

# Past abrupt climate change:

## Dansgaard–Oeschger events from the perspective of dynamical systems and uncertainty-sensitive inference

Keno Riechers, M.Sc.

Vollständiger Abdruck der von der TUM School of Engineering and Design der Technischen Universität München zur Erlangung eines

Doktors der Naturwissenschaften (Dr. rer. nat.)

genehmigten Dissertation.

Vorsitz:	Prof. Dr. techn. Roland Pail
Prüfer*innen der Dissertation:	1. Prof. Dr. rer. nat. Niklas Boers
	2. Prof. Dr. Georg Gottwald
	3. Assoc. Prof. Dr. Anna von der Heydt

Die Dissertation wurde am 12.06.2023 bei der Technischen Universität München eingereicht und durch die TUM School of Engineering and Design am 21.09.2023 angenommen.

## **Copyright**

Past abrupt climate change: Dansgaard–Oeschger events from the perspective of dynamical systems and uncertainty-sensitive inference

©2023 Keno Riechers, Technical University of Munich, Munich, Germany

# Acknowledgments

This work may be published under my name, but it has emerged from the contributions, inputs and collaborations of many people. This said I would like to thank all my co-authors for the inspiring joint work which led to the completion of five research articles. More importantly, through the numerous and intense discussions we had I gained knowledge and experience that books could never have taught me. The same holds true for the regular seminars with my colleagues that have accompanied me over the last few years. Even though we had fewer coffee room conversations — which are considered an important source of inspiration in academia — than usual due to COVID-19, my colleagues have contributed significantly to my work and my experience at the Potsdam Institute of Climate Impact Research.

I would like to express a special thanks to Leonardo for his seemingly endless patience during hours-long zoom meetings. Likewise, Georg Gottwald, Takahito Mitsui, Michael Ghil and Eirik Myrvoll-Nielsen have played a major role in creating the incredibly inspiring experience that the past few years have been for me. After all, this work would not have been possible without the great support of my supervisor Niklas Boers. Niklas provided me with considerable freedom in my work, allowing me to explore and pursue my ideas. Simultaneously, he consistently made himself available whenever I sought his guidance or input. It was, to some extent, a coincidence that led Niklas to become the supervisor of my dissertation. Today, I know how lucky I was in that regard. Furthermore, I was supported by the PIK staff in bureaucratic and organizational matters and in particular by Gabriele Pilz, Till Hollmann and Sophia Kostial.

Many factors contributed to the fact that I was able to write this dissertation in the first place. I am aware that I benefited from a number of privileges along the way. However, I want to express my gratitude to my parents for their unconditional support throughout my life, which gave me the confidence needed to pursue a doctoral degree. Furthermore, I am deeply grateful to my friends, family, and partner Johanna for their constant support, whether it was through their simple presence during times of smooth progress or their active assistance during challenging moments. A special thanks goes to Bene, Benni, Leonie, Frederic and Johanna for proofreading this thesis. Finally, I would like to thank my shared office ‘Metrogap’ for hosting me during the final phase of my PhD.



# List of publications

This cumulative dissertation is based on the following publications.

- P1 Riechers, K., Mitsui, T., Boers, N. & Ghil, M.:** Orbital insolation variations, intrinsic climate variability, and Quaternary glaciations. *Climate of the Past*, 18, 863–893. (2022)  
DOI: <https://doi.org/10.5194/cp-18-863-2022>
- P2 Riechers, K., Gottwald, G. & Boers, N.:** Glacial abrupt climate change as a multi-scale phenomenon resulting from monostable excitable dynamics. Submitted to *Journal of Climate*. (2023)  
DOI (arXiv preprint): <https://doi.org/10.48550/arXiv.2303.04063>
- P3 Riechers, K., Gorjão, L.R., Hassanibesheli, F., Witthaut, D., Lind, G.P. & Boers, N.:** Stable stadial and interstadial states of the last glacial's climate identified in a combined stable water isotope and dust record from Greenland. *Earth System Dynamics*, 14, 593–607. (2023)  
DOI: <https://doi.org/10.5194/esd-14-593-2023>
- P4 Riechers, K. & Boers, N.:** Significance of uncertain phasing between the onsets of stadial–interstadial transitions in different Greenland ice core proxies. *Climate of the Past*, 17, 1751–1775. (2021)  
DOI: <https://doi.org/10.5194/cp-17-1751-2021>
- P5 Myrvoll-Nilsen, E., Riechers, K., Rypdal, M.W. & Boers, N.:** Comprehensive uncertainty estimation of the timing of Greenland warmings in the Greenland ice core records. *Climate of the Past*, 18, 1275–1294. (2022)  
DOI: <https://doi.org/10.5194/cp-18-1275-2022>



# Summary

## Background

In view of current global warming of already 1.1°C above pre-industrial levels and the continued rise of global greenhouse gas emissions (c.f. Fig. 1.1, Jones et al., 2023b; NOAA National Centers for Environmental information, 2023), scientists warn that climate tipping points (CTPs) might be crossed in the future (Lenton et al., 2008, 2019; Armstrong McKay et al., 2022). Contrary to the widespread perception of climate change as a mostly linear process, CTPs could trigger qualitative, abrupt, and potentially irreversible changes in several components of the climate system, such as the Amazon rainforest, the Atlantic meridional overturning circulation (AMOC) or the Greenland ice sheet (GrIS) (e.g. Armstrong McKay et al., 2022; Wang et al., 2023). The destructive potential of climate tipping events — should they occur — is repeatedly emphasized in the scientific literature (e.g. Lapola et al., 2018; Lenton et al., 2019; Armstrong McKay et al., 2022). However, substantial uncertainties remain on both the critical level of warming that triggers CTPs and the impacts of potential climate tipping events.

The understanding that climatic conditions may change drastically on a relatively short time scale is based to a considerable extent on findings from paleoclimate research. Proxy data provide empirical evidence that the climate system or components thereof have undergone abrupt and qualitative state transitions in the past (e.g. Brovkin et al., 2021; Boers et al., 2022). Therefore, similar transitions cannot be excluded for the future in particular in view of the drastic human influence on the climate system. At the same time, global climate models have until recently struggled to reproduce major abrupt climatic changes of the past. This limits the confidence in their ability to reflect the underlying nonlinear dynamics and poses an important caveat to the credibility of corresponding climate projections (Valdes, 2011).

In this context, this doctoral thesis investigates past abrupt climatic changes with the aim to further the understanding of climatic tipping dynamics. If the physics of past abrupt tipping processes can be deciphered this would provide important information for the assessment and improvement of climate model performances.

This thesis investigates the so-called Dansgaard–Oeschger (DO) events, a series of abrupt warming events evident in Greenland ice core records. These events were followed by phases of milder conditions before the temperatures dropped back to their pre-event levels (Dansgaard et al., 1984; Johnsen et al., 1992a; Dansgaard et al., 1993). Mild and cold intervals, termed Greenland interstadials (GIs) and Greenland stadials (GSs), respectively, both lasted from centuries to millennia. The imprint of these millennial-scale cycles can be found in numerous proxy archives across the globe with strongest expression in the North Atlantic region (e.g. Voelker, 2002; Menviel et al., 2020, and references therein). The combined proxy evidence led to the widely shared conviction that switches between stadial and interstadial climate involved sudden changes in the strength of the AMOC, an ocean circulation

whose susceptibility to tipping is confirmed by climate model experiments (Jackson et al., 2015; Lynch-Stieglitz, 2017; Weijer et al., 2019; Jackson et al., 2023). The fact that DO events and the climate variability associated therewith are relatively well documented by paleoclimate proxy data makes them a suitable subject for the study of nonlinear and abrupt climate dynamics. Furthermore, recent findings that the AMOC might already be approaching a tipping point underline the need for a precise understanding of its vulnerability to tipping (Boers, 2021). Although the DO events occurred during glacial times, their investigation might shed further light on the AMOC's stability.

The results presented in this thesis contribute to the understanding of the last glacial's DO variability and therewith to the wider debate on CTPs. The thesis contains new methodological approaches and formulates a potential mechanism for (past) abrupt climatic shifts in terms of a conceptual climate model in P2. Recent climate simulations appear to reproduce DO variability reasonably well (Zhang et al., 2021; Kuniyoshi et al., 2022; Vettoretti et al., 2022; Malmierca-Vallet et al., 2023), but it remains to be shown that the simulations are truly governed by the same physics that drove the DO variability of the past. Both the results and the methods of this thesis can help bridge the gap between the paleoclimatic evidence and climate model simulations and facilitate an informed assessment of the corresponding climate model output.

## Scope of the dissertation

The overarching research question of this thesis is:

### Research Question

**Q1** *What has caused the last glacial's repeated abrupt climatic changes and the millennial-scale climate variability associated therewith?<sup>a</sup>*

<sup>a</sup>Notice that DO variability has been reported also for previous glacial intervals (e.g. Barker et al., 2011; Rousseau et al., 2020). However, Greenland ice core records, which are the main source of evidence for DO variability, do not extend beyond the last interglacial. This thesis is centered around the highly resolved Greenland ice core data, and therefore its conclusions primarily concern the DO variability of the last glacial. It seems likely that during previous glacial intervals, the same physical mechanism was active. However, the DO variability of previous glacial cycles is beyond the scope of this thesis.

Despite substantial efforts, to date, no conclusive theory of the emergence of DO events has been given. An unambiguous reconstruction and theoretical explanation of DO variability have so far been prevented by the scarcity of climate proxy data, their insufficient spatial coverage and temporal resolution and the associated uncertainties in quantitative and qualitative terms. First, the dating and the measurement of the climate proxies are subject to quantitative uncertainty. And second, a one-to-one correspondence between proxies and climate variables does clearly not exist and proxy data interpretation always remains subject to qualitative uncertainty. Nevertheless, the DO events are among the best-documented abrupt changes of the past.

In this context, this thesis must be understood as a part of an ongoing in-

cremental research process that continuously furthers the understanding of DO variability. The contributions of this thesis approach Q1 by exploring the two more specific questions Q2 and Q3:

#### Research Question

- Q2** *Can Dansgaard–Oeschger (DO) variability be explained in terms of a low-dimensional random and / or non-autonomous dynamical system?*
- Q3** *Can the relative phasing of abrupt climatic shifts in different Earth system components (ESCs) during Dansgaard–Oeschger events be inferred from paleoclimate proxy data?*

The following section clarifies the context of these research questions and summarizes the corresponding results obtained in the course of this work.

**Q2|Background.** Q2 is based on the notion of the climate system as a dynamical system. In paleoclimatic research, the state of spatially extended ESCs is often summarized in a few or only a single dynamical variable. This facilitates the description of climate phenomena by means of low-dimensional conceptual climate models as explained in detail in P1. For example, the state of the GrIS may be represented by its volume  $V_{\text{GrIS}}(t)$ , or the AMOC may be described in terms of meridional temperature and salinity gradients  $T(t)$  and  $S(t)$  in the North Atlantic which depend of the time  $t$ . This framework offers a versatile toolkit to explain climate variability on millennial time scale and above as discussed in P1. In particular, the following issues related to Q2 can be usefully addressed from a dynamical systems perspective: Did the climate system transition between different stable states during the last glacial? Or do Dansgaard–Oeschger cycles represent the signature of a stable limit-cycle that potentially governed past climate dynamics? If so, how can the variations of the cycle period be explained? Which physical feedbacks could explain the potentially multiple stable states? And what could be potential sources of noise, that would push the climate from one state into the other? Or similarly, what would be the drivers of the oscillation if DO variability was caused by a limit cycle? What was the effect of external influences such as orbital forcing and changing atmospheric CO<sub>2</sub> concentrations on these dynamics? Can the slow changes of the ice sheet configuration be regarded as external forcing or should they be considered as part of the DO variability? Under the umbrella of dynamical systems P1–3 target these kinds of questions from slightly different perspectives and with the use of different methods.

**Q2|Key findings.** P1 summarizes the central aspects of dynamical system theory and shortly reviews how it entered the realm of paleoclimate research. It explains how the glacial–interglacial cycles of the Pleistocene can be understood in terms of a non-autonomous dynamical system driven by orbital insolation forcing. In particular, it demonstrates how the action of external forcing on nonlinear dynamical systems may evoke variability on time scales which are neither inherent to the internal system dynamics nor to the forcing. Such a mechanism could explain the spectral mismatch between the time series of global ice volume proxies and past

orbital insolation variations. Following a similar reasoning, **P1** shows how **DO**-like cycles can emerge in a FitzHugh–Nagumo model driven by past atmospheric  $\text{CO}_2$  concentrations. The model undergoes repeated dynamic Hopf bifurcations switching on and off a self-sustained oscillation in response to variations in its external control.

**P2** develops a multi-scale climate model which combines an excitation mechanism with  $\alpha$ -stable driving noise to reproduce the joint **DO** variability of four climate variables: the **AMOC**, Greenlandic temperatures and Nordic Seas' sea ice extent and temperatures. In response to rare but strong stochastic removal of sea ice, the model system takes a prolonged state space excursion before it relaxes back to its single stable fixed point. The transient excited state and the stable state can be identified with interstadial and stadial climatic regimes from the last glacial interval. To date, the stochastic excitability paradigm has received only little attention in the study of **DO** variability and so has the role of non-Gaussian components in the climatic noise. Given the remarkable performance of the model, further investigation of these two aspects seems worthwhile. In agreement with previous research, **P2** highlights the role of sea ice in actively controlling the state of the North Atlantic climate system (e.g. [Li et al., 2005](#); [Dokken et al., 2013](#); [Li and Born, 2019](#); [Sadatzki et al., 2020](#)).

Finally, **P3** approaches the Dansgaard–Oeschger cycles from the viewpoint of random dynamical systems and stochastic differential equations. It presents a reconstruction of the deterministic drift function from a bivariate ice core record, whose components represent past Greenland temperatures and the state of the large-scale atmospheric circulation. The study identifies two stable fixed points in the reconstructed drift. This suggests that Dansgaard–Oeschger cycles were in fact repeated noise-driven transitions between two stable climate states. The fact that the bistability can be attributed to the atmospheric circulation proxy, hints at an active role of atmospheric reorganizations in stabilizing the two distinct climatic states. This view aligns well with previously reported atmospherically driven climatic transitions in the North Atlantic region observed in general circulation model (**GCM**) simulations ([Drijfhout et al., 2013](#); [Kleppin et al., 2015](#)).

Taken together **P2** and **P3** support the view that the deterministic dynamics of the glacial climate was rather not governed by a limit cycle but instead featured one stable and a second at least meta-stable state. Both studies conclude that **DO** events were noise-induced. While **P2** emphasizes the role of the North Atlantic sea ice as a receiver and propagator of the stochastic perturbations, **P3** suggests that atmospheric reorganizations have played an important role in the emergence of **DO** events. **P1** and **P2** highlight the role of changing climate background conditions in shaping **DO** cycles.

**Q3|Background.** The **DO** events manifest most prominently as repeated abrupt transitions in temperature-proxy time series from Greenland ice cores (e.g. [North Greenland Ice Core Project Members, 2004](#)). Concomitant and similarly abrupt transitions are found in other Greenland ice core proxies and even in proxy records from remote archives. These findings prove that warming events over Greenland were accompanied by pronounced and sudden changes in several components of the climate system (e.g. [Erhardt et al., 2019](#); [Corrick et al., 2020](#); [Menviel et al., 2020](#), and references therein). The question is, whether a temporal sequence

of transitions in different ESCs can be inferred, that is consistent across all DO events. This endeavor is hampered by two types of uncertainties: first, the dating uncertainty that is inherent to paleoclimate time series, and second, the uncertainty in the detection of transition onsets in noisy and often poorly resolved proxy data. P4 and P5 are both concerned with the mathematically robust incorporation of these uncertainties in the assessment of temporal leads and lags between DO transitions in different paleoclimate proxy records. In doing so, they rely on Bayesian methods.

**Q3|Key findings.** A previous study concluded that over the course of DO events, atmospheric reorganizations preceded a sudden warming of Greenland and a decline in sea ice in the North Atlantic by about a decade (Erhardt et al., 2019). This assessment relied on an uncertainty-sensitive Bayesian detection of transition onset times in corresponding proxy time series. P4 shows that under rigorous treatment of this uncertainty, the reported lag is not statistically significant, i.e. the data does not contradict the null hypothesis of synchronous transitions in the different ESCs represented by the proxies.

P5 reassesses the layer-counted age–depth model for the North Greenland Ice Core Project (NGRIP) ice core (North Greenland Ice Core Project Members, 2004; Rasmussen et al., 2006; Vinther et al., 2006; Andersen et al., 2006; Svensson et al., 2008). The high absolute dating uncertainties towards the bottom of the core hinder the comparison of the NGRIP DO event ages with their counterparts from remote archives such as speleothems from tropical monsoon regions (e.g. Corrick et al., 2020). P5 presents a new Bayesian age–depth model for the NGRIP ice core that reduces the overall dating uncertainty and provides a mathematically consistent way to generate ensembles of chronologies required for uncertainty propagation. Combining the new age–depth model with a Bayesian transition onset detection (P4), this study updates the DO event ages for the NGRIP record under full consideration of uncertainties. Given the central role of the DO events seen in the NGRIP ice core in the puzzle of leads and lags, the new Bayesian age–depth model is pivotal for Q3. However, the improvements of the new dating still remain to be leveraged in terms of a revised assessment of temporal leads and lags between DO transitions in proxy records from different archives.

## Conclusions and Outlook

The challenge of paleoclimate research is to find the best possible explanation for the existing proxy evidence. A given topic must therefore be considered from different perspectives and studied by means of complementary methodological approaches. Together, the latter shed light on different aspects of past climate phenomena. It may happen that the results obtained do not coalesce into a fully consistent narrative. In that case, further research is required to reconcile existing discrepancies. This applies also to the study of DO events.

Like numerous studies before, this thesis cannot conclusively answer Q1, but it provides important insights along the way. The key findings of this work corroborate some previous hypotheses while contradicting others. Beyond that, it places new emphasis on aspects that did not receive much attention before.

In order to put the key conclusions of this thesis into context and to discuss potential future research questions, it should first be pointed out that there is a growing number of GCM simulations that reproduce DO variability in a reasonable manner (Vettoretti and Peltier, 2018; Zhang et al., 2021; Armstrong et al., 2022; Kuniyoshi et al., 2022; Malmierca-Vallet et al., 2023). On the one hand, it remains to be shown that the mechanisms that drive DO-like variability in these simulations reflect the physics of the past real-world's DO variability. On the other hand, these simulations open up a huge playing field to explore the dynamics that give rise to abrupt AMOC changes, irrespective of whether the physics of DO variability are accurately reproduced or not. The following section picks up some of the results described above and derives further research questions from them. The latter are often related to the new availability of corresponding GCM data.

Two major lines of thought are followed in this thesis. P1-3 explore DO variability from the perspective of dynamical systems and P4-5 draw direct (Bayesian) inference on the past and in particular about the course of DO events. With regard to Q2, P1-2 corroborates the perception that the interplay of external forcing and nonlinear dynamics is central to the emergence of complex climate variability. Accordingly, DO variability was most likely shaped by the changes in the climatic background conditions that took place over the course of the last glacial. Under constant background conditions, GCMs seem to generate DO cycles of fairly stable period (Vettoretti et al., 2022). It will be interesting to see if changes in the background state in GCM experiments may give rise to a variability of DO cycles in terms of shape, amplitude and duration, which is comparable to that observed in the proxy data.

Related to that, the  $\alpha$ -stable noise postulated in P2 constitutes an additional source for the model's variability. Given that only a few studies have explicitly targeted the structure of the climate noise that characterizes Greenland ice core records (Ditlevsen, 1999), the role of noise in DO variability merits further investigation. Potential next steps could include the attempt to identify non-Gaussian noise contributions in the fluctuations of recent and upcoming proxy records by estimating Kramers–Moyal (KM) coefficients according to P3. This could be complemented by analog investigations of climate model output where temporal and data availability do not limit the applicability of the method. P3 further supports the idea, that climate noise is crucial for the emergence of DO variability. The study identifies two stable climate states and thus relies on stochastic transitions between these to explain DO cycles.

Clearly, P2 and P3 disagree on the number of stable states in the last glacial's North Atlantic climate. Remarkable modeling results reported in P2 suggest that DO variability resulted from excitations of a monostable climate system. Furthermore, P2 and P3 differ in identifying sea ice, on the one hand, and the large-scale atmospheric circulation, on the other hand, as central drivers of DO variability.

To date, the excitability paradigm proposed in P2 has received only little attention in the study of DO variability and it merits further investigation in the future. In a perfect world, the reconstruction of corresponding drift functions from proxy records according to P3 would disclose the stability of the interstadial state. However, sufficiently highly resolved and independently dated proxy records that reflect corresponding ESCs are currently not available. Once such records become available, the framework presented in P3 can be readily applied and potentially

be extended into further dimensions. Meanwhile, estimating the drift function of climate summary variables like the AMOC strength and the Nordic Seas' sea ice extent from the output of climate model experiments could be a suitable way to construct informative low-order models in the sense of Q2 from simulation data. The excitability paradigm could also be further tested in tailored GCM studies with forced sea ice removal.

P4 concludes that currently available multi-proxy records from Greenland ice cores do not allow for inferring an unambiguous temporal sequence of changes in different ESCs at DO events. With regard to Q3, the null hypothesis of synchronous changes in Greenland temperatures, the North Atlantic sea ice and the atmospheric circulation must be retained for now. Here again, the framework developed in P4 can be readily applied to new proxy data as it becomes available.

With regard to Q3, in view of methodological discrepancies in recent investigations of leads and lags between speleothem and ice core recorded DO event ages (Adolphi et al., 2018; Corrick et al., 2020), P5 prepares the stage for a corresponding reassessment of the available data. The new age–depth model for the NGRIP ice core reduces the absolute dating uncertainties and quantifies the joint dating uncertainty of all data in the record.

On a higher level, the increasing number of GCM simulations apparently showing DO cycles open up a whole new perspective for the investigation of DO variability. For example, rare-event algorithms could be used in combination with glacial climate simulations to better understand the role of noise, i.e. which parts of natural variability potentially acted as facilitators for DO events. Finally, the envisaged development of proxy-enabled climate models would certainly be another big step forward for the study of DO variability and paleoclimate research in general. Such models would allow for a direct comparison of model output with observations.



# Zusammenfassung

## Hintergrund

Angesichts der derzeitigen globalen Erwärmung um bereits 1.1°C gegenüber dem vorindustriellen Niveau und dem weiter steigenden Ausstoß von Treibhausgasen (vgl. Abb. 1.1, Jones et al., 2023b; NOAA National Centers for Environmental information, 2023) warnen Wissenschaftler\*Innen davor, dass in Zukunft Kippunkte im Klimasystem erreicht werden könnten (Lenton et al., 2008, 2019; Armstrong McKay et al., 2022). Im Gegensatz zur weit verbreiteten Wahrnehmung des Klimawandels als hauptsächlich linearen Prozess könnten Kippunkte qualitative, abrupte und potenziell irreversible Veränderungen in mehreren Komponenten des Klimasystems auslösen, wie zum Beispiel dem Amazonas-Regenwald, der Atlantischen meridionalen Umwälzzirkulation oder dem Grönländischen Eisschild (z.B. Armstrong McKay et al., 2022; Wang et al., 2023). Das zerstörerische Potenzial von Klimakippereignissen - sollten diese eintreten - wird in der wissenschaftlichen Literatur immer wieder betont (z.B. Lapola et al., 2018; Lenton et al., 2019; Armstrong McKay et al., 2022). Es bleiben jedoch erhebliche Unsicherheiten sowohl bezüglich des kritischen Maßes globaler Erwärmung, welches die Kippunkte auslösen könnte, als auch hinsichtlich der Auswirkungen potenzieller Klimakippereignisse.

Das Verständnis, dass die klimatischen Bedingungen sich auf vergleichsweise kurzen Zeitskalen drastisch ändern können, basiert zu erheblichem Anteil auf Ergebnissen der Paläoklimaforschung. Proxy-Daten liefern empirische Beweise dafür, dass das Klimasystem oder Teile davon in der Vergangenheit abrupte und qualitative Zustandsübergänge durchlaufen hat bzw. haben (z.B. Brovkin et al., 2021; Boers et al., 2022). Ähnliche Übergänge können daher für die Zukunft nicht ausgeschlossen werden, insbesondere angesichts des drastischen menschlichen Einflusses auf das Klimasystem. Gleichzeitig gelang es lange Zeit nicht, wichtige abrupte Klimaveränderungen der Vergangenheit mit globalen Klimamodellen zu reproduzieren. Diese Tatsache stellt die Fähigkeit dieser Modelle, die nichtlineare Dynamik von Kippprozessen korrekt zu simulieren, in Frage. Dies wiederum ist ein wichtiger Vorbehalt gegenüber der Aussagekraft entsprechender Klimaprojektionen (Valdes, 2011).

In diesem Zusammenhang untersucht diese Dissertation vergangene abrupte Klimaveränderungen mit dem Ziel, das Verständnis für klimatische Kippdynamiken zu erweitern. Wenn es gelingt die Physik vergangener abrupter Kippvorgänge zu entschlüsselt, so könnten daraus wichtige Informationen für die Bewertung und Verbesserung von aktuellen Klimamodellen gewonnen werden. Diese Arbeit untersucht die sogenannten Dansgaard-Oeschger (DO) Ereignisse, eine Serie von abrupten Erwärmungen, die zuerst in Eisbohrkernen aus dem Grönländischen Eisschild identifiziert wurden. Auf jedes dieser Ereignisse folgte eine Phase milderer Klimas im nordatlantischen Raum, bevor eine etwas weniger abrupte Abkühlung die ursprünglichen Bedingungen wiederherstellte (Dansgaard et al., 1984; Johnsen et al., 1992a; Dansgaard et al., 1993). Milde und kalte Intervalle werden als Grönland-Interstadiale und Grönland-Stadiale bezeichnet. Sie dauerten jeweils von

einigen hundert bis wenige tausend Jahre. Diese zyklischen Klimaveränderungen hinterließen ihre Spur in zahlreichen Proxy-Archiven auf der ganzen Welt, wobei das Signal in den Daten aus der nordatlantischen Region am stärksten ausgeprägt ist (z.B. [Voelker, 2002](#); [Menviel et al., 2020](#), und darin enthaltene Referenzen).

Das Gesamtbild, welches sich aus den Proxy Daten ergibt, spricht dafür, dass die Wechsel zwischen stadialen und interstadialen Klimabedingungen mit plötzlichen Änderungen der Stärke der Atlantischen Umwälzzirkulation einher gingen ([Lynch-Stieglitz, 2017](#)). Die Fähigkeit dieser Ozeanzirkulation zu abrupten Zustandsänderungen ist durch Klimamodelle weitestgehend bestätigt ([Jackson et al., 2015](#); [Weijer et al., 2019](#); [Jackson et al., 2023](#)). Die Tatsache, dass DO-Ereignisse und die damit verbundene Klimavariabilität relativ gut durch paleoklimatische Proxy-Daten dokumentiert sind, macht sie zu einem geeigneten Gegenstand für die Untersuchung nichtlinearer und abrupter Klimadynamik. Jüngste Forschungsergebnisse zeigen, dass die Atlantische Umwälzzirkulation bereits einen Kipppunkt zustrebt, und unterstreichen daher die Notwendigkeit eines genauen Verständnisses ihrer Anfälligkeit für Kippereignisse ([Boers, 2021](#)). Obwohl sich die DO-Ereignisse während der Eiszeit ereigneten, könnte ihre Untersuchung weitere Erkenntnisse über die Stabilität der Umwälzzirkulation liefern.

Ergebnisse dieser Arbeit tragen zum Verständnis der DO-Variabilität der letzten Eiszeit und damit zur breiteren Debatte über klimatische Kipppunkte bei. Die Arbeit enthält neue methodische Ansätze und formuliert einen möglichen Mechanismus für (vergangene) abrupte Klimaveränderungen in Form eines konzeptionellen Klimamodells (P2). Aktuelle Klimasimulationen konnten zuletzt DO-Variabilität erfolgreich reproduzieren ([Zhang et al., 2021](#); [Kuniyoshi et al., 2022](#); [Vettoretti et al., 2022](#); [Malmierca-Vallet et al., 2023](#)). Es ist jedoch nicht von vornherein offensichtlich, dass der verantwortliche physikalische Mechanismus der Modelle mit dem tatsächlichen Mechanismus der DO Variabilität übereinstimmt. Sowohl die Ergebnisse als auch die Methoden dieser Arbeit können dazu beitragen, die Simulationsergebnisse mit den paleoklimatischen Proxy-Daten abzugleichen und eine fundierte Bewertung der entsprechenden Klimamodelle vorzunehmen.

## Umfang der Dissertation

Die übergreifende Forschungsfrage dieser Arbeit lautet wie folgt:

### Forschungsfrage

**Q1** *Was hat zu den wiederholten abrupten klimatischen Veränderungen der letzten Eiszeit und der damit verbundenen Klimavariabilität auf der Skala von Jahrtausenden geführt?<sup>a</sup>*

<sup>a</sup>Es ist wahrscheinlich, dass DO-Variabilität auch frühere Glaziale geprägt hat (z.B. [Barker et al., 2011](#); [Rousseau et al., 2020](#)). Allerdings reichen die Datensätze grönländischer Eisbohrkerne, welche die wichtigste empirische Evidenz für DO-Variabilität darstellen, nicht über das letzte Interglazial hinaus. Diese Arbeit konzentriert sich auf die Auswertung ebendieser hochaufgelösten Daten. Von daher gelten entsprechende Resultate in erster Linie für die DO-Variabilität der letzten Eiszeit, auch wenn es plausibel erscheint, dass während früherer Glaziale der gleiche physikalische Mechanismus aktiv war. Eine genauere Untersuchung der DO-Variabilität vorheriger Glaziale geht jedoch über den Rahmen dieser Arbeit hinaus.

Trotz intensiver Forschung besteht bisher keine allgemein akzeptierte abschließende Theorie zur Entstehung von DO-Ereignissen vor. Eine eindeutige Rekonstruktion und theoretische Erklärung der DO-Variabilität scheitert an der Knappheit von Klimaproxy-Daten, ihrer unzureichenden räumlichen Abdeckung und zeitlichen Auflösung sowie der mit den Daten verbundenen Unsicherheiten in quantitativer und qualitativer Hinsicht. Sowohl die Messung als auch die Datierung von Klimaproxys unterliegt quantitativen Unsicherheiten. Ferner existiert keine direkte Entsprechung zwischen Proxys und Klimavariablen. Die Interpretation von Proxy-Daten birgt daher stets qualitative Unsicherheiten. Dennoch gehören die DO-Ereignisse zu den am besten dokumentierten abrupten Klimaveränderungen der Vergangenheit.

Diese Arbeit muss als Teil eines fortlaufenden und inkrementellen Forschungsprozesses verstanden werden, der das Verständnis der DO-Variabilität kontinuierlich erweitert. Ihre Beiträge adressieren **Q1** durch Untersuchung der beiden spezifischeren Fragen **Q2** und **Q3**.

#### Forschungsfrage

**Q2** *Kann Dansgaard-Oeschger-Variabilität mit Hilfe eines niedrig-dimensionalen stochastischen und / oder nicht-autonomen dynamischen Systems erklärt werden?*

**Q3** *Kann die zeitliche Abfolge abrupter Veränderungen in verschiedenen Komponenten des Klimasystems im Zusammenhang von Dansgaard-Oeschger-Ereignissen aus paläoklimatischen Proxy-Daten abgeleitet werden?*

Der folgende Abschnitt erläutert den Kontext dieser Forschungsfragen und fasst die entsprechenden Ergebnisse zusammen, die im Laufe dieser Arbeit erzielt wurden.

**Q2|Hintergrund.** **Q2** basiert auf der Konzeption des Klimasystems als dynamisches System. In der paläoklimatischen Forschung wird der Zustand räumlich ausgedehnter Erdsystemkomponenten oft in einer oder in wenigen dynamischen Variablen zusammengefasst. Dies ermöglicht die Beschreibung von Klimaphänomenen durch niedrig-dimensionale konzeptionelle Klimamodelle, wie in **P1** detailliert erläutert wird. Zum Beispiel kann der Zustand des Grönländischen Eisschildes durch sein Volumen  $V(t)$  ausgedrückt werden. Analog dazu, lässt sich der Zustand der Atlantischen Umwälzzirkulation durch meridionale Gradienten der Temperatur  $T(t)$  und des Salzgehaltes  $S(t)$  im Nordatlantik beschreiben, die von der Zeit  $t$  abhängen. Dieser theoretische Rahmen bietet ein mathematisches Werkzeug zur Erklärung von Klimavariabilität auf paläoklimatischen Zeitskalen (**P1**). Insbesondere lassen sich folgende oder ähnliche Fragen im Zusammenhang mit **Q2** sinnvoll aus der Perspektive dynamischer Systeme erörtern: Ist das nordatlantische Klimasystem während des letzten Glazials zwischen verschiedenen stabilen Zuständen hin und her gewechselt? Oder stellen Dansgaard-Oeschger-Zyklen die Signatur eines stabilen Grenzyklus dar, der möglicherweise die vergangene Klimadynamik bestimmte? Wenn ja, wie können die Variationen der Zyklusdauer erklärt werden? Welche physikalischen Rückkopplungen könnten die möglicherweise multiplen stabilen Zustände erklären? Und was sind potenzielle Quellen von Rauschen,

welches Übergänge des Klimas von einem Zustand in den anderen Erklären könnte? Was wären die Ursachen einer möglichen oszillatorischen Klimadynamik? Welche Auswirkungen hatten externe Einflüsse wie Veränderungen der orbitalen Sonneneinstrahlung und oder sich ändernde atmosphärische CO<sub>2</sub>-Konzentrationen? Können langsame Veränderungen der Eisschilde als externe Einflüsse betrachtet werden oder sollten sie als Teil der DO-Variabilität betrachtet werden? **P1–3** untersuchen ebensolche Fragen aus der Perspektive dynamischer Systeme, wobei sie jeweils unterschiedliche unterschiedliche Ansätze und Methoden verfolgen.

**Q2|Ergebnisse.** **P1** fasst die zentralen Aspekte der Theorie dynamischer Systeme zusammen und beschreibt, wie diese Einzug den Bereich der Paläoklimaforschung erhielt. Die Publikation erklärt, wie die Glazial-Interglazial-Zyklen des Pleistozäns im Sinne eines nicht-autonomen dynamischen Systems verstanden werden können, das durch orbitale Veränderungen in der Sonneneinstrahlung angetrieben wird. Insbesondere zeigt **P1**, wie die Wirkung externer Einflüsse auf nichtlineare dynamische Systeme Variabilität auf Zeitskalen hervorrufen kann, die weder der internen Systemdynamik noch der externen Antriebskraft inhärent sind. Ein solcher Mechanismus könnte die Diskrepanz zwischen den Spektra von Proxy-Zeitreihen, welche den Glazial-Interglazial-Zyklus abbilden, einerseits und Zeitreihen orbitaler Veränderungen andererseits erklären. Ferner zeigt **P1**, wie DO-ähnliche Zyklen mit einem FitzHugh-Nagumo-Modell erzeugt werden können. Wird das Modell durch vergangene atmosphärische CO<sub>2</sub>-Konzentrationen getrieben lassen sich die Oszillationen in zeitliche Übereinstimmung mit Phasen starker DO-Aktivität bringen. Dabei durchläuft das Modell wiederholten dynamischen Hopf-Bifurkationen, wodurch abwechselnd ein stabiler Grenzzyklus oder ein stabiler Fixpunkt die Systemdynamik bestimmt. **P2** kombiniert einen Anregungsmechanismus mit  $\alpha$ -stabilem Rauschen in einem mehrskaligen Modells des nordatlantischen Klimasystems. Dieses Modell erklärt die gemeinsame DO-Variabilität der Atlantischen Umwälzzirkulation, der Grönländischen Lufttemperatur sowie der Meereis-Ausdehnung und den Temperaturen im Europäischen Nordmeer. Stochastisch getriebene starke Rückgänge des Meereises können das Modellsystem von einem stabilen stadialen Zustand in einen meta-stabilen interstadialen Zustand anregen. Ausgehend von diesem relaxiert das Modellsystem über einen ausgedehnten Pfad durch den Zustandsraum zurück zum stadialen Klima. Bisher wurde stochastisch anregbaren dynamischen Systemen in der Untersuchung von DO-Variabilität wenig Aufmerksamkeit zuteil. Gleiches gilt für nicht-Gauß'sche Anteile im Rauschen. Angesichts der bemerkenswerten Simulationsergebnisse die diese Modell liefert, scheint eine weitere Untersuchung beider Aspekte lohnenswert. In Übereinstimmung mit früheren Forschungsergebnissen betont **P2** die Rolle des Meereises für den Zustand des nordatlantischen Klimasystems (z.B. [Li et al., 2005](#); [Dokken et al., 2013](#); [Li and Born, 2019](#); [Sadatzki et al., 2020](#)).

**P3** betrachtet die Dansgaard-Oeschger-Zyklen aus der Perspektive stochastischer dynamischer Systeme. Ausgehend von einer bivariaten Zeitreihe aus einem grönländischen Eisbohrkern präsentiert die Studie eine Rekonstruktion der deterministischen entsprechenden Driftfunktion. Die Komponenten dieser Zeitreihe repräsentieren vergangene Temperaturen in Grönland und den Zustand der großräumigen atmosphärischen Zirkulation. Es lassen sich zwei stabile Fixpunkte in der rekonstruierten Drift identifizieren. Dies legt nahe, dass die Dansgaard-Oeschger-Zyklen tat-

sächlich wiederholte, durch Rauschen ausgelöste Übergänge zwischen zwei stabilen Klimazuständen waren. Diese Bistabilität kann eindeutig dem atmosphärischen Proxy zugeschrieben werden, was auf eine aktive Rolle der Atmosphärendynamik bei der Stabilisierung der beiden verschiedenen Klimazustände hindeutet. In Simulationen mit globalen Zirkulationsmodellen wurden DO-ähnliche klimatische Übergang in der Nordatlantik-Region beobachtet, welche von atmosphärischen Anomalien getrieben wurden (Drijfhout et al., 2013; Kleppin et al., 2015). Die in P3 erzielten Ergebnisse sind konsistent mit diesen atmosphärisch getriebenen Übergängen.

Zusammenfassend lässt sich sagen, dass P2 und P3 der Annahme entgegen stehen, dass die deterministische Dynamik des letzten Glazials durch einen stabilen Grenzyklus bestimmt wurde. Vielmehr scheint es, dass diese Dynamik von einem stabilen und einem zweiten mindestens meta-stabilen Zustand geprägt war. Beide Studien kommen zu dem Schluss, dass DO-Ereignisse durch stochastische Effekte verursacht wurden. Während P2 die Rolle des Meereises im Nordatlantik als Empfänger und Überträger der stochastischen Störungen betont, legt P3 nahe, dass atmosphärische Reorganisationen eine wichtige Rolle bei der Entstehung von DO-Ereignissen gespielt haben könnten. P1 und P2 betonen den Einfluss sich verändernder klimatischer Hintergrundbedingungen auf die Ausprägung der DO-Zyklen.

**Q3|Hintergrund.** Der deutlichste und prominenteste Nachweis für DO-Ereignisse sind die wiederholten abrupte Übergänge in Zeitreihen von Temperatur-Proxies aus grönländischen Eisbohrkernen (z.B. [North Greenland Ice Core Project Members, 2004](#)). Gleichzeitig treten ähnlich abrupte Übergänge in weiteren Proxy-Zeitreihen aus Grönland und sogar aus entfernten Archiven auf. Diese Befunde zeigen, dass die Erwärmungen über Grönland von deutlichen und plötzlichen Veränderungen mehrerer Komponenten des Klimasystems begleitet wurden (z.B. [Erhardt et al., 2019](#); [Corrick et al., 2020](#); [Menviel et al., 2020](#), und darin enthaltene Referenzen). Es stellt sich die Frage, ob eine zeitliche Abfolge von Veränderungen in den betroffenen Komponenten des Klimasystems abgeleitet werden kann, die über alle DO-Ereignisse hinweg konsistent ist. Dieses Vorhaben wird durch zwei Arten von Unsicherheiten erschwert: Erstens ist die Datierung paläoklimatischer Proxy-Daten stets mit Unsicherheit verbunden und zweitens besteht eine Unsicherheit bei der Detektion von Übergängen in verrauschten und oft zeitlich niedrig aufgelösten Proxy-Daten. P4 und P5 befassen sich beide mit der Frage, wie diese Unsicherheiten mathematisch konsistent in der Bewertung der zeitlichen Abfolge von DO-Übergängen in verschiedenen paläoklimatischen Proxy-Datensätzen berücksichtigt werden kann und stützen sich dabei auf Bayessche Methoden.

**Q3|Ergebnisse.** Eine frühere Studie kam zu dem Schluss, dass im Verlauf von DO-Ereignissen atmosphärische Reorganisationen einer plötzlichen Erwärmung in Grönland und einem Rückgang des Meereises im Nordatlantik um etwa ein Jahrzehnt vorausgingen ([Erhardt et al., 2019](#)). Dieses Ergebnis beruht auf einer unsicherheits-sensiblen Bayesschen Methode zur Detektion von Übergängen, oder genauer deren Startzeitpunkt, in entsprechenden Proxy-Zeitreihen. P4 zeigt, dass unter strenger Berücksichtigung dieser Unsicherheiten der Zeitversatz zwischen den Übergängen in den unterschiedlichen Proxy-Zeitreihen statistisch nicht sig-

nifikant ist. D.h. der Nullhypothese synchroner Übergänge in den durch die Proxy-repräsentierten Komponenten des Klimasystems, kann auf Basis der vorliegenden Daten nicht widersprochen werden.

P5 befasst sich mit dem Alters-Tiefen-Modell für des NGRIP-Eisbohrkerns (North Greenland Ice Core Project) (North Greenland Ice Core Project Members, 2004; Rasmussen et al., 2006; Vinther et al., 2006; Andersen et al., 2006; Svensson et al., 2008). Die hohen absoluten Datierungsunsicherheiten im älteren Teil des Kerns erschweren den Vergleich des Alters von DO-Ereignissen die in den Daten des NGRIP Bohrkerens beobachtet werden mit ihren entsprechenden Übergängen in Daten aus geografisch entfernten Archiven wie Tropfsteinen aus tropischen Monsunregionen (Corrick et al., 2020). P5 präsentiert ein neues Bayessches Alters-Tiefen-Modell für den NGRIP-Eisbohrkern, das einerseits die absoluten Unsicherheiten reduziert und andererseits eine mathematisch konsistenten Methode zur Berücksichtigung dieser Unsicherheiten in etwaigen Analysen der Daten bietet. Die Studie aktualisiert die Alter der DO-Ereignisse für den NGRIP-Datensatz unter vollständiger Berücksichtigung der Unsicherheiten. Dies gelingt durch die Kombination des neuen Alters-Tiefen-Modells mit einer Bayesschen Methode zur Charakterisierung von Übergängen (P4). Angesichts der zentralen Bedeutung der DO-Ereignisse aus dem NGRIP-Bohrkern hinsichtlich der Erforschung der zeitlichen Abfolge von entsprechenden klimatischen Veränderungen weltweit, ist das neue Bayessche Alters-Tiefen-Modell für ein wichtiger Beitrag zur Beantwortung von Q3. Die neuen Möglichkeiten, die dieses Modell bietet müssen jedoch noch voll ausgeschöpft werden.

## Schlussfolgerungen und Ausblick

Ein wichtiger Teil paläoklimatischer Forschung besteht darin, die bestmögliche Erklärung für die vorhandenen Proxy-Daten zu finden. Dazu müssen paleoklimatische Phänomene aus verschiedenen Perspektiven betrachtet und mit Hilfe von komplementären methodischen Ansätzen untersucht werden. Es kann vorkommen, dass die erzielten Ergebnisse kein konsistentes Bild ergeben und sich gegebenenfalls sogar widersprechen. In diesem Fall sind weitere Untersuchungen erforderlich, um vorhandene Diskrepanzen auszuräumen. Dies ist aktuell der Fall bei der Erforschung von DO-Ereignissen und gilt im speziellen auch für die Ergebnisse dieser Arbeit. Wie zahlreiche Studien zuvor kann diese Arbeit die Frage Q1 nicht abschließend beantworten. Sie liefert jedoch wichtige Erkenntnisse auf dem Weg dorthin. Die Ergebnisse dieser Arbeit bestärken einige der bestehenden Hypothesen, widersprechen jedoch anderen. Darüber hinaus beleuchtet diese Arbeit Aspekte, die zuvor wenig Beachtung fanden.

Um wichtigsten Erkenntnisse dieser Arbeit zu diskutieren und einzuordnen sei darauf hingewiesen, dass die Anzahl vermeintlicher Reproduktionen der DO-Variabilität mit Hilfe von komplexen Klimamodellen Verlauf der letzten Jahre stark zugenommen hat (Vettoretti and Peltier, 2018; Zhang et al., 2021; Armstrong et al., 2022; Kuniyoshi et al., 2022; Malmierca-Vallet et al., 2023). Einerseits bleibt noch zu zeigen, ob die Mechanismen die diesen Simulationen zugrunde liegen, der tatsächlichen Physik der DO-Variabilität der Vergangenheit entsprechen. Andererseits eröffnen diese Simulationen ein neue Möglichkeiten, um die Dynamik abrupter

Veränderungen insbesondere der Atlantischen Umwälzströmung zu erforschen. Dies ist schlussendlich unabhängig davon, ob die Physik der DO-Variabilität korrekt wiedergegeben wird oder nicht. Der folgende Abschnitt greift einige der oben beschriebenen Ergebnisse auf und leitet weitere Forschungsfragen daraus ab. Diese stehen oft im Zusammenhang mit der neuen Verfügbarkeit entsprechender Simulationen verbunden.

Diese Arbeit verfolgt zwei Hauptgedankenstränge. **P1-3** untersuchen DO-Variabilität aus der Perspektive dynamischer Systeme, während **P4-5** direkte (Bayessche) Rückschlüsse über den Verlauf von der DO-Ereignisse aus paleoklimatischen Proxy-Daten ziehen. Hinsichtlich **Q2** bestätigen **P1-2**, dass das Zusammenspiel von externen Einflüssen und nichtlinearer Dynamik zentral für das Auftreten komplexer Variabilität ist. Demnach wurde die DO-Variabilität höchstwahrscheinlich durch Veränderungen der klimatischen Hintergrundbedingungen geprägt. Unter konstanten Hintergrundbedingungen scheinen die oben erwähnten Klimamodelle DO-Zyklen mit relativ stabiler Periode zu simulieren (Vettoretti et al., 2022). Eine zentrale Frage wird sein, ob Veränderungen des Hintergrundklimas in den Simulationen die DO-Zyklen hinsichtlich Form, Amplitude und Dauer auf eine Art beeinflussen können, die mit den in den Proxy-Daten Variabilität der Zyklen vergleichbar ist. Das  $\alpha$ -stabile Rauschen, welches in **P2** als Auslöser von DO-Ereignissen dient, ist darüber hinaus eine zusätzliche Quelle für die Variabilität des Modells dar. Da bisher nur wenige Studien explizit die Struktur des Rauschen in den Daten aus grönländischen Eisbohrkernen untersucht haben (Ditlevsen, 1999), sollte die Rolle stochastischer Einflüsse auf die Variabilität von DO-Zyklen weiter untersucht werden. Mögliche nächste Schritte könnten darin bestehen, nicht-Gaußsche Rauschanteile in aktuellen und wie auch in zukünftigen Proxy-Daten durch Schätzung von Kramers-Moyal Koeffizienten gemäß **P3** zu identifizieren. Dies könnte durch analoge Untersuchungen von Simulationsdaten ergänzt werden, bei denen zeitliche Auflösung und Datenverfügbarkeit die Anwendung der Methode nicht behindern. **P3** unterstützt ebenfalls die These, dass das Auftreten der von DO-Ereignissen rauschinduziert ist. Die Studie identifiziert zwei stabile Klimazustände und beruft sich somit auf stochastische Übergänge zwischen diesen, um die DO-Zyklen zu erklären.

**P2** und **P3** widersprechen sich jedoch hinsichtlich der Anzahl der stabilen Zustände im nordatlantischen Klima des letzten Glazials. Die bemerkenswerten Ergebnisse, die mit dem in **P2** entwickelten Modell erzielt werden konnten, legen nahe, dass die DO-Variabilität als Anregungen eines mono-stabilen Klimasystems zu verstehen ist. Darüber hinaus unterscheiden sich **P2** und **P3** darin, dass sie Meereis einerseits und die großräumige atmosphärische Zirkulation andererseits als zentralen Akteur der DO-Variabilität identifizieren.

Die in **P2** formulierte These, dass DO-Zyklen durch Anregungen eines metastabilen Zustandes entstanden hat bisher nur wenig Aufmerksamkeit erfahren und sollte daher eingehender untersucht werden. Idealerweise könnten Rekonstruktionen entsprechender Driftfunktionen aus Proxy-Aufzeichnungen gemäß **P3** die Stabilität des interstadialen Zustands klären. Allerdings sind derzeit keine ausreichend hochaufgelösten und unabhängig datierten Proxy-Aufzeichnungen verfügbar, die die beteiligten Komponenten des Klimasystems repräsentieren. Sobald solche Aufzeichnungen verfügbar sind, kann die in **P3** angewandte Methode direkt darauf übertragen und möglicherweise in weitere Dimensionen erweitert wer-

den. Die Schätzung von Driftfunktion von Klimavariablen wie z.B. der Stärke der Atlantischen Umwälzströmung und der Ausdehnung des Meereises im Nordatlantik anhand von neuen Simulationsdaten stellt ebenfalls einen vielversprechenden Ansatz dar. So könnten informative Klimamodelle niedriger Dimension aus den komplexen Modellen destilliert werden. Ferner könnte die These, dass Interstadiale als rauschinduzierte Anregungen verstanden werden müssen, auch in maßgeschneiderten Experimenten mit komplexen Klimamodellen weiter erforscht werden, indem zum Beispiel das stadiale Meereis manuell entfernt und die Relaxation des System analysiert wird.

# Contents

<b>Acknowledgments</b>	<b>iii</b>
<b>List of publications</b>	<b>v</b>
<b>Summary</b>	<b>vii</b>
<b>Zusammenfassung</b>	<b>xv</b>
<b>1 Introduction</b>	<b>1</b>
1.1 Climate tipping points and why they matter . . . . .	1
1.2 The study of climate tipping points . . . . .	4
1.3 Outline of the thesis . . . . .	8
<b>2 A formalization of tipping points</b>	<b>11</b>
2.1 Phenomenology . . . . .	11
2.2 Mathematical description . . . . .	12
<b>3 The Stommel box model</b>	<b>19</b>
<b>4 Past abrupt climate change: the Dansgaard–Oeschger events</b>	<b>25</b>
4.1 The proxy evidence . . . . .	26
4.2 The dynamical systems view . . . . .	30
4.3 Uncertainty-sensitive inference . . . . .	34
<b>5 DO events from the perspective of dynamical systems</b>	<b>37</b>
P1 Orbital insolation variations, intrinsic climate variability, and Quaternary glaciations . . . . .	37
P2 Glacial abrupt climate change as a multi-scale phenomenon resulting from monostable excitable dynamics . . . . .	69
P3 Stable stadial and interstadial states of the last glacial’s climate identified in a combined stable water isotope and dust record from Greenland . . . . .	91
<b>6 Uncertainty-sensitive inference on the course of DO events</b>	<b>107</b>
P4 Significance of uncertain phasing between the onsets of stadial–interstadial transitions in different Greenland ice core proxies . . . . .	107
P5 Comprehensive uncertainty estimation of the timing of Greenland warmings in the Greenland ice core records . . . . .	133
<b>7 Synthesis</b>	<b>155</b>
7.1 Discussion . . . . .	155

P1–3	DO variability from the perspective of dynamical systems . . .	157
P4–5	Uncertainty-sensitive inference on the course of DO events . . .	167
7.2	Conclusions and outlook . . . . .	174
<b>List of Figures</b>		<b>181</b>
<b>List of Tables</b>		<b>181</b>
<b>Bibliography</b>		<b>183</b>

# 1 Introduction

## 1.1 Climate tipping points and why they matter

Climate tipping points (CTPs) have made headlines in mainstream media recently (e.g. Kaplan, 2021; Briggs, 2022; Carrington, 2022; Habekuß, 2022). In view of current global warming of already 1.1°C above pre-industrial levels and the continued rise of global greenhouse gas emissions (c.f. Fig. 1.1, Jones et al., 2023b; NOAA National Centers for Environmental information, 2023), Scientists warn that several Earth system components (ESCs) might undergo drastic, qualitative change if global warming exceeds certain critical thresholds (e.g. Lenton et al., 2008, 2019; Armstrong McKay et al., 2022; Boers et al., 2022; Kemp et al., 2022; Wang et al., 2023). For example, the Amazon Rainforest could turn into a savanna (Cox et al., 2004; Nobre and Borma, 2009), the Atlantic meridional overturning circulation (AMOC) — an important ocean circulation that comprises the Gulf Stream (c.f. Fig. 1.3) — could lose substantial momentum or even come to a halt (Manabe and Stouffer, 1993; Stocker and Schmittner, 1997; Liu et al., 2017; Lohmann and Ditlevsen, 2021) and the Greenland ice sheet (GrIS) could collapse partially or completely (Robinson et al., 2012; Bochow et al., 2023). Such qualitative changes in the climate system that occur in response to an incremental change in the level of global warming are referred to as *climate tipping events* or simply *climate tipplings*. The critical temperature threshold beyond which tipping becomes inevitable constitutes the corresponding CTP.<sup>1</sup> A climate tipping is commonly associated with a certain sense of abruptness and irreversibility. That is, the change of state unfolds at untypically high rates of change and restoring the pre-tipping level of warming levels does not revert the tipping itself. Consider, for example, a tipping scenario for the AMOC. The overturning could weaken by approximately 50–90% within decades and thus at an average rate that exceeds the natural rate of change on comparable time scales by far (Jackson and Wood, 2018; Jackson et al., 2023). Furthermore, once tipped, even if global temperatures returned below the AMOC-specific critical threshold again, the AMOC would probably reside in the tipped state of weak overturning (e.g. Jackson et al., 2023). Only further cooling below a second critical threshold would bring the AMOC back into its strong overturning state. This phenomenon is known as hysteresis and is illustrated in Fig. 2.2. Further prominent examples for so-called climate tipping elements (CTEs) — ESCs believed to be prone to tipping — are given by the West Antarctic ice sheet (WAIS), low latitude coral reefs and boreal forests among others (compare Fig. 1.2 and see Lenton et al., 2008; Armstrong McKay et al., 2022; Wang et al., 2023).

The possible impacts of (multiple) tipping events are the subject of highly topical research. While many details remain elusive it must be stated that tipping of one or more large-scale components of the Earth system bears tremendous

---

<sup>1</sup>Notice that there is some inconsistency in the use of the term *climate tipping point* in the media as well as in the scientific literature. A more precise definition will be given in Sect. 2.2.

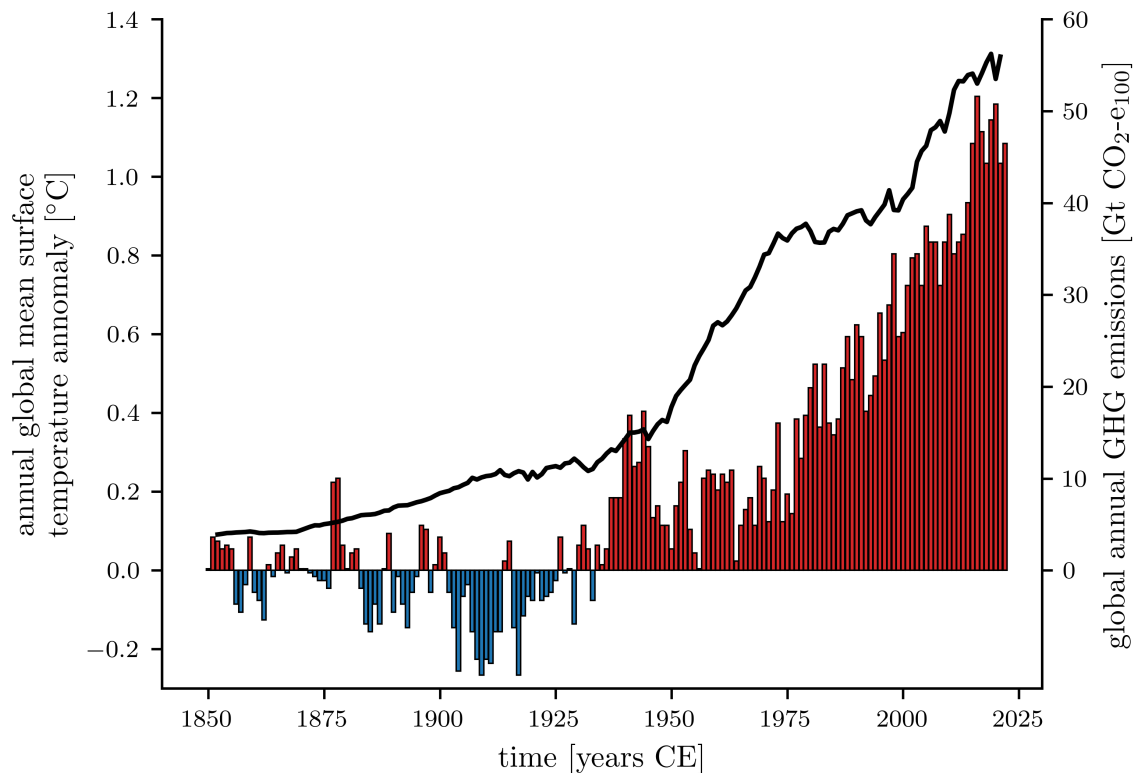


Figure 1.1: Global warming and greenhouse gas emission. Blue and red bars show the global annual-mean surface temperature anomalies with respect to the reference period 1850–1900 (NOAA National Centers for Environmental information, 2023); originally the reference period is 1901–2000. The black line shows the cumulative global emissions of the three dominant greenhouse gases (GHGs), namely  $\text{CO}_2$ ,  $\text{CH}_4$  and  $\text{N}_2\text{O}$ , including emissions from land use, land use change and forestry (LULUCF) (Jones et al., 2023b). The total emissions are specified in gigatons of  $\text{CO}_2$  equivalent emissions over a 100-year time horizon. This means that emissions of  $\text{CH}_4$  and  $\text{N}_2\text{O}$  are converted into a corresponding amount of  $\text{CO}_2$  emissions which has the same global warming potential over a time span of 100 years (Jones et al., 2023b). The data is directly available from Jones et al. (2023a).

destructive potential for societies and for other parts of the Earth system itself (Steffen et al., 2018; Lenton et al., 2019; Kemp et al., 2022). This includes at worst the risk of a tipping cascade wherein the tipping of one CTE triggers the tipping of the next (Wunderling et al., 2021). The consequences of versatile climate tipping scenarios cannot be discussed here in detail. For an overview see please see Wang et al. (2023).

To make the term climate tipping point (CTP) more tangible in terms of both mechanisms and impacts, the example of an AMOC tipping shall be sketched in the following. In rough terms, the AMOC is comprised of a near-surface northward flow and a return flow at intermediate depth in the Atlantic (e.g. Buckley and Marshall, 2016). On their way northward southern-sourced warm and salty surface waters release heat to the atmosphere and become denser. The effective northward heat transport governs the mild European climate. At high latitudes, the water masses eventually sink and travel back southward in the form of very dense North Atlantic deep water (NADW) balancing the northward surface mass transport. Upwelling of NADW in the Southern Ocean closes the circulation (Marshall and

Speer, 2012). The overturning motion is driven by a combination of prevailing winds and density gradients in the ocean. Among other drivers, the meridional density gradient is sustained by the *AMOC itself*. This self-sustainability is referred to as the salt–advection feedback and explains why the *AMOC* is prone to tipping (e.g. Weijer et al., 2019): an initial weakening of the *AMOC* would entail reduced northward salt transport and thus less efficient deep water formation, which in turn would lead to further *AMOC* weakening. This self-amplifying process could be triggered by enhanced freshwater influx into the regions of deep water formation sourced from either changes in precipitation patterns or from accelerated melting of the *GrIS* that occur in response to global warming *GrIS* (e.g. Wang et al., 2023).

The reduced northward oceanic heat transport associated with an *AMOC* collapse would entail local cooling over the Nordic Seas of up to 15°C and around 5°C on a wider regional scale over the northern North Atlantic (Jackson et al., 2015). Consequently, the climate in Europe would generally be colder and drier, with severe negative impacts on vegetation and agriculture (Jackson et al., 2015). Moreover, the atmosphere would respond to the altered oceanic heat transport in terms of substantial global-scale reorganizations and in particular a southward migration of the intertropical Convergence Zone (*ITCZ*) (Orihuela-Pinto et al., 2022; Wang et al., 2023). In turn, predicted impacts include the predominance of *la Niña*-like conditions in the tropical Pacific, substantially altered rainfall patterns in the tropical monsoon regions and potential reductions in rainfall in the Sahel region (Jackson et al., 2015; Orihuela-Pinto et al., 2022; Wang et al., 2023). Based on the assessment of so-called early warning signals (Dakos et al., 2008; Lenton, 2011), a recent study suggests that the *AMOC* might already approach its tipping point (Boers, 2021). As opposed to many other *CTE*, a tipping of the *AMOC* would most likely have a negative impact on global mean surface temperatures and potentially stabilize other *CTEs* such as the Amazon rainforest and the *GrIS* (Wunderling et al., 2021; Armstrong McKay et al., 2022; Nian et al., 2023).

For further illustration of the concept of *CTPs* the case of the Amazon rainforest is briefly discussed here as a second example. The stability of the forest crucially relies on atmosphere–vegetation feedbacks wherein large fractions of the precipitation originally sourced from the Atlantic Ocean are recycled (Salati et al., 1979; Zemp et al., 2014, 2017). Forest dieback may thus reduce water availability for the remaining forest and consequently induce further dieback. In short, this self-amplifying effect is what renders the Amazon rainforest susceptible to tipping from a forest to a savanna state in response to climate change induced water scarcity. Human activity may additionally reduce the forest’s resilience and potentially act as a trigger of forest dieback itself (Boers et al., 2017; Boulton et al., 2022) with devastating consequences: Already a (partial) tipping of the Amazon rainforest would transform the forest from an important terrestrial carbon sink into a source (Gatti et al., 2021) and estimated cumulative emissions from (partial) forest dieback of (30) 75 Gt of carbon might translate into additional (0.1°C) 0.2°C of global warming (Armstrong McKay et al., 2022). At the regional level, overall livelihoods, food security, hydropower generation and public health would suffer from an Amazon dieback among others (Lapola et al., 2018), not to mention the tremendous loss of biodiversity that an Amazon tipping would entail. Some studies highlight potential teleconnections between the Amazon and

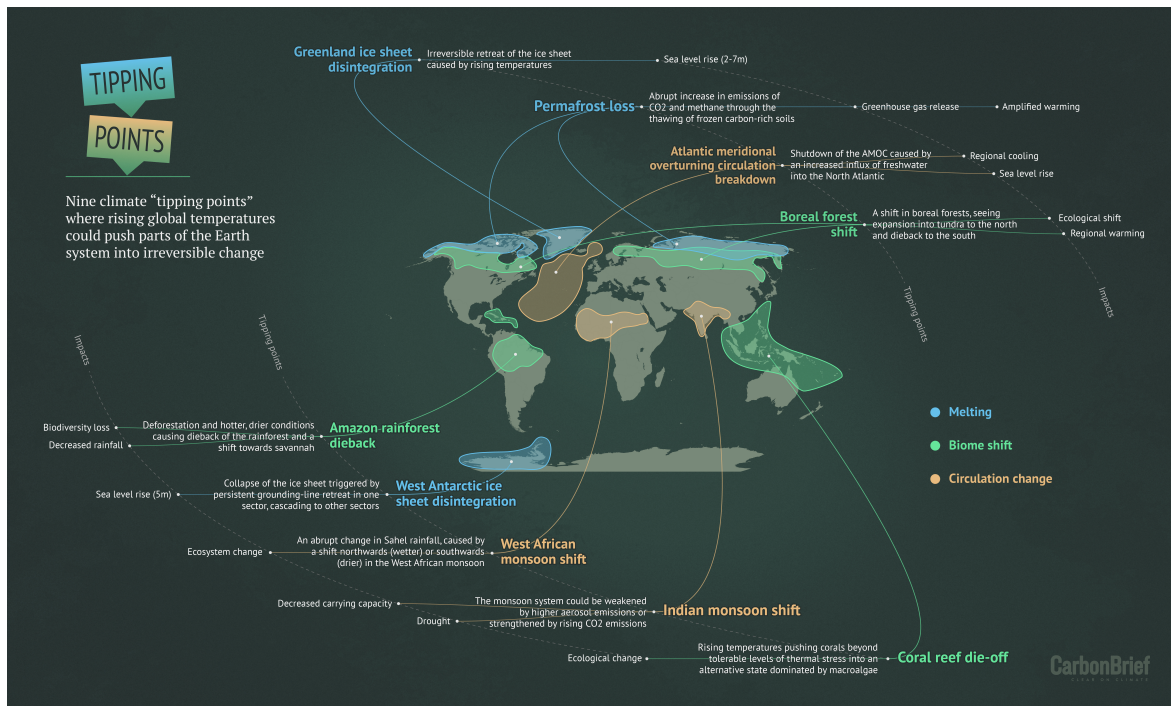


Figure 1.2: Map of important CTEs. With permission from [McSweeney \(2020\)](#). Similar illustrations can be found in [Armstrong McKay et al. \(2022\)](#), [Lenton et al. \(2019\)](#), or [Lenton and Schellnhuber \(2007\)](#). Notice, however, that the specific CTEs shown in these illustrations may differ between the sources. This may be due to a shift in the scientific evaluation of certain ESCs in their capacity as CTEs, or to disparities in assessments made by individual authors.

other remote areas in the sense that Amazon forest dieback could alter climatic conditions over Central and North America and the Indian Ocean ([Werth and Avissar, 2002](#); [Medvigy et al., 2013](#)). As for the AMOC early warning signals of tipping have also been reported for the Amazon rainforest ([Boulton et al., 2022](#)).

Both AMOC and Amazon rainforest act on time scales of several decades to a few centuries and therefore may impact the livelihoods of the very next generations ([Jackson and Wood, 2018](#); [Ritchie et al., 2021](#); [Armstrong McKay et al., 2022](#)). In contrast, the tipping of ice sheets unfolds only on much longer time scales but would entail maybe even more severe consequences. On millennial time scales the global mean sea level could rise by approximately 7m if the GrIS tips ([Morlighem et al., 2017](#); [Boers and Rypdal, 2021](#); [Bochow et al., 2023](#)) and tipping of the WAIS could add another 3-5m ([Feldmann and Levermann, 2015](#); [Morlighem et al., 2020](#)) — let alone the 52m of sea-level equivalent currently stored in form of ice in the East Antarctic Ice sheet ([Morlighem et al., 2020](#)), which is considered much less likely yet not impossible to tip ([Armstrong McKay et al., 2022](#)).

## 1.2 The study of climate tipping points

Despite recent advances in the study of CTEs, large uncertainties remain in both the quantification of CTPs in terms of critical warming thresholds and the assessment of the impacts of potential tipping events (see e.g. [Armstrong McKay et al., 2022](#); [Wang et al., 2023](#)). Researchers in this field are confronted with multiple challenges important for the context of this thesis:

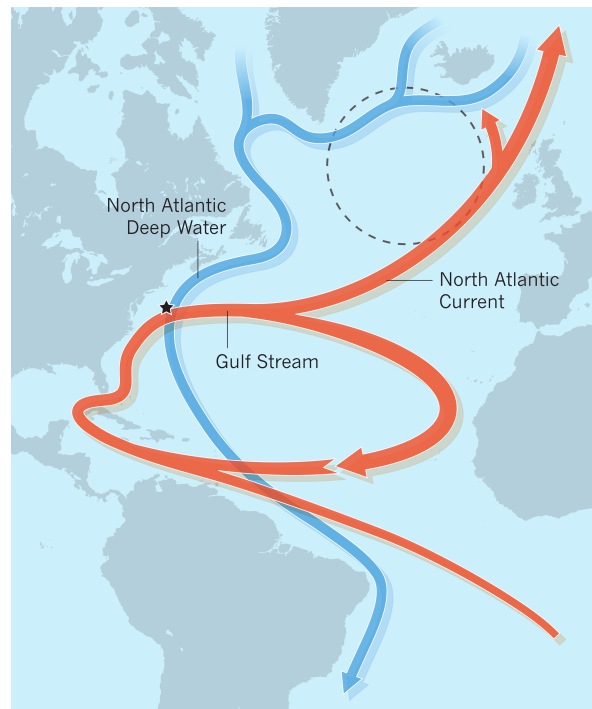


Figure 1.3: Schematic illustration of the AMOC. Red arrows indicate warm near-surface currents, while blue arrows indicate cold deep-water return flows. As the warm water masses travel northward, they lose heat to the atmosphere and become denser. This facilitates deep convection in the Labrador Sea and in the Nordic Seas. The sinking water masses form the NADW that eventually returns South at large depth. Figure reprinted with permission of Springer Nature BV, from: Praetorius (2018), North Atlantic circulation slows down, *Nature*, vol. 556, ©2018 Macmillan Publishers Limited, part of Springer Nature. All rights reserved; permission conveyed through Copyright Clearance Center, Inc..

1. No major climate tipping event has ever been observed directly. Observational evidence that ESC or the climate system as a whole can transition more or less abruptly between different (stable) states can only be obtained from paleoclimate proxy records. These are physical quantities preserved in so-called climate archives which are known to correlate with certain climate variables (Brovkin et al., 2021; Boers et al., 2022).
2. General circulation models (GCMs) and Earth system models (ESMs) are suspected to inherently simulate a potentially overly stable climate (Valdes, 2011; Liu et al., 2017). Tipping dynamics often rely on a delicate interplay of complex and potentially small-scale feedbacks, many of which are not properly resolved in state-of-the-art climate models often in the interest of computational costs (Wang et al., 2023). E.g. while the Amazon Rainforest alone hosts ~14,000 plant species (Cardoso et al., 2017), recent ESMs rely on the order of tens of so-called plant-functional types to represent global vegetation (e.g. Rolinski et al., 2018). Similarly, elevated meltwater influx into the high-latitude North Atlantic from the GrIS — a potential source of instability of the AMOC — is typically not considered in Coupled Model Intercomparison Project Phase (CMIP) phase 6 models. These models further do not resolve convective processes in the ocean and the atmosphere, which are also relevant for the AMOC and the Amazon rainforest, respectively. Still, a number of abrupt transitions have been identified in the CMIP climate

projections (Drijfhout et al., 2015) and there is increasing success in reproducing a series of high Northern latitude abrupt warming events from the last glacial (Vettoretti and Peltier, 2018; Zhang et al., 2021; Kuniyoshi et al., 2022; Izumi et al., 2023; Malmierca-Vallet et al., 2023),

3. In the presence of two or more alternative stable states, the question of climate tipping is one of probabilities, be it due to stochastic parameterizations or the chaotic sensitivity to initial conditions. To assess these, large ensembles of model runs would be required exceeding the currently affordable computational costs.
4. Typical time scales for the dynamics of CTE range from decades to millennia. Despite this separation in terms of time scales, these CTE may be strongly coupled. In order to assess the coupled dynamics, fully coupled climate models need to be run over several thousands of years which clearly exceeds the currently affordable computational costs.

To overcome these challenges the ongoing investigation of climate tipping points draws on a range of complementing strategies:

**Study of Paleoclimate proxy records.** As already mentioned, the only observational evidence for climate tipping events stems from paleoclimate proxy data (Brovkin et al., 2021; Boers et al., 2022). Figure 1.4 presents a selection of proxy records showing indicative of past abrupt climatic changes. The recovery of new proxy data (e.g. Kjær et al., 2021; Skiba et al., 2023), improvement of data interpretation (e.g. Vallelonga et al., 2021) as well as the identification of abrupt climatic changes in the available data are ongoing efforts (e.g. Bagniewski et al., 2021). Provided that proxy records indicate past abrupt climatic changes, the next task is to reconstruct the corresponding climate dynamics to understand how exactly positive climate feedbacks have unfolded in the past and thus may unfold future tipping scenarios. This thesis fully belongs to this last research category.

The study of past abrupt climatic changes is a valuable source of information in two ways: On the one hand, it may provide empirical evidence that certain ESCs have undergone abrupt changes in the past, which renders them potential candidates to undergo an abrupt change of state, again. This applies for example to the AMOC (Lynch-Stieglitz, 2017), which repeatedly switched between different operational modes during the last glacial interval, and to the Sahara, which transitioned from a savanna state to a desert state around 5500 years ago (DeMenocal et al., 2000; Brovkin et al., 2021). While the AMOC might already be approaching a tipping point in response to global warming (Boers, 2021), it seems less likely that the Sahara would transition back to the Savanna state. On the other hand, even though future tipplings are likely to rely on different mechanisms than past ones, understanding the dynamics of past abrupt climate changes contributes to a comprehensive understanding of CTE. Past abrupt climatic changes provide a benchmark for ESMs in the sense that ESMs should reasonably well reproduce the tipplings of the past before one should rely on their projections with respect to future climate tipping or not-tipping.

This said it is important to emphasize that past abrupt climatic changes do not serve as a template for potential future tipping events. In contrast, the drivers,

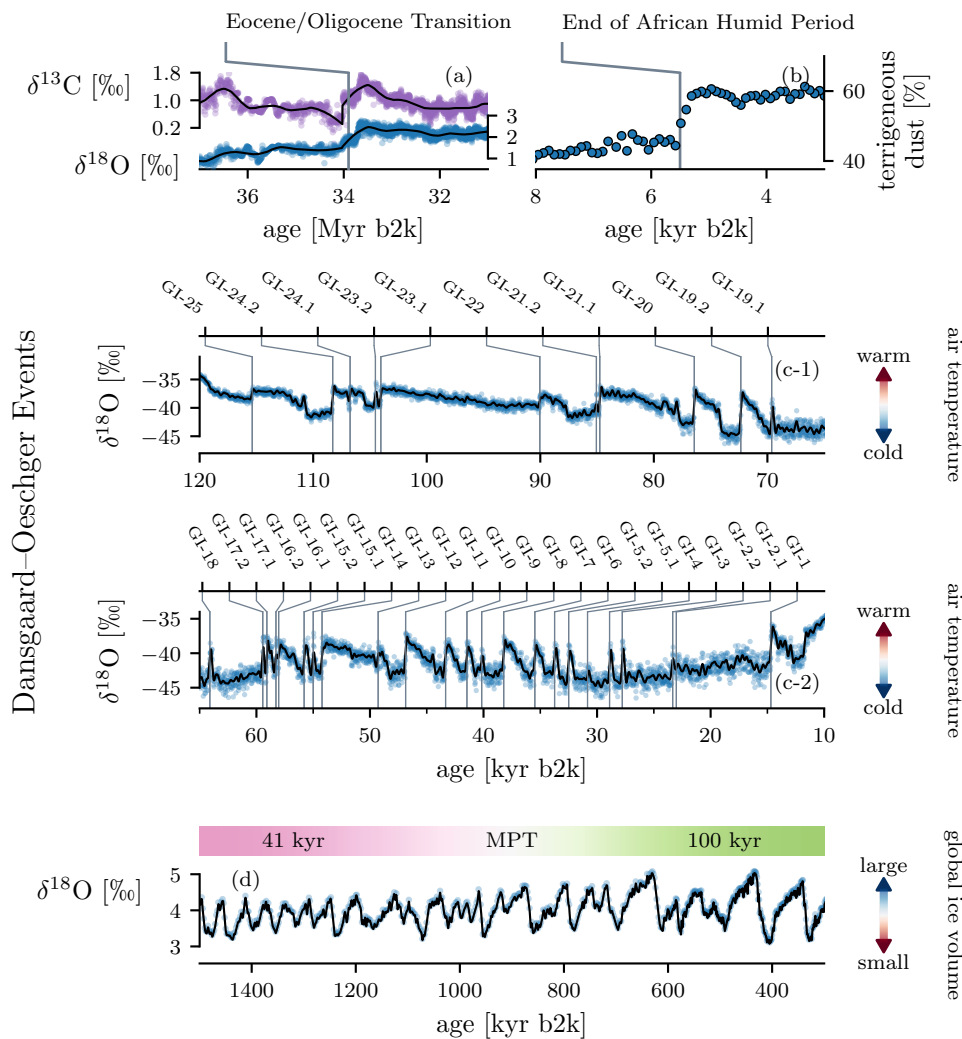


Figure 1.4: Paleoclimatic proxy evidence for past abrupt climatic changes. a) Composite records of deep-sea benthic foraminifer carbon ( $\delta^{13}\text{C}$ ) and oxygen  $\delta^{18}\text{O}$  isotope ratios as presented by [Westerhold et al. \(2020\)](#). 33.9 million years ago, a pronounced shift in both records indicates the so-called Eocene/Oligocene transition, marking the transition from an almost ice-free planet to Antarctic glaciation ([Hutchinson et al., 2021](#); [Boers et al., 2022](#)). The data are provided in the file `TableS34.tab` of the [supplementary material](#) [last accessed: 08.05.2023] to the original publication. b) Terrigenous sediment concentrations from a marine sediment core off the coast of Mauritania ([DeMenocal et al., 2000](#)); the data are available as a [supplement](#) [last accessed: 08.05.2023] to [Brovkin et al. \(2021\)](#). The steep increase seen at 5.5 kyr b2k provides evidence for rapid desertification of the previously savanna-like Sahara region ([Boers et al., 2022](#), and references therein). c) Stable water isotope records from the North Greenland Ice Core Project (NGRIP) ice core ([North Greenland Ice Core Project Members, 2004](#)). The repeated sudden increases are the so-called Dansgaard–Oeschger (DO) events — the main subject of this thesis. They are associated with sudden warming of the local air temperatures of 8–16.5°C. The black line is obtained by applying a 100 yr Chebyshev low-pass filter to the original data (blue dots). The data are available as a [supplement](#) [last accessed: 08.05.2023] to [Seierstad et al. \(2014\)](#). d) Stack of benthic foraminiferal  $\delta^{18}\text{O}$  data from 57 globally distributed marine sediment cores (LR04 stack) ([Lisiecki and Raymo, 2005a](#)). Benthic  $\delta^{18}\text{O}$  is a function of global ice volume and deep ocean temperature. As such, the record documents past glacial–interglacial cycles with fairly abrupt deglaciations. Furthermore, a qualitative transition from a 41 kyr cycle periodicity to a 100 kyr periodicity took place at about 1 Myr b2k, which is discussed in detail in [P1](#). The data is available from [Lisiecki and Raymo \(2005b\)](#).

feedbacks and potentially even the ESCs involved would be different given that today's climatic background conditions differ substantially from those of known past abrupt climatic changes.

**A hierarchy of models.** In contrast to the general trend towards a predominance of GCMs and comprehensive ESMs in climate science, to date these types of models play a subordinate role in CTP research due to the reasons described in the challenges 2.-4.. Instead, researchers draw on conceptual climate models to work out fundamental physical mechanisms of climate tipping events. So-called Earth system models of intermediate complexity (EMICs) may be used to test these mechanisms in a physically more realistic setup. Moreover, high-resolution stand-alone models are being used to study the tipping behavior of specific CTEs in isolation (Salazar and Nobre, 2010; Robinson et al., 2012; Feldmann and Levermann, 2015; Lohmann and Ditlevsen, 2021; Bochow et al., 2023). Taken together, a hierarchy of models is invoked to examine past and future climate tipping points in an isolated and coupled fashion. Given the steady increase in computational power and the recent successes in reproducing past abrupt climate change, the role of GCMs and ESMs can reasonably be expected to grow also in this field.

### 1.3 Outline of the thesis

This thesis contributes to the study of abrupt climatic changes from the past as evidenced by paleoclimate proxy records. In particular, it investigates the famous DO events from the last glacial interval (115–11.7 kyr b2k) and the millennial-scale climate variability associated therewith, referred to as DO variability in this work (see Sect. 4). It further touches upon the glacial–interglacial cycles of the Pleistocene (2.6 Myr – 11.7 kyr b2k) and the emergence of the so-called mid-Pleistocene transition (MPT). Its overarching research question is the following:

#### Research Question

**Q1** *What has caused the last glacial's repeated abrupt climatic changes and the millennial-scale climate variability associated therewith?<sup>a</sup>*

<sup>a</sup>Notice that DO variability has been reported also for previous glacial intervals (e.g. Barker et al., 2011; Rousseau et al., 2020). However, Greenland ice core records, which are the main source of evidence for DO variability, do not extend beyond the last interglacial. This thesis is centered around the highly resolved Greenland ice core data, and therefore its conclusions primarily concern the DO variability of the last glacial. It seems likely that during previous glacial intervals the same physical mechanism was active. However, the DO variability of previous glacial cycles is beyond the scope of this thesis.

Methodologically, this work pursues two main approaches. On the one hand, it adopts the framework of dynamical systems to explain past climate dynamics underlying the evident abrupt shifts. On the other hand, it uses Bayesian methods to draw direct inference from the available paleoclimatic time series. Correspondingly, the overarching research question can be subdivided into the following more

specific questions:

### Research Question

- Q2** *Can Dansgaard–Oeschger (DO) variability be explained in terms of a low-dimensional random and / or non-autonomous dynamical system?*
- Q3** *Can the relative phasing of abrupt climatic shifts in different Earth system components (ESCs) during Dansgaard–Oeschger events be inferred from paleoclimate proxy data?*

The main part of the thesis is comprised of five research articles reprinted here in the form in which they were published by scientific journals. **P2**, which is still under review, is included here in the form it has been published on the preprint server *arXiv*. The publications **P1-3** address the research question **Q2** and the publications **P4-5** are concerned with **Q3**. Among **P1-3**, **P1** was placed first, because it introduces the theory of dynamical systems.

Sections **1-4** serve as an introduction to **P1-5**. Concretely, Sect. **2** formalizes the term climate tipping point (**CTP**) and introduces the framework of dynamical systems used for their mathematical description. Sect. **3** presents the Stommel and the Stommel–Cessi box models of the Atlantic meridional overturning circulation (**AMOC**). As mentioned previously, the **AMOC** is thought to have played a major role in the emergence of **DO** variability by transitioning between different modes of operation. These simple dynamical system models provide a tangible explanation for why the **AMOC** is considered a **CTE** and how it can transition between two different states. Finally, Sect. **4** introduces the **DO** events themselves and the global climate variability associated with them. It further summarizes the challenges faced in the study of these events and the strategies used to overcome these. Sections **5** and **6** are comprised of the corresponding research articles and constitute the main part of this thesis. Subsequent to that main part, a concluding section finalizes this thesis by synthesizing the key findings of the presented research, discussing their role in the current scientific debate and sketching research questions that follow from the presented findings.



## 2 A formalization of tipping points

### 2.1 Phenomenology

Given the high level of attention the term *tipping point* currently attracts, it is no surprise that it is used in a somewhat inconsistent manner both across the media and the scientific literature. Most researchers would probably understand it as a *threshold* in the space of a system's external control which is *critical* in the sense that exceedance thereof (for at least a certain amount of time) would qualitatively alter the system's trajectory as compared to not exceeding it. A formalization of this concept was sought by [Lenton et al. \(2008\)](#) and the present work shares this very understanding. In contrast, one often reads statements like

*'Politicians, economists and even some natural scientists have tended to assume that tipping points in the Earth system — such as the loss of the Amazon rainforest or the West Antarctic ice sheet — are of low probability and little understood.'* ([Lenton et al., 2019](#))

in which the term *tipping point* clearly refers to the *process* that is triggered by the crossing of a corresponding critical threshold. This process is called *tipping event* or simply *tipping* in this thesis. According to the Intergovernmental Panel on Climate Change ([IPCC](#)), the *critical threshold* is localized in the system's state space and not in the space of its (external) control.

*'Tipping points refer to critical thresholds in a system that, when exceeded, can lead to a significant change in the state of the system, often with an understanding that the change is irreversible.'* ([Hoegh-Guldberg et al., 2018](#))

Finally, the concepts of *noise-induced tipping (points)* and *rate-induced tipping (points)* are reconciled with the slightly different notions of *tipping points* in one way or another (e.g. [Ashwin et al., 2012, 2017](#)). Fortunately, these inaccuracies are more of a nuisance than a major obstacle with respect to the general public and scientific debate. Usually, it is clear from the context which notion of CTPs underlies a certain statement. The box *Tipping points: A phenomenological definition* concisely defines the term *tipping point* and several related terms for the scope of this thesis.

In summary, the central aspect of the notion of *tipping points* is a qualitative state transition of a *tipping element* that unfolds in response to a marginal yet critical change of an external control. In the case of CTEs, this external control is either exerted directly by the global mean surface temperature or indirectly by other correlated climate variables such as local precipitation (e.g. [Lenton et al., 2008](#); [Hoegh-Guldberg et al., 2018](#); [Armstrong McKay et al., 2022](#)). The transitioning phase between the un-tipped and the tipped state is typically governed by extraordinarily high rates of change. This abruptness must be understood in relative terms compared to the natural change rates seen prior to the transition. To some extent and for some CTPs, the threat posed by a potential tipping is due to

this abruptness: If triggered, the speed of associated environmental changes could outpace capacities for societal adaptation. Once a tipping has fully materialized it is commonly considered to be irreversible in the sense that a simple backward crossing of the critical level of forcing (global warming) would not recover the un-tipped state. Instead, further reversal of the forcing (further cooling) beyond a second critical threshold would be required to induce a reverse transition from the tipped to the un-tipped state. This phenomenon is called *hysteresis* and is illustrated in Fig. 2.2. Notice that a hysteresis behavior is not required by all definitions of (climate) tipping points.

### Tipping points: A phenomenological definition

In this thesis, the term **tipping point** shall exclusively refer to a critical threshold in the level of external forcing or control that acts on a system from the outside. Here, the term critical implies that permanent exceedance of this threshold qualitatively impacts the dynamics of the systems and triggers a process of substantial change.

This process of qualitative change is called a **tipping event** or simply **tipping** within this thesis. Tipping events do not necessarily require the crossing of a **tipping point** but can also be triggered by random perturbations or by extraordinarily high rates of change of the external control as will be discussed later. Yet, this thesis preconditions the occurrence of a **tipping event** on the existence of a **tipping point**, irrespective of whether it is crossed or not. This criterion distinguishes tipping dynamics from other nonlinear mechanisms that likewise entail abrupt changes of a system's state.

In the case of climate tipping points (CTPs), and in particular, in the case of climate tipping, there is commonly a feedback of the system to its control, i.e. to global warming. Thus the required externality of the control must not be understood in a strict sense here.

For ease of language, in this thesis, past abrupt climatic changes evident in paleoclimate proxy records will also sometimes be referred to as **tipping events**, although it cannot be judged with certainty if they strictly qualify as such in the above sense.

## 2.2 Mathematical description

The mathematical concept underlying the notion of tipping points is that of a dynamical bifurcation. Consider bi- or multi-stable dynamical systems exposed to an external control  $\alpha$ . In climate science  $\alpha$  usually represents the level of global warming, the concentration of atmospheric CO<sub>2</sub> or on longer time scales the orbital insolation forcing, i.e. the spatiotemporal distribution of sunlight that reaches the Earth's surface over the course of an annual cycle. If a marginal change  $\alpha < \alpha_{\text{crit}} \rightarrow \alpha + \delta\alpha > \alpha_{\text{crit}}$  changes the number of stable states, the system is said to undergo a bifurcation. The point  $\alpha_{\text{crit}}$ , termed bifurcation point, constitutes a tipping point for the system provided that the crossing of  $\alpha_{\text{crit}}$  destabilizes the prevailing system state. Closely following [Dijkstra \(2013\)](#) and [Caraballo and Han](#)

(2017) the next paragraph provides a concise yet sufficiently formal introduction of this mathematical framework which is central to the modern scientific discourse on CTPs and for this thesis.

**Dynamical systems and bifurcations.** Let  $\mathbb{T} \subset \mathbb{R}$  denote a continuous time interval and let  $\mathbf{X} \subset \mathbb{R}^n$  be an  $n$ -dimensional state space of a real-valued system.<sup>1</sup> The map

$$\phi_\alpha : \mathbb{T} \times \mathbf{X} \rightarrow \mathbf{X}, \quad (2.1a)$$

$$(\mathbf{x}, t) \mapsto \phi_\alpha(\mathbf{x}, t) \quad (2.1b)$$

is termed flow and the subscript  $\alpha$  expresses an explicit dependency of the flow on the control parameter  $\alpha$ . Here, for simplicity,  $\alpha$  is assumed to be real-valued, but in a more general setting, it can also be complex or vector-valued.

Formally, the tuple  $\Sigma = (\mathbb{T}, \mathbf{X}, \phi)$  defines a so-called dynamical system. In practice, dynamical systems are often given in terms of an associated ordinary differential equation (ODE)

$$\frac{d}{dt}\mathbf{x}(t) = \mathbf{f}_\alpha(\mathbf{x}, t), \quad (2.2)$$

wherein  $\mathbf{f}_\alpha(\mathbf{x}, t)$  is induced by the flow by assigning each point in state space  $\mathbf{X} \ni \mathbf{x} = \phi_\alpha(\mathbf{x}_0, t)$  the vector

$$\mathbf{f}_\alpha(\mathbf{x}, t) = \frac{d}{dt}\phi_\alpha(\mathbf{x}_0, t) \in \mathbb{R}^n. \quad (2.3)$$

A solution  $\mathbf{x}(t)$  with initial conditions  $\mathbf{x}(t_0) = \mathbf{x}_0$  of the ODE (2.2) is called a trajectory or orbit and  $\mathbf{f}_\alpha(\mathbf{x}(t), t)$  is tangent to any of the orbit's points  $\mathbf{x}(t)|_{t \in \mathbb{T}}$ . If  $\mathbf{f}_\alpha(\mathbf{x}, t)$  does not explicitly depend on time, then the system is called autonomous and (2.2) simplifies to

$$\frac{d}{dt}\mathbf{x}(t) = \mathbf{f}_\alpha(\mathbf{x}). \quad (2.4)$$

In that case, under a set of suitable assumptions on  $\mathbf{f}_\alpha(\mathbf{x})$  (e.g. continuity and differentiability) any initial condition  $(\mathbf{x}_0, t_0)$  can be associated with a trajectory  $\mathbf{x}(t)_{(x_0, t_0)}$  in a unique manner (Caraballo and Han, 2017). This implies that trajectories of autonomous dynamical systems may not cross in their state space  $\mathbf{X}$ .

While dynamical systems, in general, possess a multitude of features worth studying, to understand the fundamental concept of CTPs the focus may be laid exclusively on so-called (stable) fixed points or equilibria, i.e. points  $\mathbf{x}^*$  in the state space where the vector field  $\mathbf{f}_\alpha$  vanishes:

$$\mathbf{f}_\alpha(\mathbf{x}^*) = 0. \quad (2.5)$$

If additionally, all eigenvalues of the Jacobian  $d\mathbf{f}_\alpha(\mathbf{x}^*)$  have negative real part, these points attract trajectories with suitable initial conditions in the sense that  $|\mathbf{x}(t) - \mathbf{x}^*| \rightarrow 0$  as time goes to infinity. This *forward attraction* renders these fixed

---

<sup>1</sup>For discrete time dynamical systems one has  $\mathbb{T} \subset \mathbb{Z}$ . In general dynamical systems may as well be complex-valued, but this thesis is limited to real-valued systems.

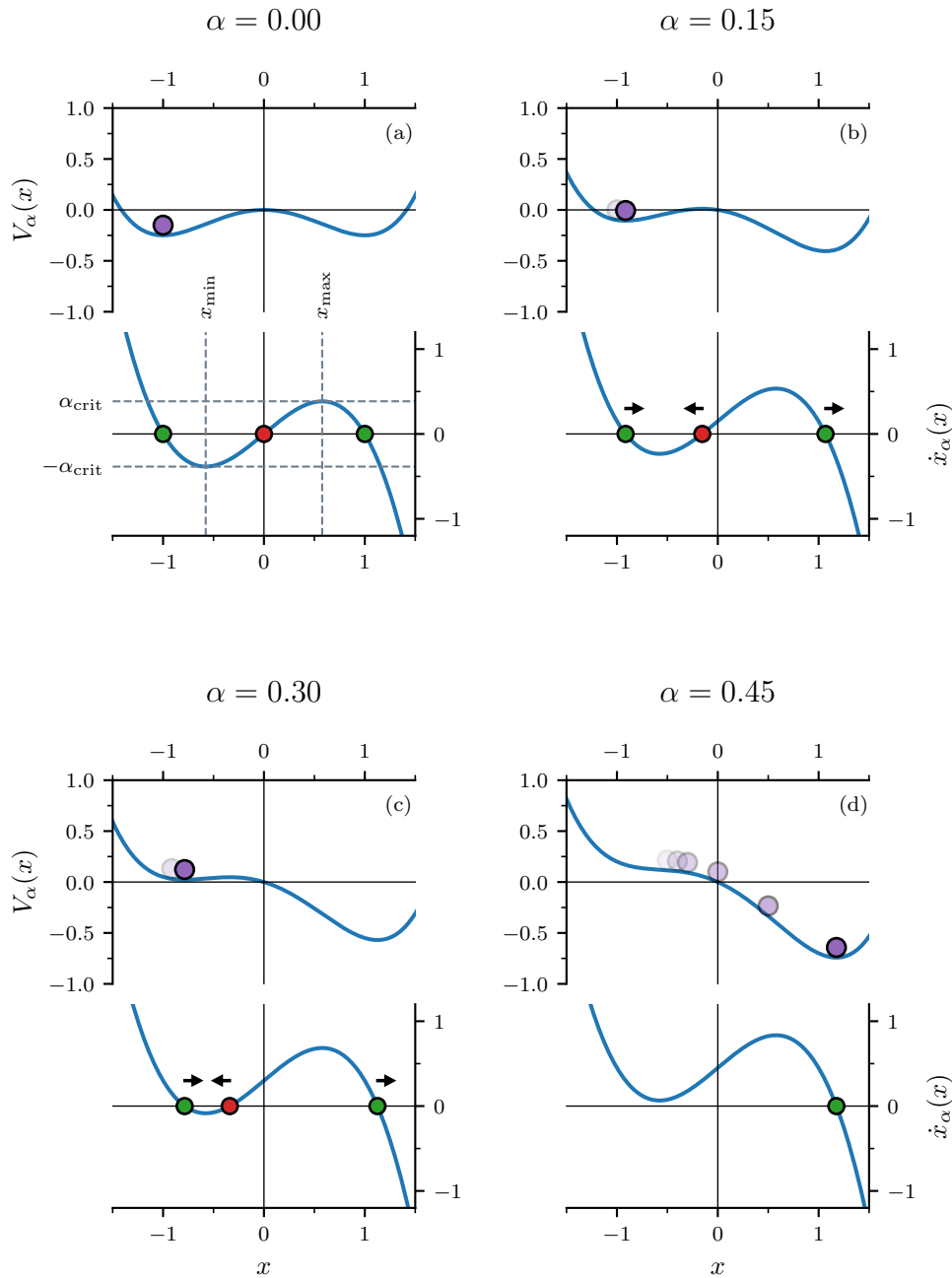


Figure 2.1: Tipping in a double-well potential. Based on Eqs. (2.6) and (2.9) panels a) to d) illustrate how a tipping materializes if  $\alpha$  is increased past the bifurcation point  $\alpha_{\text{crit}}$ . In each panel shows the potential  $V_\alpha(x)$  and the function  $f_\alpha(x)$  for increasing values of  $\alpha$ . Green (red) dots indicate stable (unstable) fixed points of  $f_\alpha$ . For  $\alpha = 0$  the two potential wells are equally deep and the system (violet dot) resides in the left well. Increasing  $\alpha$  flattens the left well and deepens the right one. At the same time, the stable fixed points are shifted to the right while the unstable fixed moves to the left approaching the left-hand side's stable fixed point. The system keeps track of this shift of the left-hand side's fixed point. For  $\alpha = 0.45$  the left well no longer exists and the 'marble rolls down the hill' into the remaining well, i.e. the system tips in response to a bifurcation.

points *stable*. In contrast, *unstable* fixed points are characterized by at least one eigenvalue of the Jacobian having positive real part. If all eigenvalues of  $\mathbf{d}f_\alpha(\mathbf{x}^*)$  are positive, they attract trajectories in a backward sense, i.e.  $|\mathbf{x}(t) \rightarrow \mathbf{x}^*|$  as  $t \rightarrow -\infty$ . Loosely speaking, the set of all initial conditions  $\mathcal{S}_{\mathbf{x}^*}$  attracted by a stable fixed point  $\mathbf{x}^*$  is called the *basin of attraction* of  $\mathbf{x}^*$ .<sup>2</sup>

How can dynamical systems help to understand tipping points? Consider, for example, the simple ODE

$$\dot{x}(t) = -x^3 + x + \alpha. \quad (2.6)$$

For  $\alpha = 0$  the equation's right-hand-side vanishes for  $x = \pm 1$  and  $x = 0$ . The Jacobian is negative for the first two roots ( $df(\pm 1) = -2$ ) and positive for the third ( $df(0) = 1$ ). This renders  $x_{+,-}^* = \pm 1$  stable fixed points and  $x_0^* = 0$  an unstable fixed point (c.f. Fig. 2.1a). Therefore, all trajectories initialized on the positive (negative) half-axis will converge to  $x_+^*$  ( $x_-^*$ ) while a trajectory initialized in the origin stays there forever. Note that  $x_{\min} = -1/\sqrt{3}$  and  $x_{\max} = 1/\sqrt{3}$  constitute local extremes of  $f$  with

$$f_{\alpha=0}(\pm 1/\sqrt{3}) = \pm 2/\sqrt{27}. \quad (2.7)$$

Hence, shifting  $f$  globally upwards or downwards by a value  $\alpha$  with  $|\alpha| > \alpha_{\text{crit}} = 2/\sqrt{27}$  leads to a collision of the unstable with one of the stable fixed points in which both are annihilated (c.f. Figs. 2.1 and 2.2). As a consequence, for  $|\alpha| > \alpha_{\text{crit}}$  all trajectories are attracted by the remaining stable fixed point  $x_{+,-}^*(\alpha)$ , irrespective of the initial conditions. Such a qualitative change of a system's stability configuration in response to a (marginal) change of a control parameter is called a *bifurcation* and  $\pm\alpha_{\text{crit}}$  are bifurcation points in the space of the system's control.

Strictly speaking, introducing a time dependency for the control parameter  $\alpha$  converts the system defined by Eq. (2.6) from an autonomous into a non-autonomous system. Typically, the external control is assumed to change on a time scale that is slower than the internal system dynamics. In that case, the quasi-autonomous analysis of the system as presented here is sufficient to understand the essentials of the dynamics. P1 discusses explicitly some particularities of non-autonomous systems, where the time scale separation is not so clear.

For a better illustration, in one dimension, one often introduces a potential  $V_\alpha(x)$  with

$$f_\alpha(x) = -\frac{dV_\alpha(x)}{dx}. \quad (2.8)$$

Stable fixed points of  $f_\alpha$  translate into minima of  $V_\alpha$  and one can think of the system's dynamics as a marble that always rolls into the valleys of a hilly environment. Equation (2.6) yields a double-well potential for  $-\alpha_{\text{crit}} < \alpha < \alpha_{\text{crit}}$  of the form

$$V_\alpha = \frac{1}{4}x^4 - \frac{1}{2}x^2 - \alpha x. \quad (2.9)$$

Figure 2.1 illustrates how the double-well transforms into a single-well potential upon increasing  $\alpha$  past the bifurcation point and how the system tips in response

<sup>2</sup>Stable fixed points are in fact a special case of so-called *attractors*. The term *basin of attraction* is commonly defined in a more general sense based on a formal introduction of the term *attractor* (Caraballo and Han, 2017). However, for the purpose of this work, it suffices to identify attractors with *stable fixed points* and rely on the simpler notion of *basins of attraction* associated therewith.

to that, i.e. how the marble rolls into the respective other valley. Similarly, Fig. 2.2 shows the position of the fixed points of Eq. (2.6) in dependence on  $\alpha$  in form of a bifurcation diagram together with a trajectory of a corresponding random dynamical system.

In a nutshell, to establish the connection between Eq. (2.6) and a climate tipping point, think of  $x(t)$  as a measure of biomass in the Amazon rainforest, for example. Identify  $\alpha$  with the amount of precipitation in the Amazon basin which is negatively affected by global warming.<sup>3</sup> For an intermediate range of warming, and hence precipitation, there are two stable configurations that the Amazon basin’s vegetation could assume due to the atmosphere–vegetation feedback briefly introduced in Sect. 1 (Nobre and Borma, 2009). The first is given by the current forest state wherein a dense tree–cover maintains itself by efficiently recycling the precipitated water in a transpiration–evaporation–precipitation cycle (e.g. Salati et al., 1979; Zemp et al., 2014, 2017). The second possible state is a savanna state, wherein the absence of trees yields highly elevated drain rates of the available rainfall. The resulting drier conditions stabilize the savanna state in the sense that they prevent the growth of dense rainforest vegetation. Conceptually, the two stable states  $x_+^*$  and  $x_-^*$  of Eq. (2.6) can be identified with the forest state and the savanna state of the Amazon rainforest, respectively. In this simple model, the reduction in precipitation due to anthropogenic global warming is reflected by a steady decrease in the parameter  $\alpha$ . If precipitation decreases past the bifurcation point  $-\alpha_{\text{crit}}$  and remains below this level, the forest state  $x_+^*$  becomes unstable and the Amazon basin’s vegetation  $x(t)$  transitions abruptly and inevitably towards the only remaining stable state, which is given by the savanna state  $x_-^*$ . This analogy should of course be taken with a grain of salt. The highly complex dynamics of the Amazon basin’s vegetation are certainly not captured by Eq. (2.6) to their full extent. Yet, structurally similar one-dimensional ODEs have been used to model Amazon rainforest dynamics, because the important tipping dynamics believed to be inherent to the Amazon rainforest are indeed well reflected in these simple model equations (Ritchie et al., 2021; Wunderling et al., 2021).

**From deterministic to random dynamics.** The previous section has introduced the fundamental mathematical considerations underlying the concept of climate tipping point (CTP). The tipping point itself was identified with the bifurcation point in the space of the external control acting on the system. A permanent exceedance of this critical level of forcing inevitably destabilizes the current attractor of the system and entails a state transition, the *tipping* of the system. So far, this framework was exclusively formulated in terms of deterministic model equations. However, real-world CTEs are subject to fluctuations and thus require a random dynamical systems formulation. Importantly, in the presence of multiple attractors these fluctuations may push a system across basin boundaries separating different basins of attraction. Once pushed across a basin boundary, a system is likely to transition to the respective other attractor and thus a tipping may unfold without the crossing of bifurcation point. In other words, a system can tip, before

<sup>3</sup>In fact, global warming negatively impacts the Amazon rainforest via a complex mixture of increasing dry season length, elevated drought and forest fire frequency and decreasing overall precipitation (e.g. Wang et al., 2023; Parsons, 2020). Human deforestation additionally destabilizes the rainforest (Boers et al., 2017).

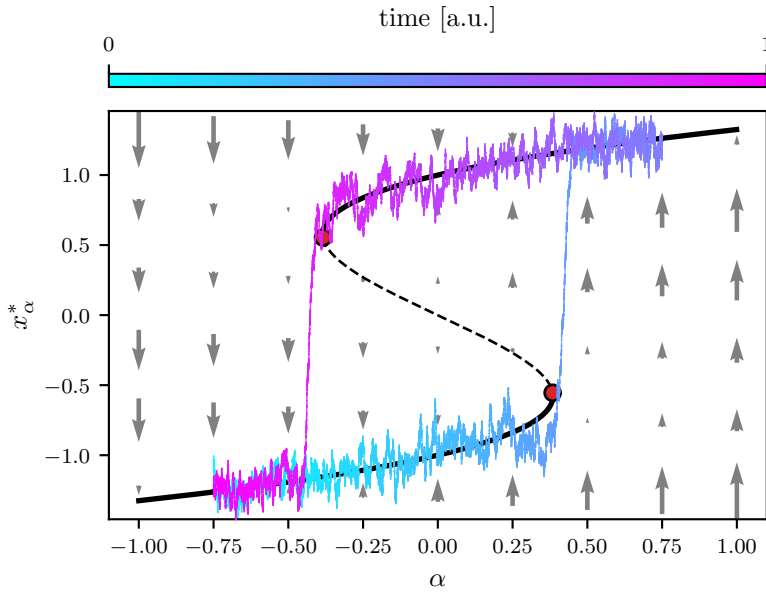


Figure 2.2: Double fold bifurcation with simulated trajectory. The gradient-colored line shows a trajectory of a random dynamical system defined by  $dx = (-x^3 + x + \alpha)dt + \sigma dW$  with  $\sigma = 0.2$ . The colorbar indicates the time in arbitrary units. The black line shows the nullcline of the system, i.e. the fixed points of the system's deterministic part in dependence on  $\alpha$ . The solid parts of the line correspond to stable fixed points, while the dashed part represents unstable fixed points. Red dots indicate corresponding bifurcation points and gray arrows represent the deterministic drift. Over the integration time interval, the control parameter  $\alpha$  is ramped in a triangle shape from  $-0.75$  to  $+0.75$  and back. The system tracks the changing position of the closest stable fixed point until that is annihilated in a dynamic fold bifurcation. This entails a tipping of the system to the remaining stable fixed point. One can see that the transition from the upper to the lower stable branch of the nullcline is actually noise-induced. The noise pushes the system across the unstable fixed point by chance slightly before the bifurcation point is crossed. The integration was carried out using the Euler–Maruyama method based on the Itô interpretation of the defining SDE (e.g. Tabar, 2019).

it reaches its tipping point in what is called noise-induced tipping (Ashwin et al., 2012).

Let  $x(t)$  denote some macroscopic variable that conveniently describes the state of a CTE, such as the Amazon rainforest's total biomass, the water mass transport of the AMOC or the volume of the GrIS. Assume that the overall temporal evolution of  $x(t)$  can be expressed in terms of an ODE similar to Eq. (2.6). Such an equation can neither resolve the microscopic dynamics of the CTE nor fast external influences acting on the system. For example, in the Amazon rainforest, the growth and dying of individual plants give rise to what is known as internal variability, on the one hand. On the other hand, the forest is exposed to the external influence of fluctuating rainfall. Similarly, the AMOC is exposed to fluctuations of the winds driving it and the GrIS may receive more or less snowfall in a particular year at a particular location. Both, internal unresolved scales and external unresolved influences can be summarized in a noise term  $\xi_t$  (e.g. Hasselmann, 1976) whose consideration transforms the ordinary differential equation (ODE) (2.2) into a stochastic differential equation (SDE) of the form

$$d\mathbf{x}(t) = f_{\alpha}(\mathbf{x}(t), t)dt + \sigma(\mathbf{x}(t))d\xi_t. \quad (2.10)$$

The noise  $\xi_t$  constitutes a time-dependent stochastic force and hence contributes

to the incremental temporal evolution of  $x(t)$  in a random fashion (e.g. Gardiner, 1985; Risken, 1989). The strength of the stochastic force on the system  $\sigma$  may depend on the system's state  $x(t)$  itself. A dynamical system that is given in terms of an SDE is called a random dynamical system (see P1). The function  $f_\alpha$  — commonly referred to as the drift in the context of SDEs — still defines the underlying deterministic stability landscape in terms of basins of attractions, bifurcations and so on. However, the random perturbations exerted by  $\xi_t$  may now push the system  $x(t)$  from one basin of attraction into another triggering a noise-induced tipping (Ashwin et al., 2012). Figure 2.2 illustrates how a random dynamical tips in response to a dynamical bifurcation.

For the sake of completeness, it shall be mentioned, a system can also tip in response to rapid relocation of its basins of attraction. This phenomenon is known as rate-induced tipping and it does not require the crossing of a bifurcation point (Ashwin et al., 2012). This can be understood by considering a double-well potential as shown in Fig. 2.1a that is being shifted to the left at a high rate. Above a critical rate, the system fails to track the changing position of the left well and tips to the right well.

**The role of dynamical systems in this work.** P1 specifies how dynamical system theory facilitates paleoclimate research. In particular, it emphasizes the role of external forcing in the emergence of variability in non-autonomous and nonlinear dynamical systems. In concrete terms, it elaborates on how the changing orbital insolation forcing has paced the glacial cycles of the Pleistocene (2588-12 kyr b2k), wherein orbital insolation takes the role of an external forcing and the Earth's climate that of a non-autonomous dynamical system. Equation (2.10) is the starting point for P2 and P3 which approach past abrupt climate change from the perspective of random dynamical systems. P3 presents a reconstruction of the drift  $f$  from a paleoclimate time series which comprises numerous abrupt transitions. The reconstructed drift features two stable fixed points that can be identified with two climate regimes that prevailed during the last glacial cycle. From this perspective, the transitions between the two climate regimes evident from the proxy data appear as noise-induced tipping events. P2 is concerned with the same series of abrupt climatic changes, but follows a modeling instead of a time-series analysis approach. It explains the abrupt transitions in terms of noise-induced excitations of a multi-scale climate system.

### 3 The Stommel box model

The previous section has built the bridge from complex ESC to simple model equations. A standard double-fold bifurcation was introduced as a generic model for CTEs. It reflects tipping dynamics in terms of a state transition that unfolds as a consequence of a dynamic bifurcation, i.e. the crossing of a CTP. The tipping ability of the considered ESC was phenomenologically justified but not mathematically derived. This section will briefly introduce the Stommel (or Stommel-Cessi) box model for the AMOC. The model equations are derived from fundamental physical considerations. From these, a tipping ability follows strictly mathematically and is not per se prescribed as in the previous example.

Already in 1961, Stommel presented his famous box model of thermohaline convection. Later, Cessi (1994) adopted the model with minor modifications to explicitly describe the AMOC. The original and the modified version are now referred to as the Stommel and Stommel–Cessi models, respectively. They predict the coexistence of a strong and a weak mode of the meridional overturning flow in the Atlantic. According to these models changes in the global distribution of freshwater fluxes can annihilate either of the stable modes via a smooth and a non-smooth saddle-node bifurcation, respectively.

The Stommel model provides a very tangible explanation for abrupt AMOC changes. Such changes are widely accepted as a central element of the last glacial’s DO variability studied in this thesis (e.g. Lynch-Stieglitz, 2017; Menviel et al., 2020). In the study of DO variability (e.g. Roberts and Saha, 2017; Gottwald, 2021; Lohmann et al., 2021) the model was picked up repeatedly and it forms a central building block of the model developed in P2. While unambiguous evidence from proxy records for two disjoint circulation modes was missing for a long time, the assessment of Pa/Th records from the Bermuda Rise (c.f. Fig. 4.2) presented by Henry et al. (2016b), among others, has solidified the prevailing conviction that AMOC–switches have occurred in the past. The tipping mechanism and the corresponding hysteresis suggested by the Stommel–Cessi model were later also found in both EMICs and GCMs (Ganopolski and Rahmstorf, 2001; Dijkstra and Weijer, 2005; Rahmstorf et al., 2005; Jackson and Wood, 2018; Weijer et al., 2019; Jackson et al., 2023; Lohmann et al., 2023). The study of the AMOC constitutes a very instructive example for how conceptual modeling, proxy evidence, process-based EMICs and fully coupled GCMs acted in concert to shape the perception of the AMOC as a CTE.

The model considers two neighboring volumes of water representing the equatorial Atlantic (box 1) and the northern North Atlantic (box 2) as illustrated in Fig. 3.1 (Stommel, 1961; Cessi, 1994). Each volume is characterized by a uniform temperature  $T_i$  and salinity  $S_i$ , with  $i = \{1, 2\}$  indexing the boxes. The density of each box follows from an idealized equation of state

$$\rho_i(T_i, S_i) = \rho_0 - \alpha T_i + \beta S_i, \quad (3.1)$$

wherein  $\alpha$  and  $\beta$  describe the linearized effects of temperature and salinity changes with respect to a reference density  $\rho_0$ . The density gradient between the two

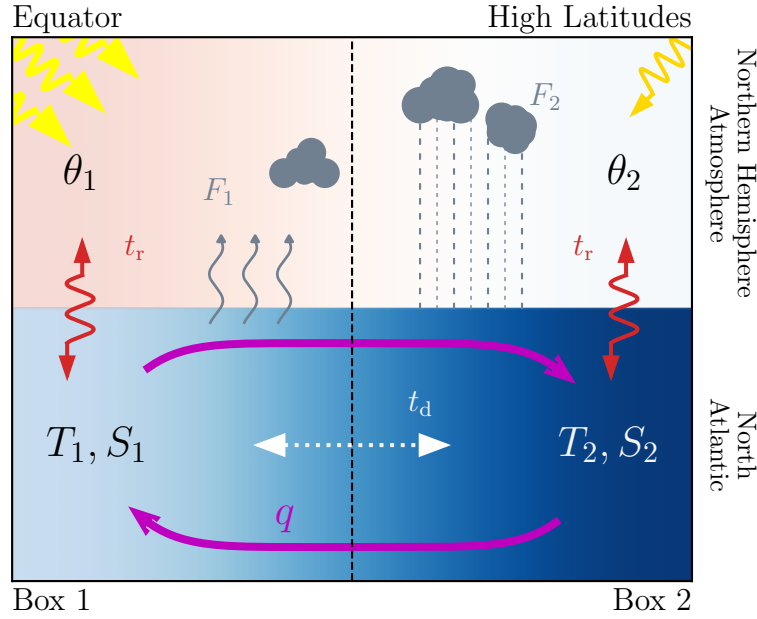


Figure 3.1: Schematic presentation of the Stommel model. Two North Atlantic is subdivided into two boxes, an equatorial box and a high-latitude box. Each box is described by a homogeneous temperature  $T_i$  and salinity  $S_i$ . The temperature of each box relaxes against a box-specific atmospherically prescribed temperature  $\theta_i$  at the rate  $t_r^{-1}$ . The dominance of evaporation over precipitation in the equatorial region and the inverse relation in the high northern latitudes give rise to salinity forcings  $F_i$ . Diffusive transport counteracts existing gradients between the boxes at the rate  $t_d^{-1}$ . A density difference between the two boxes drives an overturning flow  $q$  representative of the AMOC.

volumes

$$\Delta\rho = \beta[S_1 - S_2] - \alpha[T_1 - T_2] \quad (3.2)$$

drives a proportional flow from the denser to the less dense volume at the bottom of the ocean:

$$\begin{aligned} Q &= -k\Delta\rho \\ &= k(\alpha[T_1 - T_2] - \beta[S_1 - S_2]), \end{aligned} \quad (3.3)$$

where  $k$  determines the linear dependence of the bottom flow on the density gradient. This mass flux must be balanced by a counteracting flow at the surface, which closes the overturning loop. This mass flux must be balanced by a counteracting flow at the surface, which closes the overturning loop.

To find the strength of the overturning in a steady state, one has to consider the temporal evolution of the boxes' temperatures and salinities. The temperature of each box is assumed to relax against the temperature  $\theta_i$  of the atmosphere above it at a rate  $t_r^{-1}$ . The atmospheric temperatures  $\theta_i$  are controlled by the differences in the incoming solar radiation between the equator and high northern latitudes. Furthermore, diffusive transport counteracts the existing temperature gradient between the two boxes at a diffusion rate  $t_d^{-1}$ . Finally, the overturning flow will replace water of temperature  $T_i$  with that of  $T_{j \neq i}$ . These considerations give rise to the following equations of motion for the temperatures of both boxes:

$$\frac{d}{dt}T_1 = -t_r^{-1}(T_1 - \theta_1) - t_d^{-1}(T_1 - T_2) - |Q|(T_1 - T_2), \quad (3.4a)$$

$$\frac{d}{dt}T_2 = -t_r^{-1}(T_2 - \theta_2) - t_d^{-1}(T_2 - T_1) - |Q|(T_2 - T_1). \quad (3.4b)$$

For the case of the salinities, the relaxation to a surrounding reservoir is replaced by a constant salinity flux  $F_i$  into each box. Differences between  $F_1$  and  $F_2$  result from an excess of evaporation over precipitation and river runoff in the equatorial region and an inverse relation in the high northern latitudes. Diffusive and advective transport processes enter the equations of motion as above:

$$\frac{d}{dt}S_1 = F_1 - t_d^{-1}(S_1 - S_2) - |Q|(S_1 - S_2), \quad (3.5a)$$

$$\frac{d}{dt}S_2 = F_2 - t_d^{-1}(S_2 - S_1) - |Q|(S_2 - S_1). \quad (3.5b)$$

Introducing a gradient notation  $A = A_1 - A_2$  and absorbing factors of 2 in the constants  $t_d^{-1}$  and  $k$  the above equations simplify to

$$\frac{d}{dt}T = -t_r^{-1}(T - \theta) - (t_d^{-1} + |Q|)T, \quad (3.6a)$$

$$\frac{d}{dt}S = F - (t_d^{-1} + |Q|)S. \quad (3.6b)$$

It is convenient to rescale the dynamical variables and the time according to

$$x = \frac{T}{\theta}, \quad y = \frac{\beta S}{\alpha \theta}, \quad \tau = t/t_d. \quad (3.7)$$

This gives rise to the dimensionless equations

$$\frac{d}{d\tau}x = -\gamma(x - 1) - (1 + \mu|x - y|)x, \quad (3.8a)$$

$$\frac{d}{d\tau}y = \sigma - (1 + \mu|x - y|)y, \quad (3.8b)$$

where  $\gamma = t_d/t_r$  denotes the ratio between the diffusive time scale and that of the temperature relaxation. The effective freshwater (or salinity) forcing imbalance between high and low latitudes is given by  $\sigma = (\beta F t_d)/(\alpha \theta)$  and  $\mu = \alpha \theta q t_d$  indicates the ratio between the diffusive time scale and the advective time scale  $t_a^{-1} = \alpha \theta q$ .<sup>1</sup> Rescaling also the flow

$$q = Q/(\alpha \theta) = x - y \quad (3.9)$$

yields the steady solutions

$$x^* = \frac{\gamma}{\gamma + 1 + \mu|q^*|}, \quad (3.10a)$$

$$y^* = \frac{\sigma}{1 + \mu|q^*|} \quad (3.10b)$$

---

<sup>1</sup>Notice, that in the formulation provided by Cessi (1994) additional constants express physical quantities such as the box volume or typical meridional length scale. These are omitted here for sake of simplicity. Other formulations of the Stommel–Cessi model additionally take into account different diffusion rates for salinity and temperature (Lohmann et al., 2021).

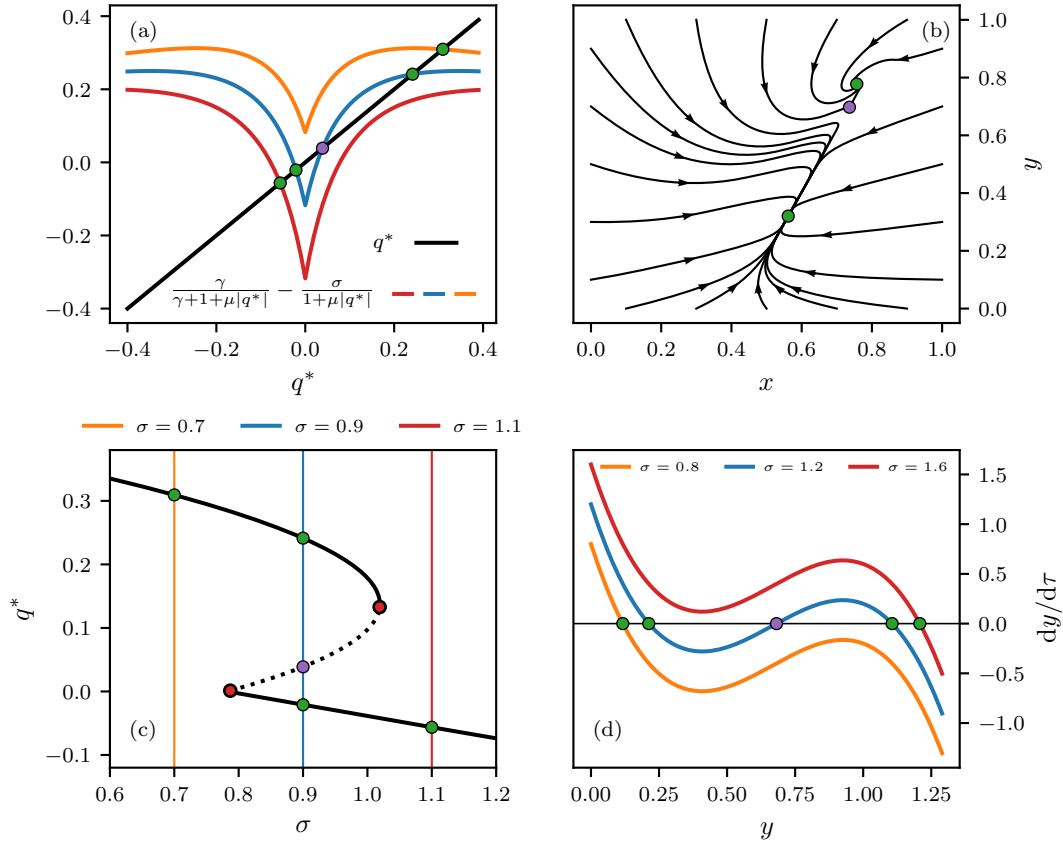


Figure 3.2: Fixed points of the Stommel model. a) red, blue and orange lines display the right side of Eq. (3.11) for  $\sigma = 1.1, 0.9$  and  $0.7$ , respectively. The black line shows the right side of the same equations. Stable solutions of Eq. (3.11) are marked by green dots and unstable ones by violet dots in all panels. b) Phase portrait of the Stommel model for  $\sigma = 0.9$ . c) Bifurcation diagram of the Stommel model. Red dots mark the bifurcation points. d) Temporal derivative of the dimensionless salinity from the Stommel–Cessi model defined by Eq. (3.14) for different values of  $\sigma$ . For all panels,  $\gamma = 3.6$  and  $\mu = 7.5$  were used.

for Eq. (3.8). Inserting these into Eq. (3.9) gives rise to

$$q^* = \frac{\gamma}{\gamma + 1 + \mu|q^*|} - \frac{\sigma}{1 + \mu|q^*|}. \quad (3.11)$$

Figure 3.2a demonstrates graphically that this equation has either three or only a single root, depending of the value of  $\sigma$ . The remaining parameters were set to  $\gamma = 3.6$  and  $\mu = 7.5$  according to [Gottwald \(2021\)](#). These values follow from considerations on the actual configuration in the North Atlantic.

Figure 3.2c shows the resulting bifurcation diagram for  $q^*(\sigma)$ . For low differences in the salinity forcing between the boxes (small  $\sigma$ ), there is only a single stable mode of overturning, with positive surface flow from low to high latitudes. A non-smooth fold bifurcation occurs at around  $\sigma_1 \sim 0.79$ , giving rise to two additional solutions of Eq. (3.11), one being stable and the other being unstable. The additional stable solution is characterized by a reversed flow, i.e. at the surface the water flows from the low the high latitudes. Finally, at  $\sigma_2 \sim 1.02$ , the unstable and the initial stable solution annihilate in a fold bifurcation. For the range of values for  $\sigma$  considered here the flow is consistently stronger in the upper stable branch.

This branch is therefore often referred to as the strong **AMOC** mode as opposed to the weak mode, which labels the lower branch of stable solutions. The strong mode is said to be temperature-driven, because the dimensionless temperature gradient  $x$  exceeds the salinity gradient  $y$ . Reversely, the weak mode is salinity driven.

Physically, starting in the strong operational mode, this model suggests that the **AMOC** undergoes a transition to the weak mode, if the latitudinal gradient in the salinity forcing is increased beyond the second bifurcation point  $\sigma_2$ . In **EMIC** and **GCM** experiments this transition is typically triggered by (unphysically) injecting freshwater into the northern North Atlantic (e.g. [Rahmstorf et al., 2005](#); [Menviel et al., 2014](#); [Jackson et al., 2015](#); [Weijer et al., 2019](#); [Jackson et al., 2023](#)). With respect to future climate tipping scenarios, the concern is that a combination of amplified warming of the polar atmosphere, increasing high-latitude precipitation and elevated meltwater fluxes from the **GrIS** could drive the **AMOC** past this tipping point (e.g. [Bakker et al., 2016](#); [Liu et al., 2017](#); [Wang et al., 2023](#)).

Although a reversal of the flow is not observed in complex models, the analogy is remarkable and demonstrates how simple model equations can help to understand complex climate phenomena. The reversed transition from a weak mode of operation to the strong mode may in the simple model be triggered a decrease of  $\sigma$  past  $\sigma_1$ . Repeated transitions between the two modes of operation are commonly invoked to explain past **DO** variability (e.g. [Lynch-Stieglitz, 2017](#); [Menviel et al., 2020](#)).

Notice also, that the Stommel model locates the upwelling of the bottom flow in the equatorial region. In fact, most of this upwelling happens as far south as the Southern Ocean ([Marshall and Speer, 2012](#); [Manta et al., 2021](#)). Also, the Stommel model is ignorant towards the influence of winds, which actually play an important role in driving the **AMOC** ([Buckley and Marshall, 2016](#)).

Opposed to [Stommel \(1961\)](#), [Cessi \(1994\)](#) assumed a quadratic dependence of the flow on the density gradient

$$q \propto (x - y)^2. \quad (3.12)$$

Furthermore, she assumed a very high temperature relaxation rate and estimated  $\gamma = 3.6 \cdot 10^6$ . The relaxation term's predominance in the temporal evolution of the temperature gradient given by Eq. (3.8a) can then be used to approximate

$$x^* = 1 + \mathcal{O}(\gamma^{-1}) \simeq 1. \quad (3.13)$$

Inserting Eqs. (3.12) and (3.13) into Eq. (3.8b) yields

$$\begin{aligned} \frac{d}{d\tau}y &= \sigma - (1 + \mu(1 - y)^2)y \\ &= -\mu[y^3 - 2y^2 + (1 + \mu^{-1})y] + \sigma. \end{aligned} \quad (3.14)$$

This equation is structurally resembles the generic double-fold model for **CTEs** given by Eq. (2.6). It exhibits two local extremes resulting in a 90° tilted s-shape, and an offset parameter to shift the function globally up or down (c.f. Fig. 3.2d). As a result, the bifurcation structure of the Stommel–Cessi model is given by the classical double-fold bifurcation shown in Fig. 2.2 as is the case for Eq. (2.6).



## 4 Past abrupt climate change: the Dansgaard–Oeschger events

In the history of the Earth, the planet’s climate has repeatedly undergone substantial changes (e.g. [Westerhold et al., 2020](#); [Boers et al., 2022](#)). To assess the implications of human intervention, it is mandatory to understand the dynamics of the climate system. Any theory of climate dynamics must account for the history of the Earth’s climate and explain past changes to a reasonable degree or at least not contradict them. Accordingly, the study of past climate is an integral part of climate system science and the knowledge gained informs modern climate theories and models (e.g. [Haywood et al., 2019](#)). In particular, this reasoning also holds true with respect to climate tipping points (CTPs). There is multiple evidence that the climate has undergone substantial and relatively abrupt changes in the past ([Brovkin et al., 2021](#); [Boers et al., 2022](#)) and one must thus consider the possibility of similar changes in the future. This is all the more true as anthropogenic GHG emissions exert an enormous exogenous forcing that pushes the climate system far away from its pre-industrial equilibrium.

However, assessing past climate dynamics is not straightforward. The study of past climate and in particular of abrupt transitions therein suffers from the fact that instrumental weather records at high spatiotemporal resolution cover only the most recent century if not decades. In order to reconstruct past climatic conditions, researchers draw on climate proxies — physical quantities preserved in so-called proxy archives such as speleothems, tree rings and ice cores. An illustrative example is given by past atmospheric CO<sub>2</sub> concentrations which can be inferred directly by measuring the composition of air bubbles trapped in ancient ice (e.g. [Lüthi et al., 2008](#); [Bereiter et al., 2015](#)). Other proxies which are known to correlate with specific climate variables, can be used for indirect inference of past climatic conditions. For example, the ratios of stable water isotopes ( $\delta^{18}\text{O}$ ) in ice cores from Greenland and Antarctica indicate, at least qualitatively, local air temperature variations at the drilling site and are therefore commonly regarded as a *paleothermometer* ([Dansgaard, 1964](#); [Jouzel et al., 1997](#); [Mook, 2001](#)). The age of the ice and therewith that of the trapped air increases with increasing depth in the core as illustrated in Fig. 4.1. While the ice at the bottom of the Antarctic Dome-C core reaches an age of 800 kyr, Greenland ice cores are constrained to a maximum age of 130 kyr ([Jouzel, 2013](#); [NEEM community members, 2013](#); [Bereiter et al., 2015](#)). Together with a suitable age–depth model (see Section 4.3), measurements taken along the core translate into paleoclimatic time series.

This section introduces the main subject of this thesis: the so-called Dansgaard–Oeschger (DO) events and the millennial-scale climate variability associated therewith. DO events are a series of past abrupt climatic transitions well documented in paleoclimate records. As such, although not yet fully understood, they are of great importance in the field of CTPs. Despite substantial efforts, a conclusive explanation of the physical mechanism of DO events is still lacking. This thesis adds several pieces to the paleoclimatic puzzle and provides important insights for

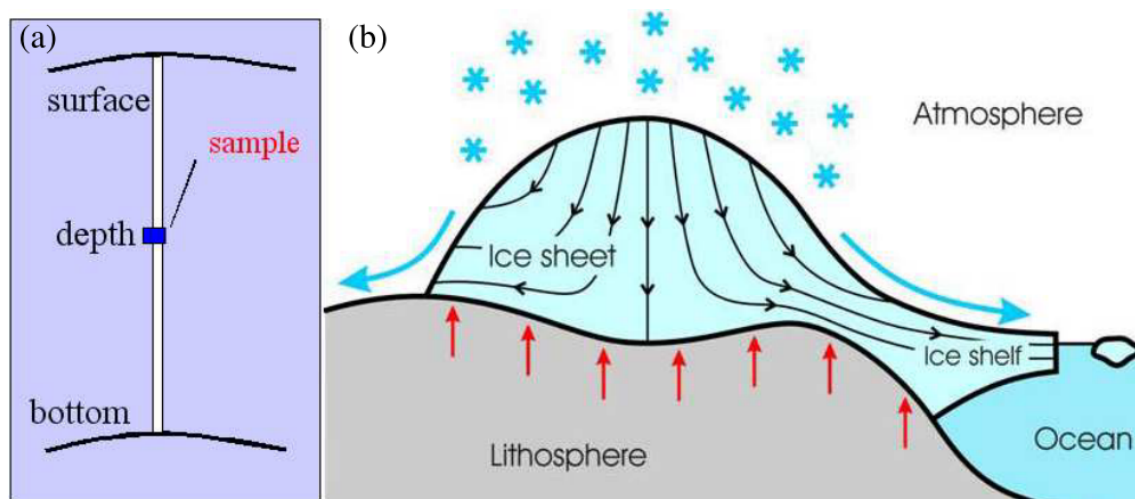


Figure 4.1: Schematic illustration of an ice sheet (b) and an ice core taken from it (a). The snow accumulates at the surface of the ice sheet and transforms into ice at approximately 50–100 m of depth (Kindler et al., 2014). Black arrows in (b) indicate the flow of the ice. Along the core (a) the age of the deposited material increases with increasing depth. Reprinted with permission of John Wiley & Sons - Books, from Placidi et al. (2006), A Critical Review of the Mechanics of Polycrystalline Polar Ice, GAMM–Mitteilungen, vol. 29, p. 80–117, ©2006 WILEY-VCH Verlag GmbH & Co. KGaA, Weinheim; permission conveyed through Copyright Clearance Center, Inc..

the understanding of these past abrupt climatic changes. The following section gives an overview of DO variability and puts the research presented in this thesis into context. On this basis, it will later be discussed in detail how the included publications contribute to the ongoing debate on DO events and the associated climate variability. All publications comprised in this thesis are concerned with DO events and thus each of them gives an individual corresponding introduction to the topic. Here, the focus is laid on the interplay between different levels of modeling and paleoclimate time series analysis in the field.

## 4.1 The proxy evidence

Analyzing the first deep Greenland ice core records that captured the full last glacial interval (also termed the Wisconsin) from Camp Century (Dansgaard et al., 1969) and Dye3 (Dansgaard et al., 1982), Dansgaard et al. (1984) noted ‘*abrupt environment changes in the Wisconsin*’, evident as ‘*large amplitude oscillations of  $\delta^{18}\text{O}$  in both records*’. By that time, the interpretation of stable water isotope ratios ( $\delta^{18}\text{O}$ ) in the ice as a paleothermometer was already established, with higher values of  $\delta^{18}\text{O}$  indicating warmer temperatures at the site and time of the snow deposition, and vice versa (Dansgaard, 1964; Dansgaard et al., 1984). The shifts in the records were thus interpreted as past abrupt warming events over Greenland. Additional evidence from the younger Renland Ice Cap Project (RECAP) (Johnsen et al., 1992b) and European Greenland Ice Core Project (GRIP) removed last doubts that the observed  $\delta^{18}\text{O}$  shifts were, in fact, signatures of substantial climatic changes (Johnsen et al., 1992a; Dansgaard et al., 1993). Nowadays, these abrupt shifts are referred to as Dansgaard–Oeschger (DO) events and they are commonly regarded as the archetype of past abrupt climate change. Figures 1.4c and 4.2a show the

#### 4. Past abrupt climate change: the Dansgaard–Oeschger events

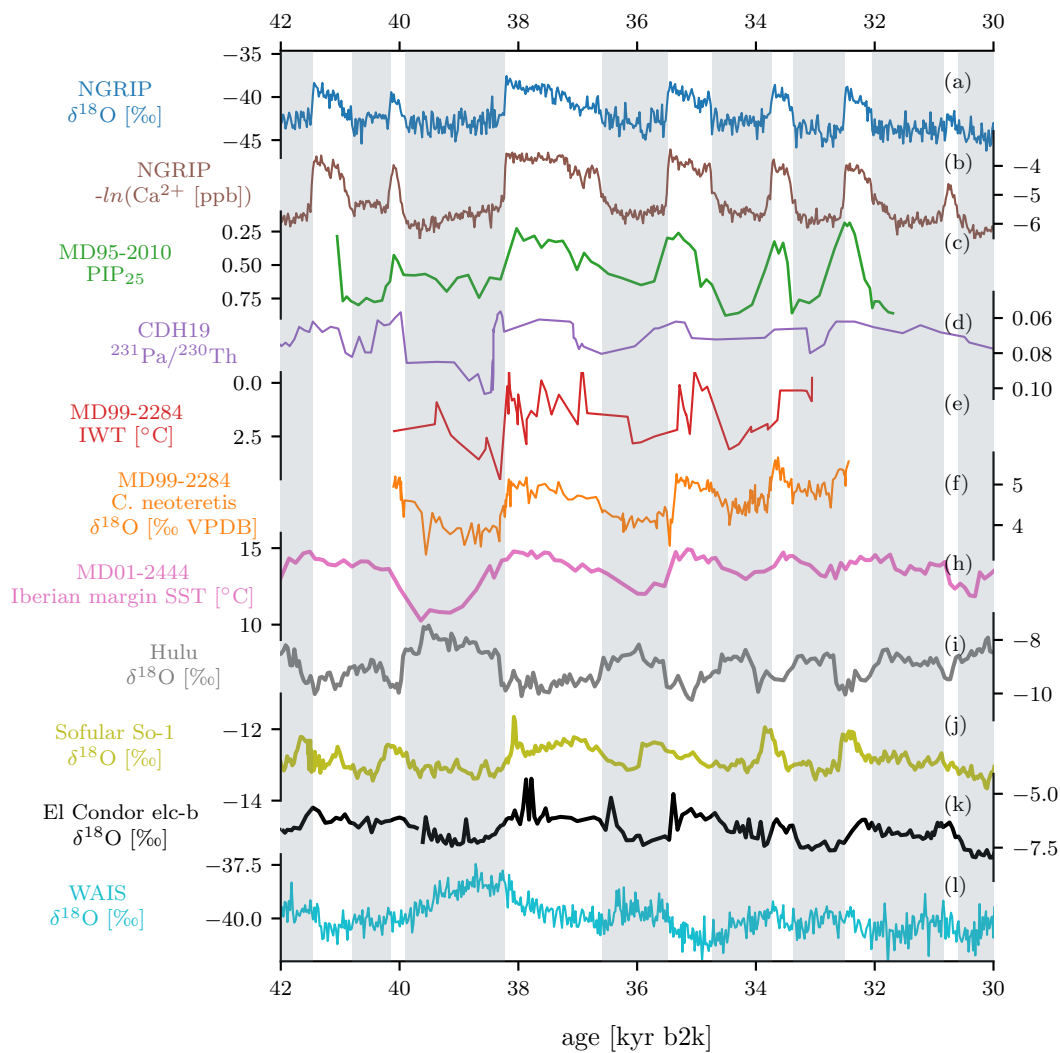


Figure 4.2: Proxy evidence of Dansgaard–Oeschger (DO) variability. a) 20-year mean stable water isotope ratios from the NGRIP ice core (North Greenland Ice Core Project Members, 2004). DO events are manifest as sudden shifts to higher values. b) 20-year mean calcium ion concentrations (negative logarithm) from NGRIP. The calcium is mainly sourced from Asian deserts. High concentrations during stadials indicate dry conditions at the source and efficient transport and deposition (e.g. Fischer et al., 2007; Erhardt et al., 2019). Abrupt decreases at DO events indicate sudden changes in the Asian hydroclimate and the large-scale atmospheric circulation (Ruth et al., 2007; Erhardt et al., 2019). Both time series are available as a supplement to Seierstad et al. (2014). c) PIP<sub>25</sub> index from the Nordic Seas’ marine sediment core MD95-2010 (data supplement to Sadatzki et al., 2020). The index serves as a qualitative sea ice proxy. High values during stadials indicate the presence of perennial sea ice cover and low values during interstadials reflect mostly open waters. d) Protactinium/thorium ratios from the marine core KNR191-CDH19 recovered from the Bermuda rise (Henry et al., 2016b). These ratios are interpreted as a direct measure of the AMOC strength with lower values indicating stronger overturning. The data are available from (Henry et al., 2016a). e) Intermediate water temperature reconstructions from the Nordic Seas marine sediment core MD99-2284 (Sessford et al., 2019) shown here on a revised age–scale (Berben et al., 2020). f) stable water isotope ratios from benthic foraminifera from the same core, originally presented by (Dokken et al., 2013) and shown here on a revised age-scale (Berben et al., 2020). Lower values reflect warmer deep ocean temperatures and vice versa. The data shown in e) and f) are available as supplements to Sadatzki et al. (2020). h) Sea surface temperature reconstructions from the marine sediment core MD01-2444 from the Iberian margin (Martrat et al., 2007a). The data are available from Martrat et al. (2007b). i–k) Speleothem stable water isotope records from the Hulu (China), Sofular (Turkey) and El Condor (Peru) caves, respectively. In all cases changes in  $\delta^{18}\text{O}$  are interpreted as changes in the hydroclimate at the cave location. The Hulu data constitute a composite record and are available as a supplement [last accessed: 09.05.2023] to Cheng et al. (2016). Sofular data [last accessed: 09.05.2023] are provided by Fleitmann et al. (2009a) and were published in conjunction with Fleitmann et al. (2009b). The data from the El Condor cave [last accessed: 09.05.2023] are provided by Cheng et al. (2013a) and have been discussed in Cheng et al. (2013b). l) stable water isotope ratios from the WAIS divide ice core (Buizert et al., 2015a). As for Greenland,  $\delta^{18}\text{O}$  is a qualitative measure for past temperatures in Antarctica. Greenlandic DO events are followed by so-called Antarctic isotopic maxima (AIMs), which indicate a reversal from a warming to cooling trend in Antarctica. An AIM typically lags a corresponding DO event by about 120 years (Svensson et al., 2020). The WAIS divide data are provided as a supplement [last accessed: 09.05.2023] to Buizert et al. (2015a).

record of stable water isotope ratios from the younger and higher resolved NGRIP ice core wherein the DO events appear as a series of sudden transitions from low ( $\sim -45\text{‰}$ ) to high ( $\sim -35\text{‰}$ ) levels of  $\delta^{18}\text{O}$  (North Greenland Ice Core Project Members, 2004; Gkinis et al., 2014). The high resolution and the precise dating of the NGRIP ice core allowed for the inference of typical transition times from cold to milder conditions of less than a century (Steffensen et al., 2008; Erhardt et al., 2019; Capron et al., 2021). Quantifications based on other proxies revealed amplitudes ranging from 5 to 16.5°C of warming (Landais et al., 2005; Huber et al., 2006; Kindler et al., 2014). Judging from Greenland ice core records, the sudden warming events were followed by phases of milder, yet continuously cooling climate termed Greenland interstadials (GIs). GI typically ended with an again relatively abrupt temperature decline back to pre-event levels. The cold and relatively stable conditions persisted until the next DO event would start a new cycle (e.g. Wolff et al., 2010). These phases are called Greenland stadials (GSs) and in succession with GIs they form what is often referred to as DO cycles.

### Nomenclature

This section describes global climate variability associated with DO events and cycles. In the literature, this variability is often referred to as the last glacial's *millennial-scale variability*. Here, the term *DO variability* is used instead for two reasons: Most importantly, the term *DO-variability* emphasizes the causal relationship between the DO events evidenced in Greenland ice cores and corresponding coherent changes found in remote archives across the globe. Further, the time scale of this variability varied considerably. Over the course of the last glacial several DO cycles observed in Greenland ice core records lasted less than 1,000 years (e.g. the cycles comprised of GI and GS 15.1, 15.2, 16.2 or 23.2), while others exceeded 6,000 years in duration such (e.g. the cycles 25, 23.1 or 2.1) (compare Rasmussen et al., 2014).

The labeling of GI and GS used in this thesis strictly follows Rasmussen et al. (2014). Furthermore, the terms *Greenland stadial* and *Greenland interstadial* shall strictly refer to the two climatic regimes and according time intervals that can be identified in Greenland ice core records on the corresponding ice core chronology. If used without *Greenland*, the terms *stadial* and *interstadial* refer more generally to the global climatic conditions during corresponding intervals.

Numerous proxy records from outside of Greenland show abrupt transitions which are causally related to the DO events evidenced in Greenland ice core records. For ease of language, such transitions will also be referred to as DO transitions or DO events, although formally, the term is reserved for the events seen in Greenland ice core records.

The  $\delta^{18}\text{O}$  records from Greenland ice cores are by far not the only proxy data to bear the signature of DO variability (c.f. Fig. 4.2). First, other proxies from Greenland ice cores covary with  $\delta^{18}\text{O}$  and show the same abrupt shifts at the beginning of GIs. These include among others concentrations of dust, calcium and sodium, the so-called deuterium excess, methane or the annual layer thickness (Fuhrer et al., 1999; Ruth et al., 2003; Masson-Delmotte et al., 2005; Ruth et al.,

2007; Baumgartner et al., 2014; Erhardt et al., 2019; Capron et al., 2021). Second, proxy records from remote archives such as cave speleothems and marine or lake sediment cores also show variability in phase with the ice core evidence (Corrick et al., 2020; Menviel et al., 2020, and references therein). In rough terms, the concomitant shifts in these proxies provide evidence that the DO events were not limited to sudden local warming over Greenland but instead were accompanied by substantial changes in other parts of the climate system. In particular major reorganizations of the atmospheric circulation at DO events are encoded in dust concentration records (Ruth et al., 2007; Erhardt et al., 2019, e.g.). These large-scale atmospheric circulation changes are confirmed by sudden shifts in speleothem data from tropical monsoon regions (Wang et al., 2001; Kanner et al., 2012; Cheng et al., 2013b, 2016; Zhang et al., 2017; Corrick et al., 2020). Even Southern Hemisphere mid-latitude storm tracks are supposed to have changed concomitantly (Markle et al., 2017; Buizert et al., 2018). Marine sediment cores document a sudden retreat of sea ice in the Nordic Seas and the Labrador Sea in concert with DO events. They further reveal changes in the oceanic stratification in phase with Greenland ice core's DO cycles (Rasmussen et al., 1996; Rasmussen and Thomsen, 2004; Dokken et al., 2013; Ezat et al., 2014; Rasmussen et al., 2016; Hoff et al., 2016; Sadatzki et al., 2020; Scotto and Sadatzki, 2022). Rainfall and temperature reconstructions from Europe and the Mediterranean likewise show the imprint of DO cycles with colder and drier conditions prevailing over most of Europe during stadials (e.g. Genty et al., 2003; Fleitmann et al., 2009b; Budsky et al., 2019; Menviel et al., 2020). Ice core records from Antarctica reveal a phenomenon known as the bipolar seesaw (Stocker and Johnsen, 2003; Buizert et al., 2015a; Pedro et al., 2018): During stadials Antarctica typically was subject to a warming trend which reversed shortly after a Greenland DO event. When the subsequent interstadial in the North Atlantic region ended, the cooling trend in Antarctica turned into a warming trend again.

Already in 1985 Broecker et al. hypothesized that the changes in the Arctic atmospheric temperatures could be related to changes in the thermohaline ocean circulation and in particular the Arctic deep water formation. Indeed, much of the reconstructed global variability associated with DO cycles aligns remarkably well with switches between a weak and strong mode of operation of the AMOC as introduced in Sect. 3 (e.g. Lynch-Stieglitz, 2017; Menviel et al., 2020). While evidence for such switches remained elusive for a long time, indications for reduced and shallower overturning during stadials and AMOC reinvigoration in synchrony with DO events have accumulated from the study of marine sediment cores (Böhm et al., 2015; Gottschalk et al., 2015; Henry et al., 2016b; Lynch-Stieglitz, 2017). Today, a close relation between DO variability and AMOC strength has become widely accepted and is consistently confirmed by most recent GCM results (e.g. Vettoretti and Peltier, 2018; Zhang et al., 2021; Malmierca-Vallet et al., 2023). A complete shutdown of the AMOC is suggested to have occurred only during so-called Heinrich stadials, i.e. stadials which were accompanied by massive discharges of icebergs from the Laurentide ice sheet (Heinrich, 1988; Bond et al., 1992; Hemming, 2004). Several authors suggest that Heinrich and DO events are in fact physically entangled (Bond et al., 1993; Schulz et al., 2002; Clark et al., 2007; Rousseau et al., 2022, e.g.). Yet, this thesis focuses exclusively on DO events and DO variability, with the argument that Heinrich events likely modulated DO

cycles only quantitatively but not qualitatively.

In summary, while the expression of DO variability was strongest in the North Atlantic region, its impact was felt globally. Most likely, DO events comprised major changes in both oceanic and atmospheric circulations, that reallocated the heat fluxes between the Hemispheres. During stadials, the North Atlantic and in particular the European climate was dictated by the reduced northward oceanic heat transport associated with the weak Atlantic meridional overturning. Generally colder and drier conditions prevailed over Europe and the Mediterranean and substantial sea ice cover was present in the Nordic Seas and the northern North Atlantic. In turn, the South Atlantic region experienced a mild warming trend. As a consequence of the redistribution of heat, the Intertropical convergence zone was shifted southward during stadials, impacting in particular precipitation patterns in the tropical monsoon regions. For a comprehensive overview of the global expression of DO variability, please see the review by Menviel et al. (2020). The overall picture that emerges from the combined proxy record reveals dramatic changes in different ESCs that are consistent with one another. However, the available information is too coarse-grained to decipher the underlying physical (trigger) mechanisms with certainty. The study of past climate processes is ultimately limited by the lack of comprehensive data. It is the goal of paleoclimate research to extract the maximum amount of information from available proxy data and to provide the most plausible theory for past climate dynamics in light of these. This thesis contributes to this endeavor by following two approaches that be explained in the next two sections. On the one hand, it assumes the perspective of dynamical systems to explore the climate dynamics of DO variability and on the other hand, it uses Bayesian methods to draw inference on the actual course of DO events.

## 4.2 The dynamical systems view

The previous section summarized the knowledge of DO variability gained from paleoclimate proxy records. The ‘proxy perspective’ is complemented by numerous modeling studies, that contributed substantially to the prevailing physical conception of DO variability. For the context of this thesis, it is important to understand the interplay between models and proxy data analysis. The achievements of modeling studies shall be illustrated by means of a few prominent examples, wherein contributions from the three types of models will be distinguished: conceptual models, EMICs and GCMs.

Conceptual modeling can be understood as the translation of physical considerations into mathematical equations, i.e., commonly into (random) dynamical systems, as demonstrated in Sect. 3. The resulting low-dimensional models are tractable and thus useful to formulate and test the plausibility of hypotheses DO variability. As such they have played an important role in streamlining the debate. E.g. the aforementioned consideration by Broecker et al. that related GS and GI observed in Greenland ice core records to different states of the thermohaline circulation drew on the theoretical prediction of two stable modes of operation derived from conceptual climate models (Stommel, 1961; Rooth, 1982). Most proposed models targeting DO variability cluster around one of the following two

paradigms:

- a) **General bi- or multi-stability of the glacial climate in the North Atlantic region.** Several studies investigate the hypothesis that transitions between stadial and interstadial climate were stochastic transitions between two (or more) stable states of the North Atlantic climate system (e.g. Ditlevsen, 1999; Timmermann and Lohmann, 2000; Ditlevsen et al., 2005, 2007; Livina et al., 2010; Kwasniok, 2013; Mitsui and Crucifix, 2017; Lohmann and Ditlevsen, 2019).
- b) **Self-sustained (relaxation) oscillation.** Many studies invoke models that feature self-sustained oscillations of the thermohaline oscillation to explain DO variability (Winton, 1993; Sakai and Peltier, 1999; Timmermann et al., 2003; Saha, 2015; Vettoretti et al., 2022). Other studies draw on more abstract oscillatory models such as the FitzHugh–Nagumo (FHN) model (FitzHugh, 1961; Nagumo et al., 1962) which might be less physically grounded, but still provide useful insights into the general DO cycle dynamics (e.g. Rial and Saha, 2011; Kwasniok, 2013; Mitsui and Crucifix, 2017; Roberts and Saha, 2017; Lohmann and Ditlevsen, 2019, and P1)

Many of the above-mentioned studies also explore a coupling of the corresponding models to slowly changing climate background conditions, be it orbital insolation variations, changing atmospheric CO<sub>2</sub> or the waxing and waning of ice sheets. Such a coupling transforms the otherwise autonomous (random) dynamical systems into non-autonomous systems and may give rise to more sophisticated phenomena. These include stochastic resonance (Alley et al., 2001; Vélez-Belchí et al., 2001), a changing number of stable state (Livina et al., 2010; Cimatoribus et al., 2013; Mitsui and Crucifix, 2017) or even switches between residence in a stable fixed point and oscillation via transient crossing of a Hopf bifurcation as discussed in P1 (Vettoretti et al., 2022). Somewhat simpler, external forcing may also be used to modulate cycle durations or amplitudes in conceptual models (e.g. Roberts and Saha, 2017, and similarly P2). Conceptual modeling often goes hand in hand with time series analysis e.g. by tuning the model's summary statistics to those derived from the data (e.g. Lohmann and Ditlevsen, 2019; Boers et al., 2022).

In this thesis, P1-3 assume a dynamical systems perspective on paleoclimate in general and the DO variability of the last glacial in particular and follow the line of research sketched above. P1 presents the fundamental concepts of dynamical system theory (including non-autonomous and random dynamical systems) and traces how it shaped the understanding of glacial–interglacial cycles and DO variability. The study introduces the notion of pullback attractors and demonstrates how external forcing may substantially enrich the variability of a given system in the presence of non-linearities. It furthermore illustrates these theories in form applications: an FHN model is used to mimic the  $\delta^{18}\text{O}$  record from the NGRIP ice core and the pullback attractor of a simple glacial cycle model driven by the changing orbital insolation forcing is analyzed.

P2 follows a strict modeling approach and proposes a somewhat new paradigm for DO variability, namely that of noise-induced excitation. It models interstadials as prolonged transient state space excursions that occur in response to supercritical perturbations of a stable stadial state. A similar excitation mechanism was already

studied by [Timmermann et al. \(2003\)](#) but as part of a coherence resonance framework for [DO](#) variability. **P2** draws on  $\alpha$ -stable noise to generate rare and strong perturbations that can excite the system. The presence of an  $\alpha$ -stable component in Greenland ice core records was demonstrated by [Ditlevsen \(1999\)](#) and further explored by [Gottwald \(2021\)](#) in a modeling study. The model's excitation path is shaped by the different time scales introduced for the variables that represent ocean, sea ice and atmospheric dynamics. A coupling to a proxy record of past global ice volume aligns the frequency of simulated [DO](#) events with that inferred from proxy observation, in a transient simulation of the last glacial interval.

Finally, **P3** investigates the combined  $\delta^{18}\text{O}$  and dust concentration record from the [NGRIP](#) ice core from a random dynamical systems perspective. The study regards the bivariate record as the outcome of a Markovian stochastic process and reconstructs the deterministic drift in the two-dimensional state space by estimating the corresponding Kramers–Moyal ([KM](#)) coefficients. This approach does not require any upfront model specification beyond [Eq. \(2.10\)](#) but has the drawback that it is applicable only for time-homogeneous dynamics. Hence, the analysis was applied only to a selected time window from the last glacial interval and is by design not suited to assess the effects of changing background conditions.

Conceptual models have arguably shaped the prevailing conception of [DO](#) variability. However, their explanatory power is limited and they cannot prove or falsify hypotheses on the physics of [DO](#) variability with certainty.<sup>1</sup> The next more complex category of climate models are so-called Earth system models of intermediate complexity ([EMICs](#)). As opposed to conceptual models, these are anchored in the partial differential equations that govern atmospheric and oceanic dynamics and usually obey physical conservation laws. The low spatial and temporal resolution of these models allows for simulating long physical time spans like the last glacial interval. Even if neither [EMICs](#), nor the next more complex [GCMs](#) were deployed for this thesis, their role in the study of [DO](#) events along the hierarchy of model shall be illustrated here by giving several examples.

By means of the [EMIC CLIMBER-2](#) [Ganopolski and Rahmstorf \(2001\)](#) demonstrated that the glacial [AMOC](#) could indeed switch between three modes of operation in response to prescribed quasi-periodic changes in freshwater forcing. Apparently, in their simulation [DO](#) events are triggered by short-lived crossings of a bifurcation point from higher to lower freshwater influx into the North Atlantic. Corresponding temporary reinvigorations of the [AMOC](#) entail a warming of the North Atlantic region at least in qualitative agreement with the proxy record. Using a different [EMIC](#), [Meniel et al. \(2014\)](#) showed in greater detail that forced [AMOC](#) switches could explain many features of the global [DO](#) variability, including the abrupt Greenland warming events, changes in global precipitation patterns and the bipolar seesaw. These authors hypothesize that the control of the freshwater flux into the North Atlantic is exerted by ice sheet dynamics, whose growth yields net negative freshwater forcing while their surging results in freshwater pulses into the North Atlantic. Both studies constitute important contributions and their results starkly corroborate the importance of the [AMOC](#) in the emergence of [DO](#) variability. Their explanatory power is constrained by the fact that the trigger

<sup>1</sup>For a given paleoclimate observation, one can only ever try to narrow down the set of possible explanation and find the most plausible one. A comprehensive *proof* can certainly never be given.

for the simulated DO events is imposed externally by prescribed changes in the freshwater flux.<sup>2</sup> Note that under specific boundary conditions, the LOVECLIM model used by Menviel et al. may also exhibit self-sustained oscillations of the AMOC (Friedrich et al., 2010).

A reproduction of DO events by means of comprehensive GCMs with glacial climate boundary conditions was not achieved until recently (Vettoretti and Peltier, 2018; Peltier and Vettoretti, 2014; Zhang et al., 2014). Today, a growing number of model simulations show promising similarity with the paleoclimate proxy evidence of DO cycles including changes in the strength of the AMOC. (Zhang et al., 2021; Vettoretti et al., 2022; Kuniyoshi et al., 2022; Izumi et al., 2023; Malmierca-Vallet et al., 2023). Importantly, in these simulations, DO-like abrupt events occur spontaneously and do not rely on externally prescribed freshwater forcings. Consensus appears to exist among these models regarding the pivotal role of the salt-advection feedback in the North Atlantic in driving the oscillatory behavior of the AMOC.

The essential task for the upcoming years will be a meticulous investigation of the model output: First, the simulations must pass a benchmarking procedure in terms of a detailed model–data comparison on the basis of available proxy records potentially supplemented by EMIC model output. In a second step, the dynamical mechanism that generates abrupt climatic changes in the models needs to be identified and understood. Both processes will be guided by the understanding of DO variability that has emerged from the rich history of paleoclimate time series analysis, conceptual modeling and EMIC-based paleoclimate modeling. Both the methods and the results presented in this work suggest possible approaches for the investigation of GCM simulations of DO variability that will be detailed in Sect. 7.1. If the model output can be reconciled with the proxy evidence and if underlying mechanisms for DO variability are physically plausible and consistent across the different models, then this will be a big step forward in climate modeling. To bridge back to CTP, if specific features or parameterizations can be identified in GCMs that enable the reproduction of past abrupt climate changes, then the effects of these model configurations should also be explored with respect to future climate projections. These configurations could impact the stability of the AMOC under global warming scenarios in GCMs and ESMs. Eventually, these activities facilitate a more robust risk assessment with respect to a potential AMOC tipping event.

---

<sup>2</sup>Whereas Ganopolski and Rahmstorf (2001) introduced the freshwater flux variations more or less ad-hoc, Menviel et al. (2014) relate these to according proxy records and thus obtain a high level of consistency in the study design.

### 4.3 Uncertainty-sensitive inference

The previous section placed P1-3 in their specific research context. This section will introduce the background of P4-5 in a similar manner. P1-3 all attempt to express past climate dynamics in terms of stochastic or ordinary differential equations (ODEs). P4-5 follow strictly data-driven approaches and primarily aim at better constraining past climate phenomena as opposed to explaining them.

As described in Section 4.1, DO events are comprised of a number of concomitant sudden changes in several ESCs. E.g., it is widely accepted that the warming events detected in Greenland ice cores are accompanied by abrupt changes in precipitation patterns in the tropical monsoon regions that are evident as sudden changes in the isotopic composition of corresponding speleothem records (Wang et al., 2001; Kanner et al., 2012; Zhang et al., 2017; Corrick et al., 2020). The question that arises is, whether the low-latitude precipitation changes are a cause or a consequence of the high-latitude warming events. Assuming a data-driven perspective, this question translates into the question, which of the different paleoclimate time series that reflect these changes first undergoes a corresponding abrupt transition associated with a DO event.

More generally speaking, P4 is concerned with the inference of the sequence of abrupt changes in different ESC at DO events by investigating the phasing of corresponding transitions in the available proxy record. If a characteristic sequence of events could be identified that is consistent across all DO events, this would provide important boundary conditions for hypotheses on the emergence of DO events. In particular, deciphering the sequence of transitions in spatially distributed ESCs at DO events would reveal the spatiotemporal propagation of the climate signal.

In the same context, P5 provides an associated preparatory work by reassessing the age-scale of the NGRIP ice core. It provides a method to rigorously propagate the associated dating uncertainty while reducing it at the same time. Both aspects facilitate improved comparability of the ages of DO events as inferred from the NGRIP record with their counterparts from remote archives.

To date, the only temporal order of DO-related climatic changes that has been firmly established is that of the bipolar seesaw: The change from a warming to a cooling trend in Antarctica is estimated to lag behind the sudden warming in Greenland by about 120 years which is in line with an oceanic propagation of the climate signal (Svensson et al., 2020; Buizert et al., 2015a). Beyond that, the inference of a characteristic temporal sequence of events from available paleoclimate data is hampered by the following obstacles:

- **Dating uncertainties.** The measurement of proxy variables is accompanied by a corresponding dating procedure, wherein the depositional age of the measured sample is estimated. However, the assigned ages are subject to substantial uncertainties and the relative dating uncertainties between different archives are often times larger than physically expected temporal lags between DO transitions in different ESCs.
- **Dependent dating.** Important marine sediment records that evidence DO transitions for example in the AMOC strength or the Nordic Seas' sea ice cover are not independently dated. That is, their age-scales are at least

in parts tuned to the Greenland Ice Core Chronology 2005 (GICC05) — a chronology for Greenland ice cores (Rasmussen et al., 2006; Vinther et al., 2006; Andersen et al., 2006; Svensson et al., 2008) — by an alignment of DO related abrupt shifts (Henry et al., 2016b; Sadatzki et al., 2020; Berben et al., 2020). Clearly, the inference of leads and lags between previously aligned transitions is not meaningful. In contrast, speleothem records are dated radiometrically and thus independently, which makes transitions in speleothem records suited for comparison with those in Greenland ice cores.

- **Temporal resolution.** Many records that show DO-related shifts have only low temporal resolution on the order of tens to hundreds of years (c.f. Fig. 4.2). Sometimes the transition happens from one data point to the next. In that case, the age of the transition can only be constrained to the interval between the two data points.
- **Transition detection.** Even in records with temporal resolution on the order of years such as the NGRIP  $\delta^{18}\text{O}$  records, the estimation of the exact transition age is not trivial. Erhardt et al. (2019) have provided a suitable method to infer Bayesian posterior distributions for transition onsets in noisy time series. Application to DO events in ice core records, however, yielded uncertainties that are comparable to physically plausible temporal lags between transitions in different climate subsystems.

Several attempts have been made to place the evident changes that occur in different ESC at DO events in a consistent temporal order. A recent study concludes that climatic shifts in the tropical monsoon region occurred in synchrony with Greenlandic DO events (Corrick et al., 2020). The combination of positive and negative temporal lags observed for different DO events further suggest that neither is the driver of the other, but that instead both abrupt changes have a common external trigger which could possibly lie in AMOC reinvigorations.

The overall assessment that low- and high-latitude abrupt changes occurred in synchrony has previously also been reported by Adolphi et al. (2018). However, these authors base their conclusions on age estimates for both Greenlandic DO events and their low-latitude speleothem counterparts that are younger and therefore inconsistent with the ages used by Corrick et al. (2020). These discrepancies showcase that the topic remains controversial and that further research is required to reconcile contradictory results. In both studies synchrony could only be attested within the limits of relative dating uncertainties. Hence, lead-lag relationships on the order of decades cannot be ruled out. In the context of climate tipping dynamics, however, decadal-scale leads and lags between spatially distant events do not seem implausible, in particular in situations where a climate signal is mediated by the atmosphere (Markle et al., 2017; Buizert et al., 2018; Svensson et al., 2020).

To understand the contribution of P4 to the debate on leads of lags, some further context is required. First, in order to avoid inter-archive dating uncertainties, several studies investigated the relative phasing of transitions in so-called multi-proxy records from Greenland ice cores (Steffensen et al., 2008; Erhardt et al., 2019; Capron et al., 2021). In ice cores, alongside with  $\delta^{18}\text{O}$  commonly other proxies such as dust or sodium concentrations are measured which exhibit similarly

abrupt shifts concomitant with  $\delta^{18}\text{O}$ -indicated DO events. The individual proxies have different climatological interpretations, but they share the same age–depth relationship. This allows to assess the relative phasing between abrupt transitions in different ESCs free of relative dating uncertainty. For example, changes in dust concentrations are commonly interpreted as indications of large-scale atmospheric reorganizations (Fuhrer et al., 1999; Fischer et al., 2007; Ruth et al., 2007; Erhardt et al., 2019).<sup>3</sup> Accordingly, a consistent lead of the dust transition with respect to the  $\delta^{18}\text{O}$  transitions across DO events would hint at an atmospheric trigger of these events. Using a mathematically sound Bayesian inference scheme, Erhardt et al. (2019) compared transition onsets from several DO events between different proxy variables and concluded

*‘[...] that the collapse of the North Atlantic sea-ice cover may not be the initial trigger for the DO events and [...] that synoptic and hemispheric atmospheric circulation changes started before the reduction of the high-latitude sea-ice cover that ultimately coincided with the Greenland warming.’ (Erhardt et al., 2019)*

However, P4 reassesses the Bayesian posterior distributions of the proxy-transition onsets and shows that the attested lag is not statistically significant, if uncertainties are rigorously propagated.

Finally, the contribution of P5 to the assessment of the spatiotemporal evolution of DO events is an indirect one whose benefits still remain to be exploited. It presents a statistically inspired new age–depth model for the NGRIP ice core that brings two major advantages. First, it allows for a mathematically consistent generation of ensembles of chronologies. Such ensembles are commonly used for rigorous propagation of the dating uncertainty to any subsequent analysis. Prior to the publication of P5, it was not per se clear how correlations in the dating uncertainties should be treated, due to the particularities of the NGRIP age-scale. Second, at the same time, this age–depth model narrows down the chronology’s cumulative dating uncertainty. Due to its extraordinary high resolution, the NGRIP record has a pivotal role in the paleoclimate puzzle of leads and lags around DO events and P5 places it on a uncertainty-sensitive yet less uncertain age-scale. Taken together, P5 paves the way for a comprehensive (re)assessment of leads and lags between DO transitions evidenced in the NGRIP records and that observed in remote independently dated archives.

---

<sup>3</sup>Calcium ions are a central component of the dust and thus calcium ion concentrations and dust concentrations are to some degree treated equivalently (Erhardt et al., 2019).

# 5 DO events from the perspective of dynamical systems

## P1 Orbital insolation variations, intrinsic climate variability, and Quaternary glaciations

**Keno Riechers**, Takahito Mitsui, Niklas Boers, & Michael Ghil, 2022. *Climate of the Past*, 18, 863-893. DOI: 10.5194/cp-18-863-2022

**Copyright.** The article is published open access under the terms of the [Creative Commons Attribution 4.0](#) license. The copyright remains with the authors.

**Contribution.** MG conceived and designed the study. KR and TM carried out the major part of the article's new research in close interaction with MG and NB. All authors interpreted and discussed the results and wrote the manuscript.

Clim. Past, 18, 863–893, 2022  
<https://doi.org/10.5194/cp-18-863-2022>  
 © Author(s) 2022. This work is distributed under  
 the Creative Commons Attribution 4.0 License.



## Orbital insolation variations, intrinsic climate variability, and Quaternary glaciations

Keno Riechers<sup>1,2</sup>, Takahito Mitsui<sup>2,3</sup>, Niklas Boers<sup>2,3,4</sup>, and Michael Ghil<sup>5,6</sup>

<sup>1</sup>Department of Mathematics and Computer Science, Freie Universität Berlin, Berlin, Germany

<sup>2</sup>Potsdam Institute for Climate Impact Research, Potsdam, Germany

<sup>3</sup>Earth System Modelling, School of Engineering & Design, Technical University of Munich, Munich, Germany

<sup>4</sup>Department of Mathematics and Global Systems Institute, University of Exeter, Exeter, UK

<sup>5</sup>Geosciences Department and Laboratoire de Météorologie Dynamique (CNRS and IPSL),

Ecole Normale Supérieure and PSL University, Paris, France

<sup>6</sup>Department of Atmospheric and Oceanic Science, University of California at Los Angeles, Los Angeles, USA

**Correspondence:** Keno Riechers (riechers@pik-potsdam.de)

Received: 8 October 2021 – Discussion started: 14 October 2021

Revised: 1 March 2022 – Accepted: 3 March 2022 – Published: 21 April 2022

**Abstract.** The relative role of external forcing and of intrinsic variability is a key question of climate variability in general and of our planet’s paleoclimatic past in particular. Over the last 100 years since Milankovic’s contributions, the importance of orbital forcing has been established for the period covering the last 2.6 Myr and the Quaternary glaciation cycles that took place during that time. A convincing case has also been made for the role of several internal mechanisms that are active on timescales both shorter and longer than the orbital ones. Such mechanisms clearly have a causal role in Dansgaard–Oeschger and Heinrich events, as well as in the mid-Pleistocene transition. We introduce herein a unified framework for the understanding of the orbital forcing’s effects on the climate system’s internal variability on timescales from thousands to millions of years. This framework relies on the fairly recent theory of non-autonomous and random dynamical systems, and it has so far been successfully applied in the climate sciences for problems like the El Niño–Southern Oscillation, the oceans’ wind-driven circulation, and other problems on interannual to interdecadal timescales. Finally, we provide further examples of climate applications and present preliminary results of interest for the Quaternary glaciation cycles in general and the mid-Pleistocene transition in particular.

### 1 Introduction and motivation

In the early 20th century, Milutin Milankovic presented his theory of ice ages (Milankovitch, 1920). Based on his own calculations and on insightful suggestions from Wladimir Köppen and Alfred Wegener (Imbrie and Imbrie, 1986), he proposed that the transitions between glacial and interglacial climate conditions were primarily caused by variations of incoming solar radiation, which by that time was known to vary in a quasi-periodic manner on slow timescales of tens of thousands to hundreds of thousands of years (Poincaré, 1892–1899). These variations of insolation, which arise as a consequence of the gravitational interaction of the Earth with the other planets and with its own Moon, are typically referred to as orbital forcing.

The orbital forcing comprises variations in (i) the eccentricity of the Earth’s orbit around the sun with dominant spectral peaks around 400 and 100 kyr; (ii) the obliquity, or axial tilt, i.e., the angle between the Earth’s rotational and its orbital axis, with dominant periodicity around 41 kyr; and (iii) the climatic precession, which determines the phase of the summer solstice along the Earth’s orbit and has its most pronounced spectral power around 23 and 19 kyr (Berger, 1978).

For 2 centuries or so of modern geology, records of our planet’s physical and biological past were merely discrete sequences of strata with specific properties, like coloration

and composition (Imbrie and Imbrie, 1986). This state of affairs led, after the initial success of the Milankovitch (1920) theory of the ice ages, to severe criticism of the temporal mismatch between insolation minima and glaciation maxima (e.g., Flint, 1971).

The advent of marine-sediment cores after World War II led, for the first time, to the availability of records that were more or less continuous in time. Like all climate records, these cores covered limited time intervals and did so with limited resolution and with inaccuracies in absolute dating, as well as in the quantities being measured. Moreover, they posed the problem of inverting proxy records of isotopic and microbiotic counts to physical quantities like temperature and precipitation.

In spite of these limitations, the spectral analysis of deep-sea records allowed Hays et al. (1976) to overcome the difficulties previously encountered by the orbital theory of Quaternary glaciations, in particular the absence of the imprint of precessional and obliquity peaks in glaciation proxy records. Specifically, Hays et al. (1976) were able to create a composite record – back to over 400 kyr b2k, i.e., over 400 000 years before the year 2000 CE – from two relatively long marine-sediment records of the best quality available in the early 1970s. The authors demonstrated therewith that significant precessional and obliquity peaks near 20 and 40 kyr were present in this record's spectral analysis; see Fig. 1. The power spectrum in the figure also made it quite clear that these peaks were superimposed on a continuous background – the stippled area in the figure – whose total variance much exceeded the sum of the variances present in the peaks.

The work of Hays et al. (1976) and of the subsequent CLIMAP and SPECMAP projects resulted in a much more detailed spatiotemporal mapping of the Quaternary and extended the belief in the pacemaking role of orbital variations into the more remote past. The spectral peaks near 20 and 40 kyr have been widely interpreted within the geological community as evidence for a linear response of the climate system to the orbital forcing (Imbrie and Imbrie, 1986). A third spectral peak at 100 kyr was, however, the most pronounced but much more difficult to reconcile with the orbital theory of Quaternary glaciations. Since no sufficiently pronounced counterpart can be found in the spectra of the seasonal insolation forcing, Hays et al. (1976) hypothesized a nonlinear response of the climate system in order to explain this dominant periodicity of the Late Pleistocene glacial–interglacial cycles. At the same time, the advent of higher-resolution marine cores and especially ice cores from both Greenland and Antarctica, led to the discovery of Heinrich events (Heinrich, 1988), Dansgaard–Oeschger (D–O) events (e.g., Dansgaard et al., 1993), and Bond cycles (Bond et al., 1997), which were hard to explain by orbital forcing given their shorter timescales.

In fact, interest in past climates was heightened not only by these striking observational discoveries but also by the growing concerns about humanity's impact on the climate (SMIC,

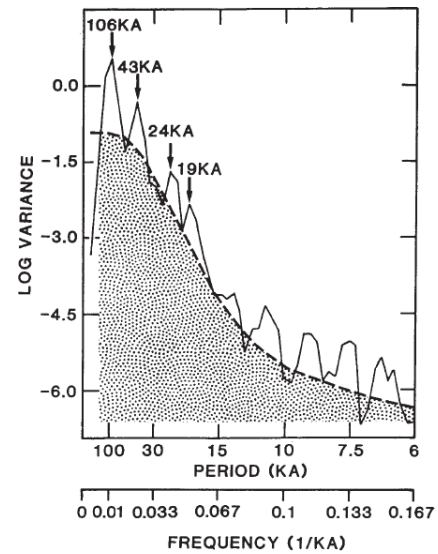


**Figure 1.** Power spectrum of a composite  $\delta^{18}\text{O}$  record using deep-sea cores RC11-120 and E49-18. This figure is based on the work of Hays et al. (1976), as presented by Imbrie and Imbrie (1986). Reprinted by permission from Springer Nature Customer Service Centre GmbH: Springer Nature. Topics in Geophysical Fluid Dynamics: Atmospheric Dynamics, Dynamo Theory, and Climate Dynamics by Ghil and Childress (1987), © 1987 by Springer Science+Business Media New York. All rights reserved. 1987.

1971; National Research Council, 1975). Given the declining temperatures between the 1940s and 1970s, on the one hand, as shown in Fig. 2 (see also Ghil and Vautard, 1991, Fig. 3), and the substantial advances in the description of the Quaternary glaciations, on the other hand, it is clear that interest was mainly on the planet's falling into another ice age (e.g., National Research Council, 1975).

As a result of the twofold stimulation provided by data about past glaciations and concern about future ones, a number of researchers in the early-to-mid 1970s worked on energy balance models (EBMs) of climate with multiple stable steady states (Held and Suarez, 1974; North, 1975; Ghil, 1976). Two such stable “equilibria” corresponded to the present climate and to a “deep-freeze”, as it was called at the time, i.e., to a totally ice-covered Earth. At the time there was some disbelief about this second climate, as its calculated temperatures were much lower than those associated with the Quaternary glaciations and incompatible with paleoclimatic evidence available in the 1970s.

New geochemical evidence, however, led in the early 1990s to the discovery of a “snowball” or, at least, “slushball” Earth prior to the emergence of multicellular life, sometime before 650 Myr b2k (Hoffman et al., 1998). It thus turned out that this climate state – predicted by several EBMs and confirmed by a general circulation model (GCM) with much higher spatial resolution (Wetherald and Manabe, 1975) – had actually occurred and is now being modeled in

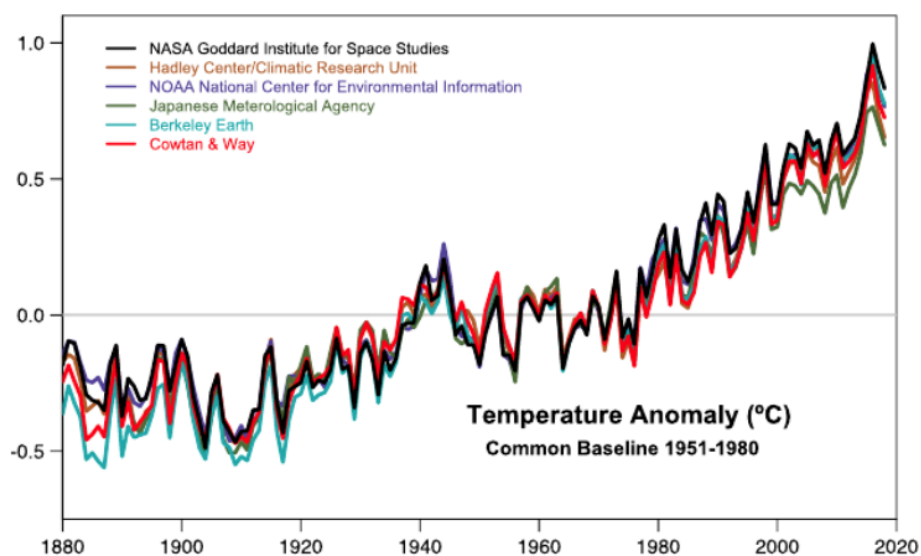


**Figure 2.** Comparison of six analyses of the annually and globally averaged surface temperature anomalies through 2018. The abscissa is time in years, and the ordinate is temperature anomalies in °C with respect to a 30-year climatological average for 1951–1980. NASA stands for the National Aeronautics and Space Administration; NOAA stands for the National Oceanic and Atmospheric Administration. Reprinted by permission from John Wiley & Sons Inc.: American Geophysical Union. *Journal of Geophysical Research: Atmospheres*. Improvements in the GISTEMP Uncertainty Model. Lenssen et al. (2019), © 2019. American Geophysical Union. All Rights Reserved. 2019.

much greater detail (Pierrehumbert, 2004; Ghil and Lucarini, 2020).

On the other hand, it also became clear that these early models, whose only stable solutions were stationary, could not reproduce the wealth of variability that the proxy records were describing very well, not even in the presence of stochastic forcing (e.g., Ghil, 1994). Certain theoretical paleoclimatologists therefore turned to coupling a “climate” equation, with temperature as its only dependent variable, with an ice sheet equation (Källén et al., 1979; Ghil and Le Treut, 1981) or a carbon dioxide equation (Saltzman et al., 1981; Saltzman and Maasch, 1988). These coupled climate models, albeit highly idealized, did produce oscillatory solutions that captured some of the features of the Quaternary glaciation cycles as known at that time. For instance, the models of Ghil and associates (Källén et al., 1979; Ghil and Le Treut, 1981) captured the phase differences between peak ice sheet extent and minimum temperatures in the North Atlantic suggested by Ruddiman and McIntyre (1981), while the work of Saltzman and associates (e.g., Saltzman and Maasch, 1988) captured the asymmetry of the glaciation cycles with their more rapid “terminations” (Broecker and Van Donk, 1970).

The stable self-sustained oscillations of these coupled models, however, were totally independent of any orbital or other time-dependent forcing, i.e., the solar input to their radiative budget was constant in time. Hence, they could not capture the wealth of spectral features, with their orbital and other peaks, of the paleo-records available by the 1980s. The basic quandary of the Quaternary glaciation cycles – at least

from the point of view of theoretical climate dynamics (Ghil and Childress, 1987, Part IV) – is formulated in Fig. 3 below; see also Ghil (1994): How does the quasi-periodic orbital forcing, with its relatively narrow spectral peaks, act on the climate’s internal variability to produce a response that is characterized by significant spectral peaks superimposed on a broad continuous background? In addition, how does the climate’s spectral peak at 100 kyr arise given its absence in the power spectrum of the forcing?

In this paper, we try to show a path toward resolving the four fundamental questions listed in Box 1. In the next section, we summarize existing results on how the climate system’s intrinsic variability arises on Quaternary timescales and on how this variability is modified by the time-dependent orbital forcing, which was added to the previously autonomous climate models as the next step in paleoclimate modeling evolution; see, for instance, Le Treut and Ghil (1983) and Le Treut et al. (1988) vs. Ghil and Le Treut (1981). In Sect. 3, we outline a more general framework for the study of such mechanisms, as given by the theory of non-autonomous and random dynamical systems (NDSs and RDSs), and sketch an application of this theory to other climate problems. An application to the problem at hand is proposed in Sect. 4 and conclusions follow in Sect. 5.

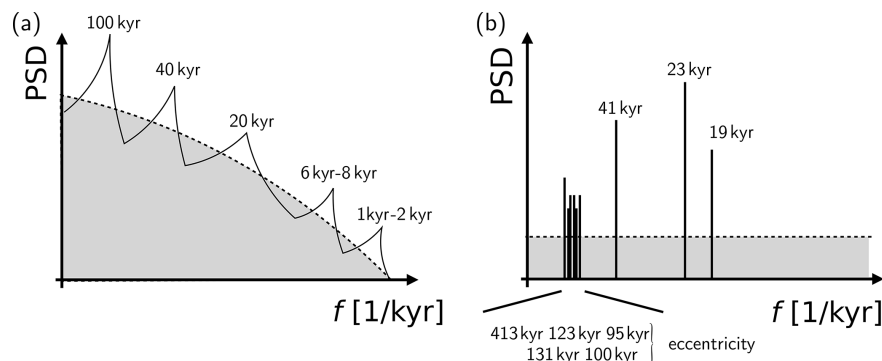


**Figure 3.** The theoretical quaternity of modeling the Quaternary glaciation cycles, illustrated here by schematic diagrams of the composite power spectral densities (PSD) of (a) the paleo-records and (b) the orbital forcing. In panel (a), the dominant peak for the Late Pleistocene is near 100 kyr, while in panel (b) eccentricity forcing is distributed over several spectral lines. The peaks at 6–8 and 1–2 kyr in panel (a) correspond to Bond cycles (Bond et al., 1992, 1993) and to the mean recurrence of D-O events, and they lack a match in the forcing lines of panel (b).

Based on the discussion so far and on the discrepancy between Fig. 3a and b, we propose herein the following questions that still need to be resolved for a thorough understanding of Quaternary climate variability.

1. How does the dominant peak of the observed variability near 100 kyr arise, given the rather diffuse orbital forcing close to this periodicity?
2. What causes the continuous part of the observed spectrum, which contains most of the variance?
3. What gives rise to the high-frequency peaks due to the sudden warmings and to the approximate periodicities associated with Heinrich and D-O events, among others?
4. What are the contributions of the orbital forcing and the climate system's intrinsic variability to items (1)–(3), and how does the former factor modify the latter?

**Box 1.** Fundamental questions regarding the Quaternary glacial–interglacial cycles.

## 2 Self-sustained climate oscillators

### 2.1 A simple mechanism for climate oscillations

We follow Ghil (1994) in sketching the simplest physical mechanism for a self-sustained climate oscillation at fixed insolation forcing. Consider the Källén et al. (1979, hereafter KCG) oscillator, to the best of our knowledge the first such self-sustained climate oscillator. The model itself was built from the ground up, coupling a scalar version of the Ghil (1976) energy balance model (EBM) with a simplified, scalar version of the Weertman (1964, 1976) ice sheet model

(ISM). The model's details and further analyses of its ingredients and variants can be found in several references (e.g., Craford and Källén, 1978; Ghil and Tavantzis, 1983; Ghil, 1984; Bódaí et al., 2015).

The basic workings of this climate oscillator can be represented by two coupled ordinary differential equations (ODEs), written symbolically as follows:

$$\dot{T} \simeq -V, \quad (1a)$$

$$\dot{V} \simeq T. \quad (1b)$$

Here  $T$  stands for global temperature and  $V$  for global ice volume, while Eq. (1a) is an EBM and Eq. (1b) is an ice sheet model (ISM). The “ $\simeq$ ” symbol stands for a binary relation of rough proportionality and is intended to neglect the details of the equation's right-hand side (RHS), including its nonlinearities. The EBM represents the well-known ice–albedo feedback used by both Budyko (1969) and Sellers (1969), while the ISM relies on the precipitation–temperature feedback postulated by KCG and used also by Ghil and Le Treut (1981), who coined the term.

The latter feedback can be better understood by writing the following equations:

$$\dot{V} \simeq p, \quad (2a)$$

$$p \simeq p_{ac} - p_{ab}, \quad (2b)$$

$$p_{ac} \simeq T. \quad (2c)$$

Here  $p$  is net precipitation on the single ice sheet of the globally integrated model, given by the difference in Eq. (2b) between the accumulation  $p_{ac}$  and the ablation  $p_{ab}$  (KCG).

As first observed by George C. Simpson – the meteorologist of Robert F. Scott's *Terra Nova* expedition to Antarctica in 1910–1912 and later the longest-serving Director of the U.K. Meteorological Office – warmer winters have more snow, and hence, at least in central Antarctica, the increase of  $p_{ac}$  with  $T$  exceeds the more obvious increase of  $p_{ab}$  with

$T$ . Hence,  $p \simeq T$ , and we have derived therewith Eq. (1b), i.e.,  $V \simeq p \simeq T$ . For more recent studies of the precipitation–temperature feedback, see Tziperman and Gildor (2002).

More generally, the presence of feedbacks of opposite sign in a system of two linear coupled ODEs,

$$\dot{x} = y, \quad \dot{y} = -x,$$

leads to an oscillation, with the solution given by two trigonometric functions in quadrature with each other,  $x(t) = \sin(t)$ ,  $y(t) = \cos(t) = \sin(t + \pi/2)$ , and the trajectory describing a circle in the  $(x, y)$  phase plane,  $x^2(t) + y^2(t) = 1$ . In a nonlinear system, however – like the full KCG model or any other climate oscillator mentioned so far – the possibility of an oscillation, as indicated by the system (1), is actually realized in the explicit, full set of equations only for certain parameter values and not for others.

This can be understood by considering the so-called normal form of a Hopf bifurcation, which leads from a stable steady state, called a fixed point in dynamical systems theory, to a stable oscillatory solution, called a limit cycle. The easiest way to see this transition is by writing the normal form in polar coordinates, as in Arnold (1988) and in Ghil and Childress (1987, Sect. 12.2), namely,

$$\dot{z} = (\mu + i\omega)z + c(z\bar{z})z. \quad (3)$$

Here  $z = x + iy$  is complex, where  $i = \sqrt{-1}$  is the imaginary unit, while  $\mu$  is a real bifurcation parameter, and  $c, \omega$  are real and nonzero. Note that the KCG model per se is not in the normal form above, and we will discuss its bifurcation parameter  $\mu_*$  in the next subsection.

A very natural transformation of variables,

$$\rho = z\bar{z} > 0, \quad z = \rho^{1/2} \exp(i\theta), \quad (4)$$

leads from the complex ODE (3) to the system of two real and decoupled ODEs,

$$\dot{\rho} = 2\rho(\mu + c\rho), \quad (5a)$$

$$\dot{\theta} = \omega. \quad (5b)$$

Equation (5b) simply provides an angular rotation around the origin  $\rho = 0 = x = y$ , since the complex exponential in Eq. (4) is periodic with period  $2\pi$ . Equation (5a) is quadratic in  $\rho$ , and thus it can have two real roots,  $\rho = \rho_0 = 0$  and  $\rho = \rho_* = -\mu/c$ . But  $\rho$  has to be positive, and thus in the case in which  $c < 0$ , the only possible solution for  $\mu < 0$  is the origin, and it is stable since  $\rho(\mu + c\rho)$  is negative for  $\rho > 0$  in this case; hence,  $\rho$  has to be monotonically decreasing, i.e., all the solutions of Eq. (5) spiral into the origin. The Hopf bifurcation from this stable steady state to a periodic solution, i.e., a limit cycle with radius  $\rho^{1/2} = \rho_*^{1/2}$ , occurs as  $\mu$  crosses 0. Since now  $\rho(\mu + c\rho) > 0$  for  $0 < \rho < \rho_*$  and  $\rho(\mu + c\rho) < 0$  for  $\rho > \rho_*$ , the limit cycle is stable and trajectories spiral out from inside this cycle and into it from outside; see Fig. 4 for the so-called supercritical (or soft) Hopf bifurcation case with  $c < 0$ .

## 2.2 Intrinsic climate oscillations and the mid-Pleistocene transition (MPT)

In this subsection, we present an argument for the role of intrinsic oscillations in the mid-Pleistocene transition (MPT). The first point to be made is that while orbital forcing clearly plays a major role in the power spectrum of the Quaternary’s climatic variability, it cannot be, in and of itself, the cause of the MPT. Indeed, changes in the solar system’s orbital periodicities only occur on much longer timescales than the entire Quaternary’s duration (Varadi et al., 2003; Laskar et al., 2004a). Our argument continues with a further analysis of the Hopf bifurcation presented in the previous subsection. Such an analysis was carried out for the KCG model by Ghil and Tavantzis (1983).

Physically speaking, the presence or absence of the regular, purely periodic oscillations obtained by KCG and illustrated in Ghil and Childress (1987, Fig. 12.6) depends on whether  $c \geq 0$  in Eq. (5a). The KCG model’s bifurcation parameter is  $\mu_* = c_T/c_L$ , where  $c_T$  is the heat capacity in its EBM, while  $c_L$  is the “mass capacity” in its ISM (Ghil and Tavantzis, 1983). Large  $\mu_*$  corresponds physically to a very small, possibly pre-Pleistocene ice cap (Ghil, 1984; Saltzman and Sutera, 1987). At these values of  $\mu_*$ , the KCG model’s nullclines and fixed points – the latter being given by the intersection of the former – are very different from those that are obtained for Quaternary-sized ice sheets, for which  $c_L$  is comparable in value to  $c_T$ ; see Ghil and Tavantzis (1983, Figs. 3–5). As  $\mu_*$  decreases to  $O(1)$ , i.e., as we proceed from very small to more substantial ice sheets, the fixed point transfers its stability to a branch of periodic solutions via a subcritical Hopf bifurcation (Källén et al., 1979; Ghil and Tavantzis, 1983); see also Ghil and Childress (1987, Figs. 12.8 and 12.9).

To clarify the simple physical concepts that underlie subcritical and supercritical Hop bifurcations, let us consider a purely mechanical oscillator with mass  $m$ , a spring  $kx$ , and a dashpot  $\alpha\dot{x}$  (Landau and Lifshitz, 1960; Jordan and Smith, 1987),

$$m\ddot{x} = -\alpha(x)\dot{x} - k(x)x. \quad (6)$$

If  $k = \text{const.}$  and  $\alpha = \text{const.}$ , we have the simplest, linear setup, but we will be interested in the nonlinear cases here. Normalizing by the mass  $m$  and not changing notation otherwise, by rearranging terms and adding a periodic forcing we get the following equation:

$$\ddot{x} + \alpha(x)\dot{x} + k(x)x = F \cos(\omega t). \quad (7)$$

Two classical nonlinear cases are those of the Duffing (1918) equation, in which  $k(x) = x^2$  and  $\alpha = \text{const.}$ , and of the Van der Pol (1926) equation, in which  $k = \text{const.}$  and  $\alpha(x) = \nu(x^2 - 1)$ . The fully nonlinear case in which both the spring and the damping are nonlinear, with  $k(x) = x^2$  and  $\alpha(x) = \nu(x^2 - 1)$ , is known as the Van der Pol–Duffing oscillator

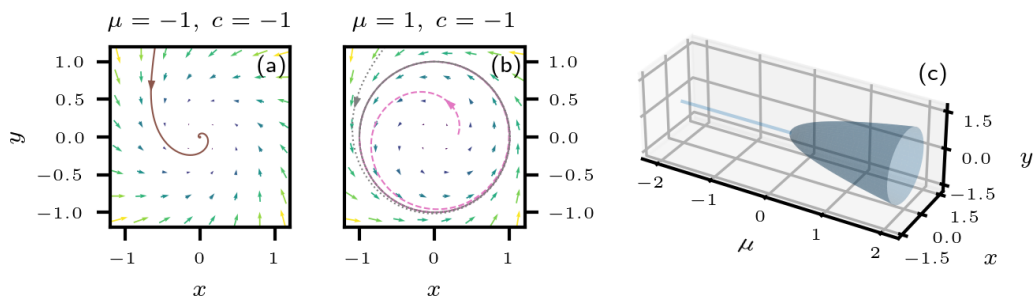


**Figure 4.** Supercritical Hopf bifurcation. **(a)** Vector field  $\dot{z}(z)$  of Eq. (3) for the parameter values  $\mu = -1$  and  $c = -1$ ;  $z = x + iy$ . In this case, the origin constitutes the only stable fixed point, and all trajectories will spiral into this point, as illustrated by the single brown trajectory. **(b)** Vector field  $\dot{z}(z)$  and three trajectories for  $\mu = 1$ . In this case, the origin is an unstable fixed point, while the limit cycle with radius  $\rho_*^{1/2} = 1$  constitutes the only stable solution. Trajectories that start inside this limit cycle, with  $\rho(t_0) < \rho_*$ , tend to it by spiraling out – as illustrated by the magenta trajectory – while trajectories that start outside the limit cycle, with  $\rho(t_0) > \rho_*$ , approach it by spiraling inward, as illustrated by the gray trajectory. **(c)** Dependence of the stable solution of Eq. (3) on the parameter  $\mu$ , for  $c = -1$ . For  $\mu \leq 0$ , the single stable solution is the fixed point located at the origin,  $\rho \equiv 0$ . For  $\mu > 0$ , the stable solution is the limit cycle given by  $\rho = \mu$ .

(e.g., Jackson, 1991; Pierini et al., 2018). Note that all three types of nonlinear oscillators can exhibit chaotic behavior even in the presence of simple periodic forcing (e.g., Guckenheimer and Holmes, 1983; Pierini et al., 2018, and references therein). The idea of using such simple, classical oscillators in modeling Quaternary glaciation cycles goes back to Saltzman et al. (1981).

Jordan and Smith (1987, Sect. 5.6) specifically discuss the case of a soft and a hard spring for a generalized Duffing equation, with  $k(x) = k_0 + \epsilon h(x)$ , where  $0 < |\epsilon| \ll 1$ ,  $h(-x) = h(x)$ , and  $h'' > 0$ . A spring is soft if it is sublinear,  $\epsilon < 0$ , and hard if it is superlinear,  $\epsilon > 0$ ; see their Eq. (5.37) and Fig. 5.4a, b, with  $h(x) = x^2$ .

The supercritical Hopf bifurcation in the absence of forcing is analogous to the nonlinear response of a soft, sublinear spring to periodic forcing in which the oscillations in the position  $x$  of the mass  $m$  increase gradually in amplitude as the spring constant  $k_0$  increases past a critical value  $k_*$ , while the subcritical case is analogous to the response of a hard, superlinear spring, for which the oscillations in  $x$  jump suddenly from zero amplitude to a finite amplitude as the spring constant  $k_0$  crosses the value  $k_*$ . Please compare the behavior of supercritical and subcritical Hopf bifurcations in Ghil and Childress (1987, Sect. 12.2 and Figs. 12.7–12.9) and see Jordan and Smith (1987, Fig. 5.7) for the change in the nonlinear response of a Duffing oscillator as its spring changes from soft, with  $\epsilon < 0$ , to hard, with  $\epsilon > 0$ .

There is a clear-cut analogy with the mid-Pleistocene transition, occurring at roughly 0.8 Ma b2k, at which small-amplitude climate variability with a dominant periodicity near 40 kyr becomes larger, dominated by a periodicity that is close to 100 kyr, as well as being more irregular (e.g., Huybers, 2009; Quinn et al., 2018; Rousseau et al., 2020). A fair number of distinct dynamical theories for this transition have been formulated (e.g., Maasch and Saltzman, 1990; Ghil, 1994; Crucifix, 2012; Ashwin and Ditlevsen, 2015; Daruka

and Ditlevsen, 2016; Omta et al., 2016; Ditlevsen and Ashwin, 2018). A rather obvious one is that a Hopf bifurcation occurs at that point, which leads to a more vigorous response to the multi-periodic orbital forcing; thus, the latter does not need to change in the least in order to explain the observed phenomena. In Saltzman and Sutera (1987), there is only a comment on the likely role of a Hopf bifurcation in the transition, but their Fig. 3 suggests that in their model such a bifurcation would have to be of the supercritical type and lead to a fairly gradual transition.

In contrast, the subcritical Hopf bifurcation of the KCG and Ghil and Le Treut (1981) oscillators would have to lead to a more abrupt transition, as suggested by Ghil (1984). Later, Crucifix (2012) showed that the models by Saltzman and Maasch (1990, 1991) exhibit MPT-like behavior via supercritical or subcritical Hopf bifurcations, depending on the parameter values. The existing  $\delta^{18}\text{O}$  and  $\delta^{13}\text{C}$  records might or might not have sufficient resolution back in time up to 1.2 Ma to settle this question about the abruptness of the transition. In case some of them do, an objective test of suddenness – as proposed by Bagniewski et al. (2021) for the high-resolution NGRIP record (North Greenland Ice Core Project members, 2004) – will have to be applied to such records.

### 3 Time-dependent forcing, NDSs, and RDSs

#### 3.1 Orbital forcing of a climate oscillator

We start this section by describing some fairly simple ways in which the orbital forcing might have modified intrinsic climate variability, thus helping to solve the mismatch between Fig. 3a and b in Sect. 1. To explore this possibility, Le Treut and Ghil (1983) used somewhat simplified insolation forcing based on the calculations of Berger (1978) and applied it to a slightly modified version of the Ghil and Le Treut (1981) oscillator. These authors found that, as expected for a nonlinear oscillator, its internal frequency  $f_0$  is affected strongly by

the forcing ones,  $\{f_1, \dots, f_5\}$ , resulting in both nonlinear resonance and combination tones (Landau and Lifshitz, 1960).

Depending on parameter values, the periodicity  $P_0 = 1/f_0$  of the Ghil and Le Treut (1981) oscillator is  $P_0 \simeq 6\text{--}7$  kyr. The lines in the simplified insolation spectrum used by Le Treut and Ghil (1983) had the following periodicities:  $P_1 = 19$  kyr,  $P_2 = 23$  kyr,  $P_3 = 41$  kyr,  $P_4 = 100$  kyr, and  $P_5 = 400$  kyr. These periodicities correspond to the two precessional ones, the obliquity one, and the two eccentricity ones. The actual celestial-mechanics calculations that Berger (1978) based his insolation calculations on have been substantially updated since (e.g., Varadi et al., 2003; Fienga et al., 2015). However, these advances have not modified the spectrum of the planetary-orbit solutions over the 2.6 Myr of the Quaternary very much, which is a rather short interval in celestial-mechanics terms.

The results of the Le Treut and Ghil (1983) model on the evolution of the primary climate variables  $T$  and  $V$  were converted to  $\delta^{18}\text{O}$  values in simulated isotopic records of marine sediment and ice cores by Le Treut et al. (1988); the spectra of the latter are plotted in Fig. 5. The values on the abscissa of Fig. 5a are values of the logarithm of frequency, while those in Fig. 5b are values of the frequency itself; the values on the ordinate of both panels are powers of 10. One refers to such figures as being in (a) log–log coordinates vs. (b) log–linear coordinates for short.

Aside from the spectral features noted in the figure caption and discussed in greater detail by Ghil (1994), it is important to realize (i) that the large continuous background in Fig. 5a is purely of deterministically chaotic origin since there is no stochastic element whatsoever in the Le Treut and Ghil (1983) model or in its forcing and (ii) that the dominant peak at 109 kyr is not directly forced by the  $f_4 = 1/100 \text{ kyr}^{-1}$  eccentricity line but rather it is due to the difference tone between the two precessional frequencies,  $f_1$  and  $f_2$ . Finally, it is the nonlinear, broad resonance of the model's  $f_0$  frequency with the quasi-periodic forcing that produces the bump in the spectrum of Fig. 5a to the right of the orbital frequencies.

In returning to the “fundamental question no. 2” in Box 1, one must recall that on the paleoclimatic timescales of interest – apart from deterministic chaos à la Lorenz (1963), as obtained by Le Treut and Ghil (1983) and Le Treut et al. (1988) and shown here in Fig. 5a – stochastic contributions à la Hasselmann (1976) to the continuous part of the spectrum must also play an important role. In fact, RDS theory, as outlined in the next subsection, provides an excellent framework for a “grand unification” of these two complementary points of view (Ghil, 2014, 2019). In the paleoclimatic context, Ditlevsen et al. (2020) have suggested that, aside from red noise processes, dating uncertainties in the proxy records from which the spectra are derived may contribute, in all likelihood, to this background; see also Boers et al. (2017a, b). In this context, Verbitsky and Crucifix (2020) also provide a simple theory that addresses scaling properties in the glacial

cycles and their spectra, based on the so-called Buckingham  $\pi$ -theorem (e.g., Barenblatt, 1996).

### 3.2 Basic facts of NDS and RDS life

The highly preliminary results summarized in Sect. 3.1 encourage us to pursue the effects of the orbital forcing on intrinsic climatic variability in a more systematic way, effects that may have contributed to generate the rich paleoclimate spectrum on Quaternary and longer timescales (e.g., Westerhold et al., 2020). In fact, several research groups in the climate sciences have carried out during the past 2 decades an important extension of the dynamical systems and model hierarchy framework presented by Ghil and Childress (1987) and by Ghil (2001), from deterministically autonomous to non-autonomous and random dynamical systems (NDSs and RDSs, e.g., Ghil et al., 2008; Chekroun et al., 2011; Bóday and Tél, 2012).

On the road to including deterministically time-dependent and random effects, one needs to realize first that the climate system – as well as any of its subsystems on any timescale – is not closed: it exchanges energy, mass, and momentum with its surroundings, whether this pertains to other subsystems or the interplanetary space and the solid earth. The typical applications of dynamical systems theory to climate variability until not so long ago have only taken into account exchanges that are constant in time, thus keeping the model – whether governed by ordinary, partial, or other differential equations – autonomous; i.e., the models had coefficients and forcings that were constant in time.

Alternatively, the external forcing or the parameters were assumed to change either much more slowly than a model's internal variability, meaning that the changes could be assumed to be quasi-adiabatic, or much faster, meaning that they could be approximated by stochastic processes. Some of these issues are covered in much greater detail by Ghil and Lucarini (2020, Sect. III.G). The key concepts and tools of NDSs and RDSs go beyond such approaches that rely in an essential way on a scale separation between the characteristic times of the forcing and the internal variability of a given system; such a separation is rarely if ever actually present in the climate sciences.

The presentation of the key NDS and RDS concepts and tools in this subsection is aimed at as large a readership as possible and follows Ghil (2014). Slightly more in-depth but still fairly expository presentations can be found in Crauel and Kloeden (2015) and in Caraballo and Han (2017). Readers who are less interested in this mathematical framework – which allows a truly thorough understanding of the way that orbital forcing acts on intrinsic climate variability on Quaternary timescales – may skip at a first reading the remainder of this section and continue with Sect. 4.

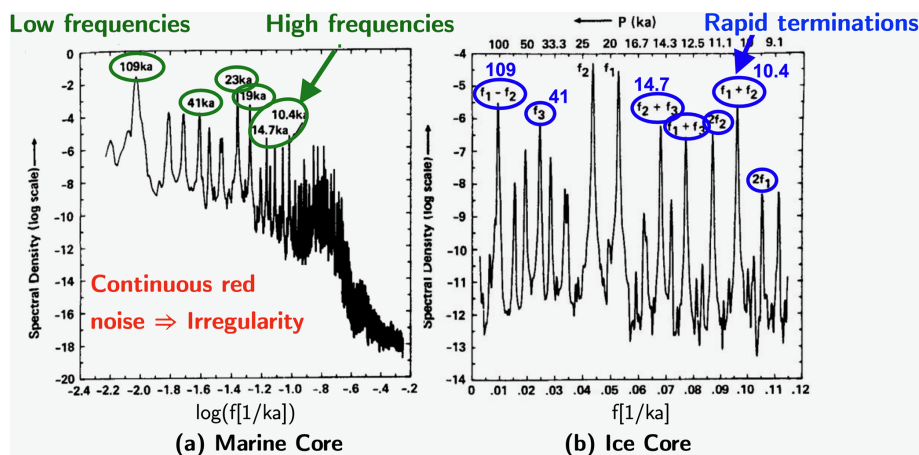


**Figure 5.** Power spectra of simulated (a) deep-sea and (b) ice core records for the forced climate oscillator of Le Treut et al. (1988) with idealized orbital forcing. Panel (a) is in log–log coordinates and clearly shows a dominant peak at 109 kyr and a very large amount of variance in the continuous spectrum, which has a roughly  $-2$  power law slope. The orbital peaks at  $P_1 = 19$  kyr,  $P_2 = 23$  kyr and  $P_3 = 41$  kyr are also present, along with peaks at 14.7 and 10.4 kyr, which correspond to the sum tones  $f_2 + f_3$  and  $f_1 + f_2$ , respectively. Panel (b) is in log–linear coordinates and shows additional harmonics and sum tones, as well as the difference tone  $f_1 - f_2$ , which corresponds to the dominant peak at 109 kyr. Inside the figure, the notation ka instead of kyr has been kept unchanged from the original publication. Adapted by permission from John Wiley & Sons Inc.: American Geophysical Union. Journal of Geophysical Research: Atmospheres. Isotopic Modeling of Climatic Oscillations: Implications for a Comparative Study of Marine and Ice Core Records by Le Treut et al. (1988), © 1988 by the American Geophysical Union. 1988.

### 3.2.1 Autonomous and non-autonomous systems

Succinctly, one can write an autonomous system as

$$\dot{X} = F(X; \mu), \quad (8)$$

where  $X$  stands for any state vector or climate field. While  $F$  is a smooth function of  $X$  and of the parameter  $\mu$ , it does not depend explicitly on time. This autonomous character of Eq. (8) greatly facilitates the analysis of its solutions' properties.

For instance, two distinct trajectories,  $X_1(t)$  and  $X_2(t)$ , of a well-behaved, smooth autonomous system cannot intersect – i.e., they cannot pass through the same point in phase space – because of the uniqueness of solutions. This property helps one draw the phase portrait of an autonomous system, as does the fact that we only need to consider the behavior of solutions  $X(t)$  as time  $t$  tends to  $+\infty$ . The sets of points so obtained are (possibly multiple) equilibria, periodic and quasi-periodic solutions, and chaotic sets. In the language of dynamical systems theory, these are called, respectively: fixed points, limit cycles, tori, and strange attractors.

We know only too well, however, that the seasonal cycle plays a key role in climate variability on interannual timescales, while orbital forcing is crucial on the Quaternary timescales of many millennia. In addition, more recently it has become obvious that anthropogenic forcing is of utmost importance on the interdecadal timescales between these two extremes.

How can one take into account these types of time-dependent forcings and analyze the non-autonomous systems

that they lead us to formulate? One succinctly writes such a system as follows:

$$\dot{X} = F(X, t; \mu). \quad (9)$$

In Eq. (9), the dependence of  $F$  on  $t$  may be periodic,  $F(X, t + P) = F(X, t)$ , as in various El Niño–Southern Oscillation (ENSO) models, where the period  $P = 12$  months, or monotonic,  $|F|(X, t + \tau) \geq |F|(X, t)$ , as it is when studying scenarios of anthropogenic climate forcing. An even more general situation includes time dependence in one or more parameters  $\{\mu_1, \dots, \mu_p\}$ .

To illustrate the fundamental distinction between an autonomous system like Eq. (8) and a non-autonomous one like Eq. (9), consider the simple scalar version of these two equations:

$$\dot{X} = -\beta X, \quad (10a)$$

and

$$\dot{X} = -\beta X + \gamma t, \quad (10b)$$

respectively. We assume that both systems are dissipative, i.e.,  $\beta > 0$ , and that the forcing is monotonically increasing,  $\gamma \geq 0$ , as would be the case for anthropogenic forcing in the industrial era. Lorenz (1963) pointed out the key role of dissipativity in giving rise to strange but attracting solution behavior, while Ghil and Childress (1987) emphasized its importance and pervasive character in climate dynamics. Clearly the only attractor for the solutions of Eq. (10a), given

any initial point  $X(0) = X_0$ , is the stable fixed point  $X_* = 0$ , attained as  $t \rightarrow +\infty$ .

In the case of Eq. (10b), however, this forward-in-time approach yields blow-up from  $t \rightarrow +\infty$  for any initial point. To make sense of what happens in the case of time-dependent forcing, one instead introduces the pullback approach, in which solutions are allowed to still depend on the time  $t$  at which we observe them but also on a time  $s$  from which the solution is started, with  $X(s) = X_0$  and  $s \ll t$ . With this little change of approach, one can easily verify that

$$|X(s, t; X_0) - \mathcal{A}_t| \rightarrow 0 \quad \text{as } s \rightarrow -\infty, \quad (11)$$

for all  $t$  and  $X_0$ , where  $\mathcal{A}_t = (\gamma/\beta)(t-1/\beta)$ . We obtain therefore, in this pullback sense, the intuitively obvious result that the solutions, if we start them far enough in the past, all approach the family of attracting sets  $\mathcal{A}_t$ ; this family follows the forcing  $\gamma t$ , and it thus has a linear growth in time  $t$ . Hence, the fixed point  $X_*$  of Eq. (10b) is in fact a moving target and it is given by  $X_* = \gamma t/\beta$ . Due to the system's inertia, the set  $\mathcal{A}_t$  that is approached by the trajectories lags this time-dependent fixed point by a constant offset of  $\gamma/\beta^2$ .

### 3.2.2 Pullback attractor (PBA)

Formally, the indexed family  $\mathcal{A}$  of all pullback attracting sets  $\mathcal{A}_t$ ,

$$\mathcal{A} = \{\mathcal{A}_t\}_{t \in \mathbb{R}}, \quad (12)$$

is termed the *pullback attractor* (PBA) of an NDS if the following two conditions are fulfilled:

- i. each snapshot  $\mathcal{A}_t$  is compact and the family of snapshots  $\{\mathcal{A}(t)\}_{t \in \mathbb{R}}$  is invariant with respect to the dynamics,

$$X(t, s; X_0) \in \mathcal{A}_t \quad \forall s \leq t \text{ and } X_0 \in \mathcal{A}_s, \quad (13)$$

and

- ii. the pullback attraction occurs for all times,

$$\lim_{s \rightarrow -\infty} |X(t, s; X_0) - \mathcal{A}_t| = 0 \quad \forall t. \quad (14)$$

To further improve the reader's intuition for PBAs, we provide a second illustrative example here. A system defined in polar coordinates by

$$\dot{\rho} = \alpha(\mu - \rho), \quad \dot{\phi} = \omega, \quad (15)$$

with  $\rho, \mu \in \mathbb{R}^+$ , and  $\phi \in \mathbb{R}/2\pi$  can easily be seen to exhibit a limit cycle in the  $(x, y)$  plane with  $(x = \rho \cos \phi, y = \rho \sin \phi)$ . An initial deviation of  $\rho$  from  $\mu$  will decay exponentially, and the system converges to an oscillation of radius  $\mu$  with the angular velocity  $\omega$ . Here, we transform this

autonomous dynamical system into a non-autonomous one by modulating the target radius  $\mu$  with a sinusoidal forcing,

$$\mu \rightarrow \mu(t) = \mu_0 + \beta \sin(\nu t), \quad (16)$$

where the modulation is moderate to guarantee that  $\mu_0 + \beta \sin(\nu t) > 0$  for all  $t$ .

Since the dynamics of the phase  $\phi$  and of the radius  $\rho$  are decoupled, the corresponding equations can be solved and analyzed separately. While the temporal development of the phase is trivial, the pullback-invariant attracting set of the radius for the initial condition  $\rho(s) = \rho_0$  is given by

$$\mathcal{A}^{(\rho)}(t; \rho_0) = \lim_{s \rightarrow -\infty} \rho(t, s; \rho_0) = \alpha\beta \sin(\nu t + \vartheta) + \mu_0, \quad (17a)$$

with

$$\vartheta = \arctan(-\nu/\alpha), \quad (17b)$$

as shown in Appendix B. Note that in the limit  $s \rightarrow -\infty$ , the dependence on the initial value  $\rho_0$  vanishes and the attracting set  $\mathcal{A}_t^{(\rho)}$  performs an oscillation of the same frequency as the forcing. It lags the phase of the time-dependent fixed point  $\mu(t)$  by the constant  $\vartheta$ , while its amplitude is amplified by the factor  $\alpha$ . Since  $\rho$  is restricted to positive values, this solution requires  $\alpha\beta < \mu_0$ .

The PBA with respect to the coordinate  $\rho$  is comprised of the family of all the sets  $\mathcal{A}_t^{(\rho)}$  as defined in Eq. (18) and thus reads

$$\mathcal{A}^{(\rho)} = \{\alpha\beta \sin(\nu t + \vartheta) + \mu_0\}_{t \in \mathbb{R}}. \quad (18)$$

Since the pullback limit for the phase  $\phi$  does not exist, no constraints on it other than  $\phi \in [0, 2\pi)$  are imposed by the dynamics. Hence, for the system (15) comprised of radius and phase, we find that the distance of any trajectory at time  $t$  – i.e.  $(\rho(t; t_0, \rho_0), \phi(t; t_0, \phi_0))$  – to the set  $\mathcal{A}_t = \{(\alpha\beta \sin(\nu t + \vartheta) + \mu_0, \varphi) : \varphi \in [0, 2\pi)\}$  tends to zero as we pullback the initial time  $t_0$  to  $-\infty$ . The pullback attracting sets  $\mathcal{A}_t$  at time  $t$  are circles in the  $(x, y)$  plane with a radius that oscillates in time, and the system's PBA is given by the family of these circles

$$\mathcal{A} = \{(\alpha\beta \sin(\nu t + \vartheta) + \mu_0, \varphi) : \varphi \in [0, 2\pi)\}_{t \in \mathbb{R}}. \quad (19)$$

Figure 6 shows trajectories of the system starting from different points in the past. In Fig. 6a, the trajectories are depicted in the three-dimensional (3-D) space spanned by the two Cartesian coordinates  $(x, y)$  and the time  $t$ , where the usual transformation from polar to Cartesian coordinates was applied. The shaded surface in this panel represents the PBA of the system. Corresponding trajectories of  $\rho(t)$  and their convergence to the PBA  $\mathcal{A}_t^{(\rho)}$  are shown Fig. 6b. Figure 6f shows a heat map (Wilkinson and Friendly, 2009) that approximates a portion of the PBA's invariant measure projected onto the  $(x, y)$  plane. For a clean definition of such

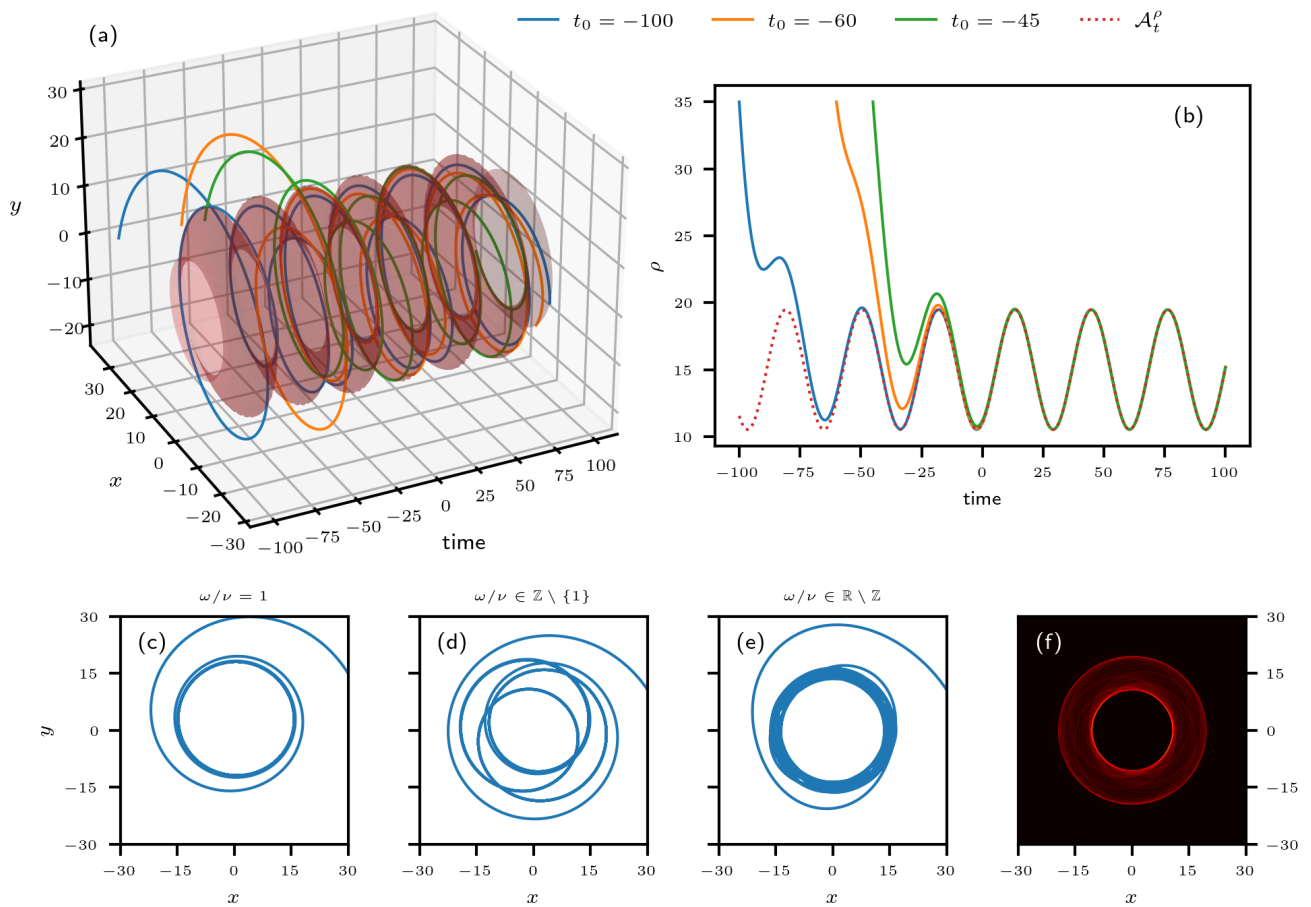


**Figure 6.** Trajectories and PBA of the system defined by Eqs. (15) and (16); in all the panels the parameter values are  $\mu_0 = 15$ ,  $\alpha = 10$ ,  $\nu = 0.2$ , and  $\omega = 0.3$ , unless stated otherwise. **(a)** Trajectories  $(\rho(t), \phi(t))$  of the system starting from different times in the past in the 3-D space spanned by  $(x, y)$  and time  $t$ ; the system’s PBA lies on the red-shaded surface. **(b)** Temporal evolution of the radius (solid colors) of the three trajectories shown in **(a)** together with its PBA (dotted red). **(c–e)** Trajectories integrated from  $t_0 = -100$  to  $t_f = 200$  for  $\nu = 0.3, 0.2, 0.5^{1/2}$  in panels **(c)**, **(d)**, and **(e)**, respectively. The values are chosen such that the ratio between  $\nu$  and  $\omega$  is  $\omega/\nu = 1$ ,  $\omega/\nu \in \mathbb{Z} \setminus \{1\}$  and  $\omega/\nu \in \mathbb{R} \setminus \mathbb{Z}$  in panels **(c)** to **(e)**. Correspondingly, in **(c)** the trajectory quickly converges to a circle, whose center is slightly shifted from the origin. In panel **(d)** a quasi-closed three-fold loop can be observed, since  $\omega/\nu = 3/2$ . In panel **(e)** the trajectories will densely fill the annular disk defined in the video supplement statement. **(f)** Heat map of numerous trajectories projected onto the  $(x, y)$  plane. The trajectories start at random points in state space and are integrated from  $t_i = -200$  to  $t_f = 200$ . A video of the heat map filling up as more and more trajectories with different initial conditions are added is provided in the video supplement. The heat map shown here is a snapshot of the video taken at time  $t = 0.20$ ; see details in the video supplement.

a measure in NDSs and RDSs, please see Caraballo and Han (2017), Chekroun et al. (2011), Crauel and Kloeden (2015), or Ghil et al. (2008). Essentially, the heat map here counts the number of times that 100 trajectories integrated from  $t = -200$  to  $t = 200$ , with randomized initial conditions like the ones shown in Fig. 6a, cross small pixels in the  $(x, y)$  plane.

Figure 6c–e demonstrate a particularity of this system, which is characteristic of dynamics confined to a torus. Namely, the structure of the system’s trajectories depends on the frequency ratio  $\omega/\nu$ , and three different cases must be distinguished. If the radius is modulated with the same frequency as the oscillation itself, i.e.  $\omega = \nu$  as in panel (c), the forcing and the system have a fixed phase relation. That is,

for a given phase of the system, its radius is always attracted by the same fixed point. Hence, the system practically repeats its orbit after a short time. More precisely, the radius of the oscillation does differ from one “round trip” around the torus to the next, but this difference tends to zero as  $\rho(t)$  approaches the PBA  $\mathcal{A}_t^{(\rho)}$ .

If  $\omega$  and  $\nu$  are rationally related, i.e.,  $m\omega = n\nu$  with  $n, m \in \mathbb{N}$ , as in Fig. 6d, then – after  $n$  periods of the radial modulation and  $m$  periods of the system’s oscillation – the phase relation between the system and its forcing will repeat itself, and hence we observe the same quasi-repetition of the orbit after the time  $n 2\pi/\nu = m 2\pi/\omega$ . That is, such a trajectory will appear as an  $n$ -fold quasi-closed loop.

Finally, if  $\omega/\nu \notin \mathbb{Z}$ , as in Fig. 6e, then a given phase of the system will never coincide with the same phase of the radius modulation more than once. Hence, the trajectory does not repeat itself but instead densely covers the annular disk  $\mathcal{D} = \{(\rho, \phi) : \rho \in [\mu_0 - \alpha\beta, \mu_0 + \alpha\beta] \text{ and } \phi \in [0, 2\pi)\}$ .

### 3.2.3 Random attractor

Let us return now to the more general, nonlinear case of Eq. (9) and add not only deterministic time dependence  $F(X, t)$  but also random forcing,

$$dX = F(X, t)dt + G(X)d\eta, \quad (20)$$

where  $\eta = \eta(t, \omega)$  represents a Wiener process – with  $d\eta$  commonly referred to as “white noise” – and  $\omega$  now labels the particular realization of this random process. When  $G = \text{const.}$ , the noise is additive, while for  $\partial G/\partial X \neq 0$  we speak of multiplicative noise. The distinction between  $dt$  and  $d\eta$  in the stochastic differential Eq. (20) is necessary since, roughly speaking and following the Einstein (1905) paper on Brownian motion, it is the variance of a Wiener process that is proportional to time and thus  $d\eta \propto (dt)^{1/2}$ . In Eq. (20), we dropped the dependence on a parameter  $\mu$  for the sake of simplicity.

The noise processes may include “weather” and volcanic eruptions when  $X(t)$  is “climate”, thus generalizing the linear model of Hasselmann (1976), or cloud processes when dealing with the weather itself: one person’s signal is another person’s noise, as the saying goes. In the case of random forcing of Eq. (20), the concepts introduced by the simple deterministic examples of Eq. (10b) and Eqs. (15) and (16) above can be illustrated by the random attractor  $\mathcal{A}(\omega)$  in Fig. 7.

A key feature of the pullback point of view on noise-perturbed dynamical systems that characterizes RDS theory is the use of a single noise realization, as opposed to the traditional, forward viewpoint of the Fokker–Planck equation and associated concepts, in which multiple noise realizations play a role. For a precise definition of a random attractor – as well as the commonalities and differences between the deterministic and random cases of time-dependent forcing – please see Caraballo and Han (2017).

Chekroun et al. (2011) studied a specific case of such a random attractor for the paradigmatic, climate-related Lorenz (1963) convection model. The authors introduced multiplicative noise into each of the ODEs of the original, deterministically chaotic system, as shown below:

$$dX = P_r(Y - X)dt + \sigma X d\eta, \quad (21a)$$

$$dY = (rX - Y - XZ)dt + \sigma Y d\eta, \quad (21b)$$

$$dZ = (-bZ + XY)dt + \sigma Z d\eta, \quad (21c)$$

where  $r = 28$ ,  $P_r = 10$ , and  $b = 8/3$  are the standard parameter values for chaotic behavior in the absence of noise and  $\sigma$  is a constant variance of the Wiener process that is not

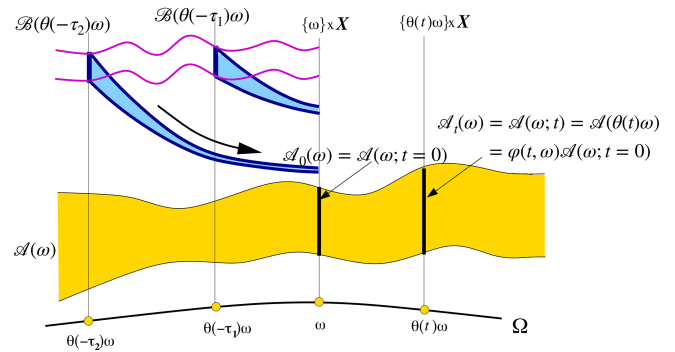


**Figure 7.** Schematic diagram of a random attractor  $\mathcal{A}(\omega)$  and of the pullback attraction to it; here  $\omega$  labels the particular realization of the random process  $\theta(t)\omega$  that drives the system. We illustrate the evolution in time  $t$  of the random process  $\theta(t)\omega$  (light solid black line at the bottom), the random attractor  $\mathcal{A}(\omega)$  itself (yellow band in the middle), with the snapshots  $\mathcal{A}_0(\omega) = \mathcal{A}(\omega; t = 0)$  and  $\mathcal{A}(\omega; t)$  (the two vertical sections, heavy solid lines), and the flow of an arbitrary compact set  $\mathcal{B}$  from “pullback times”  $t = -\tau_2$  and  $t = -\tau_1$  onto the attractor (heavy blue arrows). See Ghil et al. (2008, Appendix A) for the requisite properties of the random process  $\theta(t)\omega$  that drives the RDS formulated by Eq. (20). Adapted from Physica D: Nonlinear Phenomena, 237, Ghil et al. (2008), Climate dynamics and fluid mechanics: natural variability and related uncertainties, 2111–2126, © 2008 Elsevier B.V. All rights reserved. 2008, with permission from Elsevier.

necessarily small; both the noise realization  $\eta(t)$  and  $\sigma$  are the same in all three equations. The well-known strange attractor of the deterministic case is replaced by the Lorenz model’s random attractor, dubbed LORA by the authors. Four snapshots  $\mathcal{A}_t(\omega)$  of LORA are plotted in Fig. 8 and a video of its evolution in time  $\mathcal{A}(\omega) = \{\mathcal{A}_t(\omega)\}_{t \in \mathbb{R}}$  is available as supplementary material to Chekroun et al. (2011) at <https://doi.org/10.1016/j.physd.2011.06.005>.

Charó et al. (2021) have further analyzed the striking effects of the noise on the nonlinear dynamics that are visible in Fig. 8 and in the video of Chekroun et al. (2011) and gathered further insights into the abrupt changes of the snapshots’ topology at critical points in time. These remarkable changes suggest the possibility of random processes giving rise to qualitative jumps, such as the MPT, in paleoclimatic variability.

### 3.3 Application to Dansgaard–Oeschger (D–O) events

Before discussing conceptual glacial cycle models, we take a little detour and introduce a simpler – yet interesting and at the same time highly instructive – application of NDS theory to another important climate phenomenon. During past glacial periods, Greenland experienced a series of sudden decadal-scale warming events that left a clear trace in ice core records (Dansgaard et al., 1993). These so-called D–O events were followed by intervals of steady moderate cooling, be-

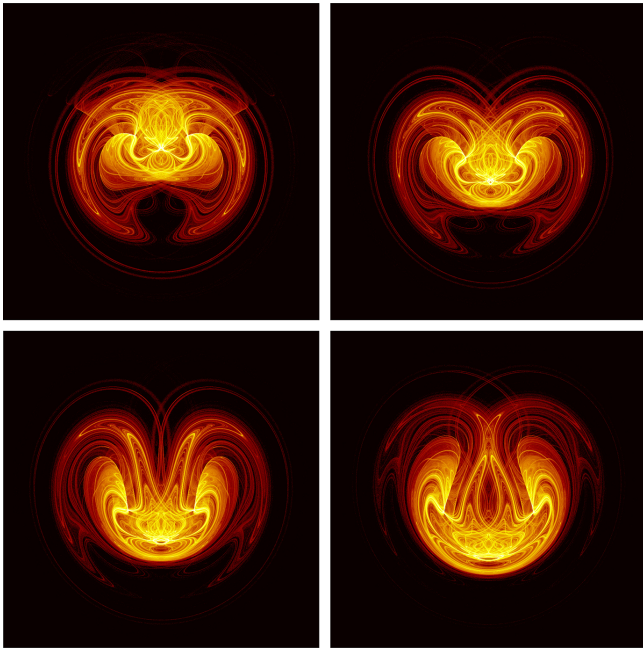


**Figure 8.** Heat maps of the time-dependent invariant measure  $\nu_t(\omega)$  supported on four snapshots  $\mathcal{A}_t(\omega)$  of LORA. The values of the parameters  $r$ ,  $s$ , and  $b$  are the classical ones, where the variance of the noise  $\sigma = 0.5$ . The color bar is on a log scale, and it quantifies the probability of landing in a particular region of phase space; a projection is shown of the 3-D phase space  $(X, Y, Z)$  onto the  $(X, Z)$  plane. Note the complex, interlaced filament structures between highly populated regions (in yellow) and moderately populated ones (in red). Reprinted from *Physica D: Nonlinear Phenomena*, 240, Chekroun et al. (2011), *Stochastic climate dynamics: Random attractors and time-dependent invariant measures*, 1685–1700, © 2011 Elsevier B.V. All rights reserved. 2011, with permission from Elsevier.

fore a short phase of enhanced cooling brought the temperatures back to their pre-event levels (e.g., Rasmussen et al., 2014). This pattern is very clearly apparent in NGRIP  $\delta^{18}\text{O}$  records (North Greenland Ice Core Project members, 2004), and it can be qualitatively simulated by the fast component of a FitzHugh–Nagumo (FHN) model (FitzHugh, 1961; Nagumo et al., 1962), as pointed out by Mitsui and Crucifix (2017), among others; see also Kwasniok (2013), Rial and Yang (2007), Roberts and Saha (2017), and Vettoretti et al. (2022).

We discuss the example of the FHN model at some length in order to illustrate how external forcing can act on a system's internal variability and thereby give rise to more complex dynamics. This model's concise mathematical formulation and its widespread application in paleoclimate modeling and other fields make it ideally suited for this goal. We start with a description of the autonomous model with no time-dependent forcing. Subsequently, we introduce a simple sinusoidal forcing and numerically compute the corresponding PBA. We then extend these consideration into the realm

of random dynamical systems by adding stochastic forcing and discuss the resulting random attractor. Finally, we replace the synthetic forcings by one that corresponds to a paleoclimate proxy record of past  $\text{CO}_2$  concentrations retrieved from Antarctic ice cores (Bereiter et al., 2015a) and show that this setup brings the model's trajectories into good qualitative agreement with the D-O patterns observed in  $\delta^{18}\text{O}$  records from Greenland ice cores. In doing so, we pay less attention to the physical interpretation of the model's variables, while focusing on the detailed explanation of model behavior and on the role of the forcing in the resulting dynamics.

### 3.3.1 The FitzHugh–Nagumo (FHN) model of fast–slow oscillations

The FHN model consists of two coupled ODEs that govern behavior alternating between slow evolutions and fast transitions. Typically, the timescales of the two variables are separated by introducing the parameters  $\tau_x$  and  $\tau_y$ , with  $x(t)$  being the slow component and  $y(t)$  the fast one:

$$\dot{x} = \frac{1}{\tau_x}(y - \gamma), \quad (22a)$$

$$\dot{y} = \frac{1}{\tau_y}[\alpha(y - y^3) - x]. \quad (22b)$$

In order to develop an understanding for the way that such a model can simulate the rapid D-O warmings, followed by slow coolings, we start by discussing its autonomous behavior for time-independent  $\gamma$ .

First, consider the case of large timescale separation

$$\tau_x \gg \tau_y. \quad (23)$$

This choice guarantees that the fast  $y$  component adjusts adiabatically to quasi-static changes of the slow  $x$  component. The time derivative of  $y(t)$ , as shown in Fig. 10a, exhibits either three real roots or a single one, depending on the value of  $x(t)$ , which shifts the graph of the cubic polynomial  $P_3(x, y) = \alpha(y - y^3) - x$  globally upwards or downwards. Of the three potential roots, the outer two are stable fixed points for  $y(t)$  at a fixed value of  $x$ , while the inner one is unstable. Note that the two stable fixed points are always located either left or right of the local minimum or maximum of  $P_3(x, y)$ , respectively. Accordingly, we label them  $y_1$  and  $y_r$ . The positions of the local extrema, namely  $y_{\min} = -\sqrt{1/3}$  and  $y_{\max} = \sqrt{1/3}$ , provide an upper and a lower bound for the left and right stable fixed point, respectively.

Now, let us investigate the coupled dynamics of the slow and fast variables  $x(t)$  and  $y(t)$ . Assume we are in a state where  $x > 2\alpha/\sqrt{27}$  such that  $y_1$  is the only root of  $P_3(x, y)$ . Provided that  $|\gamma| < \sqrt{1/3}$ , the time derivative  $\dot{x}$  and  $x$  itself will have opposite signs, with the consequence that a slow adjustment process of  $x(t)$  sets in. This will shift the polynomial  $P_3(x, y)$  upwards in Fig. 10a, which in turn revives the other two roots of  $P_3(x, y)$ . The fast  $y(t)$  closely follows

$y_l$ , which is shifted accordingly. Once  $x(t) = -2\alpha/\sqrt{27}$ , the root  $y_l$  stops existing and a fast transition to the neighborhood of the opposite root  $y_r$  ensues. This transition switches the sign of  $\dot{x}(t)$  and the slow adjustment of  $x(t)$  now happens in the opposite direction.

In the  $(x, y)$  plane, this behavior manifests itself as a stable limit cycle. However, any value  $|\gamma| > \sqrt{1/3}$  prevents  $\dot{x}(t)$  from switching sign and therefore interrupts the cyclic destruction and revival of the respective opposite root of  $P_3(x, y)$ . Instead,  $|\gamma| > \sqrt{1/3}$  gives rise to a single stable fixed point for the entire system in the  $(x, y)$  plane and in this case both variables relax towards it.

In fact, in the autonomous setting, the system's qualitative behavior is controlled by the value of the parameter  $\gamma$ , which decides between internal oscillations along a limit cycle and relaxation towards a fixed point in the  $(x, y)$  plane. Note that previously we referred to the roots  $y_l$  and  $y_r$  also as stable fixed points of  $y$  for a given value of  $x$ . Here, the term stable fixed point refers to the entire system defined by the coupled ODEs (22a) and (22b). Both  $\gamma = \pm\sqrt{1/3}$  are critical values of  $\gamma$  that give rise to supercritical Hopf bifurcations of the coupled system's fixed points; recall Fig. 4 of Sect. 2.1.

This behavior can be better understood by considering the nullclines of Eqs. (22b) and (22a) in the  $(x, y)$  plane, as shown in Fig. 9. If the branches of the  $y$  nullcline that correspond to  $y_l$  and  $y_r$ , and thus to stable fixed points of Eq. (22b) for a given value of  $x$ , intersect with the  $x$  nullcline given by  $y = \gamma$ , then this intersection constitutes a stable fixed point for the entire system.

If they do not, the system first relaxes along the fast direction toward the  $y$  nullcline. Only then does the adjustment of the slow component start to drag the system along the  $y$  nullcline in the direction where the distance to the  $x$  nullcline decreases. At the point where the  $y$  nullcline reverses, the fast component is immediately attracted by the other branch of the fast nullcline and the same process starts all over again.

So far we have described the formation of the limit cycle in the FHN model under the assumption of clear timescale separation and the independence of the  $x$  nullcline  $\{y = \gamma\}$  from  $x$ . See Rocsoreanu et al. (2000) for the emergence of the limit cycle in the more general FHN model.

The highly nonlinear, two-time behavior of the FHN model somewhat modifies the way that stable limit cycles arise in it. While we saw the oscillation's radius grow with the square root of the bifurcation parameter in the case of the normal form given by Eqs. (3)–(5), in the case of the FHN model, the radius of the oscillations actually grows exponentially over a small range of  $\gamma$  values right after the bifurcation point and then stabilizes. These exponentially growing stable limit cycles have been termed “canard cycles” (Benoît, 1983). Roberts and Saha (2017) have pointed out a possible link between canard cycles and D-O cycles, and they play a role in other excitable climate models; see Pierini and Ghil (2022) and references therein.

### 3.3.2 A pullback attractor of a periodically forced FHN model

Introducing a sinusoidal time dependence

$$\gamma \rightarrow \gamma(t) \propto \sin(t/\tau_f) \quad (24)$$

into the slow Eq. (22a) makes the system non-autonomous, as discussed in general terms in Sect. 3.2, and it periodically switches the self-oscillatory behavior on and off. We consider here the case in which the variations of the external forcing  $\gamma(t; \tau_f)$  occur on a slower timescale than the entire internal dynamics, i.e.,

$$\tau_f > \tau_x > \tau_y. \quad (25)$$

Note that we give up here on the restriction of strict timescale separation between  $x(t)$  and  $y(t)$ , as expressed by Eq. (23).

The trajectories plotted in Fig. 10c–e and f–h represent the solutions of such a periodically forced FHN model starting at different points in the past. The time units are arbitrary and the two sets of solutions are for two different forcing timescales  $\tau_f$ . These trajectories illustrate the applicability of the pullback perspective suggested by Sect. 3.2 and Fig. 6 to the periodically forced FHN model. In contrast to the illustrative examples of Sect. 3.2, an analytical solution is not available in this case. However, this small sample of numerically computed trajectories, together with the phenomenological discussion herein, is quite sufficient for an intuitive understanding of the system's pullback behavior.

For Fig. 10c–e, the forcing's timescale is much slower than the internal timescales. The amplitude of the forcing  $\gamma(t)$  was chosen such that it repeatedly crosses the two thresholds  $\pm\sqrt{1/3}$  and thus induces a sequence of Hopf bifurcations by switching between intervals of self-sustained oscillation and attraction to a stable fixed point. Crossing such a bifurcation point due to slow changes in the forcing is referred to as a bifurcation-induced tipping or “B-tipping” (Ashwin et al., 2012; Ghil, 2019; Ghil and Lucarini, 2020).

Strikingly, all trajectories converge to one another during non-oscillatory time intervals, when they are simultaneously attracted by the single existing fixed point. During oscillatory intervals, phase differences between individual trajectories may, in principle, persist. Still, convergence during a single non-oscillatory interval is so strong that after it the trajectories can no longer be discriminated visually. Numerically, however, the distance between trajectories only tends to zero but never reaches it. At the end of non-oscillatory intervals, the trajectories always re-enter the oscillatory regime from the same location in the  $(x, y)$  plane – to within negligible numerical differences – and hence very nearly repeat themselves. Qualitatively speaking, the PBA  $\mathcal{A}$  – i.e., the family of invariant snapshots  $\{\mathcal{A}(t)\}_{t \in \mathbb{R}}$  of Eq. (13) – is an infinite repetition of the common trajectory structure that can be observed in Fig. 10d, e between –5000 and 15 000 time units. In the case at hand, each snapshot  $\mathcal{A}(t)$  consists of a single point.

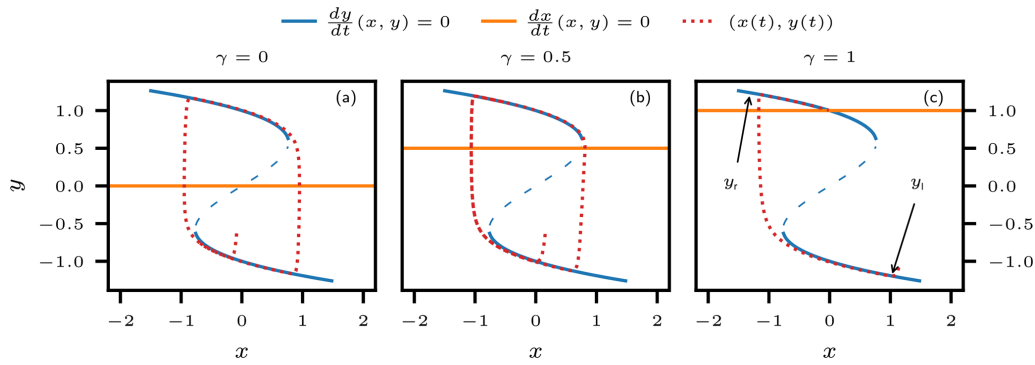


**Figure 9.** Nullclines of the autonomous FHN model governed by Eq. (22) with large timescale separation, for  $\alpha = 2$ ,  $\tau_x = 100$ , and  $\tau_y = 10$ ; the nullclines of the fast  $y$  component are in blue, and those of the slow  $x$  component are in orange. **(a–c)** One illustrative trajectory (red dotted) for  $\gamma = 0, 0.5$ , and  $1.0$ , respectively. The upper branch and the lower branch of the  $y$  nullcline (solid blue) correspond to the roots  $y_r$  and  $y_l$ , respectively, as defined in the text. For fixed values of  $x$ , they constitute stable fixed points for Eq. (22b). The middle branch (dashed blue) corresponds to the unstable fixed point for Eq. (22b) for a given  $x$ . The trajectories for panels **(a)** and **(b)** follow a limit cycle, as the  $x$  nullcline does not intersect with either of the stable branches of the  $y$  nullcline, given that  $|\gamma| < \sqrt{1/3}$ , while the trajectory in panel **(c)** approaches a single stable fixed point for the coupled system formed by the intersection of the  $x$  nullcline with the  $y_l$  branch of the  $y$  nullcline.

For Fig. 10f–h, the timescale separation between the forcing and the internal dynamics is reduced, resulting in a qualitatively different behavior of the non-autonomous system. The frequency of occurrence of B-tipping points is much higher, and hence the trajectories do not even execute a full oscillation during a single time interval that permits oscillations. As a result, two stable patterns of trajectories are formed. These two patterns can be brought into agreement by switching the sign of one pattern and shifting it in time by  $\tau_f/2$ . This symmetry reflects the symmetry of the stable nullcline of the fast system component, as shown in Fig. 9.

Again, the PBA of this non-autonomous system can be thought of as an infinite repetition of the common trajectory structure that can be observed in Fig. 10g, h between  $-5000$  and  $15000$  time units. In contrast to the slow-forcing case, each snapshot  $\mathcal{A}(t)$  now is comprised of two points in the  $(x, y)$  plane. This example illustrates how the action of an external force on an autonomous system can give rise to considerably richer dynamics, which crucially depends on both the system’s internal variability and the nature of the forcing.

### 3.3.3 A random attractor of a periodically and stochastically forced FHN model

Based on the brief introduction to RDSs in Sect. 3.2, we take our investigation of the periodically forced FHN model one step further and include a random component into the external forcing, acting on the model’s fast  $y$  component:

$$dx = \frac{1}{\tau_x}(y - \gamma(t))dt, \tag{26a}$$

$$dy = \frac{1}{\tau_y} \left[ \alpha (y - y^3) - x \right] dt + \sigma d\eta. \tag{26b}$$

Here,  $\eta$  denotes a Wiener process, as in Eq. (20) – i.e., a continuous stochastic process whose increments  $d\eta$  are inde-

pendently and normally distributed, with mean zero and unit variance – and  $\gamma(t)$  remains a periodic forcing of the  $x$  component proportional to  $\sin(\tau_f t)$ .

In order to study the random attractor of this system, we compute trajectories with random initial conditions over a time span long enough to reveal the asymptotic behavior, as shown in Fig. 11. For both the slower and faster deterministic forcing – i.e.,  $\tau_f = 1000$  and  $\tau_f = 350$ , respectively, as studied in the previous paragraphs – several random attractors are approximated for increasing noise variance values  $\sigma$  in Eq. (26b). For each attractor approximation, we use 20 trajectories with the same noise realization. Each random attractor (red) is shown together with the corresponding PBA of the FHN system subject to purely periodic forcing (blue and green).

For the long periodic forcing with  $\tau_f = 1000$ , the trajectories in Fig. 11a converge fairly rapidly to a single one, as in the case with no noise in Fig. 10d, e. Furthermore, there is a clear similarity of pattern and proximity in phase between the PBA of the deterministic system and the random attractor. However, the deviations of the random attractor from the PBA increase in both pattern and phase as the noise variance increases. These deviations are most striking during the oscillatory intervals because the noise can induce phase shifts in the oscillations, which then persist for the duration of the oscillatory interval. During non-oscillatory intervals, the random attractor is less susceptible to the noise because the resulting perturbations decay in the presence of a stable fixed point of the underlying deterministic system.

For the shorter period forcing with  $\tau_f = 350$ , the PBA of the deterministic system features two stable branches, which could in principle persist in the random attractor. As for the case of  $\tau_f = 1000$ , a rapid convergence of the trajectories can be observed for all noise variances. However, two separate

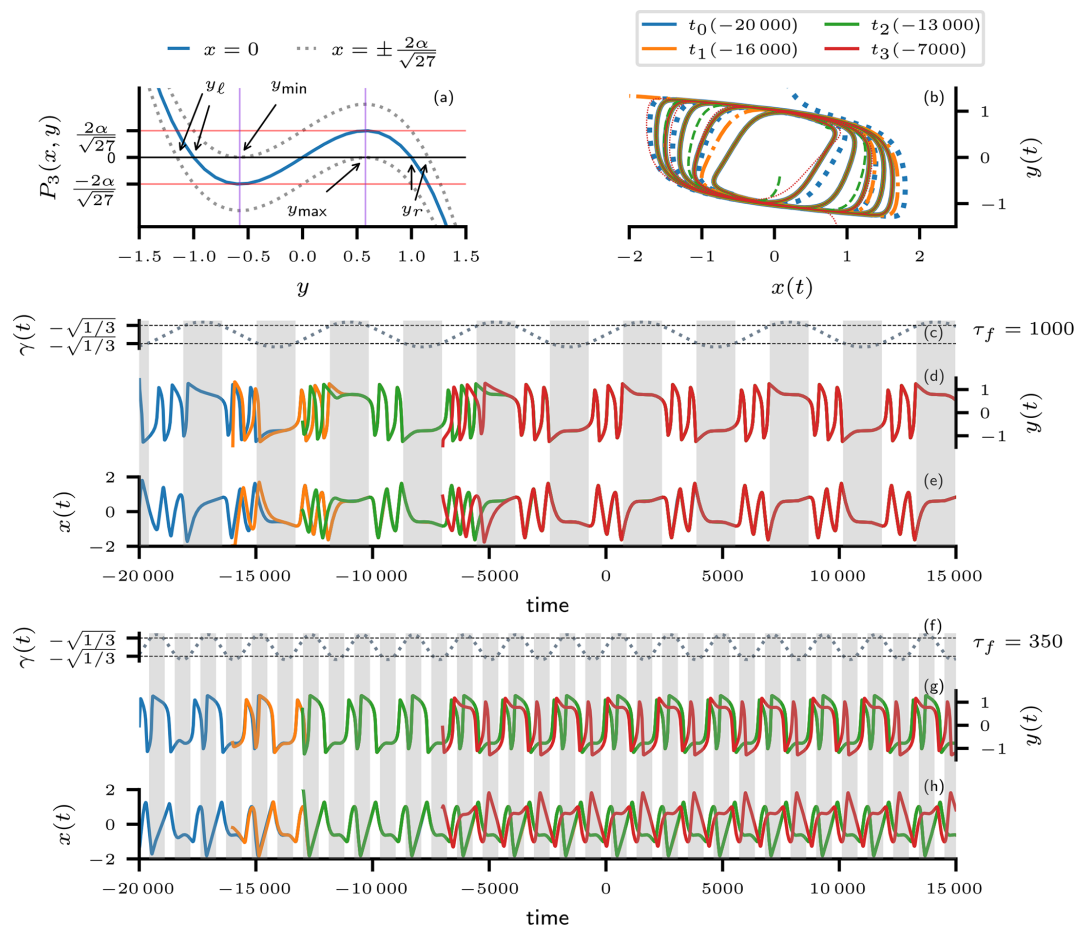


**Figure 10.** FitzHugh–Nagumo (FHN) model with parameters  $\tau_x = 100$ ,  $\tau_y = 60$ , and  $\alpha = 2$ . **(a)** The cubic polynomial  $P_3(x, y)$  of the fast derivative as a function of  $y$  for  $x = 0$  (solid blue line); the red lines point to the local maximal and minimal values of  $P_3(x, y)$ , namely  $\pm 2\alpha/\sqrt{27}$ , respectively – these are the maximal values by which  $P_3$  can be shifted up or down, while maintaining all of its three roots; the dotted gray lines indicate the shifted function with  $x = \pm 2\alpha/\sqrt{27}$ . The purple lines labeled  $y_{\min}$  and  $y_{\max}$  mark the right and left boundaries for the roots  $y_l$  and  $y_r$ , respectively:  $y_l$  and  $y_r$  can never be located in between the two purple lines. **(b)** Trajectories of the non-autonomous model with  $\gamma(t) = 0.8 \sin(t/\tau_f)$  and  $\tau_f = 1000$ , plotted in the  $(x, y)$  phase plane; the trajectories are colored by their starting times  $\{t_0 = -20\,000, t_1 = -16\,000, t_2 = -13\,000, t_3 = -7\,000\}$ , and the initial positions were drawn from a standard Gaussian bivariate distribution. **(c)** The slow time-dependent forcing  $\gamma(t) = 0.8 \sin(t/1000)$ . **(d, e)** The same trajectories as in **(b)** but plotted in time as  $y = y(t)$  and  $x = x(t)$ , respectively. Panels **(f–h)** are same as panels **(c)–(e)** but for the fast time-dependent forcing  $\gamma(t) = 0.8 \sin(t/350)$ . The gray shading in panels **(c)–(h)** indicates intervals during which  $|\gamma| > \sqrt{1/3}$ , and the internal oscillation is hence suppressed.

bundles of trajectories persist, each associated with one of the two separate branches of the deterministic PBA. Only after some time do the two bundles merge and subsequently follow either one of the two branches of the PBA or the other. This phenomenon is called noise-induced synchronization (e.g., Arnold, 1998; Chekroun et al., 2011). Which of the two PBA branches the random attractor follows depends on the exact noise realization. The random attractor may also switch irregularly from one branch of the PBA to the other (not shown). Already in the simple setup explored here, one notices that the higher the noise variance, the faster the synchronization of the trajectories. This statement must be understood probabilistically: it may certainly happen for two given noise realizations that the random attractor with the

higher noise level takes longer to synchronize, as is the case for  $\sigma = 0.7$  and  $\sigma = 0.8$  in Fig. 11b.

The investigation carried out herein assesses a very special case of an FHN model's random attractor. Random attractors of FHN-type models have been studied intensively (e.g., Wang, 2009; Yamakou et al., 2019). Most studies so far, however, have concentrated on the excitable regime of the stochastically forced FHN model, i.e., the deterministic model's parameters were chosen so as to exhibit a single stable fixed point in the absence of the noise. The noise variance was then chosen sufficiently high to ensure that random fluctuations can push the system out of equilibrium and allow it to take a round trip on what would be the deterministic model's limit cycle, given different parameter values.

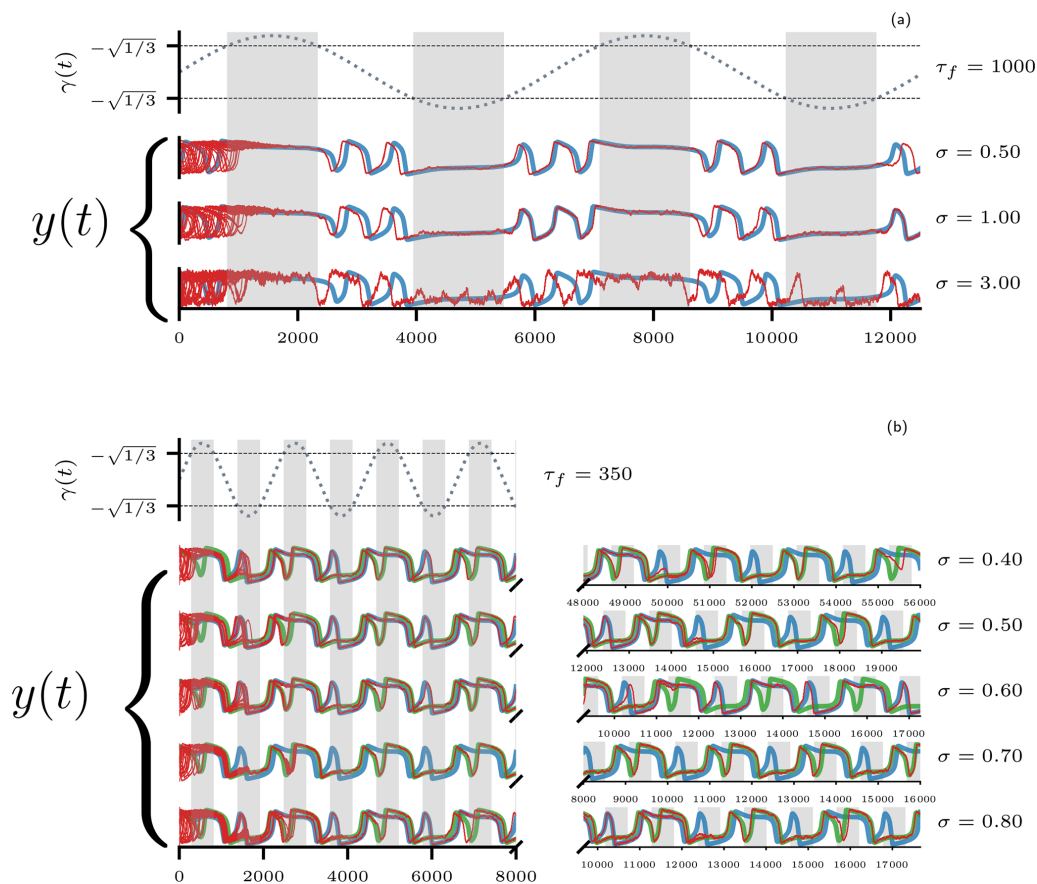


**Figure 11.** Random attractor of the periodically and stochastically forced FHN model governed by Eq. (26). **(a)** Results for slow periodic forcing with period  $\tau_f = 1000$ . The top graph shows the periodic forcing, with non-oscillatory intervals marked by gray shading. The next three graphs show the fast  $y$  component of the approximate random attractors, as per Eq. (26b); the noise variance  $\sigma$  increases from top to bottom. Each random attractor is approximated by integrating 20 trajectories (solid red) with different initial conditions over time and using the same Wiener process as their common stochastic forcing; the corresponding deterministic PBA is shown in blue. The random attractors and the PBA are very similar for small noise variances, but they differ more and more as the noise variance increases. **(b)** Results for faster periodic forcing with period  $\tau_f = 350$ . The forcing is only shown for the first 8000 time units, with non-oscillatory intervals again shaded gray. The left part of panel **(b)** shows five approximate random attractors, computed as in panel **(a)**, on a common time axis. The panel's right-hand side shows their continuations on individual time axes in order to display the moment when full noise-induced synchronization of the trajectories takes place. Prior to this point, the random attractor is split into two branches, which closely follow the PBA of the deterministic system (blue and green). For  $\sigma = 0.7$ , the synchronization already takes place during the first 8000 time units.

The situation studied here is rather different, as shown across Figs. 9–11.

### 3.3.4 An FHN model of the NGRIP record

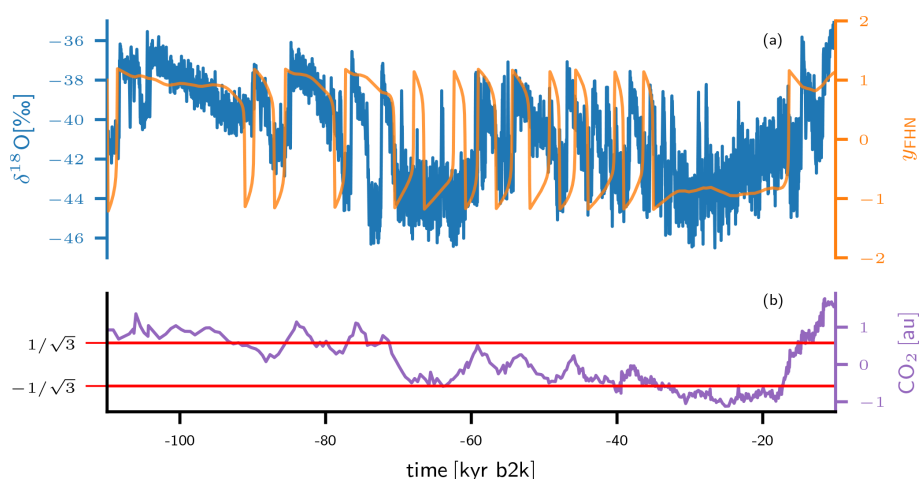
Readers who are familiar with the NGRIP  $\delta^{18}\text{O}$  record (North Greenland Ice Core Project members, 2004) might have already realized the qualitative resemblance between the proxy data and the fast component's trajectory of the periodically forced FHN model in Fig. 10d. In particular, the prominent sawtooth pattern of the data is satisfactorily captured by the fast and slow dynamics of the model.

Figure 12 shows a trajectory of the FHN model for which the sinusoidal forcing used in Fig. 10 was replaced by a rescaled time series of atmospheric  $\text{CO}_2$  concentrations re-

trieved from Antarctic ice cores (Bereiter et al., 2015a):

$$\gamma(t) \propto \text{CO}_2(t). \quad (27)$$

Is it remarkable how well this simple forcing brings the oscillatory intervals of the FHN model into agreement with the time intervals of the record that are dominated by D-O cycles without any systematic tuning of the model parameters. Clearly, the  $\text{CO}_2$ -forced FHN model fails to reproduce the exact waiting times between D-O events. However, with these waiting times being at least in part stochastically determined (Ditlevsen et al., 2007), the purely deterministic FHN model is not meant to reproduce the exact pattern of D-O events. Vettoretti et al. (2022) have carried out a detailed



**Figure 12.** FHN model fit to the NGRIP  $\delta^{18}\text{O}$  dataset of 20-year means, as published as a supplement to Seierstad et al. (2014) (see also Rasmussen et al., 2014). Originally, the North Greenland Ice Core Project members (2004) reported a 50-year-mean dataset. **(a)** The fast component  $y_{\text{FHN}}(t)$  of an FHN model forced with historical  $\text{CO}_2$  concentrations (orange), together with the observed  $\delta^{18}\text{O}$  record (blue) from the NGRIP ice core (Seierstad et al., 2014). **(b)** Rescaled atmospheric  $\text{CO}_2$  concentrations from Antarctic ice cores in arbitrary units (au) (Bereiter et al., 2015a); the horizontal red lines indicate the lower and upper bounds,  $y_{\min} = -\sqrt{1/3}$  and  $y_{\max} = \sqrt{1/3}$ , respectively, of the free-oscillation regime.

study on the use of a  $\text{CO}_2$ -forced FHN-type model to simulate D-O variability.

In fact, Rousseau et al. (2022, Fig. 6) describe in detail a somewhat more complex, proxy-record-based picture of the interaction between episodes full of D-O events, (Heinrich, 1988) events, and longer-term cooling trends. It is quite possible that a simple model like the one in this section but including explicitly continental ice sheets could capture such a detailed picture.

In the present framework, the FHN model's fast variable  $y(t)$  may be interpreted as the intensity of the Atlantic meridional overturning circulation (AMOC), which switches between on and off states during self-oscillatory behavior; see, for instance, Henry et al. (2016), Ghil (1994, Table 5), and Ghil and Lucarini (2020, Table I). The slower  $x$  variable that drives the transition between the on and off states of the AMOC may then be taken, for instance, as the waxing and waning of Northern Hemisphere ice sheets (e.g., Ghil et al., 1987), linked in turn to varying ice shelf extent (e.g., Boers et al., 2018), or as the weakening and strengthening of Antarctic bottom water production (Vettoretti et al., 2022).

The interaction between the fast variable and the slow one happens here in the presence of a climate forcing represented by  $\text{CO}_2$  concentration. On the much slower timescales of Quaternary glaciations, an interplay between the  $\text{CO}_2$  concentration and mean global temperature might also occur, as we shall see in the next section.

#### 4 An NDS for the Quaternary glaciations

Apparently, it was Crucifix (2013) who first applied pull-back ideas to the problems of Quaternary glaciations, independently of earlier work on the topic in the climate literature (Ghil et al., 2008; Chekroun et al., 2011; Bódai and Tél, 2012). His work concentrated mainly on the connection between the pacemaking role of the orbital forcing and the observed irregularity of the glacial terminations during the Late Pleistocene; cf. Broecker and Van Donk (1970) and Ghil and Childress (1987, Fig. 11.2).

Based on the considerable success of NDS and RDS applications to other climate problems – such as ENSO (Ghil et al., 2008; Ghil and Zaliapin, 2015; Chekroun et al., 2018; Marangio et al., 2019), the wind-driven ocean circulation (Pierini et al., 2016, 2018), or the evaluation of the ensemble simulations routinely performed in support of the Assessment Reports of the Intergovernmental Panel on Climate Change (Drótos et al., 2015; Vissio et al., 2020) – it would appear worthwhile to proceed further along these lines.

Box 2 summarizes open questions with respect to Quaternary glaciations whose investigation should be aided by NDS and RDS theory. Of course, each of these problems requires one or more distinct climate models, as well as very careful modeling of the kinds of time-dependent changes in forcing and parameters that are most enlightening, as well as most relevant and plausible. A good way would be to start testing ideas with relatively simple models and pursue the investigation systematically across a hierarchy of models – through intermediate ones and on to the most detailed ones – in order to further increase understanding of the climate system and

The concepts and tools summarized in Sect. 3.2 could shed further light on several problems that not yet quite solved concerning Quaternary glaciations and paleoclimate in general. A short and highly incomplete list of the interesting problems that might gain by such a treatment is given below.

1. What are the causes of the MPT, and what are the contributions of intrinsic climate variability and orbital forcing therein? See discussion in Sec. 2.2 for more details.
2. What causes the large continuous background of the observed spectrum: is it deterministic chaos, stochastic forcing, or both? See discussion in the caption of Fig. 4 for more details.
3. Particularly complex problems are associated with Heinrich and D-O events and their modulation over longer time intervals by orbital forcing and other slow-acting changes in atmospheric composition, geology, ocean circulation, and so on. See, for instance, Rousseau et al. (2021, and references therein) for more details.
4. It is well established by now that a snowball mode occurred several times in Earth's geologic history, but we still know fairly little about how the planet got into, and especially out of, such a mode (e.g., Pierrehumbert, 2004).

**Box 2.** Some open questions concerning Quaternary glaciations.

of its predictability on the various paleoclimatic time scales mentioned in the list above.

Such an approach can usefully complement the more common one of merely pushing onwards to higher and higher model resolution in order to achieve ever more detailed simulations of the system's behavior for a limited set of semi-empirical parameter values. Ghil (2001) and Held (2005), among others, have emphasized the need to pursue such a model hierarchy, as originally proposed by Schneider and Dickinson (1974), in order to balance the need to broaden the number of plausible hypotheses vs. the need for confronting them with spatiotemporal details derived from observations.

In this section, we illustrate how the PBA concept can help shed more light upon the dynamics of ice age models. As pointed out in Sect. 3.1 and elsewhere in this paper, there is a long history of modeling the climate of the Quaternary by means of conceptual models, and many non-autonomous models have been proposed to simulate glacial–interglacial cycles of the last 400 kyr to 2.6 Myr based on the orbital forcing. In Appendix A, we provide a long but still not exhaustive list of glacial-cycle models and specify some of their key characteristics, including the degree of their success at simulating the MPT; see also the discussion in Sect. 2.2.

Among these glacial-cycle models, the model of Daruka and Ditlevsen (2016, DD16 hereafter) belongs to the more abstract ones, as it is not derived from detailed physical considerations. Still, its concise form, interesting nonlinear dynamics, and ability to simulate glacial cycles, as well as the MPT, make the DD16 model well suited for our illustrative purposes. We first modify this model slightly from its original formulation. We do so mainly in order for the model to better approximate the benthic  $\delta^{18}\text{O}$  proxy reconstruction of glacial–interglacial cycles due to Lisiecki and Raymo (2005a), especially the timing of glacial terminations; compare our Fig. 13 with Fig. 1 in DD16. Thereafter, we compute the PBAs of the modified DD16 model (hereafter M-DD16) to investigate the dynamical stability of its glacial cycles over the past 2.6 Myr.

Our model's variables, following DD16, are a global temperature anomaly  $y$  that is proportional to minus the global ice volume and an effective climatic memory term  $x$  that represents the internal degrees of freedom. In the deterministic case, the governing equations of the M-DD16 model are given by

$$\tau \dot{x} = \lambda y, \quad (28a)$$

$$\tau \dot{y} = -\alpha(t) + x - x^3 - \beta(t)F(t)x - \kappa y; \quad (28b)$$

here  $t$  is the time (in kyr) and  $F(t)$  is the normalized 21 June insolation at  $65^\circ\text{N}$ , based on the calculations of Laskar et al. (2004a), as shown in Fig. 13a. The constant parameter values are chosen as  $\kappa = 1$ ,  $\tau = 100$ , and  $\lambda = 10$ . Note that with this choice of  $\lambda$  and unlike in the FHN model of D–O oscillations in Sect. 3.3,  $x$  is the fast variable and  $y$  is the slow one.

In the original DD16 model, MPT-like behavior was produced by a slow sigmoid variation of the parameter  $\kappa$  in Eq. (28b),

$$\kappa(t) = \kappa_1 + 0.5(\kappa_0 - \kappa_1) \left( 1.0 - \tanh\left(\frac{t-t_0}{t_s}\right) \right). \quad (29)$$

In our M-DD16 model, we introduce instead a slow change in the parameters  $\alpha(t)$  and  $\beta(t)$  of Eq. (28b) as follows:

$$\alpha(t) = 2.1 - 1.4 \tanh((t + 1100)/500), \quad (30a)$$

$$\beta(t) = 2.5 + 1.4 \tanh((t + 1100)/500). \quad (30b)$$

The functions  $\alpha(t)$  and  $\beta(t)$  so defined are plotted in Fig. 13b, and they induce, as we shall see forthwith, a change in model behavior that not only resembles the MPT but also shows correct timings for most of the terminations. Moreover, to simulate  $\delta^{18}\text{O}_{\text{model}}$ , we add a linear trend to the slow variable  $y$  to mimic the overall cooling at time scales of millions of years, and thus  $\delta^{18}\text{O}_{\text{model}} = 4.3 - 1.4y + 0.0003t$ . Equation (28) generalizes a first-order ODE system that is equivalent to the Duffing form of the nonlinear spring Eq (7) discussed in Sect. 2.2. The use of such classical first-order systems – like the Duffing and Van der Pol ones – in paleoclimate models was initiated by Saltzman et al. (1981); see also Sect. 2.2 herein.

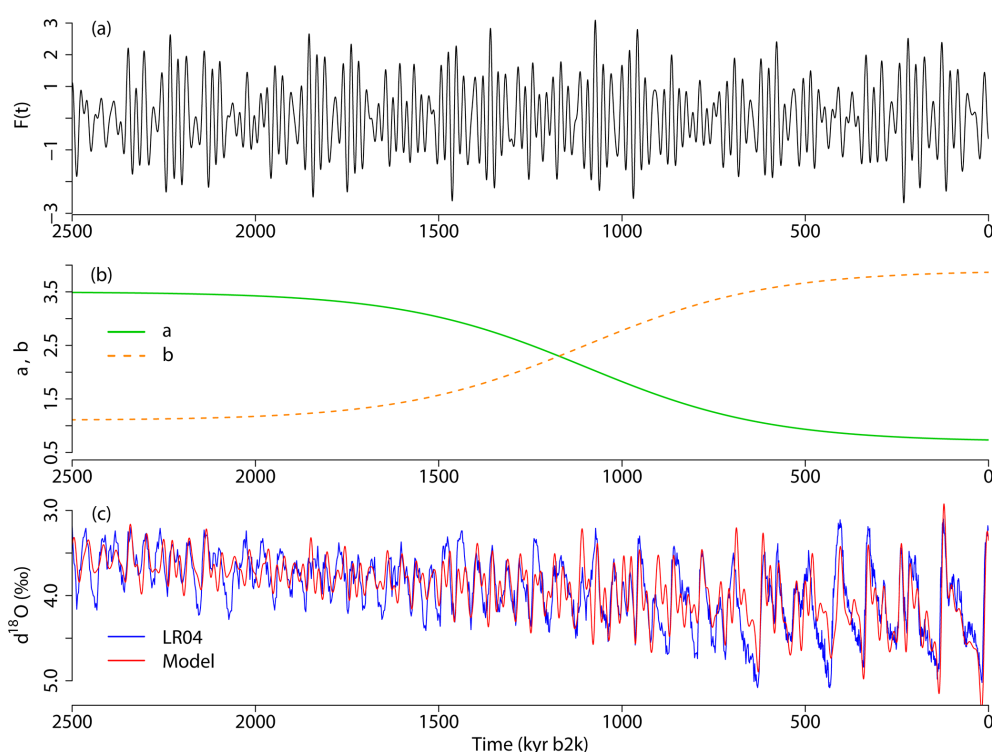


**Figure 13.** Glacial–interglacial cycles simulated by the modified Daruka and Ditlevsen model of Eqs. (28) and (30): (a) 21 June insolation  $F(t)$  at  $65^\circ$  N, normalized to have mean zero and unit standard deviation over the last 1000 kyr, according to Laskar et al. (2004a). (b) Slowly changing parameters  $\alpha(t)$  and  $\beta(t)$  introduced to give rise to the MPT. (c) Simulated glacial–interglacial cycles  $\delta^{18}\text{O}_{\text{model}}$  (red) in comparison with the benthic  $\delta^{18}\text{O}$  data (blue); the latter dataset, provided by Lisiecki and Raymo (2005a), is also known as the LR04 stack.

Figure 13c shows a time series of simulated glacial–interglacial changes  $\delta^{18}\text{O}_{\text{model}}$  (red) in comparison with the benthic  $\delta^{18}\text{O}$  (blue) of Lisiecki and Raymo (2005a). The model’s initial condition is taken to be  $x = -1$  and  $y = 0$  at  $t = 10\,000$  kyr b2k and, since the insolation forcing in Fig. 13a is prescribed as a time series with 100-year sampling, we solved Eq. (28) using Heun’s predictor–corrector method (Isaacson and Keller, 2012, chap. 8) with a step size of 100 years. A large spin-up time is chosen to guarantee that transient effects caused by the initial conditions have abated by the year 2.6 Ma b2k, which is the starting point for the time interval under study. The correlation between the model simulation and the proxy record is 0.75 for the time interval from 2600 to 0 kyr b2k and 0.72 over the interval from 1000 to 0 kyr b2k. Varying the parameters slowly across the time interval of interest, as shown in Fig. 13b, leads to a change in the frequency – from a dominant 41 kyr periodicity prior to the MPT, at roughly 1.2 Ma kyr b2k, to a dominant 100 kyr periodicity after the MPT, at roughly 800 kyr b2k – and a substantial increase in the amplitude.

We next approximate the PBA by taking 40 random initial conditions at 10 Ma b2k and integrating the model of Eqs. (28) and (30) up to the present time. The PBA in this case is simply a moving fixed point, as plotted in Fig. 14a, since the model dynamics is predominantly stable in the long

time interval prior to the MPT. It would thus appear that the orbital forcing simply moves this fixed point around and fully determines Earth’s climate. This agrees with the clear statement in DD16 that “first and foremost, our model does not have any internal periods of oscillation”.

However, when keeping the parameters  $\alpha$  and  $\beta$  fixed at their post-MPT values  $\alpha = 0.7$  and  $\beta = 3.9$  throughout the simulation interval and repeating the computation of the PBA, a more complex picture arises. In the latter case, Fig. 14b shows a bunching of trajectories into separate fuzzy clusters, subject to the quasi-periodic orbital forcing of Fig. 13a.

There are two interesting inferences to be drawn. First, post-MPT dynamics is much more irregular and unstable than the more stable dynamics prior to the MPT. The robustness of the 40 kyr glacial cycles and instability of 100 kyr glacial cycles against perturbations is in line with the conclusions of previous studies (Mitsui et al., 2015; Quinn et al., 2018). It also appears to be consistent with the Willeit et al. (2019) simulation of the last 3 Myr of Earth’s history that used an Earth system model of intermediate complexity (CLIMBER-2) that included ice sheets and a carbon cycle, along with atmosphere–ocean dynamics. In their work, trajectories starting from different initial states tended to converge to a single attracting trajectory in the Early Pleistocene,

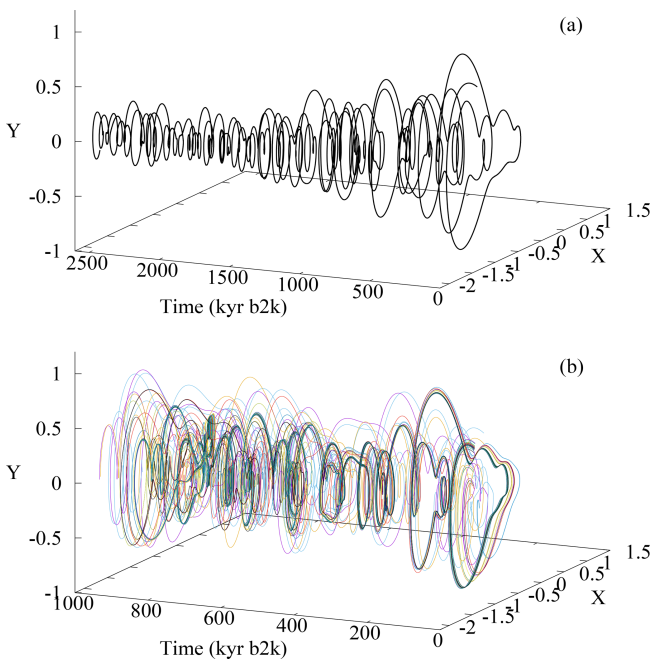


**Figure 14.** PBA of the M-DD16 model governed by Eq. (28), approximated by 40 trajectories starting from random initial conditions in  $(x, y) \in [-2, 2] \times [-2, 2]$  at  $t = -10000$  kyr. **(a)** The PBA corresponding to Fig. 13, with the slowly changing parameters  $\alpha(t)$  and  $\beta(t)$  given by Eq. (30). **(b)** The PBA for  $\alpha(t)$  and  $\beta(t)$  kept constant at the post-MPT values of  $\alpha = 0.7$  and  $\beta = 3.9$ . In panel **(b)**, the PBA is shown over a shorter time interval of the last 1000 kyr so that the detailed structure is more clearly visible. Without changes in  $\alpha$  and  $\beta$  in time, the overall structure of the PBA is similar before and after 1000 kyr b2k.

while several distinct trajectories survived in the Late Pleistocene after the MPT.

Second, the separate bundles or “ropes” of trajectories in Fig. 14b seem to point to the type of generalized synchronization discussed in the paleoclimate context by De Saedeleer et al. (2013) and in the context of interannual and interdecadal climate variability by Pierini and Ghil (2022) and Vannitsem et al. (2021). Generalized synchronization in the strict sense of the existence of a map between a time-dependent control and the system’s asymptotic behavior has only been shown to hold for non-chaotic systems. Work is under way, however, to further generalize this concept to chaotic systems as well (e.g., Rulkov et al., 1995; Zhang et al., 2007).

## 5 Conclusions

In this review and research paper, we have covered the contributions of the 1970s to the rebirth of the Milankovitch (1920) theory of the ice ages in Sect. 1 and the 1980s advances in modeling the Quaternary climate’s intrinsic variability in Sect. 2. In Sect. 3, we presented first results on the effects of

the orbital insolation forcing of the data discussed in Sect. 1 on the intrinsic variability of the data discussed in Sect. 2, and proceeded to introduce the novel concepts and tools of the theory of non-autonomous and random dynamical systems (NDSs and RDSs) that can help to better model and understand these effects. Section 3 concluded with the formulation and study of a FitzHugh–Nagumo (FHN)-type model of recurrent Dansgaard–Oeschger (D–O) events, in which historical  $\text{CO}_2$  concentrations induced episodes of D–O events alternating with episodes of their absence in excellent qualitative agreement with NGRIP  $\delta^{18}\text{O}$  data; see Fig. 12.

Finally, in Sect. 4, we listed a number of open issues on Quaternary and longer paleoclimate timescales and proposed to address them by using the tools of Sect. 3.2. This approach was illustrated by a Duffing-type model of Daruka and Ditlevsen (2016), modified to include slow changes in the parameters that mimic such changes in the Earth system over the duration of the Quaternary period.

When the parameters are gradually changed in time so as to exhibit the mid-Pleistocene transition (MPT), the PBA is simply a moving fixed point. However, when the parameters are fixed at their post-MPT values, the PBA so obtained is chaotic and exhibits clusters of trajectories that we termed ropes. This suggests (a) that the stability of the system is gradually lost while crossing the MPT and (b) that the Late Pleistocene climate, albeit chaotic, may well be subject to a kind of generalized synchronization (cf. De Saedeleer et al., 2013; Pierini and Ghil, 2022; Vannitsem et al., 2021) with the orbital forcing that is illustrated in Fig. 5 of Sect. 3.1 herein. In the specific situation at hand, separate ropes may be associated with various combination tones of the forcing frequencies.

In a broader perspective – and leaving aside various finer points of the MPT conversation outlined in Sect. 2.2 – one can see the work that was reviewed and extended in this paper as a confirmation of the fine intuition of Emiliani and Geiss (1959), 6 decades ago, as summarized in and further expanded by Ghil and Childress (1987, Sect. 12, pp. 446–447).

Hence the following scenario (compare Emiliani and Geiss, 1959) suggests itself for the successive climatic transitions from Pliocene to Pleistocene and from Early to Late Pleistocene: As land masses moved towards more northerly positions, small ice caps formed on mountain chains and at high latitudes. These ice caps, due to their feedback on albedo, made climate more sensitive to insolation variations than it was in the total absence of ice. The response of the climatic system to such variations during the Early Pleistocene (2000 [kyr]–1000 [kyr] ago) was still relatively weak, of a fraction of a degree centigrade in global temperature perhaps, in agreement with the quasi-equilibrium results of Sect. 10.2.

As ice caps passed, about 1000 [kyr] ago, a certain critical size, the unforced system jumped from its stable equilibrium to its stable limit-cycle state (Figures 12.5 and 12.9), increasing dramatically the climate's total variability, to a few degrees centigrade in global temperature. Furthermore, resonant response became possible (see also Oerlemans (1984) [in Berger et al. (1984)] and Sergin (1979)), enhancing abruptly the amplitude of the peak at 100 kyr, among others.

The take-home message is that slow and fast processes, both intrinsic and extrinsic, interact on all paleoclimatic timescales and that we are mastering the art of modeling such interactions.

### Appendix A: Low-order dynamical-system models of glacial cycles

The dynamical modeling of glacial cycles dates back to the 1970s. Calder (1974) proposed a model of global ice volume changes that had different sensitivities to the insolation when ice sheets were waxing and waning, respectively. His model can be written as an NDS, according to Paillard (2001). Subsequently, conceptual dynamical models were further developed (e.g., Imbrie and Imbrie, 1980; Berger, 1999). Some of the more recent models simulate the proxy records of glacial cycles remarkably well (Paillard, 1998; Imbrie et al., 2011; Parrenin and Paillard, 2012).

Shortly after Calder (1974) presented his work, Weertman (1976) proposed a simple ice sheet model based on the flow law of a perfectly plastic solid. Next, researchers extended this simple ice sheet model by coupling it with an energy balance model (Källén et al., 1979) and further with the isostatic response of the underlying bedrock (Oerlemans, 1980; Ghil and Le Treut, 1981; Le Treut and Ghil, 1983; Pollard, 1983). Källén et al. (1979) found self-sustained oscillations in their simple coupled ice sheet–energy balance model. Le Treut and Ghil (1983) showed that the dominant 100 kyr periodicity of glacial cycles is generated – in their simple oscillator coupling ice sheet volume with the bedrock's isostatic rebound, on the one hand, and with the atmosphere and ocean's energy balance, on the other hand – via nonlinear resonance with the multi-periodic orbital forcing. More recently, Verbitsky et al. (2018) developed a simple physical model through a scaling argument that respects the underlying physics. Another branch of simple models explicitly includes the carbon cycle as an essential ingredient (Saltzman and Maasch, 1990; Paillard and Parrenin, 2004; Hogg, 2008; Toggweiler, 2008; Omta et al., 2016; Talento and Ganopolski, 2021).

A deeper understanding of glaciation cycles cannot be obtained without process-based models that focus on the detailed physics and biogeochemical phenomena involved (Berger et al., 1999; Ganopolski and Calov, 2011; Abe-Ouchi et al., 2013; Ganopolski and Brovkin, 2017; Willeit et al.,

2019). Still, simple dynamical models like the ones mentioned above, as well as models based on more mathematical considerations, are also useful for understanding the climate system's behavior and changes therein, since complex systems can sometimes exhibit familiar dynamics, regardless of the details (Nicolis and Nicolis, 2012; Crucifix, 2011). As Henri Poincaré pointed out, “mathematics is the art of giving the same name to different things”.

For example, coupled nonlinear oscillators frequently exhibit synchronization with simple frequency ratios, either with each other (Pikovsky et al., 2001) or with the forcing (Ghil and Childress, 1987). Thus, mathematical models that ignore many physical details may also help us elucidate emergent properties in paleoclimatic dynamics (Tziperman et al., 2006; Crucifix, 2011, 2012; De Saedeleer et al., 2013; Mitsui et al., 2015; Ashwin and Ditlevsen, 2015; Daruka and Ditlevsen, 2016) or test different orbital hypotheses (Huybers, 2011). Many low-order models of glacial dynamics are listed in Table A1, although it is by no means exhaustive.

### Appendix B: PBA for a limit cycle with sinusoidally modulated radius

Here we study the system of two formally decoupled ODEs

$$\begin{aligned} \frac{d\rho}{dt} &= \alpha(\mu + \beta \sin(\nu t) - \rho), \\ \frac{d\phi}{dt} &= \omega \quad \text{with } \rho > 0, \mu > 0, \end{aligned} \quad (\text{B1})$$

that were introduced in Sect. 3.2 and analytically derive their invariant sets

$$\begin{aligned} \mathcal{A}(t) &= \{(\alpha\beta \sin(\nu t + \vartheta) + \mu, \varphi) : \varphi \in [0, 2\pi)\} \\ \forall t \in \mathbb{R}, \end{aligned} \quad (\text{B2})$$

as well as the corresponding pullback attractor (PBA). Following Crauel and Kloeden (2015), the PBA is given by the family

$$\mathcal{A} = \{\mathcal{A}\}_{t \in \mathbb{R}}. \quad (\text{B3})$$

First, we define  $\Delta\rho(t) = \rho(t) - \mu$ , which gives rise to

$$\frac{d\Delta\rho(t)}{dt} = -\alpha\Delta\rho(t) + \alpha\beta \sin(\nu t). \quad (\text{B4})$$

This is an inhomogeneous ODE and can thus be solved by the variation of parameters method (e.g., Boyce and DiPrima, 2005). The ansatz

$$\Delta\rho(t) = c(t) e^{-\alpha(t-t_0)}, \quad (\text{B5})$$

yields

$$\frac{d\Delta\rho(t)}{dt} = -\alpha\Delta\rho(t) + \frac{dc(t)}{dt} e^{-\alpha(t-t_0)}. \quad (\text{B6})$$

**Table A1.** List of simple conceptual glacial-cycle models with only 1–3 variables. Note that, while extensive, this list is not exhaustive.

Author(s) (year)	Succinct description	Dynamical properties	Is the mid-Pleistocene transition (MPT)-like behavior generated?	Additional comments
Low-order dynamical systems models of glacial cycles				
Calder (1974)	Model of the global ice volume with different sensitivities to the insolation during growth and retreat, respectively.	Non-chaotic. No self-sustained oscillation in the absence of forcing	Not specifically addressed.	His model can be written as a non-autonomous dynamical system (NDS) (Paillard, 2001).
Weertman (1976)	Simplified ice sheet model based on the flow law of a perfectly plastic solid.	Non-chaotic. No self-sustained oscillation in the absence of forcing.	Not specifically addressed.	
Källén et al. (1979), Ghil and Le Treut (1981), Le Treut and Ghil (1983), Ghil (1994)	Ice sheet–bedrock–temperature coupled oscillator; see the text for details.	Chaotic in the presence of orbital forcing (Ghil, 1994). Exhibits self-sustained oscillations with a period of $\approx 10$ kyr; the basic mechanism for getting $\sim 100$ kyr cycle is nonlinear resonance at a difference tone between the 19 and 23 kyr precession cycles (Le Treut and Ghil, 1983); see Sect. 2.1 herein.	Not explicitly. It can exhibit, however, the MPT in principle, since 41 kyr oscillations and dominant 100 kyr oscillations can be generated depending on the model's parameter values.	Källén et al. (1979) is an ice sheet–temperature coupled oscillator. Ghil and Le Treut (1981) introduced the bedrock and Le Treut and Ghil (1983) added the orbital forcing.
Imbrie and Imbrie (1980)	Piecewise linear model with two different timescales for ice sheet waxing and waning.	Non-chaotic. No self-sustained oscillation in the absence of forcing.	Not specifically addressed.	400 kyr periodicity is more dominant than 100 kyr periodicity.
Saltzman and Maasch (1988, 1990), Maasch and Saltzman (1990)	Coupled oscillator based on ice–CO <sub>2</sub> –ocean temperature (or NADW) coupling. Nonlinearity is only in the CO <sub>2</sub> component.	Non-chaotic. After the MPT, it exhibits self-sustained oscillations with a period of $\sim 100$ kyr in the absence of forcing.	Yes, the MPT arises via a Hopf bifurcation in the underlying system; see also Crucifix (2012).	It has a strange non-chaotic attractor, as well as a chaotic one, depending on the parameter setting (Mitsui and Aihara, 2014).
Paillard (1998), Parrenin and Paillard (2003, 2012)	Hybrid dynamical system with discrete states that switch when conditions are satisfied.	Non-chaotic but the dynamics is sensitive to parameter changes near the switching boundaries (Paillard, 2001). No self-sustained oscillations in the absence of forcing.	Yes, in Paillard (1998).	The authors call these models relaxation oscillators, in spite of their discrete-state formulation.
Berger (1999)	Delayed differential equation for ice volume,	Robustness of trajectories against random perturbations is mentioned. It exhibits damped oscillations in the absence of forcing.	Not specifically addressed.	
Paillard and Parrenin (2004)	Coupled oscillator based on Northern Hemisphere ice volume–Antarctic ice extent–CO <sub>2</sub> coupling.	Non-chaotic. It exhibits self-sustained oscillations in the absence of forcing.	Yes, the MPT is induced by a slow drift in the bottom water formation efficiency around the Antarctic.	Ashwin et al. (2018) showed that this model can exhibit chaotic dynamics when it is slightly modified.
Ashkenazy and Tziperman (2004), Tziperman et al. (2006)	An ice mass model that simplifies the sea ice switch model of Gildor and Tziperman (2000).	It exhibits self-sustained oscillations in the absence of forcing. Non-chaotic under the orbital forcing.	Yes, in Ashkenazy and Tziperman (2004), where the maximum ice volume threshold is increased in time according to the regolith hypothesis.	Uses the temperature–precipitation feedback introduced by Källén et al. (1979).
Huybers (2007, 2011)	The ice mass grows monotonically and collapses to zero when it exceeds a threshold modulated by the obliquity (Huybers, 2007) or by a hybrid measure consisting of the obliquity and climatic precession (Huybers, 2011).	Non-chaotic. It exhibits self-sustained oscillations in the absence of forcing.	Yes, in Huybers (2007).	

Table A1. Continued.

Author(s) (year)	Succinct description	Dynamical properties	Is the mid-Pleistocene transition (MPT)-like behavior generated?	Additional comments
Imbrie et al. (2011)	Data-based, phase space model for Pleistocene ice volume with thresholds.	Due to the presence of the threshold, the model is sensitive to changes in parameters or in its position in phase space.	Yes, MPT-like behavior is produced solely by changes in orbital parameters.	
Crucifix (2012), De Saedeleer et al. (2013)	Forced Van der Pol (VdP) oscillator model; closely related to the FHN model used in Sect. 3.3 herein.	Non-chaotic (Crucifix, 2012) but sensitive to the noise. It exhibits self-sustained oscillations in the absence of forcing.	Yes, MPT-like behavior is generated via a Hopf bifurcation with an explosive character (Crucifix, 2012).	Ashwin et al. (2018) showed that this model has only a small parameter region corresponding to chaotic dynamics but may have a wider chaotic region when it is generalized to the VdP–Duffing system.
Mitsui et al. (2015)	One-dimensional phase oscillator model.	Non-chaotic.	Yes, MPT-like frequency change accompanies a smooth or non-smooth saddle-node bifurcation of tori.	It has a strange non-chaotic attractor in a classical sense, i.e., not in the pullback sense.
Ashwin and Ditlevsen (2015)	Two-dimensional forced limit cycle oscillator.	Non-chaotic; overall stability of simulated glacial cycles against dynamical noise is reported.	It exhibits MPT-like behavior via a trans-critical bifurcation of the slow manifold in the fast dynamics.	
Omta et al. (2016)	Forced two-dimensional oscillator consisting of ocean alkalinity and calcifer population.	Non-chaotic or chaotic given periodic forcing, depending on the parameters. It exhibits self-sustained oscillations in the absence of forcing.	Yes.	
Daruka and Ditlevsen (2016)	Forced Duffing oscillator-type model.	No self-sustained oscillations in the absence of forcing. Can be chaotic depending on parameter values; the authors call this the “climatic butterfly effect”.	Yes, MPT-like behavior is induced by a slow change in the damping coefficient parameter $\kappa$ .	See also Sect. 4 herein.
Huybers and Langmuir (2017)	Coupled system of ice volume, temperature, and atmospheric CO <sub>2</sub> incorporating a delayed CO <sub>2</sub> contribution from ocean ridge volcanism. It is reduced to a forced 1-D delay differential equation.	A phase-locking property is reported. The underlying system has two stable and one unstable stationary states. However, it is close to a Hopf bifurcation point and is excitable by the forcing.	Yes, the MPT is modeled as a switch from small-amplitude oscillations to large-amplitude ones, which is triggered by the amplitude modulation of obliquity cycles.	
Quinn et al. (2018)	Scalar delay differential equation for ice volume, derived from the Saltzman and Maasch (1988) model via the linear chain approximation.	Non-chaotic before the MPT and temporarily chaotic after the MPT around 800 kyr b2k. In the absence of astronomical forcing, the delayed feedback leads to bistable behavior, in which stable large-amplitude oscillations and an equilibrium coexist.	Yes, MPT-like behavior is induced by summer insolation forcing as a transition from small-amplitude $\sim 41$ kyr cycles to large-amplitude $\sim 100$ kyr cycles.	
Ashwin et al. (2018)	Study of several low-order dynamical systems models, including Paillard and Parrenin (2004), Crucifix (2012), and a generalized VdP–Duffing oscillator.	Chaotic or non-chaotic depending on the model and its parameter values.	Not explicitly discussed. The models can, however, exhibit MPT-like behavior in principle because 41 kyr oscillations and dominant 100 kyr oscillations are generated depending on parameter values.	The authors stress the possibility of chaotic dynamics occurring.

**Table A1.** Continued.

Author(s) (year)	Succinct description	Dynamical properties	Is the mid-Pleistocene transition (MPT)-like behavior generated?	Additional comments
Verbitsky et al. (2018)	Coupled model relying on ice sheet basal temperature–ocean temperature coupling, deduced from physical laws via a scaling analysis.	Non-chaotic. No self-sustained oscillations in the absence of forcing. The 100 kyr cycles are attributed to a period-doubling response to 41 kyr obliquity cycles.	Yes, MPT-like behavior is induced by an enhancement of positive feedbacks against negative feedbacks in the model.	
Talento and Ganopolski (2021)	Ice volume–CO <sub>2</sub> coupled conceptual model.		Not specifically addressed.	This model was developed to simulate the last 800 kyr of glacial cycles and Earth’s future climate on the million-year timescale.
Low-order dynamical models in which stochastic processes are of the essence				
Benzi et al. (1981, 1982), Nicolis (1981)	Two independent formulations of a stochastic-resonance model. Additive noise favors the bimodal response of a periodically modified double-well potential to global annual insolation variations.	Additive stochastic perturbations play a key role.	Not specifically addressed. An MPT-like transition could be obtained by subjecting both the depth of the deterministic double well and the pure periodicity of its modulation to a more or less gradual modification.	Benzi et al. (1981, 1982) and Nicolis (1981) proposed the stochastic-resonance idea for ice age cyclicity independently of each other.
Matteucci (1989)	Generalized stochastic resonance model with obliquity and precessional forcing.	Additive stochastic perturbations play a key role.	Not specifically addressed.	
Pelletier (2003)	Model based on the coherence resonance mechanism (Pikovsky and Kurths, 1997) uses a single temperature ODE with a discrete delay.	Additive stochastic perturbations play a key role.	Yes.	The delay feedback in the temperature is based on ice sheet extent reconstructions and affects the model’s albedo.
Ditlevsen (2010)	Generalized stochastic resonance model with obliquity and precessional forcing.	Additive stochastic perturbations play a key role.	Yes.	The model has an underlying bifurcation structure following Paillard (1998).

A comparison with Eq. (B4) requires

$$\frac{d}{dt}c(t) = \alpha\beta \sin(\nu t)e^{+\alpha(t-t_0)},$$

and hence

$$\begin{aligned} c(t) &= \int_{t_0}^t \alpha\beta \sin(\nu t')e^{+\alpha(t'-t_0)} dt' + \gamma \\ &= \left[ \alpha\beta \sin(\nu t') \frac{1}{\alpha} e^{+\alpha(t'-t_0)} \right]_{t_0}^t \\ &\quad - \int_{t_0}^t \frac{\nu}{\alpha} \alpha\beta \cos(\nu t') e^{+\alpha(t'-t_0)} dt' + \gamma. \end{aligned} \tag{B8}$$

Repeated partial integration yields

$$\begin{aligned} \int_{t_0}^t \frac{\nu}{\alpha} \alpha\beta \cos(\nu t') e^{+\alpha(t'-t_0)} dt' &= \\ &= \left[ \frac{\nu}{\alpha} \alpha\beta \cos(\nu t') \frac{1}{\alpha} e^{+\alpha(t'-t_0)} \right]_{t_0}^t \\ &\quad + \int_{t_0}^t \frac{\nu^2}{\alpha^2} \alpha\beta \sin(\nu t') e^{+\alpha(t'-t_0)} dt'. \end{aligned} \tag{B9}$$

Therefore, we find

$$\begin{aligned} \left( 1 + \frac{\nu^2}{\alpha^2} \right) \int_{t_0}^t \alpha\beta \sin(\nu t') e^{+\alpha(t'-t_0)} dt' &= \\ &= \left[ \alpha\beta \sin(\nu t') \frac{1}{\alpha} e^{+\alpha(t'-t_0)} \right]_{t_0}^t \\ &\quad - \left[ \frac{\nu}{\alpha} \alpha\beta \cos(\nu t') \frac{1}{\alpha} e^{+\alpha(t'-t_0)} \right]_{t_0}^t, \end{aligned} \tag{B10}$$

and finally

$$c(t) = \frac{1}{\left(1 + \frac{v^2}{\alpha^2}\right)} \left( \underbrace{\left[ \beta \sin(vt') e^{+\alpha(t'-t_0)} \right]_{t_0}^t}_{=\beta[\sin(vt)e^{\alpha(t-t_0)} - \sin(vt_0)]} - \underbrace{\left[ \frac{v\beta}{\alpha} \cos(vt') e^{+\alpha(t'-t_0)} \right]_{t_0}^t}_{=\frac{v\beta}{\alpha} [\cos(vt)e^{\alpha(t-t_0)} - \cos(vt_0)]} + \gamma \right). \quad (\text{B11})$$

Plugging this result into the ansatz (Eq. B5) yields

$$\Delta\rho(t, t_0) = \frac{1}{\left(1 + \frac{v^2}{\alpha^2}\right)} \left( \beta [\sin(vt) - \sin(vt_0)e^{-\alpha(t-t_0)}] - \frac{v\beta}{\alpha} [\cos(vt) - \cos(vt_0)e^{-\alpha(t-t_0)}] \right) + \gamma e^{-\alpha(t-t_0)}, \quad (\text{B12})$$

with the initial conditions

$$\Delta\rho(t_0, t_0) = \gamma. \quad (\text{B13})$$

In the pullback limit, all the terms that carry a factor  $e^{-\alpha(t-t_0)}$  vanish, and thus

$$\lim_{t_0 \rightarrow -\infty} \Delta\rho(t, t_0) = \frac{1}{\left(1 + \frac{v^2}{\alpha^2}\right)} \left( \beta \sin(vt) - \frac{v\beta}{\alpha} \cos(vt) \right) = \alpha\beta \sin(vt + \vartheta), \quad (\text{B14})$$

with  $\vartheta = \arctan(-v/\alpha)$ . For comparison, the modulation of the target radius itself was given by  $\beta \sin(vt)$ , and hence it is amplified by the factor of  $\alpha$ . Since  $\rho$  is restricted to positive values, this solution requires  $\alpha\beta < \mu$ .

Since the evolution in time of the phase  $\phi(t)$  is trivial, different initial conditions for the phase do not converge. Hence, the time-dependent sets that are invariant with respect to the dynamics of the system are

$$\mathcal{A}(t) = \{(\rho(t), \phi) : \phi \in [0, 2\pi)\} = \{(\alpha\beta \sin(vt + \vartheta), \phi) : \phi \in [0, 2\pi)\}. \quad (\text{B15})$$

Defined as the indexed family of all  $\mathcal{A}(t)$ , the system's PBA is comprised of the family of circles

$$\mathcal{A} = \{A(t)\}_{t \in \mathbb{R}} = \{(\alpha\beta \sin(vt + \vartheta), \phi) : \phi \in [0, 2\pi)\}_{t \in \mathbb{R}}. \quad (\text{B16})$$

**Code and data availability.** All code used to generate the figures presented in this article is available from the authors upon

request. The NGRIP  $\delta^{18}\text{O}$  – originally published in North Greenland Ice Core Project members (2004) – and the historical  $\text{CO}_2$  data (Seierstad et al., 2014) shown in Fig. 12 are available as a supplement to Seierstad et al. (2014) or <https://www.iceandclimate.nbi.ku.dk/data/> (last access: 13 April 2022) and from <https://www.ncei.noaa.gov/access/paleo-search/study/17975> (last access: 13 April 2022, Bereiter et al., 2015b), respectively. The benthic  $\delta^{18}\text{O}$  data (Lisiecki and Raymo, 2005a) shown in Fig. 13 can be obtained from <https://doi.org/10.1594/PANGAEA.704257> (Lisiecki and Raymo, 2005b), and the 21 June insolation at  $65^\circ\text{N}$  (Laskar et al., 2004a) can be downloaded from <http://vo.imcce.fr/insola/earth/online/earth/online/index.php> (last access: 13 April 2022, Laskar et al., 2004b).

**Video supplement.** The video supplement to this article (<https://doi.org/10.5281/zenodo.6346211>, Riechers, 2022) illustrates the pullback attractor (PBA) associated with the simple system governed by Eqs. (15) and (16). It shows a heat map of the phase plane, derived from an increasing number of trajectories with common initial time  $t_i = -200$  and final time  $t_f = 200$ . The initial radius and phase of each trajectory are randomly sampled from Gaussian distributions centered at  $\mu_\rho = 20$  and  $\mu_\phi = 0$  with standard deviations of  $\sigma_\rho = 5$  and  $\sigma_\phi = 10$ , respectively. Over the course of the video, 100 trajectories are continuously added to the heat map and the annular disk  $\mathcal{D} = \{(\rho, \phi) : \rho \in [\mu - \alpha\beta, \mu + \alpha\beta] \text{ and } \phi \in [0, 2\pi)\}$  fills up. The heat map in Fig. 6b is a snapshot from this video at time  $t = 0.2$ .

**Author contributions.** MG conceived and designed the study. KR and TM carried out the major part of the article's new research in close interaction with MG and NB. All authors interpreted and discussed the results and wrote the manuscript.

**Competing interests.** The contact author has declared that neither they nor their co-authors have any competing interests.

**Disclaimer.** Publisher's note: Copernicus Publications remains neutral with regard to jurisdictional claims in published maps and institutional affiliations.

**Special issue statement.** This article is part of the special issue "A century of Milankovic's theory of climate changes: achievements and challenges (NPG/CP inter-journal SI)". It is a result of the conference "One Hundred Years of Milankovic's Theory of Climate Changes: synergy of the achievements and challenges of the next century", 17–18 November 2020.

**Acknowledgements.** We thank Andreas Groth for helpful comments on an earlier version of this manuscript. It is a pleasure to thank Tamás Bóдай and two anonymous referees for their thorough and constructive comments. István Daruka's public comments in part motivated the addition of Appendix A and its Table A1, in order

to give a broader perspective of relevant work on the Quaternary's glacial cycles and the mid-Pleistocene transition (MPT). Takahito Mitsui and Niklas Boers acknowledge funding by the Volkswagen Foundation. The present work is TiPES contribution no. 52; the TiPES (Tipping Points in the Earth System) project has received funding from the European Union's Horizon 2020 research and innovation program under grant agreement no. 820970. Michael Ghil acknowledges support by the EIT Climate-KIC; EIT Climate-KIC is supported by the European Institute of Innovation & Technology (EIT), a body of the European Union.

**Financial support.** This research has been supported by the Horizon 2020 research and innovation program under grant agreement no. 820970 (TiPES), the Volkswagen Foundation, and the European Institute of Innovation & Technology via the EIT Climate-KIC.

The publication of this article was funded by the Open Access Fund of the Leibniz Association.

**Review statement.** This paper was edited by Marie-France Loutre and reviewed by Tamas Bodai and two anonymous referees.

## References

- Abe-Ouchi, A., Saito, F., Kawamura, K., Raymo, M. E., Okuno, J., Takahashi, K., and Blatter, H.: Insolation-driven 100 000-year glacial cycles and hysteresis of ice-sheet volume, *Nature*, 500, 190–193, <https://doi.org/10.1038/nature12374>, 2013.
- Arnold, L.: *Random Dynamical Systems*, 1st edn., Springer, Berlin, Heidelberg, <https://doi.org/10.1007/978-3-662-12878-7>, 1998.
- Arnold, V.: *Geometrical Methods in the Theory of Ordinary Differential Equations*, Springer, New York, NY, <https://doi.org/10.1007/978-1-4612-1037-5>, 1988.
- Ashkenazy, Y. and Tziperman, E.: Are the 41 kyr glacial oscillations a linear response to Milankovitch forcing?, *Quaternary Sci. Rev.*, 23, 1879–1890, <https://doi.org/10.1016/j.quascirev.2004.04.008>, 2004.
- Ashwin, P. and Ditlevsen, P.: The middle Pleistocene transition as a generic bifurcation on a slow manifold, *Clim. Dynam.*, 45, 2683–2695, 2015.
- Ashwin, P., Wieczorek, S., Vitolo, R., and Cox, P.: Tipping points in open systems: bifurcation, noise-induced and rate-dependent examples in the climate system, *Philos. T. Roy. Soc. A*, 370, 1166–1184, 2012.
- Ashwin, P., David Camp, C., and von der Heydt, A. S.: Chaotic and non-chaotic response to quasiperiodic forcing: limits to predictability of ice ages paced by Milankovitch forcing, *Dynamics and Statistics of the Climate System*, 3, 1–20, <https://doi.org/10.1093/climsys/dzy002>, 2018.
- Bagniewski, W., Ghil, M., and Rousseau, D. D.: Automatic detection of abrupt transitions in paleoclimate records, *Chaos*, 31, 113129, <https://doi.org/10.1063/5.0062543>, 2021.
- Barenblatt, G. I.: Scaling, Self-similarity, and Intermediate Asymptotics: Dimensional Analysis and Intermediate Asymptotics, Cambridge University Press, <https://doi.org/10.1017/CBO9781107050242>, 1996.
- Benoit, E.: Systèmes lents-rapides dans  $R^3$  et leurs canards, in: *IIIe rencontre de géométrie du Schnepfenried Volume 2 – 10–15 mai 1982*, no. 109–110 in *Astérisque*, Société mathématique de France, [http://www.numdam.org/item/AST\\_1983\\_\\_109-110\\_\\_159\\_0/](http://www.numdam.org/item/AST_1983__109-110__159_0/) (last access: 13 April 2022), 1983.
- Benzi, R., Sutera, A., and Vulpiani, A.: The mechanism of stochastic resonance, *J. Phys. A-Math. Den.*, 14, L453, <https://doi.org/10.1088/0305-4470/14/11/006>, 1981.
- Benzi, R., Parisi, G., Sutera, A., and Vulpiani, A.: Stochastic resonance in climatic change, *Tellus*, 34, 10–15, <https://doi.org/10.3402/tellusa.v34i1.10782>, 1982.
- Bereiter, B., Eggleston, S., Schmitt, J., Nehrbass-Ahles, C., Stocker, T. F., Fischer, H., Kipfstuhl, S., and Chappellaz, J.: Revision of the EPICA Dome C CO<sub>2</sub> record from 800 to 600 kyr before present, *Geophys. Res. Lett.*, 42, 542–549, 2015a.
- Bereiter, B., Eggleston, S., Schmitt, J., Nehrbass-Ahles, C., Stocker, T. F., Fischer, H., Kipfstuhl, S., and Chappellaz, J. A.: Antarctic Ice Cores Revised 800KYr CO<sub>2</sub> Data, National Centers for Environmental Information, NESDIS, NOAA, U.S. Department of Commerce [data set], <https://www.ncei.noaa.gov/access/paleo-search/study/17975> (last access: 13 April 2022), 2015b.
- Berger, A.: Long-term variations of daily insolation and Quaternary climatic changes, *J. Atmos. Sci.*, 35, 2362–2367, 1978.
- Berger, A., Imbrie, J., Hays, J., Kukla, G., and Saltzman, B. (Eds.): *Milankovitch and Climate: Understanding the Response to Astronomical Forcing*, NATO ASI series. Series C, Mathematical and physical sciences; vol. 126, pts. 1–2, Springer, Dordrecht, <https://doi.org/10.1007/978-94-017-4841-4>, 1984.
- Berger, A., Li, X., and Loutre, M.-F.: Modelling northern hemisphere ice volume over the last 3 Ma, *Quaternary Sci. Rev.*, 18, 1–11, 1999.
- Berger, W. H.: The 100 kyr ice-age cycle: Internal oscillation or inclinational forcing?, *Int. J. Earth Sci.*, 88, 305–316, <https://doi.org/10.1007/s005310050266>, 1999.
- Bódai, T. and Tél, T.: Annual variability in a conceptual climate model: Snapshot attractors, hysteresis in extreme events, and climate sensitivity, *Chaos*, 22, 023110, <https://doi.org/10.1063/1.3697984>, 2012.
- Bódai, T., Lucarini, V., Lunkeit, F., and Boschi, R.: Global instability in the Ghil-Sellers model, *Clim. Dynam.*, 44, 3361–3381, 2015.
- Boers, N., Chekroun, M. D., Liu, H., Kondrashov, D., Rousseau, D.-D., Svensson, A., Bigler, M., and Ghil, M.: Inverse stochastic-dynamic models for high-resolution Greenland ice core records, *Earth Syst. Dynam.*, 8, 1171–1190, <https://doi.org/10.5194/esd-8-1171-2017>, 2017a.
- Boers, N., Goswami, B., and Ghil, M.: A complete representation of uncertainties in layer-counted paleoclimatic archives, *Clim. Past*, 13, 1169–1180, <https://doi.org/10.5194/cp-13-1169-2017>, 2017b.
- Boers, N., Ghil, M., and Rousseau, D.-D.: Ocean circulation, ice shelf, and sea ice interactions explain Dansgaard-Oeschger cycles, *P. Natl. Acad. Sci. USA*, 115, E11005–E11014, <https://doi.org/10.1073/pnas.1802573115>, 2018.
- Bond, G., Heinrich, H., Broecker, W., Labeyrie, L., Mcmanus, J., Andrews, J., Huonll, S., Jantschik, R., Clasen, S., Simet, C., Tedesco, K., Klas, M., Bonanitt, G., and Ivy, S.: Evi-

- dence for massive discharges of icebergs into the North Atlantic ocean during the last glacial period, *Nature*, 360, 1668–1672, <https://doi.org/10.1038/360245a0>, 1992.
- Bond, G., Broecker, W., Johnsen, S., McManus, J., Labeyrie, L., Jouzel, J., and Bonani, G.: Correlations between climate records from North Atlantic sediments and Greenland ice, *Nature*, 365, 143–147, <https://doi.org/10.1038/365143a0>, 1993.
- Bond, G., Showers, W., Cheseby, M., Peter Almasi, R. L., deMenocal, P., Priore, P., Irka Hajdas, H. C., and Bonani, G.: A pervasive millennial-scale cycle in North Atlantic Holocene and glacial climates, *Science*, 278, 1257–1266, <https://doi.org/10.1126/science.278.5341.1257>, 1997.
- Boyce, W. E. and DiPrima, R. C.: *Elementary Differential Equations and Boundary Value Problems*, 8th edn., John Wiley & Sons, ISBN 978-0-470-38334-6, 2005.
- Broecker, W. S. and Van Donk, J.: Insolation changes, ice volumes, and the O<sup>18</sup> record in deep-sea cores, *Rev. Geophys.*, 8, 169–198, 1970.
- Budyko, M. I.: The effect of solar radiation variations on the climate of the Earth, *Tellus*, 21, 611–619, 1969.
- Calder, N.: Arithmetic of ice ages, *Nature*, 252, 216–218, <https://doi.org/10.1038/252216a0>, 1974.
- Caraballo, T. and Han, X.: *Applied Nonautonomous and Random Dynamical Systems: Applied Dynamical Systems*, Springer, Cham, <https://doi.org/10.1007/978-3-319-49247-6>, 2017.
- Charó, G. D., Chekroun, M. D., Sciamarella, D., and Ghil, M.: Noise-driven topological changes in chaotic dynamics, arXiv [preprint], arXiv:2010.09611v7, 2 August 2021.
- Chekroun, M. D., Simonnet, E., and Ghil, M.: Stochastic climate dynamics: random attractors and time-dependent invariant measures, *Physica D*, 240, 1685–1700, <https://doi.org/10.1016/j.physd.2011.06.005>, 2011.
- Chekroun, M. D., Simonnet, E., and Ghil, M.: Stochastic climate dynamics: random attractors and time-dependent invariant measures, *Physica D*, 240, 1685–1700, <https://doi.org/10.1016/j.physd.2011.06.005>, 2011.
- Chekroun, M. D., Ghil, M., and Neelin, J. D.: Pullback attractor crisis in a delay differential ENSO model, in: *Advances in Nonlinear Geosciences*, edited by: Tsonis, A. A., Springer Science & Business Media, 1–33, <https://doi.org/10.1007/978-3-319-58895-7>, 2018.
- Crafoord, C. and Källén, E.: A note on the condition for existence of more than one steady state solution in Budyko-Sellers type models, *J. Atmos. Sci.*, 35, 1123–1125, 1978.
- Crauel, H. and Kloeden, P. E.: *Nonautonomous and random attractors*, *Jahresbericht der Deutschen Mathematiker-Vereinigung*, 117, 173–206, 2015.
- Crucifix, M.: How can a glacial inception be predicted?, *Holocene*, 21, 831–842, 2011.
- Crucifix, M.: Oscillators and relaxation phenomena in Pleistocene climate theory, *Philos. T. Roy. Soc. A*, 370, 1140–1165, 2012.
- Crucifix, M.: Why could ice ages be unpredictable?, *Clim. Past*, 9, 2253–2267, <https://doi.org/10.5194/cp-9-2253-2013>, 2013.
- Dansgaard, W., Johnsen, S. J., Clausen, H. B., Dahl-Jensen, D., Gundestrup, N. S., Hammer, C. U., Hvidberg, C. S., Steffensen, J. P., Sveinbjörnsdóttir, A. E., Jouzel, J., and Bond, G.: Evidence for general instability of past climate from a 250 kyr ice-core record, *Nature*, 364, 218–220, <https://doi.org/10.1038/364218a0>, 1993.
- Daruka, I. and Ditlevsen, P. D.: A conceptual model for glacial cycles and the middle Pleistocene transition, *Clim. Dynam.*, 46, 29–40, 2016.
- De Saedeleer, B., Crucifix, M., and Wiczorek, S.: Is the astronomical forcing a reliable and unique pacemaker for climate? a conceptual model study, *Clim. Dynam.*, 40, 273–294, 2013.
- Ditlevsen, P., Mitsui, T., and Crucifix, M.: Crossover and peaks in the Pleistocene climate spectrum; understanding from simple ice age models, *Clim. Dynam.*, 54, 1801–1818, 2020.
- Ditlevsen, P. D.: Extension of stochastic resonance in the dynamics of ice ages, *Chem. Phys.*, 375, 403–409, <https://doi.org/10.1016/j.chemphys.2010.05.022>, 2010.
- Ditlevsen, P. D. and Ashwin, P. B.: Complex climate response to astronomical forcing: The middle-Pleistocene transition in glacial cycles and changes in frequency locking, *AIP Conf. Proc.*, 6, 62, <https://doi.org/10.3389/fphy.2018.00062>, 2018.
- Ditlevsen, P. D., Andersen, K. K., and Svensson, A.: The DO-climate events are probably noise induced: statistical investigation of the claimed 1470 years cycle, *Clim. Past*, 3, 129–134, <https://doi.org/10.5194/cp-3-129-2007>, 2007.
- Drótos, G., Bódoi, T., and Tél, T.: Probabilistic concepts in a changing climate: A snapshot attractor picture, *J. Climate*, 28, 3275–3288, 2015.
- Duffing, G.: *Erzwungene Schwingungen bei veränderlicher Eigenfrequenz und ihre technische Bedeutung*, vol. 41/42 of *Sammlung Vieweg*, R. Vieweg & Sohn, Braunschweig, <https://doi.org/10.1002/zamm.19210010109>, 1918.
- Einstein, A.: Über die von der molekularkinetischen Theorie der Wärme geforderte Bewegung von in ruhenden Flüssigkeiten suspendierten Teilchen, *Annalen der Physik*, 322, 549–560; reprinted in *Investigations on the Theory of the Brownian Movement*, five articles by A. Einstein, edited by: Furth, R., translated by: Cowper, A. D., 1956, Dover Publ., New York, 122 pp., <https://doi.org/10.1002/andp.200590005>, 1905.
- Emiliani, C. and Geiss, J.: On glaciations and their causes, *Geol. Rundsch.*, 46, 576–601, 1959.
- Fienga, A., Laskar, J., Exertier, P., Manche, H., and Gastineau, M.: Numerical estimation of the sensitivity of INPOP planetary ephemerides to general relativity parameters, *Celestial Mechanics and Dynamical Astronomy*, 123, 325–349, 2015.
- FitzHugh, R.: Impulses and physiological states in theoretical models of nerve membrane, *Biophys. J.*, 1, 445–466, 1961.
- Flint, R. F.: *Glacial and Quaternary Geology*, Wiley New York, ISBN 978-0471264354, 1971.
- Ganopolski, A. and Brovkin, V.: Simulation of climate, ice sheets and CO<sub>2</sub> evolution during the last four glacial cycles with an Earth system model of intermediate complexity, *Clim. Past*, 13, 1695–1716, <https://doi.org/10.5194/cp-13-1695-2017>, 2017.
- Ganopolski, A. and Calov, R.: The role of orbital forcing, carbon dioxide and regolith in 100 kyr glacial cycles, *Clim. Past*, 7, 1415–1425, <https://doi.org/10.5194/cp-7-1415-2011>, 2011.
- Ghil, M.: Climate stability for a Sellers-type model, *J. Atmos. Sci.*, 33, 3–20, 1976.
- Ghil, M.: Climate sensitivity, energy balance models, and oscillatory climate models, *J. Geophys. Res.-Atmos.*, 89, 1280–1284, 1984.
- Ghil, M.: Cryothermodynamics: the chaotic dynamics of paleoclimate, *Physica D*, 77, 130–159, 1994.

- Ghil, M.: Hilbert problems for the geosciences in the 21st century, *Nonlin. Processes Geophys.*, 8, 211–211, <https://doi.org/10.5194/npg-8-211-2001>, 2001.
- Ghil, M.: Climate variability: Nonlinear and random aspects, in: *Encyclopedia of Atmospheric Sciences*, 2nd edn., edited by G. R. North, J. P. and Zhang, F., vol. 2, 38–46, Elsevier, ISBN 9780123822253, 2014.
- Ghil, M.: A century of nonlinearity in the geosciences, *Earth Space Sci.*, 6, 1007–1042, <https://doi.org/10.1029/2019EA000599>, 2019.
- Ghil, M. and Childress, S.: *Topics in Geophysical Fluid Dynamics: Atmospheric Dynamics, Dynamo Theory, and Climate Dynamics*, Springer Science+Business Media, Berlin/Heidelberg, <https://doi.org/10.1007/978-1-4612-1052-8>, 1987.
- Ghil, M. and Le Treut, H.: A climate model with cryodynamics and geodynamics, *J. Geophys. Res.-Oceans*, 86, 5262–5270, 1981.
- Ghil, M. and Lucarini, V.: The physics of climate variability and climate change, *Rev. Mod. Phys.*, 92, 035002, <https://doi.org/10.1103/RevModPhys.92.035002>, 2020.
- Ghil, M. and Tavantzis, J.: Global Hopf bifurcation in a simple climate model, *SIAM J. Appl. Math.*, 43, 1019–1041, <https://doi.org/10.1137/0143067>, 1983.
- Ghil, M. and Vautard, R.: Interdecadal oscillations and the warming trend in global temperature time series, *Nature*, 350, 324–327, 1991.
- Ghil, M. and Zaliapin, I.: Understanding ENSO variability and its extrema: A delay differential equation approach, in: *Extreme Events: Observations, Modeling and Economics*, Geophysical Monograph 214, edited by: Chavez, M., Ghil, M., and Urrutia-Fucugauchi, J., Wiley Online Library, 63–78, <https://doi.org/10.1002/9781119157052.ch6>, 2015.
- Ghil, M., Mullhaupt, A., and Pestiaux, P.: Deep water formation and Quaternary glaciations, *Clim. Dynam.*, 2, 1–10, 1987.
- Ghil, M., Chekroun, M. D., and Simonnet, E.: Climate dynamics and fluid mechanics: natural variability and related uncertainties, *Physica D*, 237, 2111–2126, <https://doi.org/10.1016/j.physd.2008.03.036>, 2008.
- Gildor, H. and Tziperman, E.: Sea ice as the glacial cycles' climate switch: Role of seasonal and orbital forcing, *Paleoceanography*, 15, 605–615, 2000.
- Guckenheimer, J. and Holmes, P. J.: *Nonlinear Oscillations, Dynamical Systems, and Bifurcations of Vector Fields*, Applied Mathematical Sciences, Springer Science & Business Media, <https://doi.org/10.1007/978-1-4612-1140-2>, 1983.
- Hasselmann, K.: Stochastic climate models. I: Theory, *Tellus*, 28, 473–485, 1976.
- Hays, J. D., Imbrie, J., and Shackleton, N. J.: Variations in the Earth's orbit: pacemaker of the ice ages, *Science*, 194, 1121–1132, 1976.
- Heinrich, H.: Origin and consequences of cyclic ice rafting in the Northeast Atlantic Ocean during the past 130 000 years, *Quaternary Res.*, 29, 142–152, [https://doi.org/10.1016/0033-5894\(88\)90057-9](https://doi.org/10.1016/0033-5894(88)90057-9), 1988.
- Held, I. M.: The gap between simulation and understanding in climate modeling, *B. Am. Meteorol. Soc.*, 86, 1609–1614, <https://doi.org/10.1175/bams-86-11-1609>, 2005.
- Held, I. M. and Suarez, M. J.: Simple albedo feedback models of the ice caps, *Tellus*, 26, 613–629, 1974.
- Henry, L. G., McManus, J. F., Curry, W. B., Roberts, N. L., Piotrowski, A. M., and Keigwin, L. D.: North Atlantic ocean circulation and abrupt climate change during the last glaciation, *Science*, 353, 470–474, <https://doi.org/10.1126/science.aaf5529>, 2016.
- Hoffman, P. F., Kaufman, A. J., Halverson, G. P., and Schrag, D. P.: A Neoproterozoic snowball earth, *Science*, 281, 1342–1346, 1998.
- Hogg, A. M. C.: Glacial cycles and carbon dioxide: A conceptual model, *Geophys. Res. Lett.*, 35, 1–5, <https://doi.org/10.1029/2007GL032071>, 2008.
- Huybers, P.: Glacial variability over the last two million years: an extended depth-derived agemodel, continuous obliquity pacing, and the Pleistocene progression, *Quaternary Sci. Rev.*, 26, 37–55, <https://doi.org/10.1016/j.quascirev.2006.07.013>, 2007.
- Huybers, P.: Pleistocene glacial variability as a chaotic response to obliquity forcing, *Clim. Past*, 5, 481–488, <https://doi.org/10.5194/cp-5-481-2009>, 2009.
- Huybers, P.: Combined obliquity and precession pacing of late Pleistocene deglaciations, *Nature*, 480, 229–232, <https://doi.org/10.1038/nature10626>, 2011.
- Huybers, P. and Langmuir, C. H.: Delayed CO<sub>2</sub> emissions from mid-ocean ridge volcanism as a possible cause of late-Pleistocene glacial cycles, *Earth Planet. Sc. Lett.*, 457, 238–249, 2017.
- Imbrie, J. and Imbrie, J. Z.: Modeling the Climatic Response to Orbital Variations, *Science*, 207, 943–953, 1980.
- Imbrie, J. and Imbrie, K. P.: *Ice Ages: Solving the Mystery*, 2nd edn., Harvard University Press, ISBN 9780674440753, 1986.
- Imbrie, J. Z., Imbrie-Moore, A., and Lisiecki, L. E.: A phase-space model for Pleistocene ice volume, *Earth Planet. Sc. Lett.*, 307, 94–102, <https://doi.org/10.1016/j.epsl.2011.04.018>, 2011.
- Isaacson, E. and Keller, H. B.: *Analysis of numerical methods*, Dover Publications, Inc., New York, NY, ISBN 9780486137988, 2012.
- Jackson, E. A.: *Perspectives of Nonlinear Dynamics*, Cambridge University Press, New York, ISBN 9780198596219, 1991.
- Jordan, D. W. and Smith, P.: *Nonlinear Ordinary Differential Equations – An Introduction for Scientists and Engineers*, 2nd edn., Oxford University Press, Oxford/New York, ISBN 0-19-859657-X, 1987.
- Källén, E., Crafoord, C., and Ghil, M.: Free oscillations in a climate model with ice-sheet dynamics, *J. Atmos. Sci.*, 36, 2292–2303, 1979.
- Kwasniok, F.: Analysis and modelling of glacial climate transitions using simple dynamical systems, *Philos. T. Roy. Soc. A*, 371, <https://doi.org/10.1098/rsta.2011.0472>, 2013.
- Landau, L. D. and Lifshitz, E. M.: *Mechanics*, vol. I of *Course on Theoretical Physics*, Pergamon Press, Oxford, 1960.
- Laskar, J., Robutel, P., Joutel, F., Gastineau, M., Correia, A., and Levrard, B.: A long-term numerical solution for the insolation quantities of the Earth, *Astron. Astrophys.*, 428, 261–285, 2004a.
- Laskar, J., Robutel, P., Joutel, F., Gastineau, M., Correia, A. C. M., and Levrard, B.: Computation of various insolation quantities for Earth, IMCCE, Observatoire de Paris/CNRS [data set], <http://vo.imcce.fr/insola/earth/online/earth/online/index.php> (last access: 13 April 2022), 2004b.
- Lenssen, N. J. L., Schmidt, G. A., Hansen, J. E., Menne, M. J., Persin, A., Ruedy, R., and Zyss, D.: Improvements in the GIS-

- TEMP uncertainty model, *J. Geophys. Res.-Atmos.*, 124, 6307–6326, 2019.
- Le Treut, H. and Ghil, M.: Orbital forcing, climatic interactions, and glaciation cycles, *J. Geophys. Res.-Oceans*, 88, 5167–5190, 1983.
- Le Treut, H., Portes, J., Jouzel, J., and Ghil, M.: Isotopic modeling of climatic oscillations: Implications for a comparative study of marine and ice core records, *J. Geophys. Res.-Atmos.*, 93, 9365–9383, 1988.
- Lisiecki, L. E. and Raymo, M. E.: A Pliocene-Pleistocene stack of 57 globally distributed benthic  $\delta^{18}\text{O}$  records, *Paleoceanography*, 20, PA1003, <https://doi.org/10.1029/2004PA001071>, 2005a.
- Lisiecki, L. E. and Raymo, M. E.: Pliocene-Pleistocene stack of globally distributed benthic stable oxygen isotope records, PAN-GAEA [data set], <https://doi.org/10.1594/PANGAEA.704257>, 2005b.
- Lorenz, E. N.: Deterministic nonperiodic flow, *J. Atmos. Sci.*, 20, 130–141, 1963.
- Maasch, K. A. and Saltzman, B.: A Low-Order Dynamical Model of Global Climatic Variability Over the Full Pleistocene, *J. Geophys. Res.*, 95, 1955–1963, 1990.
- Marangio, L., Sedro, J., Galatolo, S., Di Garbo, A., and Ghil, M.: Arnold maps with noise: Differentiability and non-monotonicity of the rotation number, *J. Stat. Phys.*, 179, 1–31, <https://doi.org/10.1007/s10955-019-02421-1>, 2019.
- Matteucci, G.: Orbital forcing in a stochastic resonance model of the Late-Pleistocene climatic variations, *Clim. Dynam.*, 3, 179–190, <https://doi.org/10.1007/BF01058234>, 1989.
- Milankovitch, M.: *Théorie mathématique des phénomènes thermiques produits par la radiation solaire*, Gauthier-Villars, Paris, 1920.
- Mitsui, T. and Aihara, K.: Dynamics between order and chaos in conceptual models of glacial cycles, *Clim. Dynam.*, 42, 3087–3099, <https://doi.org/10.1007/s00382-013-1793-x>, 2014.
- Mitsui, T. and Crucifix, M.: Influence of external forcings on abrupt millennial-scale climate changes: a statistical modelling study, *Clim. Dynam.*, 48, 2729–2749, 2017.
- Mitsui, T., Crucifix, M., and Aihara, K.: Bifurcations and strange nonchaotic attractors in a phase oscillator model of glacial-interglacial cycles, *Physica D*, 306, 25–33, 2015.
- Nagumo, J., Arimoto, S., and Yoshizawa, S.: An active pulse transmission line simulating nerve axon, *Proceedings of the IRE*, 50, 2061–2070, 1962.
- National Research Council: *Understanding Climatic Change, a Program for Action*, National Academy of Sciences, Washington, DC, 239 pp., ISBN 978-0309023238, 1975.
- Nicolis, C.: Solar variability and stochastic effects on climate, *Sol. Phys.*, 74, 473–478, <https://doi.org/10.1007/BF00154530>, 1981.
- Nicolis, G. and Nicolis, C.: *Foundations of Complex Systems*, World Scientific, 2nd edn., <https://doi.org/10.1142/8260>, 2012.
- North, G. R.: Analytical solution to a simple climate model with diffusive heat transport, *J. Atmos. Sci.*, 32, 1301–1307, 1975.
- North Greenland Ice Core Project members: High-resolution record of the Northern Hemisphere climate extending into the last interglacial period, *Nature*, 431, 147–151, 2004.
- Oerlemans, J.: Model experiments on the 100 000-year glacial cycle, *Nature*, 287, 430–432, 1980.
- Oerlemans, J.: On the origin of the ice ages, in: *Milankovitch and Climate: Understanding the Response to Astronomical Forcing*, vols. I & II, edited by: Berger, A., Imbrie, J., Hays, J., Kukla, G., and Saltzman, B., D. Reidel Publ. Co., 607–611, <https://doi.org/10.1007/978-94-017-4841-4>, 1984.
- Omta, A. W., Kooi, B. W., van Voorn, G. A., Rickaby, R. E., and Follows, M. J.: Inherent characteristics of sawtooth cycles can explain different glacial periodicities, *Clim. Dynam.*, 46, 557–569, 2016.
- Paillard, D.: The timing of Pleistocene glaciations from a simple multiple-state climate model, *Nature*, 391, 378–381, 1998.
- Paillard, D.: Glacial cycles: Toward a new paradigm, *Rev. Geophys.*, 39, 325–346, <https://doi.org/10.1029/2000RG000091>, 2001.
- Paillard, D. and Parrenin, F.: The Antarctic ice sheet and the triggering of deglaciations, *Earth Planet. Sci. Lett.*, 227, 263–271, <https://doi.org/10.1016/j.epsl.2004.08.023>, 2004.
- Parrenin, F. and Paillard, D.: Amplitude and phase of glacial cycles from a conceptual model, *Earth Planet. Sci. Lett.*, 214, 243–250, [https://doi.org/10.1016/S0012-821X\(03\)00363-7](https://doi.org/10.1016/S0012-821X(03)00363-7), 2003.
- Parrenin, F. and Paillard, D.: Terminations VI and VIII (~ 530 and ~ 720 kyr BP) tell us the importance of obliquity and precession in the triggering of deglaciations, *Clim. Past*, 8, 2031–2037, <https://doi.org/10.5194/cp-8-2031-2012>, 2012.
- Pelletier, J. D.: Coherence resonance and ice ages, *J. Geophys. Res.*, 108, 1–14, <https://doi.org/10.1029/2002jd003120>, 2003.
- Pierini, S. and Ghil, M.: Climate tipping points induced by parameter drift: an excitable system study, *Sci. Rep.*, in press, 2022.
- Pierini, S., Ghil, M., and Chekroun, M. D.: Exploring the pullback attractors of a low-order quasigeostrophic ocean model: The deterministic case, *J. Climate*, 29, 4185–4202, 2016.
- Pierini, S., Chekroun, M. D., and Ghil, M.: The onset of chaos in nonautonomous dissipative dynamical systems: a low-order ocean-model case study, *Nonlin. Processes Geophys.*, 25, 671–692, <https://doi.org/10.5194/npg-25-671-2018>, 2018.
- Pierrehumbert, R. T.: High levels of atmospheric carbon dioxide necessary for the termination of global glaciation, *Nature*, 429, 646–649, <https://doi.org/10.1038/nature02640>, 2004.
- Pikovsky, A., Rosenblum, M. G., and Kurths, J.: *Synchronization, A Universal Concept in Nonlinear Sciences*, Cambridge University Press, Cambridge, <https://doi.org/10.1017/CBO9780511755743>, 2001.
- Pikovsky, A. S. and Kurths, J.: Coherence resonance in a noise-driven excitable system, *Phys. Rev. Lett.*, 78, 775–778, <https://doi.org/10.1103/physrevlett.78.775>, 1997.
- Poincaré, H.: *Méthodes nouvelles de la Mécanique céleste*, vols. I–III, Gauthier-Villars, <https://doi.org/10.3931/e-rara-421>, 1892–1899.
- Pollard, D.: A coupled climate-ice sheet model applied to the Quaternary ice ages, *J. Geophys. Res.-Oceans*, 88, 7705–7718, 1983.
- Quinn, C., Sieber, J., Von Der Heydt, A. S., and Lenton, T. M.: The Mid-Pleistocene Transition induced by delayed feedback and bistability, *Dynamics and Statistics of the Climate System*, 3, dzy005, <https://doi.org/10.1093/climsys/dzy005>, 2018.
- Rasmussen, S. O., Bigler, M., Blockley, S. P., Blunier, T., Buchardt, S. L., Clausen, H. B., Cvijanovic, I., Dahl-Jensen, D., Johnsen, S. J., Fischer, H., Gkinis, V., Guillevic, M., Hoek, W. Z., Lowe, J. J., Pedro, J. B., Popp, T., Seierstad, I. K., Steffensen, J. P., Svensson, A. M., Vallelonga, P., Vinther, B. M., Walker, M. J., Wheatley, J. J., and Winstrup, M.: A stratigraphic framework for abrupt climatic changes during the Last Glacial period based on

- three synchronized Greenland ice-core records: refining and extending the INTIMATE event stratigraphy, *Quaternary Sci. Rev.*, 106, 14–28, 2014.
- Rial, J. A. and Yang, M.: Is the frequency of abrupt climate change modulated by the orbital insolation?, *Geophys. Monog. Ser.*, 173, 167–174, <https://doi.org/10.1029/173GM12>, 2007.
- Riechers, K.: *kriechers/Orbital-Insolation-Variations-Intrinsic-Climatic-Variability-and-Quaternary-Glaciations: Video Supplement to: Orbital Insolation Variations, Intrinsic Climate Variability, and Quaternary Glaciations (1.0)*, Zenodo [video], <https://doi.org/10.5281/zenodo.6346211>, 2022.
- Roberts, A. and Saha, R.: Relaxation oscillations in an idealized ocean circulation model, *Clim. Dynam.*, 48, 2123–2134, <https://doi.org/10.1007/s00382-016-3195-3>, 2017.
- Rocsoreanu, C., Georgescu, A., and Giurgiteanu, N.: *The FitzHugh-Nagumo model: bifurcation and dynamics*, 1st edn., Springer, Dordrecht, <https://doi.org/10.1007/978-94-015-9548-3>, 2000.
- Rousseau, D.-D., Antoine, P., Boers, N., Lacroix, F., Ghil, M., Lomax, J., Fuchs, M., Debret, M., Hatté, C., Moine, O., Gauthier, C., Jordanova, D., and Jordanova, N.: Dansgaard–Oeschger-like events of the penultimate climate cycle: the loess point of view, *Clim. Past*, 16, 713–727, <https://doi.org/10.5194/cp-16-713-2020>, 2020.
- Rousseau, D.-D., Bagniewski, W., and Ghil, M.: Abrupt climate changes and the astronomical theory: are they related?, *Clim. Past*, 18, 249–271, <https://doi.org/10.5194/cp-18-249-2022>, 2022.
- Ruddiman, W. F. and McIntyre, A.: The North Atlantic Ocean during the last deglaciation, *Palaeogeogr. Palaeoclimatol.*, 35, 145–214, 1981.
- Rulkov, N. F., Sushchik, M. M., Tsimring, L. S., and Abarbanel, H. D. I.: Generalized synchronization of chaos in directionally coupled chaotic systems, *Phys. Rev. E*, 51, 980–994, <https://doi.org/10.1103/physreve.51.980>, 1995.
- Saltzman, B. and Maasch, K. A.: Carbon cycle instability as a cause of the late Pleistocene ice age oscillations: modeling the asymmetric response, *Global Biogeochem. Cy.*, 2, 177–185, 1988.
- Saltzman, B. and Maasch, K. A.: A first-order global model of late Cenozoic climatic change, *Transactions of the Royal Society of Edinburgh: Earth Sciences*, 81, 315–325, <https://doi.org/10.1017/S0263593300020824>, 1990.
- Saltzman, B. and Maasch, K. A.: A first-order global model of late Cenozoic climatic change II. Further analysis based on a simplification of CO<sub>2</sub> dynamics, *Clim. Dynam.*, 5, 201–210, <https://doi.org/10.1007/BF00210005>, 1991.
- Saltzman, B. and Sutera, A.: The mid-Quaternary climatic transition as the free response of a three-variable dynamical model, *J. Atmos. Sci.*, 44, 236–241, 1987.
- Saltzman, B., Sutera, A., and Evenson, A.: Structural stochastic stability of a simple auto-oscillatory climatic feedback system, *J. Atmos. Sci.*, 38, 494–503, 1981.
- Schneider, S. H. and Dickinson, R. E.: Climate modelling, *Rev. Geophys. Space Ge.*, 25, 447–493, 1974.
- Seierstad, I. K., Abbott, P. M., Bigler, M., Blunier, T., Bourne, A. J., Brook, E., Buchardt, S. L., Buizert, C., Clausen, H. B., Cook, E., Dahl-Jensen, D., Davies, S. M., Guillevic, M., Johnsen, S. J., Pedersen, D. S., Popp, T. J., Rasmussen, S. O., Severinghaus, J. P., Svensson, A., and Vinther, B. M.: Consistently dated records from the Greenland GRIP, GISP2 and NGRIP ice cores for the past 104 ka reveal regional millennial-scale  $\delta^{18}\text{O}$  gradients with possible Heinrich event imprint, *Quaternary Sci. Rev.*, 106, 29–46, <https://doi.org/10.1016/j.quascirev.2014.10.032>, 2014 (data available at: <https://www.iceandclimate.nbi.ku.dk/data/>, last access: 3 April 2022).
- Sellers, W. D.: A global climatic model based on the energy balance of the Earth atmosphere, *J. Appl. Meteorol.*, 8, 392–400, 1969.
- Sergin, V. Y.: Numerical modeling of the glaciers-ocean-atmosphere global system, *J. Geophys. Res.-Oceans*, 84, 3191–3204, 1979.
- SMIC: Inadvertent Climate Modification: Report of the Study of Man’s Impact on Climate, The MIT Press, Cambridge, Mass., 308 pp., ISBN 9780262191012, 1971.
- Talento, S. and Ganopolski, A.: Reduced-complexity model for the impact of anthropogenic CO<sub>2</sub> emissions on future glacial cycles, *Earth Syst. Dynam.*, 12, 1275–1293, <https://doi.org/10.5194/esd-12-1275-2021>, 2021.
- Toggweiler, J.: Origin of the 100,000-year timescale in Antarctic temperatures and atmospheric CO<sub>2</sub>, *Paleoceanography*, 23, PA2211, <https://doi.org/10.1029/2006PA001405>, 2008.
- Tziperman, E. and Gildor, H.: The stabilization of the thermohaline circulation by the temperature–precipitation feedback, *J. Phys. Oceanogr.*, 32, 2707–2714, 2002.
- Tziperman, E., Raymo, M. E., Huybers, P., and Wunsch, C.: Consequences of pacing the Pleistocene 100 kyr ice ages by nonlinear phase locking to Milankovitch forcing, *Paleoceanography*, 21, 1–11, <https://doi.org/10.1029/2005PA001241>, 2006.
- Van der Pol, B.: On relaxation-oscillations, *The London, Edinburgh and Dublin Phil. Mag. and J. Sci.*, 2, 978–992, 1926.
- Vannitsem, S., Demaeyer, J., and Ghil, M.: Extratropical low-frequency variability with ENSO forcing: A reduced-order coupled model study, *J. Adv. Model. Earth Syst.*, 13, e2021MS002530, <https://doi.org/10.1029/2021MS002530>, 2021.
- Varadi, F., Runnegar, B., and Ghil, M.: Successive refinements in long-term integrations of planetary orbits, *Astrophys. J.*, 592, 620–630, 2003.
- Verbitsky, M. Y. and Crucifix, M.:  $\pi$ -theorem generalization of the ice-age theory, *Earth Syst. Dynam.*, 11, 281–289, <https://doi.org/10.5194/esd-11-281-2020>, 2020.
- Verbitsky, M. Y., Crucifix, M., and Volobuev, D. M.: A theory of Pleistocene glacial rhythmicity, *Earth Syst. Dynam.*, 9, 1025–1043, <https://doi.org/10.5194/esd-9-1025-2018>, 2018.
- Vettoretti, G., Ditlevsen, P., Jochum, M., and Rasmussen, S. O.: Atmospheric CO<sub>2</sub> control of Spontaneous Millennial-Scale Ice Age Climate Oscillations, *Nat. Geosci.*, 15, 300–306, <https://doi.org/10.1038/s41561-022-00920-7>, 2022.
- Vissio, G., Lembo, V., Lucarini, V., and Ghil, M.: Evaluating the performance of climate models based on Wasserstein distance, *Geophys. Res. Lett.*, 47, e2020GL089385, <https://doi.org/10.1029/2020GL089385>, 2020.
- Wang, B.: Random attractors for the stochastic FitzHugh-Nagumo system on unbounded domains, *Nonlinear Anal.-Theor.*, 71, 2811–2828, <https://doi.org/10.1016/j.na.2009.01.131>, 2009.
- Weertman, J.: Rate of growth or shrinkage of non-equilibrium ice-sheets, *J. Glaciol.*, 6, 145–158, 1964.
- Weertman, J.: Milankovitch solar radiation variations and ice-age ice-sheet sizes, *Nature*, 261, 17–20, 1976.

- Westerhold, T., Marwan, N., Drury, A. J., Liebrand, D., Agnini, C., Anagnostou, E., Barnet, J. S. K., Bohaty, S. M., Vleeschouwer, D. D., Florindo, F., Frederichs, T., Hodell, D. A., Holbourn, A. E., Kroon, D., Laurentano, V., Littler, K., Lourens, L. J., Lyle, M., Pälike, H., Röhl, U., Tian, J., Wilkens, R. H., Wilson, P. A., and Zachos, J. C.: An astronomically dated record of Earth's climate and its predictability over the last 66 million years, *Science*, 369, 1383–1387, 2020.
- Wetherald, R. T. and Manabe, S.: The effects of changing the solar constant on the climate of a general circulation model, *J. Atmos. Sci.*, 32, 2044–2059, 1975.
- Wilkinson, L. and Friendly, M.: The History of the Cluster Heat Map, *Am. Stat.*, 63, 179–184, <https://doi.org/10.1198/tas.2009.0033>, 2009.
- Willeit, M., Ganopolski, A., Calov, R., and Brovkin, V.: Mid-Pleistocene transition in glacial cycles explained by declining CO<sub>2</sub> and regolith removal, *Sci. Adv.*, 5, eaav7337, <https://doi.org/10.1126/sciadv.aav7337>, 2019.
- Yamakou, M. E., Tran, T. D., Duc, L. H., and Jost, J.: The stochastic Fitzhugh–Nagumo neuron model in the excitable regime embeds a leaky integrate-and-fire model, *J. Math. Biol.*, 79, 509–532, <https://doi.org/10.1007/s00285-019-01366-z>, 2019.
- Zhang, G., Liu, Z., and Ma, Z.: Generalized synchronization of different dimensional chaotic dynamical systems, *Chaos Soliton. Fract.*, 32, 773–779, <https://doi.org/10.1016/j.chaos.2005.11.099>, 2007.

## P2 **Glacial abrupt climate change as a multi-scale phenomenon resulting from monostable excitable dynamics**

**Keno Riechers**, Georg Gottwald & Niklas Boers, 2023. arXiv preprint. DOI: 10.48550/arXiv.2303.04063

**Copyright.** The article is published open access under the terms of the [Creative Commons Attribution-NonCommercial-NonDerivative](#) license. The copyright remains with the authors.

**Contribution.** The study was conceived by all authors in close collaboration with major contributions from KR. All numerical computations were carried out by KR. All authors analyzed and discussed the results. All authors wrote the manuscript based on an initial draft by KR.

# Glacial abrupt climate change as a multi-scale phenomenon resulting from monostable excitable dynamics

Keno Riechers  
Complexity Science  
Potsdam Institute for Climate Impact Research  
Potsdam, Germany  
riechers@pik-potsdam.de

Georg Gottwald  
School of Mathematics and Statistics  
University of Sydney  
Sydney, Australia

Niklas Boers  
Earth System Modelling - School of Engineering & Design  
Technical University of Munich  
Munich, Germany

May 23, 2023

Paleoclimate proxy records evidence repeated abrupt climatic transitions during past glacial intervals with strongest expression in the North Atlantic region. In particular, temperature reconstructions from Greenland ice cores reveal high northern latitude warming events of up to  $16^{\circ}\text{C}$  on decadal time scales, but associated impacts extend across the globe. These so-called Dansgaard-Oeschger (DO) events are followed by phases of relatively mild temperatures termed interstadials, which exhibit gradual cooling over several hundred to a few thousand years prior to a final phase of abrupt temperature decrease back to cold stadials. To date, there is no consensus on the mechanism of this millennial-scale variability. Here, we propose an excitable model system to explain the DO cycles, in which interstadials occur as noise-induced state space excursions. Our model comprises the mutual multi-scale interactions between four dynamical variables representing Arctic atmospheric temperatures, Nordic Seas' temperatures and sea ice cover, and the Atlantic Meridional Overturning Circulation (AMOC). Crucially, the model's atmosphere-ocean heat flux is moderated by the sea ice variable, which in turn is subject to large perturbations dynamically generated by fast evolving intermittent noise. If supercritical, these perturbations trigger interstadial-like state space excursions seizing all four model variables. As a physical source for such a driving noise process we propose convective events in the ocean or atmospheric blocking events. The key characteristics of DO cycles are reproduced by our model with remarkable resemblance to the proxy record; in particular, their shape, return time, as well as the dependence of the interstadial and stadial durations on the background temperatures are reproduced accurately. In contrast to the prevailing understanding that the DO variability showcases bistability in the underlying dynamics, we conclude that multi-scale, monostable excitable dynamics provides a promising alternative candidate to explain the millennial-scale climate variability associated with the DO events.

**Keywords** Dansgaard-Oeschger Events | Excitable Dynamics | Multi-scale System |  $\alpha$ -stable Noise

## 1 Introduction

Stable water isotope records from Greenland ice cores provide evidence for repeated abrupt climatic shifts during the last glacial interval. Decadal-scale transitions from low to high values of  $\delta^{18}\text{O}$  (Fig. 1a) are indicative of sudden warming events at the drilling site, which are termed Dansgaard-Oeschger (DO) events [1–5]. The temperature increases of  $\sim 8 - 16^{\circ}\text{C}$  [6–10] are followed by phases of milder, yet moderately cooling temperatures called interstadials, lasting from centuries to millennia [11–13]. Typically, a final and more abrupt decline brings the climate back to a colder state known as stadial climate. The successions of interstadials and stadials are often

referred to as DO cycles.

While the early glacial ( $\sim 115$ – $71$  kyr b2k) was dominated by long lasting interstadials and relatively warm stadial conditions, colder stadials and very short interstadials prevailed during the later part of the last glacial ( $\sim 29$ – $14$  kyr b2k, compare Fig. 1). The middle part ( $\sim 71$ – $29$  kyr b2k) was characterized by frequent DO events with intermediate-length stadials and interstadials. The ratio between interstadial and stadial duration was presumably influenced by the background climate state and orbital forcing [14–18].

The signature of DO cycles is found in numerous paleoclimatic proxy records around the globe, including speleothems and Antarctic ice cores [25, 26]. For instance, DO events

## 5. DO events from the perspective of dynamical systems

Glacial abrupt climate change as a multi-scale phenomenon resulting from monostable excitable dynamics

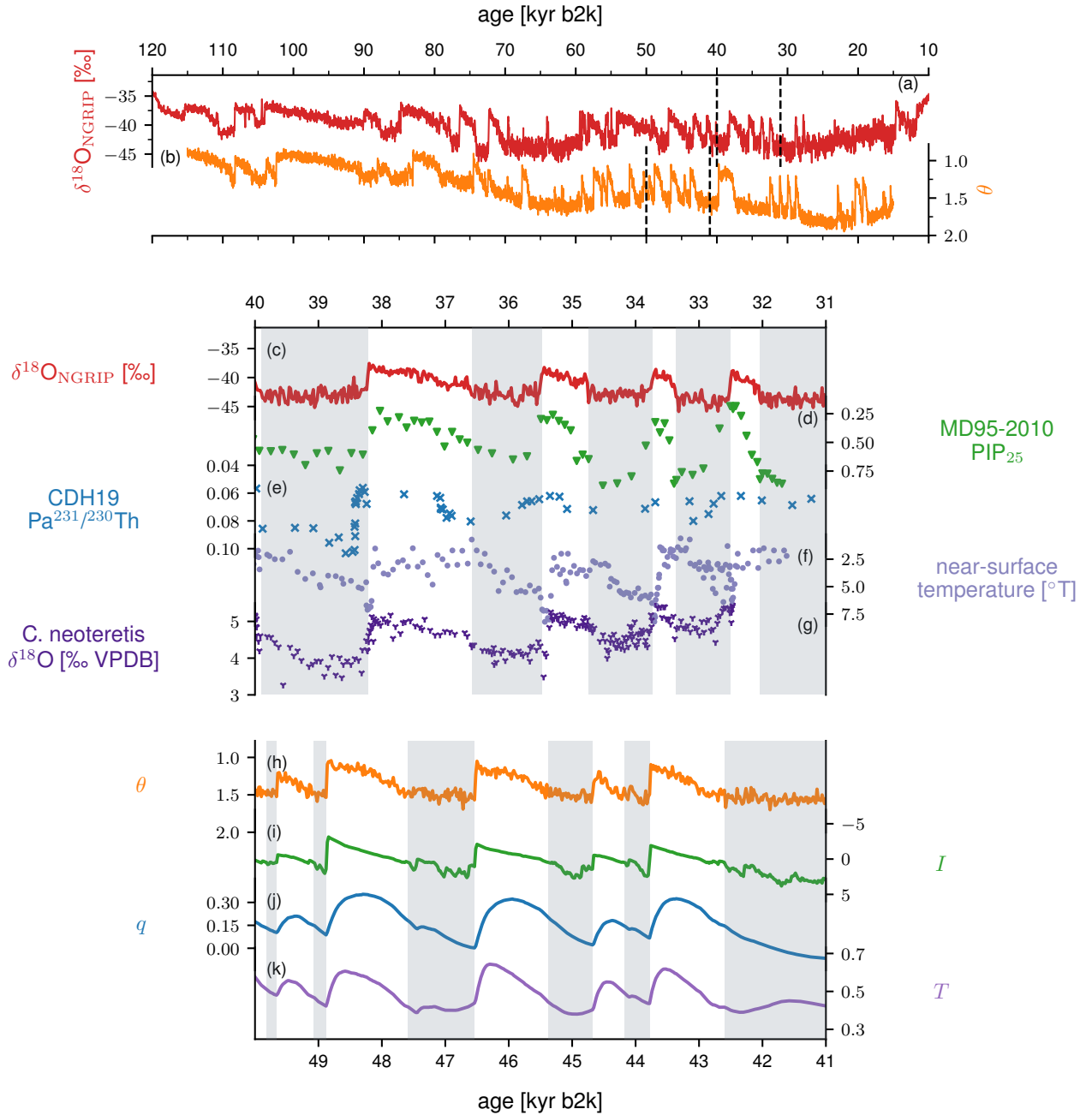


**Figure 1:** Paleoclimatic proxy evidence for characteristic features of DO variability together with corresponding results of our model defined by Eqs. 1–7. (a) 20-year mean NGRIP  $\delta^{18}\text{O}$  data [12, 19] interpreted as a qualitative proxy of air temperatures over Greenland (data available at: <https://www.iceandclimate.nbi.ku.dk/data/>, last access: 3 March 2023). (b) Simulated Arctic atmospheric air temperatures  $\theta$ . (c) Zoom into the period 40–31 kyr b2k of (a) — the period was chosen due to the availability of proxy data. (d)  $\text{PIP}_{25}$  index from the marine sediment core MD95-2010 [20]. The  $\text{PIP}_{25}$  index is indicative of past sea ice cover at the core site with values of 1 and 0 corresponding to perennial sea ice and open ocean conditions, respectively. (e)  $\text{Pa}/\text{Th}$  ratios from the marine sediment core CDH19 from the Bermuda Rise as provided by [21]. The ratios are interpreted as a direct measure of the AMOC strength, with lower values corresponding to stronger overturning and vice versa. (f) Near-surface ocean temperature reconstruction from the marine sediment core MD99-2284 [22], presented here on a revised age scale [20, 23]. (g)  $\delta^{18}\text{O}$  of the benthic species  $C. neoteretis$  [22] shown on a revised age-scale [20, 23]. According to the most recent interpretation of the data, the benthic  $\delta^{18}\text{O}$  is mostly indicative of past deep-ocean temperatures [20, 24] with higher values indicating colder temperatures and vice versa. Panels (h–k) show corresponding model results but for the period 50–41 kyr b2k, which was selected because of its high DO event frequency. (h) the Arctic atmospheric temperature  $\theta$ , (i) the Nordic Seas’ sea ice cover  $I$ , (j) the AMOC strength  $q$  and (k) the Nordic Seas intermediate to deep water temperatures  $T$ . The proxy records shown in (c)–(g) should be directly compared to the simulated trajectories shown in panels (h)–(k), respectively. All model variables are given in arbitrary units.

Glacial abrupt climate change as a multi-scale phenomenon resulting from monostable excitable dynamics

are associated with large-scale reorganizations of the Northern Hemisphere atmospheric circulation [27–29] including a northward shift of the ITCZ [26] with strong impacts on the Asian and South American Monsoon systems [30–34]. The expression of DO variability is, however, most pronounced in the North Atlantic region and climatic processes hosted by this region such as sea ice or deep water formation are believed to be central to the triggering mechanism of DO events.

To date there is no conclusive theory that fully explains the mechanism of the DO cycles. Several climatic components have been proposed to be relevant, including ocean dynamics, atmospheric events, sea ice, ice sheets and freshwater fluxes [18, 22, 35–40]. Similarly, several dynamic mechanisms have been invoked to explain the DO events, ranging from external drivers such as (periodically) changing freshwater fluxes [36, 41–43] and noise induced transitions between two stable states [17, 44–47] to dynamically self-generating mechanisms including self-sustained oscillations [18, 22, 35, 39, 48–50]. In this study, building on the results of [51] we consider a paradigm for DO variability which has to date received only little attention: We present an excitable multi-scale model, whose single stable fixed point can be identified with stadial climate conditions. In response to perturbations above a critical threshold, the system takes prolonged excursions through a region of slow transitive dynamics in state space assuming an interstadial configuration in all system dimensions. The perturbations are generated by an intermittent non-Gaussian driving noise detailed later. In particular, we reproduce the following five central aspects of DO cycles in an interpretable manner:

1. **Shape of DO cycles:** In addition to the above described characteristic evolution of past Greenland atmospheric temperatures over a DO cycle we resolve more detailed features of the record, such as the presence of short-lived interstadials and stadials (cf. Fig. 1a and c).
2. **Duration of stadials and interstadials:** A pronounced variability in stadial and interstadial duration can be observed over the last glacial (cf. Fig. 1a). It has previously been shown that the interstadial durations are positively correlated with slowly varying global mean background climate [18], while the variability in stadial durations is less clear.
3. **In-phase sea ice dynamics:** An important climate variable found to vary in phase with Greenland temperatures is the sea ice extent in the Nordic Seas and the North Atlantic. During stadials an extensive sea ice cover prevails, whereas interstadials exhibit conditions ranging from open water to seasonal sea ice cover [20, 22, 52–54] (cf. Fig. 1d).
4. **Nordic Seas’ temperature inversion:** Several studies report warming of the ice-covered stadial Nordic Seas at intermediate and large depth which they attribute to continued inflow of warm water masses from the south [22, 24, 49] (cf. Fig. 1f and g). This heat — initially trapped under the sea ice — is hypothesized to have warmed the polar atmosphere abruptly in response to sudden sea ice retreat during DO events [18, 22].

5. **AMOC switches:** Multiple lines of direct and indirect evidence, thoroughly summarized by [55], point to changes in the strength of the Atlantic Meridional Overturning Circulation (AMOC) in phase with Greenland temperatures, with weak (or no) overturning during (Heinrich) stadials and stronger overturning during interstadials (cf. Fig. 1e). An active AMOC is typically thought to have provided the necessary northward heat transport to explain the milder arctic climate during interstadials.

The model proposed here dynamically generates DO events and convincingly reproduces the subsequent interstadial phase in terms of the five features mentioned above as shown in Fig. 1. From a physical modelling point of view, the results presented below suggest that the DO events may have been caused by complex multi-scale interactions between several climate subsystems acting on separate time scales: the ocean circulation, the sea ice, the large-scale atmosphere, and intermittent atmospheric or oceanic events, ordered from slow to fast characteristic time scales.

The paper is structured as follows: We introduce the model in Section 2 and analyze its dynamics in Section 3. We interpret the results in a physical context and also perform a detailed model–data comparison in terms of the above listed five key features. Section 4 discusses the results and relates them to previous analysis. We conclude in Section 5 with a summary of our key findings.

## 2 Methods

### 2.1 Monostable excitable model of DO variability

From the slowest to the fastest time scale, the key components of our conceptual multi-scale model are: (i) the Atlantic ocean represented by the meridional temperature and salinity gradients  $T(t)$  and  $S(t)$  between the Equator and the Nordic Seas, (ii) the Nordic Seas’ sea ice extent  $I(t)$ , (iii) the Northern Hemisphere atmosphere represented by the meridional temperature gradient  $\theta(t)$  and (iv) intermittent oceanic and atmospheric anomalies  $\xi_t$  and regular Gaussian atmospheric fluctuations  $\zeta_t$ . The model set-up is schematically illustrated in Figure 2. For the ease of notation, we will omit the explicit time-dependence of the four dynamical variables in the following; driving noise processes will be subscripted with  $t$ . A detailed derivation of the individual model components is provided in the SI Appendix. Here we give only a concise description of the model.

Following the classical Stommel model [56], on the slowest time scale  $\tau_{\text{ocean}}$  the oceanic meridional gradients of temperature and salinity evolve according to

$$\tau_{\text{ocean}}\dot{T} = -\gamma(I)(T - \theta) - (1 + \mu |T - S|)T, \quad (1)$$

$$\tau_{\text{ocean}}\dot{S} = \sigma - (1 + \mu |T - S|)S \quad (2)$$

and determine the strength of the overturning flow

$$q = T - S, \quad (3)$$

representing the AMOC strength [51]. The ocean temperature  $T$  is coupled to the atmospheric temperature gradient  $\theta$  via mutual heat exchange at the (sea ice moderated) rate  $\gamma(I)$ .

Glacial abrupt climate change as a multi-scale phenomenon resulting from monostable excitable dynamics

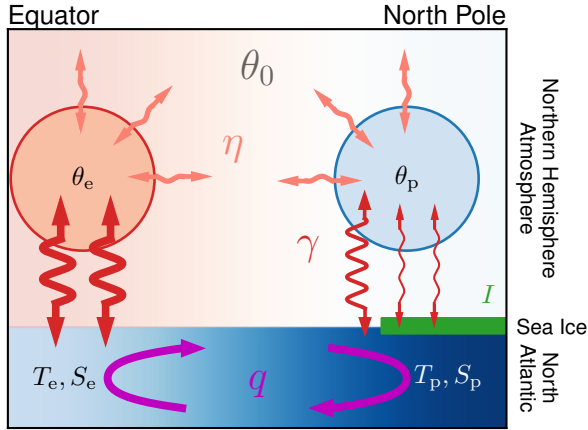


**Figure 2:** Schematic illustration of the excitable monostable model used to reproduce DO variability of the last glacial. The three key model components are the North Atlantic (bottom), the Northern Hemisphere atmosphere in the North Atlantic region (upper part) and the sea ice in the Nordic Seas (green bar on the right). Oceanic temperature and salinity in the equatorial and polar region are denoted as  $T_e, S_e$  and  $T_p, S_p$ , respectively. The corresponding meridional gradients follow as  $T = T_e - T_p$  and  $S = S_e - S_p$ . Analogously, the atmospheric temperature gradient  $\theta = \theta_e - \theta_p$  is given by the difference between equatorial and polar atmospheric temperatures. A background hemispheric meridional temperature gradient  $\theta_0$  is determined by the solar radiation with slow variation driven by changes of the global ice sheet configuration. Atmosphere and ocean exchange heat in both the equatorial and the polar region (dark red arrows). In the polar region the presence of sea ice substantially reduces the heat exchange rate  $\gamma$ . The considered atmospheric polar and equatorial parcels simultaneously dissipate heat (light red arrows) at the rate  $\eta$  such that the meridional atmospheric temperature gradient over the North Atlantic  $\theta$  relaxes against the background gradient  $\theta_0$ . The oceanic gradients  $T$  and  $S$  translate into a meridional density gradient, that in turn drives the flow  $q$  which represents the AMOC. The oceanic salinity gradient  $S$  is maintained by constant fresh water flux in the equatorial and polar regions (not shown).

The atmospheric meridional temperature gradient  $\theta$  relaxes against both a prescribed background state  $\theta_0$  and the oceanic gradient  $T$  on a fast characteristic time scale  $\tau_{\text{atm}} < \tau_{\text{ocean}}$ :

$$\tau_{\text{atm}} \dot{\theta} = -\eta(\theta - \theta_0) - \gamma(I)(\theta - T) + \zeta_t, \quad (4)$$

with  $\zeta_t$  denoting a white noise process that disturbs the atmospheric dynamics. The ratio of the atmospheric redistribution of heat and the atmosphere–ocean heat exchange is set by  $\eta$ .

It is widely accepted that changing background climate conditions strongly influenced DO variability over the course of the last glacial [14–16, 18]. This effect is considered in our model by altering the atmospheric background state  $\theta_0$  over time according to

$$\theta_0(t) = 1.59 + 0.23\delta^{18}\text{O}_{\text{LR04}}^*(t), \quad (5)$$

where the normalized benthic stable isotope data  $\delta^{18}\text{O}_{\text{LR04}}^*(t)$  is indicative of past global ice volume changes [57]. We argue that a colder background climate increases the atmospheric background temperature gradient  $\theta_0$  due to arctic amplification.

On an intermediate time scale  $\tau_{\text{ice}}$  with  $\tau_{\text{ocean}} > \tau_{\text{ice}} > \tau_{\text{atm}}$ , the temporal evolution of the sea ice is given by the seasonally averaged Eisenman model [58, 59]

$$\tau_{\text{ice}} \dot{I} = \Delta \tanh\left(\frac{I}{h}\right) - R_0 \Theta(I) I - L_0 + L_1 \theta - L_2 I + \xi_t, \quad (6)$$

where  $\Theta(I)$  denotes the Heaviside function and the term  $L_1 \theta$  represents the influence of the atmosphere on the sea ice formation, with large atmospheric temperature gradients — i.e. colder temperatures at high northern latitudes — fostering sea ice growth and vice versa. The remaining terms represent the ice–albedo feedback, sea ice export and the net incoming and outgoing radiation linearized with respect to  $I$ , respectively (see Appendix). The stochastic process  $\xi_t$  models fast intermittent random sea ice retreat events that will be explained in greater detail below. The sea ice itself couples back to the ocean and atmosphere dynamics by acting as a dynamic insulator [18, 22] and modifying the respective mutual relaxation rate according to

$$\gamma(I) = \gamma_0 + \frac{\Delta\gamma}{2} \left[ \tanh\left(\frac{-(I - I_0)}{\omega}\right) + 1 \right]. \quad (7)$$

In the presence of a stadial sea ice cover ( $I > 0.5$ ) the polar ocean is shielded from the atmosphere and the mutual heat exchange is heavily suppressed. In contrast, a reduced interstadial sea ice cover yields strong atmosphere–ocean heat exchange and correspondingly high mutual relaxation rates.

Although  $T$  and  $\theta$  are gradients, we may compare them directly with observations for oceanic and atmospheric temperature proxies from high northern latitudes, respectively. This is justified since the comparably much larger size of the equatorial region compared to the polar region implies substantially larger heat capacities for the considered equatorial boxes. We thus ascribe changes in the gradients mostly to changes in the polar regions and interpret  $T$  and  $\theta$  as direct counterparts for intermediate and deep ocean temperature proxy records from the Nordic Seas (compare Fig. 1f–g with 1k) and  $\delta^{18}\text{O}$  records from Greenland ice cores (compare Fig. 1c with 1h), respectively. The comparison of  $q$  with proxies for past AMOC strength is straightforward (compare Fig. 1e with 1j) and so is the comparison of  $I$  with proxies for past sea ice extent (compare Fig. 1d with 1i).

Values of the parameters used in our numerical simulation are summarized in Table 1.

## 2.2 Stochastic (intermittent) forcing processes $\xi_t$ and $\zeta_t$

The deterministic model defined by Eqs. 1–4 and Eqs. 6–7 without a driving force ( $\zeta_t = \xi_t = 0$ ) yields monostable dynamics for  $\theta_0 > 1.286$  and is thus as such not suited to model the last glacial’s climate variability. However, it also features a region of slow transitive dynamics located where the nullclines of the atmosphere and sea ice variables are closest (c.f. Fig. 4a and f). We will show later that this meta-stable state in the model’s state space can be identified with interstadial climate conditions of the North Atlantic region. In order to make this meta-stable state accessible to the dynamics we introduce the noise processes  $\xi_t$  and  $\zeta_t$  that

Glacial abrupt climate change as a multi-scale phenomenon resulting from monostable excitable dynamics

Parameter	Definition	Value
<b>time scales</b>		
$\tau_{\text{ocean}}$	oceanic time scale	1000
$\tau_{\text{ice}}$	sea ice time scale	200
$\tau_{\text{atm}}$	atmospheric time scale	20
<b>atmosphere–ocean model</b>		
$\gamma_0$	relaxation rate at full sea ice cover	0.5
$\Delta\gamma$	amplitude of the sea ice’s insolation effect	3.5
$\eta$	atmospheric heat dissipation rate	4
$\mu$	flux parameter	7.5
$\sigma$	freshwater influx	0.7
<b>sea ice model</b>		
$L_0$	0th order sea ice OLR	1.3
$L_1$	linear dependence of sea ice OLR on the atmosphere	1.4
$L_2$	linear dependence of sea ice OLR on the sea ice	0.35
$\Delta$	strength of sea ice albedo feedback	0.25
$h$	characteristic sea ice albedo feedback scale	0.08
$R_0$	rate of sea ice export	0.4
$\omega$	characteristic insolation scale of sea ice	0.8
$I_0$	sea ice value, at which half of the insolation effect is reached	-0.5

**Table 1:** Model parameters used in all simulations, unless stated otherwise. The parameters are chosen to reproduce the key features of DO events.

mimic the effect of unresolved events occurring on time scales faster than the characteristic time scales  $\tau_{\text{ice}}$  and  $\tau_{\text{atm}}$  of the sea ice and atmosphere dynamics, respectively.

The atmosphere variable  $\theta$  is assumed to be subjected to Gaussian white noise forcing  $\zeta_t = \sigma_\theta \dot{W}$  with standard Brownian motion  $W$ . This noise can be motivated as the effective stochastic effect of unresolved strongly chaotic atmospheric fluctuations on  $\theta$  [60]. This noise does not substantially affect the dynamics of Eqs. 1–4 and Eqs. 6–7 but generates more realistic fluctuations of  $\theta$  in accordance with the NGRIP  $\delta^{18}\text{O}$  record.

The sea ice noise  $\xi_t$ , however, will play a major role in triggering DO events. To generate rare but large forcing events which allow the system to leave the stadial fixed point and enter the meta-stable state, non-Gaussian noise is required. [51] showed that  $\alpha$ -stable noise, which is characterized by the occurrence of discrete jumps, can be dynamically generated in a multi-scale setting to produce abrupt warming events in a Stommel model driven by a simple sea-ice model. Here, we postulate that sea ice is subjected to rare and intermittent fast processes. According to the theory laid out in [61–63] and [51], this forcing, when integrated, gives rise to an effective  $\alpha$ -stable component in the resulting dynamics of the sea ice. By controlling the heat exchange rate  $\gamma(I)$  the sea ice in turn drives the atmospheric and oceanic variables  $\theta$  and  $T$  with emergent non-Gaussian noise. Indeed, signatures of non-Gaussian  $\alpha$ -stable noise have been detected by [44] in the calcium concentration record of the GRIP ice core [64].

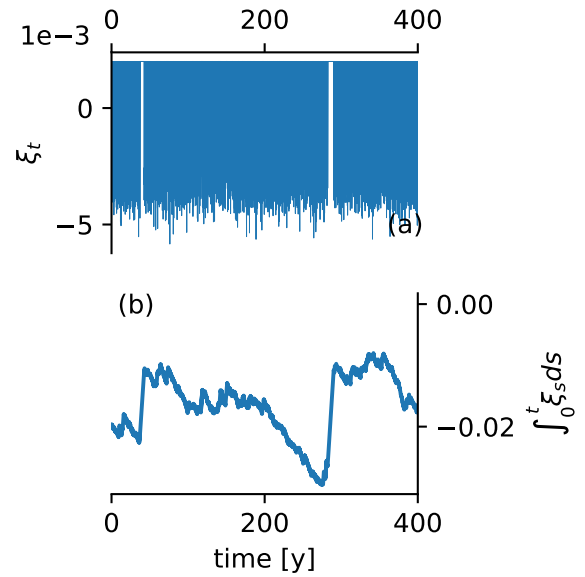


**Figure 3:** Illustration of the driving noise process  $\xi_t$  acting on the sea ice (a) and its integrated form  $\int_0^t \xi_s ds$  (b). It is clearly seen how prolonged laminar phases of the driving noise  $\xi_t$  result in jumps in the integrated  $\int_0^t \xi_s ds$ . These jumps may translate into supercritical sea ice removals and trigger DO events in our excitable model.

We propose two possible physical mechanisms which may constitute such intermittent forcing on the sea ice: oceanic convective events and atmospheric anomalies. During stadials, the Nordic Seas’ sea ice is shielded from the warmer subsurface and deep waters by a thin layer of cold and fresh water [20, 22]. We hypothesize that intermittent convective events may temporarily remove this layer and melt sea ice from below, efficiently opening up polynia through which oceanic heat could be released to the atmosphere [39]. Either, after locally releasing sufficient heat, a stable stratification of the ocean reestablishes and the polynia refreeze. Or, the convective events might remove a critical amount of sea ice and push the system into the meta-stable interstadial state.

Strong atmospheric anomalies constitute another possible source of intermittent sea ice forcing. [65] and [66] describe — although in a somewhat different setting — how persistent atmospheric anomalies can drive the high northern latitude climate into a substantially altered state.

We postulate that the mechanisms giving rise to intermittent anomalous forcing events are active only during stadials. During interstadials, convectively driven sea ice removal should not have a strong impact on the already northward displaced sea ice edge, because the warm Atlantic inflow loses too much heat before it could be subdued under the sea ice. Similarly, we argue that atmospheric anomalous forcing events require a certain meridional temperature gradient and a stadial configuration of the jet stream. Therefore, we impose a Gaussian white noise forcing of the sea ice dynamics with  $\xi_t = \sigma_I \dot{W}$  with standard Brownian motion  $W$  if no pronounced stadial sea ice cover is present ( $I < 0.5$ ). Since sea ice fluctuations are smaller, the smaller the sea ice extent, we choose relatively

Parameter	Definition	Value
<b>atmospheric noise <math>\zeta_t</math></b>		
$\sigma_\theta$	amplitude of the atmospheric noise	0.04
<b>sea ice noise <math>\xi_t</math> during stadials</b>		
$c$	laminar forcing strength	0.2
$\sigma_\Omega$	amplitude of the Brownian motion during turbulent phase	0.01
$k = 1/\alpha$	shape parameter of Pareto distribution	0.62
$\sigma_\Sigma$	scale parameter of the Pareto distribution	2
$\mu_\Sigma = \sigma_\Sigma/k$	location parameter of the Pareto distribution	3.2
<b>sea ice noise <math>\xi_t</math> during interstadials</b>		
$\sigma_I$	amplitude of interstadial Brownian motion	0.006

**Table 2:** Parameters for the stochastic processes  $\zeta_t$  and  $\xi_t$  which drive the atmosphere and sea ice in 4 and 6, respectively.

small  $\sigma_I$  as compared to the sea ice fluctuation emerging from the more complex stadial driving noise which we describe in the following.

To model intermittent convective events or atmospheric anomalies, we follow [61, 62] and design a (mean-zero) process which consists of a succession of turbulent and laminar periods. The forcing in the laminar periods is set to a constant  $\xi_t = -c$  whereas during the turbulent periods it fluctuates around  $\xi_t = c$  according to standard Brownian motion with  $\xi_t = c + \sigma_\Omega \dot{W}$ . The respective durations of these phases are themselves random variables. In particular, durations of the laminar period  $\Sigma$  can be arbitrarily long and are distributed according to a Pareto law

$$\Sigma \sim \frac{1}{\sigma_\Sigma} \left( 1 + k \left[ \frac{\Sigma - \mu_\Sigma}{\sigma_\Sigma} \right] \right)^{-(1/k+1)} \quad (8)$$

with shape parameter  $k = 1/\alpha$ , scale parameter  $\sigma_\Sigma$ , and location parameter  $\mu_\Sigma = \sigma_\Sigma/k$ . Hence, laminar periods last on average for  $\mathbb{E}[\Sigma] = \sigma_\Sigma \alpha^2 / (\alpha - 1)$  time units (assuming  $\alpha > 1$ ). The durations of turbulent periods  $\Omega$  are uniformly distributed around the mean  $\bar{\Omega} = \mathbb{E}[\Sigma]$  with  $\Omega \sim \bar{\Omega} + U[-\bar{\Omega}/2, +\bar{\Omega}/2]$ , where  $U[a, b]$  denotes the uniform distribution between the limits  $a$  and  $b$ . When such a process is integrated, the laminar periods yield ballistic flights  $\sim -c\Sigma$ . The heavy tail of the Pareto distribution assigns a probability of  $(\alpha\sigma)^\alpha \vartheta^{-\alpha}$  to durations  $\Sigma > \vartheta$ , and allows for  $\alpha < 2$  for non-vanishing probabilities of ballistic flights of arbitrary lengths. This renders  $\int \xi_t dt$  an effective  $\alpha$ -stable process. This mechanism of intermittent laminar dynamics generating  $\alpha$ -stable noise is illustrated in Figure 3, where we show the stochastic process  $\xi_t$  and its integrated form.

Long lasting laminar forcing events may remove large amounts of sea ice and thus entail an abrupt shift in the atmosphere–ocean heat exchange which determines the climatic state of the coupled atmosphere–ocean model (cf. Fig. 4). Such dynamically generated perturbations are capable of inducing meta-stable interstadial dynamics in our model as we will show in the next section. In Table 2 we list the parameters used to generate the noise.

### 3 Results

In this section we will first analyze the response of the deterministic coupled model to imposed perturbations of the sea ice cover with  $\zeta_t = \xi_t = 0$  and a constant climate background temperature  $\theta_0$ . We show that long lasting interstadial-like excursions occur as a consequence of supercritical sea ice perturbations of the stable stadial state. This phenomenon results from a complex interplay of the three separate time scales and the slow deterministic dynamics in a particular meta-stable region of the state space, which is characterized by high proximity of the  $\theta$  and  $I$  nullclines (cf. Fig. 4). We then show that the intermittent noise  $\xi_t$  is capable of generating such supercritical perturbations to the sea ice acting as triggers of interstadials. Finally, the full stochastic model, coupled to the background climate, is run over the entire last glacial.

#### 3.1 Deterministic response to sea ice perturbations

To understand how our model may explain DO variability, we investigate how the deterministic system given by Eqs. 1–4 and Eqs. 6–7 with  $\zeta_t = 0, \xi_t = 0$  recovers after large imposed perturbations of the sea ice variable for two different choices of  $\theta_0$ , corresponding to warm and intermediate glacial climate backgrounds, respectively (Fig. 4). In simulations initialized in the stadial stable state, at time  $t_p = 200$ , the sea ice is abruptly removed by manually setting  $I(t) = I_p$  with  $I_p = \{0.2, 0, -0.2, -0.5, -1, -2\}$ . Subsequently the system evolves freely and relaxes back to the unique stadial fixed point. The character of the relaxation depends on the strength of the perturbation as well as the value of the climate background  $\theta_0$ . We observe distinct phases in the system response which shall be discussed separately in the following.

**Phase A: immediate atmospheric response.** Since on small time intervals the slow ocean dynamics  $T$  and  $S$  can be considered as constants for the faster atmosphere dynamics  $\theta$ , the atmosphere rapidly increases to the value  $\theta_p$  (see Fig. 4b,g), which is approximately given as the solution to  $\gamma(I_p)(\theta_p - T_s) + \eta(\theta_p - \theta_0) = 0$  (shown as a light orange line in Fig. 4 as a guide to the eye), where the subscript  $s$  denotes the respective stadial fixed point values. Physically,  $\theta_p$  is determined as the balance of atmospheric uptake of oceanic heat  $\gamma(I_p)(\theta_p - T_s)$  and its associated atmospheric redistribution (dissipation)  $\eta(\theta_p - \theta_0)$  in response to the sudden exposure to a warm stadial ocean (small  $T$ ) which was previously shielded from the atmosphere by the stadial sea ice cover. The slow model time scale  $\tau_{\text{ocean}}$  may in this context be interpreted as the large heat capacity of the Nordic Seas, allowing them to release heat to the atmosphere while remaining themselves unchanged on short time scales.

**Phase B: system-wide relaxation.** We now discuss how the system relaxes from the perturbed state  $(\theta_p, T_s, q_s, I_p)$  back to the unique stable fixed point  $(\theta_s, T_s, q_s, I_s)$ . Notice that the sea ice bifurcation point  $I_{B2}$  marks the lowest sea ice cover of the sea ice nullcline’s stable branch with reduced sea ice cover (cf. Fig. 4). The relaxation is qualitatively different depending on whether the perturbation brings the sea ice to the low-ice regime ( $I_p < I_{B2}$ ) or not. If that is the case, the system takes a prolonged excursion in state space with a two-stage relaxation process, of which the first stage can

Glacial abrupt climate change as a multi-scale phenomenon resulting from monostable excitable dynamics

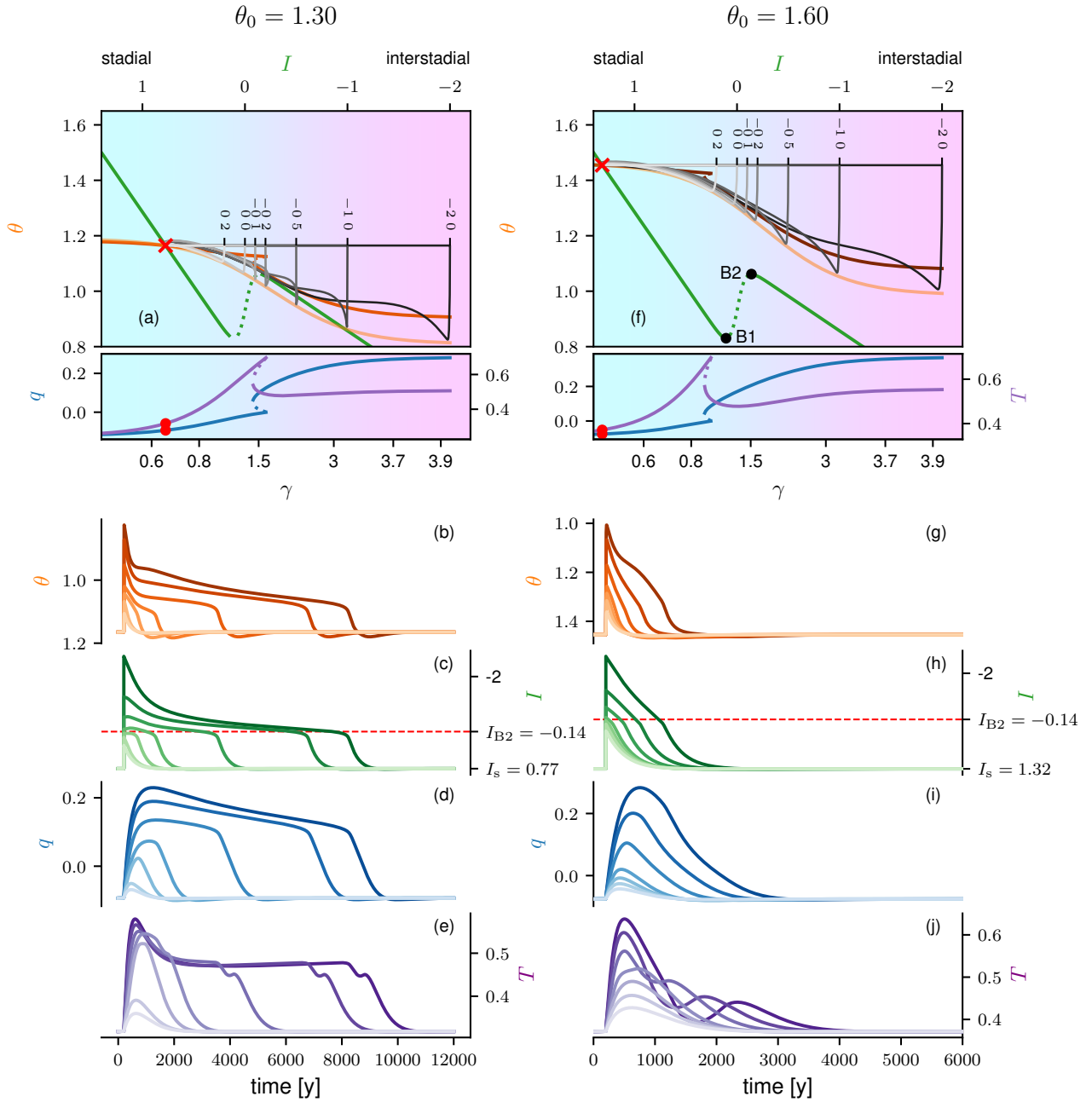


**Figure 4:** Trajectories of the deterministic system defined by Eqs. 1–7 subjected to instantaneous sea ice retreat at  $t = 200$  for several values of the perturbed sea ice state  $I_p = \{0.2, 0.0, -0.2, -0.5, -1.0, -2.0\}$  (gray horizontal lines in a and f). In panels (a–e)  $\theta_0 = 1.3$  (warmer background climate) while in panels (f–j)  $\theta_0 = 1.6$  (colder background climate). (a) and (f) show the trajectories in the  $\theta$ – $I$  plane together with the corresponding nullclines of all four model variables. A prescribed value for the sea ice variable (top axis) determines the atmosphere–ocean heat exchange rate  $\gamma$  (bottom axis), which in turn sets the fixed points of  $\theta$ ,  $T$  and  $q$ . Strong sea ice cover and a low heat exchange rate yield a cold polar atmosphere (large  $\theta$ ), warm intermediate and deep waters in the Nordic Seas (small  $T$ ) and a weak AMOC (small  $|q|$ ). This configuration corresponds to stadial climate conditions as inferred from proxy records. A small sea ice cover reversely entails a warm polar atmosphere (small  $\theta$ ), cold Nordic Seas (large  $T$ ) and an active AMOC (large  $|q|$ ) which can be identified with interstadial climate conditions. Since  $\theta$  couples back to the sea ice  $I$ , intersections of the  $I$ - and  $\theta$ -nullcline constitute fixed points of the entire system in the  $\theta$ – $I$  plane (red cross) with values for  $T$  and  $q$  (red dots) following from the heat exchange rate associated with this intersection. All trajectories are initialized at the unique stable fixed point. The remaining panels show the trajectories of the individual system variables against time for the different sea ice perturbations. The horizontal dashed lines in panels (c) and (h) mark the critical sea ice threshold  $I_{B2}$  which constitutes the highest possible sea ice cover in the low-ice regime. Vice versa, the other sea ice bifurcation point  $I_{B1}$  marks the lowest possible sea ice cover in an ice-rich regime viewed in the  $\theta$ – $I$  plane.

be identified with interstadial climate conditions. We call this scenario, which involves responses of all model variables, the supercritical case. If  $I_p > I_{B2}$ , then the system shows a straight relaxation back to stadial conditions without any substantial response of the oceanic variables to the initial perturbation. We term this scenario the subcritical case. The existence of both subcritical perturbations which rapidly relax back to the steady state and supercritical perturbations which cause long transitory dynamics back towards the steady state involving several time scales is a hallmark of so called excitable media often found in neurophysiological systems.

**Phase B: subcritical case  $I_p > I_{B2}$ .** In the subcritical case the system remains in an ice-rich state which due to the albedo feedback facilitates a fast regrowth of the sea ice. Consequently, the dynamics of  $I$  and  $\theta$  jointly relax back straight to the stadial equilibrium as the regrowing sea ice increasingly shields the atmosphere from the warmer ocean. The oceanic variables on the other hand show hardly any response due to their higher inertia and the fast sea ice recovery. Qualitatively the general system response to subcritical perturbations is the same for  $\theta_0 = 1.3$  and  $\theta_0 = 1.6$ .

**Phase B: supercritical case  $I_p < I_{B2}$  - Stage 1.** In contrast, in the supercritical case a phase of slowed-down sea ice recovery occurs, giving the oceanic variables enough time to respond to the perturbation such that all model variables temporarily assume interstadial configurations, i.e. in addition to the elevated arctic atmospheric temperature (low gradient  $\theta$ ) and the reduced Nordic Seas' ice cover (low  $I$ ), the AMOC assumes its strong circulation mode (large  $q$ ) and the Nordic Seas cool at intermediate and large depth (high gradient  $T$ ) in agreement with proxy evidence (cf. Fig. 1).

As a consequence of the substantially reduced sea ice cover the ice–albedo feedback now inhibits the reformation of the sea ice and in the presence of warm atmospheric conditions  $\theta_p$  the sea ice regrows at a slow rate towards  $I_{B2}$  or retreats even further. As the atmosphere continuously dissipates the heat it receives from the ocean, the latter starts to notably cool (increase in  $T$ ). In turn, the oceanic cooling reduces the atmospheric uptake of oceanic heat and as a result the arctic atmosphere cools in parallel (pronounced increase in  $\theta$  in Fig. 4 shortly after the perturbations). This effect inevitably prevents a stabilization of the system in the low-ice regime and ensures that the sea ice eventually regrows. A second consequence of the Nordic Seas' cooling is the transition of the AMOC from a salinity-driven weak mode to the temperature-driven strong mode. This completes the interstadial configuration of the four model variables and allows us to identify this first stage of the supercritical relaxation with the interstadial climate. Fully reactivated, the AMOC's northward oceanic heat transport stabilizes the temperatures of the Nordic Seas and over the course of the remaining interstadial the slow adjustments of the other variables are driven by the incremental sea ice regrowth.

The nature and duration of the interstadial stage depends on both the size of the initial sea ice perturbation  $I_p$  and the closeness of the sea ice nullcline and the atmosphere nullcline. If the two nullclines are close (as for  $\theta_0 = 1.3$ ) the dynamics of  $\theta$  and  $I$  is comparably slow (cf. the dynamics for  $\theta_0 = 1.3$  in Fig. 4). Sufficiently strong sea ice perturbations then result

in pronounced interstadials during which all system variables hardly change over an extended period of time. If the nullclines are further apart (as for  $\theta_0 = 1.60$ ) the interstadial state is less pronounced and characterized by continuous change in all model variables, driven by steady sea ice regrowth.

**Phase B: supercritical case ( $I_p < I_{B2}$ ) - Stage 2.** Once the sea ice has regrown past  $I_{B2}$ , its further regrowth accelerates substantially, marking the beginning of the second stage in the supercritical system-wide relaxation process. This is due to the strongly changing albedo effect around intermediate sea ice cover. The regrowing sea ice increasingly prevents oceanic heat loss to the atmosphere, which entails polar atmospheric cooling and initiates warming of the Nordic Seas. The reduction of the oceanic temperature gradient is closely followed by a corresponding reduction in the AMOC strength. Since the atmosphere equilibrates quasi-adiabatically to the declining heat exchange rate  $\gamma(I)$ , it cools at the same accelerated rate as the ice recovers and both atmosphere and sea ice reach stadial configuration within a few hundred years after the sea ice passed its threshold  $I_{B2}$ . The oceanic variables follow with some inertia; they exhibit a sustained relaxation after the faster atmosphere and sea ice have already clearly transitioned to their stadial configuration. This second stage of the supercritical relaxation process corresponds to the abrupt interstadial–stadial transitions observed in the paleoclimate record.

### 3.2 Noise-driven interstadials

We now show that the intermittent driving noise  $\xi_t$  is able to generate large sea ice perturbations which may trigger DO events provided they are supercritical. Fig. 5 shows trajectories of the dynamics determined by Eqs. 1–4 and Eqs. 6 and 7 under the influence of the driving noises  $\xi_t$  and  $\zeta_t$  with a constant atmospheric background climatic state  $\theta_0$ . Overall there is high visual agreement between simulated  $\theta$  trajectories (Fig. 5) and the DO cycles recorded in the NGRIP  $\delta^{18}\text{O}$  data (Fig. 1a and c).

For  $\theta_0 = 1.3$  the  $\theta$ -trajectory resembles DO cycles from the early glacial, with two persistent interstadials separated by a short stadial. For  $\theta_0 = 1.6$  the  $\theta$ -trajectory has a greater similarity with the mid to late glacial, with shorter interstadials and predominantly stadial conditions. Confirming the discussion in the previous section, interstadials last longer and have a more pronounced plateau in all variables for the smaller atmospheric background temperature gradient  $\theta_0 = 1.3$ . Moreover, a subtle increase in the stadial duration can be observed for larger  $\theta_0$ . The colder stadial conditions associated with larger  $\theta_0$  imply an increased distance between the sea ice's stable stadial configuration  $I_s$  and the critical sea ice threshold  $I_{B2}$ . Hence, for unchanged driving noise  $\xi_t$ , the probability for the noise to drive the system across  $I_{B2}$  is reduced for larger  $\theta_0$  and thus the waiting time between two supercritical stochastic forcing events is higher and the stadials are longer. However, this effect is attenuated by the fact that DO events can also be triggered by two pronounced yet subcritical laminar forcing periods in quick succession.

The noise process  $\zeta_t$  driving the  $\theta$  variable blurs the exact timing of DO cooling transitions in agreement with  $\delta^{18}\text{O}$  ice

Glacial abrupt climate change as a multi-scale phenomenon resulting from monostable excitable dynamics

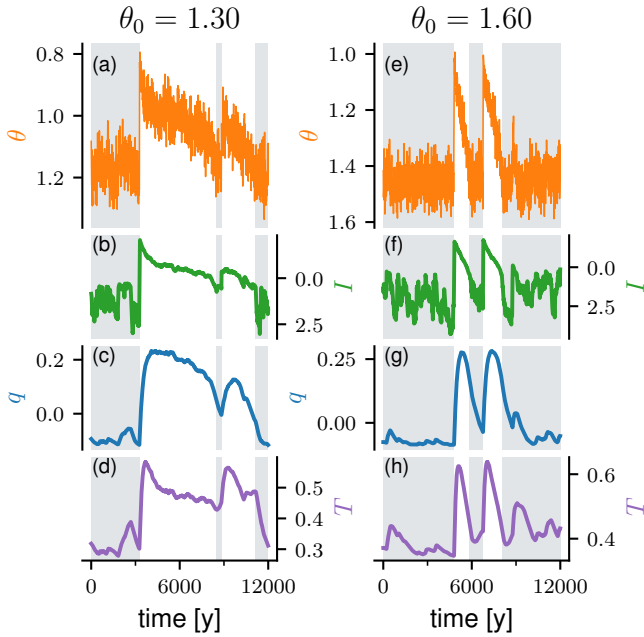


**Figure 5:** Trajectories of the model system defined by Eqs. 1–7 driven by the noise scheme as described in Sect. 2.2, i.e., with non-zero noise  $\zeta_t$  and  $\xi_t$ , for  $\theta_0 = 1.3$  (left column) and  $\theta_0 = 1.6$  (right column). The gray shading indicates stadial intervals. A DO event is defined by at least 25 consecutive years of sea ice cover  $I > I_{B2}$  within a stadial followed by at least 15 years of reduced sea ice cover of  $I < I_{B2}$ . Provided that the system is in an interstadial state, the reverse interstadial–stadial transition occurs when the sea ice regrows past  $I_c = 0.5$  and maintains this level in an average over the following 25 years. The hysteresis in the definition of climate transitions prevents a jumping back and forth between the two states when the sea ice fluctuates close to a potential critical threshold and gives rise to well defined climatic periods.

core records. In the sea ice, however, these transitions are still fairly distinct. Compared to the deterministic setup, sea ice perturbations of the same strength yield shorter interstadials. This behavior occurs, because the delicate balance of influences that yields the slow sea ice regrowth of the meta-stable interstadial is highly susceptible to small sea ice fluctuations. The latter may easily push the system across the critical threshold of  $I_{B2}$  and thereby immediately end the interstadial.

Remarkably, our model reproduces several irregular features of the original  $\delta^{18}\text{O}$  record, with respect to variability in terms of shape, duration, and amplitude of DO cycles. The different strengths of the sea ice perturbations translate into different lengths of the interstadial intervals for given background conditions. Also, the first interstadial of the  $\theta_0 = 1.3$  trajectories shows what resembles an overshoot, i.e. a pronounced peak in the arctic atmospheric temperatures that decays rapidly over the first quarter of this interstadial. Overshoots similar to this one can be observed for example at the beginning of interstadial 20c or at the beginning of interstadial 1 in the NGRIP record [12]. Both trajectories exhibit pronounced perturbations within a stadial towards a warmer arctic atmosphere that do not develop into a full interstadial. Perturbations of

this kind can also be found in the NGRIP record.

### 3.3 Realistic climate background

Finally, we run a simulation of the last glacial with the full model defined by Eqs. 1–7 with a changing atmospheric background climate (Fig.6). With the linear coupling to the LR04  $\delta^{18}\text{O}$  stack introduced in Eq. 5 the atmospheric background state  $\theta_0$  assumes low values around 1.3 during the early parts of the last glacial and increases to high values  $\theta_0 > 1.9$  around the last glacial maximum. As discussed in Sect. 3.1 and 3.2, this leads to longer lasting interstadials during the early glacial and shorter ones during the late glacial, with the opposite effect although much less pronounced for stadials. Hence, the predominance of long lasting interstadials with only short stadial inceptions in the early glacial is reversed towards the late glacial (cf. Fig. 6). In general, the time scales of the stadials and interstadials match those observed in the proxy data throughout the entire last glacial. During the very cold conditions toward the end of the last glacial, DO events are unlikely but not impossible to occur in our simulations.

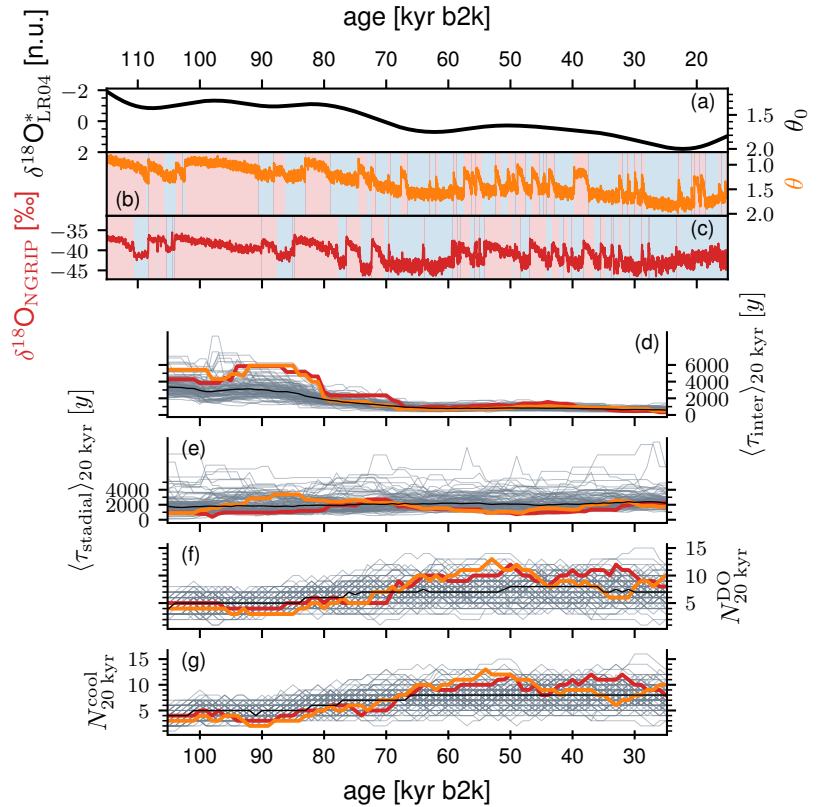
## 4 Discussion

Overall, the modelled atmospheric temperature  $\theta$  resembles the NGRIP  $\delta^{18}\text{O}$  record over the entire last glacial in terms of shape and periodicity of DO cycles (compare Fig. 1a with b). The general features of strong (reduced) sea ice cover, weak (strong) AMOC and warm (cold) Nordic Seas during stadials (interstadials) are likewise consistently reproduced by the model (compare Fig. 1c–g with h–k).

We now discuss the similarity between proxy records and our simulations with focus on the five key characteristics of DO variability as listed above, which rely on a multitude of proxy records of ocean, ice core, and terrestrial origin [20, 22, 24, 26, 49, 52, 55, 67].

- 1. Shape of DO cycles:** The general shape of the DO cycles is reproduced well by the modelled atmospheric temperature  $\theta$  (Fig. 1a,c vs. Fig. 1b,h). Our model also resolves several finer-scale features of the proxy record of the last glacial, such as precursor events – short-lived strong positive excursions in the  $\delta^{18}\text{O}$  data that do not evolve into full interstadials such as interstadial 5.1 at  $\sim 31$  kyr b2k or interstadial 16.2 at  $\sim 58$  kyr b2k (Fig. 1b and Fig. 6) or very short stadial inceptions similar to the stadial 23.1 at  $\sim 90$  kyr b2k and the stadial 21.2 at  $\sim 85$  kyr b2k which yield apparent back-to-back interstadials [12]. Furthermore, consistent with the proxy record, several interstadials exhibit a continuous trend of moderate cooling back to full stadial conditions instead of the more typical abrupt final cooling.
- 2. Duration of stadials and interstadials:** The modelled variability of stadial and interstadial durations is in good agreement with the data (cf. Fig. 6). In our simulations the coupling of the background climate  $\theta_0$  to the LR04 benthic  $\delta^{18}\text{O}$  introduced in Eq. 5 causes a gradual transition from predominantly interstadial to predominantly stadial climate across the last glacial due

**Figure 6:** Simulation of the period 115–15 kyr b2k of the full stochastic model given by Eqs. 1–7 with the coupling to the background climate. (a) 50 kyr low-pass filtered LR04 benthic  $\delta^{18}\text{O}$  stack in normalized units. The right-hand-side ordinate indicates the corresponding  $\theta_0(\delta^{18}\text{O}_{\text{LR04}}^*)$  according to Eq. 5. (b) Simulated trajectory of  $\theta$  as a direct model counterpart of the NGRIP  $\delta^{18}\text{O}$  record. The effect of the changing  $\theta_0$  on the interstadial duration and to a lesser extent on the stadial duration is apparent, with a predominance of long interstadials in the earlier part of the glacial and only short interstadial excursions from mostly stadial climate during the late glacial. (c) NGRIP  $\delta^{18}\text{O}$  data as in Fig. 1a. (d) The duration of occurring interstadials averaged in a 20 kyr running window  $\langle\tau_{\text{inter}}\rangle_{20 \text{ kyr}}$  for the proxy data (red) and the simulation (orange) and for 99 alternative realizations of the simulation (gray). The black line indicates the average over all 100 model runs. The 20 kyr mean duration takes into account all interstadials that are either fully included in the window or that end or start within the window. Interstadials that stretch across the window boundaries are considered with their full duration. (e) Same as (d) for the 20 kyr running mean duration of stadials  $\langle\tau_{\text{stadial}}\rangle_{20 \text{ kyr}}$ . (f) Number of DO events occurring in a 20 kyr running window  $N_{20 \text{ kyr}}^{\text{DO}}$  with the same color coding as before. (g) The same as (f) for the number of DO cooling events  $N_{20 \text{ kyr}}^{\text{cool}}$ .



to the mechanisms explained in Sects. 3.2 and 4. The slow variations in the overall stadial and interstadial levels are reproduced by our simulations, however with an apparent mismatch prior to the last glacial maximum, where the NGRIP  $\delta^{18}\text{O}$  record shows a persistent warming trend (within a stadial climate), while our simulation evolves to colder temperatures (cf. Fig. 6). This mismatch originates from the fact that the warming trend in the NGRIP record is in contrast to the global cooling trend prior to the last glacial maximum [68].

- In-phase sea ice dynamics:** The extensive (minimal) sea ice cover during stadials (interstadials) suggested by proxy records [20, 22, 52, 69] is well reproduced by our model; the sea ice  $I$  consistently regrows at a moderate rate over the course of the interstadial, before it returns to its stadial extent in a final phase of accelerated regrowth marking the interstadial–stadial transition. Overall, this behavior agrees with the sea ice dynamics in the Nordic Seas across DO cycles as inferred by [20] and others. While proxy records suggest a continued sea ice growth during the early stadial, the modeled sea ice  $I$  reaches its stadial extent already during the interstadial–stadial transition and the regrowth thus does not stretch significantly into the stadial phase.
- Nordic Seas’ temperature inversion:** In our interpretation of the modeled oceanic temperature gradient  $T$  we ignore surface waters and regard  $T$  as an indicator

of subsurface and deep water temperatures. Indeed, our model simulates warm Nordic Seas at full stadial conditions (Fig. 1k), in line with the proxy records [22, 24, 49]. At the beginning of interstadials, pronounced cooling sets in, which can be interpreted as a continuous convection-driven release of the heat previously stored underneath the sea ice cover. Approximately one third into an interstadial the subsurface cooling is reversed into a more gentle yet persistent warming trend caused by regrowing sea ice and decreasing heat loss which accelerates across the transition back to stadial conditions, but is sustained in the subsequent stadial. In general, this pattern agrees very well with existing paleoclimate proxies [20, 22, 24, 49]. The moderate warming that persists over the final two thirds of the interstadial can be observed in a very similar manner in the benthic  $\delta^{18}\text{O}$  from marine sediment cores indicative of deep ocean temperatures (compare Fig. 1g with Fig. 1k). The deep ocean warming is attributed to a gradual reduction of deep convection over the course of the interstadial driven by regrowing sea ice [20, 24]. Conversely, the subsurface temperature reconstructions (Fig. 1f) reveal a mild cooling trend during this phase of the DO cycle, which is not reproduced by the model. Subsequent to the interstadial–stadial transition the observed sustained warming of the intermediate and deep ocean into stadials is reproduced by our model, where a salinity driven stadial AMOC ( $q < 0$ ) counteracts an existing meridional temperature gradient and the sea ice

cover prevents heat loss to the atmosphere.

5. **AMOC switches:** The correspondence between strong (weak) overturning and interstadial (stadial) climate conditions is widely accepted [21, 26, 35, 36, 39, 55, 70]. However, limited quality of the proxy data prevents a more detailed assessment of the changes in the AMOC during the course of a typical DO cycle. It seems that the AMOC almost stopped during Heinrich stadials, while during non-Heinrich stadials it probably operated in a weak and shallow mode [55]. An AMOC reinvigoration is reported to have happened in synchrony with abrupt Greenland warmings, within the limits of dating uncertainties [55]. In general terms, simulated changes of the AMOC strength agree with this pattern apart from the specific expression of Heinrich events, which aren't explicitly targeted by our modeling setup (c.f. Fig. 1e and j). From the interstadial onsets onward the AMOC strength increases until it plateaus somewhere half way through the interstadial. Thereafter a weakening trend sets in whose strength is related to the climate background condition and which stretches well into the stadial before the AMOC recovers its stadial state.

Our four-dimensional model given by Eqs. 1–7 hence reproduces central features of DO variability in terms of arctic temperatures  $\theta$ , Nordic Seas' sea ice cover  $I$ , intermediate-to-deep water temperatures  $T$ , and the meridional overturning strength  $q$ . In particular, our modelling results align well with the characteristics of DO variability inferred from the study of marine sediment cores from the northern North Atlantic and the Nordic Seas [20, 22, 24, 49, 52, 67, 71]. First pointed out by [67, 71] a sustained inflow of North Atlantic warm water into the Nordic Seas during stadial periods was later confirmed and integrated in a conceptual explanation for the emergence of DO variability by [49]: The sustained inflow of warm and salty waters during stadials is subdued under a strong halocline which eventually separates a cold and fresh surface layer from the intermediate and deep waters. These experience a gradual warming up to the point where the growing vertical temperature gradient destabilizes the stratification and (re)initiates deep convection. This in turn reinvigorates the AMOC and cools the intermediate to deep waters in the Nordic Seas. The transition back to the stadials is more or less explicitly attributed to the prevailing glacial climate background conditions [49]. [22] and later [20] supplemented this framework by providing observational evidence for extended (reduced) Nordic Seas' ice cover during stadials (interstadials), highlighting the role of the sea ice as an insulator between atmosphere and ocean. Our model shows remarkable agreement with corresponding proxy evidence (compare Fig. 1) and integrates well into the above narrative. The insulating effect of the sea ice, which has previously also been considered by [18] as a crucial component, is modeled explicitly in our study and is confirmed to be key to the changes between stadial and interstadial climates. The observed sustained stadial inflow of warm North Atlantic waters into the intermediate depth Nordic Seas corresponds to a weak, salinity-driven AMOC in our model. Importantly, in contrast to the majority of previous work but in agreement with the above, in our model

interstadials do not correspond to stable fixed points, but rather to meta-stable states that inevitably relax back to stadial climate conditions.

However, our view of DO cycles as an excursion triggered by supercritical perturbations in an excitable medium provides a new aspect to the above narrative: The continued warming of the intermediate waters as described by [49], [22], and [18] would inevitably trigger the next DO event in a finite amount of time. According to our model, the stadial climate is stable and could persist for very long time if no supercritical forcing event occurred. In line with this, [20] suggest that DO-triggering destabilizations of the stadial halocline might have been triggered themselves by elevated Atlantic inflow, caused by stochastic atmospheric action on the subpolar gyre [40, 72]. Our model does not resolve the exact triggering mechanism and instead relies on intermittent noise, which may trigger DO events by removing sufficiently large amounts of sea ice reactivating atmosphere–ocean interaction in the high latitudes. So far, as a source of this noise, we have proposed either atmospheric anomalies as described by [65] and [40] or, inspired by [20], [22], and [49] convective events in the ocean. The interplay of both mechanism as suggested by [20] might even be better suited to justify the choice of our driving noise.

Apart from its central role as the DO event trigger, we find that the intermittent driving noise can indeed explain several details of the NGRIP  $\delta^{18}\text{O}$  record; the variable strength of the supercritical perturbations translates into a variability in terms of shape and duration of interstadials. The reproduction of back-to-back interstadials with no extended stadial separating them as well as very short interstadials follows naturally from the stochastic nature of the trigger in our simulation. Similarly, the variability of stadial durations results in our model from randomly distributed waiting times between supercritical perturbations. Taking all these arguments together, we find a purely deterministic mechanism of DO events to be more difficult to reconcile with the variable expression of interstadials in the proxy records. Furthermore, subcritical forcing events contribute to the higher fluctuations of the stadial arctic atmospheric temperatures as compared to the interstadial one in our simulation which is also observed in the NGRIP  $\delta^{18}\text{O}$  record. These subcritical events could be interpreted as local convective events that entail a partial and temporary removal of stadial sea ice associated with the release of a certain amount of oceanic heat.

It should be noted that the three different time scales introduced together with the dynamical equations for the three model components are crucial to obtain agreement between the modeled and the observed shape and duration of DO cycles. The other key ingredient for the successful simulation of sustained interstadial intervals is the proximity of the  $\theta$  and ice nullclines, which gives rise to an additional slow time scale and a meta-stable state. The existence of such a meta-stable state, whose expression is highly sensitive to background conditions, seems physically plausible in view of a delicate interplay between northward oceanic heat transport, the high latitude atmospheric temperatures and the ice-albedo feedback. The influence of warm Atlantic surface inflow in the Nordic Seas on the formation of sea ice during interstadials

has so far been neglected, but should be considered in further research.

## 5 Conclusions

In summary, we have modeled DO cycles across the last glacial period as state space excursions of an excitable monostable system, resolving the ocean, sea ice and atmosphere on increasingly fast time scales. DO events are triggered by an intermittent noise scheme that acts on the stadial sea ice cover. The associated effect on the atmospheric Arctic temperatures  $\theta$  is consistent with the observed  $\alpha$ -stable noise signature in the GRIP calcium record [44]. We propose as potential sources for the driving intermittent noise local and temporary convective instabilities in the stadial stratification of the Nordic Seas [73, 74] or persistent atmospheric anomalies [40, 65], or combinations thereof [20]. Our model reproduces the observed DO cycle patterns of four climate variables central to the physics of DO cycles: the typical saw-tooth shape of arctic atmospheric temperatures [1, 7], the reduced (extended) sea ice cover during interstadials (stadials) [20, 22, 52, 69], the strong interstadial AMOC, with sustained northward heat transport during stadials at a weaker level [22, 49, 55, 67], and the corresponding stadial warming of the Nordic Seas [20, 22, 24, 49]. Furthermore, detailed aspects of the NGRIP  $\delta^{18}\text{O}$  record, such as the variability of the interstadial shape and duration, higher-amplitude stadial fluctuations, and very short interstadials (stadials) during the colder (warmer) parts of the late glacial, are reproduced.

Here, we summarize the most important features of our model that provide plausible mechanistic explanations to the last glacial's millennial-scale climate variability:

1. The rate of ocean–atmosphere heat exchange in the high northern latitudes is decisive for the state of the North Atlantic climate system. The heat exchange is controlled by the sea ice.
2. Stochastic removal of the sea ice may abruptly expose the atmosphere to the influence of a large oceanic heat reservoir and entail abrupt atmospheric warming and oceanic cooling facilitated by reactivated deep convection. The latter happens at a much slower rate due to the ocean's much larger heat capacity.
3. If sea ice is absent the oceanic heat loss to the atmosphere yields a strong meridional oceanic temperature gradient which in turn drives the AMOC's strong circulation mode.
4. In the interstadial configuration the North Atlantic climate system is – although close – not in an equilibrium state. Generally prevailing cold atmospheric temperatures in the high latitudes entail sea ice regrowth, which inevitably drive the system back to the stadial state.
5. The persistence of the interstadial state is highly sensitive to the background conditions.
6. The time-scale separation between ocean, sea ice, and atmosphere (from slow to fast) is central to the characteristic shape of Greenland interstadials in terms of Greenland temperature changes.
7. DO events are stochastically triggered by asymmetric intermittent noise, mimicking abrupt large sea ice removal events.

We hope that our findings will provide a helpful conceptual framework to eventually solve the puzzle of DO variability. The proposed mechanisms should be further tested against new proxy data and by further investigations with Earth system model simulations.

## Acknowledgments

This is TiPES contribution #215; the TiPES ('Tipping Points in the Earth System') project has received funding from the European Union's Horizon 2020 research and innovation programme under grant agreement No. 820970. NB acknowledges further funding by the Volkswagen Foundation, the European Union's Horizon 2020 research and innovation programme under the Marie Skłodowska-Curie grant agreement No. 956170, as well as from the German Federal Ministry of Education and Research under grant No. 01LS2001A.

## References

- [1] North Greenland Ice Core Project Members. High-resolution record of Northern Hemisphere climate extending into the last interglacial period. *Nature*, 431: 147–151, 2004. doi: 10.1038/nature02805.
- [2] Dansgaard, W., Clausen, H.B., Gundestrup, N., Hammer, C.U., Johnsen, S.F., Kristinsdottir, P.M., and Reeh, N. A New Greenland Deep Ice Core. *Science*, 218:1273–1277, 1982. doi: 10.1126/science.218.4579.1273.
- [3] Dansgaard, W., Johnsen, S., Clausen, H., Dahl-Jensen, D., Gundestrup, N., Hammer, C., and Oeschger, H. North Atlantic climatic oscillations revealed by deep Greenland ice cores. In *Climate processes and climate sensitivity*, edited by Hansen, J. and Takahashi, T., pages 288–298. American Geophysical Union (AGU), 1984. doi: 10.1029/GM029p0288.
- [4] Johnsen, S.J., Clausen, H.B., Dansgaard, W., Fuhrer, K., Gundestrup, N., Hammer, C.U., Iversen, P., Jouzel, J., Stauffer, B., and Steffensen, J. Irregular glacial interstadials recorded in a new Greenland ice core. *Nature*, 359: 311–313, 1992. doi: 10.1038/359311a0.
- [5] Dansgaard, W., Johnsen, S.J., Clausen, H.B., Dahl-Jensen, D., Gundestrup, N.S., Hammer, C.U., Hvidberg, C.S., Steffensen, J.P., Sveinbjörnsdottir, A.E., Jouzel, J., and Bond, G. Evidence for general instability of past climate from a 250-kyr ice-core record. *Nature*, 364:218–220, 1993. doi: 10.1038/364218a0.
- [6] Jouzel, J., Alley, R.B., Cuffey, K.M., Dansgaard, W., Grootes, P., Hoffmann, G., Johnsen, S.J., Koster, R.D., Peel, D., Shuman, C.A., Stievenard, M., Stuiver, M., and White, J. Validity of the temperature reconstruction from water isotopes in ice cores. *Journal of Geophysical*

Glacial abrupt climate change as a multi-scale phenomenon resulting from monostable excitable dynamics

- Research: Oceans*, 102:26471–26487, 1997. doi: 10.1029/97JC01283.
- [7] Johnsen, S.J., Dahl-Jensen, D., Gundestrup, N., Steffensen, J.P., Clausen, H.B., Miller, H., Masson-Delmotte, V., Sveinbjörnsdóttir, A.E., and White, J. Oxygen isotope and palaeotemperature records from six Greenland ice-core stations: Camp Century, Dye-3, GRIP, GISP2, Renland and NorthGRIP. *Journal of Quaternary Science*, 16:299–307, 2001. doi: 10.1002/jqs.622.
- [8] Landais, A., Jouzel, J., Masson-Delmotte, V., and Caillon, N. Large temperature variations over rapid climatic events in Greenland: a method based on air isotopic measurements. *Comptes Rendus - Geoscience*, 337:947–956, 2005. doi: 10.1016/j.crte.2005.04.003.
- [9] Huber, C., Leuenberger, M., Spahni, R., Flückiger, J., Schwander, J., Stocker, T.F., Johnsen, S., Landais, A., and Jouzel, J. Isotope calibrated Greenland temperature record over Marine Isotope Stage 3 and its relation to CH4. *Earth and Planetary Science Letters*, 243:504–519, 2006. doi: 10.1016/j.epsl.2006.01.002.
- [10] Kindler, P., Guillevic, M., Baumgartner, M., Schwander, J., Landais, A., and Leuenberger, M. Temperature reconstruction from 10 to 120 kyr b2k from the NGRIP ice core. *Climate of the Past*, 10:887–902, 2014. doi: 10.5194/cp-10-887-2014.
- [11] Wolff, E.W., Chappellaz, J., Blunier, T., Rasmussen, S.O., and Svensson, A. Millennial-scale variability during the last glacial: The ice core record. *Quaternary Science Reviews*, 29:2828–2838, 2010. doi: 10.1016/j.quascirev.2009.10.013.
- [12] Rasmussen, S.O., Bigler, M., Blockley, S.P., Blunier, T., Buchardt, S.L., Clausen, H.B., Cvijanovic, I., Dahl-Jensen, D., Johnsen, S.J., Fischer, H., Gkinis, V., Guillevic, M., Hoek, W.Z., Lowe, J.J., Pedro, J.B., Popp, T., Seierstad, I.K., Steffensen, J.P., Svensson, A.M., Vallenga, P., Vinther, B.M., Walker, M.J., Wheatley, J.J., and Winstrup, M. A stratigraphic framework for abrupt climatic changes during the Last Glacial period based on three synchronized Greenland ice-core records: Refining and extending the INTIMATE event stratigraphy. *Quaternary Science Reviews*, 106:14–28, 2014. doi: 10.1016/j.quascirev.2014.09.007.
- [13] Lohmann, J. and Ditlevsen, P.D. Objective extraction and analysis of statistical features of Dansgaard-Oeschger events. *Climate of the Past*, 15:1771–1792, 2019. doi: 10.5194/cp-15-1771-2019.
- [14] Rial, J.A. and Saha, R. Modeling Abrupt Climate Change as the Interaction Between Sea Ice Extent and Mean Ocean Temperature Under Orbital Insolation Forcing. In *Abrupt Climate Change: Mechanisms, Patterns, and Impacts*, edited by Rashid, H., Polyak, L., and Mosley-Thompson, E., pages 57–74. American Geophysical Union (AGU), 2011. ISBN 9781118670040. doi: 10.1029/2010GM001027.
- [15] Roberts, A. and Saha, R. Relaxation oscillations in an idealized ocean circulation model. *Climate Dynamics*, 48:2123–2134, 2017. doi: 10.1007/s00382-016-3195-3.
- [16] Mitsui, T. and Crucifix, M. Influence of external forcings on abrupt millennial-scale climate changes: a statistical modelling study. *Climate Dynamics*, 48:2729–2749, 2017. doi: 10.1007/s00382-016-3235-z.
- [17] Lohmann, J. and Ditlevsen, P.D. Random and externally controlled occurrences of Dansgaard-Oeschger events. *Climate of the Past*, 14:609–617, 2018. doi: 10.5194/cp-14-609-2018.
- [18] Boers, N., Ghil, M., and Rousseau, D.D. Ocean circulation, ice shelf, and sea ice interactions explain Dansgaard-Oeschger cycles. *Proceedings of the National Academy of Sciences of the United States of America*, 115:E11005–E11014, 2018. doi: 10.1073/pnas.1802573115.
- [19] Seierstad, I.K., Abbott, P.M., Bigler, M., Blunier, T., Bourne, A.J., Brook, E., Buchardt, S.L., Buizert, C., Clausen, H.B., Cook, E., Dahl-Jensen, D., Davies, S.M., Guillevic, M., Johnsen, S.J., Pedersen, D.S., Popp, T.J., Rasmussen, S.O., Severinghaus, J.P., Svensson, A., and Vinther, B.M. Consistently dated records from the Greenland GRIP, GISP2 and NGRIP ice cores for the past 104ka reveal regional millennial-scale  $\delta^{18}O$  gradients with possible Heinrich event imprint. *Quaternary Science Reviews*, 106:29–46, 2014. doi: 10.1016/j.quascirev.2014.10.032.
- [20] Sadatzki, H., Maffezzoli, N., Dokken, T.M., Simon, M.H., Berben, S.M., Fahl, K., Kjær, H.A., Spolaor, A., Stein, R., Vallenga, P., Vinther, B.M., and Jansen, E. Rapid reductions and millennial-scale variability in Nordic Seas sea ice cover during abrupt glacial climate changes. *Proceedings of the National Academy of Sciences of the United States of America*, 117:29478–29486, 2020. doi: 10.1073/pnas.2005849117.
- [21] Henry, L.G., McManus, J.F., Curry, W.B., Roberts, N.L., Piotrowski, A.M., and Keigwin, L.D. North Atlantic ocean circulation and abrupt climate change during the last glaciation. *Science*, 353:470–474, 2016. doi: 10.1126/science.aaf5529.
- [22] Dokken, T.M., Nisancioglu, K.H., Li, C., Battisti, D.S., and Kissel, C. Dansgaard-Oeschger cycles: Interactions between ocean and sea ice intrinsic to the Nordic seas. *Paleoceanography*, 28:491–502, 2013. doi: 10.1002/palo.20042.
- [23] Berben, S.M., Dokken, T.M., Abbott, P.M., Cook, E., Sadatzki, H., Simon, M.H., and Jansen, E. Independent tephrochronological evidence for rapid and synchronous oceanic and atmospheric temperature rises over the Greenland stadial-interstadial transitions between ca. 32 and 40 ka b2k. *Quaternary Science Reviews*, 236:106277, 2020. doi: 10.1016/j.quascirev.2020.106277.
- [24] Ezat, M.M., Rasmussen, T.L., and Groeneveld, J. Persistent intermediate water warming during cold stadials

- in the southeastern Nordic seas during the past 65 k.y. *Geology*, 42:663–666, 2014. doi: 10.1130/G35579.1.
- [25] Voelker, A.H. Global distribution of centennial-scale records for Marine Isotope Stage (MIS) 3: A database. *Quaternary Science Reviews*, 21:1185–1212, 2002. doi: 10.1016/S0277-3791(01)00139-1.
- [26] Menviel, L.C., Skinner, L.C., Tarasov, L., and Tzedakis, P.C. An ice–climate oscillatory framework for Dansgaard–Oeschger cycles. *Nature Reviews Earth & Environment*, 1:677–693, 2020. doi: 10.1038/s43017-020-00106-y.
- [27] Ruth, U., Bigler, M., Röthlisberger, R., Siggaard-Andersen, M.L., Kipfstuhl, S., Goto-Azuma, K., Hansson, M.E., Johnsen, S.J., Lu, H., and Steffensen, J.P. Ice core evidence for a very tight link between North Atlantic and east Asian glacial climate. *Geophysical Research Letters*, 34:L03706, 2007. doi: 10.1029/2006GL027876.
- [28] Fischer, H., Siggaard-Andersen, M.L., Ruth, U., Röthlisberger, R., and Wolff, E. Glacial/interglacial changes in mineral dust and sea-salt records in polar ice cores: Sources, transport, and deposition. *Reviews of Geophysics*, 45:RG1002, 2007. doi: 10.1029/2005RG000192.
- [29] Schüpbach, S., Fischer, H., Bigler, M., Erhardt, T., Gfeller, G., Leuenberger, D., Mini, O., Mulvaney, R., Abram, N.J., Fleet, L., Frey, M.M., Thomas, E., Svensson, A., Dahl-Jensen, D., Kettner, E., Kjaer, H., Seierstad, I., Steffensen, J.P., Rasmussen, S.O., Vallelonga, P., Winstrup, M., Wegner, A., Twarloh, B., Wolff, K., Schmidt, K., Goto-Azuma, K., Kuramoto, T., Hirabayashi, M., Uetake, J., Zheng, J., Bourgeois, J., Fisher, D., Zhiheng, D., Xiao, C., Legrand, M., Spolaor, A., Gabrieli, J., Barbante, C., Kang, J.H., Hur, S.D., Hong, S.B., Hwang, H.J., Hong, S., Hansson, M., Iizuka, Y., Oyabu, I., Muscheler, R., Adolphi, F., Maselli, O., McConnell, J., and Wolff, E.W. Greenland records of aerosol source and atmospheric lifetime changes from the Eemian to the Holocene. *Nature Communications*, 9:1476, 2018. doi: 10.1038/s41467-018-03924-3.
- [30] Corrick, E.C., Drysdale, R.N., Hellstrom, J.C., Capron, E., Rasmussen, S.O., Zhang, X., Fleitmann, D., Couchoud, I., Wolff, E., and Monsoon, S.A. Synchronous timing of abrupt climate changes during the last glacial period. *Science*, 369:963–969, 2020.
- [31] Zhang, Y., Chiessi, C.M., Mulitza, S., Sawakuchi, A.O., Häggi, C., Zabel, M., Portilho-Ramos, R.C., Schefuß, E., Crivellari, S., and Wefer, G. Different precipitation patterns across tropical South America during Heinrich and Dansgaard-Oeschger stadials. *Quaternary Science Reviews*, 177:1–9, 2017. doi: 10.1016/j.quascirev.2017.10.012.
- [32] Cheng, H., Sinha, A., Cruz, F.W., Wang, X., Edwards, R.L., D’Horta, F.M., Ribas, C.C., Vuille, M., Stott, L.D., and Auler, A.S. Climate change patterns in Amazonia and biodiversity. *Nature Communications*, 4:1411, 2013. doi: 10.1038/ncomms2415.
- [33] Kanner, L.C., Burns, S.J., Cheng, H., and Edwards, R.L. High-Latitude Forcing of the South American Summer Monsoon During the Last Glacial. *Science*, 335:570–573, 2012. doi: 10.1126/science.1213397.
- [34] Wang, Y.J., Cheng, H., Edwards, R.L., An, Z.S., Wu, J.Y., Shen, C.C., and Dorale, J.A. A high-resolution absolute-dated late pleistocene monsoon record from Hulu Cave, China. *Science*, 294:2345–2348, 2001. doi: 10.1126/science.1064618.
- [35] Broecker, W.S., Peteet, D.M., and Rind, D. Does the ocean-atmosphere system have more than one stable mode of operation? *Nature*, 315:21–26, 1985. doi: 10.1038/315021a0.
- [36] Ganopolski, A. and Rahmstorf, S. Rapid changes of glacial climate simulated in a coupled climate model. *Nature*, 409:153–158, 2001.
- [37] Petersen, S.V., Schrag, D.P., and Clark, P.U. A new mechanism for Dansgaard-Oeschger cycles. *Paleoceanography*, 28:24–30, 2013. doi: 10.1029/2012PA002364.
- [38] Zhang, X., Lohmann, G., Knorr, G., and Purcell, C. Abrupt glacial climate shifts controlled by ice sheet changes. *Nature*, 512:290–294, 2014. doi: 10.1038/nature13592.
- [39] Vettoretti, G. and Peltier, W.R. Fast physics and slow physics in the nonlinear Dansgaard-Oeschger relaxation oscillation. *Journal of Climate*, 31:3423–3449, 2018. doi: 10.1175/JCLI-D-17-0559.1.
- [40] Li, C. and Born, A. Coupled atmosphere-ice-ocean dynamics in Dansgaard-Oeschger events. *Quaternary Science Reviews*, 203:1–20, 2019. doi: 10.1016/j.quascirev.2018.10.031.
- [41] Ganopolski, A. and Rahmstorf, S. Abrupt Glacial Climate Changes due to Stochastic Resonance. *Physical Review Letters*, 88:038501, 2002. doi: 10.1103/PhysRevLett.88.038501.
- [42] Timmermann, A., Gildor, H., Schulz, M., and Tziperman, E. Coherent resonant millennial-scale climate oscillations triggered by massive meltwater pulses. *Journal of Climate*, 16:2569–2585, 2003. doi: 10.1175/1520-0442(2003)016<2569:CRMCOT>2.0.CO;2.
- [43] Menviel, L., Timmermann, A., Friedrich, T., and England, M.H. Hindcasting the continuum of Dansgaard-Oeschger variability: Mechanisms, patterns and timing. *Climate of the Past*, 10:63–77, 2014. doi: 10.5194/cp-10-63-2014.
- [44] Ditlevsen, P.D. Observation of  $\alpha$ -stable noise induced millennial climate changes from an ice-core record. *Geophys. Geophysical Research Letters*, 26:1441–1444, 1999.
- [45] Ditlevsen, P.D., Kristensen, M.S., and Andersen, K.K. The recurrence time of Dansgaard-Oeschger events and limits on the possible periodic component. *Journal of Climate*, 18:2594–2603, 2005. doi: 10.1175/JCLI3437.1.

Glacial abrupt climate change as a multi-scale phenomenon resulting from monostable excitable dynamics

- [46] Ditlevsen, P.D., Andersen, K.K., and Svensson, A. The DO-climate events are probably noise induced: Statistical investigation of the claimed 1470 years cycle. *Climate of the Past*, 3:129–134, 2007. doi: 10.5194/cp-3-129-2007.
- [47] Lohmann, J. and Svensson, A. Ice core evidence for major volcanic eruptions at the onset of Dansgaard-Oeschger warming events. *Climate of the Past Discussions*, 18: 2021–2043, 2022.
- [48] Broecker, W.S., Bond, G., Klas, M., Bonani, G., and Wolffi, W. A salt oscillator in the glacial Atlantic? 1. The concept. *Paleoceanography*, 5:469–477, 1990. doi: 10.1029/PA005i004p00469.
- [49] Rasmussen, T.L. and Thomsen, E. The role of the North Atlantic Drift in the millennial timescale glacial climate fluctuations. *Palaeogeography, Palaeoclimatology, Palaeoecology*, 210:101–116, 2004. doi: 10.1016/j.palaeo.2004.04.005.
- [50] Vettoretti, G., Ditlevsen, P., Jochum, M., and Rasmussen, S.O. Atmospheric CO<sub>2</sub> control of spontaneous millennial-scale ice age climate oscillations. *Nature Geoscience*, 15, 2022. doi: 10.1038/s41561-022-00920-7.
- [51] Gottwald, G.A. A model for Dansgaard-Oeschger events and millennial-scale abrupt climate change without external forcing. *Climate Dynamics*, 56:227–243, 2021. doi: 10.1007/s00382-020-05476-z.
- [52] Hoff, U., Rasmussen, T.L., Stein, R., Ezat, M.M., and Fahl, K. Sea ice and millennial-scale climate variability in the Nordic seas 90 kyr ago to present. *Nature Communications*, 7:12247, 2016. doi: 10.1038/ncomms12247.
- [53] Li, C., Battisti, D.S., and Bitz, C.M. Can North Atlantic Sea Ice Anomalies Account for Dansgaard – Oeschger Climate Signals ? *Journal of Climate*, 23:5457–5475, 2010. doi: 10.1175/2010JCLI3409.1.
- [54] Li, C., Battisti, D.S., Schrag, D.P., and Tziperman, E. Abrupt climate shifts in Greenland due to displacements of the sea ice edge. *Geophysical Research Letters*, 32:1–4, 2005. doi: 10.1029/2005GL023492.
- [55] Lynch-Stieglitz, J. The Atlantic Meridional Overturning Circulation and Abrupt Climate Change. *Annual Review of Marine Science*, 9:83–104, 2017. doi: 10.1146/annurev-marine-010816-060415.
- [56] Stommel, H. Thermohaline Convection with Two Stable Regimes. *Tellus*, 13:224–230, 1961.
- [57] Lisiecki, L.E. and Raymo, M.E. A Pliocene-Pleistocene stack of 57 globally distributed benthic  $\delta$  18O records. *Paleoceanography*, 20:1–17, 2005. doi: 10.1029/2004PA001071.
- [58] Eisenman, I. Factors controlling the bifurcation structure of sea ice retreat. *Journal of Geophysical Research Atmospheres*, 117:1–18, 2012. doi: 10.1029/2011JD016164.
- [59] Lohmann, J., Castellana, D., Ditlevsen, P.D., and Dijkstra, H.A. Abrupt climate change as a rate-dependent cascading tipping point. *Earth System Dynamics*, 12: 819–835, 2021. doi: 10.5194/esd-12-819-2021.
- [60] Hasselmann, K. Stochastic climate models: Part I. Theory. *Tellus A: Dynamic Meteorology and Oceanography*, 28:473, 1976. doi: 10.3402/tellusa.v28i6.11316.
- [61] Gottwald, G.A. and Melbourne, I. A Huygens principle for diffusion and anomalous diffusion in spatially extended systems. *Proceedings of the National Academy of Sciences of the United States of America*, 110:8411–8416, 2013. doi: 10.1073/pnas.1217926110.
- [62] Gottwald, G.A. and Melbourne, I. Homogenization for deterministic maps and multiplicative noise. *Proceedings of the Royal Society A*, 469, 2013. doi: https://doi.org/10.1098/rspa.2013.0201.
- [63] Gottwald, G.A., Crommelin, D.T., and Franzke, C.L. Stochastic climate theory. In *Nonlinear and Stochastic Climate Dynamics*, edited by Franzke, C.L.E. and O’Kane, T., pages 209–240. Cambridge University Press, Cambridge, 2017. ISBN 9781316339251. doi: 10.1017/9781316339251.009.
- [64] Fuhrer, K., Neftel, A., Anklin, M., and Maggi, V. Continuous measurements of hydrogen peroxide, formaldehyde, calcium and ammonium concentrations along the new grip ice core from summit, Central Greenland. *Atmospheric Environment Part A, General Topics*, 27:1873–1880, 1993. doi: 10.1016/0960-1686(93)90292-7.
- [65] Kleppin, H., Jochum, M., Otto-Bliesner, B., Shields, C.A., and Yeager, S. Stochastic atmospheric forcing as a cause of Greenland climate transitions. *Journal of Climate*, 28: 7741–7763, 2015. doi: 10.1175/JCLI-D-14-00728.1.
- [66] Drijfhout, S., Gleeson, E., Dijkstra, H.A., and Livina, V. Spontaneous abrupt climate change due to an atmospheric blocking-Sea-Ice-Ocean feedback in an unforced climate model simulation. *Proceedings of the National Academy of Sciences of the United States of America*, 110 :19713–19718, 2013. doi: 10.1073/pnas.1304912110.
- [67] Rasmussen, T.L., Thomsen, E., Van Weering, T.C., and Labeyrie, L. Rapid changes in surface and deep water conditions at the Faeroe Margin during the last 58,000 years. *Paleoceanography*, 11:757–771, 1996. doi: 10.1029/96PA02618.
- [68] Clark, P.U., Dyke, A.S., Shakun, J.D., Carlson, A.E., Clark, J., Wohlfarth, B., Mitrovica, J.X., Hostetler, S.W., and McCabe, A.M. The Last Glacial Maximum. *Science*, 325:710–714, 2009. doi: 10.1126/science.1172873.
- [69] Sadatzki, H., Dokken, T.M., Berben, S.M., Muschiatiello, F., Stein, R., Fahl, K., Menviel, L., Timmermann, A., and Jansen, E. Sea ice variability in the southern norwegian sea during glacial dansgaard-oeschger climate cycles. *Science Advances*, 5:1–11, 2019. doi: 10.1126/sciadv.aau6174.

- [70] Gottschalk, J., Skinner, L.C., Misra, S., Waelbroeck, C., Meniel, L., and Timmermann, A. Abrupt changes in the southern extent of North Atlantic Deep Water during Dansgaard-Oeschger events. *Nature Geoscience*, 8:950–954, 2015. doi: 10.1038/ngeo2558.
- [71] Rasmussen, T.L., Thomsen, E., Labeyrie, L., and Van Weering, T.C. Circulation changes in the Faeroe-Shetland Channel correlating with cold events during the last glacial period (58-10 ka). *Geology*, 24:937–940, 1996. doi: 10.1130/0091-7613(1996)024<0937:CCITFS>2.3.CO;2.
- [72] Klockmann, M., Mikolajewicz, U., Kleppin, H., and Marotzke, J. Coupling of the Subpolar Gyre and the Overturning Circulation During Abrupt Glacial Climate Transitions. *Geophysical Research Letters*, 47, 2020. doi: 10.1029/2020GL090361.
- [73] Jensen, M.F., Nilsson, J., and Nisancioglu, K.H. The interaction between sea ice and salinity-dominated ocean circulation: implications for halocline stability and rapid changes of sea ice cover. *Climate Dynamics*, 47:3301–3317, 2016. doi: 10.1007/s00382-016-3027-5.
- [74] Singh, H.A., Battisti, D.S., and Bitz, C.M. A heuristic model of dansgaard-oeschger cycles. part i: Description, results, and sensitivity studies. *Journal of Climate*, 27: 4337–4358, 2014. doi: 10.1175/JCLI-D-12-00672.1.

## Supporting information for

### Glacial abrupt climate change as a multi-scale phenomenon resulting from monostable excitable dynamics

Keno Riechers, Georg Gottwald & Niklas Boers (2023) [arXiv preprint]

*Corresponding Author:* Keno Riechers, riechers@pik-potsdam.de

**Ocean component** We adopt the classical Stommel model [1] for the dynamics of the oceanic meridional gradients of temperature  $T = T_e - T_p$  and salinity  $S = S_e - S_p$ , where the subscripts denote the respective equatorial and northern polar variables [2, 3]

$$\tau_{\text{ocean}} \dot{T} = -\gamma(I)(T - \theta) - (1 + \mu |T - S|)T, \quad (1)$$

$$\tau_{\text{ocean}} \dot{S} = \sigma - (1 + \mu |T - S|) S. \quad (2)$$

In Eq. 2  $\sigma$  denotes a freshwater forcing that sustains a meridional salinity gradient. The term  $(1 + \mu |T - S|)$  represents diffusive and advective transport of heat and salt within the ocean, both counteracting existing meridional gradients. The flux parameter  $\mu$  is a measure for the relative strength of the advective transport with respect to the diffusive transport. The flow  $q = T - S$  quantifies the strength of the AMOC, which is driven by a meridional density gradient resulting from temperature and salinity differences between the equatorial and polar boxes. The term  $\gamma(I)(T - \theta)$  describes the relaxation of the oceanic temperatures to the prevailing atmospheric temperatures  $\theta$ . The key modifications that we apply to the Stommel model are related to this term. First, in the original Stommel model the atmospheric temperature gradient  $\theta$  is a constant and describes a static climatic background. Given that the relaxation of oceanic temperatures  $T$  to atmospheric temperatures  $\theta$  requires mutual exchange of heat between atmosphere and ocean, we argue that the heat transfer should impact the atmospheric temperature gradient as well. We therefore treat  $\theta$  as an additional dynamic variable as described in the next section. Second, we model the rate of the atmosphere–ocean heat exchange  $\gamma$ , which is also a constant in the original Stommel model, as a function of the Nordic Seas’ sea ice cover  $I$ . The latter acts as an insulator between the two media. With sea ice being the fourth dynamical variable of our model, the rate  $\gamma(I)$  is subject to dynamic changes. This mechanism will be described in detail further below.

**Atmosphere component** We explicitly take into account the effect of the atmosphere–ocean heat exchange on the atmospheric meridional temperature gradient by writing

$$\dot{\theta} = -\Gamma(\theta - \theta_0) - \gamma(\theta - T)/\kappa. \quad (3)$$

Here,  $\theta_0$  is the atmospheric temperature gradient determined by the background climate state, which would dictate  $\theta(t)$  in the absence of the ocean–atmosphere feedback. The relaxation of  $\theta(t)$  towards  $\theta_0$  at the rate  $\Gamma$  competes with the relaxation of the atmosphere towards the oceanic temperature gradient  $T$  which acts at a rate  $\gamma/\kappa$ . The introduction of an atmospheric heat capacity  $\kappa$  guarantees that the heat flux between ocean and atmosphere is consistently incorporated in the equations of motion of  $\theta$  and  $T$  in compliance with energy conservation. In the limit of infinitely fast relaxation of the atmospheric temperature gradient  $\theta$  against the background climate  $\theta_0$ , the original Stommel model with constant  $\theta = \theta_0$  is recovered. Multiplication of Eq. 3 by  $\kappa$  yields the atmosphere dynamics

$$\tau_{\text{atm}} \dot{\theta} = -\eta(\theta - \theta_0) - \gamma(I)(\theta - T) \quad (4)$$

with  $\tau_{\text{atm}} = \kappa$ ; in this case  $\eta = \kappa\Gamma$  represents an effective atmospheric heat dissipation rate. The heat capacity of the atmosphere thus introduces a time scale separation between the oceanic and atmospheric components of our model. In the following we call the ocean–atmosphere system defined by Eqs. 1–4 with a constant relaxation rate  $\gamma$  and without the stochastic forcing  $\zeta_t$  used in the main text the extended Stommel model.

**Dynamics of the extended Stommel model** We now discuss the dynamics of the extended Stommel model defined by Eqs. 1–4 for constant relaxation rate  $\gamma$  and constant background state  $\theta_0$ . Figure 1 shows the model’s bifurcation diagram with  $\gamma$  acting as a bifurcation parameter. As the standard Stommel model, the extended model has two stable fixed point branches. For  $1.1 < \gamma < 1.21$  the system is bistable with an unstable branch separating the two stable ones. The lower branch is associated with a weak mode of overturning (smaller  $|q|$ ) while the upper branch represents a strong mode (larger  $|q|$ ), with the former being salinity-driven ( $S > T$ ) and the latter being temperature-driven ( $T > S$ ). We note that the increase of  $q$  with increasing  $\gamma$  is stronger in the standard Stommel model because in the extended model a strengthening of the AMOC weakens the atmospheric temperature gradient.

Given the interpretation of the model variables established in the main text, with  $\theta$  corresponding to arctic atmospheric temperatures,  $T$  representing the Nordic Seas’ deep and intermediate water temperatures and  $q$  indicating the AMOC strength, we can identify stadial and interstadial climate conditions with different configurations of the extended Stommel model. The ocean–atmosphere heat exchange rate  $\gamma$  controls the state of the high latitude climate (Fig. 1). Varying  $\gamma$  from low to high

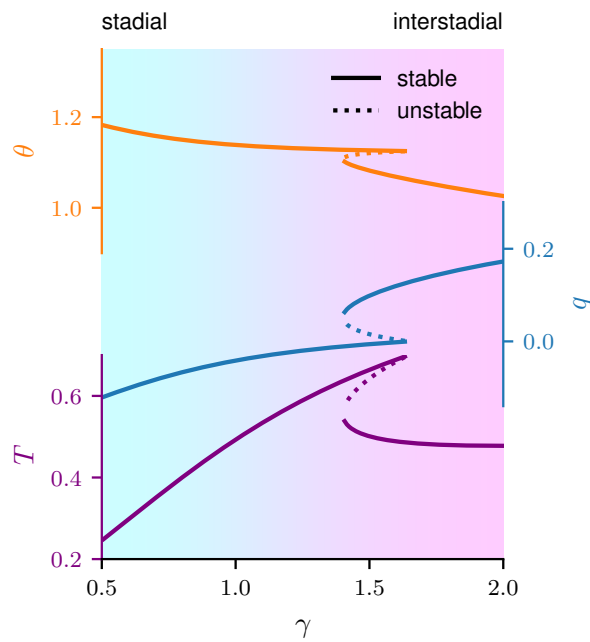


**Figure 1:** Bifurcation diagram of the extended Stommel model defined by Eqs. 1-4. The heat exchange rate  $\gamma$  acts as a control parameter with two bifurcations occurring at  $\gamma_{c1} = 1.1$  and  $\gamma_{c2} = 1.21$ . Solid (dashed) lines represent stable (unstable) branches. The atmospheric meridional temperature gradient  $\theta$  declines with increasing heat exchange rate  $\gamma$  due to the action of the ocean on the atmosphere. The stable branch of the model that is associated with higher  $\gamma$  is commonly referred to as the strong mode (temperature driven), while the stable branch associated with lower  $\gamma$  is called the weak mode (salinity driven). For low  $\gamma < 0.8$  all model variables assume a stadial configuration (blue shading), while for  $\gamma > 1.5$  they assume an interstadial configuration (magenta shading). Here, the atmospheric background climate was set to  $\theta_0 = 1.3$  and all other parameters are as given in the main text.

Supporting Information for: Glacial abrupt climate change as a multi-scale phenomenon resulting from monostable excitable dynamics

values yields changes in all three model variables that consistently match the changes of the true climate system observed between stadial and interstadial periods. Low values of  $\gamma \lesssim 0.7$  are associated with a weak AMOC state (lower  $|q|$  as compare to the strong stable AMOC branch), cold polar atmosphere (large  $\theta$ ) and warm Nordic Seas (small  $T$ ), while high values of  $\gamma \gtrsim 1.5$  reverse this configuration. This allows to interpret the stable states of the extended Stommel model at low and high  $\gamma$  as stadial and interstadial states, respectively.

Although higher values of  $\gamma$  entail enhanced oceanic northward heat transport, the Nordic Seas are colder in this configuration because of the stronger release of heat into the atmosphere. In the stadial state (small values of  $\gamma$ ) the model shows sustained northward heat transport provided by the salinity-driven weak AMOC. However, with the corresponding smaller heat exchange rate  $\gamma$  even a reduced northward heat transport warms the northern ocean as it hardly loses any heat to the atmosphere. This model behavior is in line with the findings by [4–6] who report a sustained warm water inflow into the Nordic seas at intermediate depth during stadials.

**Sea ice component** The sea ice variable  $I$  represents the sea ice cover in the polar box (i.e. in the Nordic Seas). Acting as an insulator, the sea ice controls the heat exchange rate  $\gamma$  between the polar atmosphere and ocean [5, 7]. We adopt the seasonally averaged version of the [8] sea ice model introduced by [9]:

$$\dot{I} = \Delta \tanh\left(\frac{I}{h}\right) - R_0 \Theta(I) I + L - B I, \quad (5)$$

where  $\Theta(I)$  denotes the Heaviside function. The first term represents the ice-albedo feedback to the incoming solar short-wave radiation. The sea ice transport, which is absent in open ocean conditions ( $I < 0$ ), is controlled by  $R_0$ . The term  $L - BI$  describes the change of sea ice due to the net outgoing longwave radiation (OLR) according to a linearized Stefan Boltzmann law. The incoming longwave radiation depends on the atmospheric temperature  $\theta$ . In order to incorporate dynamic changes of the polar atmospheric temperature in Eq. 5 and to couple the sea ice model with the extended Stommel model, we assume a linear relationship between the net incoming (or outgoing) longwave radiation and the atmospheric temperature and write

$$L = L_0 + L_1(\theta - \theta^*), \quad (6)$$

where  $\theta - \theta^*$  denotes deviations from some default atmospheric temperature. Since larger  $\theta$  corresponds to a colder polar atmosphere with positive effect on the sea ice growth,  $L_1$  is positive. Inserting Eq. 6 into Eq. 5 finally leads to our sea ice model used in the main text

$$\tau_{\text{ice}} \dot{I} = \Delta \tanh\left(\frac{I}{h}\right) - R_0 \Theta(I) I - L_0 + L_1 \theta - L_2 I + \xi_t, \quad (7)$$

yet without the stochastic forcing  $\xi_t$ . We ignore influences of the oceanic temperatures on the sea ice.

In the original Eisenman model  $I$  is the negative of the enthalpy which is proportional to the thickness of the sea ice if  $I > 0$ . [8] considered an oceanic box of limited size, such that the sea ice can be regarded as homogeneous along the horizontal dimensions of the box. In our case, the polar oceanic box is identified with the Nordic Seas and is thus too large for such a homogeneity assumption to hold and therefore the variable  $I$  in our model should be interpreted as a measure of the annually averaged sea ice volume in the Nordic Seas (and the northern North Atlantic) with  $I = 0$  indicating intermediate sea ice cover.

As mentioned previously, sea ice insulates atmosphere and ocean from one another and hence controls their mutual heat exchange. Note that the heat flux  $\psi$  between any two reservoirs with different temperatures is proportional to their temperature difference  $\Delta T$ . If separated by an insulator,  $\psi$  is moreover inversely proportional to the insulator's thickness. Based on our altered interpretation of the sea ice variable  $I$ , we model the effect of the sea ice on the ocean–atmosphere heat exchange in form of a hyperbolic tangent with saturation towards high and low values of sea ice

$$\gamma(I) = \gamma_0 + \frac{\Delta\gamma}{2} \left[ \tanh\left(\frac{-(I - I_0)}{\omega}\right) + 1 \right]. \quad (8)$$

This yields a heat flux  $\psi \propto \gamma(I) (T - \theta)$  that in turn controls the mutual atmosphere–ocean relaxation in terms of temperatures. The parameters  $\gamma_0$  and  $\gamma_0 + \Delta\gamma$  in Eq. 8 define the heat exchange rate at maximum ice cover and open ocean conditions, respectively, and  $\omega$  moderates the steepness of the heat exchange decline with increasing sea ice thickness  $I$ . Shifting the hyperbolic tangent along the sea ice axis by setting  $I_0 = -0.5$  yields an already substantially reduced heat exchange rate at intermediate sea ice cover ( $I = 0$ ; cf. Fig. 2). At maximum sea ice cover the heat exchange between the high-latitude ocean and atmosphere is considered to be (almost) shut off. At low latitudes, the heat flux is unaffected by the sea ice and thus the total ocean–atmosphere heat flux is sustained at the reduced rate  $\gamma_0$  even with fully sea ice covered Nordic Seas. We assume that the atmosphere–ocean temperature difference is larger in the polar box than in the equatorial box, with the effect that polar heat exchange contributes stronger to the relaxation of the gradients  $\theta$  and  $T$  to one another. This justifies a relatively small minimum exchange rate  $\gamma_0 = 0.5$  compared to the maximum heat exchange rate  $\gamma_0 + \Delta\gamma = 4$ .

We now examine the joint bifurcation structure of the sea ice model and the atmospheric temperature  $\theta$  in the deterministic setting — i.e. we assess the nullclines of Eqs. 4 and 7. Our sea ice model features a double fold bifurcation with respect

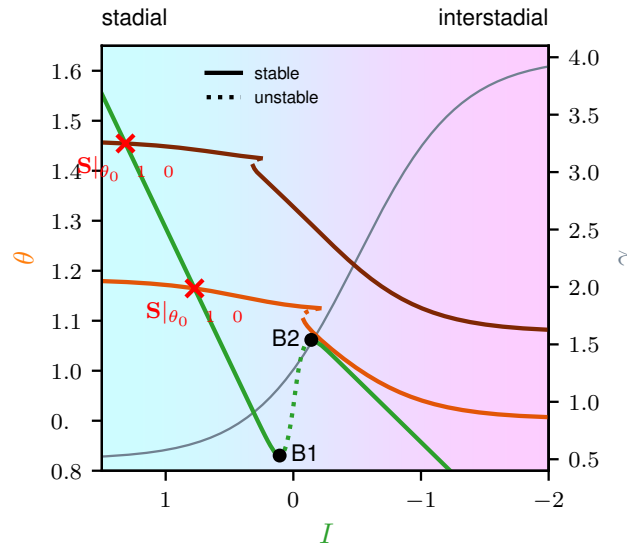


**Figure 2:** Nullcline of the seasonally averaged sea ice  $I$  (green) together with the nullcline of the Stommel atmosphere  $\theta$  (orange). Due to the ice-albedo feedback the sea ice model features a bistable region where an ice-rich and a low-ice solution coexist. The difference in the slope of the two stable branches is controlled by the strength of the sea ice export  $R_0$ . The upper  $\theta$ -nullcline (dark orange) is the same as in Fig. 1 with  $\theta_0 = 1.45$  upon using the transformation  $\gamma = \gamma(I)$  given by Eq. 8. The lower  $\theta$ -nullcline (lighter orange) results from setting  $\theta_0 = 1.3$ . The heat exchange rate  $\gamma(I)$  as a function of the sea ice is shown in light gray on the right ordinate. Intersections of the  $\theta$  and  $I$  nullclines define fixed points of the entire coupled system defined by Eqs. 1–8. Larger atmospheric backgrounds  $\theta_0$  yield more pronounced stadial conditions with colder arctic atmosphere and larger sea ice cover.

to  $\theta$  (Fig. 2). The associated bistability is an effect of the ice–albedo feedback. The bifurcation points are given by  $B1 = (\theta = 0.83, I = 0.11)$  and  $B2 = (\theta = 1.06, I = -0.14)$ . Intersections of the sea ice’s and the atmosphere’s nullclines constitute fixed points of the full coupled system. The stable fixed points that correspond to the two climate background states  $\theta_0 = 1.3$  and  $\theta_0 = 1.45$  are  $(\theta_s \sim 1.16, I_s \sim 0.77)$  and  $(\theta_s \sim 1.31, I_s \sim 1.05)$ , respectively, and represent stadial climate states with large sea ice cover and cold temperatures over Greenland (crosses in Figure 2). Note that larger atmospheric background gradients yield a more severe stadial climate with larger  $I_s$  and  $\theta_s$ . The corresponding stadial fixed point in the ocean model, i.e. in Eqs. 1 and 2 is  $T_s \approx 0.3$  for both values of  $\theta_0$ , implying relatively warm Nordic Seas. Moreover, the AMOC strength  $q_s \sim -0.09$  is negative and thus salinity driven and weak.

A key feature of the bifurcation diagram is the proximity of the low-ice stable branch of the sea ice nullcline and the strong-mode stable branch of the  $\theta$  nullcline around  $I \approx -0.25$ . The closer the nullclines are to each other, the slower is the deterministic dynamics in nearby regions of the state space. Their distance is controlled by the atmospheric climate background  $\theta_0$  and decreases with decreasing  $\theta_0$  provided that  $\theta_0 > 1.29$ . If the nullclines are sufficiently close, once the system enters this region of the state space, the dynamics allows for prolonged periods in which  $I$  and  $\theta$  do not vary much, giving rise to what we term a meta-stable state. It is the existence of this transient meta-stable state that allows us to model interstadials.

To bring the system close to the meta-stable state we require sufficiently large perturbations. In our model these will be provided by substantial stochastic sea ice removals which reactivate the ocean–atmosphere interaction and thereby trigger temporary state space excursions into the interstadial regime. This is achieved by introducing a non-Gaussian intermittent stochastic process which acts as a forcing on the sea ice and is capable of inducing the required large abrupt sea ice removal.

## References

- [1] Stommel, H. Thermohaline Convection with Two Stable Regimes of Flow. *Tellus*, 13:224–230, 1961. doi: 10.1111/j.2153-3490.1961.tb00079.x.
- [2] Cessi, P. A Simple Box Model of Stochastically Forced Thermohaline Flow. *Journal of Physical Oceanography*, 24: 1911–1920, 1994. doi: [https://doi.org/10.1175/1520-0485\(1994\)024<1911:ASBMOS>2.0.CO;2](https://doi.org/10.1175/1520-0485(1994)024<1911:ASBMOS>2.0.CO;2).
- [3] Roeber, P.J. Climate variability in a low-order coupled atmosphere-ocean model. *Tellus A*, 47:473–494, 1995. doi: 10.1034/j.1600-0870.1995.t01-3-00006.x.

Supporting Information for: Glacial abrupt climate change as a multi-scale phenomenon resulting from monostable excitable dynamics

- [4] Rasmussen, T.L. and Thomsen, E. The role of the North Atlantic Drift in the millennial timescale glacial climate fluctuations. *Palaeogeography, Palaeoclimatology, Palaeoecology*, 210:101–116, 2004. doi: 10.1016/j.palaeo.2004.04.005.
- [5] Dokken, T.M., Nisancioglu, K.H., Li, C., Battisti, D.S., and Kissel, C. Dansgaard-Oeschger cycles: Interactions between ocean and sea ice intrinsic to the Nordic seas. *Paleoceanography*, 28:491–502, 2013. doi: 10.1002/palo.20042.
- [6] Ezat, M.M., Rasmussen, T.L., and Groeneveld, J. Persistent intermediate water warming during cold stadials in the southeastern Nordic seas during the past 65 k.y. *Geology*, 42:663–666, 2014. doi: 10.1130/G35579.1.
- [7] Boers, N., Ghil, M., and Rousseau, D.D. Ocean circulation, ice shelf, and sea ice interactions explain Dansgaard–Oeschger cycles. *Proceedings of the National Academy of Sciences of the United States of America*, 115:E11005–E11014, 2018. doi: 10.1073/pnas.1802573115.
- [8] Eisenman, I. Factors controlling the bifurcation structure of sea ice retreat. *Journal of Geophysical Research Atmospheres*, 117:D01111, 2012. doi: 10.1029/2011JD016164.
- [9] Lohmann, J., Castellana, D., Ditlevsen, P.D., and Dijkstra, H.A. Abrupt climate change as a rate-dependent cascading tipping point. *Earth System Dynamics*, 12:819–835, 2021. doi: 10.5194/esd-12-819-2021.

### **P3 Stable stadial and interstadial states of the last glacial's climate identified in a combined stable water isotope and dust record from Greenland**

**Keno Riechers** Leonardo Rydin Gorjão, Forough Hassanibesheli, Pedro G. Lind, Dirk Witthaut & Niklas Boers, 2023. *Earth System Dynamics*, 14, 593–607.

**Copyright.** The article is published open access under the terms of the [Creative Commons Attribution-NonCommercial](#) license. The copyright remains with the authors.

**Contribution.** KR and LRG designed the study with contributions from all authors. KR and LRG conducted the numerical analysis. KR and LRG wrote the paper with contributions from all authors.



## Stable stadial and interstadial states of the last glacial's climate identified in a combined stable water isotope and dust record from Greenland

Keno Riechers<sup>1,2,★</sup>, Leonardo Rydin Gorjão<sup>3,4,5,6,★</sup>, Forough Hassanibesheli<sup>7</sup>, Pedro G. Lind<sup>8,9,10</sup>, Dirk Witthaut<sup>4,5</sup>, and Niklas Boers<sup>2,1,11</sup>

<sup>1</sup>Research Domain IV – Complexity Science, Potsdam Institute for Climate Impact Research, Telegrafenberg A31, 14473 Potsdam, Germany

<sup>2</sup>Earth System Modelling, School of Engineering & Design, Technical University of Munich, 80333 Munich, Germany

<sup>3</sup>Faculty of Science and Technology, Norwegian University of Life Sciences, 1432 Ås, Norway

<sup>4</sup>Institute of Energy and Climate Research, Forschungszentrum Jülich, 52428 Jülich, Germany

<sup>5</sup>Institute for Theoretical Physics, University of Cologne, 50937 Cologne, Germany

<sup>6</sup>Institute of Networked Energy Systems, German Aerospace Center (DLR), 26129 Oldenburg, Germany

<sup>7</sup>Earth System Modelling, Helmholtz Centre Potsdam, GFZ German Research Center for Geosciences, 14473 Potsdam, Germany

<sup>8</sup>Department of Computer Science, OsloMet – Oslo Metropolitan University, 0130 Oslo, Norway

<sup>9</sup>NordSTAR – Nordic Center for Sustainable and Trustworthy AI Research, 0166 Oslo, Norway

<sup>10</sup>Artificial Intelligence Lab, Oslo Metropolitan University, 0166 Oslo, Norway

<sup>11</sup>Global Systems Institute, Department of Mathematics, University of Exeter, EX4 4QF Exeter, UK

★These authors contributed equally to this work.

**Correspondence:** Keno Riechers ([keno.riechers@pik-potsdam.de](mailto:keno.riechers@pik-potsdam.de))

Received: 20 November 2021 – Discussion started: 7 December 2021

Revised: 10 March 2023 – Accepted: 28 March 2023 – Published: 16 May 2023

**Abstract.** During the last glacial interval, the Northern Hemisphere climate was punctuated by a series of abrupt changes between two characteristic climate regimes. The existence of stadial (cold) and interstadial (milder) periods is typically attributed to a hypothesised bistability in the glacial North Atlantic climate system, allowing for rapid transitions from the stadial to the interstadial state – the so-called Dansgaard–Oeschger (DO) events – and more gradual yet still fairly abrupt reverse shifts. The physical mechanisms driving these regime transitions remain debated. DO events are characterised by substantial warming over Greenland and a reorganisation of the Northern Hemisphere atmospheric circulation, which are evident from concomitant shifts in the  $\delta^{18}\text{O}$  ratios and dust concentration records from Greenland ice cores. Treating the combined  $\delta^{18}\text{O}$  and dust record obtained by the North Greenland Ice Core Project (NGRIP) as a realisation of a two-dimensional, time-homogeneous, and Markovian stochastic process, we present a reconstruction of its underlying deterministic drift based on the leading-order terms of the Kramers–Moyal equation. The analysis reveals two basins of attraction in the two-dimensional state space that can be identified with the stadial and interstadial regimes. The drift term of the dust exhibits a double-fold bifurcation structure, while – in contrast to prevailing assumptions – the  $\delta^{18}\text{O}$  component of the drift is clearly mono-stable. This suggests that the last glacial's Greenland temperatures should not be regarded as an intrinsically bistable climate variable. Instead, the two-regime nature of the  $\delta^{18}\text{O}$  record is apparently inherited from a coupling to another bistable climate process. In contrast, the bistability evidenced in the dust drift points to the presence of two stable circulation regimes of the last glacial's Northern Hemisphere atmosphere.

## 1 Introduction

Recently, evidence was reported for the destabilisation of climatic subsystems likely caused by continued anthropogenically driven climate change (e.g. Boers, 2021; Rosier et al., 2021; Boers and Rypdal, 2021). Conceptually, such destabilisation is commonly formulated in terms of bistable dynamical systems that approach a bifurcation in response to the gradual change in a control parameter. This setting offers three mechanisms for the system to transition between two alternative stable states (Ashwin et al., 2012). First, the control parameter may cross a bifurcation, which dissolves the currently attracting state and necessarily entails a transition to the remaining alternative stable state (bifurcation-induced transition). Second, random perturbations may push the system across a basin boundary (noise-induced transition); this is generally more likely the closer the system is to a bifurcation. Third, rapid change in the control parameter may shift the basin boundaries at a rate too high for the system to track the moving domain of its current attractor (rate-induced transition). If global warming – viewed as the control parameter – were to exceed certain thresholds, several elements of the climate system are thought to be at risk to “tip” to alternative stable states (Lenton and Schellnhuber, 2007; Lenton et al., 2008; Armstrong McKay et al., 2022), among them the Greenland ice sheet (Boers and Rypdal, 2021), the Amazon rainforest (Boulton et al., 2022), the Atlantic Meridional Overturning Circulation (AMOC) (Boulton et al., 2014; Boers, 2021), and the West Antarctic ice sheet (Rosier et al., 2021).

The possibility of alternative stable states of the entire climate system or its subsystems (and transitions between these) has been discussed at least since the 1960s (e.g. Ghil, 1975; North, 1975; Stommel, 1961). Empirical evidence, however, that the climate system or its subsystems can indeed abruptly transition between alternative equilibria is available only from proxy records which allow reconstruction of past climatic conditions prior to the instrumental period (e.g. Brovkin et al., 2021; Boers et al., 2022; and references therein). Given that comprehensive Earth system models continue to have problems in simulating abrupt climate changes and especially in reproducing abrupt changes evidenced in proxy records (Valdes, 2011), studying abrupt changes recorded by paleoclimate proxies is key for gaining a better understanding of the physical mechanisms involved and for assessing the risks of future abrupt transitions.

In this context, our study investigates the Dansgaard–Oeschger (DO) events, a series of abrupt warming events over Greenland first evidenced in stable water isotope records from Greenland ice cores (Dansgaard et al., 1982, 1984, 1993; Johnsen et al., 1992; North Greenland Ice Core Projects members, 2004). While locally the temperature increases are estimated to be as large as 16 °C in the annual

mean temperature (Kindler et al., 2014), a (weaker) signature of these events can be found in numerous records across the globe (e.g. Voelker, 2002; Menviel et al., 2020; and references therein) indicating changes in other climatic subsystems such as Antarctic average temperatures (e.g. WAIS Divide Project Members, 2015; EPICA Community Members, 2006), the Asian and South American Monsoon system (e.g. Wang et al., 2001; Kanner et al., 2012; Cheng et al., 2013; Li et al., 2017; Corrick et al., 2020), or the Atlantic Meridional Overturning Circulation (AMOC) (e.g. Lynch-Stieglitz, 2017; Henry et al., 2016; Gottschalk et al., 2015). The global puzzle of more or less abrupt shifts in synchrony (within the limits of dating uncertainties) with DO events found in versatile paleoclimate proxy records point to a complex scheme of interactions between climatic subsystems involved in the DO variability that dominated the last glacial period. While multiple lines of evidence indicate a central role of changes in the overturning strength of the AMOC (e.g. Lynch-Stieglitz, 2017; Menviel et al., 2020), to date, there is no consensus about the ultimate trigger of DO events.

An important branch of research has assessed the performance of low-dimensional conceptual models in explaining the DO variability in the Greenland ice core records (e.g. Ditlevsen, 1999; Livina et al., 2010; Kwasniok, 2013; Mitsui and Crucifix, 2017; Roberts and Saha, 2017; Boers et al., 2017, 2018; Lohmann and Ditlevsen, 2018a; Vettoretti et al., 2022). Typically, one-dimensional multi- or bistable models (Ditlevsen, 1999; Livina et al., 2010; Kwasniok, 2013; Lohmann and Ditlevsen, 2018a) or two-dimensional relaxation oscillators (Kwasniok, 2013; Mitsui and Crucifix, 2017; Roberts and Saha, 2017; Lohmann and Ditlevsen, 2018a; Vettoretti et al., 2022) have been invoked, forced by either slowly changing climate background variables such as CO<sub>2</sub> or changing orbital parameters, by noise, or by both. To the best of our knowledge, to date Boers et al. (2017) presented the only inverse-modelling approach to simulate a two-dimensional Greenland ice core proxy record –  $\delta^{18}\text{O}$  and dust – with regards to its DO variability. Likewise in two dimensions, we present here a data-driven investigation of the couplings between Greenland temperatures and the larger-scale Northern Hemisphere state of the atmosphere represented by the North Greenland Ice Core Project (NGRIP)  $\delta^{18}\text{O}$  ratio and dust concentration records, respectively (North Greenland Ice Core Projects members, 2004; Gkinis et al., 2014; Ruth et al., 2003). Treating the combined  $\delta^{18}\text{O}$  and dust record as the realisation of a time-homogeneous Markovian stochastic process (Kondrashov et al., 2005, 2015), we reconstruct the corresponding deterministic two-dimensional drift using the Kramers–Moyal equation (Kramers, 1940; Moyal, 1949; Tabar, 2019) and reveal evidence for bistability of the coupled  $\delta^{18}\text{O}$ –dust “system”. Compared to the previously mentioned studies, this approach has the advantage that the estimation of the drift is

non-parametric (i.e. it assumes no a priori functional structure for the drift) and that it assesses the stability configuration of the two-dimensional record as opposed to the numerous studies concerned with one-dimensional proxy records.

In the state space spanned by  $\delta^{18}\text{O}$  ratios and dust concentrations, based on our results we identify two regions of convergence concentrated around two stable fixed points, which can be associated with Greenland stadials and interstadials. We show that the global bistability is rooted in the dust component of the drift, exhibiting what seems to be a double-fold bifurcation parameterised by  $\delta^{18}\text{O}$ . This asserts a genuine bistability to the glacial Northern Hemisphere atmosphere. In contrast, the  $\delta^{18}\text{O}$  drift component is mono-stable across all dust values, suggesting that the two regimes evidenced in past Greenland temperature reconstructions are not the signature of intrinsic bistability but that of coupling another bistable subsystem, which – according to our results – may be the atmospheric large-scale circulation.

This article is structured as follows. We first present the paleoclimate proxies analysed in this study and explain how we pre-processed the data to make them suitable for estimating the two-dimensional drift (Sect. 2). Subsequently, we introduce the two-dimensional Kramers–Moyal equation, which is key for the analysis (Sect. 3). Section 4 provides the reconstruction of the two-dimensional drift, and Sect. 5 discusses the results and how they relate to previous studies. In Sect. 6 we summarise our main findings and detail the research questions that follow from these.

## 2 Data and pre-processing

The analysis presented here is based primarily on the joint  $\delta^{18}\text{O}$  ratio and dust concentration time series obtained by the North Greenland Ice Core Project (NGRIP) (North Greenland Ice Core Projects members, 2004; Ruth et al., 2003; Gkinis et al., 2014). From 1404.75–2426.00 m of depth in the NGRIP ice core, data are available for both proxies at a spatially equidistant resolution of 5 cm. This translates into non-equidistant temporal resolution ranging from sub-annual resolution at the end to  $\sim 5$  years at the beginning of the period, 59944.5–10276.4 years b2k, according to the Greenland Ice Core Chronology 2005 (GICC05), the common age–depth model for both proxies (Vinther et al., 2006; Rasmussen et al., 2006; Andersen et al., 2006; Svensson et al., 2008). Lower-resolution data (20-year means) (Rasmussen et al., 2014; Seierstad et al., 2014) reaching back to the last interglacial period (see Fig. 1) are only used for illustrative purposes but not for the analysis.

The ratio of stable water isotopes, expressed as  $\delta^{18}\text{O}$  values in units of permil, is a proxy for the site temperature at the time of precipitation, and hence the abrupt shifts present in the data qualitatively indicate the abrupt warming events over Greenland (Jouzel et al., 1997; Johnsen et al., 2001). The concentration of dust, i.e. the number of particles with

a diameter above  $1\ \mu\text{m mL}^{-1}$ , is commonly interpreted as a proxy for the state of the hemispheric atmospheric circulation (e.g. Fischer et al., 2007; Ruth et al., 2007; Schüpbach et al., 2018; Erhardt et al., 2019). More specifically, it is assumed to be controlled mostly by three factors (Fischer et al., 2007): first, by climatic conditions at the emission source, i.e. the dust storm activity over East Asian deserts preconditioned on generally dry regional climate; second, by the transport efficiency, which is affected by the strength and position of the polar jet stream; and third, the depositional process, which is mostly determined by local precipitation patterns. Correspondingly, the substantial changes in the dust concentrations across DO events are interpreted as large-scale reorganisations of the Northern Hemisphere's atmospheric circulation. Typically, atmospheric changes affecting the dust flux onto the Greenland ice sheet are accompanied by changes in the snow accumulation of opposite sign (e.g. Fischer et al., 2007). This enhances the corresponding change in the recorded dust particle concentration. However, for high-accumulation Greenland ice cores – such as NGRIP – the dust concentration changes still serve as a reliable indicator of atmospheric changes according to Fischer et al. (2007). Since the dust concentrations approximately follow an exponential distribution, we consider the negative natural logarithm of the dust concentration in order to emphasise the similarity to the  $\delta^{18}\text{O}$  time series. For ease of notation, we always use the term dust (or dust concentrations), although technically we refer to its negative natural logarithm.

In Fig. 1 we show the original low-resolution (b and c) and the pre-processed high-resolution data (f and g) together with corresponding histograms (h), also given in Fig. 3a. Clearly, two regimes can be visually distinguished: Greenland stadials are characterised by low  $\delta^{18}\text{O}$  ratios and high dust concentrations. Greenland interstadials (grey shading in panels f and g of Fig. 1) in general exhibit the reversed configuration besides a mild trend toward stadial conditions, which can be more or less pronounced during the individual interstadials. In our study, we use the categorisation of the climatic periods as presented by Rasmussen et al. (2014). The two-regime character of the time series translates into a bimodal histogram of the dust data, as seen in Fig. 1h. In the case of the  $\delta^{18}\text{O}$  data, the stronger trend during interstadials and the higher relative noise amplitude mask a potential bimodality, and the histogram appears unimodal. Notice that the somewhat counterintuitive combination of meta-stable distinct dynamical regimes and unimodal distributions of the associated variables has also been discussed in the context of atmospheric dynamics (Majda et al., 2006).

The analysis conducted in this work relies on the following assumptions and technical conditions:

- i. The data-generating process is sufficiently time-homogeneous over the considered time period.
- ii. The process is Markovian at the sampled temporal resolution.

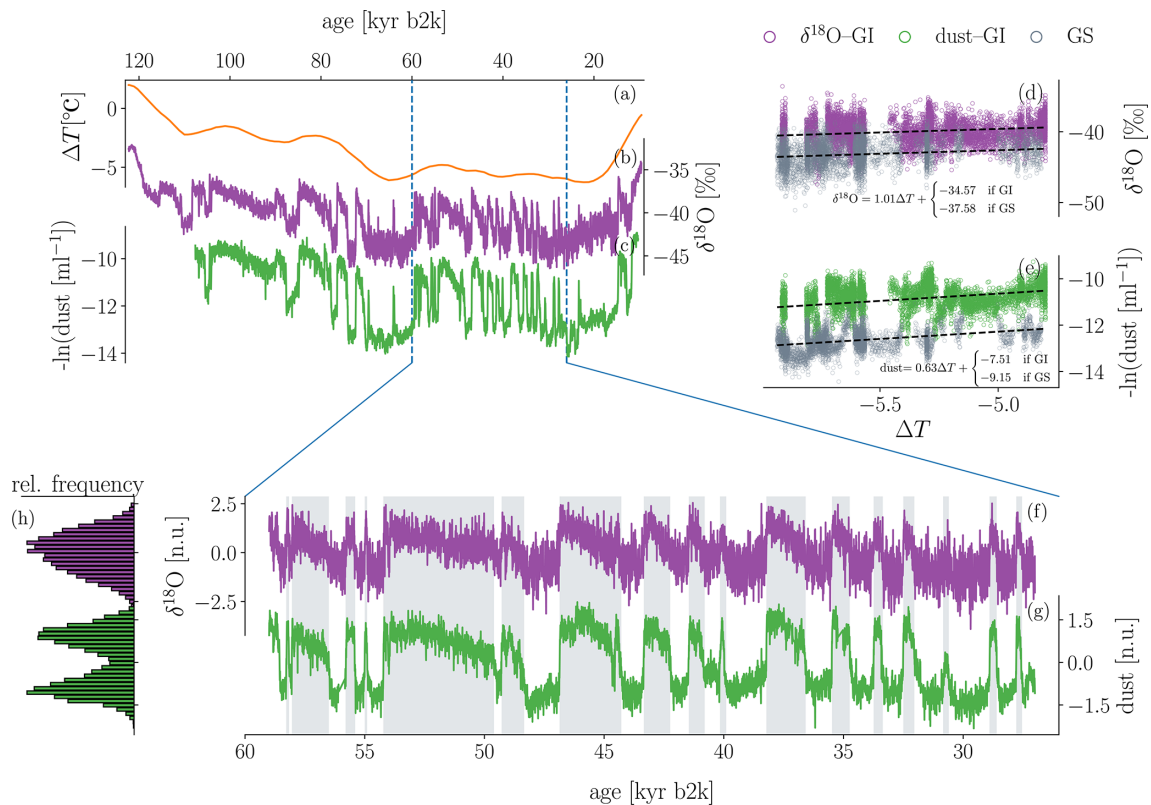


**Figure 1.** (a) Global-mean surface temperature reconstruction for the last glacial interval as provided by Snyder (2016) and linearly interpolated to a 20-year temporal resolution. The reconstruction is based on a multi-proxy database which comprises over 20 000 sea surface temperature reconstructions from 59 marine sediment cores. The figure shows the anomaly with respect to modern climate (5–0 kyr b2k average; b2k: before 2000 CE). The 20-year mean of  $\delta^{18}\text{O}$  ratios (b) and accordingly resampled dust concentrations (c) from the NGRIP ice core in Greenland, from 122 kyr and 107 kyr to 10 kyr b2k (Rasmussen et al., 2014; Seierstad et al., 2014; Ruth et al., 2003). The dust data are given as the negative natural logarithm of the actual dust concentrations in order to facilitate visual comparison to the  $\delta^{18}\text{O}$  data. Panels (d) and (e) show the linear regressions of  $\delta^{18}\text{O}$  and dust onto the reconstructed global-mean surface temperatures (Snyder, 2016) from (a), carried out separately for Greenland stadials (GSs) and Greenland interstadials (GIs). Panels (f) and (g) show the same proxies as shown in (b) and (c) but at a higher resolution of 5 years (North Greenland Ice Core Projects members, 2004; Gkinis et al., 2014; Ruth et al., 2003) and over a shorter period from 59 to 27 kyr b2k. The analysis presented in this study was constrained to this section of the record. The two proxy time series in (f) and (g) have been detrended by removing the slow non-linear change induced by changes in the global background temperatures, based on the regressions from (d) and (e). The data were then binned to equidistant time resolution from the original 5 cm depth resolution. The grey shadings mark the GI intervals according to Rasmussen et al. (2014). Panel (h) shows the histograms of the two time series shown in (f) and (g), respectively. All data are shown on the GICC05 chronology (Vinther et al., 2006; Rasmussen et al., 2006; Andersen et al., 2006; Svensson et al., 2008).

- iii. The data are equidistant in time.
- iv. The relevant region of the state space is sampled sufficiently densely by the available data.

With regard to (i), a low-frequency influence of the background climate on the proxy values and on the frequency of DO events is evident (see Fig. 1), with suppressed DO variability during the coldest parts of the glacial and longer interstadials for its warmer parts (e.g. Rial and Saha, 2011; Roberts and Saha, 2017; Mitsui and Crucifix, 2017; Lohmann and Ditlevsen, 2018b; Boers et al., 2017, 2018). We therefore restrict our analysis to the period 59–27 kyr b2k, which is characterised by a fairly sta-

ble background climate and persistent co-variability between dust and  $\delta^{18}\text{O}$  (Boers et al., 2017). To remove the remaining influence of the background climate on the climate proxy records we remove a trend that is non-linear in time from both time series. This trend is obtained by linearly regressing the proxy data against reconstructed global-average surface temperatures (Snyder, 2016). Figure 1 illustrates the detrending scheme; due to the two-regime nature of the time series, a simple linear regression of the proxy variables onto the global-average surface temperatures would overestimate the temperature dependencies. Instead, we separate the data from Greenland stadials and Greenland interstadials and then

minimise the quantity

$$R = \left( \sum_{i=1}^N x(t_i) - a \Delta T(t_i) - \begin{cases} b_{GI}, & \text{if } t_i \in GI \\ b_{GS}, & \text{if } t_i \in GS \end{cases} \right)^2 \quad (1)$$

once for  $x = \delta^{18}\text{O}$  and once for  $x$ , taken as dust concentrations. The optimisations yield optimal values for the parameters  $a$ ,  $b_{GI}$ , and  $b_{GS}$  for dust and  $\delta^{18}\text{O}$  (see Fig. 1 panels d and e for  $\delta^{18}\text{O}$  and dust concentration, respectively). For a given time  $t_i$  we write  $t_i \in GS$  ( $GI$ ) to indicate that  $t_i$  falls into a stadial (interstadial) period. The index  $i$  runs over all data points, and  $N$  denotes the total number of data points. The resulting slope  $a$  is used to detrend the original data with respect to the time-dependent background temperature:

$$x_{\text{detrended}}(t_i) = x(t_i) - a \Delta T(t_i). \quad (2)$$

Subsequently, the detrended data are normalised by subtracting their respective means and dividing by their respective standard deviations. After the detrending, all stadial (or interstadial) periods exhibit almost the same level of values, which allows the data to be considered as the outcome of a time-homogeneous and long-term stationary process (compare Fig. 1f and g). As a consequence of the regime transitions the process is certainly not stationary on short timescales but only on timescales larger than typical DO cycle periods. Levelling out the differences between the recurring climate periods guarantees a sufficiently dense sampling of the relevant region of the state space (iv) and prevents a blurring of the drift reconstruction (i).

Stationarity tests provide further confirmation that the detrended data are free of any slow underlying trends: we have applied two separate tests to assess the stationarity of the detrended data on timescales beyond single DO cycles. These tests are the augmented Dickey–Fuller test (ADF) and the augmented Dickey–Fuller–GLS test (ADF-GLS). Both tests test the possibility of a unit root in the time series (null hypothesis). The alternative hypothesis is that the time series does not have a unit root; i.e. it is stationary. We can safely reject the presence of a unit root in each time series at  $p < 0.05$  (see Table 1).

There is a trade-off between conditions (i) and (iv) concerning the choice of the data window. While an even shorter window would assure time homogeneity of the dynamics with higher confidence, the sampling of the state space would become insufficiently sparse. The above choice (59–27 kyr b2k) guarantees a sufficient number of recurrences of the pre-processed two-dimensional trajectory to the relevant state space regions to perform statistical analysis. To obtain time-equidistant records (iii), the data are binned into temporally equidistant increments of 5 years.

The question of Markovianity (ii) is the most difficult to answer unambiguously. Here we draw on the following heuristic argument: the autocorrelation functions of the increments of both proxies shown in Fig. 2 exhibit weak anti-

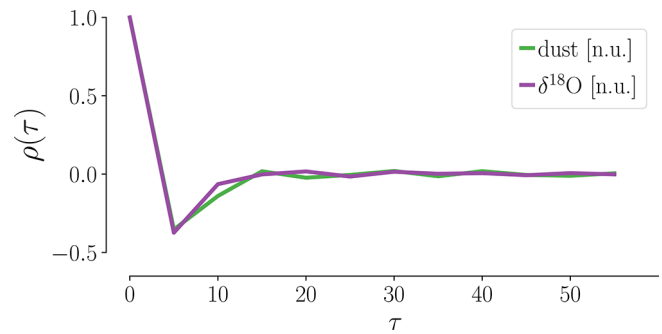


**Figure 2.** Autocorrelation  $\rho(\tau)$  of the increments  $\Delta x_t$  of  $\delta^{18}\text{O}$  and dust records. Both records show a weak anti-correlation at the shortest lag  $\tau = 5$  years and no correlation for  $\tau > 5$  years. We thus consider the data Markovian.

correlation at a shift of one time step, while correlations beyond this are negligible. Such a small level of correlation certainly rules out the notion that long-term memory effects played a major role in the emergence of the given time series. Bear in mind that this is a necessary yet not sufficient criterion to consider the data Markovian. For practical reasons, we refrained from further Markovianity tests.

Finally, further preconditions for our endeavour are the fact that the NGRIP record exhibits an exceptionally high resolution (iv) compared to other paleoclimate archives and that the two time series share the same time axis.

### 3 Methods

In this work, we treat the combined  $\delta^{18}\text{O}$  and dust record as a trajectory of a two-dimensional, time-homogeneous, and Markovian stochastic process of the form

$$d\mathbf{x} = \mathbf{F}(\mathbf{x})dt + d\xi, \quad (3)$$

where  $\xi$  denotes a general  $\delta$ -correlated driving noise in the Itô sense. It may be state-dependent – i.e. explicitly depend on  $\mathbf{x}$  – and contain discontinuous elements. No further specification is needed for the analysis presented here. The reconstruction of the two-dimensional drift  $\mathbf{F}(\mathbf{x})$  is based on the Kramers–Moyal (KM) equation, which reads

$$\begin{aligned} \frac{\partial}{\partial t} p(x_1, x_2, t | x'_1, x'_2, t') \\ = \sum_{i,j=1}^{\infty} (-1)^{i+j} \left( \frac{\partial^{i+j}}{\partial x_1^i \partial x_2^j} \right) \\ D_{i,j}(x_1, x_2) p(x_1, x_2, t | x'_1, x'_2, t') \end{aligned} \quad (4)$$

in two dimensions, where  $p(x_1, x_2, t | x'_1, x'_2, t')$  denotes the probability for the system to assume the state  $(x_1, x_2)$  at time  $t$ , given that it was in the state  $(x'_1, x'_2)$  at the time  $t'$ . The coefficients  $D_{i,j}(x_1, x_2)$  of the two-dimensional Kramers–Moyal equation can be estimated – analogously to the one-dimensional coefficients as explained in Tabar (2019) – from

**Table 1.** Unit root test of the detrended data. ADF refers to the augmented Dickey–Fuller test; ADF-GLS refers to the augmented Dickey–Fuller–GLS test. We reject the presence of a unit root in each of the time series at  $p < 0.05$ .

		Critical value	Dust statistics ( $p$ value) [lag]	$\delta^{18}\text{O}$ statistics ( $p$ value) [lag]
ADF	No trend	−1.9410	−5.0519 ( $8.362 \times 10^{-7}$ ) [6]	−6.8037 ( $1.661 \times 10^{-10}$ ) [15]
	No constant	−2.8620	−5.0515 ( $1.753 \times 10^{-5}$ ) [6]	−6.8034 ( $2.208 \times 10^{-9}$ ) [15]
	Constant and linear trend	−3.4112	−5.3732 ( $4.082 \times 10^{-5}$ ) [5]	−7.3196 ( $2.644 \times 10^{-9}$ ) [15]
	Constant, linear, and quadratic trends	−3.8333	−5.4810 ( $1.382 \times 10^{-4}$ ) [5]	−7.5415 ( $4.278 \times 10^{-9}$ ) [15]
ADF-GLS	Constant	−1.9470	−3.4422 ( $6.373 \times 10^{-4}$ ) [6]	−3.7747 ( $1.904 \times 10^{-4}$ ) [15]
	Constant and linear trend	2.8499	−5.2217 ( $9.989 \times 10^{-6}$ ) [5]	−6.6558 ( $1.487 \times 10^{-8}$ ) [15]

a realisation of a two-dimensional stochastic process  $\mathbf{x}(t) = (x_1(t), x_2(t))$ . The terms  $D_{1,0}(\mathbf{x})$  and  $D_{0,1}(\mathbf{x})$  combine to the deterministic drift that governs the stochastic process:

$$\mathbf{F}(x_1, x_2) = (D_{1,0}(x_1, x_2), D_{0,1}(x_1, x_2))^T. \quad (5)$$

In this work, we only consider the first-order KM coefficients. These are sufficient to uncover the deterministic non-linear features behind the stochastic data. Notice that we could formulate our method equally well in terms of the simpler Fokker–Planck equation (Risken and Frank, 1996). However, operating with the Fokker–Planck equation implicitly assumes that the stochastic process under investigation follows a Langevin equation in a strict sense; i.e. the noise term in Eq. (3) would be restricted to the case of Brownian motion. This conflicts with findings from ongoing research which indicate that the description of the driving noise  $\xi(t)$  as Brownian motion might not be valid (Rydin Gorjão et al., 2022). The use of the KM instead of the Fokker–Planck equation in this work aims at emphasising that  $\xi(t)$  might be more complex than Brownian motion and contain for example discontinuous elements. In principle, for a given stochastic process model, the higher-order KM coefficients can be used to estimate the corresponding noise parameters (see e.g. Anvari et al., 2016; Lehnertz et al., 2018; Rydin Gorjão et al., 2019; Tabar, 2019). However, this is not straightforward in two dimensions, and we deliberately refrain from an upfront selection of a process model in this work. Furthermore, a reliable estimate of higher-order coefficients in two dimensions is prevented by insufficient data density. A general derivation of the Kramers–Moyal equation can be found in Kramers (1940), Moyal (1949), Risken and Frank (1996), Gardiner (2009), and Tabar (2019).

In practice, in order to carry out the estimation of the first-order KM coefficients as defined in Eq. (4) we map each data point in the corresponding state space to a kernel density and then take a weighted average over all data points:

$$D_{1,0}(\mathbf{x}) \sim \frac{1}{\Delta t} \langle (x_1(t + \Delta t) - x_1(t)) | \mathbf{x}(t) = \mathbf{x} \rangle \sim \frac{1}{\Delta t} \frac{1}{N} \sum_{i=1}^{N-1} K(\mathbf{x} - \mathbf{x}_i) (x_{1,i+1} - x_{1,i}) \quad (6)$$

$$D_{0,1}(\mathbf{x}) \sim \frac{1}{\Delta t} \langle (x_2(t + \Delta t) - x_2(t)) | \mathbf{x}(t) = \mathbf{x} \rangle \sim \frac{1}{\Delta t} \frac{1}{N} \sum_{i=1}^{N-1} K(\mathbf{x} - \mathbf{x}_i) (x_{2,i+1} - x_{2,i}), \quad (7)$$

with  $\mathbf{x} = (x_1, x_2)^T$ .

Similar to selecting the number of bins in a histogram, when employing kernel density estimation with a Nadaraya–Watson estimator for the Kramers–Moyal coefficients  $D_{m,n}(\mathbf{x})$ , one needs to select both a kernel and a bandwidth (Nadaraya, 1964; Watson, 1964; Lamouroux and Lehnertz, 2009). Firstly, the choice of the kernel is the choice of a function  $K(\mathbf{x})$  for the estimator  $\hat{f}_h(\mathbf{x})$ , where  $h$  is the bandwidth at a point  $\mathbf{x}$

$$\hat{f}_h(\mathbf{x}) = \frac{1}{nh} \sum_{i=1}^n K\left(\frac{\mathbf{x} - \mathbf{x}_i}{h}\right) \quad (8)$$

for a collection  $\{\mathbf{x}_i\}$  of  $n$  random variables. The kernel  $K(\mathbf{x})$  is normalised as  $\int_{-\infty}^{\infty} K(\mathbf{x}) d\mathbf{x} = 1$  and has a bandwidth  $h$ , such that  $K(\mathbf{x}) = 1/h K(\mathbf{x}/h)$  (Rydin Gorjão et al., 2019; Tabar, 2019; Davis and Buffett, 2022). The bandwidth  $h$  is equivalent to the selection of the number of bins, except that binning in a histogram is always “placing numbers into non-overlapping boxes”. The optimal kernel is the commonly denoted Epanechnikov kernel (Epanechnikov, 1967), also used here for the analysis of the data:

$$K(\mathbf{x}) = \frac{3}{4}(1 - \mathbf{x}^2), \text{ with support } |\mathbf{x}| < 1. \quad (9)$$

Gaussian kernels are commonly used as well. Note that these require compact support in  $(-\infty, \infty)$ ; thus on a computer they require some sort of truncation (even in Fourier space, as the Gaussian shape remains unchanged).

The selection of an appropriate bandwidth  $h$  can be aided – unlike the selection of the number of bins – by Silverman’s rule of thumb (Silverman, 1998), given by

$$h_S = \left(\frac{4\hat{\sigma}^5}{3n}\right)^{\frac{1}{5}}, \quad (10)$$

where again  $\sigma^2$  is the variance of the time series. We note that the above formula for the ideal bandwidth has been developed for the estimation of the probability density function. As there is currently no consensus on the optimal kernel and bandwidth for the estimation of the KM coefficients, we employ an Epanechnikov kernel with bandwidth  $h_s$  throughout our work.

All numerical analyses were performed with Python's NumPy (Harris et al., 2020), SciPy (Virtanen et al., 2020), and pandas (McKinney, 2010). Kramers–Moyal analysis was performed with `kramersmoyal` (Rydin Gorbão and Meirinhos, 2019). Figures were generated with Matplotlib (Hunter, 2007).

## 4 Results

We first discuss the two drift components  $D_{1,0}$  and  $D_{0,1}$  (see Eq. 5) separately as functions of the two-dimensional space spanned by  $\delta^{18}\text{O}$  ratios and dust concentrations. In the component-wise analysis, the analysed component takes the role of a dynamical variable, while the respective other assumes the role of a controlling parameter. In this setting, corresponding nullclines can be computed, which reveals the bifurcation and stability structure of the two individual drift components. Intersections of the two components' nullclines yield fixed points of the coupled system, which are stable if both nullclines are stable at the intersection.

### 4.1 Double-fold bifurcation of the dust

The estimated dust drift  $D_{0,1}(x_1 = \delta^{18}\text{O}, x_2 = \text{dust})$  is displayed in Fig. 3c. This coefficient dictates the deterministic motion of the system along the dust direction; therein the  $\delta^{18}\text{O}$  ratio takes the role of the controlling parameter. We can trace the nullcline's branches, which take a general "S" shape as we vary  $\delta^{18}\text{O}$ . Hence, depending on the value of  $\delta^{18}\text{O}$ , there is either one or three fixed points for the motion along the dust direction: for approximately  $\delta^{18}\text{O} < -1.0$ , there is one stable fixed point; for approximately  $-1.0 < \delta^{18}\text{O} < 0.9$ , there are three fixed points, two stable ones and an unstable one between them; for approximately  $\delta^{18}\text{O} > 0.9$ , there is again just one stable fixed point. In fact, the merger of the nullcline's lower stable branch and unstable branch is not fully captured by the reconstruction due to too-low data density in the corresponding region (see Fig. 3c). With the position of these stable fixed points depending continuously on  $\delta^{18}\text{O}$  ratios, we find here the characteristic form of a *double-fold bifurcation*, in which  $\delta^{18}\text{O}$  takes the role of a control parameter.

The dust nullclines' structure supports the possibility for abrupt transitions in two ways: either random fluctuations move the system across the unstable branch (if present, depending on the value of the control parameter), or the control parameter, in this case  $\delta^{18}\text{O}$ , crosses a bifurcation point, and the currently attracting stable branch merges with the unsta-

ble branch. In both cases, the system will transition fairly abruptly to the alternative stable branch. A rate-induced transition seems implausible in this case since the unstable branch is approximately constant with respect to a change in the control parameter (i.e.  $\delta^{18}\text{O}$ ). Thus, a crossing of the unstable branch by means of a rapid shift in  $\delta^{18}\text{O}$  seems highly unlikely.

### 4.2 Coupling of the $\delta^{18}\text{O}$ drift with the dust

We now focus on the reconstructed drift  $D_{1,0}(\delta^{18}\text{O}, \text{dust})$  of the  $\delta^{18}\text{O}$  ratios (Fig. 3d). Its nullcline appears to be an explicit function of the dust; i.e. for each value of dust concentration there is a single stable fixed point along the  $\delta^{18}\text{O}$  dimension. The position of the fixed point changes with the value for dust in a continuous manner, with a high rate of change for intermediate dust values and a small change for more extreme dust values. These findings suggest that  $\delta^{18}\text{O}$  follows a mono-stable process whose fixed point is subject to change in response to an "external control" imposed by the dust.

### 4.3 Combined two-dimensional drift

Figure 3b shows the two-dimensional drift field  $F(\delta^{18}\text{O}, \text{dust})$  of the coupled system given by Eq. (5). The two fixed points which arise from the intersections of the dust nullcline's stable branches with the  $\delta^{18}\text{O}$  stable nullcline fall well within the regions of the state space associated with Greenland stadials and interstadials, respectively. The stable regime ( $\delta^{18}\text{O} \sim -1$ , dust  $\sim -1$ ) can be identified with Greenland stadials, while the stable regime ( $\delta^{18}\text{O} \sim 0.5$ , dust  $\sim 1$ ) corresponds to Greenland interstadials. Similarly, we can locate an unstable fixed point roughly in between the two observed stable fixed points of the coupled system. Judging from Fig. 3b the unstable fixed point resembles a saddle with a convergent drift along the  $\delta^{18}\text{O}$  direction and divergence along the connection line between the two stable fixed points. The system's bistability is inherited from the dust's drift and is not enshrined in the  $\delta^{18}\text{O}$  ratios. As mentioned previously, Fig. 3b suggests that – starting from a stable fixed point – perturbations along the  $\delta^{18}\text{O}$  direction will not entail state transitions but instead simply decay until the system reaches the  $\delta^{18}\text{O}$  nullcline again. In contrast, perturbations along the dust direction may shift the system into the other respective basin of attraction.

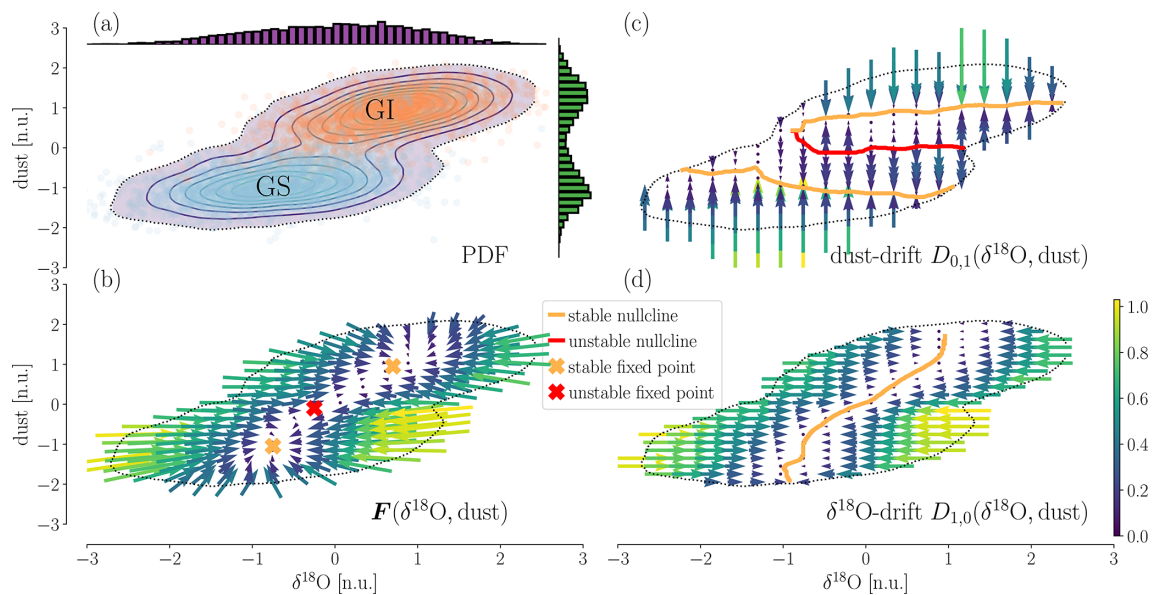


**Figure 3.** Two-dimensional drift reconstruction. **(a)** PDF of the two-dimensional record, with projections onto both dimensions. Blue and orange dots represent the individual data points from Greenland stadials (GSs) and Greenland interstadials (GIs), respectively. Contour lines are obtained from a kernel density estimate of the data distribution. The dotted contour line indicates a chosen cutoff data density of  $> 0.015$  data points per pixel; regions in the state space with lower data density are not considered in the analysis. One pixel has the size of  $0.015 \times 0.015$  in normalised units. **(b)** The reconstructed vector field  $F$  according to Eq. (5). Regions of convergence are apparent and correspond to the GI and GS states of the record. **(c)** The dust component  $D_{0,1}$  of the reconstructed drift. The dust's nullcline exhibits an S shape, with two stable branches (orange) and an unstable one in between (red), indicative of a double-fold bifurcation with  $\delta^{18}\text{O}$  as a control parameter. **(d)** The  $\delta^{18}\text{O}$  component  $D_{1,0}$  of the reconstructed drift. Here, the nullcline is comprised of a single stable branch (orange). The position of the  $\delta^{18}\text{O}$  fixed point varies with the value of the dust. Fixed points of the coupled system are given by the intersections of the two components' nullclines, marked with an X in panel (b).

#### 4.4 Rotation of the state space and the presence of a non-negligible interplay of the dust and $\delta^{18}\text{O}$

Above we argue for the existence of a double-fold bifurcation in the dust variable. In order to show that the coupling of the dust and  $\delta^{18}\text{O}$  is not a spurious result of the initial state space, we conduct an analogue analysis using a rotated state space. To rotate the state space we employ principal component analysis and obtain a new set of variables  $\mathbf{p} = (p_1, p_2)$ , with  $\mathbf{p} = \mathbf{U}(\delta^{18}\text{O}, \text{dust})^\top$ , where  $\mathbf{U}$  is given by

$$\mathbf{U} = \begin{bmatrix} -0.707 & -0.707 \\ -0.707 & 0.707 \end{bmatrix}. \quad (11)$$

In Fig. 4 we redraw Fig. 3 in the rotated state space; we observe that (i) the nullcline of  $p_1$  is now almost independent of  $p_2$ , and (ii) the  $p_2$  nullcline is still strongly dependent on  $p_1$ , while none of the rotated variables show any bifurcation. Overall, the dynamics of the dust– $\delta^{18}\text{O}$  can be explained as we introduce in Sect. 4.2, with two basins of attraction being separated by a saddle. In particular, the assessment of the drift in the rotated state space shows that the data cannot be described by a simple two-dimensional double-well potential with two axes of symmetry and decoupled dynamics along them.

## 5 Discussion

We use the two-dimensional Kramers–Moyal equation to investigate the deterministic drift of the combined dust and  $\delta^{18}\text{O}$  record from the NGRIP ice core for the time interval 59–27 kyr b2k, which exhibits pronounced DO variability. The reconstructed stability structure with two basins of attraction and a separating saddle is consistent with the regime switches observed simultaneously in both components of the record: in the  $\delta^{18}\text{O}$ –dust plane, the basins of attraction are located such that a transition from one to the other entails a change in both components. However, the analysis of the vector field (Fig. 3b) does not indicate any clear paths the system takes in order to transition between stadial and interstadial states. The shape of the nullclines can, in principle, allow for a situation where a perturbation along the  $\delta^{18}\text{O}$  direction pushes the dust across its bifurcation point, triggering a transition of the dust, which in turn stabilises the  $\delta^{18}\text{O}$  perturbation. The combined drift  $F(\mathbf{x}_1, \mathbf{x}_2)$ , however, exhibits strong restoring forces along the  $\delta^{18}\text{O}$  direction, which render this mechanism rather implausible. Viewed from either stable fixed point, perturbations along the dust direction could in contrast push the system across the basin boundary relatively easily. Certainly, a combination of noise along both

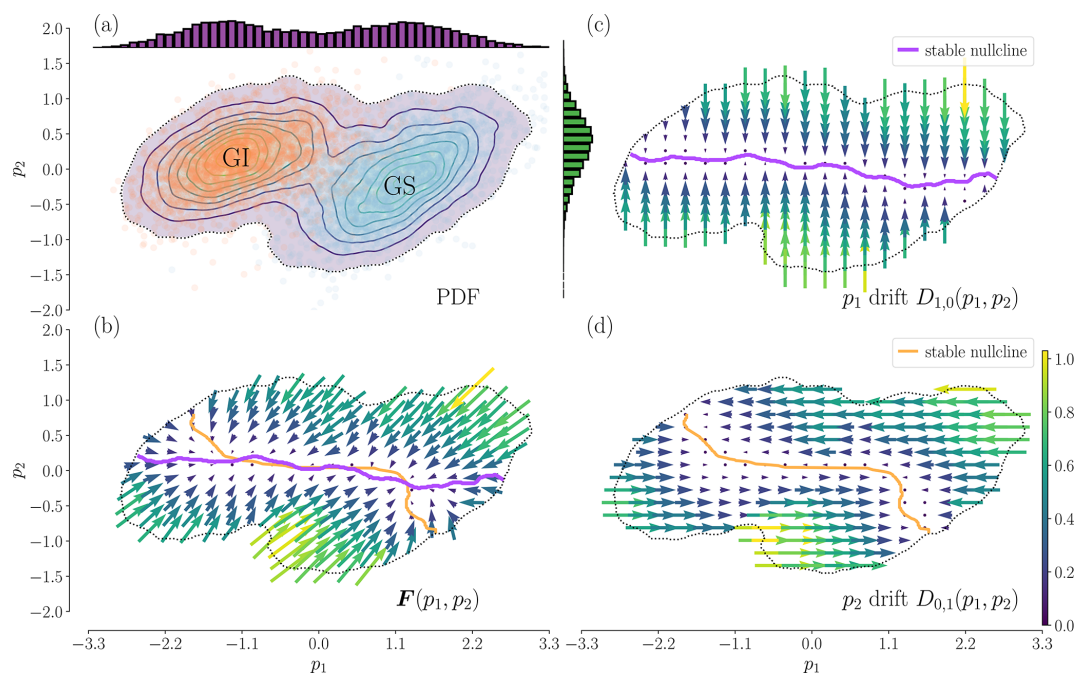


**Figure 4.** Redrawing of Fig. 3 in a rotated state space. The variables  $p_1$  and  $p_2$  represent the rotated time series, onto which the same KM analysis is performed as before. We can observe that even in this rotated setting we cannot disregard the coupling of the two variables. The doubled-fold structure is occluded by the rotation (see drift of the variable  $p_1$  in panel c). The drift of  $p_2$  remains dependent on  $p_1$  (see panel d). We can thus conclude that the observed coupling is not an artefact of the initial state space used and is an intrinsic characteristic of the two proxies.

directions may also be able to drive the system across the region of weak divergence that separates the two attractors. We note that the mild relaxation that is typical for Greenland interstadials cannot be explained by the results of this analysis alone. As mentioned previously, an estimation of the KM coefficients for the individual, univariate  $\delta^{18}\text{O}$  and dust time series indicates that at least the  $\delta^{18}\text{O}$  noise comprises non-Gaussian and potentially discontinuous components, which could play a central role with respect to the transition between the two identified stable states of the drift (Rydin Gorjão et al., 2022). However, there remain discrepancies to be reconciled in the analysis of the higher-order KM coefficients of the individual  $\delta^{18}\text{O}$  and dust time series such that arguments about the role of non-Gaussian noise in the regime transitions remain speculative at this point. Ideally, higher-order KM coefficients should be computed for the two-dimensional record; however, this is prevented by the low data resolution.

In the following, we discuss how the results presented here relate to the findings of previous studies. An important branch of research around DO events draws on low-dimensional conceptual modelling and, related to that, inverse modelling approaches with model equations being fitted to ice core data. Many of these studies build on stochastic differential equations and in particular on Langevin-type equations. Our study follows the same key paradigm, regard-

ing the paleoclimate record as the realisation of a stochastic process. However, as far as we know, it is the first study to assess the two-dimensional drift non-parametrically in the  $\delta^{18}\text{O}$ –dust plane.

For the period investigated here Livina et al. (2010) attested bistability to both the  $\delta^{18}\text{O}$  and the dust component individually by fitting a Langevin process to a 20-year-mean version of the NGRIP record. Later Kwasniok (2013) and Lohmann and Ditlevsen (2018a) showed – using techniques from Bayesian model inference – that a two-dimensional relaxation oscillator model outperforms a simple double-well potential in terms of simulating the NGRIP  $\delta^{18}\text{O}$  record. Such a relaxation oscillation still relies on a fundamental bistability in the variable that is identified with  $\delta^{18}\text{O}$  ratios. A physical interpretation for a FitzHugh–Nagumo-type DO model is provided by Vettoretti et al. (2022).

Our results contradict the interpretation that  $\delta^{18}\text{O}$  ratios and therewith Greenland temperatures bear an intrinsic bistability. In the two-dimensional setting, the apparent two-regime nature of the  $\delta^{18}\text{O}$  record can be explained by the control that the dust exerts on the  $\delta^{18}\text{O}$  fixed points and the corresponding location of the two stable fixed points in the two-dimensional drift. Since we find the bistability of the reconstructed coupled system rooted in the dust, our analysis suggests that the atmosphere may have played a more active role in stabilising the two regimes that dominated the last

glacial's Northern Hemisphere climate than many AMOC-based explanations of the DO variability suggest (Ganopolski and Rahmstorf, 2002; Clark et al., 2002; Vettoretti and Peltier, 2018; Li and Born, 2019; Menviel et al., 2020). Similarly, the observation that dust perturbations may induce state transitions may be seen as a hint that random perturbation of the atmospheric circulation can trigger DO events as proposed by, for example, Kleppin et al. (2015). In this regard, it should be noted that a multistability of the latitudinal jet stream position has been suggested – although in a somewhat different setting and sense – based on an investigation of re-analysis data of modern climate (Woollings et al., 2010). In contrast, one would not expect two distinct stable Greenland temperature regimes with all controlling factors kept fixed. This is in line with the bistability of the dust drift and the mono-stable  $\delta^{18}\text{O}$  drift revealed in our analysis.

Clearly, the state space spanned by  $\delta^{18}\text{O}$  and dust is a very particular one. On the one hand, the interpretation of the two proxies as indicators of Greenland temperatures and the hemispheric circulation state of the atmosphere bears qualitative uncertainties and should certainly not be considered a one-to-one mapping. On the other hand, other climate subsystems not directly represented in the data analysed here, like the AMOC for example, are likely to have played an important role in the physics of DO variability as well. Even if  $\delta^{18}\text{O}$  ratios and dust concentrations were to exclusively represent Greenland temperatures and the atmospheric circulation state, the recorded climate variables were certainly highly entangled with other climate variables such as the AMOC strength, the Nordic Sea's and North Atlantic's sea ice cover, or potentially North American ice sheet height (e.g. Menviel et al., 2020; Li and Born, 2019; Boers et al., 2018; Zhang et al., 2014; Dokken et al., 2013). In our analysis, such couplings are subsumed in the  $\delta$ -correlated noise term  $\xi$  – an approach which may rightfully be criticised to be overly simplistic. However, given the lack of climate proxy records that jointly represent more DO-relevant components of the climate system on the same chronology, the chosen method reasonably complements existing data-driven investigations of DO variability. For example Boers et al. (2017) similarly examined the dynamical features of the combined  $\delta^{18}\text{O}$ –dust record. They proposed a third-order polynomial two-dimensional drift in combination with a non-Markovian term and Gaussian white noise to model the coupled dynamics. While our approach is limited to a Markovian setting, it allows for more general forms of drift (and noise). Being non-parametric, it does not rely on prior model assumptions in this regard. It is not per se clear how the couplings to “hidden” climate variables (i.e. those not represented by the analysed proxy record) influence the presented drift reconstruction, and there is certainly a risk of missing a relevant part of the dynamics.

## 6 Conclusions

We have analysed the records of  $\delta^{18}\text{O}$  ratios and dust concentrations from the NGRIP ice core from a data-driven perspective. The central point of our study was to examine the stability configuration of the coupled  $\delta^{18}\text{O}$ –dust process by reconstructing its two-dimensional drift. Our findings indicate a mono-stable  $\delta^{18}\text{O}$  drift whose fixed point's position is an explicit function of the dust. The dust variable, in contrast, seems to undergo a *double-fold bifurcation* parameterised by  $\delta^{18}\text{O}$ , with a change from a single (stable) fixed point to three fixed points (two stable, one unstable) and again to a single (stable) fixed point, from small to large values of the  $\delta^{18}\text{O}$  ratio. Together, the drift components yield two stable fixed points in the coupled system surrounded by convergent regions in the  $\delta^{18}\text{O}$ –dust state space, in agreement with the two-regime nature of the coupled record. Judging from the reconstructed drift, perturbations along the dust dimension are more likely to trigger a state transition, which points to an active role of atmospheric circulation in DO variability.

Importantly, our findings question the prevailing interpretation of the two regimes observed in the isolated  $\delta^{18}\text{O}$  record as the direct signature of an intrinsic bistability. Such an intrinsic bistability can be confirmed only for the dust variable. Regarding  $\delta^{18}\text{O}$  ratios as a direct measure of the local temperature, it seems plausible that not the temperature itself is bistable but rather that the bistability is enshrined in another climate variable – or at least a regional-scale climate process or a combination of processes – that drives Greenland temperatures. The apparent two-regime nature of the  $\delta^{18}\text{O}$  record would thus only be inherited from the actual bistability of other processes. This may be the atmospheric circulation as represented by the dust proxy or another external driver not directly represented by the analysed data.

Similar investigations to ours should be applied to other pairs of Greenland proxies to investigate the corresponding two-dimensional drift. Finally, our study underlines the need for higher-resolution data, as the scarcity of data points is a limiting factor for the quality of non-parametric estimates of the KM coefficients.

**Code availability.** The code to reproduce the analysis and all figures is available at <https://doi.org/10.5281/zenodo.7898825> (Kriechers, 2023) or upon request to the corresponding author.

**Data availability.** All ice core data were obtained from the website of the Niels Bohr Institute of the University of Copenhagen <https://www.iceandclimate.nbi.ku.dk/data> (Niels Bohr Institute, 2023). The original measurements of  $\delta^{18}\text{O}$  ratios and dust concentrations go back to North Greenland Ice Core Projects members (2004) and Ruth et al. (2003), respectively. The 5 cm resolution  $\delta^{18}\text{O}$  ratio and dust concentration data together with corresponding GICC05 ages used for this study can be downloaded from [https://www.iceandclimate.nbi.ku.dk/data/NGRIP\\_d18O\\_](https://www.iceandclimate.nbi.ku.dk/data/NGRIP_d18O_)

and\_dust\_5cm.xls (last access: 4 May 2023). The  $\delta^{18}\text{O}$  data shown in Fig. 1 with 20-year resolution that cover the period 122–10 kyr b2k are available from [https://www.iceandclimate.nbi.ku.dk/data/GICC05modelext\\_GRIP\\_and\\_GISP2\\_and\\_resampled\\_data\\_series\\_Seierstad\\_et\\_al.\\_2014\\_version\\_10Dec2014-2.xlsx](https://www.iceandclimate.nbi.ku.dk/data/GICC05modelext_GRIP_and_GISP2_and_resampled_data_series_Seierstad_et_al._2014_version_10Dec2014-2.xlsx) (last access: 4 May 2023) likewise hosted on website indicated above (Niels Bohr Institute, 2023). They were published in conjunction with the work by Rasmussen et al. (2014) and Seierstad et al. (2014). The corresponding dust data, also shown in Fig. 1 and covering the period 108–10 kyr b2k, is due to Ruth et al. (2003) and can be retrieved from the website of the Niels Bohr Institute (2023) ([https://www.iceandclimate.nbi.ku.dk/data/NGRIP\\_dust\\_on\\_GICC05\\_20y\\_december2014.txt](https://www.iceandclimate.nbi.ku.dk/data/NGRIP_dust_on_GICC05_20y_december2014.txt), last access: 4 May 2023). The global-average surface temperature reconstructions is available as a supplement to Snyder (2016) and the direct link for the download is [https://static-content.springer.com/esm/art%3A10.1038%2Fnature19798/MediaObjects/41586\\_2016\\_BFnature19798\\_MOESM258\\_ESM.xlsx](https://static-content.springer.com/esm/art%3A10.1038%2Fnature19798/MediaObjects/41586_2016_BFnature19798_MOESM258_ESM.xlsx) (last access: 4 May 2023).

**Author contributions.** KR and LRG designed the study with contributions from all authors. KR and LRG conducted the numerical analysis. KR and LRG wrote the paper with contributions from all authors.

**Competing interests.** The contact author has declared that none of the authors has any competing interests.

**Disclaimer.** Publisher's note: Copernicus Publications remains neutral with regard to jurisdictional claims in published maps and institutional affiliations.

**Acknowledgements.** Leonardo Rydin Gorjão and Dirk Witthaut gratefully acknowledge support from the Helmholtz Association via the grant “Uncertainty Quantification – From Data to Reliable Knowledge” (UQ; grant agreement no. ZT-I-0029). This work was performed by Leonardo Rydin Gorjão as part of the Helmholtz School for Data Science in Life, Earth and Energy (HDS-LEE). Niklas Boers acknowledges funding from the Volkswagen Foundation. This is TiPES contribution no. 162; the “Tipping Points in the Earth System” (TiPES) project has received funding from the European Union's Horizon 2020 research and innovation programme under grant agreement no. 820970.

**Financial support.** This research has received funding from the European Union's Horizon 2020 research and innovation programme (TiPES; grant no. 820970), the Helmholtz-Gemeinschaft (grant nos. ZT-I-0029 and HIDD-0004), and the Volkswagen Foundation.

This work was supported by the Technical University of Munich (TUM) in the framework of the Open Access Publishing Program.

**Review statement.** This paper was edited by Valerio Lucarini and reviewed by Peter Ditlevsen, Tamas Bodai, Christian Franzke, Mohammed Reza Rahimi Tabar, and one anonymous referee.

## References

- Andersen, K. K., Svensson, A., Johnsen, S. J., Rasmussen, S. O., Bigler, M., Röthlisberger, R., Ruth, U., Siggaard-Andersen, M. L., Peder Steffensen, J., Dahl-Jensen, D., Vinther, B. M., and Clausen, H. B.: The Greenland Ice Core Chronology 2005, 15–42 ka, Part 1: constructing the time scale, *Quaternary Sci. Rev.*, 25, 3246–3257, <https://doi.org/10.1016/j.quascirev.2006.08.002>, 2006.
- Anvari, M., Tabar, M. R. R., Peinke, J., and Lehnertz, K.: Disentangling the stochastic behavior of complex time series, *Sci. Rep.*, 6, 35435, <https://doi.org/10.1038/srep35435>, 2016.
- Armstrong McKay, D. I., Staal, A., Abrams, J. F., Winkelmann, R., Sakschewski, B., Loriani, S., Fetzer, I., Cornell, S. E., Rockström, J., and Lenton, T. M.: Exceeding 1.5 °C global warming could trigger multiple climate tipping points, *Science*, 377, eabn7950, <https://doi.org/10.1126/science.abn7950>, 2022.
- Ashwin, P., Wieczorek, S., Vitolo, R., and Cox, P.: Tipping points in open systems: Bifurcation, noise-induced and rate-dependent examples in the climate system, *Philos. T. R. Soc. A*, 370, 1166–1184, <https://doi.org/10.1098/rsta.2011.0306>, 2012.
- Boers, N.: Observation-based early-warning signals for a collapse of the Atlantic Meridional Overturning Circulation, *Nat. Clim. Change*, 11, 680–688, <https://doi.org/10.1038/s41558-021-01097-4>, 2021.
- Boers, N. and Rypdal, M.: Critical slowing down suggests that the western Greenland Ice Sheet is close to a tipping point, *P. Natl. Acad. Sci. USA*, 118, e2024192118, <https://doi.org/10.1073/pnas.2024192118>, 2021.
- Boers, N., Chekroun, M. D., Liu, H., Kondrashov, D., Rousseau, D.-D., Svensson, A., Bigler, M., and Ghil, M.: Inverse stochastic-dynamic models for high-resolution Greenland ice core records, *Earth Syst. Dynam.*, 8, 1171–1190, <https://doi.org/10.5194/esd-8-1171-2017>, 2017.
- Boers, N., Ghil, M., and Rousseau, D. D.: Ocean circulation, ice shelf, and sea ice interactions explain Dansgaard-Oeschger cycles, *P. Natl. Acad. Sci. USA*, 115, E11005–E11014, <https://doi.org/10.1073/pnas.1802573115>, 2018.
- Boers, N., Ghil, M., and Stocker, T. F.: Theoretical and paleoclimatic evidence for abrupt transitions in the Earth system, *Environ. Res. Lett.*, 17, 093006, <https://doi.org/10.1088/1748-9326/ac8944>, 2022.
- Boulton, C. A., Allison, L. C., and Lenton, T. M.: Early warning signals of Atlantic Meridional Overturning Circulation collapse in a fully coupled climate model, *Nat. Commun.*, 5, 5752, <https://doi.org/10.1038/ncomms6752>, 2014.
- Boulton, C. A., Lenton, T. M., and Boers, N.: Pronounced loss of Amazon rainforest resilience since the early 2000s, *Nat. Clim. Change*, 12, 271–278, <https://doi.org/10.1038/s41558-022-01287-8>, 2022.
- Brovkin, V., Brook, E., Williams, J. W., Bathiany, S., Lenton, T. M., Barton, M., DeConto, R. M., Donges, J. F., Ganopolski, A., McManus, J., Praetorius, S., de Vernal, A., Abe-Ouchi, A., Cheng, H., Claussen, M., Crucifix, M., Gallopín, G., Iglesias, V., Kaufman, D. S., Kleinen, T., Lambert, F., van der Leeuw, S., Liddy,

- H., Loutre, M.-f., McGee, D., Rehfeld, K., Rhodes, R., Seddon, A. W. R., Trauth, M. H., Vanderveken, L., and Yu, Z.: Past abrupt changes, tipping points and cascading impacts in the Earth system, *Nat. Geosci.*, 14, 550–558, <https://doi.org/10.1038/s41561-021-00790-5>, 2021.
- Cheng, H., Sinha, A., Cruz, F. W., Wang, X., Edwards, R. L., D'Horta, F. M., Ribas, C. C., Vuille, M., Stott, L. D., and Auler, A. S.: Climate change patterns in Amazonia and biodiversity, *Nat. Commun.*, 4, 1411, <https://doi.org/10.1038/ncomms2415>, 2013.
- Clark, P. U., Pisias, N. G., Stocker, T. F., and Weaver, A. J.: The role of the thermohaline circulation in abrupt climate change, *Nature*, 415, 863–869, <https://doi.org/10.1038/415863a>, 2002.
- Corrick, E. C., Drysdale, R. N., Hellstrom, J. C., Capron, E., Rasmussen, S. O., Zhang, X., Fleitmann, D., Couchoud, I., Wolff, E., and Monsoon, S. A.: Synchronous timing of abrupt climate changes during the last glacial period, *Science*, 369, 963–969, <https://doi.org/10.1126/science.aay5538>, 2020.
- Dansgaard, W., Clausen, H. B., Gundestrup, N., Hammer, C. U., Johnsen, S. F., Kristinsdottir, P. M., and Reeh, N.: A New Greenland Deep Ice Core, *Science*, 218, 1273–1278, <https://doi.org/10.1126/science.218.4579.1273>, 1982.
- Dansgaard, W., Johnsen, S., Clausen, H., Dahl-Jensen, D., Gundestrup, N., Hammer, C., and Oeschger, H.: North Atlantic Climatic Oscillations Revealed by Deep Greenland Ice Cores, *American Geophysical Union*, 29, 288–298, <https://doi.org/10.1029/GM029p0288>, 1984.
- Dansgaard, W., Johnsen, S. J., Clausen, H. B., Dahl-Jensen, D., Gundestrup, N. S., Hammer, C. U., Hvidberg, C. S., Steffensen, J. P., Sveinbjörnsdottir, A. E., Jouzel, J., and Bond, G.: Evidence for general instability of past climate from a 250-kyr ice-core record, *Nature*, 364, 218–220, <https://doi.org/10.1038/364218a0>, 1993.
- Davis, W. and Buffett, B.: Estimation of drift and diffusion functions from unevenly sampled time-series data, *Phys. Rev. E*, 106, 014140, <https://doi.org/10.1103/PhysRevE.106.014140>, 2022.
- Ditlevsen, P. D.: Observation of  $\alpha$ -stable noise induced millennial climate changes from an ice-core record, *Geophys. Res. Lett.*, 26, 1441–1444, <https://doi.org/10.1029/1999GL900252>, 1999.
- Dokken, T. M., Nisancioglu, K. H., Li, C., Battisti, D. S., and Kissel, C.: Dansgaard–Oeschger cycles: Interactions between ocean and sea ice intrinsic to the Nordic seas, *Paleoceanography*, 28, 491–502, <https://doi.org/10.1002/palo.20042>, 2013.
- Epanechnikov, V. A.: Non-Parametric Estimation of a Multivariate Probability Density, *Theory Probab. Appl.*, 14, 153–158, <https://doi.org/10.1137/1114019>, 1967.
- EPICA Community Members: One-to-one coupling of glacial climate variability in Greenland and Antarctica, *Nature*, 444, 5–8, <https://doi.org/10.1038/nature05301>, 2006.
- Erhardt, T., Capron, E., Olander Rasmussen, S., Schüpbach, S., Bigler, M., Adolphi, F., and Fischer, H.: Decadal-scale progression of the onset of Dansgaard–Oeschger warming events, *Clim. Past*, 15, 811–825, <https://doi.org/10.5194/cp-15-811-2019>, 2019.
- Fischer, H., Siggaard-Andersen, M. L., Ruth, U., Röthlisberger, R., and Wolff, E.: Glacial/interglacial changes in mineral dust and sea-salt records in polar ice cores: Sources, transport, and deposition, *Rev. Geophys.*, 45, 1–26, <https://doi.org/10.1029/2005RG000192>, 2007.
- Ganopolski, A. and Rahmstorf, S.: Abrupt Glacial Climate Changes due to Stochastic Resonance, *Phys. Rev. Lett.*, 88, 038501, <https://doi.org/10.1103/PhysRevLett.88.038501>, 2002.
- Gardiner, C.: *Stochastic Methods: A Handbook for the Natural and Social Sciences*, Springer-Verlag Berlin Heidelberg, 4th Edn., ISBN 3-540-15607-0, 2009.
- Ghil, M.: *Steady-State Solutions of a Diffusive Energy-Balance Climate Model and Their Stability*, Tech. Rep. IMM410, Courant Institute of Mathematical Sciences, New York University, New York, <https://ntrs.nasa.gov/api/citations/19750014903/downloads/19750014903.pdf> (last access: 28 April 2023), 1975.
- Gkinis, V., Simonsen, S. B., Buchardt, S. L., White, J. W., and Vinther, B. M.: Water isotope diffusion rates from the North-GRIP ice core for the last 16,000 years – Glaciological and paleoclimatic implications, *Earth Planet. Sc. Lett.*, 405, 132–141, <https://doi.org/10.1016/j.epsl.2014.08.022>, 2014.
- Gottschalk, J., Skinner, L. C., Misra, S., Waelbroeck, C., Menviel, L., and Timmermann, A.: Abrupt changes in the southern extent of North Atlantic Deep Water during Dansgaard-Oeschger events, *Nat. Geosci.*, 8, 950–954, <https://doi.org/10.1038/ngeo2558>, 2015.
- Harris, C. R., Millman, K. J., van der Walt, S. J., Gommers, R., Virtanen, P., Cournapeau, D., Wieser, E., Taylor, J., Berg, S., Smith, N. J., Kern, R., Picus, M., Hoyer, S., van Kerkwijk, M. H., Brett, M., Haldane, A., Fernández del Río, J., Wiebe, M., Peterson, Pearu and Gérard-Marchant, P., Sheppard, K., Reddy, T., Weckesser, W., Abbasi, H., Gohlke, C., and Oliphant, T. E.: Array programming with NumPy, *Nature*, 585, 357–362, <https://doi.org/10.1038/s41586-020-2649-2>, 2020.
- Henry, L. G., McManus, J. F., Curry, W. B., Roberts, N. L., Piotrowski, A. M., and Keigwin, L. D.: North Atlantic ocean circulation and abrupt climate change during the last glaciation, *Science*, 353, 470–474, <https://doi.org/10.1126/science.aaf5529>, 2016.
- Hunter, J. D.: Matplotlib: A 2D Graphics Environment, *Comput. Sci. Eng.*, 9, 90–95, <https://doi.org/10.1109/MCSE.2007.55>, 2007.
- Johnsen, S. J., Clausen, H. B., Dansgaard, W., Fuhrer, K., Gundestrup, N., Hammer, C. U., Iversen, P., Jouzel, J., Stauffer, B., and Steffensen, J.: Irregular glacial interstadials recorded in a new Greenland ice core, *Nature*, 359, 311–313, <https://doi.org/10.1038/359311a0>, 1992.
- Johnsen, S. J., Dahl-Jensen, D., Gundestrup, N., Steffensen, J. P., Clausen, H. B., Miller, H., Masson-Delmotte, V., Sveinbjörnsdottir, A. E., and White, J.: Oxygen isotope and palaeotemperature records from six Greenland ice-core stations: Camp Century, Dye-3, GRIP, GISP2, Renland and NorthGRIP, *J. Quaternary Sci.*, 16, 299–307, <https://doi.org/10.1002/jqs.622>, 2001.
- Jouzel, J., Alley, R. B., Cuffey, K. M., Dansgaard, W., Grootes, P., Hoffmann, G., Johnsen, S. J., Koster, R. D., Peel, D., Shuman, C. A., Stievenard, M., Stuiver, M., and White, J.: Validity of the temperature reconstruction from water isotopes in ice cores, *J. Geophys. Res.-Ocean.*, 102, 26471–26487, <https://doi.org/10.1029/97JC01283>, 1997.
- Kanner, L. C., Burns, S. J., Cheng, H., and Edwards, R. L.: High-Latitude Forcing of the South American Summer Monsoon During the Last Glacial, *Science*, 335, 570–573, <https://doi.org/10.1126/science.1213397>, 2012.

- Kindler, P., Guillevic, M., Baumgartner, M., Schwander, J., Landais, A., and Leuenberger, M.: Temperature reconstruction from 10 to 120 kyr b2k from the NGRIP ice core, *Clim. Past*, 10, 887–902, <https://doi.org/10.5194/cp-10-887-2014>, 2014.
- Kleppin, H., Jochum, M., Otto-Bliesner, B., Shields, C. A., and Yeager, S.: Stochastic atmospheric forcing as a cause of Greenland climate transitions, *J. Clim.*, 28, 7741–7763, <https://doi.org/10.1175/JCLI-D-14-00728.1>, 2015.
- Kondrashov, D., Kravtsov, S., Robertson, A. W., and Ghil, M.: A Hierarchy of Data-Based ENSO Models, *J. Clim.*, 18, 4425–4444, <https://doi.org/10.1175/JCLI3567.1>, 2005.
- Kondrashov, D., Chekroun, M. D., and Ghil, M.: Data-driven non-Markovian closure models, *Physica D*, 297, 33–55, <https://doi.org/10.1016/j.physd.2014.12.005>, 2015.
- Kramers, H. A.: Brownian motion in a field of force and the diffusion model of chemical reactions, *Physica*, 7, 284–304, [https://doi.org/10.1016/S0031-8914\(40\)90098-2](https://doi.org/10.1016/S0031-8914(40)90098-2), 1940.
- Kriechers, R.: kriechers/esd-2021-95: esd-2021-95 (Version v1), Zenodo [code], <https://doi.org/10.5281/zenodo.7898825>, 2023.
- Kwasniok, F.: Analysis and modelling of glacial climate transitions using simple dynamical systems, *Philos. T. R. Soc. A*, 371, 20110472, <https://doi.org/10.1098/rsta.2011.0472>, 2013.
- Lamouroux, D. and Lehnertz, K.: Kernel-based regression of drift and diffusion coefficients of stochastic processes, *Phys. Lett. A*, 373, 3507–3512, <https://doi.org/10.1016/j.physleta.2009.07.073>, 2009.
- Lehnertz, K., Zabawa, L., and Tabar, M. R. R.: Characterizing abrupt transitions in stochastic dynamics, *New J. Phys.*, 20, 113043, <https://doi.org/10.1088/1367-2630/aaf0d7>, 2018.
- Lenton, T., Held, H., Kriegler, E., Hall, J. W., Lucht, W., Rahmstorf, S., and Schellnhuber, H. J.: Tipping elements in the Earth's climate system, *P. Natl. Acad. Sci. USA*, 105, 1786–1793, <https://doi.org/10.1073/pnas.0705414105>, 2008.
- Lenton, T. M. and Schellnhuber, H. J.: Tipping the Scales, *Nat. Clim. Change*, 1, 97–98, <https://doi.org/10.1038/climate.2007.65>, 2007.
- Li, C. and Born, A.: Coupled atmosphere-ice-ocean dynamics in Dansgaard-Oeschger events, *Quaternary Sci. Rev.*, 203, 1–20, <https://doi.org/10.1016/j.quascirev.2018.10.031>, 2019.
- Li, T.-Y., Han, L.-Y., Cheng, H., Edwards, R. L., Shen, C.-C., Li, H.-C., Li, J.-Y., Huang, C.-X., Zhang, T.-T., and Zhao, X.: Evolution of the Asian summer monsoon during Dansgaard/Oeschger events 13–17 recorded in a stalagmite constrained by high-precision chronology from southwest China, *Quaternary Res.*, 88, 121–128, <https://doi.org/10.1017/qua.2017.22>, 2017.
- Livina, V. N., Kwasniok, F., and Lenton, T. M.: Potential analysis reveals changing number of climate states during the last 60 kyr, *Clim. Past*, 6, 77–82, <https://doi.org/10.5194/cp-6-77-2010>, 2010.
- Lohmann, J. and Ditlevsen, P. D.: A consistent statistical model selection for abrupt glacial climate changes, *Clim. Dynam.*, 52, 6411–6426, <https://doi.org/10.1007/s00382-018-4519-2>, 2018a.
- Lohmann, J. and Ditlevsen, P. D.: Random and externally controlled occurrences of Dansgaard-Oeschger events, *Clim. Past*, 14, 609–617, <https://doi.org/10.5194/cp-14-609-2018>, 2018b.
- Lynch-Stieglitz, J.: The Atlantic Meridional Overturning Circulation and Abrupt Climate Change, *Annu. Rev. Mar. Sci.*, 9, 83–104, <https://doi.org/10.1146/annurev-marine-010816-060415>, 2017.
- Majda, A. J., Franzke, C. L., Fischer, A., and Crommelin, D. T.: Distinct metastable atmospheric regimes despite nearly Gaussian statistics: A paradigm model, *P. Natl. Acad. Sci. USA*, 103, 8309–8314, <https://doi.org/10.1073/pnas.0602641103>, 2006.
- McKinney, W.: Data Structures for Statistical Computing in Python, in: *Proceedings of the 9th Python in Science Conference*, 28 June–3 July 2010, Austin, Texas, edited by: van der Walt, S. and Millman, J., 56–61, <https://doi.org/10.25080/Majora-92bf1922-00a>, 2010.
- Menviel, L. C., Skinner, L. C., Tarasov, L., and Tzedakis, P. C.: An ice-climate oscillatory framework for Dansgaard-Oeschger cycles, *Nat. Rev. Earth Environ.*, 1, 677–693, <https://doi.org/10.1038/s43017-020-00106-y>, 2020.
- Mitsui, T. and Crucifix, M.: Influence of external forcings on abrupt millennial-scale climate changes: a statistical modelling study, *Clim. Dynam.*, 48, 2729–2749, <https://doi.org/10.1007/s00382-016-3235-z>, 2017.
- Moyal, J. E.: Stochastic processes and statistical physics, *J. R. Stat. Soc. Ser. B*, 11, 150–210, 1949.
- Nadaraya, E. A.: On Estimating Regression, *Theor. Probab. Appl.*, 9, 141–142, <https://doi.org/10.1137/1109020>, 1964.
- Niels Bohr Institute: Center for Ice and Climate – Data ice-samples and software, University of Copenhagen, Copenhagen, Denmark, [data sets], <https://www.iceandclimate.nbi.ku.dk/data/> and [https://www.iceandclimate.nbi.ku.dk/data/NGRIP\\_dust\\_on\\_GICC05\\_20y\\_december2014.txt](https://www.iceandclimate.nbi.ku.dk/data/NGRIP_dust_on_GICC05_20y_december2014.txt), last access: 28 April 2023.
- North, G. R.: Analytical Solution to a Simple Climate Model with Diffusive Heat Transport, *J. Atmos. Sci.*, 32, 1301–1307, [https://doi.org/10.1175/1520-0469\(1975\)032<1301:ASTASC>2.0.CO;2](https://doi.org/10.1175/1520-0469(1975)032<1301:ASTASC>2.0.CO;2), 1975.
- North Greenland Ice Core Project members: High-resolution record of Northern Hemisphere climate extending into the last interglacial period, *Nature*, 431, 147–151, <https://doi.org/10.1038/nature02805>, 2004.
- Rasmussen, S. O., Andersen, K. K., Svensson, A. M., Steffensen, J. P., Vinther, B. M., Clausen, H. B., Siggaard-Andersen, M. L., Johnsen, S. J., Larsen, L. B., Dahl-Jensen, D., Bigler, M., Röthlisberger, R., Fischer, H., Goto-Azuma, K., Hansson, M. E., and Ruth, U.: A new Greenland ice core chronology for the last glacial termination, *J. Geophys. Res.-Atmos.*, 111, D06102, <https://doi.org/10.1029/2005JD006079>, 2006.
- Rasmussen, S. O., Bigler, M., Blockley, S. P., Blunier, T., Buchardt, S. L., Clausen, H. B., Cvijanovic, I., Dahl-Jensen, D., Johnsen, S. J., Fischer, H., Gkinis, V., Guillevic, M., Hoek, W. Z., Lowe, J. J., Pedro, J. B., Popp, T., Seierstad, I. K., Steffensen, J. P., Svensson, A. M., Vallelonga, P., Vinther, B. M., Walker, M. J., Wheatley, J. J., and Winstrup, M.: A stratigraphic framework for abrupt climatic changes during the Last Glacial period based on three synchronized Greenland ice-core records: Refining and extending the INTIMATE event stratigraphy, *Quaternary Sci. Rev.*, 106, 14–28, <https://doi.org/10.1016/j.quascirev.2014.09.007>, 2014.
- Rial, J. A. and Saha, R.: Modeling Abrupt Climate Change as the Interaction Between Sea Ice Extent and Mean Ocean Temperature Under Orbital Insolation Forcing, in: *Abrupt Climate Change: Mechanisms, Patterns, and Impact in 2011*, edited by: Rashid, H., Polyak, L., and Mosley-Thompson, E., American Geophysical Union (AGU), 57–74, <https://doi.org/10.1029/2010GM001027>, 2011.

- Risken, H. and Frank, T.: The Fokker–Planck equation, Springer-Verlag, Berlin, Heidelberg, 2nd Edn., <https://doi.org/10.1007/978-3-642-61544-3>, 1996.
- Roberts, A. and Saha, R.: Relaxation oscillations in an idealized ocean circulation model, *Clim. Dynam.*, 48, 2123–2134, <https://doi.org/10.1007/s00382-016-3195-3>, 2017.
- Rosier, S. H. R., Reese, R., Donges, J. F., De Rydt, J., Gudmundsson, G. H., and Winkelmann, R.: The tipping points and early warning indicators for Pine Island Glacier, West Antarctica, *The Cryosphere*, 15, 1501–1516, <https://doi.org/10.5194/tc-15-1501-2021>, 2021.
- Ruth, U., Wagenbach, D., Steffensen, J. P., and Bigler, M.: Continuous record of microparticle concentration and size distribution in the central Greenland NGRIP ice core during the last glacial period, *J. Geophys. Res.-Atmos.*, 108, 4098, <https://doi.org/10.1029/2002JD002376>, 2003.
- Ruth, U., Bigler, M., Röthlisberger, R., Siggaard-Andersen, M. L., Kipfstuhl, S., Goto-Azuma, K., Hansson, M. E., Johnsen, S. J., Lu, H., and Steffensen, J. P.: Ice core evidence for a very tight link between North Atlantic and east Asian glacial climate, *Geophys. Res. Lett.*, 34, L03706, <https://doi.org/10.1029/2006GL027876>, 2007.
- Rydin Gorjão, L. and Meirinhos, F.: `kramersmoyal`: Kramers–Moyal coefficients for stochastic processes, *J. Open Sour. Softw.*, 4, 1693, <https://doi.org/10.21105/joss.01693>, 2019.
- Rydin Gorjão, L., Heysel, J., Lehnertz, K., and Tabar, M. R. R.: Analysis and data-driven reconstruction of bivariate jump-diffusion processes, *Phys. Rev. E*, 100, 062127, <https://doi.org/10.1103/PhysRevE.100.062127>, 2019.
- Rydin Gorjão, L., Riechers, K., Hassanibesheli, F., Lind, P. G., Boers, N., and Witthaut, D.: Disentangling discontinuous trajectories in paleoclimate data with the Kramers–Moyal equation, in preparation, 2023.
- Schüpbach, S., Fischer, H., Bigler, M., Erhardt, T., Gfeller, G., Leuenberger, D., Mini, O., Mulvaney, R., Abram, N. J., Fleet, L., Frey, M. M., Thomas, E., Svensson, A., Dahl-Jensen, D., Kettner, E., Kjaer, H., Seierstad, I., Steffensen, J. P., Rasmussen, S. O., Vallelonga, P., Winstrup, M., Wegner, A., Twarloh, B., Wolff, K., Schmidt, K., Goto-Azuma, K., Kuramoto, T., Hirabayashi, M., Uetake, J., Zheng, J., Bourgeois, J., Fisher, D., Zhiheng, D., Xiao, C., Legrand, M., Spolaor, A., Gabrieli, J., Barbante, C., Kang, J. H., Hur, S. D., Hong, S. B., Hwang, H. J., Hong, S., Hansson, M., Iizuka, Y., Oyabu, I., Muscheler, R., Adolphi, F., Maselli, O., McConnell, J., and Wolff, E. W.: Greenland records of aerosol source and atmospheric lifetime changes from the Eemian to the Holocene, *Nat. Commun.*, 9, 1476, <https://doi.org/10.1038/s41467-018-03924-3>, 2018.
- Seierstad, I. K., Abbott, P. M., Bigler, M., Blunier, T., Bourne, A. J., Brook, E., Buchardt, S. L., Buizert, C., Clausen, H. B., Cook, E., Dahl-Jensen, D., Davies, S. M., Guillevic, M., Johnsen, S. J., Pedersen, D. S., Popp, T. J., Rasmussen, S. O., Severinghaus, J. P., Svensson, A., and Vinther, B. M.: Consistently dated records from the Greenland GRIP, GISP2 and NGRIP ice cores for the past 104 ka reveal regional millennial-scale  $\delta^{18}\text{O}$  gradients with possible Heinrich event imprint, *Quaternary Sci. Rev.*, 106, 29–46, <https://doi.org/10.1016/j.quascirev.2014.10.032>, 2014.
- Silverman, B. W.: Density Estimation for Statistics and Data Analysis, Routledge, Boca Raton, 1st Edn., <https://doi.org/10.1201/9781315140919>, 1998.
- Snyder, C. W.: Evolution of global temperature over the past two million years, *Nature*, 538, 226–228, <https://doi.org/10.1038/nature19798>, 2016.
- Stommel, H.: Thermohaline Convection with Two Stable Regimes, *Tellus*, 13, 224–230, 1961.
- Svensson, A., Andersen, K. K., Bigler, M., Clausen, H. B., Dahl-Jensen, D., Davies, S. M., Johnsen, S. J., Muscheler, R., Parrenin, F., Rasmussen, S. O., Röthlisberger, R., Seierstad, I., Steffensen, J. P., and Vinther, B. M.: A 60 000 year Greenland stratigraphic ice core chronology, *Clim. Past*, 4, 47–57, <https://doi.org/10.5194/cp-4-47-2008>, 2008.
- Tabar, M. R. R.: Analysis and Data-Based Reconstruction of Complex Nonlinear Dynamical Systems, Springer International Publishing, <https://doi.org/10.1007/978-3-030-18472-8>, 2019.
- Valdes, P.: Built for stability, *Nat. Geosci.*, 4, 414–416, <https://doi.org/10.1038/ngeo1200>, 2011.
- Vettoretti, G. and Peltier, W. R.: Fast physics and slow physics in the nonlinear Dansgaard–Oeschger relaxation oscillation, *J. Clim.*, 31, 3423–3449, <https://doi.org/10.1175/JCLI-D-17-0559.1>, 2018.
- Vettoretti, G., Ditlevsen, P., Jochum, M., and Rasmussen, S. O.: Atmospheric CO<sub>2</sub> control of spontaneous millennial-scale ice age climate oscillations, *Nat. Geosci.*, 15, 300–306, <https://doi.org/10.1038/s41561-022-00920-7>, 2022.
- Vinther, B. M., Clausen, H. B., Johnsen, S. J., Rasmussen, S. O., Andersen, K. K., Buchardt, S. L., Dahl-Jensen, D., Seierstad, I. K., Siggaard-Andersen, M. L., Steffensen, J. P., Svensson, A., Olsen, J., and Heinemeier, J.: A synchronized dating of three Greenland ice cores throughout the Holocene, *J. Geophys. Res.-Atmos.*, 111, D13102, <https://doi.org/10.1029/2005JD006921>, 2006.
- Virtanen, P., Gommers, R., Oliphant, T. E., Haberland, M., Reddy, T., Cournapeau, D., Burovski, E., Peterson, P., Weckesser, W., Bright, J., van der Walt, S. J., Brett, M., Wilson, J., Millman, K. J., Mayorov, N., Nelson, A. R. J., Jones, E., Kern, R., Larson, E., Carey, C. J., Polat, İ., Feng, Y., Moore, E. W., VanderPlas, J., Laxalde, D., Perktold, J., Cimrman, R., Henriksen, I., Quintero, E. A., Harris, C. R., Archibald, A. M., Ribeiro, A. H., Pedregosa, F., van Mulbregt, P., and SciPy 1.0 contributors: SciPy 1.0: Fundamental Algorithms for Scientific Computing in Python, *Nat. Method.*, 17, 261–272, <https://doi.org/10.1038/s41592-019-0686-2>, 2020.
- Voelker, A. H.: Global distribution of centennial-scale records for Marine Isotope Stage (MIS) 3: A database, *Quaternary Sci. Rev.*, 21, 1185–1212, [https://doi.org/10.1016/S0277-3791\(01\)00139-1](https://doi.org/10.1016/S0277-3791(01)00139-1), 2002.
- WAIS Divide Project Members: Precise inter-polar phasing of abrupt climate change during the last ice age, *Nature*, 520, 661–665, <https://doi.org/10.1038/nature14401>, 2015.
- Wang, Y. J., Cheng, H., Edwards, R. L., An, Z. S., Wu, J. Y., Shen, C. C., and Dorale, J. A.: A high-resolution absolute-dated late pleistocene monsoon record from Hulu Cave, China, *Science*, 294, 2345–2348, <https://doi.org/10.1126/science.1064618>, 2001.
- Watson, G. S.: Smooth Regression Analysis, *Sankhyā: Smooth Regression Analysis, Sankhya A*, 26, 359–372, 1964.

Woollings, T., Hannachi, A., and Hoskins, B.: Variability of the North Atlantic eddy-driven jet stream, *Q. J. Roy. Meteor. Soc.*, 136, 856–868, <https://doi.org/10.1002/qj.625>, 2010.

Zhang, X., Lohmann, G., Knorr, G., and Purcell, C.: Abrupt glacial climate shifts controlled by ice sheet changes, *Nature*, 512, 290–294, <https://doi.org/10.1038/nature13592>, 2014.

## 6 Uncertainty-sensitive inference on the course of DO events

### P4 Significance of uncertain phasing between the onsets of stadial–interstadial transitions in different Greenland ice core proxies

**Keno Riechers** & Niklas Boers, 2021. *Climate of the Past*, 17, 1751–1775.

**Copyright.** The article is published open access under the terms of the [Creative Commons Attribution-NonCommercial](#) license. The copyright remains with the authors.

**Contribution.** KR and NB conceived the study. KR carried out the numerical analysis. KR and NB discussed and interpreted the results and wrote the paper.

Clim. Past, 17, 1751–1775, 2021  
<https://doi.org/10.5194/cp-17-1751-2021>  
 © Author(s) 2021. This work is distributed under  
 the Creative Commons Attribution 4.0 License.



## Significance of uncertain phasing between the onsets of stadial–interstadial transitions in different Greenland ice core proxies

Keno Riechers<sup>1,2</sup> and Niklas Boers<sup>1,2,3</sup>

<sup>1</sup>Department of Mathematics and Computer Science, Freie Universität Berlin, Berlin, Germany

<sup>2</sup>Potsdam Institute for Climate Impact Research (PIK), Member of the Leibniz Association, P.O. Box 60 12 03, 14412 Potsdam, Germany

<sup>3</sup>Department of Mathematics and Global Systems Institute, University of Exeter, Exeter, UK

**Correspondence:** Keno Riechers ([riechers@pik-potsdam.de](mailto:riechers@pik-potsdam.de))

Received: 21 October 2020 – Discussion started: 10 November 2020

Revised: 1 July 2021 – Accepted: 5 July 2021 – Published: 26 August 2021

**Abstract.** Different paleoclimate proxy records evidence repeated abrupt climate transitions during previous glacial intervals. These transitions are thought to comprise abrupt warming and increase in local precipitation over Greenland, sudden reorganization of the Northern Hemisphere atmospheric circulation, and retreat of sea ice in the North Atlantic. The physical mechanism underlying these so-called Dansgaard–Oeschger (DO) events remains debated. A recent analysis of Greenland ice core proxy records found that transitions in  $\text{Na}^+$  concentrations and  $\delta^{18}\text{O}$  values are delayed by about 1 decade with respect to corresponding transitions in  $\text{Ca}^{2+}$  concentrations and in the annual layer thickness during DO events. These delays are interpreted as a temporal lag of sea-ice retreat and Greenland warming with respect to a synoptic- and hemispheric-scale atmospheric reorganization at the onset of DO events and may thereby help constrain possible triggering mechanisms for the DO events. However, the explanatory power of these results is limited by the uncertainty of the transition onset detection in noisy proxy records. Here, we extend previous work by testing the significance of the reported lags with respect to the null hypothesis that the proposed transition order is in fact not systematically favored. If the detection uncertainties are averaged out, the temporal delays in the  $\delta^{18}\text{O}$  and  $\text{Na}^+$  transitions with respect to their counterparts in  $\text{Ca}^{2+}$  and the annual layer thickness are indeed pairwise statistically significant. In contrast, under rigorous propagation of uncertainty, three statistical tests cannot provide evidence against the null hypothesis. We thus

confirm the previously reported tendency of delayed transitions in the  $\delta^{18}\text{O}$  and  $\text{Na}^+$  concentration records. Yet, given the uncertainties in the determination of the transition onsets, it cannot be decided whether these tendencies are truly the imprint of a prescribed transition order or whether they are due to chance. The analyzed set of DO transitions can therefore not serve as evidence for systematic lead–lag relationships between the transitions in the different proxies, which in turn limits the power of the observed tendencies to constrain possible physical causes of the DO events.

### 1 Introduction

In view of anthropogenic global warming, concerns have been raised that several subsystems of the earth's climate system may undergo abrupt and fundamental state transitions if temperatures exceed corresponding critical thresholds (Lenton and Schellnhuber, 2007; Lenton et al., 2008, 2019). Under sustained warming, the Atlantic Meridional Overturning Circulation (AMOC), the Amazon rainforest, or the Greenland ice sheet are, among others, possible candidates to abruptly transition to new equilibrium states that may differ strongly from their current states (Lenton et al., 2008). Understanding the physical mechanisms behind abrupt shifts in climatic subsystems is crucial for assessing the associated risks and for defining safe operating spaces in terms of cumulative greenhouse gas emissions. To date, empirical evidence for abrupt climate transitions only comes from paleoclimate

proxy records encoding climate variability in the long-term past. First discovered in the  $\delta^{18}\text{O}$  records from Greenland ice cores, the so-called Dansgaard–Oeschger (DO) events are considered the archetype of past abrupt climate changes (see Fig. 1) (Johnsen et al., 1992; Dansgaard et al., 1993; Bond et al., 1993; North Greenland Ice Core Project members, 2004). These events constitute a series of abrupt regional warming transitions that punctuated the last and previous glacial intervals at millennial recurrence periods. Amplitudes of these decadal-scale temperature increases reach from 5 to 16.5 °C over Greenland (Kindler et al., 2014; Huber et al., 2006; Landais et al., 2005). The abrupt warming is followed by gradual cooling over centuries to millennia before the climate abruptly transitions back to cold conditions. The relatively cold (warm) intervals within the glacial episodes have been termed Greenland stadials (GSs) (Greenland interstadials (GIs)). GSs typically show millennial-scale persistence before another abrupt warming starts a new cycle (Rasmussen et al., 2014; Ditlevsen et al., 2007). Despite being less pronounced, a global impact of DO events on climate and ecosystems is evident in many proxy records (e.g. Moseley et al., 2020; Buizert et al., 2015; Lynch-Stieglitz, 2017; Kim et al., 2012; Fleitmann et al., 2009; Voelker, 2002; Cheng et al., 2013).

Apart from  $\delta^{18}\text{O}$ , other Greenland ice core proxy records, such as  $\text{Ca}^{2+}$  and  $\text{Na}^+$  concentrations as well as the annual layer thickness  $\lambda$ , also bear the signature of DO cycles, as can be seen in Fig. 1 (e.g., Erhardt et al., 2019; Fuhrer et al., 1999; Ruth et al., 2007). While  $\delta^{18}\text{O}$  is interpreted as a qualitative proxy for ice core site temperatures (e.g. Gkinis et al., 2014; Jouzel et al., 1997; Johnsen et al., 2001), changes in  $\text{Ca}^{2+}$  concentrations – or equivalently dust – are believed to reflect changes in the atmospheric circulation (Ruth et al., 2007; Erhardt et al., 2019).  $\text{Na}^+$  concentration records indicate past sea-salt aerosol concentrations and are thought to negatively correlate with North Atlantic sea-ice cover (Erhardt et al., 2019; Schüpbach et al., 2018). The annual layer thickness depends on past accumulation rates at the drilling site and hence indicates local precipitation driven by synoptic circulation patterns (Erhardt et al., 2019). According to this proxy record interpretation, DO events comprise not only sudden warming but also a sudden increase in local precipitation amounts, retreat of the North Atlantic sea-ice cover, and changes in hemispheric circulation patterns.

In the search for the mechanism(s) causing or triggering DO events, several attempts have been made to deduce the relative temporal order of these abrupt changes by analyzing the phasing of corresponding abrupt shifts detected in multi-proxy time series from Greenland ice cores (Erhardt et al., 2019; Thomas et al., 2009; Steffensen et al., 2008; Ruth et al., 2007). While Thomas et al. (2009) and Steffensen et al. (2008) report delayed Greenland warming with respect to atmospheric changes for the onsets of GI-8 and GI-1 and the Holocene, Ruth et al. (2007) find no systematic lead or lag across the onsets of GI-1 to GI-24. However, the comprehen-

sive study conducted by Erhardt et al. (2019) concludes that, on average, initial changes in both terrestrial dust aerosol concentrations ( $\text{Ca}^{2+}$ ) and local precipitation ( $\lambda$ ) have preceded the changes in local temperatures ( $\delta^{18}\text{O}$ ) and sea-salt aerosol concentrations ( $\text{Na}^+$ ) by roughly 1 decade at the onset of DO events during the last glacial cycle.

These observation-based studies are complemented by numerous conceptual theories and modeling studies that explore a variety of mechanisms to explain the DO events. Many studies emphasize the role of the AMOC in the emergence of DO events (Broecker et al., 1985; Clark et al., 2002; Ganopolski and Rahmstorf, 2001; Henry et al., 2016). In this context, Vettoretti and Peltier (2018) identified a self-sustained sea-salt oscillation mechanism to initiate transitions between stadials and interstadials in a comprehensive general circulation model (GCM) run, while Boers et al. (2018) proposed a coupling between sea-ice growth, subsurface warming, and AMOC changes to explain the DO cycles. Moreover, Li and Born (2019) draw attention to the subpolar gyre, a sensitive region that features strong interactions between atmosphere, ocean, and sea ice. In line with the empirical studies that suggest a delayed Greenland warming with respect to atmospheric changes, Kleppin et al. (2015) and Zhang et al. (2014) find DO-like transitions in GCM studies triggered by an abrupt reorganization of atmospheric circulation patterns.

Here, we refine the investigation of a potential pairwise lead–lag relationship between the four climate proxies  $\text{Ca}^{2+}$ ,  $\text{Na}^+$ ,  $\delta^{18}\text{O}$ , and the annual layer thickness  $\lambda$  at DO transition onsets, as previously presented by Erhardt et al. (2019), by rigorously taking into account the uncertainties of the DO onset detection in the different proxy records. We use the same data and the same probabilistic transition onset detection method as provided by Erhardt et al. (2019). The data comprise piecewise high-resolution (7 years or higher) multi-proxy time series around 23 major DO events from the later half of the last glacial cycle, from the NEEM and the NGRIP ice cores (Erhardt et al., 2019). The fact that high-frequency internal climate variability blurs abrupt transitions limits the ability to precisely detect their onset in the proxy data and thereby constitutes the main obstacle for the statistical analysis of the succession of events. The method designed by Erhardt et al. (2019) very conveniently takes this into account and instead of returning scalar estimators it quantifies the transition onsets in terms of Bayesian posterior probability densities that indicate the plausibility of a transition onset at a certain time in view of the data. This gives rise to a set of uncertain DO transition onset lags for each pair of proxies under study, whose statistical interpretation is the goal of this study.

While Erhardt et al. (2019) report transition onsets, midpoints, and endpoints, we restrict our investigation to the transition onset points, since we consider the leads and lags between the initial changes in the different proxy records to be the relevant quantity for a potential identification of the

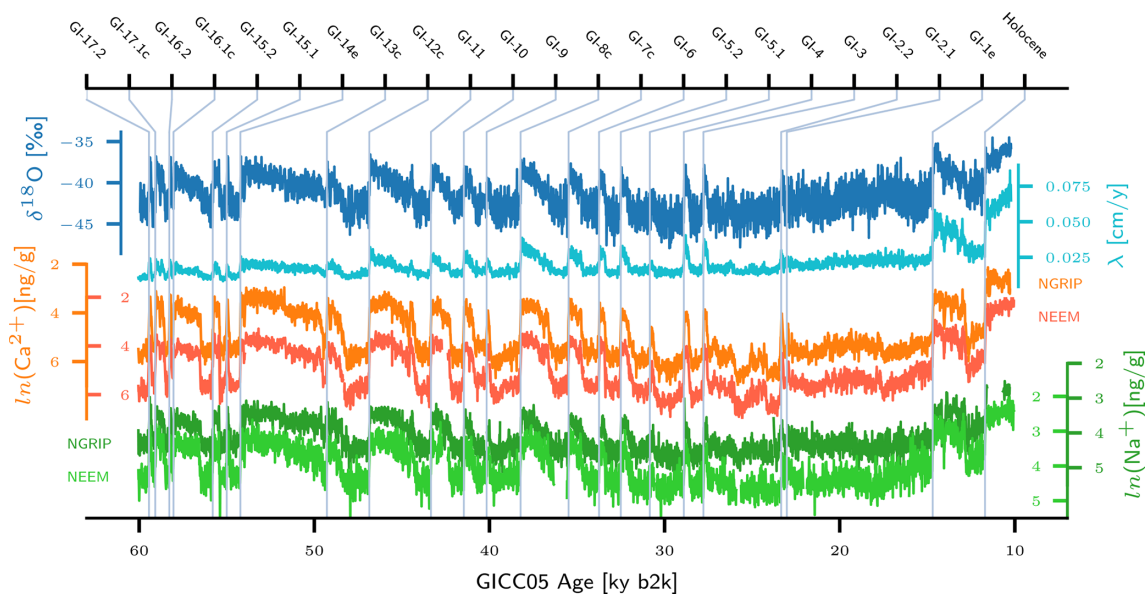


**Figure 1.** Time series of  $\delta^{18}\text{O}$  (blue), annual layer thickness  $\lambda$  (cyan),  $\text{Ca}^{2+}$  (orange), and  $\text{Na}^+$  (green) from the NGRIP ice core, together with time series of  $\text{Ca}^{2+}$  (red) and  $\text{Na}^+$  (light green) from the NEEM ice core on the GICC05 timescale in ky b2k, at 10-year resolution. Light blue vertical lines mark the timings of major DO events. All time series are retrieved from Erhardt et al. (2019), and for the DO event timings and Greenland interstadial (GI) notation we followed Rasmussen et al. (2014). Originally, the  $\delta^{18}\text{O}$  record was published by NGRIP project members (2004) as 50-year mean values and later at higher resolution (5 cm) as a Supplement to Gkinis et al. (2014). The GICC05 age scale for the NGRIP ice core was compiled by Vinther et al. (2006), Rasmussen et al. (2006), Andersen et al. (2006), and Svensson et al. (2008). For the NEEM ice core, the GICC05 presented by Rasmussen et al. (2013) is used here.

physical trigger of the DO events. We extend the previous work by interpreting the sets of uncertain lags as samples generated in random experiments from corresponding unknown populations – each proxy pair is associated with its own population of lags. This allows for the investigation of whether the reported average lags (Erhardt et al., 2019) are a systematic feature or whether they might have emerged by chance. In order to review the statistical evidence for potential systematic lags, we formalize the notion of a “systematic lag”: we call a lag systematic if it is enshrined in the random experiment in form of a population mean different from 0. Samples generated from such a population with a non-zero mean would systematically (and not by chance) exhibit sample means different from 0. Accordingly, we formulate the null hypothesis that the proposed transition sequence is in fact not physically favored. In mathematical terms this corresponds to an underlying population of lags with a mean equal to 0 or with reversed sign with respect to the observed lags. A rejection of this null hypothesis would statistically corroborate the interpretation that transitions in  $\delta^{18}\text{O}$  and  $\text{Na}^+$  systematically lag their counterparts in  $\lambda$  and  $\text{Ca}^{2+}$ . On the other hand, acceptance of the hypothesis would prevent us from ruling out that the observed lag tendencies are a coincidence and not a systematic feature. We have identified three different statistical tests suitable for this task, which all rely on slightly different assumptions. Therefore, in combination they yield a robust assessment of the observations. Most im-

portantly, we propagate the uncertainties that arise from the transition onset detection to the level of  $p$  values of the different tests.

We will show that, if the uncertainties are averaged out at the level of the individual transition onset lags – thus ignoring the uncertainties in the onset detection – all tests indicate statistical significance (at 5 % confidence level) of the observed tendencies toward delayed  $\delta^{18}\text{O}$  and  $\text{Na}^+$  transition onsets with respect to the corresponding onsets in  $\lambda$  and  $\text{Ca}^{2+}$ . Rigorous uncertainty propagation, however, yields substantial probabilities for the observed transition onset lags to be non-significant with respect to the null hypothesis. We thus argue that the uncertainties in the transition onset detection are too large to infer a population mean different from 0 in the direction of the observed tendencies. In turn, this prevents the attribution of the observed lead–lag relations to a fundamental mechanism underlying the DO events. We discuss the difference between our approach and the one followed by Erhardt et al. (2019) in detail below.

In addition to the quantitative uncertainty discussed here, there is always qualitative uncertainty about the interpretation of climate proxies. Clearly, there is no one-to-one mapping between proxy variables and the climate variables they are assumed to represent. To give an example, changes in the atmospheric circulation will simultaneously impact the transport efficiency of sea-salt aerosols to Greenland. Schüpbach et al. (2018) discuss in detail the entanglement of transport

efficiency changes and source emission changes for aerosol proxies measured in Greenland ice cores. We restrict our analysis to those proxy pairs that have been found to show decadal-scale time lags by Erhardt et al. (2019) and leave aside those pairs which show almost simultaneous transition onsets according to Erhardt et al. (2019).

This article is structured as follows: first, the data used for the study are described. Second, we introduce our methodology in general terms, in order to facilitate potential adaptation to structurally similar problems. Within this section, we pay special attention to clarifying the differences between the approaches chosen in this study and by Erhardt et al. (2019). This is followed by the presentation of our results including a comparison to previous results. In the subsequent discussion, we give a statistical interpretation and explain how the two lines of inference lead to different conclusions. The last section summarizes the key conclusions that can be drawn from our analysis.

## 2 Data

In conjunction with their study, Erhardt et al. (2019) published 23 highly resolved time series for  $\text{Ca}^{2+}$  and  $\text{Na}^{+}$  concentrations from the NGRIP and NEEM ice cores for time intervals of 250 to 500 years centered around DO events from the later half of the last glacial. The data set covers all major interstadial onsets from GI-17.2 to the Holocene, as determined by Rasmussen et al. (2014). The time resolution decreases from 2 to 4 years with increasing depth in the ice cores due to the thinning of the core. In addition, Erhardt et al. (2019) derived the annual layer thickness from the NGRIP aerosol data and published these records likewise for the time intervals described above. Furthermore, continuous 10-year resolution versions of the proxy records were published, which cover the period 60–10 kyr BP, shown in Fig. 1 (Erhardt et al., 2019). Finally, the NGRIP  $\delta^{18}\text{O}$  record at 5 cm resolution (corresponding to 4–7 years for the respective time windows) (North Greenland Ice Core Project members, 2004) completes the data set used in the study by Erhardt et al. (2019) and correspondingly in our study.

While  $\text{Ca}^{2+}$  and  $\text{Na}^{+}$  mass concentrations are interpreted as indicators of the past state of the atmospheric large-scale circulation and the past North Atlantic sea-ice extent, respectively, the annual layer thickness and  $\delta^{18}\text{O}$  records give qualitative measures of the local precipitation and temperature, respectively (Erhardt et al., 2019, and references therein). The high resolution and the shared origin of the time series make them ideally suited to study the succession of events at the beginning of DO transitions. On top of that, the aerosol data have been co-registered in a continuous flow analysis allowing for the highest possible comparability (Erhardt et al., 2019).

For their analysis, Erhardt et al. (2019) only considered time series around DO events that do not suffer from sub-

stantial data gaps. For the sake of comparability, we adopt their selection. From Fig. 2 it can be inferred which proxy records around which DO events have been included in this study. For details on the data and the proxy interpretations we refer to Erhardt et al. (2019) and the manifold references therein.

## 3 Methods

We first briefly review the probabilistic method that we adopted from Erhardt et al. (2019) in order to estimate the transition onset time  $t_0$  of each proxy variable for each DO event comprised in the data (see Fig. 3). The Bayesian method accounts for the uncertainty inherent to the determination of  $t_0$  by returning probability densities  $\rho_{T_0}(t_0)$  instead of scalar estimators. From these distributions, corresponding probability distributions for the pairwise time lags between two proxies can be derived for all DO events. Second, a statistical perspective on the series of DO events is established. For a given proxy pair, the set of transition onset lags from the different DO events is treated as a sample of observations from an unknown underlying population. In this very common setup, naturally one would use hypothesis tests to constrain the population. In particular, the question of whether any lag tendencies observed in the data are a systematic feature or whether they have instead occurred by chance can be assessed by testing a convenient null hypothesis. However, the particularity that the individual observations that comprise the sample are themselves subject to uncertainty requires a generalization of the hypothesis tests. We propagate the uncertainty of the transition onset timings to the  $p$  values of the tests and hence obtain uncertain  $p$  values in terms of probability densities (see Figs. 4 and 7). While in common hypothesis tests the scalar  $p$  value is compared to a predefined significance level, here we propose two criteria to project the  $p$ -value distribution onto the binary decision between acceptance and rejection of the null hypothesis. After this general characterization of the statistical problem, we introduce the tests which we employ for the analysis. Finally, we compare our approach to the one followed by Erhardt et al. (2019).

### 3.1 Transition onset detection

Consider a fluctuating time series  $\mathcal{D} = \{x(t_i)\}_{i=1,\dots,n}$  with  $n$  data points, which includes one abrupt transition from one level of values to another, as shown in Fig. 3b. For this setting, Erhardt et al. (2019) have designed a method to estimate the transition onset time  $t_0$  in a probabilistic, Bayesian sense. The application of the method to NGRIP  $\text{Ca}^{2+}$  and  $\text{Na}^{+}$  concentration data around the onset of GI-12c is illustrated in Fig. 3. Instead of a point estimate, their method returns a so-called posterior probability density that indicates the plausibility of the respective onset time in view of the data (see Fig. 3a). For technical reasons, this probability density can-

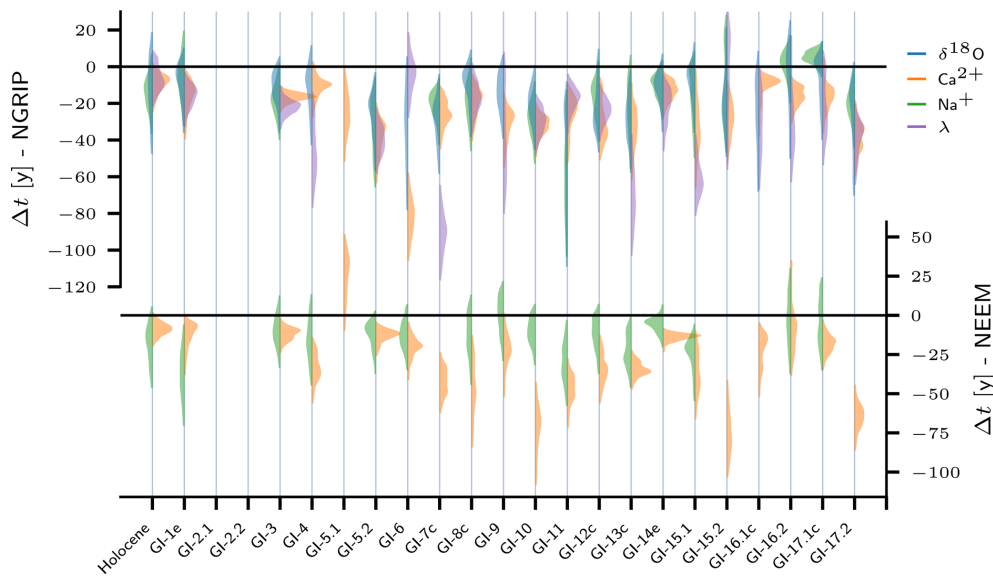


**Figure 2.** DO events (Greenland interstadial onsets) for which Erhardt et al. (2019) provide high-resolution proxy data ( $\text{Ca}^{2+}$ ,  $\text{Na}^+$ , and  $\lambda$ ) for windows centered around the transitions.  $\delta^{18}\text{O}$  data for the corresponding windows were retrieved from continuous  $\delta^{18}\text{O}$  time series measured in 5 cm steps in the NGRIP ice core (see Fig. 1). The posterior probability densities for the transition onsets with respect to the timing of the DO events according to Rasmussen et al. (2014) are shown in arbitrary units for all proxies. They were recalculated using the data and the method provided by Erhardt et al. (2019). The uncertain transition onsets are only shown for those transitions investigated in this study – the selection is adopted from Erhardt et al. (2019) to guarantee comparability.

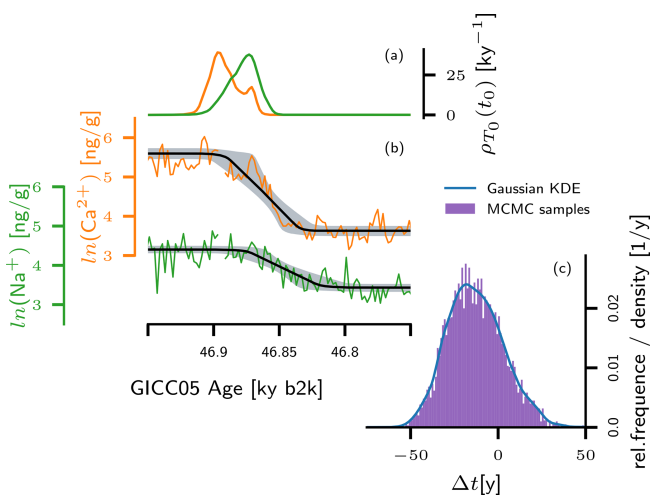


**Figure 3.** (a) Posterior probability distribution  $\rho_{T_0}(t_0)$  for the onset of NGRIP  $\text{Ca}^{2+}$  and  $\text{Na}^+$  transitions associated with the onset of GI-12c, derived from  $\text{Ca}^{2+}$  (orange) and  $\text{Na}^+$  (green) values around the GI-12c onset at 2-year resolution, using the probabilistic ramp-fitting shown in (b). The black lines in (b) indicate the expected ramp, i.e., the average over all ramps determined by the posterior distributions of the ramp parameters. The grey shaded area indicates the 5th–95th percentiles of these ramps. (c) Histogram sampled from the posterior distribution for the transition onset lag  $\Delta t$  between the two proxies (violet), together with the corresponding Gaussian kernel density estimate (KDE, blue).

not be derived in form of a continuous function but only in form of a representative set of values generated from it by means of a Markov chain Monte Carlo (MCMC) algorithm (Goodman and Weare, 2010).

The key idea is to model the transition as a linear ramp  $\mathcal{L}(t_i)$  perturbed by red noise  $\epsilon(t_i)$ , which is an autoregressive process of first order:

$$y(t_i) = \underbrace{\begin{cases} y_0 & t_i \leq t_0 \\ y_0 + \Delta y \frac{t_i - t_0}{\tau} & t_0 < t_i < t_0 + \tau \\ y_0 + \Delta y & t_i \geq t_0 + \tau \end{cases}}_{\text{linear ramp } \mathcal{L}(t_i)} + \underbrace{\epsilon(t_i)}_{\text{AR}(1)_{\sigma, \alpha}}. \quad (1)$$

This model is fully determined by the four ramp parameters  $\{t_0, y_0, \tau, \Delta y\}$ , the amplitude  $\sigma$ , and the autoregressive coefficient  $\alpha$  of the AR(1) process. For a given configuration  $\theta$  of these six parameters, the probability of this stochastic model to exactly reproduce the data  $\mathcal{D}$  reads

$$\begin{aligned} \pi(\mathcal{D}|\theta) &:= \pi(y(t_i) = x(t_i) \forall i \in \{1, \dots, n\}|\theta) \\ &= \frac{1}{(\sqrt{2\pi}\sigma^2)^n} \prod_{i=1}^n \exp\left(-\frac{1}{2} \frac{(\delta_i - \alpha\delta_{i-1})^2}{\sigma^2}\right), \end{aligned} \quad (2)$$

where  $\delta_i = x(t_i) - \mathcal{L}(t_i)$  denotes the residuals between the linear ramp and the observations and  $\delta_0 = 0$ . Bayes' theorem immediately yields the posterior probability density for the model parameters  $\pi(\theta|\mathcal{D})$  upon introduction of convenient

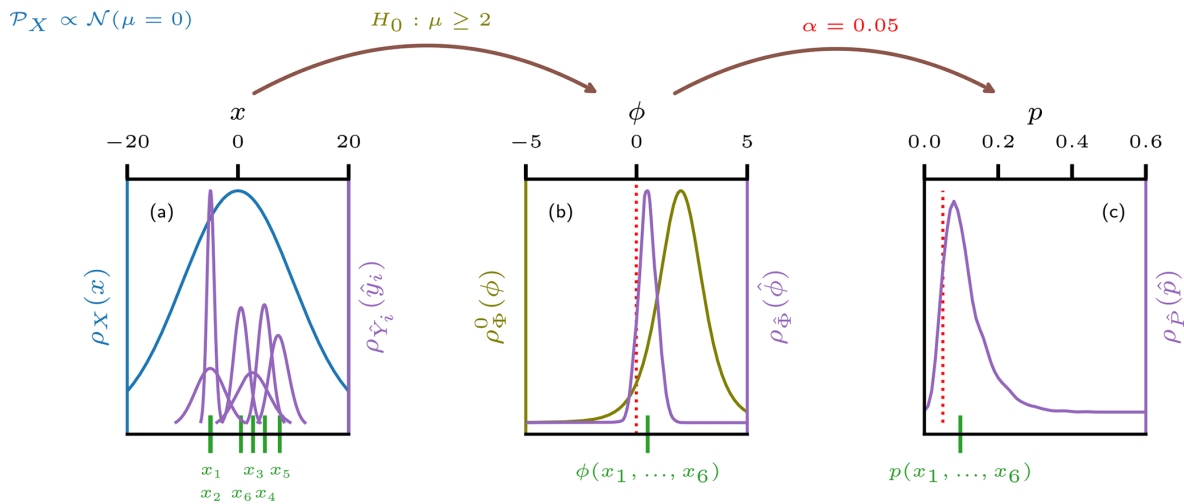


**Figure 4.** (a) Schematic representation of an uncertain observation of a sample (purple) generated from a population (blue) in a random experiment. The blue line indicates the probability density of the generating population  $\mathcal{P}_X$ . Green lines indicate the true value of a sample  $\mathbf{x} = (x_1, \dots, x_6)$  realized from  $\mathcal{P}_X$ . If the observational process involves uncertainty, a second level of randomness is introduced and the values can at best be approximated by probability density functions depicted in purple. These uncertainty distributions indicate the informed estimate of the observer about how likely a certain value  $\hat{y}_i$  for the estimator  $\hat{Y}_i$  is to coincide with the true value  $x_i$ . Depending on the measurement process, the uncertainty distributions of the sample members may all exhibit individual shapes or they may share a common one. (b) Distribution of the uncertain test statistic  $\hat{\Phi} = \phi(\hat{Y})$  derived from the uncertain sample (purple) together with the corresponding value derived from the true sample (green). In olive, the distribution of  $\Phi$  under the null hypothesis is shown. The dotted red line separates the rejection region (left) from the acceptance region in a one-sided test setup. (c) Distribution of the uncertain  $p$  value corresponding to the uncertain sample. In green, the  $p$  value of the certain sample is marked. The red line indicates the significance level  $\alpha$ .

priors  $\pi(\boldsymbol{\theta})$ :

$$\pi(\boldsymbol{\theta}|\mathcal{D}) = \frac{\pi(\mathcal{D}|\boldsymbol{\theta}) \pi(\boldsymbol{\theta})}{\pi(\mathcal{D})}, \quad (3)$$

where the normalization constant  $\pi(\mathcal{D}) = \int \pi(\mathcal{D}|\boldsymbol{\theta})\pi(\boldsymbol{\theta})d\boldsymbol{\theta}$  is the a priori probability of the observations. Since the parameter space is six-dimensional, Eq. (3) cannot be evaluated explicitly on a grid with reasonably fine spacing. Instead, an MCMC algorithm is used to sample a representative set  $\{\boldsymbol{\theta}_1, \dots, \boldsymbol{\theta}_m\}$  of parameter configurations from the posterior distribution that approximates the continuous distribution in the sense that for smooth functions  $f$

$$\int f(\boldsymbol{\theta})\rho_{\boldsymbol{\Theta}}(\boldsymbol{\theta}) d\boldsymbol{\theta} \simeq \int f(\boldsymbol{\theta})\bar{\rho}_{\boldsymbol{\Theta}}(\boldsymbol{\theta}) d\boldsymbol{\theta} = \frac{1}{m} \sum_{j=1}^m f(\boldsymbol{\theta}_j), \quad (4)$$

where the notion of a so-called empirical distribution  $\bar{\rho}_{\boldsymbol{\Theta}}(\boldsymbol{\theta}) = \frac{1}{m} \sum_{j=1}^m \delta(\boldsymbol{\theta} - \boldsymbol{\theta}_j)$  has been used. The use of the MCMC algorithm further allows us to omit the normalization constant  $\pi(\mathcal{D})$ . The number  $m$  of individuals comprised in the MCMC sample must be chosen large enough to ensure a good approximation in Eq. (4). The marginal distribution for the parameter  $t_0$  relevant for our study can be obtained by integration over the remaining parameters  $\boldsymbol{\theta}^*$ :

$$\rho_{T_0|\mathcal{D}}(t_0) = \int \pi(\boldsymbol{\theta}|\mathcal{D}) d\boldsymbol{\theta}^*, \quad (5)$$

which reads

$$\bar{\rho}_{T_0}(t_0) = \frac{1}{m} \sum_{j=1}^m \delta(t_0 - t_{0,j}) \quad (6)$$

in terms of the empirical density induced by the MCMC sample.

Given the probability densities for the transition onsets of two proxy variables  $p$  and  $q$  at a chosen DO event  $i$ , the probability density for the lag  $\Delta t_i^{p,q} = t_0^{p,i} - t_0^{q,i}$  between them reads

$$\rho_{\Delta T_i^{p,q}}(\Delta t_i^{p,q}) = \iint \delta(t_0^{p,i} - t_0^{q,i} - \Delta t_i^{p,q}) \rho_{T_0}^{p,i}(t_0^{p,i}) \times \rho_{T_0}^{q,i}(t_0^{q,i}) dt_0^{p,i} dt_0^{q,i}. \quad (7)$$

$\Delta T_i^{p,q}$  was chosen to denote the time lag which inherits the uncertainty from the transition onset detection and must thus mathematically be treated as a random variable.  $\Delta t_i^{p,q}$  denotes a potential value that  $\Delta T_i^{p,q}$  may assume. The set of probability densities  $\{\rho_{\Delta T_i^{p,q}}(\Delta t_i^{p,q})\}_i$  derived from the different DO events conveniently describes the random vector of uncertain DO onset lag observations  $\boldsymbol{\Delta T}^{p,q} = (\Delta T_1^{p,q}, \dots, \Delta T_n^{p,q})$  for the  $(p, q)$  proxy pair in the sense that

$$\rho_{\boldsymbol{\Delta T}^{p,q}}(\boldsymbol{\Delta t}^{p,q}) = \prod_{i=1}^n \rho_{\Delta T_i^{p,q}}(\Delta t_i^{p,q}). \quad (8)$$

Note that the entries  $\Delta T_i^{p,q}$  of the random vector  $\mathbf{\Delta T}^{p,q}$  are independent from each other and follow their individual distributions  $\rho_{\Delta T_i^{p,q}}(\Delta t_i^{p,q})$ , such that the joint distribution is given by the product of the individual distributions. A cross-core comparison is not possible because the relative dating uncertainties between the cores exceed the magnitude of the potential time lags.

For the sake of simplicity, we omit the difference between the posterior density distribution and the empirical posterior density distribution induced by an MCMC sample. It is shown in Appendix A that all methods can be equivalently formulated in terms of the empirical posterior density distribution. The numerical computations themselves have of course been carried out with the empirical densities obtained from the MCMC sampler. Appendix B discusses the construction of numerically manageable empirical densities  $\bar{\rho}_{\mathbf{\Delta T}^{p,q}}(\mathbf{\Delta t}^{p,q})$ . Since a substantial reduction in the available MCMC sampled data is required, a control group of alternative realizations of  $\bar{\rho}_{\mathbf{\Delta T}^{p,q}}(\mathbf{\Delta t}^{p,q})$  is introduced. The high agreement of the results obtained from the control group with the results discussed in the main text confirms the validity of the initial  $\bar{\rho}_{\mathbf{\Delta T}^{p,q}}(\mathbf{\Delta t}^{p,q})$  construction.

In the following, all probability densities that represent uncertainties with origin in the transition onset observation will be referred to as uncertainty distributions or uncertainty densities. This helps to distinguish them from probability distributions that generically characterize random experiments. The random variables described by uncertainty distributions will be termed uncertain variables and will be marked with a hat. Generally, we denote all random (uncertain) variables by capital letters  $X$  ( $\hat{X}$ ), while realizations will be denoted with lower-case letters  $x$  ( $\hat{x}$ ). Furthermore, distributions will always be subscripted with the random variables that they characterize, e.g.,  $\rho_X(x)$  ( $\rho_{\hat{X}}(\hat{x})$ ). For the sake of readability, sometimes we omit the index  $p, q$  when it is clear that a quantity refers to a pair of proxies ( $p, q$ ).

### 3.2 Statistical setting

Despite their diversity in terms of temperature amplitude, duration, and frequency across the last glacial, the reoccurring patterns and their common manifestation in different proxies suggest that the DO events follow a common physical mechanism. If this assumption holds true, this mechanism prescribes a fixed pattern of causes and effects for all DO events – at least on the scale of interactions between climatic subsystems represented by the proxies under study. However, natural variability randomly delays or advances the individual parts of the event chain of the DO mechanism in each single realization, without violating the mechanistic causality. The observed pairwise transition onset lags can thus be regarded as realizations of independent and identically distributed (i.i.d.) random variables generated in a random experiment  $(\Omega, \mathcal{F}, \mathcal{P}_{\Delta T}^{p,q})$  on the sample space  $\Omega = \mathbb{R}$ . Here,  $\mathcal{F}$  is a  $\sigma$  algebra defined on  $\Omega$  and may be taken as the Borel

algebra.  $\mathcal{P}_{\Delta T}^{p,q}$  – the so-called population – denotes a probability measure with respect to  $\mathcal{F}$  and fully characterizes the random lag  $\Delta T^{p,q}$  between the proxies  $p$  and  $q$ . Importantly, if any of the proxy variables investigated here was to represent a climate variable associated with the DO event trigger, we would expect an advanced initial change in the record of this proxy with respect to other proxies at DO events. In turn, a pronounced delay of a proxy record's transition onset contradicts the assumption that the proxy represents a climate variable associated with the trigger. Therefore, the identification of leads and lags between the transition onsets in the individual proxy time series may help in the search for the trigger of the DO events. Here, we formalize the investigation of systematic lead–lag relationships between the proxy transitions. The random experiment framework allows us to relate a suspected transition sequence to a mean of the generating population  $\mathcal{P}_{\Delta T}^{p,q}$  differing from 0 in the according direction. Evidence for the suspected sequence can then be obtained by testing the null hypothesis of a population mean equal to 0 or with a sign opposed to the suspected lag direction. If this null hypothesis can be rejected based on the observations, this would constitute a strong indication of a systematic, physical lag and would hence potentially yield valuable information on the search for the mechanism(s) and trigger(s) of the DO transitions.

According to the data selection by Erhardt et al. (2019) as explained in Sect. 2, for all studied pairs of proxies we compute either 16 or 20 transition lags from the different DO events, which we interpret as samples  $\mathbf{\Delta t}^{p,q} = (\Delta t_1^{p,q}, \dots, \Delta t_n^{p,q})$  from their respective populations  $\mathcal{P}_{\Delta T}^{p,q}$ . Studying these samples, Erhardt et al. (2019) deduced a decadal-scale delay in the transition onsets in  $\text{Na}^+$  and  $\delta^{18}\text{O}$  records with respect to their counterparts in  $\text{Ca}^{2+}$  and  $\lambda$ . In order to test if the data support evidence for this lag to be systematic in a statistical sense, the notion of a “systematic lag” first needs to be formalized mathematically. We argue that a physical process that systematically delays one of the proxy variable transitions with respect to another must in the random experiment framework be associated with a population that exhibits a mean different from 0:  $\mu^{p,q} = E(\Delta T^{p,q}) \neq 0$ . The outcomes of such a random experiment will systematically exhibit sample means different from 0 in accordance with the population mean. Samples generated from a population with a mean equal to 0 may as well yield sample means that strongly differ from 0. However, their occurrence is not systematic but rather a coincidence. Given a limited number of observations, hypothesis tests provide a consistent yet not unambiguous way to distinguish systematic from random features. If the mean of the observed sample  $u^{p,q}(\mathbf{\Delta t}^{p,q}) = \frac{1}{n} \sum \Delta t_i^{p,q}$  indicates an apparent lag between the proxies  $p$  and  $q$ , testing whether the sample statistically contradicts a population that favors no ( $\mu^{p,q} = 0$ ) or the opposite lag (or  $\text{sign}(\mu^{p,q}) \neq \text{sign}(u^{p,q})$ ) can provide evidence at the significance level  $\alpha$  for the observed mean lag to be systematic in the sense that  $\text{sign}(\mu^{p,q}) = \text{sign}(u^{p,q})$ . How-

ever, as long as the null hypothesis cannot be rejected, the observed average sample lag cannot be regarded as statistical evidence for a systematic lag.

Before we introduce the tests deployed for this study, we discuss the particularity that the individual observations of the i.i.d. variables that comprise our samples are themselves subject to uncertainty and hence are represented by probability densities instead of scalar values. The common literature on hypothesis tests assumes that an observation of a random variable yields a scalar value. Given a sample of  $n$  scalar observations

$$\mathbf{x} = (x_1, x_2, \dots, x_n), \tag{9}$$

the application of hypothesis tests to the sample is in general straight forward and has been abundantly discussed (e.g. Lehmann and Romano, 2006). In short, a test statistic  $\phi_{\mathbf{x}} = \phi(\mathbf{x})$  is computed from the observed sample, where

$$\phi : \mathbb{R}^n \rightarrow \mathbb{R}, \mathbf{x} \mapsto \phi(\mathbf{x}) \tag{10}$$

denotes the mapping from the space of  $n$ -dimensional samples to the space of the test statistic and  $\phi_{\mathbf{x}}$  denotes the explicit value of the function when applied to the observed sample  $\mathbf{x}$ . Subsequently, integration of the so-called null distribution over all values  $\phi'$ , which under the null hypothesis  $H_0$  are more extreme than the observed  $\phi_{\mathbf{x}}$ , yields the test's  $p$  value. In this study, a hypothesis on the lower limit of a parameter will be tested. In this one-sided left-tailed application of hypothesis testing, the  $p$  value explicitly reads

$$p_{\mathbf{x}} = \int_{-\infty}^{\phi_{\mathbf{x}}} \rho_{\Phi}^0(\phi') \, d\phi', \tag{11}$$

which defines the mapping

$$p : \mathbb{R} \rightarrow [0, 1], \phi_{\mathbf{x}} \mapsto p(\phi_{\mathbf{x}}) = p_{\mathbf{x}}. \tag{12}$$

Analogous expressions may be given for one-sided right-tailed and two-sided tests. The null distribution  $\rho_{\Phi}^0(\phi')$  is the theoretical distribution of the random test statistic  $\Phi = \phi(X)$  under the assumption that the null hypothesis on the population  $\mathcal{P}_X$  holds true. If  $p_{\mathbf{x}}$  is less than a predefined significance level  $\alpha$ , the observed sample  $\mathbf{x}$  is said to contradict the null hypothesis at the significance level  $\alpha$ , and the null hypothesis should be rejected.

In contrast to this setting, the DO transition onset lags  $\Delta t_i^{p,q}$  between the proxies  $p$  and  $q$ , which are thought to have been generated from the population  $\mathcal{P}_{\Delta T}^{p,q}$ , are observed with uncertainty. In our case, the entries in the vector of observations are uncertain variables themselves, which are characterized by the previously introduced uncertainty distributions  $\rho_{\Delta \hat{T}_i^{p,q}}(\Delta \hat{t}_i^{p,q})$ . Figure 4a illustrates this situation: from an underlying population  $\mathcal{P}_X$  a sample  $\mathbf{x} = (x_1, \dots, x_6)$  is realized, with  $x_i$  denoting the true values of the individual

realizations. However, the exact value of  $x_i$  cannot be measured precisely due to measurement uncertainties. Instead, an estimator  $\hat{Y}_i$  is introduced together with the uncertainty distribution  $\rho_{\hat{Y}_i}(\hat{y}_i)$  that expresses the observer's belief about how likely a specific value  $\hat{y}_i$  for the estimator  $\hat{Y}_i$  is to agree with the true value  $x_i$ . The  $\hat{Y}_i$  correspond to the  $\Delta \hat{T}_i^{p,q}$ . For the  $x_i$  there is no direct correspondence in the problem at hand because this quantity cannot be accessed in practice and is thus not denoted explicitly. We call the vector of estimators  $\hat{\mathbf{Y}} = (\hat{Y}_1, \dots, \hat{Y}_n)$  an uncertain sample in the following. Omitting the  $(p, q)$  notation, we denote an uncertain sample of time lags as

$$\Delta \hat{\mathbf{T}} = (\Delta \hat{T}_1, \Delta \hat{T}_2, \dots, \Delta \hat{T}_n), \tag{13a}$$

with

$$\rho_{\Delta \hat{\mathbf{T}}}(\Delta \hat{\mathbf{t}}) = \prod_{i=1}^n \rho_{\Delta \hat{T}_i}(\Delta \hat{t}_i). \tag{13b}$$

Note that the uncertainty represented by the uncertain sample originates from the observation process – the sample no longer carries the generic randomness of the population  $\mathcal{P}_{\Delta T}$  it was generated from. The  $\Delta \hat{T}_i$  are no longer identically but yet independently distributed.

A simplistic approach to test hypotheses on an uncertain sample would be to average over the uncertainty distribution and subsequently apply the test to the resulting expected sample

$$\begin{aligned} E(\Delta \hat{\mathbf{T}}) &= (E(\Delta \hat{T}_1), \dots, E(\Delta \hat{T}_n)) \\ &= \left( \int \Delta \hat{t}_1 \rho_{\Delta \hat{T}_1}(\Delta \hat{t}_1) \, d\Delta \hat{t}_1, \dots, \right. \\ &\quad \left. \int \Delta \hat{t}_n \rho_{\Delta \hat{T}_n}(\Delta \hat{t}_n) \, d\Delta \hat{t}_n \right). \end{aligned} \tag{14}$$

Averaging out uncertainties, however, essentially implies that the uncertainties are ignored and is thus always associated with a loss of information. The need for a more thorough treatment, with proper propagation of the uncertainties, may be illustrated by a simple consideration. Assume that a random variable  $X$  can be observed at a given precision  $\sigma_{\text{obs}}$ , where  $\sigma_{\text{obs}}$  may be interpreted as the typical width of the corresponding uncertainty distribution. For any finite number of observations of  $X$ , the measurement uncertainty limits the ability to infer properties of the population. For example, one cannot distinguish between potential candidates  $\mu_0$  and  $\mu_1$  for the population mean, whose difference  $\Delta\mu = |\mu_0 - \mu_1|$  is a lot smaller than the observational precision, unless the number of observations tends to infinity. If uncertainties are averaged out, testing  $H_0 : \mu = \mu_0$  against the alternative  $H_1 : \mu = \mu_1$  can eventually still yield significance, even in the case where  $|\mu_0 - \mu_1| \ll \sigma_{\text{obs}}$ . For relatively small sample sizes, such an attested significance would be statistically meaningless. The uncertainties in the individual measurements considered here are on the order of a few decades,

while the proposed size of the investigated time lag is roughly 1 decade. In combination with the relatively small sample sizes of either 16 or 20 events, the scales involved in the analysis require a suitable treatment of the measurement uncertainties.

The uncertainty propagation relies on the fact that applying a function  $f: \mathbb{R} \rightarrow \mathbb{R}$  to a real valued random (uncertain) variable  $X$  yields a new random (uncertain) variable  $G = f(X)$ , which is distributed according to

$$\rho_G(g) = \int \delta(f(x) - g) \rho_X(x) dx. \quad (15)$$

Analogously, the uncertain test statistic  $\hat{\Phi} = \phi(\Delta\hat{T})$  follows the distribution

$$\rho_{\hat{\Phi}}(\hat{\phi}) = \int \delta(\phi(\Delta\hat{t}) - \hat{\phi}) \rho_{\Delta\hat{T}}(\Delta\hat{t}) d\Delta\hat{t}. \quad (16)$$

Repeated application of Eq. (15) yields the uncertainty distribution of a given test's  $p$  value  $\hat{P} = p(\phi(\Delta\hat{T}))$ :

$$\begin{aligned} \rho_{\hat{P}}(\hat{p}) &= \int \delta(p(\hat{\phi}) - \hat{p}) \rho_{\hat{\Phi}}(\hat{\phi}) d\hat{\phi} \\ &= \int \int \delta(p(\hat{\phi}) - \hat{p}) \delta(\phi(\Delta\hat{t}) - \hat{\phi}) \\ &\quad \times \rho_{\Delta\hat{T}}(\Delta\hat{t}) d\Delta\hat{t} d\hat{\phi} \\ &= \int \delta(p(\phi(\Delta\hat{t})) - \hat{p}) d\Delta\hat{t}. \end{aligned} \quad (17)$$

In the example shown in Fig. 4 the initial uncertainties in the observations translate into an uncertain  $p$  value that features both probability for significance and probability for non-significance. This illustrates the need for a criterion to project the uncertain  $p$  value onto a binary decision space comprised of rejection and acceptance of the null hypothesis. We propose to consider the following criteria to facilitate an informed decision:

- The hypothesis shall be rejected at the significance level  $\alpha$  if and only if the expected  $p$  value is less than  $\alpha$ , that is

$$\int_0^1 \hat{p} \rho_{\hat{P}}(\hat{p}) d\hat{p} < \alpha. \quad (18)$$

- The hypothesis shall be rejected at the significance level  $\alpha$  if and only if the probability of  $p$  to be less than  $\alpha$  is greater than a predefined threshold  $\eta$  (we propose  $\eta = 90\%$ ), that is

$$\pi(\hat{P} < \alpha) = \int_0^{\alpha} \rho_{\hat{P}}(\hat{p}) d\hat{p} > \eta. \quad (19)$$

While the  $p$  value of a certain sample indicates its extremeness with respect to the null distribution, the expected  $p$  value may be regarded as a measure of the uncertain sample's extremeness. Given the measurement uncertainty, the quantity  $\pi(\hat{P} < \alpha)$  constitutes an informed assessment of how likely or plausible the true value of the measured sample is to be statistically significant with respect to the null hypothesis. Thus, the first criterion assesses how “strongly” the uncertain sample contradicts the null hypothesis, while the second criterion evaluates the likelihood of the uncertain sample to contradict the null hypothesis. The choice of  $\eta$  is arbitrary and may be tailored to the specific circumstances of the test. In some situations, one might want to reject the null hypothesis only in the case of a high probability of significance and therefore choose a large value for  $\eta$  – e.g., when mistakenly attested significance is associated with high costs. In other situations, even small probabilities for significance may be important, e.g., if a significant test result would be associated with high costs or with high risks. We propose to assess the two criteria in combination. In the case of them not yielding the same result, the weighing between the criteria must be adapted to the statistical problem at hand.

### 3.3 Hypothesis tests

We have introduced the notion of uncertain samples and its consequences for the application of hypothesis tests. Here, we briefly introduce the tests used to test our null hypothesis that the observed tendency for delayed transition onsets in  $\text{Na}^+$  and  $\delta^{18}\text{O}$  with respect to  $\text{Ca}^{2+}$  and  $\lambda$  has occurred by chance and that the corresponding populations  $\mathcal{P}_{\Delta T}^{p,q}$  that characterize the pairwise random lags  $\Delta T^{p,q}$  in fact do not favor the tentative transition orders apparent from the observations. Mathematically, this can be formulated as follows:

- Let  $\rho_{\Delta T}^{p,q}(\Delta t)$  be the probability density associated with the population of DO transition onset lags  $\mathcal{P}_{\Delta T}^{p,q}$  between the proxy variables  $p$  and  $q$  and let the observations  $\Delta\hat{T}^{p,q}$  suggest a delayed transition of the proxy  $q$  – that is, the corresponding uncertainty distributions  $\rho_{\Delta\hat{T}_i}^{p,q}(\Delta\hat{t}_i^{p,q})$  indicate high probabilities for negative  $\Delta\hat{T}_i^{p,q}$  across the sample according to Eq. (7). We then test the hypothesis  $H_0$ : The mean value  $\mu^{p,q} = \int \rho_{\Delta T}^{p,q}(\Delta t) d\Delta t$  of the population  $\mathcal{P}_{\Delta T}^{p,q}$  is greater than or equal to zero.

We identified three tests that are suited for this task, namely the  $t$  test, the Wilcoxon signed-rank (WSR) test, and a bootstrap test. The WSR and the  $t$  test are typically formulated in terms of paired observation  $\{x_i, y_i\}$  that give rise to a sample of differences  $\{d_i = x_i - y_i\}$  which correspond to the time lags  $\{\Delta t_i^{p,q}\}$  of different DO events (Rice, 2007; Lehmann and Romano, 2006, e.g.). The null distributions of the tests rely on slightly different assumptions regarding the populations. Since we cannot guarantee the compliance of these as-

sumptions, we apply the tests in combination to obtain a robust assessment.

3.3.1 *t* test

The *t* test (Student, 1908) relies on the assumption that the population of differences  $\mathcal{P}_D$  is normally distributed with mean  $\mu$  and standard deviation  $\sigma$ . For a random sample  $\mathbf{D} = (D_1, \dots, D_n)$  the test statistic

$$Z(\mathbf{D}) = \frac{U(\mathbf{D}) - \mu}{S(\mathbf{D})/\sqrt{n}} \tag{20}$$

follows a *t* distribution  $t_{n-1}(z)$  with  $n - 1$  degrees of freedom. Here,  $U = \frac{1}{n} \sum D_i$  is the sample mean and  $S = \frac{1}{n-1} \sum (U - D_i)^2$  is the samples' standard deviation. This allows us to test whether an observed sample  $\mathbf{d} = (d_1, \dots, d_n)$  contradicts a hypothesis on the mean  $\mu$ . To compute the *p* value for the hypothesis  $H_0 : \mu \geq 0$  (left-handed application) the null distribution is integrated from  $-\infty$  to the observed value  $z(\mathbf{d})$ :

$$p_z(z(\mathbf{d})) = \int_{-\infty}^{z(\mathbf{d})} t_{n-1}(z') dz' \tag{21}$$

The resulting *p* value must then be compared to the predefined significance level  $\alpha$ .

The *t* test can be generalized for application to an uncertain sample of the form  $\Delta\hat{\mathbf{T}} = (\Delta\hat{T}_1, \dots, \Delta\hat{T}_n)$  as follows: let  $\rho_{\Delta\hat{\mathbf{T}}}(\Delta\hat{\mathbf{t}})$  denote the uncertainty distribution of  $\Delta\hat{\mathbf{T}}$ . Then according to Eq. (15) the distribution of the uncertain statistic  $\hat{Z}(\Delta\hat{\mathbf{T}})$  reads

$$\rho_{\hat{Z}}(\hat{z}) = \int \delta\left(\frac{u(\Delta\hat{\mathbf{t}})}{s(\Delta\hat{\mathbf{t}})/\sqrt{n}} - \hat{z}\right) \rho_{\Delta\hat{\mathbf{T}}}(\Delta\hat{\mathbf{t}}) d\Delta\hat{\mathbf{t}} \tag{22}$$

Finally, the distribution of the uncertain *p* value may again be computed according to Eq. (15)

$$\begin{aligned} \rho_{\hat{p}_z}(\hat{p}_z) &= \int \delta(p_z(\hat{z}) - \hat{p}_z) \rho_{\hat{Z}}(\hat{z}) d\hat{z} \\ &= \int \delta\left(\int_{-\infty}^{\hat{z}} t_{n-1}(z) dz - \hat{p}_z\right) \rho_{\hat{Z}}(\hat{z}) d\hat{z} \end{aligned} \tag{23}$$

and then be evaluated according to the two criteria formulated above.

3.3.2 Wilcoxon signed rank

Compared to the *t* test, the WSR test (Wilcoxon, 1945) allows us to relax the assumption of normality imposed on the generating population  $\mathcal{P}_D$  and replaces it by the weaker assumption of symmetry with respect to its mean  $\mu$  in order to

test the null hypothesis  $H_0 : \mu \geq 0$ . The test statistic  $W$  for this test is defined as

$$W(\mathbf{D}) = \sum_{i=1}^n R(|D_i|) \Theta(D_i), \tag{24}$$

where  $R(|D_i|)$  denotes the rank of  $|D_i|$  within the sorted set of the absolute values of differences  $\{|D_i|\}$ . The Heaviside function  $\Theta(D_i)$  guarantees that exclusively  $D_i > 0$  values are summed. The derivation of the null distribution is a purely combinatorial problem and its explicit form can be found in lookup tables. Because  $W \in \mathbb{N}_{[0, n(n+1)/2]}$  we denote the null distribution by  $\mathcal{P}_W^0(w)$  to signal that this is not a continuous density. Explicitly, the null distribution can be derived as follows: first, the assumption of symmetry around 0 (for the hypothesis  $H_0 : \mu \geq 0$ , the relevant null distribution builds on  $\mu = 0$ ) guarantees that the chance for  $D_i$  to be positive is equal to  $\frac{1}{2}$ . Hence, the number of positive outcomes  $m$  follows a symmetric binomial distribution  $\pi(m) = \binom{n}{m} (\frac{1}{2})^n$ . For  $m$  positive observations, there are  $\binom{n}{m}$  different sets of ranks  $\{r_1, \dots, r_m\}$  that they may assume and which are again, due to the symmetry of  $\mathcal{P}_D$ , equally likely. Hence, for a given number of positive outcomes  $m$  the probability to obtain a test statistic  $w$  is given by the share of those  $\binom{n}{m}$  configurations that yield a rank sum equal to  $w$ . Summing these probabilities over all possible values of  $m$  yields the null distribution for the test statistic  $w$ .

For a given sample  $\mathbf{d}$  we test the hypothesis  $H_0 : \mu \geq 0$  by computing the corresponding one-sided *p* value  $p_w$ , which is given by the cumulative probability that the null distribution assigns to  $w'$  values smaller than the observed  $w(\mathbf{d})$ :

$$p_w(w(\mathbf{d})) = \sum_{i=1}^n \mathcal{P}_W^0(w'_i) \Theta(w(\mathbf{d}) - w'_i). \tag{25}$$

Since  $W \in \mathbb{N}_{[0, n(n+1)/2]}$  it follows that  $P_w$  assumes only discrete values in  $[0, 1]$  with the null distribution determining the mapping between these two sets.

The generalization of the WSR test to the uncertain sample  $\Delta\hat{\mathbf{T}}$  can be carried out almost analogously to the *t* test. However, the fact that  $W \in \mathbb{N}_{[0, n(n+1)/2]}$  makes it inconvenient to use a continuous probability density distribution. We denote the distribution for the uncertain  $\hat{W}(\Delta\hat{\mathbf{T}})$  by

$$\begin{aligned} \mathcal{P}_{\hat{W}}(\hat{w}) &= \int \delta\left(\sum_{i=1}^n R(|\Delta\hat{t}_i|) \Theta(\Delta\hat{t}_i) - \hat{w}\right) \\ &\quad \rho_{\Delta\hat{\mathbf{T}}}(\Delta\hat{\mathbf{t}}) d\Delta\hat{\mathbf{t}} \end{aligned} \tag{26}$$

Given the one-to-one map from all  $w \in \mathbb{N}_{[0, n(n+1)/2]}$  to the set of discrete potential values  $p_w$  for  $P_w$  in  $[0, 1]$  determined by Eq. (25), the probability to obtain  $\hat{p}_w$  is already given by the probability to obtain the corresponding  $\hat{w}$ . Hence, we find

$$\mathcal{P}_{\hat{p}_w}(p_w(\hat{W}) = \hat{p}_w) = \mathcal{P}_{\hat{W}}(\hat{w}). \tag{27}$$

3.3.3 Bootstrap test

Given an observed sample of differences  $\mathbf{d} = (d_1, \dots, d_n)$ , a bootstrap test constitutes a third option to test the compatibility of the sample with the hypothesis that the population of differences features a mean equal to or greater than 0:  $H_0 := \mu_0 \geq 0$ . Guidance for the construction of a bootstrap hypothesis test can be found in Lehmann and Romano (2006) and Hall and Wilson (1991). The advantage of the bootstrap test lies in its independence from assumptions regarding the distributions' shape. Lehmann and Romano (2006) propose the test statistic

$$v = \sqrt{nu}, \tag{28}$$

with  $u(\mathbf{d}) = \frac{1}{n} \sum_{i=1}^n d_i$  denoting the sample mean. In contrast to the above two tests, the bootstrap test constructs the null distribution directly from the observed data. In the absence of assumptions, the best available approximation of the population  $\mathcal{P}_D$  is given by the empirical density

$$\mathcal{P}_D(d) \sim \frac{1}{n} \sum_{i=1}^n \delta(d - d_i). \tag{29}$$

However, the empirical density does not necessarily comply with the null hypothesis and it thus has to be shifted accordingly:

$$\tilde{\rho}_D(d) = \sum_{i=1}^n \delta(d - d_i + u). \tag{30}$$

$\tilde{\rho}_D(d)$  corresponds to the borderline case of the null hypothesis  $\mu = 0$ . The null distribution for  $v$  is then derived by re-sampling  $m$  synthetic samples  $\tilde{\mathbf{d}}_j = (\tilde{d}_1, \dots, \tilde{d}_n)_j$  of size  $n$  from  $\tilde{\rho}_D(d)$  and computing  $\tilde{v}_j = v(\tilde{\mathbf{d}}_j)$  for each of them. This corresponds to randomly drawing  $n$  values from the set  $\mathbf{d} - u$  with replacement and computing  $v$  for the resampled vectors  $m$  times, where the index  $j$  labels the iteration of this process. The resulting set  $\{\tilde{v}_j\}_j$  induces the data-driven null distribution for the test statistic

$$\rho_V^0(v) = \frac{1}{m} \sum_{j=1}^m \delta(v - \tilde{v}_j). \tag{31}$$

Setting  $m = 10000$  we obtain robust null distributions for the two cases relevant here ( $n = 16$  and  $n = 20$ ). The  $p$  value of this bootstrap test is then computed as before in a one-sided manner:

$$p_v(v(\mathbf{d})) = \int_{-\infty}^{v(\mathbf{d})} \rho_V^0(v) dv = \frac{1}{m} \sum_{j=1}^m \Theta(v(\mathbf{d}) - \tilde{v}_j), \tag{32}$$

where the right-hand side equals the fraction of resampled  $\tilde{v}_j$  that are smaller than  $v(\mathbf{d})$  of the original sample.

In the case where the sample of differences is uncertain, as for  $\Delta\hat{T} = (\Delta\hat{T}_1, \dots, \Delta\hat{T}_n)$ , the construction scheme for  $\rho_V^0$  needs to be adjusted to reflect these uncertainties. In principle, each possible value  $\Delta\hat{t}$  for the uncertain  $\Delta\hat{T}$  is associated with its own null distribution  $\rho_V^0(v, \Delta\hat{t})$ . In this sense, the value for the test statistic  $v(\Delta\hat{t})$  should be compared to the corresponding  $\rho_V^0(v, \Delta\hat{t})$  to derive a  $p$  value for this  $\Delta\hat{t}$ . Equations (31) and (32) define a mapping from  $\Delta\hat{t}$  to its corresponding  $p$  value. To compute the uncertainty distribution for the  $p$  value, this map has to be evaluated for all potential  $\Delta\hat{t}$ , weighted by the uncertainty distribution  $\rho_{\Delta\hat{T}}(\Delta\hat{t})$ :

$$\rho_{\hat{p}_v}(\hat{p}_v) = \int \delta(\hat{p}_v - p_v(\Delta\hat{t})) \rho_{\Delta\hat{T}}(\Delta\hat{t}) d\Delta\hat{t}. \tag{33}$$

The three tests are applied in combination in order to compensate for their individual deficits. If the population  $\mathcal{P}_{\Delta T}$  was truly Gaussian, the  $t$  test would be the most powerful test; i.e., its rejection region would be the largest across all tests on the population mean (Lehmann and Romano, 2006). Since normality of  $\mathcal{P}_{\Delta T}$  cannot be guaranteed, the less powerful Wilcoxon signed-rank test constitutes a meaningful supplement to the  $t$  test, relying on the somewhat weaker assumption that  $\mathcal{P}_{\Delta T}$  is symmetric around 0. Finally, the bootstrap test is non-parametric and in view of its independence from any assumptions adds a valuable contribution.

3.4 Comparison to previous analysis

For the derivation of the transition lag uncertainty distributions  $\rho_{\Delta\hat{T}_i^{p,q}}(\Delta\hat{t}_i^{p,q})$  of the  $i$ th DO event between the proxies  $p$  and  $q$ , we have directly adopted the methodology designed by Erhardt et al. (2019). However, our statistical interpretation of the resulting sets of uncertainty distributions  $\{\rho_{\Delta\hat{T}_1^{p,q}}(\Delta\hat{t}_1^{p,q}), \dots, \rho_{\Delta\hat{T}_n^{p,q}}(\Delta\hat{t}_n^{p,q})\}$  derived from the set of DO events differs from the one proposed by Erhardt et al. (2019). In this section we explain the subtle yet important differences between the two statistical perspectives.

Given a pair of variables  $(p, q)$ , Erhardt et al. (2019) define what they call ‘‘combined estimate’’  $\rho_{\Delta T^*}(\Delta t^*)$  as the product over all corresponding lag uncertainty distributions:

$$\rho_{\Delta T^*}(\Delta t^*) \propto \prod_{i=1}^n \rho_{\Delta\hat{T}_i}(\Delta t^*). \tag{34}$$

This implicitly assumes that all DO events share the exact same time lag  $\Delta t^*$  between the variables  $p$  and  $q$ . This is realized by inserting a single argument  $\Delta t^*$  into the different distributions  $\rho_{\Delta\hat{T}_i}(\cdot)$ . Hence, the product on the right-hand side of Eq. (34) in fact indicates the probability that all DO events assume the time lag  $\Delta t^*$ , provided that they all assume the same lag:

$$\begin{aligned} \rho_{\Delta T^*}(\Delta t^*) &= \rho_{\Delta T^*}(\Delta t^* | \Delta\hat{t}_1 = \dots = \Delta\hat{t}_n = \Delta t^*) \\ &= \frac{\prod \rho_{\Delta\hat{T}_i}(\Delta t^*)}{\int_{\Omega} \prod \rho_{\Delta\hat{T}_i}(\Delta\hat{t}_i) d\Delta\hat{t}_i}, \Omega = \{\Delta\hat{t} : \Delta\hat{t}_i = \Delta\hat{t}_j \forall i, j\}. \end{aligned} \tag{35}$$

The denominator on the right-hand side equals the probability that all DO events share a common time lag. Equation (34) strongly emphasizes those regions where all uncertainty distributions  $\rho_{\Delta\hat{t}_i}(\Delta\hat{t}_i)$  are simultaneously substantially larger than 0. The combined estimate answers the question: provided that all DO events exhibit the same lag between the transition onsets of  $p$  and  $q$ , then how likely is it that this lag is given by  $\Delta t^*$ . Drawing on this quantity, Erhardt et al. (2019) conclude that  $\delta^{18}\text{O}$  and  $\text{Na}^+$  “on average” lag  $\text{Ca}^{2+}$  and  $\lambda$  by about 1 decade.

Thinking of the DO transition onset lags as i.i.d. random variables of a repeatedly executed random experiment takes into account the natural variability between different DO events, and hence it removes the restricting a priori assumption  $\Delta\hat{t}_1 = \dots = \Delta\hat{t}_n$ . In our approach we have related the potentially systematic character of lags to the population mean. Since the sample mean is the best point estimate of a population mean, we consider it to reasonably indicate potential leads and lags, whose significance should be tested in a second step. Thus, we ascribe to the sample mean a similar role as Erhardt et al. (2019) ascribe to the combined estimate, and therefore we present a comparison of these two quantities in Sect. 4.1.

The mean of an uncertain sample  $\hat{U} = u(\Delta\hat{T})$  is again an uncertain quantity and its distribution reads

$$\rho_{\hat{U}}(\hat{u}) = \int \delta(\hat{u} - u(\Delta\hat{t})) \rho_{\Delta\hat{T}}(\Delta\hat{t}) d\Delta\hat{t}. \quad (36)$$

While the combined estimate multiplies the distributions  $\rho_{\Delta\hat{t}_i}(\Delta t^*)$ , the uncertain sample mean convolutes them pairwise (see Appendix C). We thus expect the distributions for uncertain sample means to be broader than the corresponding distributions for the combined estimate. This can be motivated by considering the simple example of two Gaussian variables  $X$  and  $Y$ . According to the convolution their sample mean  $U = \frac{X+Y}{2}$  is normally distributed with variance  $\sigma_{x*y}^2 = \frac{\sigma_x^2 + \sigma_y^2}{4}$ . In contrast, a combined estimate would yield a normal distribution with variance  $\sigma_{xy}^2 = \frac{\sigma_x^2 + \sigma_y^2}{\sigma_x^2 \sigma_y^2}$ . Thus, the convolution will appear broader for all  $\sigma_x^2 \sigma_y^2 > 4$ , which is the case for the distributions considered in this study.

## 4 Results

In the following we apply the above methodology to the different pairs of proxies that Erhardt et al. (2019) found to exhibit a decadal-scale time lag, based on an assessment of the combined estimate, namely  $(\text{Ca}^{2+}, \text{Na}^+)$ ,  $(\lambda, \text{Na}^+)$ ,  $(\text{Ca}^{2+}, \delta^{18}\text{O})$ , and  $(\lambda, \delta^{18}\text{O})$  from the NGRIP ice core and  $(\text{Ca}^{2+}, \text{Na}^+)$  from the NEEM ice core. For each individual proxy we estimate the uncertain transition onsets relative to the timing of the DO events as given by Rasmussen et al. (2014) (see Fig. 2). From these uncertain transition onsets, the uncertainty distributions for the sets of uncertain lags

$\Delta\hat{T}^{p,q}$  between the proxies  $p$  and  $q$  are derived according to Eq. (7). As mentioned previously, we study the same selection of transitions evidenced in the multi-proxy records as Erhardt et al. (2019). This selection yields sample sizes of either 16 or 20 lags per pair of proxies but not 23, which is the total number of DO events present in the data.

We first study the uncertain sample means. As already mentioned, the sample mean is the best available point estimate for the population mean. Hence, sample means different from 0 may be regarded as first indications for potential systematic lead–lag relationships and thus motivate the application of hypothesis tests. We compare the results obtained for the uncertain sample means with corresponding results for the combined estimate. Both quantities indicate a tendency towards a delayed transition in  $\text{Na}^+$  and  $\delta^{18}\text{O}$ . Accordingly, in the subsequent section we apply the generalized hypothesis tests introduced above to the uncertain samples of transition lags to test the null hypothesis that pairwise, the apparent transition sequence is not systematically favored, that is, that the populations have mean equal to or greater than 0.

### 4.1 Uncertain sample mean and combined estimate

Based on their assessment of the combined estimate, Erhardt et al. (2019) concluded that on average, transitions in  $\text{Ca}^{2+}$  and  $\lambda$  started approximately 1 decade earlier than their counterparts in  $\text{Na}^+$  and  $\delta^{18}\text{O}$ . Figure 5 shows a reproduction of their results together with the uncertainty distributions of the sample means for all proxy pairs under study ( $(\text{Ca}^{2+}, \delta^{18}\text{O})$  and  $(\lambda, \delta^{18}\text{O})$  are not shown in Erhardt et al., 2019). For an uncertain sample of lags  $\Delta\hat{T}^{p,q}$  between the proxies  $p$  and  $q$ , the combined estimate and the uncertain sample mean are computed according to Eqs. (35) and (36), respectively. The reproduction of the combined estimate deviates from the original publication by no more than 1 year with respect to the mean and the 5th and 95th percentiles across all pairs. These deviations might originate from the stochastic MCMC-sampling process used for the analysis.

With the sample mean being the best point estimator of the population mean, it serves as a suitable indicator for a potential population mean different from 0. The expectations

$$E(\hat{U}) = \int \hat{u} \rho_{\hat{U}}(\hat{u}) d\hat{u} \quad (37)$$

for the sample means of all proxy pairs do in fact suggest a tendency towards negative values in all distributions, i.e., a delay of the  $\text{Na}^+$  and  $\delta^{18}\text{O}$  transition onsets with respect to  $\text{Ca}^{2+}$  and  $\lambda$ . This indication is weakest for  $(\text{Ca}^{2+}, \text{Na}^+)$  and  $(\text{Ca}^{2+}, \delta^{18}\text{O})$  from NGRIP, since for these pairs we find a non-zero probability of a positive sample mean. For the other pairs the indication is comparably strong, with the 95th percentiles of the uncertainty distributions for the sample mean still being less than 0. Overall, the results for the uncertain mean confirm the previously reported tendencies, and in very rough terms, the distributions qualitatively agree with those

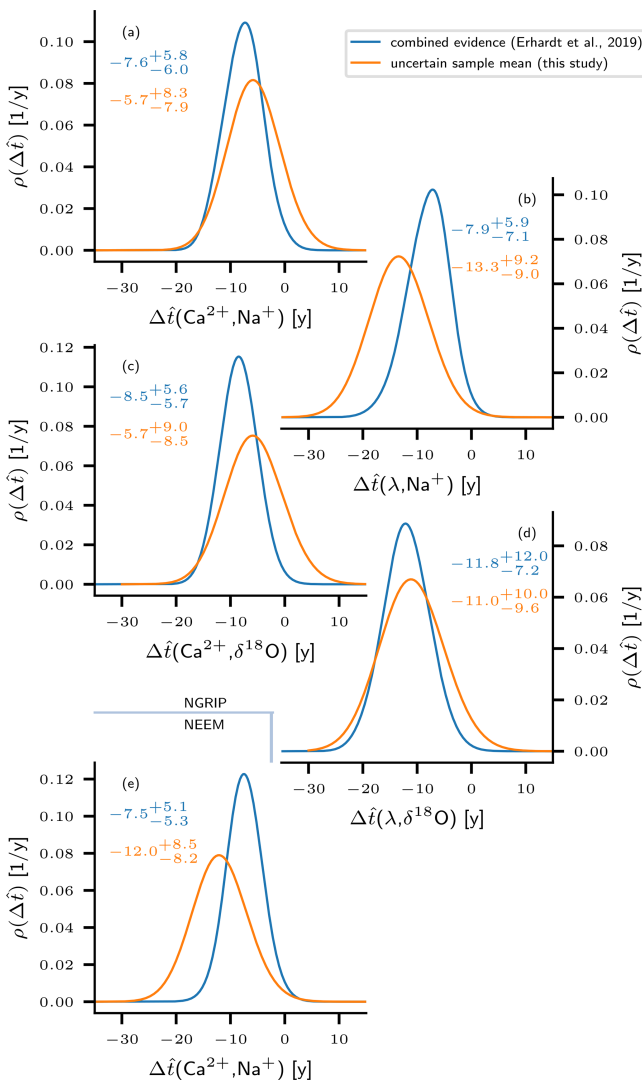


**Figure 5.** Comparison between the uncertain sample means (this study) and “combined estimates” according to Erhardt et al. (2019). The probability densities for the combined estimate are derived from the samples of uncertain time lags according to Eq. (34). Correspondingly, the uncertain sample means are computed according to Eq. (36). The numbers in the plots indicate the mean, the 5th, and the 95th percentile of the respective quantity. Both computations use Gaussian kernel density estimates of the MCMC-sampled transition onset lags. Panels (a–d) refer to proxy pairs from the NGRIP ice core, and panel (e) shows results from the NEEM ice core. The distributions for both the combined estimate and the uncertain sample mean point towards a delayed transition onset in  $\delta^{18}\text{O}$  and  $\text{Na}^+$  with respect to  $\lambda$  and  $\text{Ca}^{2+}$ .

for the combined estimate. In agreement with the heuristic example from Sect. 3.4, we find the sample mean distributions to be broader than the combined estimate distributions in all cases. The expected sample means indicate less pronounced lags for  $(\text{Ca}^{2+}, \text{Na}^+)$  (Fig. 5a) and  $(\text{Ca}^{2+}, \delta^{18}\text{O})$  (Fig. 5c) from the NGRIP ice core compared to the expecta-

tions of the corresponding combined estimate. In combination with the broadening of the distribution, this yields considerable probabilities for  $U > 0$  of 12 % and 14 %, respectively, indicating a delayed transition of  $\text{Ca}^{2+}$  in the sample mean with respect to  $\text{Na}^+$  or  $\delta^{18}\text{O}$ . Contrarily, for  $(\lambda, \text{Na}^+)$  (NGRIP, Fig. 5b) and  $(\text{Ca}^{2+}, \text{Na}^+)$  (NEEM, Fig. 5e) the expected sample means point towards more distinct lags than reported by Erhardt et al. (2019) based on the combined estimate. For  $(\lambda, \delta^{18}\text{O})$  (NGRIP, Fig. 5d) the sample mean and the combined estimate are very close. Note that the analysis of the uncertain sample values yields a more inconsistent picture with regard to the  $(\text{Ca}^{2+}, \text{Na}^+)$  lag in the two different cores. While the distribution is shifted to less negative (less pronounced lag) for the NGRIP data, it tends to more negative values in the case of NEEM (stronger lag), suggesting a slight discrepancy between the cores.

Both quantities, the uncertain sample mean and the combined estimate point towards delayed transition onsets in  $\text{Na}^+$  and  $\delta^{18}\text{O}$  with respect to  $\text{Ca}^{2+}$  and  $\lambda$ , with major fractions of their uncertainty densities being allocated to negative values. This provides motivation to test whether the observations significantly contradict the hypothesis of a population mean equal to or greater than 0. Accordingly, the subsequent section presents the results obtained from the application of three different hypothesis tests that target the population mean. As discussed in Sect. 3, the tests have been modified to allow for a rigorous uncertainty propagation and return an uncertainty distribution for their corresponding  $p$  values rather than scalars.

#### 4.2 Statistical significance of the proposed lead–lag relations

Above, we identified three tests for testing the hypothesis that the samples  $\Delta\hat{T}^{p,q}$  were actually generated from populations that on average feature no or even reversed time lags compared to what the sign of the corresponding uncertain sample mean suggests. Mathematically, this is equivalent to testing the hypothesis that the mean  $\mu^{p,q}$  of the population  $\mathcal{P}_{\Delta\hat{T}}^{p,q}$  is greater than or equal to 0:  $H_0 : \mu^{p,q} \geq 0$ . A rejection of this hypothesis would confirm that the assessed sample is very unlikely to stem from a population with  $\mu^{p,q} \geq 0$  and would thereby provide evidence for a systematic lag. Under the constraints indicated above this would in turn yield evidence for an actual lead of the corresponding climatic process. We have chosen a significance level of  $\alpha = 0.05$ , which is a typical choice. Figure 7 summarizes the final uncertainty distributions of the three tests for all proxy pairs under study. Corresponding values are given in Table 1.

Figure 6 exemplarily illustrates the application of the three tests to the empirical densities obtained for  $\Delta\hat{T}(\text{Ca}^{2+}, \text{Na}^+)$  (NGRIP). In Fig. 6 the initial uncertainty in the observations – i.e., the uncertainty encoded by the distributions of transition onset lags – is propagated to an uncertain test statistic according to Eq. (16). In turn, the uncertain test statistic

**Table 1.** Results from the application of the  $t$  test, the WSR test, and a bootstrap test to uncertain samples of DO transition onset lags  $\Delta\hat{T}^{p,q}$ .  $E(\hat{P})$  denotes the expected  $p$  value, derived from the uncertainty-propagated  $p$ -value distribution. The probability of significant test results associated with the same distribution is indicated by  $\pi(\hat{P} < 0.05)$ . For comparison, the  $p$  values from the application of the tests to the expected sample  $E(\Delta\hat{T}) = \int \rho_{\Delta\hat{T}}(\Delta\hat{T})\Delta\hat{T} d\Delta\hat{T}$  are given in the bottom row.

	NGRIP												NEEM		
	(Ca <sup>2+</sup> , Na <sup>+</sup> )			(λ, Na <sup>+</sup> )			(Ca <sup>2+</sup> , δ <sup>18</sup> O)			(λ, δ <sup>18</sup> O)			(Ca <sup>2+</sup> , Na <sup>+</sup> )		
	$t$ test	WSR	BS	$t$ test	WSR	BS	$t$ test	WSR	BS	$t$ test	WSR	BS	$t$ test	WSR	BS
$E(\hat{P})$	0.22	0.17	0.22	0.09	0.09	0.09	0.23	0.18	0.23	0.13	0.11	0.13	0.08	0.08	0.07
$\pi(\hat{P} < 0.05)$	0.26	0.32	0.3	0.47	0.48	0.52	0.24	0.31	0.26	0.37	0.44	0.41	0.57	0.58	0.61
$p(E(\Delta\hat{T}))$	0.04	0.01	0.02	0.02	0.02	0.02	0.04	0.01	0.04	0.02	0.01	0.02	0.01	0.01	0.01

yields an uncertain  $p$  value (see Eq. 17). Since the numerical computation is based on empirical densities as generated by the MCMC sampling, we show the corresponding histograms instead of continuous densities – for  $\rho_{\Delta\hat{T}_i}(\Delta\hat{T}_i)$ , Gaussian kernel density estimates are presented only for the sake of visual clarity. On the level of the test statistics the red dashed line separates the acceptance from the rejection region, based on the null distributions given in black. Qualitatively, the three tests yield the same results. The histograms clearly indicate non-zero probabilities for the test statistic in both regions. Correspondingly, the histograms for the  $p$  values stretch well across the significance threshold. The shapes of the histograms resemble an exponential decay towards higher  $p$  values. This results from the non-linear mapping of the test statistics to the  $p$  values. Despite the pronounced bulk of empirical  $p$  values below the significance level, the probability of non-significant  $p$  values is still well above 50% for the three tests (see Table 1). Also, the expected  $p$  value exceeds the significance level for all tests. Hence, neither of the two criteria for rejecting the null hypothesis formulated in Sect. 3.2 is met for the proxy pair (Ca<sup>2+</sup>, Na<sup>+</sup>). In contrast, if the observational uncertainties are averaged out on the level of the transition onset lags, all tests yield  $p$  values below the significance level, which would indicate that the lags were indeed significant. Hence, the rigorous propagation of uncertainties qualitatively changes the statistical assessment of the uncertain sample of lags  $\Delta\hat{T}(\text{Ca}^{2+}, \text{Na}^+)$  (NGRIP). While the expected sample rejects the null hypothesis, rigorous uncertainty propagation leads to acceptance. This holds true for all tests.

Figure 7 summarizes the results obtained for all proxy pairs under study. Qualitatively, our findings are the same for the other pairs as for the (Ca<sup>2+</sup>, Na<sup>+</sup>) (NGRIP) case discussed in detailed above. All expected  $p$  values, as indicated by the pink bars, are above the significance level. Also, the probability for significance is below 60% for all pairs and all tests as shown by the pie charts. Therefore, for all proxy pairs and for all tests, the formulated decision criteria do thus not allow us to reject the null hypothesis of a population mean greater than or equal to 0. In contrast, all expected samples

are significant across all tests with corresponding  $p$  values indicated by the yellow bars. The proxy pairs with the lowest expected  $p$  values and the highest probability of  $\hat{P} < \alpha$  are (λ, Na<sup>+</sup>) from NGRIP and (Ca<sup>2+</sup>, Na<sup>+</sup>) from NEEM, as already suggested by the analysis of the uncertain sample mean. For the NGRIP ice core the delay of Na<sup>+</sup> and δ<sup>18</sup>O with respect to Ca<sup>2+</sup> has a very low probability to be significant (approximately one-third). The pair (λ, δ<sup>18</sup>O) ranges in between the latter two.

## 5 Discussion

Erhardt et al. (2019) have reported an average time lag between the transition onsets in Na<sup>+</sup> and δ<sup>18</sup>O proxy values and their counterparts in Ca<sup>2+</sup> and λ at the onset of DO events. This statement is based on the assessment of the combined estimate derived from uncertain samples of time lags  $\Delta\hat{T}^{p,q}$ . The samples were obtained by applying a well-suited Bayesian transition onset detection scheme to high-resolution time series of the different proxies. The combined estimate indicates leads of the Ca<sup>2+</sup> and λ transition onsets with respect to Na<sup>+</sup> and δ<sup>18</sup>O by approximately 1 decade, with the 90% confidence interval ranging from 0 to approximately 15 years. The combined estimate implicitly assumes that for a given proxy pair all DO events share a common time lag ( $\Delta\hat{T}_i^{p,q} = \Delta\hat{T}_j^{p,q}$ ).

We argue that the variability across different DO events cannot be ignored in the assessment of the data. Although the DO events are likely to be caused by the same physical mechanism, changing boundary conditions and other natural climate fluctuations will lead to deviations in the exact timings of the different processes involved in triggering the individual DO events. Figure 2 clearly shows that the different events exhibit different time lags. Provided that the DO events were driven by the same process, physically they constitute different realizations, and they exhibit great variability also in other variables such as the amplitude of the temperature change (Kindler et al., 2014) or the waiting times with respect to the previous event (Ditlevsen et al., 2007; Boers et al., 2018). The random experiment framework introduced

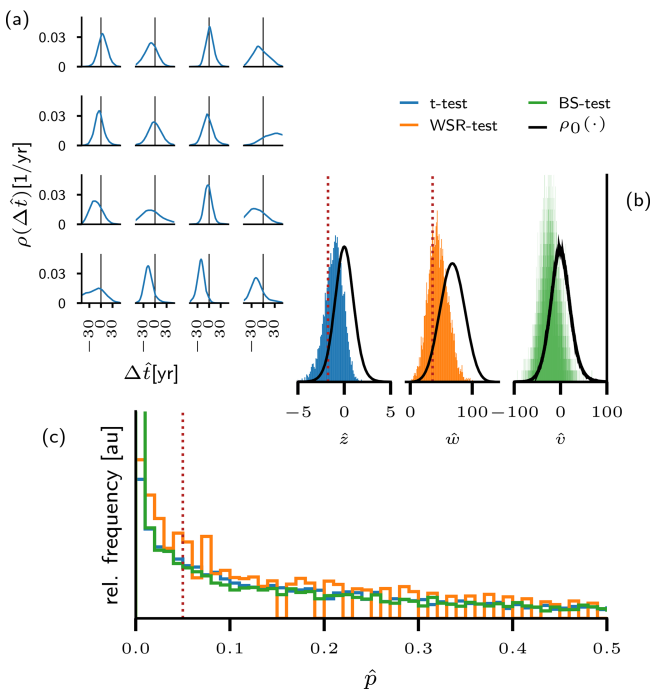


**Figure 6.** Exemplary application of the analysis to the proxy pair ( $\text{Ca}^{2+}$ ,  $\text{Na}^{+}$ ) from the NGRIP ice core. Panel (a) shows 16 uncertain time lags  $\Delta\hat{T}_i$  derived from the proxy data around DO events. The continuous densities have been obtained via a Gaussian kernel density estimate from the corresponding MCMC samples (see Sect. 3.1). In panel (b) the uncertain test statistics induced by the uncertain sample are shown for the  $t$  test (blue), the WSR test (orange), and a bootstrap test (green). The values that comprise the histograms are immediately derived from the MCMC samples. Panel (c) shows the empirical uncertainty distribution for the  $p$  values of the three tests, following from the uncertain test statistics in panel (b). Dotted red lines separate rejection from acceptance regions in panels (b) and (c). In the case of the bootstrap test, the rejection regions cannot be defined consistently on the level of the test statistic, since each possible value  $\Delta\hat{T}$  for the uncertain  $\Delta\hat{T}$  generates its individual null distribution. The null distribution shown here is in fact the pooled distribution of resampled  $\tilde{v}_j$  obtained from all MCMC-sampled values for  $\Delta\hat{T}$ . For the other proxy pairs investigated in this study, corresponding plots would appear structurally similar.

in this study allows us to relax the constraint of a common time lag  $\Delta t^*$  shared across all events and reflects the fact that natural variability will cause different expressions of the same mechanism across different DO events. Moreover, this framework relates potential systematic leads and lags in the physical process that drives DO events to a corresponding non-zero mean of a population of lags between proxy variables. This allows for the physically meaningful formulation of a statistical hypothesis and a corresponding null hypothesis. By applying different hypothesis tests we have followed a well-established line of statistical inference. Motivated by the apparent transition onset delays in  $\text{Na}^{+}$  and  $\delta^{18}\text{O}$  with respect to the transitions in  $\lambda$  and  $\text{Ca}^{2+}$ , as reported by Er-

hardt et al. (2019) and confirmed here on the level of uncertain sample means, we tested the null hypothesis that the corresponding populations do not favor the proposed transition sequence. Rejection of this hypothesis would have provided evidence that the observed lag tendency is an imprint of the underlying physical process and therefore a systematic feature. However, generalized versions of three different hypothesis tests consistently fail to reject the null hypothesis under rigorous propagation of the observational uncertainties originating from the MCMC-based transition onset detection. This holds true for all proxy pairs. The fact that the tests rely on different assumptions on the population's shape but nonetheless qualitatively yield the same results makes our assessment robust. We conclude that the possibility that the observed tendencies towards advanced transitions in  $\text{Ca}^{2+}$  and  $\lambda$  have occurred simply by chance cannot be ruled out. If the common physical interpretation of the studied proxies holds true, our results imply that the hypothesis that the trigger of the DO events is associated directly with the North Atlantic sea-ice cover rather than the atmospheric circulation – be it on a synoptic or hemispheric scale – cannot be ruled out. We emphasize that our results should not be misunderstood as evidence against the alternative hypothesis of a systematic lag. In the presence of a systematic lag ( $\mu < 0$ ) the ability of hypothesis tests to reject the null hypothesis of no systematic lag ( $(H_0 : \mu = 0)$ ) depends on the sample size  $n$ , the ratio between the mean lag  $|\mu|$ , the variance of the population, and the precision of the measurement. Neither of these quantities is favorable in our case, and thus it is certainly possible that the null hypothesis cannot be rejected despite the alternative being true.

Our main purpose was the consistent treatment of observational uncertainties and we have largely ignored the vibrant debate on the qualitative interpretation of the proxies. Surprisingly, we could not find any literature on the application of hypothesis tests to uncertain samples of the kind discussed here. The theory of fuzzy  $p$  values is in fact concerned with uncertainties either in the data or in the hypothesis. However, it is not applicable to measurement uncertainties that are quantifiable in terms of probability density functions (Filzmoser and Viertl, 2004). We have proposed to propagate the uncertainties to the level of the  $p$  values and to then consider the expected  $p$  values and the share of  $p$  values which indicate significance, in order to decide between rejection and acceptance. The  $p$  value measures the extremeness of a sample with respect to the null distribution, and we hence regard the expected  $p$  value to be a suitable measure for the uncertain samples' extremeness. In cases of a high cost of a wrongly rejected null hypothesis, one might want to have a high degree of certainty that the uncertain sample actually contradicts the null hypothesis and hence a high probability of the uncertain  $p$  value being smaller than  $\alpha$ . In contrast, if the observational uncertainties are averaged out beforehand, crucial information is lost. The expected sample may either be significant or

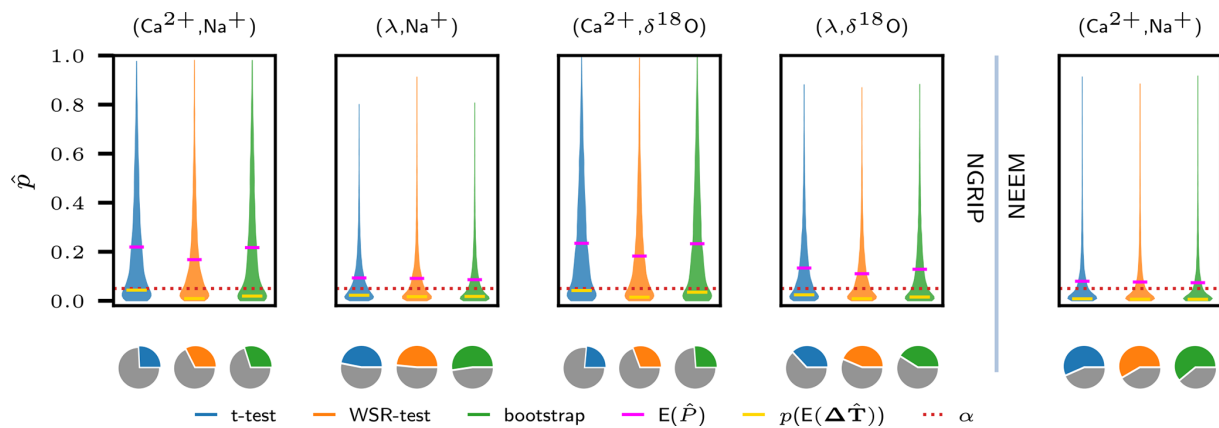


**Figure 7.** Results of the hypothesis tests applied to the uncertain samples of transition onset lags  $\Delta \hat{T}_i^{p,q}$ . The violin plots show the Gaussian kernel density estimates of the empirical uncertainty distributions for  $p$  values (see Fig. 6) obtained for all tests and for all proxy pairs investigated. Pink bars indicate the corresponding expected  $p$  values  $E(\hat{P})$  and yellow bars indicate the  $p$  values obtained from testing the expected samples  $E(\Delta \hat{T})$ . All expected  $p$  values are above the significance level  $\alpha = 0.05$  (red dotted line), while the expected samples appear to be significant consistently across all proxy pairs and all tests. The pie charts indicate the probability of the respective  $p$  values to be less than  $\alpha$ .

not, but the uncertainty about the significance can no longer be accurately quantified.

The potential of the availability of data from different sites has probably not been fully leveraged in this study. Naively, one could think of the NEEM and NGRIP ( $\text{Ca}^{2+}$ ,  $\text{Na}^+$ ) lag records as two independent observations of the same entity. However, given the discrepancies in the corresponding sample mean uncertainty distributions, changes in sea-ice cover and atmospheric circulation could in fact have impacted both cores differently. Proxy-enabled modeling studies as presented by Sime et al. (2019) could shed further light on the similarity of the signals at NEEM and NGRIP as a function of change in climatic conditions. Also, a comparison of the NGRIP and NEEM records on an individual event level could provide further insights into how to combine these records statistically. There might be ways to further exploit the advantage of having two recordings of the same signal.

## 6 Conclusions

We have presented a statistical reinterpretation of the high-resolution proxy records provided and analyzed by Erhardt et al. (2019). The probabilistic transition onset detection also designed by Erhardt et al. (2019) very conveniently quantifies the uncertainty in the transition onset estimation by returning probability densities instead of scalar estimates. While the statistical quantities “combined estimate” (Erhardt et al., 2019) and “uncertain sample mean” (this study) indicate a tendency for a pairwise delayed transition onset in  $\text{Na}^+$  and  $\delta^{18}\text{O}$  proxy values with respect to  $\text{Ca}^{2+}$  and  $\lambda$ , a more rigorous treatment of the involved uncertainties shows that these tendencies are not statistically significant. That is, at the significance level  $\alpha = 5\%$  they do not contradict the null

hypothesis that no or the reversed transition sequence is in fact physically favored. Thus, a pairwise systematic lead–lag relation cannot be evidenced for any of the proxies studied here. We have shown that if uncertainties on the level of transition onset lags are averaged out beforehand, the samples of lags indeed appear to be significant, which underpins the importance of rigorous uncertainty propagation in the analysis of paleoclimate proxy data. We have focused on the quantitative uncertainties and have largely ignored qualitative uncertainty stemming from the climatic interpretation of the proxies. However, if the common proxy interpretations hold true, our findings suggest that, for example, the hypothesis of an atmospheric trigger – either of hemispheric or synoptic scale – for the DO events should not be favored over the hypothesis that a change in the North Atlantic sea-ice cover initiates the DO events.

Even though we find that the uncertainty of the transition onset detection combined with the small sample size prevents the deduction of statistically unambiguous statements on the temporal order of events, we think that multi-proxy analysis is a promising approach to investigate the sequential order at the beginning of DO events. In this study, we refrained from analyzing the lags between the different proxies in a combined approach and focused on the marginal populations. However, a combined statistical evaluation – that is, treating the transition onsets of all proxy variables as a four-dimensional random variable – merits further investigation. Also, we propose to statistically combine measurements from NEEM and NGRIP (and potentially further ice cores) of the same proxy pairs. Finally, hierarchical models may be invoked to avoid switching from a Bayesian perspective in the transition onset estimation to a frequentist perspective in the statistical interpretation of the uncertain samples. Finally,

effort in conducting modeling studies should be sustained. Especially proxy-enabled modeling bears the potential to improve comparability between model results and paleoclimate records. Together, these lines of research are promising to further constrain the sequence of events that have caused the abrupt climate changes associated with DO events.

**Appendix A: Numerical treatment of high-dimensional probability densities**

In Sect. 3.1 we introduced the probabilistic transition onset detection designed by Erhardt et al. (2019). Given a single time series, the formulation of a stochastic ramp model induces a posterior probability density for the set of model parameters  $\theta$  in a Bayesian sense:

$$\pi(\theta|\mathcal{D}) = \frac{\pi(\mathcal{D}|\theta) \pi(\theta)}{\pi(\mathcal{D})}. \tag{A1}$$

However, a classical numerical representation of this density on a discretized grid is inconvenient. Due to its high dimensionality for a reasonable grid spacing the number of data points easily overloads the computational power of ordinary computers. For example, representing each dimension with a minimum of 100 points would amount to a total of  $10^{12}$  data points. On top of that, the application of any methods to such a grid is computationally very costly. Here, the MCMC sampler constitutes an efficient solution. By sampling a representative set  $\{\theta_j\}_j$  from the posterior probability density it may be used to construct an empirical density in the sense of Eq. (4). For the sake of simplicity in the main text we have formulated the methods in terms of continuous probability densities, although all computations in fact rely on empirical densities obtained from MCMC samples. Here, we show that all steps in the derivation of the methods can be performed equivalently under stringent use of the empirical density. With regards to hypothesis tests, the use of empirical densities for the uncertain transition lag samples  $\Delta T_i^{p,q}$  essentially boils down to an application of the tests to each individual value comprised in the respective empirical density.

For a given proxy and a given DO event, in a first step the MCMC algorithm samples from the joint posterior probability density for the models parameter configuration  $\theta = (t_0, \tau, y_0, \Delta y, \alpha, \sigma)$ , giving rise to the empirical density  $\bar{\rho}_{\Theta}(\theta) = \frac{1}{m} \sum \delta(\theta - \theta_j)$ . Integration over the nuisance parameters then yields the marginal empirical density for the transition onset:

$$\bar{\rho}_{T_0}^{p,i}(t_0^{p,i}) = \frac{1}{m} \sum_{j=1}^m \delta(t_0^{p,i} - t_{0,j}^{p,i}), \tag{A2}$$

where the index  $i$  indicates the DO event and  $p$  denotes the proxy variable while  $j$  runs over the MCMC sampled values. We use bars to mark empirical densities in contrast to continuous densities. The uncertainty distribution for the lag  $\Delta T_i^{p,q}$  between the variables  $p$  and  $q$  as defined by Eq. (7) may then be approximated as follows (omitting the index  $i$ ):

$$\begin{aligned} &\rho_{\Delta T}^{p,q}(\Delta t^{p,q}) \\ &= \iint \delta(t_0^p - t_0^q - \Delta t^{p,q}) \rho_{T_0}^p(t_0^p) \rho_{T_0}^q(t_0^q) dt_0^p dt_0^q \\ &\simeq \iint \delta(t_0^p - t_0^q - \Delta t^{p,q}) \bar{\rho}_{T_0}^p(t_0^p) \bar{\rho}_{T_0}^q(t_0^q) dt_0^p dt_0^q \\ &= \iint \delta(t_0^p - t_0^q - \Delta t^{p,q}) \frac{1}{m} \sum_{j=1}^m \delta(t_0^p - t_{0,j}^p) \\ &\quad \times \frac{1}{m} \sum_{k=1}^m \delta(t_0^p - t_{0,k}^q) dt_0^p dt_0^q \\ &= \frac{1}{m^2} \sum_{j,k=1}^m \delta(t_{0,j}^p - t_{0,k}^q - \Delta t^{p,q}) = \bar{\rho}_{\Delta T}^{p,q}(\Delta t^{p,q}). \end{aligned} \tag{A3}$$

Thus, the empirical uncertainty distribution for the time lag is induced by the set of all possible differences between members of the two MCMC samples for the respective transition onsets:

$$\left\{ \Delta t_j^{p,q} \right\}_{j \in [1, m^2]} = \left\{ t_{0,k}^p - t_{0,l}^q \right\}_{p,q \in [1, m]}. \tag{A4}$$

For this study  $m = 6000$  values have been sampled with the MCMC algorithm for each transition under study. This yields  $m^2 = 36 \times 10^6$  potential values for the empirical  $\Delta T$  uncertainty distribution. To keep the computation efficient, the sets of lags were restricted to combinations  $k = l$  and thus to 6000 empirical values. We thus approximate

$$\bar{\rho}_{\Delta T}^{p,q}(\Delta t^{p,q}) \simeq \frac{1}{m} \sum_{j=1}^m \delta(t_{0,j}^p - t_{0,j}^q - \Delta t^{p,q}). \tag{A5}$$

This drastic reduction in values certainly requires justification, which we give later by comparing final results of the analysis to those obtained from control runs. The control runs analogously construct the empirical densities for the transition onset lags from 6000 out of the  $36 \times 10^6$  possible values, but use randomly shuffled versions of the original sets of transition onset times for the variables  $p$  and  $q$ :

$$\bar{\rho}_{\Delta T}^{p,q,ctrl}(\Delta t^{p,q}) \simeq \frac{1}{m} \sum_{j=1}^m \delta(t_{0,s(j)}^p - t_{0,s'(j)}^q - \Delta t^{p,q}). \tag{A6}$$

Here,  $s$  and  $s'$  denote randomly chosen permutations of the set  $\{1, 2, \dots, m\}$ .

As in the main text, in the following we denote uncertain quantities with a hat. For a given proxy pair the starting point for the statistical analysis however, is the uncertain sample  $\Delta \hat{T}^{p,q} = (\Delta \hat{T}_1^{p,q}, \dots, \Delta \hat{T}_n^{p,q})$ , which is characterized by the  $n$ -dimensional uncertainty distribution  $\rho_{\Delta \hat{T}^{p,q}}(\Delta \hat{t}^{p,q}) = \prod \rho_{\Delta \hat{T}_i^{p,q}}(\Delta \hat{t}_i^{p,q})$ . Its empirical counterpart is given by

$$\begin{aligned} \bar{\rho}_{\Delta\hat{T}^{p,q}}(\Delta\hat{\mathbf{t}}^{p,q}) &= \prod_{i=1}^n \bar{\rho}_{\Delta\hat{T}_i^{p,q}}(\Delta\hat{t}_i^{p,q}) \\ &= \frac{1}{m^n} \prod_{i=1}^n \sum_{j=1}^m \delta(\Delta\hat{t}_i^{p,q} - \Delta t_{i,j}^{p,q}). \end{aligned} \quad (A7)$$

This empirical density is comprised of  $m^n$  possible values for the  $n$ -dimensional random vector  $\Delta\hat{\mathbf{T}}^{p,q}$ , and again, a substantial reduction in the representing set is required for practical computation. Defining the reduced empirical density for  $\Delta\hat{\mathbf{T}}^{p,q}$  as

$$\begin{aligned} \tilde{\rho}_{\Delta\hat{T}^{p,q}}(\Delta\hat{\mathbf{t}}^{p,q}) &= \frac{1}{m} \sum_{j=1}^m \prod_{i=1}^n \delta(\Delta\hat{t}_i^{p,q} - \Delta t_{i,j}^{p,q}) \\ &= \frac{1}{m} \sum_{j=1}^m \delta(\Delta\hat{\mathbf{t}}^{p,q} - \Delta\mathbf{t}_j^{p,q}) \end{aligned} \quad (A8)$$

constrains the set that determines  $\tilde{\rho}_{\Delta\hat{T}^{p,q}}(\Delta\hat{\mathbf{t}}^{p,q})$  to  $m$  values, where those values from different DO events with the same MCMC index  $j$  are combined:

$$\Delta\mathbf{t}_j^{p,q} = (\Delta t_{1,j}^{p,q}, \dots, \Delta t_{n,j}^{p,q}). \quad (A9)$$

Again, the validity is checked by randomly permuting the sets  $\{\Delta t_{i,j}^{p,q}\}$  for the individual DO events with respect to the index  $j$  before the set reduction in the control runs.

Having found a numerically manageable expression for the empirical uncertainty distribution of the sample  $\Delta\hat{\mathbf{T}}^{p,q}$  it remains to be shown how the hypothesis tests can be formulated on this basis. If  $\{\Delta\mathbf{t}_j\}_j$  denotes the set of  $n$ -dimensional vectors forming the empirical uncertainty distribution for the sample of lags obtained from  $n$  DO events, then the naive intuition holds true and the corresponding set  $\{\phi_j = \phi(\Delta\mathbf{t}_j)\}_j$  represents the empirical uncertainty distribution of the test statistic and correspondingly  $\{p_\phi(\phi_j)\}_j$  characterizes the uncertain  $p$  value. In the following, we exemplarily derive this relation for the  $t$  test – the derivations for the WSR and the bootstrap test are analogous.

Recall the statistic of the  $t$  test:

$$z(\mathbf{d}) = \frac{u(\mathbf{d}) - \mu}{s(\mathbf{d})/\sqrt{n}}. \quad (A10)$$

The empirical uncertainty distribution for a sample  $\Delta\hat{\mathbf{T}}$  induces a joint uncertainty distribution for the sample's mean and standard deviation:

$$\begin{aligned} \bar{\rho}_{\hat{U},\hat{S}}(\hat{u},\hat{s}) &= \int \delta\left(u - \frac{1}{n} \sum_{i=1}^n \Delta\hat{t}_i\right) \\ &\quad \times \delta\left(s - \frac{1}{n-1} \sum_{i=1}^n (u - \Delta\hat{t}_i)^2\right) \\ &\quad \times \frac{1}{m} \sum_{j=1}^m \prod_{i=1}^n \delta(\Delta\hat{t}_i - \Delta t_{i,j}) \, d\Delta\hat{t}_1 \dots d\Delta\hat{t}_n \\ &= \frac{1}{m} \sum_{j=1}^m \delta\left(\hat{u} - \frac{1}{n} \sum_{i=1}^n \Delta t_{i,j}\right) \\ &\quad \times \delta\left(\hat{s} - \frac{1}{n-1} \sum_{i=1}^n (\hat{u} - \Delta t_{i,j})^2\right). \end{aligned} \quad (A11)$$

Let  $u_j = \frac{1}{n} \sum_{i=1}^n \Delta t_{i,j}$  and  $s_j = \frac{1}{n-1} \sum_{i=1}^n (u_j - \Delta t_{i,j})^2$ . Then, the empirical uncertainty distribution for  $(\hat{U}, \hat{S})$  can be written as

$$\bar{\rho}_{\hat{U},\hat{S}}(\hat{u},\hat{s}) = \frac{1}{m} \sum_{j=1}^m \delta(\hat{u} - u_j) \delta(\hat{s} - s_j). \quad (A12)$$

The  $(u_j, s_j)$  that forms the empirical uncertainty distribution is simply the mean and standard deviation of those  $\Delta\mathbf{t}_j = (\Delta t_{1,j}, \Delta t_{2,j}, \dots, \Delta t_{n,j})$  that form the vector valued empirical uncertainty distribution for  $\Delta\hat{\mathbf{T}}$ . From  $\bar{\rho}_{\hat{U},\hat{S}}(\hat{u},\hat{s})$ , the empirical uncertainty distribution for the uncertain test statistic  $\hat{Z}$  can be computed as follows:

$$\begin{aligned} \bar{\rho}_{\hat{Z}}(\hat{z}) &= \int \delta\left(\hat{z} - \frac{\hat{u} - \mu}{\hat{s}/\sqrt{n}}\right) \rho_{\hat{U},\hat{S}}(\hat{u},\hat{s}) \, d\hat{u} \, d\hat{s} \\ &= \frac{1}{m} \sum_{j=1}^m \delta\left(\hat{z} - \underbrace{\frac{u_j - \mu}{s_j/\sqrt{n}}}_{=z_j}\right). \end{aligned} \quad (A13)$$

This shows that for a given empirical uncertainty distribution for a sample of time lags  $\bar{\rho}_{\Delta\hat{\mathbf{T}}}(\Delta\hat{\mathbf{t}}) = \frac{1}{m} \sum_{i=1}^m \delta(\Delta\hat{\mathbf{t}} - \Delta\mathbf{t}_i)$ , the corresponding distribution for the test statistic  $\hat{Z} = z(\Delta\hat{\mathbf{T}})$  is formed by the set  $\{z(\Delta\mathbf{t}_j) | j \in [1, m]\}$  where each  $\Delta\mathbf{t}_j$  is a vector in  $n$  dimensions. The uncertain (left-handed)  $p$  value remains to be derived from  $\bar{\rho}_{\hat{Z}}(\hat{z})$ :

$$\begin{aligned} \bar{\rho}_{\hat{p}_z}(\hat{p}_z) &= \int \delta\left(\hat{p}_z - \int_{-\infty}^{\hat{z}} t_{n-1}(z) \, dz\right) \bar{\rho}_{\hat{Z}}(\hat{z}) \, d\hat{z} \\ &= \frac{1}{m} \sum_{j=1}^m \delta\left(\hat{p}_z - \underbrace{\int_{-\infty}^{z_j} t_{n-1}(z') \, dz'}_{=p_{z,j}}\right). \end{aligned} \quad (A14)$$

Finally, the practical computation of the uncertain  $p$  values boils down to an application of the test to all members of

the set  $\Delta \mathbf{t}_j$  that originates from the MCMC sampling used to approximate the posterior probability density for the ramp parameter configuration  $\Theta$ . For the WSR test the expression

$$\bar{\rho}_{\hat{p}_w}(\hat{p}_w) = \frac{1}{m} \sum_{j=1}^m \delta(\hat{p}_w - p_{w,j}) \quad (\text{A15})$$

with

$$p_{w,j} = p_w(\Delta \mathbf{t}_j)$$

can be derived analogously. The bootstrap test bears the particularity that each  $\Delta \mathbf{t}_j$  induces its own null distribution. Yet, the application of the test to each individual  $\Delta \mathbf{t}_j$  induces a set of  $p_{v,j} = p_v(\Delta \mathbf{t}_j)$  that determines the empirical density:

$$\bar{\rho}_{\hat{p}_v}(\hat{p}_v) = \frac{1}{m} \sum_{j=1}^m \delta(\hat{p}_v - p_{v,j}). \quad (\text{A16})$$

**Appendix B: Results of the analysis for the control group**

As explained in Sect. A, we drastically reduce the cardinality of the sets that form the empirical densities  $\bar{\rho}_{\Delta \hat{\mathbf{T}}^{p,q}}(\Delta \hat{\mathbf{T}}^{p,q})$  at two points in the analysis. First, for the representation of the uncertain time lag  $\Delta \hat{\mathbf{T}}_i^{p,q}$  between the proxies  $p$  and  $q$  at a given DO event, only 6000 out of the  $6000^2$  possible values are utilized. Second, the set of vectors considered in the representation of  $\bar{\rho}_{\Delta \hat{\mathbf{T}}^{p,q}}(\Delta \hat{\mathbf{T}}) = \frac{1}{6000} \sum_{j=1}^{6000} \delta(\Delta \hat{\mathbf{T}}^{p,q} - \Delta \mathbf{t}_j^{p,q})$  is comprised of only 6000 out of the  $6000^{16}$  theoretically available vectors. To cross-check the robustness of the results obtained within the limits of this approximation, we applied our analysis to a control group of nine alternative realizations of the empirical uncertainty density for  $\Delta \hat{\mathbf{T}}^{p,q}$  for each proxy pair. The control group uncertainty densities are constructed as follows: first, the empirical uncertainty distributions for the event-specific lags  $\Delta \hat{\mathbf{T}}_i^{p,q}$  are obtained via Eq. (A6). In a second step, the joint empirical uncertainty distribution for  $\Delta \hat{\mathbf{T}}^{p,q}$  is constructed from randomly shuffled empirical sets  $\Delta \mathbf{t}_{i,s_i(j)}^{p,q}$  of each DO event:

$$\tilde{\rho}_{\Delta \hat{\mathbf{T}}^{p,q}}^{\text{ctrl}}(\Delta \hat{\mathbf{T}}^{p,q}) = \frac{1}{m} \sum_{j=1}^m \prod_{i=1}^n \delta(\Delta \hat{\mathbf{T}}_i^{p,q} - \Delta \mathbf{t}_{i,s_i(j)}^{p,q}). \quad (\text{B1})$$

Here  $s_i$  denotes an event-specific permutation of the index set  $\{1, \dots, 6000\}$ . Thus the empirical  $\Delta \mathbf{t}_{i,j}^{p,q}$  recombines between events and gives rise to a new set of 6000 vectors that constitute 6000 empirical realizations of the uncertain  $\Delta \hat{\mathbf{T}}^{p,q}$ .

The results obtained from the control runs show only minor deviations from the results presented in the main text and thus confirm the validity of the reduction in the corresponding sets. Table B1 summarizes the results obtained by the application of the hypothesis tests to the control group.

**Appendix C: Computation of the uncertain sample mean**

In the main text, we stated that the uncertain sample mean is given by the pairwise convolution of the individual uncertainty distributions that describe the uncertain sample members. Here, we show how the uncertain sample mean can be computed if the individual uncertainty distributions are known.

Consider  $n$  random variables which are independently yet not identically distributed:

$$\mathbf{X} = (X_1, \dots, X_n) \text{ with } X_i \sim \rho_{X_i}(x_i) dx_i \quad (\text{C1})$$

in analogy to the

$$\Delta \hat{\mathbf{T}}^{p,q} = (\Delta \hat{\mathbf{T}}_1^{p,q}, \dots, \Delta \hat{\mathbf{T}}_n^{p,q})$$

with  $\Delta \hat{\mathbf{T}}_i^{p,q} \sim \rho_{\Delta \hat{\mathbf{T}}_i^{p,q}}(\Delta \hat{\mathbf{T}}_i^{p,q}) \quad (\text{C2})$

from the main text. Further, let

$$U = \frac{1}{n} \sum_{i=1}^n X_i \quad (\text{C3})$$

denote the mean of the sample of random variables, which is in turn a random variable by itself. In order to compute the distribution  $\rho_U(u) du$  we introduce the variable  $V = nU$  and the sequence of variables

$$V_j = \sum_{i=1}^j X_i, \quad (\text{C4})$$

such that  $V_n = V$ . From Eq. (C4) it follows that

$$V_{j+1} = V_j + X_{j+1} \quad (\text{C5})$$

and hence

$$\begin{aligned} &\rho_{V_{j+1}}(v_{j+1}) dv_{j+1} \\ &= \int_{-\infty}^{\infty} \int_{-\infty}^{\infty} \rho_{V_j}(v_j) \rho_{X_{j+1}}(x_{j+1}) \\ &\quad \times \delta(v_{j+1} - v_j - x_{j+1}) dx_{j+1} dv_j dv_{j+1} \\ &= \int_{-\infty}^{\infty} \rho_{V_j}(v_j) \rho_{X_{j+1}}(v_{j+1} - v_j) dv_j dv_{j+1}. \end{aligned} \quad (\text{C6})$$

**Table B1.** Results obtained from the application of hypothesis tests to the control group. Reported are the mean  $p$  values  $E(p(\Delta\hat{T}))$  together with the probability of the uncertain sample to yield a  $p$  value below the significance level  $\pi(p(\Delta\hat{T}) < 0.05)$  and the  $p$  values of the expected samples  $p(E(\Delta\hat{T}))$  for all three tests. All results were derived from the corresponding empirical densities  $\bar{p}_{\Delta\hat{T}^{p,q}}(\Delta\hat{T}^{p,q})$ . The column sub-labels  $z$ ,  $w$ , and  $bs$  indicate results obtained from the  $t$  test, the WSR test, and the bootstrap test. The results presented in the main text are given by the  $p-q-0$  run for each proxy variable. The data presented here are provided in the Supplement to this article.

Proxies	Run	$E(\hat{P})$			$\pi(\hat{P} < 0.05)$			$p(E(\Delta\hat{T}))$		
		$z$	$w$	$bs$	$z$	$w$	$bs$	$z$	$w$	$bs$
NGRIP: Ca <sup>2+</sup> -Na <sup>+</sup>	0	0.219	0.168	0.217	0.258	0.324	0.299	0.044	0.009	0.02
NGRIP: Ca <sup>2+</sup> -Na <sup>+</sup>	1	0.218	0.166	0.215	0.246	0.316	0.292	0.044	0.009	0.019
NGRIP: Ca <sup>2+</sup> -Na <sup>+</sup>	2	0.219	0.165	0.216	0.258	0.324	0.294	0.044	0.009	0.018
NGRIP: Ca <sup>2+</sup> -Na <sup>+</sup>	3	0.22	0.166	0.217	0.254	0.322	0.295	0.044	0.009	0.02
NGRIP: Ca <sup>2+</sup> -Na <sup>+</sup>	4	0.219	0.166	0.217	0.255	0.32	0.296	0.044	0.009	0.02
NGRIP: Ca <sup>2+</sup> -Na <sup>+</sup>	5	0.218	0.166	0.216	0.254	0.319	0.293	0.044	0.009	0.019
NGRIP: Ca <sup>2+</sup> -Na <sup>+</sup>	6	0.219	0.167	0.217	0.255	0.319	0.299	0.044	0.009	0.021
NGRIP: Ca <sup>2+</sup> -Na <sup>+</sup>	7	0.219	0.167	0.217	0.252	0.319	0.295	0.044	0.009	0.019
NGRIP: Ca <sup>2+</sup> -Na <sup>+</sup>	8	0.219	0.164	0.217	0.257	0.316	0.3	0.044	0.009	0.02
NGRIP: Ca <sup>2+</sup> -Na <sup>+</sup>	9	0.218	0.165	0.216	0.261	0.32	0.302	0.044	0.009	0.02
NGRIP: $\lambda$ -Na <sup>+</sup>	0	0.093	0.091	0.086	0.469	0.484	0.524	0.023	0.017	0.017
NGRIP: $\lambda$ -Na <sup>+</sup>	1	0.092	0.091	0.085	0.467	0.482	0.516	0.023	0.017	0.014
NGRIP: $\lambda$ -Na <sup>+</sup>	2	0.093	0.092	0.086	0.462	0.489	0.519	0.023	0.017	0.015
NGRIP: $\lambda$ -Na <sup>+</sup>	3	0.092	0.09	0.085	0.465	0.482	0.516	0.023	0.017	0.016
NGRIP: $\lambda$ -Na <sup>+</sup>	4	0.093	0.09	0.086	0.471	0.488	0.529	0.023	0.017	0.014
NGRIP: $\lambda$ -Na <sup>+</sup>	5	0.093	0.092	0.086	0.468	0.492	0.522	0.023	0.017	0.015
NGRIP: $\lambda$ -Na <sup>+</sup>	6	0.092	0.089	0.085	0.47	0.488	0.521	0.023	0.017	0.013
NGRIP: $\lambda$ -Na <sup>+</sup>	7	0.092	0.091	0.085	0.461	0.486	0.515	0.023	0.017	0.016
NGRIP: $\lambda$ -Na <sup>+</sup>	8	0.093	0.091	0.086	0.477	0.486	0.525	0.023	0.017	0.015
NGRIP: $\lambda$ -Na <sup>+</sup>	9	0.093	0.091	0.086	0.475	0.488	0.524	0.023	0.017	0.015
NGRIP: Ca <sup>2+</sup> - $\delta^{18}O$	0	0.234	0.182	0.233	0.235	0.306	0.262	0.042	0.015	0.037
NGRIP: Ca <sup>2+</sup> - $\delta^{18}O$	1	0.234	0.182	0.232	0.231	0.294	0.257	0.042	0.015	0.035
NGRIP: Ca <sup>2+</sup> - $\delta^{18}O$	2	0.234	0.18	0.232	0.226	0.3	0.254	0.042	0.015	0.039
NGRIP: Ca <sup>2+</sup> - $\delta^{18}O$	3	0.234	0.182	0.233	0.236	0.314	0.261	0.042	0.015	0.036
NGRIP: Ca <sup>2+</sup> - $\delta^{18}O$	4	0.234	0.181	0.232	0.234	0.308	0.261	0.042	0.015	0.031
NGRIP: Ca <sup>2+</sup> - $\delta^{18}O$	5	0.233	0.181	0.231	0.23	0.304	0.253	0.042	0.015	0.032
NGRIP: Ca <sup>2+</sup> - $\delta^{18}O$	6	0.234	0.181	0.232	0.228	0.306	0.253	0.042	0.015	0.037
NGRIP: Ca <sup>2+</sup> - $\delta^{18}O$	7	0.234	0.18	0.232	0.235	0.31	0.261	0.042	0.015	0.033
NGRIP: Ca <sup>2+</sup> - $\delta^{18}O$	8	0.234	0.183	0.232	0.236	0.313	0.263	0.042	0.015	0.034
NGRIP: Ca <sup>2+</sup> - $\delta^{18}O$	9	0.234	0.182	0.232	0.231	0.307	0.257	0.042	0.015	0.035
NGRIP: $\lambda$ - $\delta^{18}O$	0	0.133	0.11	0.129	0.369	0.436	0.414	0.024	0.009	0.017
NGRIP: $\lambda$ - $\delta^{18}O$	1	0.134	0.111	0.129	0.37	0.441	0.416	0.024	0.009	0.016
NGRIP: $\lambda$ - $\delta^{18}O$	2	0.133	0.11	0.127	0.379	0.44	0.422	0.024	0.009	0.017
NGRIP: $\lambda$ - $\delta^{18}O$	3	0.135	0.112	0.13	0.38	0.435	0.42	0.024	0.009	0.017
NGRIP: $\lambda$ - $\delta^{18}O$	4	0.134	0.111	0.129	0.378	0.442	0.419	0.024	0.009	0.018
NGRIP: $\lambda$ - $\delta^{18}O$	5	0.133	0.109	0.128	0.373	0.437	0.416	0.024	0.009	0.018
NGRIP: $\lambda$ - $\delta^{18}O$	6	0.133	0.111	0.128	0.384	0.446	0.426	0.024	0.009	0.017
NGRIP: $\lambda$ - $\delta^{18}O$	7	0.133	0.109	0.128	0.376	0.445	0.416	0.024	0.009	0.017
NGRIP: $\lambda$ - $\delta^{18}O$	8	0.134	0.11	0.129	0.381	0.443	0.424	0.024	0.009	0.018
NGRIP: $\lambda$ - $\delta^{18}O$	9	0.134	0.11	0.129	0.376	0.441	0.418	0.024	0.009	0.019
NEEM: Ca <sup>2+</sup> -Na <sup>+</sup>	0	0.08	0.076	0.074	0.566	0.584	0.61	0.008	0.007	0.006
NEEM: Ca <sup>2+</sup> -Na <sup>+</sup>	1	0.08	0.076	0.074	0.57	0.581	0.61	0.008	0.007	0.006
NEEM: Ca <sup>2+</sup> -Na <sup>+</sup>	2	0.079	0.075	0.073	0.571	0.587	0.614	0.008	0.007	0.005
NEEM: Ca <sup>2+</sup> -Na <sup>+</sup>	3	0.079	0.076	0.073	0.573	0.586	0.615	0.008	0.007	0.006
NEEM: Ca <sup>2+</sup> -Na <sup>+</sup>	4	0.08	0.077	0.074	0.572	0.584	0.612	0.008	0.007	0.005
NEEM: Ca <sup>2+</sup> -Na <sup>+</sup>	5	0.08	0.076	0.074	0.571	0.579	0.608	0.008	0.007	0.005
NEEM: Ca <sup>2+</sup> -Na <sup>+</sup>	6	0.08	0.077	0.074	0.565	0.577	0.609	0.008	0.007	0.006
NEEM: Ca <sup>2+</sup> -Na <sup>+</sup>	7	0.08	0.077	0.074	0.57	0.583	0.612	0.008	0.007	0.006
NEEM: Ca <sup>2+</sup> -Na <sup>+</sup>	8	0.079	0.075	0.073	0.57	0.58	0.614	0.008	0.007	0.006
NEEM: Ca <sup>2+</sup> -Na <sup>+</sup>	9	0.078	0.075	0.072	0.567	0.576	0.608	0.008	0.007	0.006

Self-iteration of Eq. (C6) yields

$$\begin{aligned}
 & \rho_{V_{j+1}}(v_{j+1}) \, dv_{j+1} \\
 &= \int_{-\infty}^{\infty} \int_{-\infty}^{\infty} \underbrace{\rho_{V_{j-1}}(v_{j-1}) \rho_{X_j}(v_j - v_{j-1}) \, dv_{j-1}}_{=\rho_{V_j}(v_j)} \\
 & \quad \times \rho_{X_{j+1}}(v_{j+1} - v_j) \, dv_j \, dv_{j+1} \\
 &= \dots \\
 &= \int_{-\infty}^{\infty} \dots \int_{-\infty}^{\infty} \prod_{i=1}^{j+1} \rho_{X_i}(v_i - v_{i-1}) \, dv_{i-1} \, dv_{j+1}, \quad (C7)
 \end{aligned}$$

where  $v_0 = 0$ . With  $V_n/n = U$ , the distribution for the uncertain sample mean reads

$$\rho_{V_n}(v_n) \, dV_n = \rho_{V_n}(nu) \, n \, du = \rho_U(u) \, du, \quad (C8)$$

and thus

$$\rho_U(u) \, du = \int_{-\infty}^{\infty} \prod_{i=1}^n \rho_{X_i}(v_i - v_{i-1}) \, dv_{i-1} \, n \, du, \quad (C9)$$

with  $v_0 = 0$  and  $v_n = nu$ .

**Code and data availability.** The 10-year resolution time series of  $\text{Ca}^{2+}$  and  $\text{Na}^{+}$  for both the NEEM and NGRIP ice cores, together with corresponding data for  $\delta^{18}\text{O}$  and the annual layer thickness for the NGRIP ice core as shown in Fig. 1, are available from <https://doi.org/10.1594/PANGAEA.896743> (Erhardt et al., 2018). The high-resolution data around major DO events for the same proxies and ice cores are available from the same archive.

Please note that the  $\delta^{18}\text{O}$  data were originally published at 5 cm resolution together with corresponding GICC05 ages as a Supplement to Gkinis et al. (2014) and can be downloaded from [https://www.iceandclimate.nbi.ku.dk/data/NGRIP\\_d18O\\_and\\_dust\\_5cm.xls](https://www.iceandclimate.nbi.ku.dk/data/NGRIP_d18O_and_dust_5cm.xls) (last access: 19 August 2021).

All data in preprocessed form, together with the software used to generate samples from the posterior distributions of the transition onsets for all proxies at all interstadial onsets under study, were directly obtained from <https://doi.org/10.5281/zenodo.2645176> (Erhardt, 2019).

The numerical implementation of the analysis presented here, building upon the aforementioned samples from the posterior distributions of transition onsets, is publicly available under <https://doi.org/10.5281/zenodo.5217533> (Riechers, 2021).

**Supplement.** The supplement related to this article is available online at: <https://doi.org/10.5194/cp-17-1751-2021-supplement>.

**Author contributions.** KR and NB conceived the study. KR carried out the numerical analysis. KR and NB discussed and interpreted the results and wrote the paper.

**Competing interests.** The authors declare that they have no conflict of interest.

**Disclaimer.** Publisher's note: Copernicus Publications remains neutral with regard to jurisdictional claims in published maps and institutional affiliations.

**Acknowledgements.** We thank Norbert Marwan for very helpful comments and discussions. This is TiPES contribution no. 60; the TiPES (Tipping Points in the Earth System) project has received funding from the European Union's Horizon 2020 research and innovation program under grant agreement no. 820970. Niklas Boers acknowledges funding by the Volkswagen foundation.

**Financial support.** This research has been supported by the Horizon 2020 (TiPES (grant no. 820970)) and the Volkswagen foundation.

The article processing charges for this open-access publication were covered by the Potsdam Institute for Climate Impact Research (PIK).

**Review statement.** This paper was edited by Laurie Menviel and reviewed by two anonymous referees.

## References

- Andersen, K. K., Svensson, A., Johnsen, S. J., Rasmussen, S. O., Bigler, M., Röthlisberger, R., Ruth, U., Siggaard-Andersen, M. L., Peder Steffensen, J., Dahl-Jensen, D., Vinther, B. M., and Clausen, H. B.: The Greenland Ice Core Chronology 2005, 15–42 ka. Part 1: constructing the time scale, *Quaternary Sci. Rev.*, 25, 3246–3257, <https://doi.org/10.1016/j.quascirev.2006.08.002>, 2006.
- Boers, N., Ghil, M., and Rousseau, D. D.: Ocean circulation, ice shelf, and sea ice interactions explain Dansgaard–Oeschger cycles, *P. Natl. Acad. Sci. USA*, 115, E11005–E11014, <https://doi.org/10.1073/pnas.1802573115>, 2018.
- Bond, G., Broecker, W., Johnsen, S., McManus, J., Labeyrie, L., Jouzel, J., and Bonani, G.: Correlations between climate records from North Atlantic sediments and Greenland ice, *Nature*, 365, 143–147, 1993.
- Broecker, W. S., Peteet, D. M., and Rind, D.: Does the ocean-atmosphere system have more than one stable mode of operation?, *Nature*, 315, 21–26, <https://doi.org/10.1038/315021a0>, 1985.
- Buizert, C., Adrian, B., Ahn, J., Albert, M., Alley, R. B., Baggenstos, D., Bauska, T. K., Bay, R. C., Bencivengo, B. B., Bentley, C. R., Brook, E. J., Chellman, N. J., Clow, G. D., Cole-Dai, J., Conway, H., Cravens, E., Cuffey, K. M., Dunbar, N. W., Edwards, J. S., Fegyveresi, J. M., Ferris, D. G., Fitzpatrick, J. J., Fudge, T. J., Gibson, C. J., Gkinis, V., Goetz, J. J., Gregory, S., Hargreaves, G. M., Iverson, N., Johnson, J. A., Jones, T. R., Kalk, M. L., Kippenhan, M. J., Koffman, B. G., Kreutz, K., Kuhl, T. W., Lebar, D. A., Lee, J. E., Marcott, S. A., Markle, B. R., Maselli, O. J., McConnell, J. R., McGwire, K. C., Mitchell, L. E., Mortensen, N. B., Neff, P. D., Nishiizumi, K., Nunn, R. M., Orsi, A. J., Pasteris, D. R., Pedro, J. B., Petit, E. C., Price, P. B., Priscu, J. C., Rhodes, R. H., Rosen, J. L., Schauer, A. J., Schoenemann, S. W., Sendelbach, P. J., Severinghaus, J. P., Shturmakov, A. J., Sigl, M., Slawny, K. R., Souney, J. M., Sowers, T. A., Spencer, M. K., Steig, E. J., Taylor, K. C., Twickler, M. S., Vaughn, B. H., Voigt, D. E., Waddington, E. D., Welten, K. C., Wendricks, A. W., White, J. W., Winstrup, M., Wong, G. J., and Woodruff, T. E.: Precise inter-polar phasing of abrupt climate change during the last ice age, *Nature*, 520, 661–665, <https://doi.org/10.1038/nature14401>, 2015.
- Cheng, H., Sinha, A., Cruz, F. W., Wang, X., Edwards, R. L., D'Horta, F. M., Ribas, C. C., Vuille, M., Stott, L. D., and Auler, A. S.: Climate change patterns in Amazonia and biodiversity, *Nat. Commun.*, 4, 1411, <https://doi.org/10.1038/ncomms2415>, 2013.
- Clark, P. U., Pisias, N. G., Stocker, T. F., and Weaver, A. J.: The role of the thermohaline circulation in abrupt climate change, *Nature*, 415, 863–869, <https://doi.org/10.1038/415863a>, 2002.
- Dansgaard, W., Johnsen, S. J., Clausen, H. B., Dahl-Jensen, D., Gundestrup, N. S., Hammer, C. U., Hvidberg, C. S., Steffensen, J. P., Sveinbjörnsdóttir, A. E., Jouzel, J., and Bond, G.: Evidence for general instability of past climate from a 250-kyr ice-core record, *Nature*, 364, 218–220, <https://doi.org/10.1038/364218a0>, 1993.

- Ditlevsen, P. D., Andersen, K. K., and Svensson, A.: The DO-climate events are probably noise induced: statistical investigation of the claimed 1470 years cycle, *Clim. Past*, 3, 129–134, <https://doi.org/10.5194/cp-3-129-2007>, 2007.
- Erhardt, T.: terhardt/DO-progression: First official release (v1.0), Zenodo [code], <https://doi.org/10.5281/zenodo.2645176>, 2019.
- Erhardt, T., Capron, E., Rasmussen, S. O., Schüpbach, S., Bigler, M., Adolphi, F., and Fischer, H.: High resolution aerosol, layer thickness and  $\delta^{18}\text{O}$  data around Greenland warming events (10–60 ka) from NGRIP and NEEM ice cores, PANGAEA [data set], <https://doi.org/10.1594/PANGAEA.896743>, 2018.
- Erhardt, T., Capron, E., Rasmussen, S. O., Schüpbach, S., Bigler, M., Adolphi, F., and Fischer, H.: Decadal-scale progression of the onset of Dansgaard–Oeschger warming events, *Clim. Past*, 15, 811–825, <https://doi.org/10.5194/cp-15-811-2019>, 2019.
- Filzmoser, P. and Viertl, R.: Testing hypotheses with fuzzy data: The fuzzy p-value, *Metrika*, 59, 21–29, <https://doi.org/10.1007/s001840300269>, 2004.
- Fleitmann, D., Cheng, H., Badertscher, S., Edwards, R. L., Mudelsee, M., Gökürk, O. M., Fankhauser, A., Pickering, R., Raible, C. C., Matter, A., Kramers, J., and Tüysüz, O.: Timing and climatic impact of Greenland interstadials recorded in stalagmites from northern Turkey, *Geophys. Res. Lett.*, 36, 1–5, <https://doi.org/10.1029/2009GL040050>, 2009.
- Fuhrer, K., Wolff, E. W., and Johnsen, S. J.: Timescales for dust variability in the Greenland Ice Core Project (GRIP) ice core in the last 100,000 years, *J. Geophys. Res.-Atmos.*, 104, 31043–31052, <https://doi.org/10.1029/1999JD900929>, 1999.
- Ganopolski, A. and Rahmstorf, S.: Rapid changes of glacial climate simulated in a coupled climate model, *Nature*, 409, 153–158, 2001.
- Gkinis, V., Simonsen, S. B., Buchardt, S. L., White, J. W., and Vinther, B. M.: Water isotope diffusion rates from the North-GRIP ice core for the last 16,000 years – Glaciological and paleoclimatic implications, *Earth Planet. Sc. Lett.*, 405, 132–141, <https://doi.org/10.1016/j.epsl.2014.08.022>, 2014.
- Goodman, J. and Weare, J.: *Communications in Applied Mathematics and Computational Science*, *Comm. App. Math. Com. Sc.*, 5, 1–99, 2010.
- Hall, P. and Wilson, S. R.: Two Guidelines for Bootstrap Hypothesis Testing, *Biometrics*, 47, 757–762, <https://doi.org/10.2307/2532163>, 1991.
- Henry, L. G., McManus, J. F., Curry, W. B., Roberts, N. L., Piotrowski, A. M., and Keigwin, L. D.: North Atlantic ocean circulation and abrupt climate change during the last glaciation, *Science*, 353, 470–474, <https://doi.org/10.1126/science.aaf5529>, 2016.
- Huber, C., Leuenberger, M., Spahni, R., Flückiger, J., Schwander, J., Stocker, T. F., Johnsen, S., Landais, A., and Jouzel, J.: Isotope calibrated Greenland temperature record over Marine Isotope Stage 3 and its relation to  $\text{CH}_4$ , *Earth Planet. Sc. Lett.*, 243, 504–519, <https://doi.org/10.1016/j.epsl.2006.01.002>, 2006.
- Johnsen, S. J., Clausen, H. B., Dansgaard, W., Fuhrer, K., Gundestrup, N., Hammer, C. U., Iversen, P., Jouzel, J., Stauffer, B., and Steffensen, J.: Irregular glacial interstadials recorded in a new Greenland ice core, *Nature*, 359, 311–313, 1992.
- Johnsen, S. J., Dahl-Jensen, D., Gundestrup, N., Steffensen, J. P., Clausen, H. B., Miller, H., Masson-Delmotte, V., Sveinbjörnsdóttir, A. E., and White, J.: Oxygen isotope and palaeotemperature records from six Greenland ice-core stations: Camp Century, Dye-3, GRIP, GISP2, Renland and NorthGRIP, *J. Quaternary Sci.*, 16, 299–307, <https://doi.org/10.1002/jqs.622>, 2001.
- Jouzel, J., Alley, R. B., Cuffey, K. M., Dansgaard, W., Grootes, P., Hoffmann, G., Johnsen, S. J., Koster, R. D., Peel, D., Shuman, C. A., Stievenard, M., Stuiver, M., and White, J.: Validity of the temperature reconstruction from water isotopes in ice cores, *J. Geophys. Res.-Oceans*, 102, 26471–26487, <https://doi.org/10.1029/97JC01283>, 1997.
- Kim, J. H., Romero, O. E., Lohmann, G., Donner, B., Laepple, T., Haam, E., and Sinninghe Damsté, J. S.: Pronounced subsurface cooling of North Atlantic waters off Northwest Africa during Dansgaard-Oeschger interstadials, *Earth Planet. Sc. Lett.*, 339–340, 95–102, <https://doi.org/10.1016/j.epsl.2012.05.018>, 2012.
- Kindler, P., Guillevic, M., Baumgartner, M., Schwander, J., Landais, A., and Leuenberger, M.: Temperature reconstruction from 10 to 120 kyr b2k from the NGRIP ice core, *Clim. Past*, 10, 887–902, <https://doi.org/10.5194/cp-10-887-2014>, 2014.
- Kleppin, H., Jochum, M., Otto-Bliesner, B., Shields, C. A., and Yeager, S.: Stochastic atmospheric forcing as a cause of Greenland climate transitions, *J. Climate*, 28, 7741–7763, <https://doi.org/10.1175/JCLI-D-14-00728.1>, 2015.
- Landais, A., Jouzel, J., Masson-Delmotte, V., and Caillon, N.: Large temperature variations over rapid climatic events in Greenland: a method based on air isotopic measurements, *C. R. Geosci.*, 337, 947–956, <https://doi.org/10.1016/j.crte.2005.04.003>, 2005.
- Lehmann, E. L. and Romano, J. P.: *Testing Statistical Hypothesis*, vol. 102, 3rd edit edn., Springer US, New York, <https://doi.org/10.1016/j.peva.2007.06.006>, 2006.
- Lenton, T., Held, H., Kriegler, E., Hall, J. W., Lucht, W., Rahmstorf, S., and Schellnhuber, H. J.: Tipping elements in the Earth’s climate system, *P. Natl. Acad. Sci. USA*, 105, 1786–1793, <https://doi.org/10.1073/pnas.0705414105>, 2008.
- Lenton, T. M. and Schellnhuber, H. J.: Tipping the Scales, *Nat. Clim. Change*, 1, 97–98, 2007.
- Lenton, T. M., Rockström, J., Gaffney, O., Rahmstorf, S., Richardson, K., Steffen, W., and Schellnhuber, H. J.: Climate tipping points – too risky to bet against, *Nature*, 575, 592–595, <https://doi.org/10.1038/d41586-019-03595-0>, 2019.
- Li, C. and Born, A.: Coupled atmosphere-ice-ocean dynamics in Dansgaard-Oeschger events, *Quaternary Sci. Rev.*, 203, 1–20, <https://doi.org/10.1016/j.quascirev.2018.10.031>, 2019.
- Lynch-Stieglitz, J.: The Atlantic Meridional Overturning Circulation and Abrupt Climate Change, *Annu. Rev. Mar. Sci.*, 9, 83–104, <https://doi.org/10.1146/annurev-marine-010816-060415>, 2017.
- Moseley, G. E., Spötl, C., Brandstätter, S., Erhardt, T., Luetscher, M., and Edwards, R. L.: NALPS19: sub-orbital-scale climate variability recorded in northern Alpine speleothems during the last glacial period, *Clim. Past*, 16, 29–50, <https://doi.org/10.5194/cp-16-29-2020>, 2020.
- North Greenland Ice Core Project members: High-resolution record of Northern Hemisphere climate extending into the last interglacial period, *Nature*, 431, 147–151, <https://doi.org/10.1038/nature02805>, 2004.
- Rasmussen, S. O., Andersen, K. K., Svensson, A. M., Steffensen, J. P., Vinther, B. M., Clausen, H. B., Siggaard-Andersen, M. L., Johnsen, S. J., Larsen, L. B., Dahl-Jensen, D., Bigler, M., Röthlisberger, R., Fischer, H., Goto-Azuma, K.,

- Hansson, M. E., and Ruth, U.: A new Greenland ice core chronology for the last glacial termination, *J. Geophys. Res.-Atmos.*, 111, 1–16, <https://doi.org/10.1029/2005JD006079>, 2006.
- Rasmussen, S. O., Abbott, P. M., Blunier, T., Bourne, A. J., Brook, E., Buchardt, S. L., Buizert, C., Chappellaz, J., Clausen, H. B., Cook, E., Dahl-Jensen, D., Davies, S. M., Guillevic, M., Kipfstuhl, S., Laepple, T., Seierstad, I. K., Severinghaus, J. P., Steffensen, J. P., Stowasser, C., Svensson, A., Vallelonga, P., Vinther, B. M., Wilhelms, F., and Winstrup, M.: A first chronology for the North Greenland Eemian Ice Drilling (NEEM) ice core, *Clim. Past*, 9, 2713–2730, <https://doi.org/10.5194/cp-9-2713-2013>, 2013.
- Rasmussen, S. O., Bigler, M., Blockley, S. P., Blunier, T., Buchardt, S. L., Clausen, H. B., Cvijanovic, I., Dahl-Jensen, D., Johnsen, S. J., Fischer, H., Gkinis, V., Guillevic, M., Hoek, W. Z., Lowe, J. J., Pedro, J. B., Popp, T., Seierstad, I. K., Steffensen, J. P., Svensson, A. M., Vallelonga, P., Vinther, B. M., Walker, M. J., Wheatley, J. J., and Winstrup, M.: A stratigraphic framework for abrupt climatic changes during the Last Glacial period based on three synchronized Greenland ice-core records: Refining and extending the INTIMATE event stratigraphy, *Quaternary Sci. Rev.*, 106, 14–28, <https://doi.org/10.1016/j.quascirev.2014.09.007>, 2014.
- Rice, J. A.: *Mathematical Statistics and Data Analysis*, 3rd edit edn., Thomson Brooks/Cole, Belmont, USA, 2007.
- Riechers, K.: `kriechers/testing_uncertain_DO_time_lags: testing_uncertain_DO_time_lags_publication (v1.0)`, Zenodo [code], <https://doi.org/10.5281/zenodo.5217533>, 2021.
- Ruth, U., Bigler, M., Röthlisberger, R., Siggaard-Andersen, M. L., Kipfstuhl, S., Goto-Azuma, K., Hansson, M. E., Johnsen, S. J., Lu, H., and Steffensen, J. P.: Ice core evidence for a very tight link between North Atlantic and east Asian glacial climate, *Geophys. Res. Lett.*, 34, 1–5, <https://doi.org/10.1029/2006GL027876>, 2007.
- Schüpbach, S., Fischer, H., Bigler, M., Erhardt, T., Gfeller, G., Leuenberger, D., Mini, O., Mulvaney, R., Abram, N. J., Fleet, L., Frey, M. M., Thomas, E., Svensson, A., Dahl-Jensen, D., Kettner, E., Kjaer, H., Seierstad, I., Steffensen, J. P., Rasmussen, S. O., Vallelonga, P., Winstrup, M., Wegner, A., Twarloh, B., Wolff, K., Schmidt, K., Goto-Azuma, K., Kuramoto, T., Hirabayashi, M., Uetake, J., Zheng, J., Bourgeois, J., Fisher, D., Zhiheng, D., Xiao, C., Legrand, M., Spolaor, A., Gabrieli, J., Barbante, C., Kang, J. H., Hur, S. D., Hong, S. B., Hwang, H. J., Hong, S., Hansson, M., Iizuka, Y., Oyabu, I., Muscheler, R., Adolphi, F., Maselli, O., McConnell, J., and Wolff, E. W.: Greenland records of aerosol source and atmospheric lifetime changes from the Eemian to the Holocene, *Nat. Commun.*, 9, 1476, <https://doi.org/10.1038/s41467-018-03924-3>, 2018.
- Sime, L. C., Hopcroft, P. O., and Rhodes, R. H.: Impact of abrupt sea ice loss on Greenland water isotopes during the last glacial period, *P. Natl. Acad. Sci. USA*, 116, 4099–4104, <https://doi.org/10.1073/pnas.1807261116>, 2019.
- Steffensen, J. P., Andersen, K. K., Bigler, M., Clausen, H. B., Dahl-Jensen, D., Fischer, H., Goto-azuma, K., Hansson, M., Johnsen, S. J., Jouzel, J., Masson-delmotte, V., Popp, T., Rasmussen, S. O., Röthlisberger, R., Ruth, U., Stauffer, B., Sveinbjörnsdóttir, Á. E., Svensson, A., and White, J. W. C.: High-Resolution Greenland Ice Core Data Show Abrupt Climate Change Happens in Few Years, *Science*, 321, 680–684, <https://doi.org/10.1126/science.1157707>, 2008.
- Student: The probable error of a mean, *Biometrika*, 6, 1–25, <https://doi.org/10.2307/2331554>, 1908.
- Svensson, A., Andersen, K. K., Bigler, M., Clausen, H. B., Dahl-Jensen, D., Davies, S. M., Johnsen, S. J., Muscheler, R., Parrenin, F., Rasmussen, S. O., Röthlisberger, R., Seierstad, I., Steffensen, J. P., and Vinther, B. M.: A 60 000 year Greenland stratigraphic ice core chronology, *Clim. Past*, 4, 47–57, <https://doi.org/10.5194/cp-4-47-2008>, 2008.
- Thomas, E. R., Wolff, E. W., Mulvaney, R., Johnsen, S. J., Steffensen, J. P., and Arrowsmith, C.: Anatomy of a Dansgaard-Oeschger warming transition: High-resolution analysis of the North Greenland Ice Core Project ice core, *J. Geophys. Res.-Atmos.*, 114, 1–9, <https://doi.org/10.1029/2008JD011215>, 2009.
- Vettoretti, G. and Peltier, W. R.: Fast physics and slow physics in the nonlinear Dansgaard-Oeschger relaxation oscillation, *J. Climate*, 31, 3423–3449, <https://doi.org/10.1175/JCLI-D-17-0559.1>, 2018.
- Vinther, B. M., Clausen, H. B., Johnsen, S. J., Rasmussen, S. O., Andersen, K. K., Buchardt, S. L., Dahl-Jensen, D., Seierstad, I. K., Siggaard-Andersen, M. L., Steffensen, J. P., Svensson, A., Olsen, J., and Heinemeier, J.: A synchronized dating of three Greenland ice cores throughout the Holocene, *J. Geophys. Res.-Atmos.*, 111, 1–11, <https://doi.org/10.1029/2005JD006921>, 2006.
- Voelker, A. H.: Global distribution of centennial-scale records for Marine Isotope Stage (MIS) 3: A database, *Quaternary Sci. Rev.*, 21, 1185–1212, [https://doi.org/10.1016/S0277-3791\(01\)00139-1](https://doi.org/10.1016/S0277-3791(01)00139-1), 2002.
- Wilcoxon, F.: Individual comparisons of grouped data by ranking methods, *Biometrics Bull.*, 1, 80–83, <https://doi.org/10.2307/3001968>, 1945.
- Zhang, X., Lohmann, G., Knorr, G., and Purcell, C.: Abrupt glacial climate shifts controlled by ice sheet changes, *Nature*, 512, 290–294, <https://doi.org/10.1038/nature13592>, 2014.

## P5 Comprehensive uncertainty estimation of the timing of Greenland warmings in the Greenland ice core records

Eirik Myrvoll-Nilsen, **Keno Riechers**, Martin Wibe Rypdal & Niklas Boers, 2022. *Climate of the Past*, 18, 1275–1294.

**Copyright.** The article is published open access under the terms of the [Creative Commons Attribution-NonCommercial](#) license. The copyright remains with the authors.

**Contribution.** All authors conceived and designed the study. MWR conceived the idea of modeling the layer increments as a regression model and its use for estimating dating uncertainty of DO events. This idea was reworked by EMN, NB, and KR, and adopted for a Bayesian framework by EMN. Further extensions to the model were conceived by EMN, NB, and KR. EMN wrote the code and carried out the analysis. EMN, KR, and NB discussed the results, drew conclusions, and wrote the paper with input from MWR.

Clim. Past, 18, 1275–1294, 2022  
<https://doi.org/10.5194/cp-18-1275-2022>  
 © Author(s) 2022. This work is distributed under  
 the Creative Commons Attribution 4.0 License.



## Comprehensive uncertainty estimation of the timing of Greenland warmings in the Greenland ice core records

Eirik Myrvoll-Nilsen<sup>1</sup>, Keno Riechers<sup>1,2</sup>, Martin Wibe Rypdal<sup>3</sup>, and Niklas Boers<sup>1,2,4</sup>

<sup>1</sup>Potsdam Institute for Climate Impact Research, Potsdam, Germany

<sup>2</sup>Earth System Modelling, School of Engineering & Design, Technical University of Munich, Munich, Germany

<sup>3</sup>Department of Mathematics and Statistics, The University of Tromsø – The Arctic University of Norway, Tromsø, Norway

<sup>4</sup>Department of Mathematics, Global Systems Institute, University of Exeter, Exeter, UK

**Correspondence:** Eirik Myrvoll-Nilsen ([myrvoll@pik-potsdam.de](mailto:myrvoll@pik-potsdam.de)) and Niklas Boers ([n.boers@tum.de](mailto:n.boers@tum.de))

Received: 6 December 2021 – Discussion started: 10 December 2021

Revised: 27 April 2022 – Accepted: 6 May 2022 – Published: 20 June 2022

**Abstract.** Paleoclimate proxy records have non-negligible uncertainties that arise from both the proxy measurement and the dating processes. Knowledge of the dating uncertainties is important for a rigorous propagation to further analyses, for example, for identification and dating of stadial–interstadial transitions in Greenland ice core records during glacial intervals, for comparing the variability in different proxy archives, and for model–data comparisons in general. In this study we develop a statistical framework to quantify and propagate dating uncertainties in layer counted proxy archives using the example of the Greenland Ice Core Chronology 2005 (GICC05). We express the number of layers per depth interval as the sum of a structured component that represents both underlying physical processes and biases in layer counting, described by a regression model, and a noise component that represents the fluctuations of the underlying physical processes, as well as unbiased counting errors. The joint dating uncertainties for all depths can then be described by a multivariate Gaussian process from which the chronology (such as the GICC05) can be sampled. We show how the effect of a potential counting bias can be incorporated in our framework. Furthermore we present refined estimates of the occurrence times of Dansgaard–Oeschger events evidenced in Greenland ice cores together with a complete uncertainty quantification of these timings.

### 1 Introduction

The study of past climates is based on proxy measurements obtained from natural climate archives such as cave speleothems, lake and ocean sediments, and ice cores. Paleoclimate reconstructions derived from proxies suffer from 3-fold uncertainty. First, the proxy measurement itself involves the typical measurement uncertainties. Second, the interpretation of proxy variables, such as isotope ratios in terms of physical variables, such as temperature, is often ambiguous, and typically no one-to-one mapping can be established between the measured proxies and the climatic quantities of interest. Third, the age has to be measured alongside the proxy variable. In most cases an age model can be inferred that provides a quantitative relationship between the depth in the archive under consideration and the corresponding age. Such age models are also subject to uncertainties.

This study is exclusively concerned with the dating uncertainties of so-called layer counted archives, where the dating is performed based on counting periodic signals in the proxy archives such as annual layers arising from the impact of the seasonal cycle on the deposition process (e.g., Rasmussen et al., 2006). This type of archive comprises varved lake sediments, ice cores, banded corals, tree rings, and some speleothems (Comboul et al., 2014). Using the example of the NGRIP ice core (North Greenland Ice Core Project members, 2004) and its associated chronology, the GICC05 (Vinther et al., 2006; Rasmussen et al., 2006; Andersen et al., 2006; Svensson et al., 2008), we present here a statistical approach to generate ensembles of age models

that may in turn be used to propagate the age uncertainties to any subsequent analysis of the time series derived from the NGRIP record. Our method can be directly adapted to other layer counted archives.

Layer counting assesses the age increments along the axis perpendicular to the layering, whose summation yields the total age. In turn, also the errors made in the counting process accumulate such that in chronologies obtained from counting annual layers, the absolute age uncertainty grows with increasing age (e.g., Boers et al., 2017).

Most importantly, dating uncertainties make it challenging to establish an unambiguous temporal relation between signals recorded in different, and possibly remote, archives. Therefore, it is often not possible to decipher the exact temporal order of events and distinguish causes from consequences across past climate changes. For example, abrupt Greenland warmings known as Dansgaard–Oeschger (DO) events (Dansgaard et al., 1993; Johnsen et al., 1992) evidenced in ice core records from the last glacial are accompanied by changes in the east Asian monsoon system, which are apparent from Chinese speleothem records (e.g., Zhou et al., 2014; Li et al., 2017). However, since the dating uncertainties exceed the relevant time scales of these abrupt climate shifts, a clear order of events cannot be determined. This prevents us from deducing if in the context of DO events, the abrupt Greenland warming triggered a hemispheric transition in the atmosphere, or vice versa, or if these changes happened simultaneously as part of a global abrupt climatic shift (Corrick et al., 2020).

For the quantification of dating uncertainties in radiometrically dated archives, there exist well established generalized frameworks. One example is the Bayesian Accumulation Model (Blaauw and Christeny, 2011) which models the sediment accumulation rate as a first order autoregressive process with gamma distributed innovations. Other methods or software include OxCal (Ramsey, 1995, 2008) and BChron (Haslett and Parnell, 2008; Parnell et al., 2008). Contrarily, the uncertainties of layer counted archives are targeted systematically only by few studies. Comboul et al. (2014) present a probabilistic model, where the number of missed and double-counted layers are expressed as counting processes shaped by corresponding error rates. However, this approach requires knowledge about these rates and further does not account for any uncertainty associated with them. An alternative Bayesian approach for quantifying the dating uncertainty of layer counted archives is presented in Boers et al. (2017), where the uncertainty is shifted from the time axis to the proxy value. However, this approach does not allow for generation of ensembles of chronologies as required for uncertainty propagation.

Even though dating uncertainties are conveniently quantified for many archives, many studies ignore these uncertainties and instead draw inference from “average” or “most likely” age scales, as already highlighted by McKay et al. (2021). This involves the risk of losing valuable informa-

tion, as shown, for example, in Riechers and Boers (2020). In some cases, rigorous propagation of uncertainty may yield results that qualitatively differ from results obtained by using the “average” or “best fit” age model. In this context, McKay et al. (2021) propose to apply the respective analysis to an ensemble of possible age scales to ensure the uncertainty propagation, in line with the strategy proposed by Riechers and Boers (2020).

We focus on the layer counted part of the GICC05 chronology, a synchronized age scale for several Greenland ice cores (Vinther et al., 2006; Rasmussen et al., 2006; Andersen et al., 2006; Svensson et al., 2008). It was obtained by counting the layers of different Greenland ice cores and synchronizing the results using matchpoints. While the recent part of the chronology is compiled from multiple cores, the older part (older than 15 kyr b2k) is based exclusively on the layer counting in the NGRIP core. We introduce a new method to generate realistic age ensembles for the NGRIP core, which conveniently represent the uncertainty associated with the GICC05.

Originally, the dating uncertainty of the GICC05 is quantified in terms of the maximum counting error (MCE). The MCE increases by 0.5 years for every layer which is deemed uncertain by the investigators during the counting process:

$$\text{MCE}(z) = 0.5N_u(z), \quad (1)$$

where  $N_u$  is the number of uncertain layers down to depth  $z$ . In contrast to certain layers, which can be identified unambiguously in the records, uncertain layers are less pronounced and therefore it seems less certain that these signals truly correspond to physical layers. The accumulation of uncertain layers results in high values for the MCE for the older parts of the core (MCE = 2.6 kyr at 60 kyr b2k estimated age). However, it seems highly unlikely that all uncertain layers are consistently either true layers or no layers, which is why we think that the MCE is an overly careful quantification of the age uncertainty, as already suggested by Andersen et al. (2006). One might, alternatively, be tempted to treat the uncertain layers as a Bernoulli experiment with  $N_u$  repetitions and a probability of one half for each uncertain layer to be a true layer. However, this would neglect any sort of bias in the assessment of the uncertain layers and would lead to unrealistically small uncertainties, since over- and under-counting practically cancel each other out in this Bernoulli type interpretation (see for instance Andersen et al., 2006; Rasmussen et al., 2006).

The method presented here abandons the notion of certain and uncertain layers. Instead, we separate the GICC05 chronology into contributions that can be captured by deterministic model equations and corresponding residuals. We construct a new age–depth model by complementing the deterministic part with a stochastic component designed in accordance with the statistics of the residuals. This model can be used to generate age–depth ensembles in a computationally efficient manner. In turn, these ensembles facilitate un-

certainty propagation to subsequent analysis. The model parameters are tuned with respect to the GICC05 chronology that includes every uncertain layer as half a layer.

The outline of this paper is as follows: Section 2 gives a description of the data used for this study. Section 3.1 introduces our statistical model for the dating uncertainties, and details about how we incorporate physical processes and how we deduce the noise of the model from the statistics of the residuals. In Sect. 3.2 we show how we can formulate our model in terms of a hierarchical Bayesian modeling framework that allows for the physical and noise components to be estimated simultaneously. That section also details how one can use the resulting posterior distributions of the model parameters to obtain a full description of the posterior distributions of the dating uncertainties using a sample-based approach. We finally demonstrate how a potential counting bias could be incorporated by the model, and how that would affect the results. In Sect. 4 we show how our model can be used to obtain a full description of the dating uncertainties of abrupt warming events, which takes into account the dating uncertainties as well as the uncertainties in determining their exact position in the noisy data. Further discussion and conclusions are provided in Sect. 6.

## 2 NGRIP ice core data

We use the Greenland Ice Core Chronology 2005 (GICC05) (Vinther et al., 2006; Rasmussen et al., 2006; Andersen et al., 2006; Svensson et al., 2008) as defined for the NGRIP ice core together with the corresponding  $\delta^{18}\text{O}$  proxy record (North Greenland Ice Core Project members, 2004; Gkinis et al., 2014; Ruth et al., 2003). An analogous analysis for the  $\text{Ca}^{2+}$  proxy record is presented in Appendix B. The final age of the layer counted part of the GICC05 is 59 944 yr b2k, and we consider data up to 11 703 yr b2k. The following Holocene part of the record is excluded since it is governed by a substantially different climate than the last glacial interval (Rasmussen et al., 2014). For the considered period, the NGRIP record is available at 5 cm resolution and thus equidistant in depth, but not in time. In total, the data comprises  $n = 18\,672$  data points of the form  $(z_k, y_k, x_k)$ ,  $k \in \{0, 1, \dots, n-1\}$ , where  $z_k$  denotes the  $k$ th depth,  $y_k$  the corresponding age as indicated by the GICC05, and  $x_k$  the measured proxy value.

The GICC05 is based on counting annual layers which are evident in multi-proxy continuous flow measurements from the NGRIP, DYE3, and the GRIP ice cores. While the measurements from DYE3 and GRIP only facilitate layer counting up to ages of 8.2 and 14.9 kyr b2k, respectively, the NGRIP core allowed the identification of annual layers up to an age of 60 kyr b2k. The uncertainty of the GICC05 has been quantified as follows: whenever the investigators were uncertain about whether or not a signal in the data should be considered an annual layer, half a year was added to the

cumulative number of layers while simultaneously adding  $\pm 0.5$  yr to the age uncertainty. The total age uncertainty determined by the number of all uncertain layers up to a given depth is termed the maximum counting error (MCE). The MCE amounts to a relative age uncertainty of 0.84 % at the onset of the Holocene and 4.34 % at the end of the layer counted section of the core.

$\delta^{18}\text{O}$  values from Greenland ice cores are interpreted as a qualitative measure of the site temperature at the time of precipitation (Jouzel et al., 1997; Gkinis et al., 2014). We include these data in our study since our modeling approach will make use of the relation between atmospheric temperatures and the amount of precipitation, which in turn affects the thickness of the annual layers. In addition we use the division of the record into Greenland stadial and interstadial phases as presented in Table 2 of Rasmussen et al. (2014). We label the depths at which stadial–interstadial transitions occur by  $z_1^*, \dots, z_p^*$  and the corresponding ages by  $y_1^*, \dots, y_p^*$ . Figure 1 shows the measured  $\delta^{18}\text{O}$  values as a function of the GICC05 time scale, together with the Greenland stadial and interstadial onsets.

## 3 Methods

### 3.1 Age–depth model

We assume that depths  $\mathbf{z} = (z_1, \dots, z_n)^\top$  and proxy values  $\mathbf{x} = (x_1, \dots, x_n)^\top$  are measured accurately and hence treat them as deterministic variables. In contrast, we consider the ages  $\mathbf{y} = (y_1, \dots, y_n)^\top$  as dependent stochastic variables and will in the following establish a model to map the independent depths and stable isotope concentrations onto ages, in a way that reflects the uncertainties inherent to the dating. The model will be supplemented with information on the prevailing climate period.

In order to motivate our modeling approach we give some general considerations about the deposition process as well as the counting process. The decisive quantity for us will be the incremental number of annual layers counted in a 5 cm depth increment of the ice core:

$$\Delta y_k = y_k - y_{k-1}. \quad (2)$$

This quantity is determined by the amount of precipitation (minus the snow that is blown away by winds) during the corresponding period, the thinning that the layers experience over time deeper down in the core, and potential errors made during the counting process. While the thinning process can be expected to happen mostly deterministically, the net annual accumulation of snow certainly exhibits stronger fluctuations. Finally, the counting error adds additional randomness. Thus, it is reasonable to regard the observed age increments  $\Delta \mathbf{y}$  as a realization of a random vector  $\Delta \mathbf{Y}$  which can be decomposed into a deterministic and a stochastic compo-

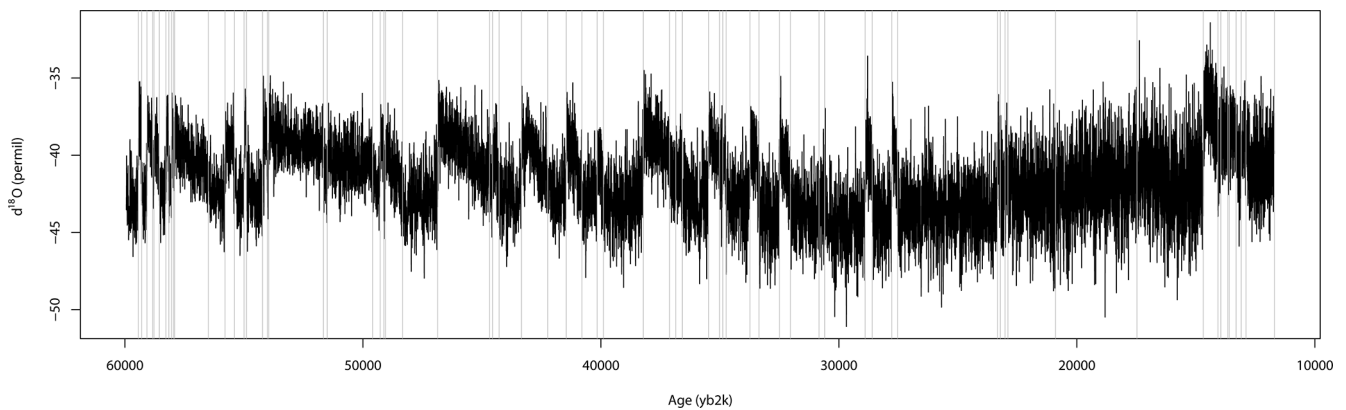


**Figure 1.** The measured  $\delta^{18}\text{O}$  isotope values plotted against the corresponding GICC05 time scale, starting from 11 793 yr b2k. The vertical gray lines denote the transitions between Greenland stadial and interstadial periods as reported by Rasmussen et al. (2014).

nent:

$$\Delta Y_k = a(z_k) + \varepsilon_k. \quad (3)$$

Note that the number of layers within a 5 cm depth increment is not necessarily an integer number. Given that the amount of precipitation co-varies with atmospheric site temperatures we can specify

$$a(z_k) = a(z_k, x(z_k)) \rightarrow a(z_k, x_k). \quad (4)$$

Based on physical arguments and the analysis of the observed age increments  $\Delta y_k$ , we will propose the structural form of the deterministic part of the model and then tune the model parameters to the data. In turn, this will allow us to design the model's noise component  $\varepsilon$  in accordance with the corresponding residuals  $\delta_k = \Delta y_k - a(z_k, x_k)$ .

### 3.1.1 Linear regression

As explained above, the thickness of the counted layers, and thereby the number of layers per depth increment  $\Delta z_k = z_k - z_{k-1}$ , is governed by two physical factors: the amount of precipitation at the time the layer was formed and the thinning of the core due to ice flow. These processes are here assumed to follow a regression model. We take into account the thinning by implementing a second order polynomial dependency of  $\Delta Y_k$  with respect to the depth  $z_k$ . Choosing this non-linear function conveniently accounts for the saturation of the layer thinning evident in the NGRIP ice core. The amount of precipitation is known to co-vary with atmospheric temperatures, since by the Clausius–Clapeyron relation the moisture holding capacity of the atmosphere increases with temperatures. This is represented using a linear response to the  $\delta^{18}\text{O}$  measurements. The same response is applied to the  $\log(\text{Ca}^{2+})$  in the alternative analysis presented in Appendix B. Finally, we observe clear trends in the incremental layers that persist over individual stadials and interstadials. Given the consistency of these trends across the different climate periods, we decided to incorporate them into

the deterministic model component. Overall, we propose a deterministic model of the form

$$a(z_k, x_k) = bz_k^2 + b_x x_k(z_k) + \sum_{i=1}^p \psi_i(z_k; a_i, c_i), \quad (5)$$

with

$$\psi_i(z_k; a_i, c_i) = \begin{cases} a_i + c_i z_k, & z_i^* < z_k < z_{i+1}^* \\ 0, & \text{otherwise} \end{cases}, \quad (6)$$

in order to capture the systematic features of the chronology. Here,  $c_i$  denotes the period specific slopes and  $a_i$  their corresponding offsets. For  $p$  transitions between stadials and interstadials we have to tune  $2p + 2$  regression parameters, which is achieved by fitting the above model for  $a(z_k, x_k)$  to the observed layer increments  $\Delta y_k$  given by the GICC05 time scale in a least squares approach. As explained above, the GICC05 ages contain the contribution of uncertain layers, which were counted as half a year each. Here, we abandon the distinction of certain and uncertain layers and regard the GICC05 ages as the best possible estimate of the true ages and accordingly use them directly for the optimization. The fitted model is shown in red in Fig. 22a.

### 3.1.2 Noise structure

After tuning the deterministic part of Eq. (3), the residuals are given by

$$\delta_k = a(z_k, x_k) - \Delta y_k. \quad (7)$$

We find the residuals to be symmetric and unimodally distributed, and apart from some degree of over-dispersion they appear to be well described by a normal distribution, as shown in Fig. 3.

Moreover, by examining the empirical autocorrelation illustrated in Fig. 3c, we observe that the residuals exhibit a fast decay of memory which is indicative of stationarity.

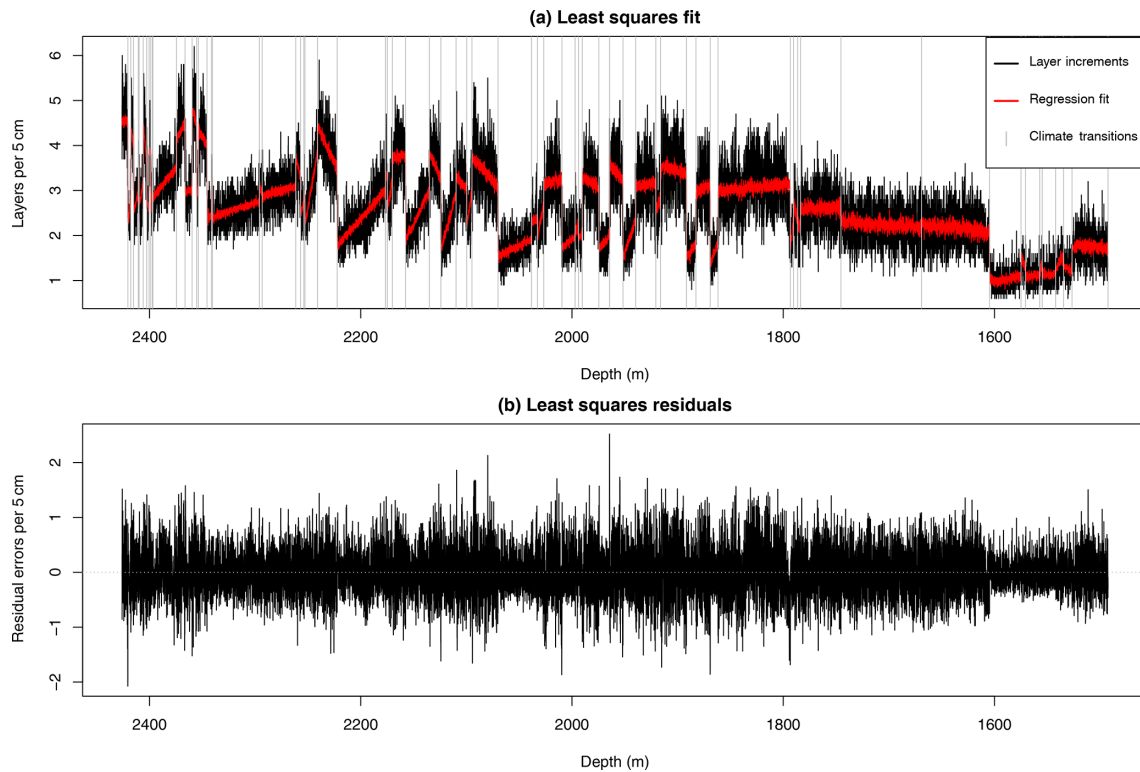


**Figure 2.** (a) Number of layers counted in the GICC05 time scale per 5 cm depth increments in the NGRIP ice core (black). The red line shows the fitted values from the regression model  $a(z_k, x_k) = bz_k^2 + b_x x(k) + \sum_{i=1}^p \psi_i(z_k; a_i, c_i)$ . The vertical gray lines represent the transitions between Greenland stadials and interstadials. (b) The residuals  $\delta_k$  obtained from fitting the regression model  $a(z_k, x_k)$  to the layer increments  $\Delta y_k$ .

This suggests that the noise can be expressed using a short-memory Gaussian stochastic process.

We explore three different models for the correlation structure of the noise  $\varepsilon$ . The first model assumes that they follow independent and identically distributed (iid) Gaussian processes:

$$\varepsilon_k \stackrel{\text{iid}}{\sim} \mathcal{N}(0, \sigma_\varepsilon^2). \quad (8)$$

The second model assumes that the noise can be described by a first order autoregressive (AR) process

$$\varepsilon_k = \phi \varepsilon_{k-1} + \xi_k, \quad (9)$$

where  $\phi$  is the first-lag autocorrelation coefficient and  $\xi_k$  is a white noise process with variance  $\sigma_\xi^2 = \sigma_\varepsilon^2 / (1 - \phi^2)$ . The third model assumes the noise follows a second order autoregressive process

$$\varepsilon_k = \phi_1 \varepsilon_{k-1} + \phi_2 \varepsilon_{k-2} + \xi_k, \quad (10)$$

where  $\phi_1$  and  $\phi_2$  are the first- and second-lag autocorrelation coefficients and  $\xi_k$  is a white noise process with variance:

$$\sigma_\xi^2 = \sigma_\varepsilon^2 \frac{1 - \phi_2}{(1 + \phi_2)((1 - \phi_2)^2 - \phi_1^2)}. \quad (11)$$

Note that a potential global or at least climate-regime-specific bias in the counting process, such as overseeing systematically 1 out of 10 layers, would be captured by the regression model and thus cannot be identified as a systematic error. We will investigate the influence of potential systematic errors below. Similarly, fluctuations in the physical processes can be captured by the noise model which aims to represent the counting errors. It would therefore be more accurate to interpret  $a(z_k, x_k)$  as a structured component representing a part of both the physical processes and a systematic counting error which can be accounted for by linear regression, and  $\varepsilon_k$  as the fluctuations of both the physical processes and counting errors. Hence,  $\varepsilon_k$  can be considered an upper boundary on the counting uncertainty.

### 3.2 Simultaneous Bayesian modeling

So far, we have fitted only the structural model component. This enabled us to investigate statistical properties of the residuals and formulate corresponding noise model candidates. Fitting both the linear regression model and the different noise models can in principle be performed in two stages: First, the linear regression model is fitted to the layer increments using the method of least squares. Thereafter, the

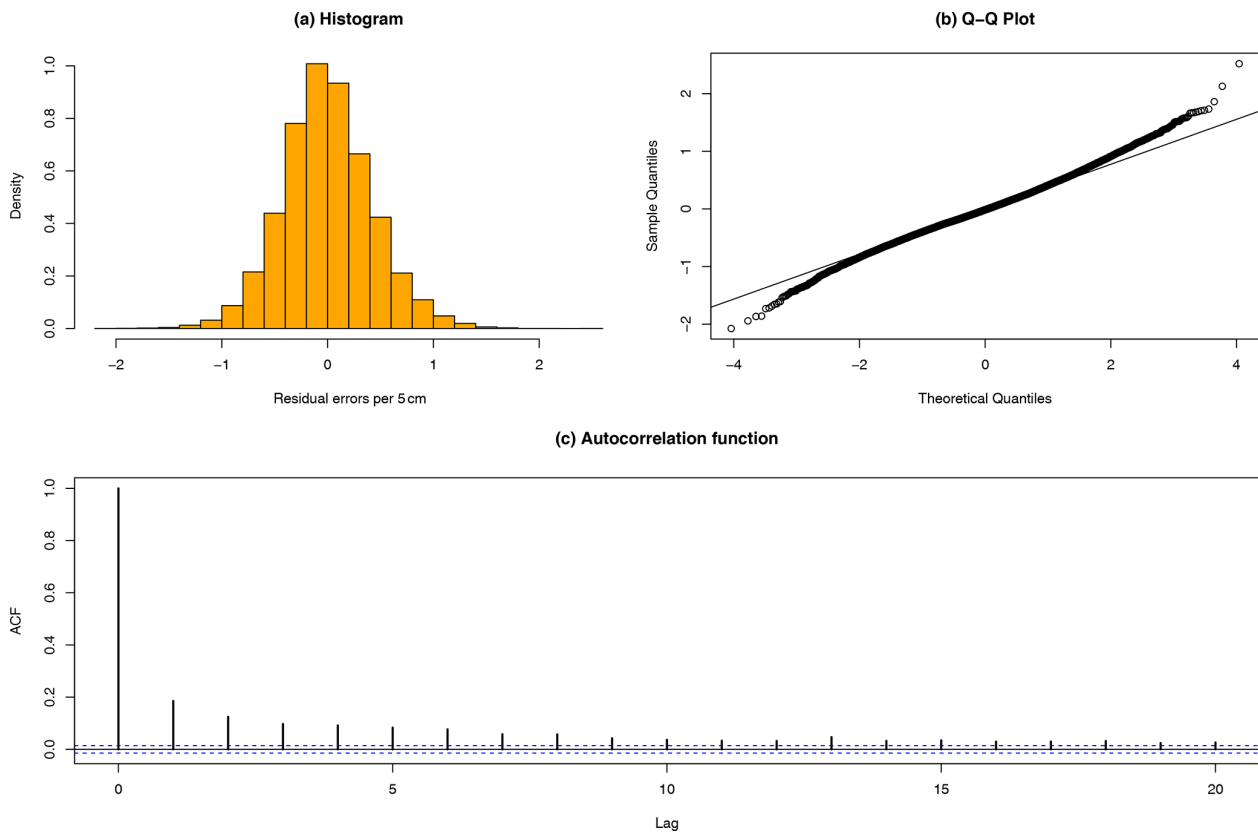


**Figure 3.** (a) Histogram of the residuals obtained from least squares fit of the regression model  $a(z_k, x_k)$ . (b) The corresponding quantile–quantile plot. We observed key properties of symmetry and unimodality indicating Gaussianity. The quantile–quantile plot indicates a small over-dispersion, but overall the data seem to be consistent with a normal distribution. (c) The autocorrelation function of the residuals from the least squares fit of the linear regression model, up to a maximum of 20 lags. A fast memory decay can be inferred.

fitted values are subtracted and the selected noise model is fitted to the residuals. However, this approach has the disadvantage that some variation that may in reality be caused by the noise process  $\varepsilon_k$  may have been attributed to the structured component  $a(z_k, x_k)$  and removed before fitting the noise model. We therefore introduce here a Bayesian approach that enables us to estimate all model parameters simultaneously. The Bayesian approach has three key advantages over the least squares fitting of the structured component: first, it treats the noise and the structured component equally. Second, it returns the joint posterior probability of all model parameters which indicates the plausibility of a certain parameter configuration in view of the data. The posterior probability distribution can be regarded as an uncertainty quantification of the model’s parameter configuration. Third, in the Bayesian parameter estimation, prior knowledge and constraints on the parameter can be incorporated via a convenient choice of the so-called prior distributions.

In general terms, let  $\mathcal{D}$  denote some observational data and  $\theta$  denote parameters that shape a model which is assumed to reasonably describe the process that generated the data. Then Bayes’ theorem can be used to deduce the posterior

probability density of the parameters  $\theta$  given the data  $\mathcal{D}$ :

$$\pi(\theta|\mathcal{D}) = \frac{\pi(\mathcal{D}|\theta)\pi(\theta)}{\pi(\mathcal{D})}. \quad (12)$$

In our case the GICC05 age  $\mathbf{y} = (y_1, \dots, y_n)$ , or more precisely their increments  $\Delta\mathbf{y}$ , represent the observational data  $\mathcal{D}$  assumed to be generated from the model defined by Eq. (3). There are  $2p+2$  parameters  $\beta = (b_2, b_x, a_1, c_1, \dots, a_p, c_p)$  for the structured component alone and the noise adds another one to three parameters, depending on the choice of the noise structure. Thus the set of model parameters reads

$$\theta = (\beta, \psi), \quad (13)$$

where  $\psi = \sigma_\varepsilon$  if the residuals are assumed to follow an iid Gaussian distribution,  $\psi = (\sigma_\varepsilon, \phi)$  if they are assumed to follow an AR(1) process, and  $\psi = (\sigma_\varepsilon, \phi_1, \phi_2)$  if they are assumed to follow an AR(2) process. For any given parameter configuration, the likelihood is for all three choices of the

noise structure defined by a multivariate Gaussian distribution,

$$\pi(\Delta \mathbf{y} | \boldsymbol{\theta}) = (2\pi)^{-n/2} |\boldsymbol{\Sigma}|^{-1} \exp \left\{ -\frac{1}{2} (\Delta \mathbf{y} - \mathbf{a})^\top \boldsymbol{\Sigma}^{-1} (\Delta \mathbf{y} - \mathbf{a}) \right\}, \quad (14)$$

where  $\mathbf{a} = (a(z_1, x_1), \dots, a(z_n, x_n))^\top$  and the entries of the autocovariance matrix  $\boldsymbol{\Sigma}$  are given by the autocovariance function  $\Sigma_{ij} = \gamma(|i - j|)$  of the assumed noise model. For the iid model, the autocovariance function is simply  $\sigma_\varepsilon^2$  if  $i = j$ , and zero otherwise, resulting in a diagonal covariance matrix. For the AR(1) model the autocovariance function is

$$\gamma(k) = \frac{\sigma_\varepsilon^2}{1 - \phi^2} \phi^{|k|}. \quad (15)$$

The autocovariance function of the AR(2) model is specified by the difference equation,

$$\gamma(k) = \phi_1 \gamma(k - 1) + \phi_2 \gamma(k - 2), \quad (16)$$

with initial conditions:

$$\gamma(0) = \left( \frac{1 - \phi_2}{1 + \phi_2} \right) \frac{\sigma_\varepsilon^2}{(1 - \phi_2)^2 - \phi_1^2} \quad (17)$$

$$\gamma(1) = \frac{\phi_1}{1 - \phi_2} \gamma(0). \quad (18)$$

A benefit of having the likelihood follow a Gaussian distribution is that it can be evaluated easily and samples can be obtained efficiently, despite the large number of parameters. Finally, we define convenient priors for the model parameters. For the parameters of the structured model component  $\boldsymbol{\beta}$  we choose vague Gaussian priors, with variances that safely cover all reasonable parameter configurations. For the noise parameters  $\boldsymbol{\psi}$  we restrict the scaling parameter  $\sigma_\varepsilon$  to be positive, and the autoregressive coefficients such that they define a stationary model. These constraints are embedded into the model by adopting suitable parameterizations. The scaling parameter  $\sigma_\varepsilon$  is assigned a gamma distribution through the parameterization  $\kappa = \log(1/\sigma_\varepsilon^2)$ . For the lag-one correlation parameter in the AR(1) model we assume a Gaussian prior on the logit transformation  $\rho = \log((1 + \phi)/(1 - \phi))$ . For the AR(2) model we instead assign priors on the logit transformation of the partial autocorrelations  $\psi_1 = \phi_1/(1 - \phi_2)$  and  $\psi_2 = \phi_2$ , using penalized complexity priors (Simpson et al., 2017).

In principle, the joint posterior density can then be sampled by using a Markov chain Monte Carlo (MCMC) algorithm (e.g., Goodman and Weare, 2010). However, to solve Eq. (12) more efficiently, we formulate the problem in terms of a latent Gaussian model and then use integrated nested Laplace approximations (INLAs) (Rue et al., 2009, 2017) to

compute the joint and marginal posterior distributions (for details see Appendix A).

The posterior distribution of  $\boldsymbol{\theta}$  enables us to generate ensembles of different realizations of the random variable  $\mathbf{Y}$ , i.e., of the age increments that correspond to the fixed depth increments  $\Delta \mathbf{z}$ . In a two-stage Monte Carlo simulation, first a value for  $\boldsymbol{\theta}$  is randomly sampled from the posterior  $\pi(\boldsymbol{\theta} | \Delta \mathbf{y})$ . Second, the noise  $\varepsilon$  is sampled according to the noise model using noise parameters sampled in the first step. An ensemble generated in this fashion simultaneously reflects the uncertainty enshrined in the stochastic process and the model thereof as well as the uncertainty about the model parameters. Each realization of age increments yields a corresponding possible chronology according to

$$y_k = y_0 + \sum_{i=1}^k (a(z_i, x_i) + \varepsilon_i), \quad (19)$$

where  $y_0$  is the number of reported layers up to the depth  $z_0$ . Figure 4 shows the 95 % credible intervals obtained from age ensembles for the three different noise models with respect to the GICC05 age. Each ensemble comprises 10 000 realizations of  $\mathbf{Y}$ . In this plot we notice a significant increase of uncertainty going from the iid to the AR(1) model. This is intuitive as when more memory is added to the model, the variation increases.

However, going from AR(1) to AR(2) adds only moderate additional uncertainty. We therefore argue that an AR(1) process is sufficient in terms of modeling the correlation structure of the residuals. The same is observed when using  $\log(\text{Ca}^{2+})$  as a proxy instead (see Fig. B1). All computations henceforth are carried out with the AR(1) noise model.

### 3.3 Incorporating an unknown counting bias

When originally quantifying the uncertainty of the GICC05 chronology, a concern was that the layer counting was potentially biased in the sense that layers were consistently overcounted or missed. As highlighted by Andersen et al. (2006), there is no way to quantify a potential bias based on the data. Here, we investigate the influence that such a bias would have on our model, assuming a given maximum bias strength. To capture the effect of a systematic bias in the layer counting we introduce a scaling parameter  $\eta$  such that

$$\Delta Y_k = \eta (a(z_k, x_k) + \varepsilon_k). \quad (20)$$

Given that we have no knowledge about the size of the bias,  $\eta$  must be regarded as a random variable whose distribution can only be estimated by experts a priori. Originally, biases on the order of 1 % in the counting performed by different investigators have been observed (Rasmussen et al., 2006; Andersen et al., 2006). Here we assume

$$\eta \sim \mathcal{U}(1 \pm \Delta \eta), \quad (21)$$

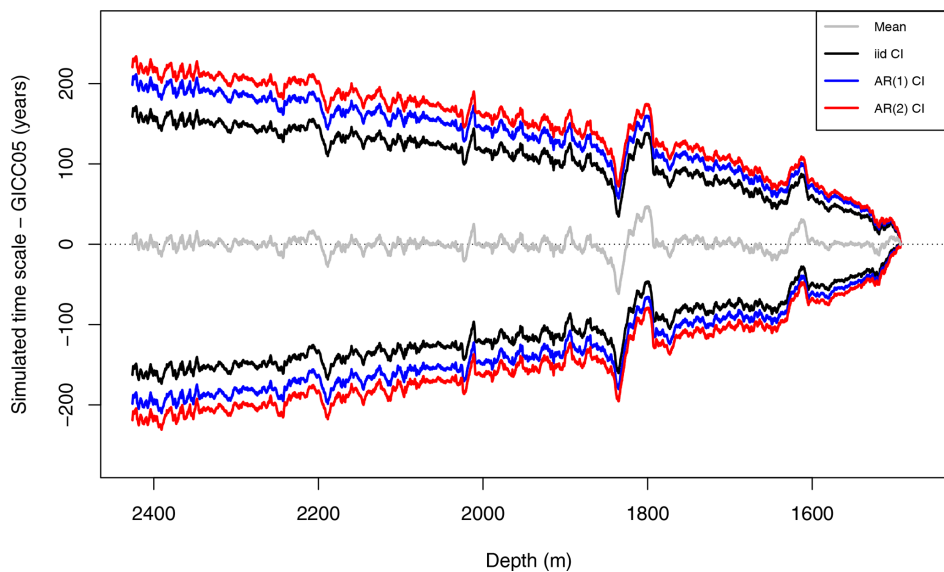


**Figure 4.** The 95 % credible intervals of the dating uncertainty distribution when  $\delta^{18}\text{O}$  is used as the proxy covariate. The GICC05 time scale has been subtracted and the noise is modeled using iid (black), AR(1) (blue), and AR(2) (red) noise models. Only the posterior marginal mean computed using AR(1) distributed noise is included (gray) since it is very similar to the mean obtained using other noise assumptions.

meaning the layer counters are just as likely to systematically over-count as to under-count, on a maximum rate of  $\Delta\eta$ . While the expectation for the age increments  $E(\Delta Y)$  remains unchanged as long as  $E(\eta) = 1$ , their variance will grow due to the additional uncertainty. Figure 5 shows the 95 % credible intervals for potentially biased chronology ensembles generated under the assumption that  $\Delta\eta$  equals 0 %, 2 %, or 4 %.

It is evident that the bias uncertainty contributes substantially to the age uncertainty. This is expected since a relatively small counting bias yields a large absolute error at a possible age of 60 kyr b2k, which in turn exceeds the uncertainty contribution of the noise by far. We also observed that one would need a maximum error rate of  $\Delta\eta \approx 4\%$  in order for the uncertainty to approach the maximum counting error at the end of the layer counted core segment.

## 4 Examples of applications

### 4.1 Dating uncertainty of DO events

Both the NGRIP  $\delta^{18}\text{O}$  and  $\log(\text{Ca}^{2+})$  records are characterized by prominent abrupt shifts from low to high values, including the so-called Dansgaard–Oeschger (DO) events (Johnsen et al., 1992; Dansgaard et al., 1993). These jumps are interpreted as sudden warming events in Greenland, which took place repeatedly during the last glacial period. In order to explain the physical relationship between these abrupt Greenland warming events and apparently concomitant abrupt climate shifts evidenced in other archives from different parts of the planet, it is crucial to disentangle the exact temporal order of these events. This requires a rigorous

treatment of the uncertainties associated with the dating of DO events in Greenland ice core records.

Rasmussen et al. (2014) provide a comprehensive list of Dansgaard–Oeschger events and other stadial–interstadial transitions, indicating depths from the NGRIP ice core at which they occur, and the corresponding GICC05 age. They report the visually identified event onsets and provide uncertainty estimates in terms of data points along the depth axis and the respective MCE associated with the estimated event onset depth. This assessment was later refined by Capron et al. (2021) using the algorithm for detecting transition onsets designed by Erhardt et al. (2019). Here, we present a rigorous combination of the depth and age uncertainties, which complicate the exact dating of abrupt warming events.

First, we adopt the Bayesian transition onset detection designed by Erhardt et al. (2019) to estimate the onset of the abrupt warming transitions in the proxy records with respect to the depth in the core. By  $Z^*$  we denote a continuous stochastic variable that represents the uncertain onset depth and by  $\mathbf{x}^*$  we denote a selected data window of the proxy record enclosing the transition. For each transition this yields a posterior distribution  $\pi(Z^*|\mathbf{x}^*)$  over potential transition onset depths, assuming a linear transition from low to high proxy values perturbed by AR(1) noise. For inference we adopt the methodology of INLA as it is particularly suited for such models, granting us a significant reduction in computational cost over traditional MCMC algorithms. The application of the transition onset detection to the onset of GI-11 is presented in Fig. 6a, with the resulting posterior marginal distribution for  $Z^*$  illustrated in Fig. 6b. Note that the dating method for the transitions is sensitive to the choice

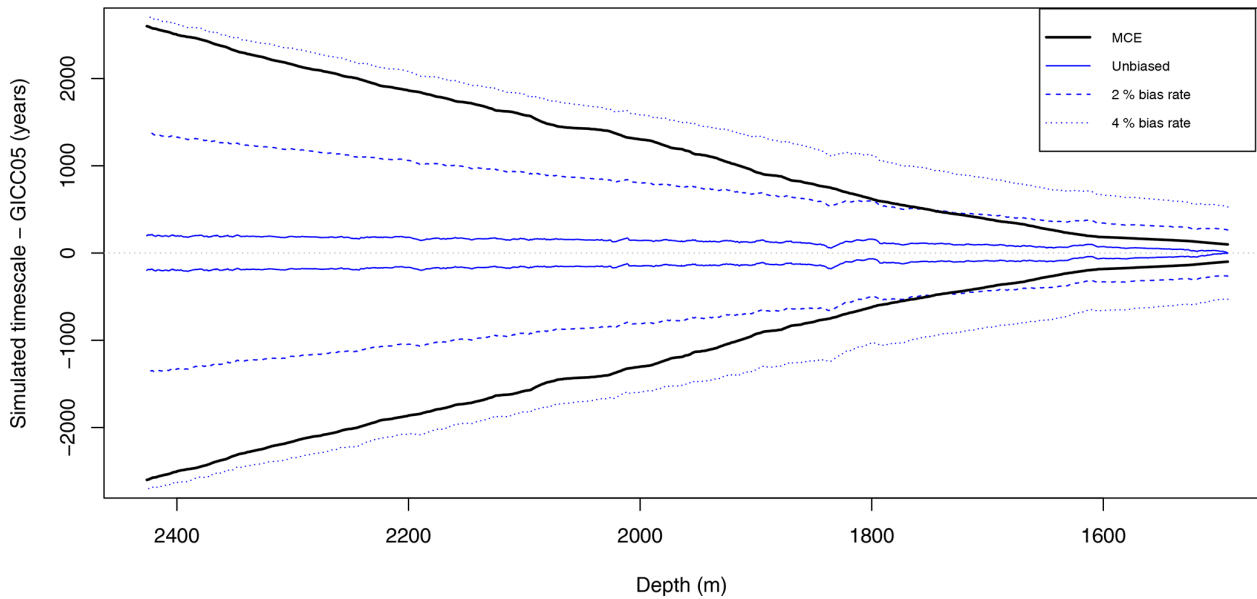


**Figure 5.** The 95 % credible intervals of the difference between estimated dating and the GICC05 time scale compared with the maximum counting error (solid black). Dating uncertainties in this case include a bias expressed by a stochastic scaling parameter drawn from a uniform  $\mathcal{U}(1 \pm \Delta\eta)$  distribution. The solid blue line represents the unbiased  $\Delta\eta = 0$  dating uncertainty, while the dashed and dotted blue lines represent the biased cases of  $\Delta\eta = 2\%$  and  $\Delta\eta = 4\%$ , respectively. The differences in dating uncertainty between iid, AR(1), and AR(2) models are dwarfed by the uncertainty introduced by the unknown bias; hence, only the AR(1) distributed residuals are shown here.

of the data window. In Appendix D we detail how the fitting windows for the linear ramps are optimally chosen. The selected data windows are listed in Table D1. Furthermore, the Bayesian transition detection fails in some cases where the transition amplitudes are small. We successfully derive posterior marginal distribution for a total of 29 events, whose summary statistics are listed in Table 1.

Each potential transition onset depth  $z^*$  yields a distribution over potential transition onset ages  $Y^*$ . This uncertainty, denoted by  $\pi(Y^* | \Delta y, z^*)$ , is determined by linearly interpolating the age ensemble members generated according to Sect. 3.1 based on the observed layer increments  $\Delta y$ . The posterior distribution for the transition onset date for a given DO event thus reads

$$\pi(Y^* | \Delta y, \mathbf{x}^*) = \int \pi(Y^* | \Delta y, Z^*) \pi(Z^* | \mathbf{x}^*) dZ^*. \quad (22)$$

Technically, we create an ensemble of potential onset ages in the following way: First, we generate an ensemble of 10 000 samples from the posterior distribution of the transition onset depth,

$$z_r^* \sim \pi(Z^* | \mathbf{x}^*), \quad r \in [1, 10000],$$

to represent the onset depth uncertainty. Second, for each onset depth sample  $z_r^*$  we produce a simulation of a chronology from the corresponding age uncertainty:

$$y_r^* | z_r^* \sim \pi(Y^* | \Delta y, z_r^*).$$

Thus, for both proxies ( $\delta^{18}\text{O}$  and  $\text{Ca}^{2+}$ ) and for each event we obtain 10 000 possible values for the transition onset age whose distribution corresponds to the posterior distribution expressed in Eq. (22). The posterior marginal mean and 95 % credible intervals for each event are reported in Table 1. This table hence gives the timing of the transitions together with the full uncertainties, stemming from the transition onset detection and the dating of the record. The estimated dating uncertainties are presented visually in Fig. 7, where they are also compared to the onset age obtained by Rasmussen et al. (2014), as well as the best estimates from Buizert et al. (2015) and Capron et al. (2021) which are presented in Table 2.

Although the GICC05 ages  $y^*$  of abrupt warming events and subevents as reported by Rasmussen et al. (2014) fall within our estimated 95 % credible intervals for all transitions, there are some transitions where there is a notable difference between the estimated posterior marginal mean  $E(Y^*)$  and the reported  $y^*$ . This can be partially explained by the fact that Rasmussen et al. (2014) uses a lower 20-year temporal resolution, and that they determine the onset from three different ice cores and two different proxies ( $\delta^{18}\text{O}$  and  $\text{Ca}^{2+}$ ), whereas our assessment is based on the univariate NGRIP proxy records only. With  $E(Y^*) - y^* \sim 120$  the difference is most prominent in the GI-11 transition, whose simulated ages are represented in the histogram in Fig. 6c. This discrepancy is caused by the difference between our estimated onset depth  $Z^*$  and  $z^*$  from our linear ramp model fit shown in Fig. 6a. Our estimated onset depth  $E(Z^*)$  dif-

**Table 1.** Linear ramp model fits for the NGRIP depth of 29 abrupt warming events, as well as the full dating uncertainty. Data include the depth  $z^*$  and dating  $y^*$  from Rasmussen et al. (2014), as well as the posterior marginal mean and 95 % credible intervals for the estimated onset depth  $Z^*$  and age  $Y^*$ .

Event	$z^*$ (m)	$Z^*$ mean (m)	$Z^*$ 95 % CI (m)	$y^*$ (yr b2k)	$Y^*$ mean (yr b2k)	$Y^*$ 95 % CI (yr b2k)
GI-1d	1574.80	1574.97	(1574.85, 1575.11)	14 075	14 078.53	(14 020.02, 14 136.57)
GI-1e	1604.64	1604.52	(1604.47, 1604.57)	14 692	14 689.13	(14 621.21, 14 758.25)
GI-2.2	1793.19	1793.87	(1793.63, 1794.08)	23 340	23 383.98	(23 269.8, 23 497.12)
GI-3	1869.12	1869.22	(1868.95, 1869.56)	27 780	27 789.43	(27 661.18, 27 916.42)
GI-4	1891.57	1891.67	(1891.32, 1892.05)	28 900	28 909.82	(28 777.57, 29 042.34)
GI-5.2	1951.65	1952.02	(1951.98, 1952.06)	32 500	32 524.76	(32 383.73, 32 662.2)
GI-6	1974.55	1974.40	(1974.36, 1974.44)	33 740	33 734.54	(33 590.28, 33 874.96)
GI-7b	1997.04	1997.25	(1997.20, 1997.31)	35 020	35 029.43	(34 881.88, 35173.95)
GI-7c	2009.44	2009.76	(2009.70, 2009.82)	35 480	35 502.41	(35 352.63, 35 649.46)
GI-8c	2070.02	2069.91	(2069.78, 2070.07)	38 220	38 216.54	(38 058.91, 38 372.02)
GI-9	2099.61	2099.65	(2099.64, 2099.66)	40 160	40 163.26	(40 001.66, 40 322.67)
GI-10	2124.03	2124.38	(2124.26, 2124.47)	41 460	41 484.34	(41 320.07, 41 647.05)
GI-11	2157.49	2159.20	(2159.02, 2159.37)	43 340	43 469.75	(43 300.83, 43 637.19)
GI-12c	2222.30	2222.27	(2222.16, 2222.39)	46 860	46 860.6	(46 685.25, 47 035.35)
GI-13b	2253.84	2254.11	(2254.05, 2254.17)	49 120	49 135.6	(48 957.52, 49 313.66)
GI-13c	2256.89	2257.39	(2257.26, 2257.54)	49 280	49 313.32	(49 134.13, 49 491.73)
GI-14b	2295.90	2296.00	(2295.81, 2296.17)	51 660	51 666.83	(51 482.6, 51 849.78)
GI-14c	2340.38	2340.03	(2339.93, 2340.13)	53 960	53 943.9	(53 753.12, 54 131.19)
GI-14d	2341.38	2341.55	(2341.52, 2341.59)	54 020	54 028.81	(53 837.72, 54 215.99)
GI-14e	2345.52	2345.65	(2345.59, 2345.70)	54 220	54 233.81	(54 042.35, 54 421.9)
GI-15.1	2355.34	2355.35	(2355.33, 2355.36)	55 000	55 002.51	(54 810.67, 55 190.97)
GI-15.2	2366.32	2366.56	(2366.47, 2366.64)	55 800	55 824.2	(55 630.79, 56 013.95)
GI-16.1b	2397.35	2397.36	(2397.28, 2397.47)	57 960	57 959.99	(57 762.56, 58 153.23)
GI-16.1c	2398.78	2398.67	(2398.58, 2398.75)	58 040	58 035.39	(57 838.32, 58 228.46)
GI-16.2	2402.55	2402.30	(2402.25, 2402.34)	58 280	58 266.31	(58 068.78, 58 459.55)
GI-17.1a	2409.78	2409.50	(2409.37, 2409.66)	58 780	58 765.24	(58 567.02, 58 960.27)
GI-17.1b	2410.65	2411.26	(2411.04, 2411.45)	58 840	58 876.59	(58 677.75, 59 072.46)
GI-17.1c	2415.01	2414.83	(2414.77, 2414.89)	59 080	59 069.05	(58 870.83, 59 265.27)
GI-17.2	2420.44	2420.70	(2420.64, 2420.76)	59 440	59 465.5	(59 266.65, 59 662.2)

fers from the value  $z^*$  reported by Rasmussen et al. (2014) by approximately 1.6 m. This discrepancy propagates into an accordingly large difference in the age estimation of the transition onset. This demonstrates the importance of incorporating proper estimation and uncertainty quantification of the onset depth. Although the absolute uncertainty added from determining the onset depth can be considered negligible compared with the much larger age–depth uncertainty, there can still be a noticeable shift in the estimated onset age propagated from the estimation of the onset depth.

## 5 Discussion

Motivated by the relationship between air temperature on the one hand and the water-holding capacity and thus precipitation on the other hand, we assumed a linear dependency of the number of incremental layers per 5 cm on respective values of  $\delta^{18}\text{O}$ , which serves as an air temperature proxy. The only other climate proxy variable which is available from the NGRIP ice core at the same resolution over the same time

period is the  $\text{Ca}^{2+}$  particle concentration (Ruth et al., 2003). From visual inspection one can already see that the negative logarithm of the  $\text{Ca}^{2+}$  mass concentration record shows high covariability with the  $\delta^{18}\text{O}$  record (see, for example, Fig. 1 of Rasmussen et al. (2014)). Changes in the  $\text{Ca}^{2+}$  concentrations are interpreted as changes in the local and hemispheric atmospheric circulation (e.g., Ruth et al., 2007; Schüpbach et al., 2018; Erhardt et al., 2019), which would also affect the amount of precipitation over Greenland. Above, we have focused on the  $\delta^{18}\text{O}$ ; and analogous analysis for  $-\log\text{Ca}^{2+}$  is presented in Appendix B. The results of the  $-\log\text{Ca}^{2+}$ -based chronology modeling are in very good agreement with the ones based on  $\delta^{18}\text{O}$ , which corroborates our methodology.

Adopting Gaussian noise models in principle allows for a negative modeled number of incremental layers in a 5 cm incremental core segment, which does not seem plausible from a physical perspective. To avoid this, for comparison one could log-transform the age increments and then apply the modeling procedure. The model output would then have to be transferred back by taking the exponential. However,

**Table 2.** Greenland interstadial transitions observed in the NGRIP record. Data include the median onset NGRIP depth and age for the  $\delta^{18}\text{O}$  and  $\text{Ca}^{2+}$  proxy records as reported in Capron et al. (2021) and the  $\delta^{18}\text{O}$  record presented in Buizert et al. (2015).

Transition	Capron et al. (2021)			Buizert et al. (2015)	
	Depth (m)	$\delta^{18}\text{O}$ onset (yr b2k)	$\text{Ca}^{2+}$ onset (yr b2k)	Depth (m)	$\delta^{18}\text{O}$ onset (yr b2k)
GI-1e	1604.89	14 700	14 708	1604.05	14 628
GI-2.2	1794.49	23 400	23 428		
GI-3	1869.35	27 788	27 797	1869.00	27 728
GI-4	1891.77	28 911	28 912	1891.27	28 838
GI-5.2	1952.26	32 528	32 540	1951.66	32 452
GI-7c	2010.12	35 510	35 507	2009.62	35 437
GI-8c	2070.22	38 231	38 239	2069.88	38 165
GI-10	2124.46	41 482	41 494	2123.98	41 408
GI-11	2159.33	43 471	43 366	2157.58	43 297
GI-12c	2222.71	46 887	46 896	2221.96	46 794
GI-14e	2345.73	54 235	54 233	2345.39	54 164
GI-15.1	2355.41	55 006	55 038	2355.17	54 940
GI-15.2	2366.71	55 831	55 831	2366.15	55 737
GI-16.2	2402.53	58 279	58 298	2402.25	59 018
GI-17.1c	2415.01	59 080	59 095	2414.82	59 018
GI-17.2	2420.98	59 480	59 483	2420.35	59 386

it turns out that the log transformation induces systematic deviations of the mean model output age from the reported GICC05 age. With the chances of negative layer increments being fairly small (less than 5%), overall the original model outperforms the log-transformed model. A more detailed discussion on the log-transformed modeling approach is given in Appendix C.

From Fig. 2b we observe that the variance of the residuals increases slightly with increasing depth down in the core. This heteroskedasticity can be incorporated into our latent Gaussian model by assuming that the variance depends on the core depth in some predefined way. As this implementation is rather technical we consider it beyond the scope of the current paper. Regardless, assuming constant variance appears to be a good first order approach.

## 6 Conclusions

We have developed a general statistical framework for quantifying the age–depth uncertainty of layer counted proxy archives. In these records the age can be determined by counting annual layers that result from seasonal variations, which in turn impact the deposition process. By counting these layers one can assign time stamps to the individual proxy measurements. However, there is a non-negligible uncertainty associated with this counting process. Proper quantification of this uncertainty is important since it carries valuable information and the error propagates to further analyses, e.g., dating of climatic events, determining cause and effect between such events, and model–data comparisons. Originally, the uncertainty of the GICC05 is quantified in terms

of the maximum counting error (MCE), defined as half the number of uncertain layers. However, since this method assumes that uncertain layers are either true or false, we believe this to be an overly conservative estimate, giving too high uncertainty for deeper layers.

In our approach we express the number of layers per depth increment as the sum of a structured component and a stochastic component. The structured component represents physical layer thinning, a positive temperature–precipitation feedback, and persisting trends over individual stadials and interstadials. The stochastic component takes into account the natural variability of the layer thickness and the errors made in the counting process. After fitting the structured component in a least squares manner, we find the residuals to be approximately stationary, Gaussian distributed, and to exhibit short-range autocorrelation. These summary statistics motivate us to employ Gaussian white noise, or an autoregressive process of first or second order, as the stochastic part of the age–depth model.

After defining the structure of the model, we estimate all model parameters simultaneously in a hierarchical Bayesian framework. The resulting joint posterior distribution on the one hand serves as a quantification of the parameter uncertainty in the model and on the other hand allows to generate chronology ensembles that reflect the uncertainty in the age–depth relationship of the NGRIP ice core. The dating uncertainties obtained from this approach are significantly smaller than those from the MCE. We also find that our estimates do not deviate much from the GICC05 in terms of best estimates for the dating.

Additional information that may help to further constrain the uncertainties, such as tie points obtained via cosmogenic

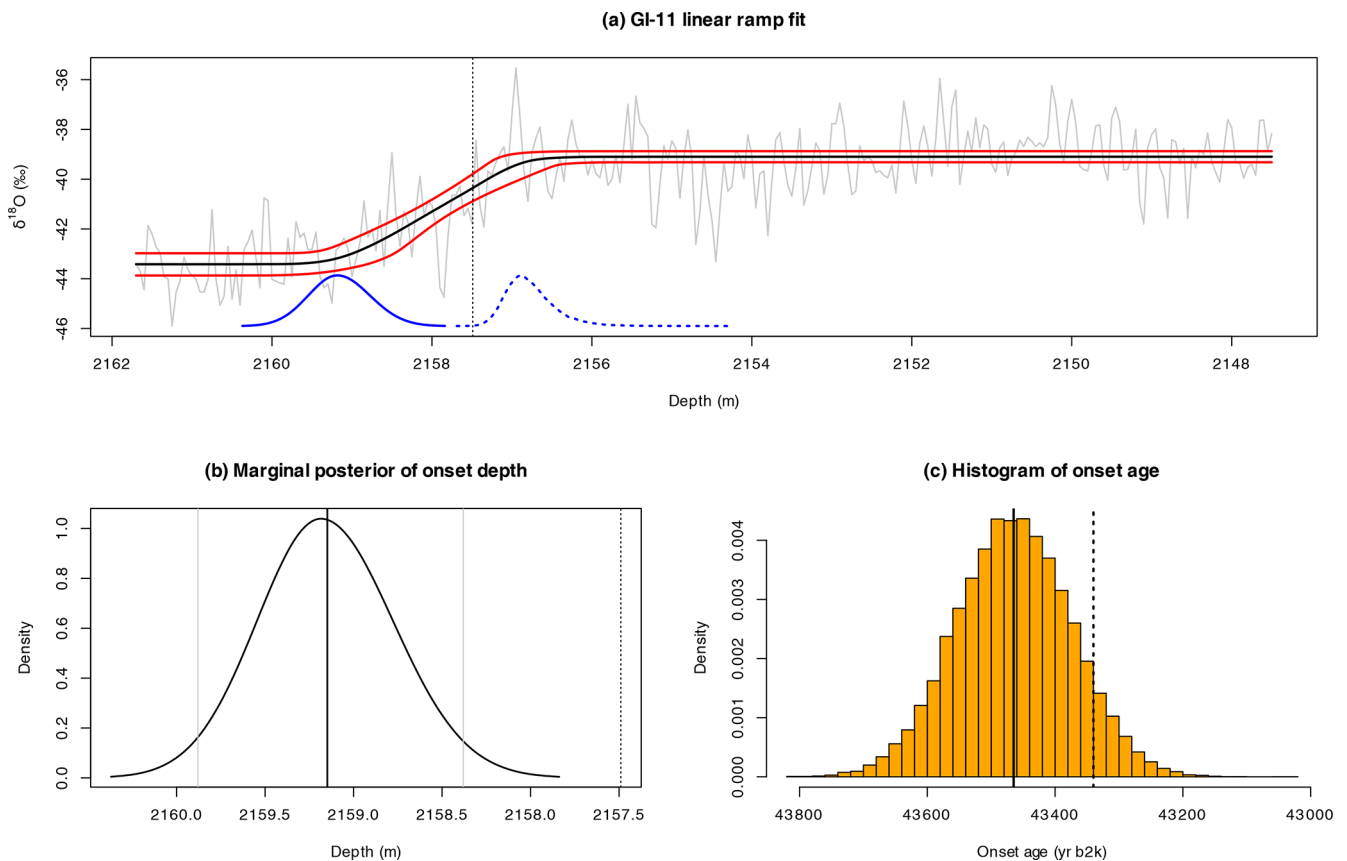


**Figure 6.** (a) The recorded  $\delta^{18}\text{O}$  of the NGRIP data  $x^*$  (gray) as a function of depth for the GI-11 transition. The black line represents the posterior marginal mean of the linear ramp model fitted using INLA. The enclosing red lines represent the corresponding 95 % credible intervals. The blue curves at the bottom illustrate the (unscaled) posterior distributions of the onset (solid) and end point (dotted) of the transition. The vertical dotted line represents the onset depth  $z^*$  as reported in Rasmussen et al. (2014). (b) The posterior marginal distribution of the onset depth  $Z^*$  following a linear ramp model fit. The solid vertical lines represent the posterior marginal mean (black) and 95 % credible intervals (gray). The dotted vertical line represents  $z^*$ . (c) Histogram describing the complete dating uncertainty of the transition to GI-11, taking into account the uncertainty of the NGRIP depth of the onset as well as the dating uncertainty at this depth. The solid vertical black line represents the mean of these samples,  $E(Y^*)$ , and the dotted vertical line represents the GICC05 onset age  $y^*$  as reported in Rasmussen et al. (2014).

radionuclides (Adolphi et al., 2018), will be fed into the model in future research.

One of the biggest concerns regarding the layer counting is that of a potential counting bias. Such a systematic error cannot be corrected after the counting and, therefore, we investigate how a potential unknown counting bias increases the uncertainty of the presented age–depth model. If such a counting bias is restricted to  $\pm 4\%$  we obtain total age uncertainties comparable to the estimates based on the MCE. Finally, we apply our method to the dating of DO events. Using a Bayesian transition onset detection we are able to combine the uncertainty of the onset depth with the corresponding age uncertainty, and to give a posterior distribution that entails the complete dating uncertainty of each transition onset. We find that previous estimates of the DO onsets reported in Rasmussen et al. (2014) are well within our estimated uncertainty ranges both in terms of depth and age. However, the

dating uncertainties of the abrupt warming event onsets are all considerably smaller than the MCE, even when accounting for the additional uncertainty associated with the onset depth.

In theory, it should be possible to apply this approach to other layered proxy records as well. However, there are some requirements that need to be fulfilled for this approach to be applicable. The first condition is that a potential layer thinning can be adequately expressed by a regression model. In our results we find the residuals to follow a Gaussian process, but it should be possible for the model to be adapted such that it supports other distributions for the residuals as well. However, depending on the model, if the residuals exhibit too long memory then this could lead to the simulation procedure having an infeasibly high computational cost. Moreover, if there are many effects in the regression model there needs to be sufficient data to achieve proper inference.

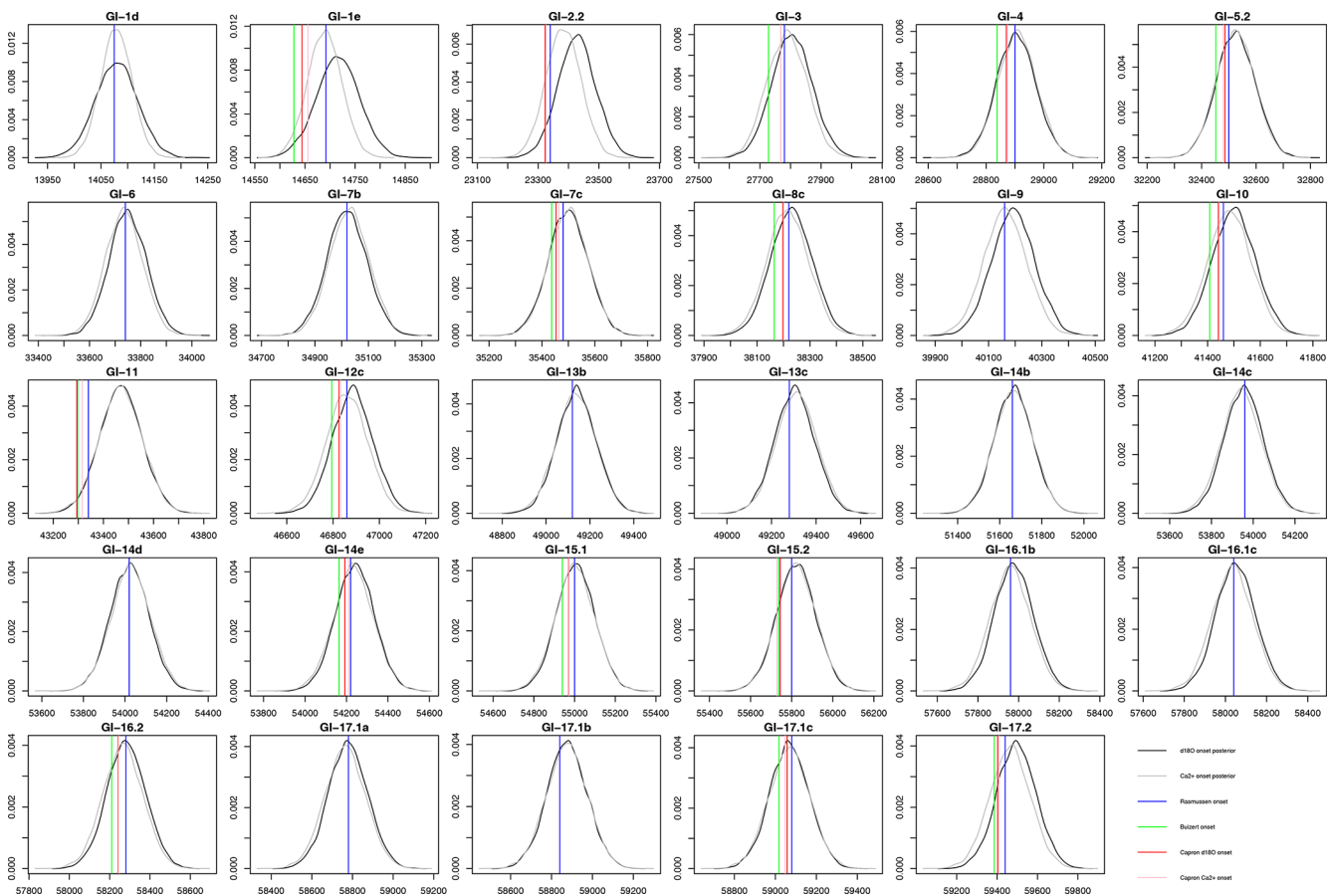


**Figure 7.** Posterior distributions of the onset ages of abrupt climate transitions for the NGRIP  $\delta^{18}\text{O}$  (black) and  $\text{Ca}^{2+}$  (gray) proxy records. The results are compared with ages reported by Rasmussen et al. (2014) (blue), Buizert et al. (2015) (green), and Capron et al. (2021) (red and pink for the  $\delta^{18}\text{O}$  and  $\text{Ca}^{2+}$  record, respectively). The  $\text{Ca}^{2+}$ -based posterior distributions rely on modeled chronologies which are presented in Appendix B and which are not shown in the main text.

### Appendix A: Latent Gaussian model formulation

In this study we consider different Gaussian models for the noise component, including independent identically distributed (iid) and first and second order autoregressive (AR) models. These models all exhibit the Markov property, meaning there is a substantial amount of conditional independence. So-called Gaussian Markov random fields are known to work really well with the methodology of integrated nested Laplace approximations (INLAs), which will grant a substantial reduction in computational cost in obtaining full Bayesian inference. However, this requires formulating our model into a latent Gaussian model where the data, here  $\mathcal{D} = (\Delta y_1, \dots, \Delta y_n)^\top$ , depend on a set of latent Gaussian variables  $\mathbf{X} = (X_1, \dots, X_N)^\top$  which in turn depend on hyperparameters  $\boldsymbol{\theta} = (\theta_1, \dots, \theta_m)^\top$ . This class of models constitutes a subset of hierarchical Bayesian models and is defined in three stages.

The first stage defines the likelihood of the data and how they depend on the latent variables. For the data and models

used in this study we assume a direct correspondence between an observation  $y_i$  and the corresponding latent variable  $X_i$ , which is achieved using a Gaussian likelihood with some negligible fixed variance and mean given by the linear predictor,

$$\eta_k = E(\Delta y_k) = bz_k^2 + b_x x_k + \sum_{i=1}^p \psi_i(z_k; a_i, c_i) + \varepsilon_k(\boldsymbol{\theta}).$$

Here,  $\boldsymbol{\beta} = (b_0, b, b_x, \{a_i\}, \{c_i\})$  are known as fixed effects, even though they are indeed stochastic variables in the Bayesian framework. The noise variables  $\varepsilon_k(\boldsymbol{\theta})$  are referred to as random effects since they depend on hyperparameters  $\boldsymbol{\theta}$ . The hyperparameters are  $\boldsymbol{\theta} = \sigma_\varepsilon$  if we assume the residuals follow an iid Gaussian process,  $\boldsymbol{\theta} = (\sigma_\varepsilon, \phi)$  if they follow an AR(1) process, and  $\boldsymbol{\theta} = (\sigma_\varepsilon, \phi_1, \phi_2)$  if they follow an AR(2) process. All random terms in the predictor, and the predictor itself, are included in the latent field  $\mathbf{X} = (\boldsymbol{\eta}, \boldsymbol{\beta}, \boldsymbol{\varepsilon})$ . The latent field is assigned a prior distribution in what is the second stage of defining a latent Gaussian model. For latent Gaus-

sian fields this prior is multivariate Gaussian:

$$X | \boldsymbol{\theta} \sim \mathcal{N}(\boldsymbol{\mu}(\boldsymbol{\theta}), \boldsymbol{\Sigma}(\boldsymbol{\theta})).$$

Specifically, we assume vague Gaussian priors for  $\boldsymbol{\beta}$ , while the prior for  $\boldsymbol{\varepsilon}(\boldsymbol{\theta})$  is either an iid, AR(1), or AR(2) process. The predictor  $\boldsymbol{\eta}$  is then a Gaussian with a mean vector corresponding to the linear regression  $\boldsymbol{a}(\boldsymbol{\beta})$  and a covariance matrix given by the covariance structure of the assumed noise model.

The third and final stage of the latent Gaussian model definition is to specify a prior distribution on the hyperparameters. We use the default prior choices included in the R-INLA package, which means that for all models of  $\boldsymbol{\varepsilon}$  considered in this paper the scaling parameter  $\sigma_{\varepsilon}^2$  is assigned a log-gamma distribution through the transformation  $\kappa = 1/\sigma_{\varepsilon}^2$ . When the residuals follow an AR(1) distribution we assume a Gaussian prior on the additional lag-one correlation parameter using a logit transformation  $\rho = \log((1 + \phi)/(1 - \phi))$ . For the AR(2) residuals we instead assign penalized complexity priors (Simpson et al., 2017) on the partial autocorrelations  $\psi_1 = \phi_1/(1 - \phi_2)$  and  $\psi_2 = \phi_2$ , also using a logit transformation.

Inference is obtained by computing the posterior marginal distributions:

$$\pi(X_k | \mathcal{D}) = \int \pi(X_k | \boldsymbol{\theta}, \mathcal{D}) \pi(\boldsymbol{\theta} | \mathcal{D}) d\boldsymbol{\theta}$$

and

$$\pi(\theta_k | \mathcal{D}) = \int \pi(\boldsymbol{\theta} | \mathcal{D}) d\boldsymbol{\theta}_{-k}.$$

The notation  $\theta_k$  refers to the  $k$ th hyperparameter, and  $\boldsymbol{\theta}_{-k}$  refers to all except the  $k$ th hyperparameter. These integrals can be approximated efficiently using R-INLA, and the resulting posterior marginal distributions are included in Fig. A1. The estimated hyperparameter posterior marginal means and credible intervals (given in parentheses) are  $\sigma_{\varepsilon}^{\text{iid}} \approx 0.427$  (0.423, 0.431) for iid residuals,  $\sigma_{\varepsilon}^{\text{AR}(1)} \approx 0.428$  (0.423, 0.434) and  $\phi^{\text{AR}(1)} \approx 0.194$  (0.178, 0.217) for AR(1) residuals, and  $\sigma_{\varepsilon}^{\text{AR}(2)} \approx 0.429$  (0.423, 0.438),  $\phi_1^{\text{AR}(2)} \approx 0.180$  (0.158, 0.210), and  $\phi_2^{\text{AR}(2)} \approx 0.108$  (0.089, 0.134) for AR(2) residuals.

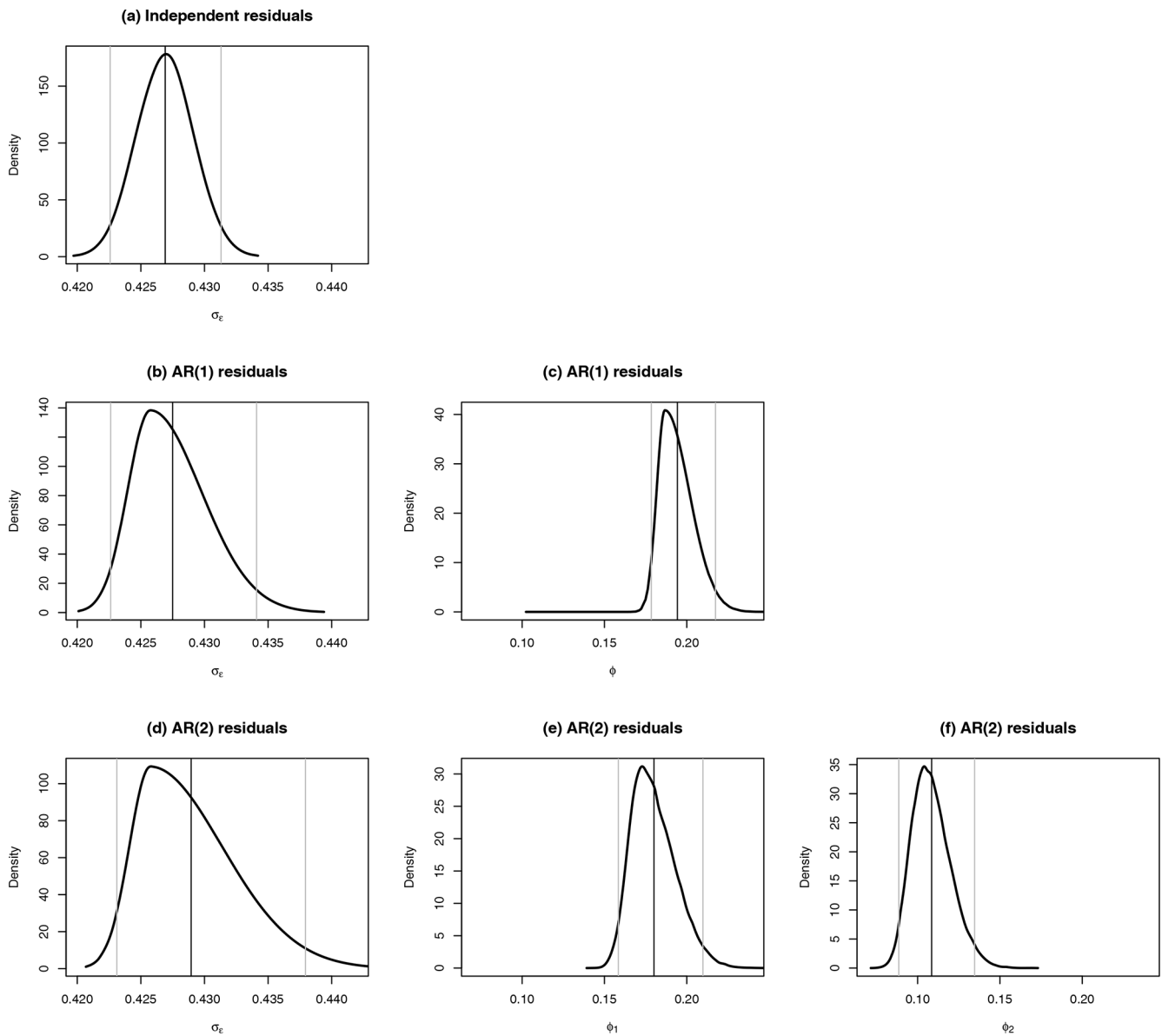


**Figure A1.** The posterior marginal distributions obtained by fitting the model with INLA. Panel (a) shows the density of  $\sigma_\varepsilon$  using iid distributed residuals. Panels (b) and (c) show the densities of  $\sigma_\varepsilon$  and  $\phi$  using AR(1) distributed residuals. Panels (d)–(f) show the densities of  $\sigma_\varepsilon$ ,  $\phi_1$ , and  $\phi_2$  using AR(2) distributed residuals. The vertical lines represent the mean (black) and 95 % credible intervals (gray).

### Appendix B: Ca<sup>2+</sup> analysis

As an alternative, we perform an analogous study using the  $\log(\text{Ca}^{2+})$  as the proxy variable  $x_k$ , which is available at the same period and resolution (Ruth et al., 2003). Missing values in the Ca<sup>2+</sup> data set are filled using linear interpolation. Performing the same analysis as described in Sect. 3 we produce joint samples of the chronologies. The resulting posterior marginal means and 95 % credible intervals of the dating uncertainties are illustrated in Fig. B1, where the credible intervals obtained using an iid, AR(1), and AR(2) noise model are compared. These results are consistent with those obtained using  $\delta^{18}\text{O}$  as the proxy variable, shown in Fig. 4.

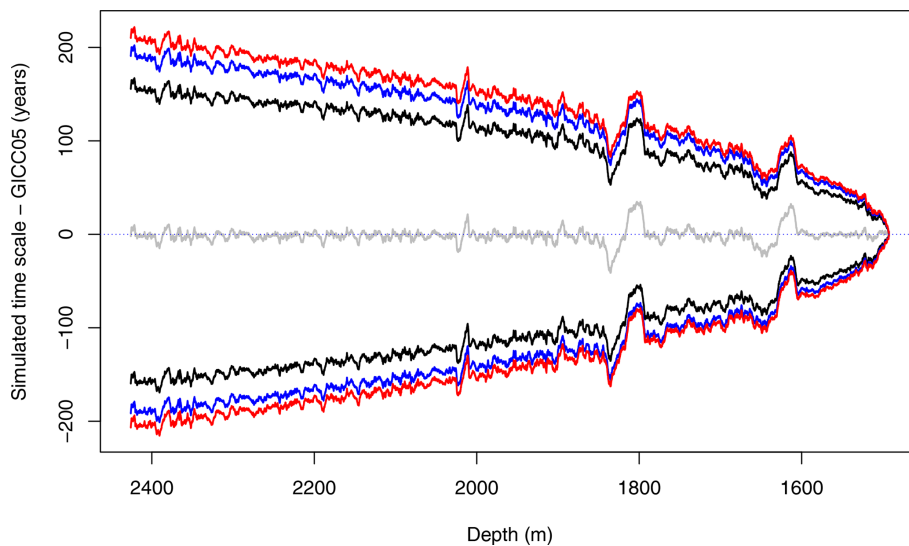


**Figure B1.** The 95 % credible intervals of the dating uncertainty distribution when  $\log(\text{Ca}^{2+})$  is used as the proxy covariate. The GICC05 time scale has been subtracted and the noise is modeled using iid (black), AR(1) (blue), and AR(2) (red) noise models. Only the posterior marginal mean computed using AR(1) distributed noise is included (gray) since it is very similar to the mean obtained using other noise assumptions.

### Appendix C: Log-normal distribution

A possible concern with the approach presented above is that assuming a normal distribution on the layer increments assigns a non-zero probability of negative depositions, violating monotonicity. Furthermore, one might be concerned by our choice of an additive thinning function rather than a multiplicative. Both of these issues are resolved by instead assuming a log-normal regression model on the layer increments, i.e.,

$$\log \Delta y_k = a(z_k, x_k) + \varepsilon_k, \quad (\text{C1})$$

where  $\varepsilon_k$  follows either an iid, AR(1), or AR(2) model as before. This results in the joint age variables being a multivariate process with marginals described by sums of log-normal distributions.

Simulations of the chronology can be produced as follows: First, the latent Gaussian model is fitted to the data and second,  $a(z_k, x_k)$  and  $\varepsilon_k$  are sampled from the resulting posterior distributions. Then compute the sampled chronologies:

$$y_k = y_0 + \sum_{i=1}^k \exp(a(z_i, x_i) + \varepsilon_i). \quad (\text{C2})$$

The resulting dating uncertainty is illustrated in Fig. C1 and is more curved than for the original model. This suggests that the normal distribution is a better fit to the observed layer increments. We will hence focus on the original Gaussian model in the analysis of this paper.

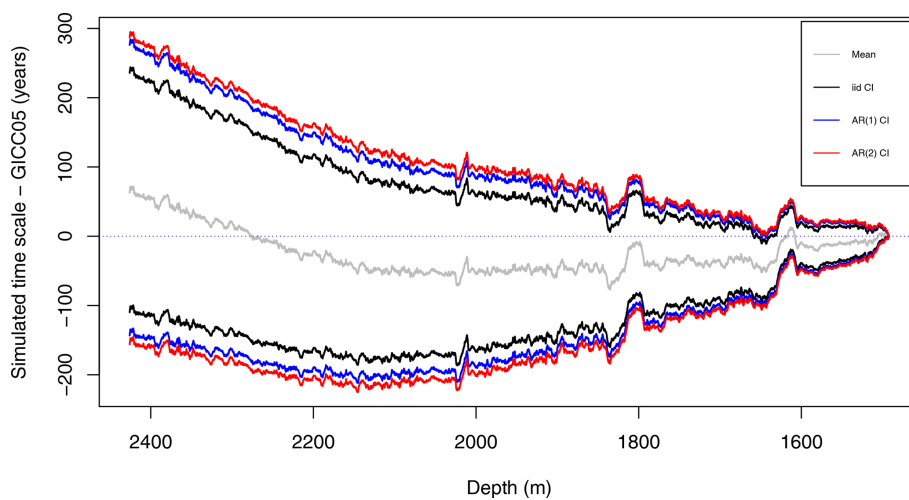


**Figure C1.** The 95 % credible intervals of the dating uncertainty distribution when the GICC05 time scale has been subtracted and a log-normal distribution is assumed, using iid (black), AR(1) (blue), and AR(2) (red) noise models. Only the posterior marginal mean computed using AR(1) distributed noise is included (gray) since it is very similar to the mean obtained using the other noise models.

#### Appendix D: Determination of the fitting windows

The estimation for the onset depth is sensitive to the choice of the data window which represents the transition. It is important to select these carefully such that the data best represent a single linear ramp function while being of a sufficient size. As some DO events are located more closely to other transitions than others, it is necessary to determine these data windows individually for each transition. As such there are indeed some transitions where it is difficult to determine a clear transition point, and a linear ramp model is not appropriate. These transitions will be omitted from our analysis. The reduction in computational cost granted by adopting the model for INLA allows us to perform repeated fits to determine the optimal data interval based on a given criteria. Specifically, we adjust both sides of the interval until we find the data window for which the fitted model yields the lowest amplitude of the AR(1) noise, measured by the posterior marginal mean of the standard deviation parameter.

We impose some restrictions on the domain of the optimal start and end points of our data interval. To achieve the best possible fit we want our interval to include both the onset and end point of the transition, which we suspect are located close to the NGRIP onset depth  $z^*$  given by Table 2 of Rasmussen et al. (2014). Unless the DO events are located too close to adjacent transitions, we assume the optimal interval always contains the points representing 1 m above to 2.5 m deeper than  $z^*$ . These are the minimum distances from the proposed onset. Similarly, we also introduce a maximum distance from  $z^*$  to be considered for the start and end points of the data interval. This is set to be 10 m above and 15 m deeper than  $z^*$ , or at the adjacent transitions if they are located closer than this. From these intervals we create a two-dimensional grid for which we perform the INLA fit for each grid point. The start and end points of the interval representing the grid point for which INLA found the lowest noise amplitude are selected. Those events that failed to provide a decent fit after the conclusion of this procedure were discarded. This left us with 29 DO events for which the results are displayed in Table D1. Although the GICC05 onset depths  $z^*$  fall outside the 95 % credible intervals for several transitions, they are still remarkably close to our best estimates, considering Rasmussen et al. (2014) used a lower 20 year resolution data set.

**Table D1.** The optimal interval for the data window for fitting a linear ramp model to 29 DO events, expressed in terms of depth and the corresponding index in our data. The Rasmussen et al. (2014) onset depths  $z^*$  were used as a starting midpoint in the optimization procedure.

Event	$k^*$	Index interval	$z^*$ (m)	Depth interval (m)
GI-1d	1648	(1622, 1711)	1574.8	(1573.5, 1577.95)
GI-1e	2245	(2175, 2285)	1604.65	(1601.15, 1606.65)
GI-2.2	6016	(5986, 6079)	1793.2	(1791.7, 1796.35)
GI-3	7534	(7482, 7574)	1869.1	(1866.5, 1871.1)
GI-4	7983	(7929, 8023)	1891.55	(1888.85, 1893.55)
GI-5.2	9185	(9106, 9223)	1951.65	(1947.7, 1953.55)
GI-6	9643	(9572, 9683)	1974.55	(1971, 1976.55)
GI-7b	10 093	(10 068, 10 142)	1997.05	(1995.8, 1999.5)
GI-7c	10 341	(10 169, 10 404)	2009.45	(2000.85, 2012.6)
GI-8c	11 552	(11 352, 11 592)	2070	(2060, 2072)
GI-9	12 144	(12 098, 12 174)	2099.6	(2097.3, 2101.1)
GI-10	12 633	(12 563, 12 690)	2124.05	(2120.55, 2126.9)
GI-11	13 302	(13 102, 13 386)	2157.5	(2147.5, 2161.7)
GI-12c	14 598	(14 417, 14 718)	2222.3	(2213.25, 2228.3)
GI-13b	15 229	(15 212, 15 274)	2253.85	(2253, 2256.1)
GI-13c	15 290	(15 245, 15 339)	2256.9	(2254.65, 2259.35)
GI-14b	16 070	(16 054, 16 110)	2295.9	(2295.1, 2297.9)
GI-14c	16 960	(16 881, 16 983)	2340.4	(2336.45, 2341.55)
GI-14d	16 980	(16 968, 16 992)	2341.4	(2340.8, 2342)
GI-14e	17 062	(16 986, 17 185)	2345.5	(2341.7, 2351.65)
GI-15.1	17 259	(17 247, 17 272)	2355.35	(2354.75, 2356)
GI-15.2	17 478	(17 365, 17 610)	2366.3	(2360.65, 2372.9)
GI-16.1b	18 099	(18 087, 18 111)	2397.35	(2396.75, 2397.95)
GI-16.1c	18 128	(18 108, 18 146)	2398.8	(2397.8, 2399.7)
GI-16.2	18 203	(18 190, 18 215)	2402.55	(2401.9, 2403.15)
GI-17.1a	18 348	(18 315, 18 371)	2409.8	(2408.15, 2410.95)
GI-17.1b	18 365	(18 353, 18 431)	2410.65	(2410.05, 2413.95)
GI-17.1c	18 452	(18 387, 18 464)	2415	(2411.75, 2415.6)
GI-17.2	18 561	(18 531, 18 608)	2420.45	(2418.95, 2422.8)

**Code and data availability.** NGRIP  $\delta^{18}\text{O}$  data (North Greenland Ice Core Projects Members, 2004; Gkinis et al., 2014) and the GICC05 chronology (Vinther et al., 2005; Rasmussen et al., 2006; Andersen et al., 2006; Svensson et al., 2008) are available at <http://www.iceandclimate.nbi.ku.dk/data/> (last access: 13 June 2022). The code used for generating the results of this paper will be uploaded as supplementary material. The code to reproduce the analysis and results is available at [https://github.com/eirikmn/dating\\_uncertainty](https://github.com/eirikmn/dating_uncertainty) (last access: 17 June 2022) and <https://doi.org/10.5281/zenodo.6637528> (Myrvoll-Nilsen, 2022) or upon request to the corresponding author.

**Supplement.** The supplement related to this article is available online at: <https://doi.org/10.5194/cp-18-1275-2022-supplement>.

**Author contributions.** All authors conceived and designed the study. MWR conceived the idea of modeling the layer increments as a regression model and its use for estimating dating uncertainty of DO events. This idea was reworked by EMN, NB, and KR, and adopted for a Bayesian framework by EMN. Further extensions to the model were conceived by EMN, NB, and KR. EMN wrote the

code and carried out the analysis. EMN, KR, and NB discussed the results, drew conclusions, and wrote the paper with input from MWR.

**Competing interests.** The contact author has declared that neither they nor their co-authors have any competing interests.

**Disclaimer.** Publisher's note: Copernicus Publications remains neutral with regard to jurisdictional claims in published maps and institutional affiliations.

**Acknowledgements.** This research is TiPES contribution #136 and has been supported by the European Union Horizon 2020 research and innovation program (grant no. 820970).

**Financial support.** This research has been supported by the European Union, Horizon 2020 (TiPES, grant no. 820970).

This work was supported by the German Research Foundation (DFG) and the Technical University of Munich (TUM) in the framework of the Open Access Publishing Program.

**Review statement.** This paper was edited by Amaelle Landais and reviewed by Anders Svensson and Frédéric Parrenin.

## References

- Adolphi, F., Bronk Ramsey, C., Erhardt, T., Edwards, R. L., Cheng, H., Turney, C. S. M., Cooper, A., Svensson, A., Rasmussen, S. O., Fischer, H., and Muscheler, R.: Connecting the Greenland ice-core and U/Th timescales via cosmogenic radionuclides: testing the synchronicity of Dansgaard–Oeschger events, *Clim. Past*, 14, 1755–1781, <https://doi.org/10.5194/cp-14-1755-2018>, 2018.
- Andersen, K. K., Svensson, A., Johnsen, S. J., Rasmussen, S. O., Bigler, M., Röthlisberger, R., Ruth, U., Siggaard-Andersen, M. L., Peder Steffensen, J., Dahl-Jensen, D., Vinther, B. M., and Clausen, H. B.: The Greenland Ice Core Chronology 2005, 15–42 ka. Part 1: constructing the time scale, *Quaternary Sci. Rev.*, 25, 3246–3257, <https://doi.org/10.1016/j.quascirev.2006.08.002>, 2006.
- Blaauw, M. and Christeny, J. A.: Flexible paleoclimate age-depth models using an autoregressive gamma process, *Bayesian Anal.*, 6, 457–474, <https://doi.org/10.1214/11-BA618>, 2011.
- Boers, N., Goswami, B., and Ghil, M.: A complete representation of uncertainties in layer-counted paleoclimatic archives, *Clim. Past*, 13, 1169–1180, <https://doi.org/10.5194/cp-13-1169-2017>, 2017.
- Buizert, C., Cuffey, K. M., Severinghaus, J. P., Baggenstos, D., Fudge, T. J., Steig, E. J., Markle, B. R., Winstrup, M., Rhodes, R. H., Brook, E. J., Sowers, T. A., Clow, G. D., Cheng, H., Edwards, R. L., Sigl, M., McConnell, J. R., and Taylor, K. C.: The WAIS Divide deep ice core WD2014 chronology – Part 1: Methane synchronization (68–31 ka BP) and the gas age–ice age difference, *Clim. Past*, 11, 153–173, <https://doi.org/10.5194/cp-11-153-2015>, 2015.
- Capron, E., Rasmussen, S. O., Popp, T. J., Erhardt, T., Fischer, H., Landais, A., Pedro, J. B., Vettoretti, G., Grinsted, A., Gkinis, V., Vaughn, B., Svensson, A., Vinther, B. M., and White, J. W.: The anatomy of past abrupt warmings recorded in Greenland ice, *Nat. Commun.*, 12, 2106, <https://doi.org/10.1038/s41467-021-22241-w>, 2021.
- Comboul, M., Emile-Geay, J., Evans, M. N., Mirnateghi, N., Cobb, K. M., and Thompson, D. M.: A probabilistic model of chronological errors in layer-counted climate proxies: applications to annually banded coral archives, *Clim. Past*, 10, 825–841, <https://doi.org/10.5194/cp-10-825-2014>, 2014.
- Corrick, E. C., Drysdale, R. N., Hellstrom, J. C., Capron, E., Rasmussen, S. O., Zhang, X., Fleitmann, D., Couchoud, I., Wolff, E., and Monsoon, S. A.: Synchronous timing of abrupt climate changes during the last glacial period, *Science*, 369, 963–969, 2020.
- Dansgaard, W., Johnsen, S. J., Clausen, H. B., Dahl-Jensen, D., Gundestrup, N. S., Hammer, C. U., Hvidberg, C. S., Steffensen, J. P., Sveinbjörnsdóttir, A. E., Jouzel, J., and Bond, G.: Evidence for general instability of past climate from a 250-kyr ice-core record, *Nature*, 364, 218–220, <https://doi.org/10.1038/364218a0>, 1993.
- Erhardt, T., Capron, E., Rasmussen, S. O., Schüpbach, S., Bigler, M., Adolphi, F., and Fischer, H.: Decadal-scale progression of the onset of Dansgaard–Oeschger warming events, *Clim. Past*, 15, 811–825, <https://doi.org/10.5194/cp-15-811-2019>, 2019.
- Gkinis, V., Simonsen, S. B., Buchardt, S. L., White, J. W., and Vinther, B. M.: Water isotope diffusion rates from the North-GRIP ice core for the last 16,000 years – Glaciological and paleoclimatic implications, *Earth Planet. Sc. Lett.*, 405, 132–141, <https://doi.org/10.1016/j.epsl.2014.08.022>, 2014.
- Goodman, J. and Weare, J.: Ensemble samplers with affine invariance, *Comm. App. Math. Com. Sc.*, 5, 1–99, 2010.
- Haslett, J. and Parnell, A.: A simple monotone process with application to radiocarbon-dated depth chronologies, *J. R. Stat. Soc. C-Appl.*, 57, 399–418, <https://doi.org/10.1111/j.1467-9876.2008.00623.x>, 2008.
- Johnsen, S. J., Clausen, H. B., Dansgaard, W., Fuhrer, K., Gundestrup, N., Hammer, C. U., Iversen, P., Jouzel, J., Stauffer, B., and Steffensen, J.: Irregular glacial interstadials recorded in a new Greenland ice core, *Nature*, 359, 311–313, 1992.
- Jouzel, J., Alley, R. B., Cuffey, K. M., Dansgaard, W., Grootes, P., Hoffmann, G., Johnsen, S. J., Koster, R. D., Peel, D., Shuman, C. A., Stievenard, M., Stuiver, M., and White, J.: Validity of the temperature reconstruction from water isotopes in ice cores, *J. Geophys. Res.-Oceans*, 102, 26471–26487, <https://doi.org/10.1029/97JC01283>, 1997.
- Li, T. Y., Han, L. Y., Cheng, H., Edwards, R. L., Shen, C. C., Li, H. C., Li, J. Y., Huang, C. X., Zhang, T. T., and Zhao, X.: Evolution of the Asian summer monsoon during Dansgaard/Oeschger events 13–17 recorded in a stalagmite constrained by high-precision chronology from southwest China, *Quaternary Res.*, 88, 121–128, <https://doi.org/10.1017/qua.2017.22>, 2017.
- McKay, N. P., Emile-Geay, J., and Khider, D.: geoChronR – an R package to model, analyze, and visualize age-uncertain data, *Geochronology*, 3, 149–169, <https://doi.org/10.5194/gchron-3-149-2021>, 2021.

- Myrvoll-Nilsen, E.: `eirikmn/dating_uncertainty: First release (v1.1.0)`, Zenodo [code], <https://doi.org/10.5281/zenodo.6637528>, 2022.
- North Greenland Ice Core Project members: High-resolution record of Northern Hemisphere climate extending into the last interglacial period, *Nature*, 431, 147–151, <https://doi.org/10.1038/nature02805>, 2004.
- Parnell, A. C., Haslett, J., Allen, J. R., Buck, C. E., and Huntley, B.: A flexible approach to assessing synchronicity of past events using Bayesian reconstructions of sedimentation history, *Quaternary Sci. Rev.*, 27, 1872–1885, <https://doi.org/10.1016/j.quascirev.2008.07.009>, 2008.
- Ramsey, C. B.: Radiocarbon calibration and analysis of stratigraphy: the OxCal program, *Radiocarbon*, 37, 425–430, <https://doi.org/10.1017/s0033822200030903>, 1995.
- Ramsey, C. B.: Deposition models for chronological records, *Quaternary Sci. Rev.*, 27, 42–60, <https://doi.org/10.1016/j.quascirev.2007.01.019>, 2008.
- Rasmussen, S. O., Andersen, K. K., Svensson, A. M., Steffensen, J. P., Vinther, B. M., Clausen, H. B., Siggaard-Andersen, M. L., Johnsen, S. J., Larsen, L. B., Dahl-Jensen, D., Bigler, M., Röthlisberger, R., Fischer, H., Goto-Azuma, K., Hansson, M. E., and Ruth, U.: A new Greenland ice core chronology for the last glacial termination, *J. Geophys. Res.-Atmos.*, 111, 1–16, <https://doi.org/10.1029/2005JD006079>, 2006.
- Rasmussen, S. O., Bigler, M., Blockley, S. P., Blunier, T., Buchardt, S. L., Clausen, H. B., Cvijanovic, I., Dahl-Jensen, D., Johnsen, S. J., Fischer, H., Gkinis, V., Guillevic, M., Hoek, W. Z., Lowe, J. J., Pedro, J. B., Popp, T., Seierstad, I. K., Steffensen, J. P., Svensson, A. M., Vallelonga, P., Vinther, B. M., Walker, M. J., Wheatley, J. J., and Winstrup, M.: A stratigraphic framework for abrupt climatic changes during the Last Glacial period based on three synchronized Greenland ice-core records: refining and extending the INTIMATE event stratigraphy, *Quaternary Sci. Rev.*, 106, 14–28, <https://doi.org/10.1016/j.quascirev.2014.09.007>, 2014.
- Riechers, K. and Boers, N.: A statistical approach to the phasing of atmospheric reorganization and sea ice retreat at the onset of Dansgaard–Oeschger events under rigorous treatment of uncertainties, *Clim. Past Discuss.* [preprint], 2020, 1–30, <https://doi.org/10.5194/cp-2020-136>, 2020.
- Rue, H., Martino, S., and Chopin, N.: Approximate Bayesian inference for latent Gaussian models using integrated nested Laplace approximations (with discussion), *J. R. Stat. Soc. Series B*, 71, 319–392, 2009.
- Rue, H., Riebler, A., Sørbye, S. H., Illian, J. B., Simpson, D. P., and Lindgren, F. K.: Bayesian Computing with INLA: A Review, *Annu. Rev. Stat. Appl.*, 4, 395–421, 2017.
- Ruth, U., Wagenbach, D., Steffensen, J. P., and Bigler, M.: Continuous record of microparticle concentration and size distribution in the central Greenland NGRIP ice core during the last glacial period, *J. Geophys. Res.-Atmos.*, 108, 1–12, <https://doi.org/10.1029/2002jd002376>, 2003.
- Ruth, U., Bigler, M., Röthlisberger, R., Siggaard-Andersen, M. L., Kipfstuhl, S., Goto-Azuma, K., Hansson, M. E., Johnsen, S. J., Lu, H., and Steffensen, J. P.: Ice core evidence for a very tight link between North Atlantic and east Asian glacial climate, *Geophys. Res. Lett.*, 34, 1–5, <https://doi.org/10.1029/2006GL027876>, 2007.
- Schüpbach, S., Fischer, H., Bigler, M., Erhardt, T., Gfeller, G., Leuenberger, D., Mini, O., Mulvaney, R., Abram, N. J., Fleet, L., Frey, M. M., Thomas, E., Svensson, A., Dahl-Jensen, D., Kettner, E., Kjaer, H., Seierstad, I., Steffensen, J. P., Rasmussen, S. O., Vallelonga, P., Winstrup, M., Wegner, A., Twarloh, B., Wolff, K., Schmidt, K., Goto-Azuma, K., Kuramoto, T., Hirabayashi, M., Uetake, J., Zheng, J., Bourgeois, J., Fisher, D., Zhiheng, D., Xiao, C., Legrand, M., Spolaor, A., Gabrieli, J., Barbante, C., Kang, J. H., Hur, S. D., Hong, S. B., Hwang, H. J., Hong, S., Hansson, M., Iizuka, Y., Oyabu, I., Muscheler, R., Adolphi, F., Maselli, O., McConnell, J., and Wolff, E. W.: Greenland records of aerosol source and atmospheric lifetime changes from the Eemian to the Holocene, *Nat. Commun.*, 9, 1476, <https://doi.org/10.1038/s41467-018-03924-3>, 2018.
- Simpson, D., Rue, H., Riebler, A., Martins, T. G., and Sørbye, S. H.: Penalising model component complexity: A principled, practical approach to constructing priors, *Stat. Sci.*, 232, 1–28, 2017.
- Svensson, A., Andersen, K. K., Bigler, M., Clausen, H. B., Dahl-Jensen, D., Davies, S. M., Johnsen, S. J., Muscheler, R., Parenin, F., Rasmussen, S. O., Röthlisberger, R., Seierstad, I., Steffensen, J. P., and Vinther, B. M.: A 60 000 year Greenland stratigraphic ice core chronology, *Clim. Past*, 4, 47–57, <https://doi.org/10.5194/cp-4-47-2008>, 2008.
- Vinther, B. M., Clausen, H. B., Johnsen, S. J., Rasmussen, S. O., Andersen, K. K., Buchardt, S. L., Dahl-Jensen, D., Seierstad, I. K., Siggaard-Andersen, M. L., Steffensen, J. P., Svensson, A., Olsen, J., and Heinemeier, J.: A synchronized dating of three Greenland ice cores throughout the Holocene, *J. Geophys. Res.-Atmos.*, 111, 1–11, <https://doi.org/10.1029/2005JD006921>, 2006.
- Zhou, H., Zhao, J. X., Feng, Y., Chen, Q., Mi, X., Shen, C. C., He, H., Yang, L., Liu, S., Chen, L., Huang, J., and Zhu, L.: Heinrich event 4 and Dansgaard/Oeschger events 5–10 recorded by high-resolution speleothem oxygen isotope data from central China, *Quaternary Res.*, 82, 394–404, <https://doi.org/10.1016/j.yqres.2014.07.006>, 2014.



# 7 Synthesis

## 7.1 Discussion

The publications comprised in this thesis all contribute to the study of the last glacial's **DO** climate variability with a particular focus on the abrupt **DO** events. Like numerous previous studies, this thesis cannot conclusively answer the central research question:

### Research Question

**Q1** *What has caused the last glacial's repeated abrupt climatic changes and the millennial-scale climate variability associated therewith?*

Yet, it provides important insights to the more specific questions **Q2** and **Q3**:

### Research Question

**Q2** *Can Dansgaard–Oeschger (**DO**) variability be explained in terms of a low-dimensional random and / or non-autonomous dynamical system?*

**Q3** *Can the relative phasing of abrupt climatic shifts in different Earth system components (**ESCs**) during Dansgaard–Oeschger events be inferred from paleoclimate proxy data?*

The main reasons that have so far prevented a clear answer to **Q1** shall be briefly summarized here. Paleoclimate research faces the challenge to reconstruct past climate conditions from a rather small number of proxy time series obtained from individual sites. Both spatial coverage and temporal resolution constitute limiting factors in this regard. Researchers cannot decide which climate variable they measure, but instead, they have to make the best of the available proxy data. The interpretation of these data is a cumbersome task and is inevitably associated with qualitative uncertainties. The qualitative interpretation of climate proxies was, however, not a matter of this thesis and is therefore not detailed any further here. The quantitative spatiotemporal data coverage of **DO** variability is well illustrated by a few numbers: For example, [Rasmussen et al. \(2016\)](#) present a map of the North Atlantic showing the locations of 27 marine sediment cores with data from the last glacial interval. [Corrick et al. \(2020\)](#) investigated the phasing between high and low-latitude **DO** transitions on the basis of speleothem records from 63 locations from three different regions and the **NGRIP** ice core record. Overall, the number of proxy records relevant to the study of **DO** variability hardly exceeds several hundred records. These translate into point-like time series (as opposed to spatially extended fields) of climate variables which often reflect past variations in a qualitative but not quantitative sense. The temporal resolution of these records typically ranges from decadal to centennial time scale and many records are not dated independently from one another. Several ice core records

exhibit extraordinarily high resolution over the last glacial interval with sub-annual resolution at the end of the last glacial and decadal-scale resolution at its beginning (North Greenland Ice Core Project Members, 2004; NEEM community members, 2013; Buizert et al., 2015b; Sigl et al., 2016).

The available data is clearly too sparse to resolve the processes often invoked to explain DO events at the desired precision. These include the (local) destabilization of a stadial halocline (Dokken et al., 2013; Vettoretti and Peltier, 2018), fast and slow displacements of the sea ice edge and of the convection sites in the North Atlantic (Vettoretti and Peltier, 2018; Sadatzki et al., 2020; Li and Born, 2019) or decadal-scale reorganizations of atmospheric circulation patterns (Markle et al., 2017; Buizert et al., 2018), just to name a few examples. This explains why a conclusive explanation of the DO variability is still lacking.

Despite these limitations, research on the topic has steadily sharpened the understanding of DO variability over the past three decades and this thesis adds to this process. This section synthesizes the key findings reported in the publications that comprise this thesis. Despite their common subjective, the publications P1–5 approach the topic from different perspectives and correspondingly draw on different methods.

P1–3 share a dynamical systems perspective on DO variability and are centered around the research question Q2. P1 provides an introduction to dynamical systems theory and demonstrates how it facilitates paleoclimate research using concrete examples of glacial–interglacial and DO cycles. P2 presents a conceptual multi-scale model of the North Atlantic climate system, wherein DO events appear as excitations induced by  $\alpha$ -stable driving noise. Finally, assuming an underlying SDE of the form of Eq. (2.10), P3 reconstructs the deterministic drift underlying the combined NGRIP  $\delta^{18}\text{O}$  and dust concentration record — one of the most prominent records of DO variability. The reconstruction suggests that the large-scale atmospheric circulation supported a genuine bistability of the past high northern latitude’s climate.

P4 and P5 aim at drawing direct inference on the past from paleoclimate data under consideration of uncertainties addressing Q3. P4 finds that previously reported lags between DO transitions observed in different proxy time series from multi-proxy ice core records are not statistically significant if uncertainties are rigorously propagated. Thus, it concludes that the null hypothesis of synchronous abrupt change in those ESC reflected by the proxies may not be rejected. P5 provides necessary preparatory work with respect to Q3 by reducing the dating uncertainties of the NGRIP ice core and providing a consistent method for their propagation to subsequent analyses. Moreover, it updates the age estimates of DO events evident in the NGRIP  $\delta^{18}\text{O}$  record under full consideration of uncertainties.

In the following, each publication will be briefly summarized and subsequently discussed with a focus on the interconnections to the respective other publications. Both consistencies and inconsistencies between the methods and the results are highlighted. The first part of this section deals with P1–3 and the second part with P4–5. The next and final section merges these two branches in a final consideration.

**P1 | Main Conclusions.**

- Q1** Past climate variability on different scales is still missing explanation. This includes the post-MPT 100 kyr glacial cycle period, the DO cycles and the Bond cycles (Bond et al., 1992, 1993). For these phenomena, there is no corresponding variability in the orbital forcing.
- Q2** Dynamical system theory provides a suitable framework for the study of past climate dynamics. Under the action of orbital insolation forcing nonlinearities in the climate system provide a possible explanation for the rich climate variability at frequencies neither supported by the forcing nor by the stand-alone system.
- Q2** Modeling results suggest that a fast-slow relaxation mechanism was present during the last glacial, wherein the AMOC potentially assumed the role of the fast component. Either ice sheets or Antarctic bottom water formation are possible candidates for the slow relaxation component. Atmospheric CO<sub>2</sub> concentrations might have shaped the oscillations.

Other findings related to glacial–interglacial cycles.

- On orbital time scales, the Earth’s climate must be understood as non-autonomous dynamical systems. Changes in the orbital insolation forcing paced the glacial–interglacial cycles of the Pleistocene.
- An investigation of a glacial cycle model’s pullback attractor (PBA) reveals a loss of stability across the MPT, suggesting that glacial cycle dynamics were more susceptible to perturbation since the MPT.

**P1–3 DO variability from the perspective of dynamical systems**

**P1 | Summary.** P1 reviews the history of paleoclimate modeling of the Pleistocene. It introduces the notion of the Earth’s climate as a non-autonomous dynamical system driven by orbital insolation forcing. It highlights the mismatch in the power spectra of proxy-recorded climate variability and orbital forcing during the late half of the Pleistocene and specifies associated pending research questions. The study recommends the consideration of nonlinear dynamical systems subjected to external forcing as a primary explanatory framework for understanding past climate variability. Correspondingly, it introduces the basic concepts of dynamical systems theory and demonstrates their usefulness in paleoclimate research using several illustrative examples. In particular, P1 shows how a periodical forcing may switch on and off an FHN model’s internal oscillations via dynamical Hopf bifurcations. This requires that the forcing has a much lower frequency than the FHN’s limit cycle. If the forcing’s frequency is increased, the model’s limit cycle is strongly deformed and the corresponding PBA splits from one into two separate branches. This showcases how the action of external forcing on a nonlinear system may give rise to complex dynamics. The example is further extended by the addition of noise to illustrate the phenomenon of noise-induced synchronization.

**P1 | Subsequent Questions.**

Although the questions listed here are not new, they still await definitive answers.

- Q2 What explains climate variability (and in particular **DO** variability) at time scales where orbital insolation forcing exhibits only limited spectral power?
- Q2 What are the contributions of internal (nonlinear) dynamics, external forcing and stochastic forcing to the observed climate variability and in particular to **DO** variability?

Other questions related to glacial–interglacial cycles.

- What has caused the **MPT**?

To demonstrate the usefulness of the above concepts in Paleoclimate research, **P1** provides two further examples. First, the oscillatory intervals of an **FHN** model are aligned with intervals of high **DO** activity observed in the **NGRIP**  $\delta^{18}\text{O}$  record by coupling the model to past atmospheric  $\text{CO}_2$  concentrations. A physical interpretation is that a fast-slow coupled climate system comprised of **AMOC** and Antarctic bottom water (**AABW**) or northern Hemisphere ice sheets, respectively, underwent dynamical Hopf bifurcations driven by past atmospheric  $\text{CO}_2$ . Similar results are in fact obtained by **Zhang et al. (2021)** and **Vettoretti et al. (2022)** in **GCM** experiments.

Second, **P1** investigates the pullback attractor of a simple glacial cycle model. Under a slow change of parameters, the model conveniently reproduces the so-called **MPT**, a transition from a 41 kyr glacial cycle period to a 100 kyr period. Even though no dynamical bifurcation occurs, the behavior of the model changes substantially across the **MPT**. In particular, the pre-**MPT** parameter configuration yields a single-branched **PBA**. In contrast, for post-**MPT** parameter values, the **PBA** comprises many separate bundles. In physical terms, this result can be interpreted as a loss of stability of the glacial–interglacial cycle across the **MPT**.

**P1 | Discussion.** **P1** must be understood as a review and research paper. The main intention of this study is to demonstrate the role of dynamical system theory in paleoclimate research, which is why it was placed first in this thesis. Addressing a wide audience, it summarizes the essentials of dynamical system theory in an appealing and digestible manner and places theoretical considerations in their historical context. In particular, **P1** shows how the Earth’s climate system can be understood in terms of a nonlinear non-autonomous system driven by orbital insolation forcing. This framework is suited to explain observed climate variability at scales that are neither inherent to the system nor to the forcing. An example of this phenomenon is given by the 100 kyr peak present in the spectrum of Pleistocene glacial cycle records which has no counterpart in the orbital insolation forcing. Correspondingly, **P1** is the only contribution in this thesis that is not exclusively concerned with **DO** variability but has an additional focus on the

## P2|Main Conclusions.

- Q2** The agreement of the simulated arctic temperatures with the **NGRIP**  $\delta^{18}\text{O}$  record is remarkable. This renders the excitability mechanism reflected by the model a plausible candidate to explain **DO** variability including the abrupt **DO** events.
- Q2** In view of the high variability of **DO** cycles in terms of duration and shape, a stochastic trigger seems more plausible than a deterministic one as invoked by limit cycle models. In the **P2** model, the excitability of the system offers a suitable mechanism to translate the variability of the  $\alpha$ -stable noise into climate variability.
- Q1** Acting as an insulator between the ocean and the atmosphere, sea ice plays a central role in controlling the state of the North Atlantic climate system. In its presence, the high-latitude atmosphere is cold while oceanic heat accumulates underneath the ice, which in turn slows down the **AMOC**. In the absence of sea ice, the release of oceanic heat warms the atmosphere and the accordingly colder oceanic temperatures drive a strong **AMOC**.
- Q2** In line with the non-autonomous system view discussed in **P1**, changing climate background conditions determine the persistence of the interstadial.

Pleistocene's glacial–interglacial cycles.

The study introduces bifurcations, non-autonomous dynamical systems and pullback attraction. It furthermore touches upon random dynamical systems, random attractors and noise-induced synchronization. In doing so, it prioritizes clarity and tangibility over mathematical rigor. It contributes to the research question **Q2** in the sense that it formulates the basic concepts underlying **Q2** and by demonstrating

*‘[...] how external forcing can act on a system’s internal variability and thereby give rise to more complex dynamics.’ (P1)*

**P1** does not aim at providing clear answers to **Q1** or to the other question it raises. Rather, its goal is to summarize and clarify the open research questions about the Pleistocene in the language of dynamical systems.

**P2|Summary.** **P2** makes strong use of the concepts introduced in **P1**. It presents a multi-scale model of the last glacial’s North Atlantic climate system and explains **DO** variability in terms of noise-induced excitations. The four dynamical model variables represent the high latitude’s atmospheric temperature, the strength of the **AMOC**, the Nordic Seas’ intermediate to deep ocean temperatures and their sea ice cover. The model reproduces the **DO** variability of all four climate variables as inferred from proxy records.

The physics of the model can be summarized as follows: Acting as an insulator the Nordic Seas’ sea ice controls the heat exchange rate between the Nordic

Seas and the high-latitude atmosphere. The model's only stable state reflects a stadial climate state with extensive sea ice cover, cold atmospheric temperatures, a weak AMOC and gentle warming of the Nordic Seas at intermediate and large depth. P2 hypothesizes that temporary destabilizations of the stadial halocline and atmospheric anomalies occasionally removed large fractions of the stadial sea ice cover. In the model, the resulting effect on the sea ice is captured by an asymmetric  $\alpha$ -stable noise. In this setup, a supercritical stochastic sea ice removal triggers a prolonged state space excursion, while the system recovers in a seemingly exponential fashion if the sea ice is perturbed only subcritically. This threshold behavior renders the system excitable and the excitations reflect the last glacial's interstadials.

After a supercritical sea ice perturbation, the adjustment of the model's atmosphere to the presence of a warm open ocean happens immediately due to its relatively low heat capacity. The corresponding cooling of the Nordic Seas takes place more gradually because of the higher oceanic heat capacity. In turn, this cooling reinvigorates the AMOC, which completes the interstadial configuration of the model. On the relaxation path back to the stadial state the system passes through a region of slowed-down transitive dynamics. During this phase, the system is almost at an equilibrium and the only gently regrowing sea ice drives the overall system relaxation. The relaxation is shaped by the three separate time scales for ocean, sea ice and atmosphere dynamics (from slow to fast). The resulting duration of the relaxation from supercritical perturbations, i.e. the model's interstadial duration, introduces a fourth time scale. Finally, a coupling to a record of past global ice volume modulates the interstadial duration in a transient simulation of the last glacial interval.

**P2|Discussion.** While P1 introduces the history and concepts of paleoclimate modeling P2 explicitly develops and discusses a novel conceptual climate model of DO variability in great detail. Certainly, numerous models of this kind have been proposed previously with the aim to explain DO variability (e.g. Ditlevsen, 1999; Timmermann and Lohmann, 2000; Timmermann et al., 2003; Rial and Saha, 2011; Singh et al., 2014; Roberts and Saha, 2017; Boers et al., 2018; Gottwald, 2021; Vettoretti et al., 2022). Some of them are derived from physical considerations while others are more abstract. Some are formulated in a deterministic way and others are provided in terms of SDEs. Most models are based on dynamical systems, whose deterministic drift features either two stable states or a stable limit cycle if considered in isolation. Typically, these models are then coupled to external forcings — be it orbital insolation forcing, past atmospheric CO<sub>2</sub> concentrations or past global mean temperatures — to simulate a climate variability, that is somewhat close that seen in stable water isotope records from Greenland. In many cases, the action of the external forcing on the internal model dynamics gives rise to very rich dynamics in the sense of P1.

The model presented in P2 builds on a mechanism that has received little attention in the context of DO events so far, namely that of noise induced excitability. The results are remarkable for two reasons: First, the model outperforms many previous conceptual models in reproducing the characteristics of the NGRIP  $\delta^{18}\text{O}$  record. And second, the model provides a consistent explanation for DO variability of four climate variables simultaneously, that are central to the North

### P2 | Subsequent Questions.

- Q2 Can  $\alpha$ -stable components be evidenced in proxy data or in GCM simulations of DO variability?
- Q2 Can temporary and localized convective events or atmospheric anomalies indeed act as a source for  $\alpha$ -stable noise on the sea ice?
- Q2 Can the threshold behavior with respect to sea ice removal be reproduced by GCMs?
- Q2 What is the influence of ocean surface temperatures on the formation of sea ice and could it be integrated into the model?
- Q2 How could the effect of brine rejection on oceanic salinity be integrated into the model?

Atlantic climate system.

P2 invokes  $\alpha$ -stable noise to generate supercritical noise pulses that trigger DO events. In the context of DO variability an  $\alpha$ -stable noise component was first evidenced by Ditlevsen (1999) in the analysis of calcium ion concentrations from the GRIP ice core. But until the work by Gottwald (2021) this aspect was apparently not taken up prominently. P2 is largely inspired by this very same study wherein DO variability is explained in a dynamic self-consistent framework through complex multi-scale interactions.

Gottwald (2021) compellingly demonstrated how time-scale-separated deterministic dynamics may lead to an effective  $\alpha$ -stable noise on the slowest time scale through appropriate coupling of the model components in the limit of large time-scale separation. Focusing on the mathematical aspects, the model presented by Gottwald (2021) exhibits a few physical shortcomings, which are addressed in P2 while retaining key aspects of the original model architecture. In particular, in the Gottwald (2021) model, the sudden climatic changes induced by  $\alpha$ -stable noise pulses do not directly correspond to transitions between the stadial and interstadial climate regimes. P2 adopts the notion that coupled and time-scale-separated atmosphere, sea ice and ocean dynamics acted in concert to produce DO variability. Compared to Gottwald (2021), P2 puts greater emphasis on the correspondence between model and proxy variables. Based on this, simulated abrupt climatic changes can indeed be identified with real-world DO events marking transitions from a stable stadial to a meta-stable interstadial climate. Further, P2 uses a more physically sound sea ice model, namely the Eisenman (2012) model, which supports bistable sea ice dynamics as a consequence of the ice–albedo feedback. However, it relies on a simpler atmosphere component and introduces the  $\alpha$ -stable driving noise process fairly ad-hoc. Instead of acting on the AMOC as in Gottwald (2021), the  $\alpha$ -stable noise acts on the sea ice in P2. Finally, while in Gottwald (2021) abrupt climatic change was induced by large sea ice cover events, in P2, DO events are triggered by supercritical sea ice removal.

In principle, P2 provides a clear and consistent answer to Q2. One caveat is that the  $\alpha$ -stable driving process is only sporadically physically motivated. Also,

the atmospheric circulation, another key actor in DO variability, is not represented in the P2 model. The excitability mechanism helps explain several features of the DO variability that other models struggle to explain, like the large variability of interstadial durations and very short-lived stadial and interstadial inceptions. This renders a stochastic trigger of DO events more plausible than self-sustained oscillatory concepts of DO variability which typically yield more regular DO cycles. Strictly speaking, the excitability mechanism does not comply with the definition of climate tipping provided in Sect. 2, since it does not rely on a steadily changing external control. In physical terms, P2 corroborates the importance of sea ice in the emergence of DO variability and its role as an insulator between the atmosphere and the ocean.

Strangely the excitability mechanism has received only little attention in the DO modeling community despite promising early results. Using a global climate model of intermediate complexity, already in 2002 Ganopolski and Rahmstorf demonstrated that DO events could be triggered by adding a stochastic component to the atmosphere–ocean freshwater fluxes north of 50°N. As the P3 model, their EMIC is monostable with the stable state corresponding to stadial climate conditions. The stochastic excitation is followed by a characteristic relaxation path that corresponds to the interstadial before the stadial state is reestablished. The resulting interstadials appear to be very regular though. The conceptual model presented by Timmermann et al. (2003) also relies on stochastic excitations. However, in their setup, an initial freshwater pulse is required to bring the system into a state that is susceptible to stochastic excitations. The authors explain the model behavior in terms of coherence resonance. Later, the excitability paradigm was picked up by Vettoretti et al. (2022) to explain the shorter interstadials. Based on the analogy between a complex climate model and a conceptual model, the authors propose that longer interstadials correspond to a limit cycle behavior in the Atlantic climate system which exists for intermediate glacial CO<sub>2</sub> concentrations. Outside of that range, the limit cycle is collapsed onto a single stable state via a Hopf bifurcation. In the high (low) CO<sub>2</sub> case, this stable state comprises a strong (weak) AMOC. From this perspective, starting from the stable weak (strong) AMOC state, short interstadials (stadials) can be viewed as singular excitations tracking the limit cycle in state space.

For the future, P2 suggests various subsequent research questions. First, existing and upcoming ice core records could be investigated with respect to a signature of  $\alpha$ -stable climate noise. Ditlevsen (1999) already showed the presence of  $\alpha$ -stable noise in the highly resolved calcium record from the GRIP ice core. In fact, a corresponding assessment of higher-order KM coefficients estimated from the NGRIP stable water isotope and dust concentration records was originally part of P3. Due to some inconsistencies it was removed from P3 but will hopefully be published as a stand-alone publication in the near future. Unfortunately, in the case of direct sea ice proxies the insufficient temporal resolution prevents any reasonable inference on the driving climate noise by means of the KM equation. However, it could be worthwhile to investigate the fluctuations in the sea ice extent in climate model simulations that show DO-like variability. GCMs could further be used to test the excitability hypothesis formulated by P2. Forced sea ice removal during stadial conditions could provide important insights into the relaxation dynamics of the models and potentially reveal a threshold behavior in

**P3 | Main Conclusions.**

- Q2 Projected onto the state space of  $\delta^{18}\text{O}$  and dust concentration as recorded by the [NGRIP](#) ice core the last glacial's North Atlantic climate system appears to have been bistable.
- Q2 The bistability is inherent to the dust variable and thus to the state of the atmospheric circulation. In contrast, the  $\delta^{18}\text{O}$  record does not feature any bistability.
- Q2 Perturbations along the dust direction seem more plausible to trigger [DO](#) events. This suggests that the atmospheric circulation played an active role in the emergence of [DO](#) variability.

the system-wide response.

**P3 | Summary.** In **P3** the bivariate [NGRIP stable water isotope and dust concentration record](#) is regarded as the outcome of a stochastic, Markovian and time-homogeneous process ([Ruth et al., 2003](#); [North Greenland Ice Core Project Members, 2004](#); [Gkinis et al., 2014](#); [Niels Bohr Institute \(University of Copenhagen\), 2023](#)). Corresponding first-order [KM](#) coefficients are estimated directly from the data and interpreted as the two-dimensional deterministic drift of the underlying dynamical system. The reconstructed drift exhibits two stable fixed points, which suggests that the transitions between stadials and interstadials were noise-induced. Furthermore, the bistability of the two-dimensional drift can be clearly attributed to the dust variable, which is commonly interpreted as a proxy for the state of the large-scale atmospheric circulation (e.g. [Fischer et al., 2007](#); [Ruth et al., 2007](#); [Erhardt et al., 2019](#)). This said, the findings presented in **P3** hint at an active role of the atmosphere in stabilizing the two different climate regimes of the last glacial interval. From a visual inspection of the reconstructed drift, it seems plausible that perturbations along the dust direction and thus of atmospheric kind could trigger a transition to the respective other stable climate state. Corresponding transitions triggered by atmospheric anomalies have been reported from [GCM](#) experiments ([Kleppin et al., 2015](#); [Drijfhout et al., 2013](#)). The reconstructed drift cannot explain the trends in the data that are characteristic of interstadial intervals.

**P3 | Discussion** **P1** and **P2** addressed **Q2** from a modeling perspective. In contrast, **P3** relies on a data-driven approach. Numerous previous studies have assumed a similar viewpoint as **P3** and have fitted time-homogeneous [SDE](#) to Greenland ice core data (e.g. [Ditlevsen, 1999](#); [Kwasniok and Lohmann, 2012](#); [Kwasniok, 2013](#); [Lohmann and Ditlevsen, 2018](#)). The novelty of **P3** is that it does not rely on an upfront specification of the model structure beyond Eq. (2.10) and that it considers a two-dimensional record. [Hassanibesheli et al. \(2020\)](#) have applied the same method used in **P3** to Greenland ice core data before, but in a univariate setting and using data with lower temporal resolution. The two-dimensional record investigated in **P3** was previously studied by [Boers et al.](#)

### P3 | Subsequent Questions.

- Q2 Can higher-order **KM** coefficients be estimated from paleoclimate data to assess the structure of the noise present in the data?
- Q2 Can drift functions be reconstructed from three-dimensional data? To date, no such three-dimensional climate proxy record is available at sufficiently high resolution, but this could probably be the case in the future.
- Q2 Can this method be applied to summary climate variables (**AMOC** strength, mean jet stream position, etc.) from **GCM** simulations of **DO** variability to assess both the underlying drift and the noise? This way, one could directly derive low-order models from the output of a complex climate model.

(2018) by fitting a stochastic delay differential equation to the data.

**P3** underwent a controversial review process, wherein in particular the assumption of Markovianity was criticized. While this is indeed a legitimate caveat, Markovianity of paleoclimate data — or more precisely Markovianity of the process that generated the data — is very hard to prove and probably never strictly fulfilled. One can certainly argue, that the data bears the signature of memory effects as done by [Boers et al. \(2018\)](#). However, excluding all methods that rely on Markovianity from paleoclimate time series analysis seems not a viable solution. Contrarily, it is plausible, that for processes with small memory Markovian methods could still reveal important information on the underlying dynamics.

The second major caveat is the assumption of time-homogeneity of the dynamics which also contradicts the insights of **P1** and **P2**, but cannot be avoided in the setting of **P3**. To make this assumption more plausible, **P3** investigates data from a limited time period over which the background climate did not change too much. Additionally, a sophisticated detrending method was applied as part of the preprocessing of the data to remove the remaining influence of changes in the background climate.

A reliable estimation of higher-order **KM** coefficients which could provide insights into the noise structure of the process was prevented by the scarcity of data, at least in two dimensions. Estimations of the higher-order **KM** coefficients of the individual, univariate time series were originally part of **P3**. These will be published in a separate publication, as soon as some remaining discrepancies have been reconciled. It seems that the noise of the  $\delta^{18}\text{O}$  record exhibits higher-order **KM** coefficients which hint at contributions from non-Gaussian noise, like for example  $\alpha$ -stable noise as used in the **P2** model.

Indeed, for the future, it would be desirable to apply the method demonstrated in **P3** to more paleoclimate records. It bears the potential to provide new insights into past (coupled) dynamics of proxy variables and therewith into the climate dynamics they represent. In particular, estimating also the higher-order **KM** coefficients could reveal potential imprints of multiplicative and non-Gaussian noise. If non-Gaussian noise contributions could be evidenced with certainty, this would have important implications for the notion of resilience with regard to **CTE** and

ESC in general. The question if and how rare but extreme noise pulses could trigger climatic transitions needed to be investigated more carefully. Moreover, multiplicative noise may have sophisticated implications on dynamical system dynamics that have not yet been explored in depth in the context of CTP. However, the estimation of KM coefficients is largely prevented by the often poor temporal resolution of the data. Promising exceptions might be the remeasurements from the Dye3 ice core (Kjær et al., 2021) or the data from the North Greenland Eemian Ice Drilling (NEEM) ice core (Erhardt et al., 2021) which would be worthwhile investigating by the means of the KM framework. As already suggested as a follow-up research question with respect to P2, the KM analysis could also be extended to GCM data that shows DO-like variability to assess both deterministic dynamics of selected climate variables and the climate noise within the models.

**P1-3|Discussion** Even though P1-3 all share the common framework of (random) dynamical systems they do approach Q2 in fairly different ways. P1 focuses on the theoretical framework given by the theory of dynamical systems and highlights the importance of an external forcing's action on internal (nonlinear) dynamics. As for P1, this combined discussion considers in particular the FHN model of DO variability presented in Section 3.3.4 of the study. P2 presents and discusses a conceptual model for the last glacial's North Atlantic climate system in great detail. Finally, P3 adopts a fully data-driven method to assess the deterministic climate dynamics underlying DO variability.

First, it should be noted that all studies are concerned with different state spaces summarized in Tab. 7.1. In P1 the fast and slow variables of the abstract FHN model are interpreted as the AMOC strength and the AABW formation or the Northern Hemisphere ice sheet height, respectively. The variables of the P2 model represent AMOC strength, high northern latitude atmospheric temperature, and the Nordic Seas' sea ice cover and their intermediate to deep ocean water temperatures. The proxies investigated in P3 are indicative of past Greenland air temperatures and, more vaguely, the state of the large-scale atmospheric circulation. In the case of P3, the choice of the state space followed naturally from the availability of corresponding high-resolution proxy records. In P1 the FHN model fulfills mostly illustrative purposes. However, the same identification of fast and slow variables of an FHN-like model was made by Vettoretti et al. (2022) based on the assessment of climate model output. As already mentioned, P2 was inspired to a large degree by Gottwald (2021) and thus adopted the same set of dynamical variables adding the interpretation of the Stommel oceanic temperature gradient. This explains why the state spaces considered in the studies are not aligned with one another.

P1 and P2 could in principle be reconciled with one another in terms of the considered state spaces and the dynamical mechanism if a fifth variable would be added to the P2 model that represented slow AABW or ice sheet height changes. Although this is not straightforward, such a slow-relaxing variable could make the deterministic core of the P2-model self-oscillatory on long time scales. It does not seem implausible, that the DO variability of the past was in fact driven by a combination of relaxation-oscillations and noise-induced excitations in the following sense: In the stadial state, a strong noise pulse can trigger DO event. If no such noise pulse occurs over a long time a slow deterministic mechanism inevitably triggers the next DO event.

feature \ study	P1-FHN	P2-model	P3-SDE
climate variables	AMOC AABW / ice sheets	AMOC sea ice Greenland temperature ocean temperature	Greenland temperature atmospheric circulation
dynamical mechanism for DO variability	self-sustained oscillations	noise-induced excitations	noise-induced transitions between two stable states
external forcings	atmospheric CO <sub>2</sub>	global ice volume & $\alpha$ -stable noise	no slow forcing, noise not specified

Table 7.1: Summary of the dynamical system approaches to DO variability chosen in P1-3.

With respect to the external forcing, it probably makes no great difference to use either atmospheric CO<sub>2</sub> or global ice volume in the conceptual setting of P1 and P2 as these two variables covary to a large degree. Another external force that is often regarded to have shaped DO variability is the orbital insolation forcing (Mitsui and Crucifix, 2017; Roberts and Saha, 2017). In fact, recent GCM results suggest a sweet spot in the combined CO<sub>2</sub> and orbital insolation forcing for the emergence of DO variability (Zhang et al., 2021; Kuniyoshi et al., 2022; Vettoretti et al., 2022; Malmierca-Vallet et al., 2023). It is noteworthy, that the FHN model in P1 undergoes dynamic Hopf bifurcations in response to the slow forcing, while the behavior of the P2 model is only quantitatively affected by the changes in global ice volume. In fact, if the coupling strength of the P2 model to the ice volume records was increased, it would also undergo qualitative transitions between mono- and bistability.

It is less clear how the results obtained in P3 fit into the picture. In suggesting a genuine bistability of the last glacial's North Atlantic climate system, P3 offers a third possible view on DO variability. Given the different state spaces, a direct comparison of the deterministic drift reconstructed in P3 with the model equations from P2 and P1 is difficult. If the model variables were aligned with the proxies, a comparison would indeed be meaningful. Still, it should be evaluated with caution since climate proxies do not provide one-to-one representations of climate variables. In particular, the dust concentrations are difficult to relate to a single specific climate variable. The bistability attested by P3 does in fact contradict the dynamical properties of the P1 and P2 models.

None of the studies presented in this thesis explicitly addresses the role of oceanic salinity in DO variability. Given that recent GCM reproductions of DO variability attribute high importance to the salt-advection feedback (Vettoretti and Peltier, 2018; Zhang et al., 2021; Kuniyoshi et al., 2022) it seems worthwhile to investigate the dynamics of the salinity gradient in P2 more closely.

Another aspect the studies have largely ignored is the interaction between DO events and Heinrich events, which add another time scale to the problem (Heinrich, 1988). The reason to neglect the influence of Heinrich events and corresponding Bond cycles was that DO cycles that comprise a Heinrich event are not qualitatively different from non-Heinrich DO cycles. Thus, to understand the fundamental physical mechanism it seems sufficient to investigate DO variability in isolation. Still, Heinrich events are suggested to be entangled with the DO

variability in quantitative terms and their respective time scale falls in between the time scales of orbital changes and that of DO variability (e.g. Bond et al., 1992, 1993; Hemming, 2004; Clark et al., 2007; Rousseau et al., 2022).

#### P4–5 Uncertainty-sensitive inference on the course of DO events

**P4|Summary.** The starting point of P4 is a set of pairwise temporal lags  $\Delta t$  between DO transitions in different proxy time series provided by Erhardt et al. (2019). More specifically, the lag is defined as the temporal difference between two transition onsets detected in a pair of proxy time series. For each individual proxy transition at each investigated DO event, the onset is estimated in a Bayesian sense. A linear transition model from one level of values to another in combination with a suitable noise model directly determines a Bayesian likelihood function. Upon multiplication with convenient priors, this likelihood function transforms into a posterior probability distribution for the transition model parameters. The marginal Bayesian posterior distribution for the transition onset parameter then follows from an integration over all nuisance parameters. The marginal distributions for the two transition onsets of a pair of proxies yields the posterior distribution for their respective temporal lag.

Only proxies from the same archive are compared to one another. While stemming from the same archive the proxies still carry different climatic interpretation. This allows to assess the phasing of abrupt changes in different ESCs at DO events free of inter-archive dating uncertainty. The investigated proxies represent the regional and large-scale atmospheric circulation, the North Atlantic sea ice cover and atmospheric temperatures over Greenland.

P4 establishes a sound statistical interpretation for the sets of pairwise transition lags. Based on the assumption that all DO events followed the same mechanism, it regards each set of lags for a given proxy pair as outcomes of a repeated random experiment, wherein the randomness reflects natural variability. This randomness must not be confused with the uncertainty in the determination of the lag. This framework allows to use hypothesis tests to infer the characteristics of the underlying (unobservable) distribution of time lags. P4 formulates the null hypothesis that for a given pair of proxies, and hence for the pair of ESCs, they represent, the transitions actually started synchronously. Natural variability is suggested to have delayed the one or the other in a random fashion and without any preference. In mathematical terms this translates into the demand that the null distribution's mean is equal to zero.

P4 identifies three hypothesis tests suited to test this null hypothesis preconditioned on different additional assumptions on the null distribution's shape. The transition lag samples bear the particularity that all sample members are given in terms of posterior distributions instead of scalars. Using an ensemble representation, this uncertainty is rigorously propagated to the tests'  $p$ -values. P4 then suggests two rules for projecting the distributions of  $p$ -values onto binary decisions between rejecting and accepting the null hypothesis. Both rules consistently accept the null hypothesis of synchronous transitions for all investigated pairs of proxies and for all applied tests. Importantly, averaging out the uncertainties of the sample members prior to the application of the tests does in fact lead to the rejection of the null hypothesis in all cases. In view of apparent lag relationships which had

**P4|Main Conclusions.**

- Q3 No significant leads or lags between abrupt changes in the atmospheric circulation, the North Atlantic sea ice cover and Greenland temperatures at DO events can be evidenced on the basis of multi-proxy records from the NEEM and NGRIP ice cores.
- Q3 The uncertainty in the transition onset detection prevents drawing more specific conclusions.
- Q3 The propagation of uncertainty qualitatively changes the outcome of the analysis as compared to averaging out uncertainties at an early stage. This finding stresses the importance of uncertainty propagation.
- Q3 The Bayesian ramp-fit method introduced by Erhardt et al. (2019) is in principle well suited to estimate transition onsets in noisy data in an uncertainty-sensitive manner.

previously been reported by Erhardt et al. (2019), the hypothesis tests are in fact applied in a one-sided manner in P4.

In physical terms P4 concludes that the null hypothesis of synchronous abrupt changes in the atmospheric circulation on regional and hemispheric scale, the North Atlantic sea ice cover and Greenland temperatures at DO events cannot be rejected on the basis of the investigated data.

**P4| Discussion.** P2 builds on the study presented by Erhardt et al. (2019). These authors addressed Q3 by investigating the phasing of DO transitions in multi-proxy records from two Greenland ice cores. The different proxies were interpreted as measures for past Greenland temperatures, the sea ice extent in the North Atlantic and local and hemispheric-scale atmospheric circulation patterns. As such, the data allowed for a comparison of the timings of abrupt transitions in different climate system components free of cross-archive dating uncertainties for a number of DO events. From these sets of uncertain time lags, inferred as described above, Erhardt et al. (2019) concluded that ‘on average’ at DO events transition onsets in atmospheric proxies lead those in sea ice and temperature proxies by about a decade.

The reassessment of the posterior distributions of the pairwise temporal transition lags presented in P4 demonstrates that the postulated lead is not statistically significant if the uncertainties are rigorously propagated. In fact, it became clear that the processing of the posterior pairwise lag distributions carried out by Erhardt et al. relied on a misconception. Assuming that for a given proxy pair, the lag distributions for all analyzed DO events were observations of one and the same quantity — namely a generic underlying time lag  $\Delta t$  — the authors multiplied the corresponding posterior distributions. The product distribution was hence confined to a region where all individual posterior lag distributions featured non-zero probability. It seems that the authors refer to the mean of the product distribution when they claim a decadal temporal lag ‘on average’, but this is not clear.

In view of this misconception, P4 first establishes a sound statistical interpretation of the samples of uncertain pairwise time lags and then presents three hypothesis tests that are suited to assess the significance of the postulated lead of the atmospheric proxies. P4 clarifies that due to climate variability, the true lag between two proxy transitions varies from one DO event to another. Even if all DO events followed the same mechanism, the true lag would be randomly distributed for different events. The different events would not share the same generic time lag as implicitly postulated by Erhardt et al. (2019).

P4 clarifies, that the mean of an underlying distribution for the true lag can best be estimated by convoluting the individual posterior lag distributions. The tendency of a delayed transition in the temperature and sea ice proxies is also apparent in the convoluted posterior distribution. However, all hypothesis tests consistently reject the significance of the lags for all pairs of proxies. P4 thus concludes that Q3 cannot be answered conclusively from the study of the particular NGRIP and NEEM multi-proxy time series investigated by Erhardt et al. (2019). While there remains a tendency of the temperature and sea ice proxies' transitions to lag those of atmospheric proxies, this lag is not significant. The non-significance of the postulated lags attested in P4 was confirmed independently by Capron et al. (2021) based on visual inspection of the posterior transition onset distributions who conclude that

*'[...] it may not be possible to infer statistically-robust leads and lags between the different components of the climate system because of their tight coupling.'*  
(Capron et al., 2021)

It is important to understand, that the attempt to identify a characteristic sequence of events for DO events is based on the assumption that all DO events were driven by the same physical mechanism. Alternative hypotheses are hardly discussed in the literature and also most conceptual models implicitly rely on this assumption. This assumption seems justified by the qualitatively consistent expression of DO events. It might, however, still be that different DO events were driven by different physical mechanisms.

One important aspect of P4 is the propagation of uncertainties. If the uncertainties of the posterior lag distributions are rigorously propagated throughout the analysis, then, as a function of uncertain variables, the  $p$ -values of the hypothesis tests also become uncertain variables. The corresponding posterior distributions of the  $p$ -values carry all the meaningful information and are therefore also reported in P4. However, the task of hypothesis testing is to produce a binary decision on whether the null hypothesis ('no time lag') should be rejected or not in view of the data. Thus, P4 proposes two different rules to project the uncertain  $p$ -value on the binary decision between rejection and acceptance of the null hypothesis. The first rule compares the expectation of the  $p$ -value with the predefined significance threshold and the second rule assesses the probability of the sample of uncertain lags to contradict the null hypothesis significantly according to the posterior  $p$ -value distribution. Surprisingly, it seems that the application of hypothesis tests to a sample of uncertain measurements has hardly been discussed in the literature and thus, these rules might be of interest for similar applications in different fields.

Together, the Bayesian ramp-fit algorithm and the statistical framework for the interpretation of the pairwise temporal lags presented in P4 constitute a sound

**P4| Subsequent Questions.**

- Q3** Can the framework developed in **P4** be transferred to **GCM** output that shows **DO**-like variability? In a simulation setting the phasing of corresponding transitions from more climate variables relevant to **DO** events could be assessed.
- Q3** Can the framework be transferred to a multi-archive setting? In the assessment of proxy data from remote archives, the relative dating uncertainty will add to the uncertainty inherent to the transition onset detection. Most likely, these uncertainties will prevent meaningful inference. However, the discussion on **P5** specifies why a reassessment of available data could be worthwhile.

mathematical approach to assess the phasing of transitions in different paleoclimate proxy records that can also be applied to data from geographically distant archives. In connection with **P5**, a faster version of the algorithm was implemented to facilitate the application to numerous events detected in different archives. The gains in computational efficiency come with the advantage, that the shape of the transition-surrounding data window can be optimized to obtain an objective and optimal posterior distribution for the transition onset.

Even though **P2** and **P3** follow very different approaches, their results are consistent with the conclusion of **P4**. If there was a significant lag between temperature and atmospheric circulation proxy transitions in the **NGRIP** record, then a signature of that lag should also be visible in the reconstructed two-dimensional drift presented in **P3**, which is not the case. In the model presented in **P2** the atmosphere responds to sea ice perturbations almost instantaneously. Assuming the model represented indeed the true mechanism of **DO** events, then in ice core records the **DO** transitions of sea ice and temperature proxies should indeed appear simultaneous. The fact that the sea ice retreat drives Greenland warming does (in the model) not translate into a temporal lag that is large enough to be detectable in climate proxy records.

Like all contributions to this thesis, **P4** does not discuss the physical interpretation of the proxies in terms of climate variables and is instead only concerned with the statistical analysis of the data. In this context, it is important to mention that the validity of sodium concentrations as a sea ice proxy is debated and that recent studies suggest using bromine enrichment records instead ([Maffezzoli et al., 2019](#)). Bromine records from Greenland ice cores are, however, not available at sufficiently high resolution for the analysis conducted in **P4**.

**P5| Summary.** **P5** is concerned with the dating uncertainty of the **NGRIP** ice core. The **NGRIP** chronology, the **GICC05**, is based on the counting of individual annual layers in the ice core which arise from seasonal variations in the accumulation process ([Rasmussen et al., 2006](#); [Vinther et al., 2006](#); [Andersen et al., 2006](#); [Svensson et al., 2008](#)). One particularity of this dating approach is that errors made in the counting accumulate and hence the absolute uncertainty in the dating grows substantially toward older ages ([Boers et al., 2017](#)). In the original counting

**P5 | Main Conclusions.**

- Q3** P5 provides a method to generate ensembles of chronologies which are required to propagate the joint dating uncertainty of the **NGRIP** record to subsequent analyses.
- Q3** It is very likely that the maximum counting error (**MCE**) is an overly conservative estimate of the **NGRIP** dating uncertainty.
- Q3** Used in combination, the new age–depth model and the Bayesian ramp-fit (**P4**) yield an uncertainty sensitive estimate of the joint **DO** transition ages that reflects both, dating uncertainties and uncertainties in the transition onset detection.

of annual layers, hereafter referred to as **GICC05**, each layer that was deemed uncertain was taken into account as half a year while at the same time, half a year was added to the so-called maximum counting error (**MCE**).

**P5** regards the resulting age–depth model, more precisely the counted layer density as a function of depth, as the realization of a stochastic process and formulates a corresponding process model. This new model introduces a set of fixed effects to capture those features of the **GICC05** that are physically explainable. These include the increasing age density with increasing depth due to the thinning of older annual layers towards the bottom of the core and the higher age density associated with stadial climate as a consequence of reduced stadial snow accumulation as compared to interstadials. The residuals between the deterministic model component and the **GICC05** are then interpreted as a combination of climate and counting noise which is reasonably well captured by an autoregressive process of first order (**AR(1)**) noise model. In combination with convenient priors, the resulting stochastic model determines a Bayesian posterior distribution for all model parameters. Accordingly, a two-stage Monte Carlo sampling scheme generates consistent realizations of the **GICC05** chronology: first, the model parameters are drawn from the Bayesian posterior distribution and second a realization of the noise, the model's stochastic component is sampled. This sampling sequence yields a possible realization of the new age–depth model and an extensive repetition of this scheme generates an ensemble of chronologies that suitably represents the joint dating uncertainty of all data points in the **NGRIP** record. Moreover, under the assumption that the original layer counting was in fact unbiased in the sense that counting spurious layers were counted comparably often as true layers were missed, this method substantially reduces the **NGRIP** record's dating uncertainty. Finally, **P5** combines the new age–depth model with the Bayesian ramp-fit introduced by [Erhardt et al. \(2019\)](#) and also used in **P4** to estimate the **DO** transition onsets in the **NGRIP**  $\delta^{18}\text{O}$  record under consideration of both sources of uncertainty, the dating uncertainty and the transitions onset detection uncertainty.

**P5 | Discussion.** The authors of the **GICC05** introduced the concept of the **MCE** to indicate the uncertainty of each measurement's associated age. Due to the

### P5 | Subsequent Questions.

- Q3** In combination with the Bayesian ramp-fit (Erhardt et al., 2019) the new age–depth model should serve as a starting point for a reassessment of the phasing of DO transitions observed in proxy time series from remote archives.
- Q3** How can the new age–depth model be synchronized to external tie-points?

specific nature of the ice core dating the ages and the respective uncertainties are correlated across the core. These correlations need to be taken into account in any dating-uncertainty-sensitive analysis. However, it is not per se clear how the MCE should be translated into a joint uncertainty distribution for all data points, i.e. into a probability for any specific ‘realization’ of the GICC05 that reflects the age correlations. A naive approach would certainly be to grant every uncertain layer a 50% chance to be a true layer and then simulate a corresponding Bernoulli experiment. However, the assumption that each uncertain layer is equally likely to be a true layer and to be a spurious layer can hardly be justified. To overcome this obstacle, P5 introduces a statistically motivated new age–depth model for the NGRIP ice core. With this new model, it is possible to assess the joint dating uncertainty of all data points in the NGRIP record.

One caveat of the age–depth model presented in P5 is that the relative incremental uncertainty increases in the original GICC05 while it does not for the new model as can be seen in Fig. 5 of P5. The relative incremental uncertainty is the additional uncertainty compared to the additional age associated with an incremental increase in depth. Also, a certain degree of heteroscedasticity is apparent in the residuals that remain after the subtraction of the deterministic model component from the data. This heteroscedasticity is ignored by the adoption of a homogeneous AR(1) noise process.

The structure of the model offers one additional advantage. Namely, the model can be synchronized to external tie-points in a mathematically consistent manner. Synchronization based on the tie-points provided by Adolphi et al. (2018) and Muscheler et al. (2020) is ongoing work. The dubious method used for the interpolation between tie-points is a clear deficit of a previous synchronization of the GICC05 presented by Adolphi et al. (2018). The age–depth model developed in P5, once synchronized, immediately yields the joint uncertainty for all data points conditioned on the tie-points and thus makes any further interpolation obsolete. Given that the DO events are distributed across the entire last glacial, a robust mathematical formulation of the synchronization for all data points is crucial to improve the age estimates for DO events and advance the debate on leads and lags. This said, P5 constitutes a preparatory work whose full potential still remains to be leveraged in terms of a revision and synthesis of the studies by Adolphi et al. (2018) and Corrick et al. (2020) based on a new synchronization of the NGRIP chronology.

**P4-5 | Discussion.** Recent studies that investigated leads and lags between different components of the climate system found synchrony between the DO transitions in the [NGRIP](#)  $\delta^{18}\text{O}$  record and corresponding transitions from low-latitude speleothem records ([Adolphi et al., 2018](#); [Corrick et al., 2020](#)). However, the reported ages for DO transitions are inconsistent between the two studies, with [Adolphi et al. \(2018\)](#) reporting older DO transition ages for both, the [NGRIP](#) record and the different speleothem records. This explains how both studies can draw the same conclusions, i.e. the synchrony between low- and high-latitude abrupt climatic change at DO events, based on different numbers.

The discrepancies in [NGRIP](#) and speleothem DO event ages are caused by three main reasons. First, [Adolphi et al. \(2018\)](#) synchronize the [NGRIP](#) chronology, the [GICC05](#), to radiocarbon-dated archives. The synchronization reveals a strong bias of the [GICC05](#) to too young ages, in particular around the last glacial maximum (LGM). Thus, on the synchronized age-scale, the DO event ages appear older than on the original [GICC05](#). Second, the studies use different transition detection methods. While [Adolphi et al. \(2018\)](#) relied on the Bayesian ramp-fit algorithm also employed by [Erhardt et al. \(2019\)](#) and **P4**, [Corrick et al. \(2020\)](#) adopt the method by [Rasmussen et al. \(2014\)](#) who identify

*'[...] the first data point of the steep part that clearly deviates from the base-line level preceding the transition'* ([Rasmussen et al., 2014](#); [Corrick et al., 2020](#))

with the interstadial onset. Third, both studies include different selections of speleothem records. Clearly, the comparison of transition onsets (or endpoints) estimated in an objective Bayesian manner is more consistent in the sense that the first data point that stands out the stadial variability may occur at a sooner or later stage within the transition.

In principle, the framework developed in **P4** could be adopted to reassess and hopefully reconcile the investigations by [Adolphi et al. \(2018\)](#) and [Corrick et al. \(2020\)](#). However, such a reassessment relies heavily on the interpretation of the absolute dating uncertainties present in the [GICC05](#). In the context of this debate, **P5** contributes to limiting the influence of the dating uncertainty associated with the [NGRIP](#) record and provides a consistent method, for how this uncertainty should be propagated to any subsequent analysis. In combination, the methods developed in **P4** and **P5** offer a good starting point to reinvestigate the temporal phasing of abrupt shifts in time series from remote climate archives at DO events. The aforementioned synchronization of the **P5** age-depth model, which is still to be published, will be central to this endeavor.

## 7.2 Conclusions and outlook

The previous section discussed the results of all publications included in this work. Special attention was paid to the relationships between P1-5 and their connections to other studies. Q1 cannot be answered conclusively within the scope of this work. Yet, P1-5 provide important insights that advance the debate on DO variability. This section summarizes once again the key findings and concludes with an outlook on future the investigation of DO events and more broadly of tipping points in the Earth system.

P1 only sketches an illustrative answer to Q1 by coupling an FHN model to past atmospheric CO<sub>2</sub> concentrations. Instead, it provides detailed guidance on how dynamical systems can contribute to the investigation of Q1 and other paleoclimate questions. P1 underlines the role of external forcing in the emergence of the past climate's variability and provides methodological guidance for the mathematical treatment thereof. In the sense of P1, the model proposed in P2 is coupled to a proxy record indicative of past global ice volume to align the simulated interstadial durations with the observed ones. In contrast, P3 deliberately investigates data from a limited period of time to exclude the influences of a changing background climate. Taken together, P1 and P2 corroborate the already prevailing perception that the state of the background climate, in terms of orbital insolation forcing, global ice sheet configuration or past atmospheric CO<sub>2</sub> concentrations shaped the expression of DO variability over the last glacial interval (e.g. Zhang et al., 2014; Roberts and Saha, 2017; Mitsui and Crucifix, 2017; Boers et al., 2018; Vettoretti et al., 2022; Zhang et al., 2021; Kuniyoshi et al., 2022). While orbital insolation forcing can safely be regarded as an external driver, this is not per se clear for the Northern hemisphere ice sheets and atmospheric CO<sub>2</sub>, which might to some extent be subjected to feedbacks from the North Atlantic climate system's state. Disentangling the contributions of these external or quasi-external factors on the DO variability remains an open challenge. The incorporation of these feedbacks into GCM or ESM model experiments is limited by the computational costs they require.

Among all studies, P2 provides the most comprehensive answer to Q1 and Q3. It explains the DO variability of four key climate variables in terms of an excitable multi-scale system wherein  $\alpha$ -stable noise triggers DO events by abruptly removing large fractions of the Nordic Seas' sea ice. To date, the excitability paradigm has remained largely unexplored in the context of DO variability and constitutes a promising alternative candidate mechanism compared to existing hypotheses. In combination with the  $\alpha$ -stable noise, it explains the variability and irregularities of the NGRIP  $\delta^{18}\text{O}$  record to a greater extent than many models previously proposed. This can be interpreted as a strong indication that DO events were in fact noise-induced. The crucial role of the sea ice in controlling the state of the North Atlantic climate system has been emphasized in previous research and is corroborated by the performance of the model introduced in P2 (e.g. Li et al., 2005; Dokken et al., 2013; Li and Born, 2019; Sadatzki et al., 2020). Exploring the excitability concept further appears to be a valuable pursuit. This could involve examining the delicate balance of influences that could cause the interstadial state to become unstable in a glacial background climate while remaining stable during interglacial periods. In particular, the stability of a reduced sea ice cover could be assessed in tailored

EMIC or GCM experiments for different climate background states. An important caveat is that the  $\alpha$ -stable stochastic sea ice forcing is motivated by somewhat indirect evidence (Ditlevsen, 1999). This suggests to explore potential sources of non-Gaussian noise in both comprehensive climate model experiments and in the available and upcoming proxy data. P2 demonstrates that such noise can on the one hand trigger DO events and on the other hand can serve as a source of variability for DO cycles. Note that unpublished research in the context of P3 also points towards non-Gaussian contributions in the noise of Greenland temperature proxy time series. Such findings would provide further arguments for the use of  $\alpha$ -stable noise in P2.

P3 agrees with P2 in that both attribute the occurrence of DO events to stochastic forcing. However, the reconstructed drift from P2 suggests that the interstadial state is also stable. Given that the attested bi-stability is rooted in the atmospheric circulation proxy, P2 suggests that the atmosphere played an active role in stabilizing the two climate regimes. This finding is in line with results obtained in GCM simulations where spontaneous atmospheric anomalies drive substantial change in the high northern latitude's climate (Drijfhout et al., 2013; Kleppin et al., 2015). Potentially, further investigations of the glacial jet stream, either by means of proxy records or by means of GCM experiments, could unravel the atmosphere's contribution to DO variability. Distinct stadial and interstadial circulation regimes could also be a source of qualitative differences in the stochastic sea ice forcing between stadials and interstadials as hypothesized in P3.

For the following reasons, P3 can answer Q1 and Q3 only partially: First, the noise term which is suggested to drive state transitions could not be estimated in P3 due to the scarcity of data. Second, a typical way to assess the performance of a suggested model is to compare simulated trajectories with the original data. P3 does not provide simulations based on the reconstructed drift, because of the missing noise term. Third, the reconstructed drift cannot explain the cooling trend observed in most interstadials.

In agreement with Capron et al. (2021) P4 ultimately concludes that currently available Greenland ice core data do not allow for the detection of significant leads and lags between DO transitions in time series of common temperature, sea ice and atmospheric circulation proxies. The methodology developed in P4 can be readily applied in future assessments of leads and lags that investigate other data. This might be proxy data from geographically distant archives, new proxy data or climate model output from simulations that reproduce DO-like variability. For the moment, the null hypothesis of a synchronous abrupt change in sea ice, Greenland temperature and atmospheric circulation patterns cannot be rejected and thus represents the best possible answer with respect to Q3.

P5 could eventually resolve the outstanding issue of how to mathematically handle and propagate the dating uncertainties of the NGRIP ice core. This is an important step forward with respect to Q3, because the DO events observed in the NGRIP ice core are pivotal to the puzzle of leads and lags between corresponding abrupt changes in different ESCs. While the updated DO event ages presented in P5 show only minor deviations from previous estimates, the model's full potential yet remains to be leveraged. Ongoing research synchronizes the new age–depth model to external tie-points and the overall reduced uncertainty allows for an

improved assessment of leads and lags between **DO** related proxy transitions from spatially remote archives.

Apart from the substantive results, this work has produced significant methodological advances with respect to the study of **DO** variability and other paleoclimate phenomena. **P4** showed how the set of temporal lags inferred from different **DO** transitions can be regarded as repeated realizations of a random experiment. In turn, this interpretation forms the basis for the application of hypothesis tests to infer characteristics of the underlying probability distribution. This framework will probably find application in the assessment of new proxy records or climate model output that shows repeated **DO**-like transitions. The age–depth model developed in **P5** can potentially be transferred to structurally similar layer counted chronologies. Prior to **P3** only a few studies have estimated **KM** coefficients from paleoclimate time series (e.g. [Hassanibesheli et al., 2020](#)). This method may prove useful to disentangle the roles of deterministic dynamics and climate noise in (paleo)climate dynamics. Low-order, tractable climate models could be derived from **GCM** output by its application. It is, however, not suited in a setting where external forcings other than noise control the dynamics of the system under study.

It appears that the study of **DO** variability is entering a new stage where comprehensive climate models take over. Given the rising number of **GCM** simulations that seemingly reproduce **DO** variability, an urgent task will be a rigorous model–data comparison. The better the agreement between observations and model output, the higher is the confidence that the model reflects the actual mechanism of **DO** variability. In turn, a decent reproduction of **DO** variability serves as an important benchmark with respect to the models’ ability to simulate nonlinear dynamics and potential abrupt climatic changes. In line with the hierarchy of models, many of the findings reported in this thesis may help to facilitate an informed assessment of climate model output and to design tailored **GCM** experiments. E.g., one could test a potential threshold behavior with respect to forced sea ice removal in **GCM** simulations. Many of the methods deployed in **P1-5** can directly be applied to the **GCM** data as mentioned before. Another big step forward expected for the future is the development of proxy-enabled models. Those will enable a direct comparison of climate model simulations with the available proxy record and thus substantially improve the ability to evaluate and improve the models’ performances.

Apart from improvements in climate modeling, obtaining new proxy data will continue to further the understanding of **DO** variability. Again, many of the methods developed in this thesis can be reused for the assessment of new data, once this becomes available.

Finally, this thesis has also important implications for the debate on future **CTP**. **P2** clearly demonstrates that the concept of a one-dimensional double-fold bifurcation might be overly simplistic for the description of **DO** variability. In particular, the additional dimensions leave room for more complex dynamics. With respect to future climate tippings, this highlights the constraints of the double-fold framework and shows that abrupt climatic changes can emerge in other mechanisms as well. One could argue, that the anthropogenic release of carbon dioxide for some parts of the climate system rather acts like a shock, in analogy to the sudden sea ice removal in **P2**, than a gradual change of forcing. If, however, global warming is regarded as the continuous change of an external

control parameter, one could also imagine that the **AMOC** enters an oscillatory state via a Hopf bifurcation as sketched in **P1**. Physically, such a scenario could look like follows: Climate change-induced warming could trigger an **AMOC** slow-down, which in turn would reduce oceanic northward heat transport. This would reduce **GrIS** melt rates and change precipitation patterns over the North Atlantic. The new North Atlantic freshwater balance would then act in favor of an **AMOC** reinvigoration and close the causal loop. Furthermore, if **CTE** were to be driven by  $\alpha$ -stable noise as suggested in **P2**, this would drastically increase the risk of noise-induced tipping way before the **CTP** is crossed and would probably change the common perception of resilience. Alongside, the predictability of corresponding upcoming tipping events would be reduced, because early warning signals can typically only be detected shortly before the **CTP** is reached. After all, the clearest way forward for paleoclimate research to inform the study of **CTP** is the following. The **DO** variability simulated by **GCMs** must be reconciled with the available and upcoming proxy record to justify the assumption that the underlying physical mechanism is correctly reflected by the models. Next, this mechanism needs to be investigated in detail in the climate models. Importantly, differences between models that reproduce **DO** variability and those who do not must be identified. Finally, the implications of model features, that enable the of reproduction **DO** cycles, on the stability of the **AMOC** must be assessed under future warming scenarios.



# Acronyms

<b>AABW</b>	Antarctic bottom water
<b>AIM</b>	Antarctic isotopic maximum
<b>AMOC</b>	Atlantic meridional overturning circulation
<b>AR(1)</b>	autoregressive process of first order
<b>CAM</b>	correlated additive and multiplicative
<b>CMIP</b>	Coupled Model Intercomparison Project Phase
<b>CTE</b>	climate tipping element
<b>CTP</b>	climate tipping point
<b>DO</b>	Dansgaard–Oeschger
<b>EAIS</b>	East Antarctic ice sheet
<b>EMIC</b>	Earth system model of intermediate complexity
<b>ESC</b>	Earth system component
<b>ESM</b>	Earth system model
<b>FHN</b>	FitzHugh–Nagumo
<b>GCM</b>	general circulation model
<b>GHG</b>	greenhouse gas
<b>GI</b>	Greenland interstadial
<b>GICC05</b>	Greenland Ice Core Chronology 2005
<b>GRIP</b>	Greenland Ice Core Project
<b>GrIS</b>	Greenland ice sheet
<b>GS</b>	Greenland stadial
<b>IPCC</b>	Intergovernmental Panel on Climate Change
<b>ITCZ</b>	intertropical Convergence Zone
<b>KM</b>	Kramers–Moyal
<b>LGM</b>	last glacial maximum
<b>LULUCF</b>	land use, land use change and forestry

**MCE** maximum counting error  
**MPT** mid-Pleistocene transition  
**NADW** North Atlantic deep water  
**NGRIP** North Greenland Ice Core Project  
**NEEM** North Greenland Eemian Ice Drilling  
**ODE** ordinary differential equation  
**PBA** pullback attractor  
**RECAP** Renland Ice Cap Project  
**SDE** stochastic differential equation  
**TiPES** Tipping Points of the Earth System  
**WAIS** West Antarctic ice sheet

# List of Figures

1.1	Global warming and greenhouse gas emission. . . . .	2
1.2	Map of important climate tipping elements. . . . .	4
1.3	Schematic illustration of the AMOC. . . . .	5
1.4	Paleoclimatic proxy evidence for past abrupt climatic changes. . . . .	7
2.1	Tipping in a double-well potential. . . . .	14
2.2	Double fold bifurcation with simulated trajectory. . . . .	17
3.1	Schematic presentation of the Stommel model. . . . .	20
3.2	Fixed points of the Stommel model. . . . .	22
4.1	Schematic illustration of an ice sheet and an ice core taken from it. . . . .	26
4.2	Proxy evidence of DO variability. . . . .	27

# List of Tables

7.1	Summary of the dynamical system approaches to DO variability chosen in P1-3. . . . .	166
-----	---	-----



# Bibliography

- Adolphi, F., Bronk Ramsey, C., Erhardt, T., Lawrence Edwards, R., Cheng, H., Turney, C. S., Cooper, A., Svensson, A., Rasmussen, S. O., Fischer, H., and Muscheler, R.: Connecting the Greenland ice-core and U/Th timescales via cosmogenic radionuclides: Testing the synchronicity of Dansgaard-Oeschger events. *Climate of the Past*, 14, 1755–1781, [10.5194/cp-14-1755-2018](https://doi.org/10.5194/cp-14-1755-2018), 2018.
- Alley, R. B., Anandakrishnan, S., Jung, P., and Clough, A.: Stochastic resonance in the north Atlantic: Further insights. in: *The Oceans and Rapid Climate Change: Past, Present, and Future*, edited by Seidov, D., Haupt, B., and Maslin, M., pp. 57–68, American Geophysical Union (AGU), [10.1029/GM126p0057](https://doi.org/10.1029/GM126p0057), 2001.
- Andersen, K. K., Svensson, A., Johnsen, S. J., Rasmussen, S. O., Bigler, M., Röthlisberger, R., Ruth, U., Siggaard-Andersen, M. L., Peder Steffensen, J., Dahl-Jensen, D., Vinther, B. M., and Clausen, H. B.: The Greenland Ice Core Chronology 2005, 15–42 ka. Part 1: constructing the time scale. *Quaternary Science Reviews*, 25, 3246–3257, [10.1016/j.quascirev.2006.08.002](https://doi.org/10.1016/j.quascirev.2006.08.002), 2006.
- Armstrong, E., Izumi, K., and Valdes, P.: Identifying the mechanisms of DO-scale oscillations in a GCM: a salt oscillator triggered by the Laurentide ice sheet. *Climate Dynamics*, [10.1007/s00382-022-06564-y](https://doi.org/10.1007/s00382-022-06564-y), 2022.
- Armstrong McKay, D. I., Staal, A., Abrams, J. F., Winkelmann, R., Sakschewski, B., Loriani, S., Fetzer, I., Cornell, S. E., Rockström, J., and Lenton, T. M.: Exceeding 1.5°C global warming could trigger multiple climate tipping points. *Science*, 377, eabn7950, [10.1126/science.abn7950](https://doi.org/10.1126/science.abn7950), 2022.
- Ashwin, P., Wieczorek, S., Vitolo, R., and Cox, P.: Tipping points in open systems: Bifurcation, noise-induced and rate-dependent examples in the climate system. *Philosophical Transactions of the Royal Society A: Mathematical, Physical and Engineering Sciences*, 370, 1166–1184, [10.1098/rsta.2011.0306](https://doi.org/10.1098/rsta.2011.0306), 2012.
- Ashwin, P., Perryman, C., and Wieczorek, S.: Parameter shifts for nonautonomous systems in low dimension: Bifurcation- and rate-induced tipping. *Nonlinearity*, 30, 2185–2210, [10.1088/1361-6544/aa675b](https://doi.org/10.1088/1361-6544/aa675b), 2017.
- Bagniewski, W., Ghil, M., and Rousseau, D. D.: Automatic detection of abrupt transitions in paleoclimate records. *Chaos*, 31, [10.1063/5.0062543](https://doi.org/10.1063/5.0062543), 2021.
- Bakker, P., Schmittner, A., Lenaerts, J. T., Abe-Ouchi, A., Bi, D., van den Broeke, M. R., Chan, W. L., Hu, A., Beadling, R. L., Marsland, S. J., Mernild, S. H., Saenko, O. A., Swingedouw, D., Sullivan, A., and Yin, J.: Fate of the Atlantic Meridional Overturning Circulation: Strong decline under continued warming and Greenland melting. *Geophysical Research Letters*, 43, 12 252–12 260, [10.1002/2016GL070457](https://doi.org/10.1002/2016GL070457), 2016.
- Barker, S., Knorr, G., Edwards, R. L., Parrenin, F., Putnam, A. E., Skinner, L. C., Wolff, E., and Ziegler, M.: 800,000 Years of abrupt climate variability. *Science*, 334, 347–351, [10.1126/science.1203580](https://doi.org/10.1126/science.1203580), 2011.
- Baumgartner, M., Kindler, P., Eicher, O., Floch, G., Schilt, A., Schwander, J., Spahni, R., Capron, E., Chappellaz, J., Leuenberger, M., Fischer, H., and Stocker, T. F.: NGRIP CH<sub>4</sub> concentration from 120 to 10 kyr before present and its relation to a  $\delta^{15}\text{N}$  temperature reconstruction from the same ice core. *Climate of the Past*, 10, 903–920, [10.5194/cp-10-903-2014](https://doi.org/10.5194/cp-10-903-2014), 2014.
- Berben, S. M., Dokken, T. M., Abbott, P. M., Cook, E., Sadatzki, H., Simon, M. H., and Jansen, E.: Independent tephrochronological evidence for rapid and synchronous oceanic and atmospheric temperature rises over the Greenland stadial-interstadial transitions between ca. 32 and 40 ka b2k. *Quaternary Science Reviews*, 236, 106 277, [10.1016/j.quascirev.2020.106277](https://doi.org/10.1016/j.quascirev.2020.106277), 2020.

- Bereiter, B., Eggleston, S., Schmitt, J., Nehrbass-Ahles, C., Stocker, T. F., Fischer, H., Kipfstuhl, S., and Chappellaz, J.: Revision of the EPICA Dome C CO<sub>2</sub> record from 800 to 600-kyr before present. *Geophysical Research Letters*, 42, 542–549, [10.1002/2014GL061957](https://doi.org/10.1002/2014GL061957), 2015.
- Bochow, N., Poltronieri, A., Robinson, A., Montoya, M., Rypdal, M., and Boers, N.: Over-shooting the critical threshold for the Greenland ice sheet. submitted to *Nature*, preprint, <https://doi.org/10.21203/rs.3.rs-2498932/v1>, 2023.
- Boers, N.: Observation-based early-warning signals for a collapse of the Atlantic Meridional Overturning Circulation. *Nature Climate Change*, 11, 680–688, [10.1038/s41558-021-01097-4](https://doi.org/10.1038/s41558-021-01097-4), 2021.
- Boers, N. and Rypdal, M.: Critical slowing down suggests that the western Greenland Ice Sheet is close to a tipping point. *Proceedings of the National Academy of Sciences of the United States of America*, 118, e2024192 118, [10.1073/pnas.2024192118](https://doi.org/10.1073/pnas.2024192118), 2021.
- Boers, N., Marwan, N., Barbosa, H. M., and Kurths, J.: A deforestation-induced tipping point for the South American monsoon system. *Scientific Reports*, 7, 41 489, [10.1038/srep41489](https://doi.org/10.1038/srep41489), 2017.
- Boers, N., Ghil, M., and Rousseau, D. D.: Ocean circulation, ice shelf, and sea ice interactions explain Dansgaard–Oeschger cycles. *Proceedings of the National Academy of Sciences of the United States of America*, 115, E11 005–E11 014, [10.1073/pnas.1802573115](https://doi.org/10.1073/pnas.1802573115), 2018.
- Boers, N., Ghil, M., and Stocker, T. F.: Theoretical and paleoclimatic evidence for abrupt transitions in the Earth system. *Environmental Research Letters*, 17, 093 006, [10.1088/1748-9326/ac8944](https://doi.org/10.1088/1748-9326/ac8944), 2022.
- Böhm, E., Lippold, J., Gutjahr, M., Frank, M., Blaser, P., Antz, B., Fohlmeister, J., Frank, N., Andersen, M. B., and Deininger, M.: Strong and deep Atlantic meridional overturning circulation during the last glacial cycle. *Nature*, 517, 73–76, [10.1038/nature14059](https://doi.org/10.1038/nature14059), 2015.
- Bond, G., Heinrich, H., Broecker, W., Labeyrie, L., Mcmanus, J., Andrews, J., Huonll, S., Jantschik, R., Clasen, S., Simet, C., Tedesco, K., Klas, M., Bonanitt, G., and Ivy, S.: Evidence for massive discharges of icebergs into the North Atlantic ocean during the last glacial period. *Nature*, 360, 1668–1672, [10.1038/360245a0](https://doi.org/10.1038/360245a0), 1992.
- Bond, G., Broecker, W., Johnsen, S., McManus, J., Labeyrie, L., Jouzel, J., and Bonani, G.: Correlations between climate records from North Atlantic sediments and Greenland ice. *Nature*, 365, 143–147, [10.1038/365143a0](https://doi.org/10.1038/365143a0), 1993.
- Boulton, C. A., Lenton, T. M., and Boers, N.: Pronounced loss of Amazon rainforest resilience since the early 2000s. *Nature Climate Change*, 12, 271–278, [10.1038/s41558-022-01287-8](https://doi.org/10.1038/s41558-022-01287-8), 2022.
- Briggs, H.: Amazon Rainforest Reaching Tipping Point, Researchers say. BBC News, <https://www.bbc.com/news/science-environment-60650415>, (last accessed 2023-05-23), 2022.
- Broecker, W. S., Peteet, D. M., and Rind, D.: Does the ocean-atmosphere system have more than one stable mode of operation? *Nature*, 315, 21–26, [10.1038/315021a0](https://doi.org/10.1038/315021a0), 1985.
- Brovkin, V., Brook, E., Williams, J. W., Bathiany, S., Lenton, T. M., Barton, M., DeConto, R. M., Donges, J. F., Ganopolski, A., McManus, J., Praetorius, S., de Vernal, A., Abe-Ouchi, A., Cheng, H., Claussen, M., Crucifix, M., Gallopín, G., Iglesias, V., Kaufman, D. S., Kleinen, T., Lambert, F., van der Leeuw, S., Liddy, H., Loutre, M.-f., McGee, D., Rehfeld, K., Rhodes, R., Seddon, A. W. R., Trauth, M. H., Vanderveken, L., and Yu, Z.: Past abrupt changes, tipping points and cascading impacts in the Earth system. *Nature Geoscience*, 14, 550–558, [10.1038/s41561-021-00790-5](https://doi.org/10.1038/s41561-021-00790-5), 2021.
- Buckley, M. W. and Marshall, J.: Observations, inferences, and mechanisms of the Atlantic Meridional Overturning Circulation: A review. *Reviews of Geophysics*, 54, 5–63, [10.1002/2015RG000493](https://doi.org/10.1002/2015RG000493), 2016.
- Budsky, A., Wassenburg, J. A., Mertz-Kraus, R., Spötl, C., Jochum, K. P., Gibert, L., and Scholz, D.: Western Mediterranean Climate Response to Dansgaard/Oeschger Events: New Insights From Speleothem Records. *Geophysical Research Letters*, 46, 9042–9053, [10.1029/2019GL084009](https://doi.org/10.1029/2019GL084009), 2019.

- Buizert, C., Adrian, B., Ahn, J., Albert, M., Alley, R. B., Baggenstos, D., Bauska, T. K., Bay, R. C., Bencivengo, B. B., Bentley, C. R., Brook, E. J., Chellman, N. J., Clow, G. D., Cole-Dai, J., Conway, H., Cravens, E., Cuffey, K. M., Dunbar, N. W., Edwards, J. S., Fegyveresi, J. M., Ferris, D. G., Fitzpatrick, J. J., Fudge, T. J., Gibson, C. J., Gkinis, V., Goetz, J. J., Gregory, S., Hargreaves, G. M., Iverson, N., Johnson, J. A., Jones, T. R., Kalk, M. L., Kippenhan, M. J., Koffman, B. G., Kreutz, K., Kuhl, T. W., Lebar, D. A., Lee, J. E., Marcott, S. A., Markle, B. R., Maselli, O. J., McConnell, J. R., McGwire, K. C., Mitchell, L. E., Mortensen, N. B., Neff, P. D., Nishiizumi, K., Nunn, R. M., Orsi, A. J., Pasteris, D. R., Pedro, J. B., Pettit, E. C., Price, P. B., Priscu, J. C., Rhodes, R. H., Rosen, J. L., Schauer, A. J., Schoenemann, S. W., Sendelbach, P. J., Severinghaus, J. P., Shturmakov, A. J., Sigl, M., Slawny, K. R., Souney, J. M., Sowers, T. A., Spencer, M. K., Steig, E. J., Taylor, K. C., Twickler, M. S., Vaughn, B. H., Voigt, D. E., Waddington, E. D., Welten, K. C., Wendricks, A. W., White, J. W., Winstrup, M., Wong, G. J., and Woodruff, T. E.: Precise inter-polar phasing of abrupt climate change during the last ice age. *Nature*, 520, 661–665, [10.1038/nature14401](https://doi.org/10.1038/nature14401), 2015a.
- Buizert, C., Cuffey, K. M., Severinghaus, J. P., Baggenstos, D., Fudge, T. J., Steig, E. J., Markle, B. R., Winstrup, M., Rhodes, R. H., Brook, E. J., Sowers, T. A., Clow, G. D., Cheng, H., Edwards, R. L., Sigl, M., McConnell, J. R., and Taylor, K. C.: The WAIS Divide deep ice core WD2014 chronology &ndash; Part 1: Methane synchronization (68-31 ka BP) and the gas age-ice age difference. *Climate of the Past*, 11, 153–173, [10.5194/cp-11-153-2015](https://doi.org/10.5194/cp-11-153-2015), 2015b.
- Buizert, C., Sigl, M., Severi, M., Markle, B. R., Wettstein, J. J., McConnell, J. R., Pedro, J. B., Sodemann, H., Goto-Azuma, K., Kawamura, K., Fujita, S., Motoyama, H., Hirabayashi, M., Uemura, R., Stenni, B., Parrenin, F., He, F., Fudge, T. J., and Steig, E. J.: Abrupt ice-age shifts in southern westerly winds and Antarctic climate forced from the north. *Nature*, 563, 681–685, [10.1038/s41586-018-0727-5](https://doi.org/10.1038/s41586-018-0727-5), 2018.
- Capron, E., Rasmussen, S. O., Popp, T. J., Erhardt, T., Fischer, H., Landais, A., Pedro, J. B., Vettoretti, G., Grinsted, A., Gkinis, V., Vaughn, B., Svensson, A., Vinther, B. M., and White, J. W.: The anatomy of past abrupt warmings recorded in Greenland ice. *Nature Communications*, 12, [10.1038/s41467-021-22241-w](https://doi.org/10.1038/s41467-021-22241-w), 2021.
- Caraballo, T. and Han, X.: *Applied Nonautonomous and Random Dynamical Systems*. Springer Cham, Cham (Switzerland), 1 edn., [10.1007/978-3-319-49247-6](https://doi.org/10.1007/978-3-319-49247-6), 2017.
- Cardoso, D., Särkinen, T., Alexander, S., Amorim, A. M., Bittrich, V., Celis, M., Daly, D. C., Fiaschi, P., Funk, V. A., Giacomini, L. L., Goldenberg, R., Heiden, G., Iganci, J., Kelloff, C. L., Knapp, S., De Lima, H. C., Machado, A. F., Dos Santos, R. M., Mello-Silva, R., Michelangeli, F. A., Mitchell, J., Moonlight, P., De Moraes, P. L. R., Mori, S. A., Nunes, T. S., Pennington, T. D., Pirani, J. R., Prance, G. T., De Queiroz, L. P., Rapini, A., Riina, R., Rincon, C. A. V., Roque, N., Shimizu, G., Sobral, M., Stehmann, J. R., Stevens, W. D., Taylor, C. M., Trovó, M., Van Den Berg, C., Van Der Werff, H., Viana, P. L., Zartman, C. E., and Forzza, R. C.: Amazon plant diversity revealed by a taxonomically verified species list. *Proceedings of the National Academy of Sciences of the United States of America*, 114, 10 695–10 700, [10.1073/pnas.1706756114](https://doi.org/10.1073/pnas.1706756114), 2017.
- Carrington, D.: World on brink of five ‘disastrous’ climate tipping points, study finds. *The Guardian*, <https://www.theguardian.com/environment/2022/sep/08/world-on-brink-five-climate-tipping-points-study-finds>, (last accessed 2023-05-23), 2022.
- Cessi, P.: A Simple Box Model of Stochastically Forced Thermohaline Flow. *Journal of Physical Oceanography*, 24, 1911–1920, [10.1175/1520-0485\(1994\)024<1911:ASBMOS>2.0.CO;2](https://doi.org/10.1175/1520-0485(1994)024<1911:ASBMOS>2.0.CO;2), 1994.
- Cheng, H., Sinha, A., Cruz, F., Wang, X., Edwards, R., D’Horta, F., Ribas, C., Vuille, M., Stott, L., and Auler, A.: NOAA/WDS Paleoclimatology - Northern Peru 250KYr Stalagmite Stable Isotope Data [dataset: condor2013elc-b]. NOAA National Centers for Environmental Information, [doi.org/10.25921/xr55-1n14](https://doi.org/10.25921/xr55-1n14), (last accessed 2023-05-23), 2013a.
- Cheng, H., Sinha, A., Cruz, F. W., Wang, X., Edwards, R. L., D’Horta, F. M., Ribas, C. C., Vuille, M., Stott, L. D., and Auler, A. S.: Climate change patterns in Amazonia and biodiversity. *Nature Communications*, 4, 1411, [10.1038/ncomms2415](https://doi.org/10.1038/ncomms2415), 2013b.

- Cheng, H., Edwards, R. L., Sinha, A., Spötl, C., Yi, L., Chen, S., Kelly, M., Kathayat, G., Wang, X., Li, X., Kong, X., Wang, Y., Ning, Y., and Zhang, H.: The Asian monsoon over the past 640,000 years and ice age terminations. *Nature*, 534, 640–646, [10.1038/nature18591](https://doi.org/10.1038/nature18591), 2016.
- Cimatoribus, A. A., Driijfhout, S. S., Livina, V., and Van Der Schrier, G.: Dansgaard-Oeschger events: Bifurcation points in the climate system. *Climate of the Past*, 9, 323–333, [10.5194/cp-9-323-2013](https://doi.org/10.5194/cp-9-323-2013), 2013.
- Clark, P. U., Hostetler, S. W., Meissner, K. J., Pisias, N. G., and Schmittner, A.: Mechanisms for an ~7-Kyr Climate and Sea-Level Oscillation During Marine Isotope Stage 3. in: *Ocean Circulation: Mechanisms and Impacts—Past and Future Changes of Meridional Overturning*, pp. 209–246, American Geophysical Union (AGU), [10.1029/173GM15](https://doi.org/10.1029/173GM15), 2007.
- Corrick, E. C., Drysdale, R. N., Hellstrom, J. C., Capron, E., Rasmussen, S. O., Zhang, X., Fleitmann, D., Couchoud, I., Wolff, E., and Monsoon, S. A.: Synchronous timing of abrupt climate changes during the last glacial period. *Science*, 369, 963–969, [10.1126/science.aay5538](https://doi.org/10.1126/science.aay5538), 2020.
- Cox, P. M., Betts, R. A., Collins, M., Harris, P. P., Huntingford, C., and Jones, C. D.: Amazonian forest dieback under climate-carbon cycle projections for the 21st century. *Theoretical and Applied Climatology*, 78, 137–156, [10.1007/s00704-004-0049-4](https://doi.org/10.1007/s00704-004-0049-4), 2004.
- Dakos, V., Scheffer, M., Van Nes, E. H., Brovkin, V., Petoukhov, V., and Held, H.: Slowing down as an early warning signal for abrupt climate change. *Proceedings of the National Academy of Sciences of the United States of America*, 105, 14 308–14 312, [10.1073/pnas.0802430105](https://doi.org/10.1073/pnas.0802430105), 2008.
- Dansgaard, W.: Stable isotopes in precipitation. *Tellus A: Dynamic Meteorology and Oceanography*, 16, 436–468, [10.3402/tellusa.v16i4.8993](https://doi.org/10.3402/tellusa.v16i4.8993), 1964.
- Dansgaard, W., Johnsen, S. J., Møller, J., and Langway, C. C.: One thousand centuries of climatic record from Camp Century on the Greenland ice sheet. *Science*, 166, 377–381, [10.1126/science.166.3903.377](https://doi.org/10.1126/science.166.3903.377), 1969.
- Dansgaard, W., Clausen, H. B., Gundestrup, N., Hammer, C. U., Johnsen, S. F., Kristinsdottir, P. M., and Reeh, N.: A New Greenland Deep Ice Core. *Science*, 218, 1273–1277, [10.1126/science.218.4579.1273](https://doi.org/10.1126/science.218.4579.1273), 1982.
- Dansgaard, W., Johnsen, S., Clausen, H., Dahl-Jensen, D., Gundestrup, N., Hammer, C., and Oeschger, H.: North Atlantic climatic oscillations revealed by deep Greenland ice cores. in: *Climate processes and climate sensitivity*, edited by Hansen, J. and Takahashi, T., pp. 288–298, American Geophysical Union (AGU), [10.1029/GM029p0288](https://doi.org/10.1029/GM029p0288), 1984.
- Dansgaard, W., Johnsen, S. J., Clausen, H. B., Dahl-Jensen, D., Gundestrup, N. S., Hammer, C. U., Hvidberg, C. S., Steffensen, J. P., Sveinbjörnsdottir, A. E., Jouzel, J., and Bond, G.: Evidence for general instability of past climate from a 250-kyr ice-core record. *Nature*, 364, 218–220, [10.1038/364218a0](https://doi.org/10.1038/364218a0), 1993.
- DeMenocal, P., Ortiz, J., Guilderson, T., Adkins, J., Sarnthein, M., Baker, L., and Yarusinsky, M.: Abrupt onset and termination of the African Humid Period: rapid climate responses to gradual insolation forcing. *Quaternary Science Reviews*, 19, 347–361, [10.1016/S0277-3791\(99\)00081-5](https://doi.org/10.1016/S0277-3791(99)00081-5), 2000.
- Dijkstra, H. A.: *Nonlinear climate dynamics*. Cambridge University Press, Cambridge, UK, 1 edn., [10.1017/CBO9781139034135](https://doi.org/10.1017/CBO9781139034135), 2013.
- Dijkstra, H. A. and Weijer, W.: Stability of the global ocean circulation: Basic bifurcation diagrams. *Journal of Physical Oceanography*, 35, 933–948, [10.1175/JPO2726.1](https://doi.org/10.1175/JPO2726.1), 2005.
- Ditlevsen, P. D.: Observation of  $\alpha$ -stable noise induced millennial climate changes from an ice-core record. *Geophysical Research Letters*, 26, 1441–1444, [10.1029/1999GL900252](https://doi.org/10.1029/1999GL900252), 1999.
- Ditlevsen, P. D., Kristensen, M. S., and Andersen, K. K.: The recurrence time of Dansgaard-Oeschger events and limits on the possible periodic component. *Journal of Climate*, 18, 2594–2603, [10.1175/JCLI3437.1](https://doi.org/10.1175/JCLI3437.1), 2005.

- Ditlevsen, P. D., Andersen, K. K., and Svensson, A.: The DO-climate events are probably noise induced: Statistical investigation of the claimed 1470 years cycle. *Climate of the Past*, 3, 129–134, [10.5194/cp-3-129-2007](https://doi.org/10.5194/cp-3-129-2007), 2007.
- Dokken, T. M., Nisancioglu, K. H., Li, C., Battisti, D. S., and Kissel, C.: Dansgaard-Oeschger cycles: Interactions between ocean and sea ice intrinsic to the Nordic seas. *Paleoceanography*, 28, 491–502, [10.1002/palo.20042](https://doi.org/10.1002/palo.20042), 2013.
- Drijfhout, S., Gleeson, E., Dijkstra, H. A., and Livina, V.: Spontaneous abrupt climate change due to an atmospheric blocking-Sea-Ice-Ocean feedback in an unforced climate model simulation. *Proceedings of the National Academy of Sciences of the United States of America*, 110, 19 713–19 718, [10.1073/pnas.1304912110](https://doi.org/10.1073/pnas.1304912110), 2013.
- Drijfhout, S., Bathiany, S., Beaulieu, C., Brovkin, V., Claussen, M., Huntingford, C., Scheffer, M., Sgubin, G., and Swingedouw, D.: Catalogue of abrupt shifts in Intergovernmental Panel on Climate Change climate models. *Proceedings of the National Academy of Sciences of the United States of America*, 112, E5777–E5786, [10.1073/pnas.1511451112](https://doi.org/10.1073/pnas.1511451112), 2015.
- Eisenman, I.: Factors controlling the bifurcation structure of sea ice retreat. *Journal of Geophysical Research Atmospheres*, 117, D01 111, [10.1029/2011JD016164](https://doi.org/10.1029/2011JD016164), 2012.
- Erhardt, T., Capron, E., Olander Rasmussen, S., Schüpbach, S., Bigler, M., Adolphi, F., and Fischer, H.: Decadal-scale progression of the onset of Dansgaard-Oeschger warming events. *Climate of the Past*, 15, 811–825, [10.5194/cp-15-811-2019](https://doi.org/10.5194/cp-15-811-2019), 2019.
- Erhardt, T., Bigler, M., Federer, U., Gfeller, G., Leuenberger, D., Stowasser, O., Röthlisberger, R., Schüpbach, S., Ruth, U., Twarloh, B., Wegner, A., Goto-Azuma, K., Takayuki, K., Kjær, H. A., Vallenga, P. T., Siggaard-Andersen, M.-L., Hansson, M. E., Benton, A. K., Fleet, L. G., Mulvaney, R., Thomas, E. R., Abram, N. J., Stocker, T. F., and Fischer, H.: High resolution aerosol concentration data from the Greenland NorthGRIP and NEEM deep ice cores [dataset]. *Pangea*, [10.1594/PANGAEA.935838](https://doi.org/10.1594/PANGAEA.935838), (last accessed 2023-05-23), 2021.
- Ezat, M. M., Rasmussen, T. L., and Groeneveld, J.: Persistent intermediate water warming during cold stadials in the southeastern Nordic seas during the past 65 k.y. *Geology*, 42, 663–666, [10.1130/G35579.1](https://doi.org/10.1130/G35579.1), 2014.
- Feldmann, J. and Levermann, A.: Collapse of the West Antarctic Ice Sheet after local destabilization of the Amundsen Basin. *Proceedings of the National Academy of Sciences of the United States of America*, 112, 14 191–14 196, [10.1073/pnas.1512482112](https://doi.org/10.1073/pnas.1512482112), 2015.
- Fischer, H., Siggaard-Andersen, M. L., Ruth, U., Röthlisberger, R., and Wolff, E.: Glacial/interglacial changes in mineral dust and sea-salt records in polar ice cores: Sources, transport, and deposition. *Reviews of Geophysics*, 45, RG1002, [10.1029/2005RG000192](https://doi.org/10.1029/2005RG000192), 2007.
- FitzHugh, R.: Impulses and Physiological States in Theoretical Models of Nerve Membrane. *Biophysical Journal*, 1, 445–466, [10.1016/S0006-3495\(61\)86902-6](https://doi.org/10.1016/S0006-3495(61)86902-6), 1961.
- Fleitmann, D., Cheng, H., Badertscher, S., Edwards, R., Mudelsee, M., Göktürk, O., Fankhauser, A., Pickering, R., Raible, C., Matter, A., Kramers, J., and Tüysüz, O.: NOAA/WDS Paleoclimatology - Fleitmann et al. 2009 Sofular Cave, Turkey 50KYr Stable Isotope Data [dataset]. NOAA National Centers for Environmental Information, [10.25921/3hwz-z793](https://doi.org/10.25921/3hwz-z793), (last accessed 2023-05-09), 2009a.
- Fleitmann, D., Cheng, H., Badertscher, S., Edwards, R. L., Mudelsee, M., Göktürk, O. M., Fankhauser, A., Pickering, R., Raible, C. C., Matter, A., Kramers, J., and Tüysüz, O.: Timing and climatic impact of Greenland interstadials recorded in stalagmites from northern Turkey. *Geophysical Research Letters*, 36, L19 707, [10.1029/2009GL040050](https://doi.org/10.1029/2009GL040050), 2009b.
- Friedrich, T., Timmermann, A., Menviel, L., Elison Timm, O., Mouchet, A., and Roche, D. M.: The mechanism behind internally generated centennial-to-millennial scale climate variability in an earth system model of intermediate complexity. *Geoscientific Model Development*, 3, 377–389, [10.5194/gmd-3-377-2010](https://doi.org/10.5194/gmd-3-377-2010), 2010.

- Fuhrer, K., Wolff, E. W., and Johnsen, S. J.: Timescales for dust variability in the Greenland Ice Core Project (GRIP) ice core in the last 100,000 years. *Journal of Geophysical Research: Atmospheres*, 104, 31 043–31 052, [10.1029/1999JD900929](https://doi.org/10.1029/1999JD900929), 1999.
- Ganopolski, A. and Rahmstorf, S.: Rapid changes of glacial climate simulated in a coupled climate model. *Nature*, 409, 153–158, [10.1038/35051500](https://doi.org/10.1038/35051500), 2001.
- Ganopolski, A. and Rahmstorf, S.: Abrupt Glacial Climate Changes due to Stochastic Resonance. *Physical Review Letters*, 88, 038 501, [10.1103/PhysRevLett.88.038501](https://doi.org/10.1103/PhysRevLett.88.038501), 2002.
- Gardiner, C.: *Handbook of stochastic methods: For Physics, Chemistry and the Natural Sciences*. Springer-Verlag, Berlin (Germany), 2. edn., 1985.
- Gatti, L. V., Basso, L. S., Miller, J. B., Gloor, M., Gatti Domingues, L., Cassol, H. L., Tejada, G., Aragão, L. E., Nobre, C., Peters, W., Marani, L., Arai, E., Sanches, A. H., Corrêa, S. M., Anderson, L., Von Randow, C., Correia, C. S., Crispim, S. P., and Neves, R. A.: Amazonia as a carbon source linked to deforestation and climate change. *Nature*, 595, 388–393, [10.1038/s41586-021-03629-6](https://doi.org/10.1038/s41586-021-03629-6), 2021.
- Genty, D., Blamart, D., Ouahdi, R., Gilmour, M., Baker, A., Jouzel, J., and Van-Exter, S.: Precise dating of Dansgaard-Oeschger climate oscillations in western Europe from stalagmite data. *Nature*, 421, 833–837, [10.1038/nature01391](https://doi.org/10.1038/nature01391), 2003.
- Gkinis, V., Simonsen, S. B., Buchardt, S. L., White, J. W., and Vinther, B. M.: Water isotope diffusion rates from the NorthGRIP ice core for the last 16,000 years - Glaciological and paleoclimatic implications. *Earth and Planetary Science Letters*, 405, 132–141, [10.1016/j.epsl.2014.08.022](https://doi.org/10.1016/j.epsl.2014.08.022), 2014.
- Gottschalk, J., Skinner, L. C., Misra, S., Waelbroeck, C., Menviel, L., and Timmermann, A.: Abrupt changes in the southern extent of North Atlantic Deep Water during Dansgaard-Oeschger events. *Nature Geoscience*, 8, 950–954, [10.1038/ngeo2558](https://doi.org/10.1038/ngeo2558), 2015.
- Gottwald, G. A.: A model for Dansgaard–Oeschger events and millennial-scale abrupt climate change without external forcing. *Climate Dynamics*, 56, 227–243, [10.1007/s00382-020-05476-z](https://doi.org/10.1007/s00382-020-05476-z), 2021.
- Habekuß, F.: Auf Katastrophenkurs. *Zeit*, <https://www.zeit.de/2022/38/klimakrise-klimawandel-kippunkte-studie>, (last accessed 2023-05-23), 2022.
- Hassanibesheli, F., Boers, N., and Kurths, J.: Reconstructing complex system dynamics from time series: a method comparison. *New Journal of Physics*, 22, [10.1088/1367-2630/ab9ce5](https://doi.org/10.1088/1367-2630/ab9ce5), 2020.
- Hasselmann, K.: Stochastic climate models: Part I. Theory. *Tellus A: Dynamic Meteorology and Oceanography*, 28, 473–485, [10.3402/tellusa.v28i6.11316](https://doi.org/10.3402/tellusa.v28i6.11316), 1976.
- Haywood, A. M., Valdes, P. J., Aze, T., Barlow, N., Burke, A., Dolan, A. M., von der Heydt, A. S., Hill, D. J., Jamieson, S. S., Otto-Bliesner, B. L., Salzmann, U., Saupe, E., and Voss, J.: What can Palaeoclimate Modelling do for you? *Earth Systems and Environment*, 3, 1–18, [10.1007/s41748-019-00093-1](https://doi.org/10.1007/s41748-019-00093-1), 2019.
- Heinrich, H.: Origin and consequences of cyclic ice rafting in the Northeast Atlantic Ocean during the past 130,000 years. *Quaternary Research*, 29, 142–152, [10.1016/0033-5894\(88\)90057-9](https://doi.org/10.1016/0033-5894(88)90057-9), 1988.
- Hemming, S. R.: Heinrich events: Massive late Pleistocene detritus layers of the North Atlantic and their global climate imprint. *Reviews of Geophysics*, 42, [10.1029/2003RG000128](https://doi.org/10.1029/2003RG000128), 2004.
- Henry, L., McManus, J., Curry, W., Roberts, N., Piotrowski, A., and Keigwin, L.: NOAA/WDS Paleoclimatology - Bermuda Rise High Resolution 60-25KYrBP Uranium Series Data [dataset: henry2016pa-th]. NOAA National Centers for Environmental Information, [10.25921/97wv-5p13](https://doi.org/10.25921/97wv-5p13), (last accessed 2023-05-09), 2016a.
- Henry, L. G., McManus, J. F., Curry, W. B., Roberts, N. L., Piotrowski, A. M., and Keigwin, L. D.: North Atlantic ocean circulation and abrupt climate change during the last glaciation. *Science*, 353, 470–474, [10.1126/science.aaf5529](https://doi.org/10.1126/science.aaf5529), 2016b.

- Hoegh-Guldberg, O., D.Jacob, Taylor, M., Bindi, M., Brown, S., Camilloni, I., Diedhiou, A., Djalante, R., Ebi, K., Engelbrecht, F., Guiot, J., Hijioka, Y., Mehrotra, S., Payne, A., Seneviratne, S., Thomas, A., Warren, R., and Zhou, G.: Impacts of 1.5°C Global Warming on Natural and Human Systems. in: *Global Warming of 1.5°C. An IPCC Special Report on the impacts of global warming of 1.5°C above pre-industrial levels and related global greenhouse gas emission pathways, in the context of strengthening the global response to the threat of climate change*, edited by Masson-Delmotte, V., Zhai, P., Pörtner, H.-O., Roberts, D., Skea, J., Shukla, P., Pirani, A., Moufouma-Okia, W., Péan, C., Pidcock, R., Connors, S., Matthews, J., Chen, Y., Zhou, X., Gomis, M., Lonnoy, E., Maycock, T., Tignor, M., and Waterfield, T., pp. 175–312, Cambridge University Press, Cambridge (UK) and New York (USA), [10.1017/9781009157940.005](https://doi.org/10.1017/9781009157940.005), 2018.
- Hoff, U., Rasmussen, T. L., Stein, R., Ezat, M. M., and Fahl, K.: Sea ice and millennial-scale climate variability in the Nordic seas 90 kyr ago to present. *Nature Communications*, 7, 12 247, [10.1038/ncomms12247](https://doi.org/10.1038/ncomms12247), 2016.
- Huber, C., Leuenberger, M., Spahni, R., Flückiger, J., Schwander, J., Stocker, T. F., Johnsen, S., Landais, A., and Jouzel, J.: Isotope calibrated Greenland temperature record over Marine Isotope Stage 3 and its relation to CH<sub>4</sub>. *Earth and Planetary Science Letters*, 243, 504–519, [10.1016/j.epsl.2006.01.002](https://doi.org/10.1016/j.epsl.2006.01.002), 2006.
- Hutchinson, D. K., Coxall, H. K., Lunt, D. J., Steinthorsdottir, M., De Boer, A. M., Baatsen, M., Von Der Heydt, A., Huber, M., Kennedy-Asser, A. T., Kunzmann, L., Ladant, J. B., Lear, C. H., Moraweck, K., Pearson, P. N., Piga, E., Pound, M. J., Salzmann, U., Scher, H. D., Sijp, W. P., Śliwińska, K. K., Wilson, P. A., and Zhang, Z.: The Eocene-Oligocene transition: A review of marine and terrestrial proxy data, models and model-data comparisons. *Climate of the Past*, 17, 269–315, [10.5194/cp-17-269-2021](https://doi.org/10.5194/cp-17-269-2021), 2021.
- Izumi, K., Armstrong, E., and Valdes, P.: Global footprints of dansgaard-oeschger oscillations in a GCM. *Quaternary Science Reviews*, 305, 108 016, [10.1016/j.quascirev.2023.108016](https://doi.org/10.1016/j.quascirev.2023.108016), 2023.
- Jackson, L. C. and Wood, R. A.: Timescales of AMOC decline in response to fresh water forcing. *Climate Dynamics*, 51, 1333–1350, [10.1007/s00382-017-3957-6](https://doi.org/10.1007/s00382-017-3957-6), 2018.
- Jackson, L. C., Kahana, R., Graham, T., Ringer, M. A., Woollings, T., Mecking, J. V., and Wood, R. A.: Global and European climate impacts of a slowdown of the AMOC in a high resolution GCM. *Climate Dynamics*, 45, 3299–3316, [10.1007/s00382-015-2540-2](https://doi.org/10.1007/s00382-015-2540-2), 2015.
- Jackson, L. C., de Asenjo, E., Bellomo, K., Danabasoglu, G., Haak, H., Hu, A., Jungclaus, J., Lee, W., Meccia, V. L., Saenko, O., Shao, A., and Swingedouw, D.: Understanding AMOC stability: the North Atlantic Hosing Model Intercomparison Project. *Geoscientific Model Development*, 16, 1975–1995, [10.5194/gmd-16-1975-2023](https://doi.org/10.5194/gmd-16-1975-2023), 2023.
- Johnsen, S. J., Clausen, H. B., Dansgaard, W., Fuhrer, K., Gundestrup, N., Hammer, C. U., Iversen, P., Jouzel, J., Stauffer, B., and Steffensen, J.: Irregular glacial interstadials recorded in a new Greenland ice core. *Nature*, 359, 311–313, [10.1038/359311a0](https://doi.org/10.1038/359311a0), 1992a.
- Johnsen, S. J., Clausen, H. B., Dansgaard, W., Gundestrup, N. S., Hansson, M., Jonsson, P., Steffensen, J. P., and Sveinbjörnsdottir, A. E.: A "deep" ice core from east Greenland. *MoG Geoscience*, 29, 1992b.
- Jones, M. W., Peters, G. P., Gasser, T., Andrew, R. M., Schwingshackl, C., Gütschow, J., Houghton, R. A., Friedlingstein, P., Pongratz, J., and Le Quééré, C.: National contributions to climate change due to historical emissions of carbon dioxide, methane and nitrous oxide [dataset]. [10.5281/zenodo.7636699](https://doi.org/10.5281/zenodo.7636699), (last accessed 2023-04-01), 2023a.
- Jones, M. W., Peters, G. P., Gasser, T., Andrew, R. M., Schwingshackl, C., Gütschow, J., Houghton, R. A., Friedlingstein, P., Pongratz, J., and Quééré, C. L.: National contributions to climate change due to historical emissions of carbon dioxide , methane , and nitrous oxide since 1850. *Sci Data*, 10, 155, [10.1038/s41597-023-02041-1](https://doi.org/10.1038/s41597-023-02041-1), 2023b.

- Jouzel, J.: A brief history of ice core science over the last 50 yr. *Climate of the Past*, 9, 2525–2547, [10.5194/cp-9-2525-2013](https://doi.org/10.5194/cp-9-2525-2013), 2013.
- Jouzel, J., Alley, R. B., Cuffey, K. M., Dansgaard, W., Grootes, P., Hoffmann, G., Johnsen, S. J., Koster, R. D., Peel, D., Shuman, C. A., Stievenard, M., Stuiver, M., and White, J.: Validity of the temperature reconstruction from water isotopes in ice cores. *Journal of Geophysical Research: Oceans*, 102, 26 471–26 487, [10.1029/97JC01283](https://doi.org/10.1029/97JC01283), 1997.
- Kanner, L. C., Burns, S. J., Cheng, H., and Edwards, R. L.: High-Latitude Forcing of the South American Summer Monsoon During the Last Glacial. *Science*, 335, 570–573, [10.1126/science.1213397](https://doi.org/10.1126/science.1213397), 2012.
- Kaplan, S.: A critical ocean system may be heading for collapse due to climate change, study finds. *The Washington Post*, <https://www.washingtonpost.com/climate-environment/2021/08/05/change-ocean-collapse-atlantic-meridional/>, (last accessed 2023-05-23), 2021.
- Kemp, L., Xu, C., Depledge, J., Ebi, K. L., Gibbins, G., Kohler, T. A., Rockstrom, J., Scheffer, M., Schellnhuber, H. J., Steffen, W., and Lenton, T. M.: Climate Endgame: Exploring catastrophic climate change scenarios. *Proceedings of the National Academy of Sciences of the United States of America*, 119, e2108146 119, [10.1073/pnas.2108146119](https://doi.org/10.1073/pnas.2108146119), 2022.
- Kindler, P., Guillevic, M., Baumgartner, M., Schwander, J., Landais, A., and Leuenberger, M.: Temperature reconstruction from 10 to 120 kyr b2k from the NGRIP ice core. *Climate of the Past*, 10, 887–902, [10.5194/cp-10-887-2014](https://doi.org/10.5194/cp-10-887-2014), 2014.
- Kjær, H. A., Harlan, M., Vallelonga, P., Svensson, A., Blunier, T., Sowers, T., Menking, J. A., de Campo, A., Venkatesh, J., Liisberg, J., Soestmeyer, D., Morris, V., Vaughn, B., and Vinther, B.: Forty years later: High resolution continuous flow analysis of the Dye3 ice core. [10.5194/egusphere-egu21-11820](https://doi.org/10.5194/egusphere-egu21-11820), (last accessed 2023-05-23), 2021.
- Kleppin, H., Jochum, M., Otto-Bliesner, B., Shields, C. A., and Yeager, S.: Stochastic atmospheric forcing as a cause of Greenland climate transitions. *Journal of Climate*, 28, 7741–7763, [10.1175/JCLI-D-14-00728.1](https://doi.org/10.1175/JCLI-D-14-00728.1), 2015.
- Kuniyoshi, Y., Abe-Ouchi, A., Sherriff-Tadano, S., Chan, W. L., and Saito, F.: Effect of Climatic Precession on Dansgaard-Oeschger-Like Oscillations. *Geophysical Research Letters*, 49, e2021GL095 695, [10.1029/2021GL095695](https://doi.org/10.1029/2021GL095695), 2022.
- Kwasniok, F.: Analysis and modelling of glacial climate transitions using simple dynamical systems. *Philosophical Transactions of the Royal Society A: Mathematical, Physical and Engineering Sciences*, 371, 20110 472, [10.1098/rsta.2011.0472](https://doi.org/10.1098/rsta.2011.0472), 2013.
- Kwasniok, F. and Lohmann, G.: A stochastic nonlinear oscillator model for glacial millennial-scale climate transitions derived from ice-core data. *Nonlinear Processes in Geophysics*, 19, 595–603, [10.5194/npg-19-595-2012](https://doi.org/10.5194/npg-19-595-2012), 2012.
- Landais, A., Jouzel, J., Masson-Delmotte, V., and Caillon, N.: Large temperature variations over rapid climatic events in Greenland: a method based on air isotopic measurements. *Comptes Rendus - Geoscience*, 337, 947–956, [10.1016/j.crte.2005.04.003](https://doi.org/10.1016/j.crte.2005.04.003), 2005.
- Lapola, D. M., Pinho, P., Quesada, C. A., Strassburg, B. B., Rammig, A., Kruijt, B., Brown, F., Ometto, J. P., Premebida, A., Marengo, J. A., Vergara, W., and Nobre, C. A.: Limiting the high impacts of Amazon forest dieback with no-regrets science and policy action. *Proceedings of the National Academy of Sciences of the United States of America*, 115, 11 671–11 679, [10.1073/pnas.1721770115](https://doi.org/10.1073/pnas.1721770115), 2018.
- Lenton, T., Held, H., Kriegler, E., Hall, J. W., Lucht, W., Rahmstorf, S., and Schellnhuber, H. J.: Tipping elements in the Earth's climate system. *Proceedings of the National Academy of Sciences of the United States of America*, 105, 1786–1793, <https://doi.org/10.1073/pnas.0705414105>, 2008.
- Lenton, T. M.: Early warning of climate tipping points. *Nature Climate Change*, 1, 201–209, [10.1038/nclimate1143](https://doi.org/10.1038/nclimate1143), 2011.

- Lenton, T. M. and Schellnhuber, H. J.: Tipping the Scales. *Nature Climate Change*, 1, 97–98, 2007.
- Lenton, T. M., Rockström, J., Gaffney, O., Rahmstorf, S., Richardson, K., Steffen, W., and Schellnhuber, H. J.: Climate tipping points — too risky to bet against. *Nature*, 575, 592–595, doi: [10.1038/d41586-019-03595-0](https://doi.org/10.1038/d41586-019-03595-0), 2019.
- Li, C. and Born, A.: Coupled atmosphere-ice-ocean dynamics in Dansgaard-Oeschger events. *Quaternary Science Reviews*, 203, 1–20, [10.1016/j.quascirev.2018.10.031](https://doi.org/10.1016/j.quascirev.2018.10.031), 2019.
- Li, C., Battisti, D. S., Schrag, D. P., and Tziperman, E.: Abrupt climate shifts in Greenland due to displacements of the sea ice edge. *Geophysical Research Letters*, 32, L19 702, [10.1029/2005GL023492](https://doi.org/10.1029/2005GL023492), 2005.
- Lisiecki, L. E. and Raymo, M. E.: A Pliocene-Pleistocene stack of 57 globally distributed benthic  $\delta^{18}\text{O}$  records. *Paleoceanography*, 20, PA1003, [10.1029/2004PA001071](https://doi.org/10.1029/2004PA001071), 2005a.
- Lisiecki, L. E. and Raymo, M. E.: (Appendix 1) Global Plio-Pleistocene stack of benthic oxygen isotope records [dataset]. PANGAEA, [10.1594/PANGAEA.701576](https://doi.org/10.1594/PANGAEA.701576), (last accessed 2023-05-23), 2005b.
- Liu, W., Xie, S. P., Liu, Z., and Zhu, J.: Overlooked possibility of a collapsed atlantic meridional overturning circulation in warming climate. *Science Advances*, 3, e1601 666, [10.1126/sciadv.1601666](https://doi.org/10.1126/sciadv.1601666), 2017.
- Livina, V. N., Kwasniok, F., and Lenton, T. M.: Potential analysis reveals changing number of climate states during the last 60 kyr. *Climate of the Past*, 6, 77–82, [10.5194/cp-6-77-2010](https://doi.org/10.5194/cp-6-77-2010), 2010.
- Lohmann, J. and Ditlevsen, P. D.: A consistent statistical model selection for abrupt glacial climate changes. *Climate Dynamics*, 52, 6411–6426, [10.1007/s00382-018-4519-2](https://doi.org/10.1007/s00382-018-4519-2), 2018.
- Lohmann, J. and Ditlevsen, P. D.: Objective extraction and analysis of statistical features of Dansgaard-Oeschger events. *Climate of the Past*, 15, 1771–1792, [10.5194/cp-15-1771-2019](https://doi.org/10.5194/cp-15-1771-2019), 2019.
- Lohmann, J. and Ditlevsen, P. D.: Risk of tipping the overturning circulation due to increasing rates of ice melt. *Proceedings of the National Academy of Sciences of the United States of America*, 118, e2017989 118, [10.1073/pnas.2017989118](https://doi.org/10.1073/pnas.2017989118), 2021.
- Lohmann, J., Castellana, D., Ditlevsen, P. D., and Dijkstra, H. A.: Abrupt climate change as a rate-dependent cascading tipping point. *Earth System Dynamics*, 12, 819–835, [10.5194/esd-12-819-2021](https://doi.org/10.5194/esd-12-819-2021), 2021.
- Lohmann, J., Dijkstra, H. A., Jochum, M., Lucarini, V., and Ditlevsen, P. D.: Multistability and Intermediate Tipping of the Atlantic Ocean Circulation. arXiv preprint, [10.48550/arXiv.2304.05664](https://doi.org/10.48550/arXiv.2304.05664), 2023.
- Lüthi, D., Le Floch, M., Bereiter, B., Blunier, T., Barnola, J. M., Siegenthaler, U., Raynaud, D., Jouzel, J., Fischer, H., Kawamura, K., and Stocker, T. F.: High-resolution carbon dioxide concentration record 650,000–800,000 years before present. *Nature*, 453, 379–382, [10.1038/nature06949](https://doi.org/10.1038/nature06949), 2008.
- Lynch-Stieglitz, J.: The Atlantic Meridional Overturning Circulation and Abrupt Climate Change. *Annual Review of Marine Science*, 9, 83–104, [10.1146/annurev-marine-010816-060415](https://doi.org/10.1146/annurev-marine-010816-060415), 2017.
- Maffezzoli, N., Vallelonga, P., Edwards, R., Saiz-Lopez, A., Turetta, C., Kjær, H. A., Barbante, C., Vinther, B., and Spolaor, A.: 120,000 year record of sea ice in the North Atlantic. *Climate of the Past*, 15, 2031–2051, [10.5194/cp-15-2031-2019](https://doi.org/10.5194/cp-15-2031-2019), 2019.
- Malmierca-Vallet, I., Sime, L. C., and the D-O community Members: Dansgaard–Oeschger events in climate models: review and baseline Marine Isotope Stage 3 (MIS3) protocol. *Climate of the Past*, 19, 915–942, [10.5194/cp-19-915-2023](https://doi.org/10.5194/cp-19-915-2023), 2023.
- Manabe, S. and Stouffer, R.: Century scale effects of increased atmospheric CO<sub>2</sub> on the ocean–atmosphere system. *Nature*, 364, 215–218, [10.1038/364215a0](https://doi.org/10.1038/364215a0), 1993.

- Manta, G., Speich, S., Karstensen, J., Hummels, R., Kersalé, M., Laxenaire, R., Piola, A., Chidichimo, M. P., Sato, O. T., Cotrim da Cunha, L., Ansorge, I., Lamont, T., van den Berg, M. A., Schuster, U., Tanhua, T., Kerr, R., Guerrero, R., Campos, E., and Meinen, C. S.: The South Atlantic Meridional Overturning Circulation and Mesoscale Eddies in the First GO-SHIP Section at 34.5°S. *Journal of Geophysical Research: Oceans*, 126, e2020JC016962, [10.1029/2020JC016962](https://doi.org/10.1029/2020JC016962), 2021.
- Markle, B. R., Steig, E. J., Buizert, C., Schoenemann, S. W., Bitz, C. M., Fudge, T. J., Pedro, J. B., Ding, Q., Jones, T. R., White, J. W., and Sowers, T.: Global atmospheric teleconnections during Dansgaard-Oeschger events. *Nature Geoscience*, 10, 36–40, [10.1038/ngeo2848](https://doi.org/10.1038/ngeo2848), 2017.
- Marshall, J. and Speer, K.: Closure of the meridional overturning circulation through Southern Ocean upwelling. *Nature Geoscience*, 5, 171–180, [10.1038/ngeo1391](https://doi.org/10.1038/ngeo1391), 2012.
- Martrat, B., Grimalt, J. O., Shackleton, N. J., de Abreu, L., Hutterli, M. A., and Stocker, T. F.: Four Climate Cycles of Recurring Deep and Surface Water Destabilizations on the Iberian Margin. *Science*, 317, 502–507, [10.1126/science.1139994](https://doi.org/10.1126/science.1139994), 2007a.
- Martrat, B., Grimalt, J. O., Shackleton, N. J., de Abreu, L., Hutterli, M. A., and Stocker, T. F.: Sea surface temperature estimation for the Iberian Margin [dataset]. PANGEA, [10.1594/PANGAEA.771894](https://doi.org/10.1594/PANGAEA.771894), (last accessed 2023-05-23), 2007b.
- Masson-Delmotte, V., Jouzel, J., Landais, A., Stievenard, M., Johnsen, S. J., White, J. W. C., Werner, M., Sveinbjornsdottir, A., and Fuhrer, K.: GRIP Deuterium Excess Reveals Rapid and Orbital-Scale Changes in Greenland Moisture Origin. *Science*, 309, 118–121, [10.1126/science.1108575](https://doi.org/10.1126/science.1108575), 2005.
- McSweeney, R.: Explainer: Nine ‘tipping points’ that could be triggered by climate change. Carbon Brief, <https://www.carbonbrief.org/explainer-nine-tipping-points-that-could-be-triggered-by-climate-change/>, (last accessed 2023-05-08), 2020.
- Medvigy, D., Walko, R. L., Otte, M. J., and Avissar, R.: Simulated changes in Northwest U.S. Climate in response to Amazon deforestation. *Journal of Climate*, 26, 9115–9136, [10.1175/JCLI-D-12-00775.1](https://doi.org/10.1175/JCLI-D-12-00775.1), 2013.
- Menziel, L., Timmermann, A., Friedrich, T., and England, M. H.: Hindcasting the continuum of Dansgaard-Oeschger variability: Mechanisms, patterns and timing. *Climate of the Past*, 10, 63–77, [10.5194/cp-10-63-2014](https://doi.org/10.5194/cp-10-63-2014), 2014.
- Menziel, L. C., Skinner, L. C., Tarasov, L., and Tzedakis, P. C.: An ice–climate oscillatory framework for Dansgaard–Oeschger cycles. *Nature Reviews Earth & Environment*, 1, 677–693, [10.1038/s43017-020-00106-y](https://doi.org/10.1038/s43017-020-00106-y), 2020.
- Mitsui, T. and Crucifix, M.: Influence of external forcings on abrupt millennial-scale climate changes: a statistical modelling study. *Climate Dynamics*, 48, 2729–2749, [10.1007/s00382-016-3235-z](https://doi.org/10.1007/s00382-016-3235-z), 2017.
- Mook, W. G.: Environmental isotopes in the hydrological cycle: Principles and applications, Volume I: Introduction: Theory, Methods, Review. International Atomic Energy Agency and United Nations Educational, Scientific and Cultural Organization, [http://www-naweb.iaea.org/napc/ih/ihresources\\_publication\\_hydrocycle\\_en.html](http://www-naweb.iaea.org/napc/ih/ihresources_publication_hydrocycle_en.html), 2001.
- Morlighem, M., Williams, C. N., Rignot, E., An, L., Arndt, J. E., Bamber, J. L., Catania, G., Chauché, N., Dowdeswell, J. A., Dorschel, B., Fenty, I., Hogan, K., Howat, I., Hubbard, A., Jakobsson, M., Jordan, T. M., Kjeldsen, K. K., Millan, R., Mayer, L., Mouginot, J., Noël, B. P., O’Cofaigh, C., Palmer, S., Rysgaard, S., Seroussi, H., Siegert, M. J., Slabon, P., Straneo, F., van den Broeke, M. R., Weinrebe, W., Wood, M., and Zinglensen, K. B.: BedMachine v3: Complete Bed Topography and Ocean Bathymetry Mapping of Greenland From Multibeam Echo Sounding Combined With Mass Conservation. *Geophysical Research Letters*, 44, 11 051–11 061, [10.1002/2017GL074954](https://doi.org/10.1002/2017GL074954), 2017.

- Morlighem, M., Rignot, E., Binder, T., Blankenship, D., Drews, R., Eagles, G., Eisen, O., Ferraccioli, F., Forsberg, R., Fretwell, P., Goel, V., Greenbaum, J. S., Gudmundsson, H., Guo, J., Helm, V., Hofstede, C., Howat, I., Humbert, A., Jokat, W., Karlsson, N. B., Lee, W. S., Matsuoka, K., Millan, R., Mouginit, J., Paden, J., Pattyn, F., Roberts, J., Rosier, S., Ruppel, A., Seroussi, H., Smith, E. C., Steinhage, D., Sun, B., den Broeke, M. R., Ommen, T. D., van Wessem, M., and Young, D. A.: Deep glacial troughs and stabilizing ridges unveiled beneath the margins of the Antarctic ice sheet. *Nature Geoscience*, 13, 132–137, [10.1038/s41561-019-0510-8](https://doi.org/10.1038/s41561-019-0510-8), 2020.
- Muscheler, R., Adolphi, F., Heaton, T. J., Bronk Ramsey, C., Svensson, A., Van Der Plicht, J., and Reimer, P. J.: Testing and Improving the IntCal20 Calibration Curve with Independent Records. *Radiocarbon*, 62, 1079–1094, [10.1017/RDC.2020.54](https://doi.org/10.1017/RDC.2020.54), 2020.
- Nagumo, J., Arimoto, S., and Yoshizawa, S.: An Active Pulse Transmission Line Simulating Nerve Axon\*. *Proceedings of the IRE*, 50, 2061–2070, [10.1109/JRPROC.1962.288235](https://doi.org/10.1109/JRPROC.1962.288235), 1962.
- NEEM community members: Eemian interglacial reconstructed from a Greenland folded ice core. *Nature*, 493, 489–494, [10.1038/nature11789](https://doi.org/10.1038/nature11789), 2013.
- Nian, D., Bathiany, S., Ben-Yami, M., Blaschke, L., Hirota, M., Rodrigues, R., and Boers, N.: The combined impact of global warming and AMOC collapse on the Amazon Rainforest. in preparation, 2023.
- Niels Bohr Institute (University of Copenhagen): Ice and Climate. <https://www.iceandclimate.nbi.ku.dk/data/>, (last accessed 2023-05-23), 2023.
- NOAA National Centers for Environmental information: Climate at a Glance: Global Time Series. <https://www.ncei.noaa.gov/access/monitoring/climate-at-a-glance/global/time-series>, (last accessed 2023-03-31), 2023.
- Nobre, C. A. and Borma, L. D. S.: 'Tipping points' for the Amazon forest. *Current Opinion in Environmental Sustainability*, 1, 28–36, [10.1016/j.cosust.2009.07.003](https://doi.org/10.1016/j.cosust.2009.07.003), 2009.
- North Greenland Ice Core Project Members: High-resolution record of Northern Hemisphere climate extending into the last interglacial period. *Nature*, 431, 147–151, [10.1038/nature02805](https://doi.org/10.1038/nature02805), 2004.
- Orihuela-Pinto, B., England, M. H., and Taschetto, A. S.: Interbasin and interhemispheric impacts of a collapsed Atlantic Overturning Circulation. *Nature Climate Change*, 12, 558–565, [10.1038/s41558-022-01380-y](https://doi.org/10.1038/s41558-022-01380-y), 2022.
- Parsons, L. A.: Implications of CMIP6 Projected Drying Trends for 21st Century Amazonian Drought Risk. *Earth's Future*, 8, [10.1029/2020EF001608](https://doi.org/10.1029/2020EF001608), 2020.
- Pedro, J. B., Jochum, M., Buizert, C., He, F., Barker, S., and Rasmussen, S. O.: Beyond the bipolar seesaw: Toward a process understanding of interhemispheric coupling. *Quaternary Science Reviews*, 192, 27–46, [10.1016/j.quascirev.2018.05.005](https://doi.org/10.1016/j.quascirev.2018.05.005), 2018.
- Peltier, W. R. and Vettoretti, G.: Dansgaard-Oeschger oscillations predicted in a comprehensive model of glacial climate: A "kicked" salt oscillator in the Atlantic. *Geophysical Research Letters*, 41, 7306–7313, [10.1002/2014GL061413](https://doi.org/10.1002/2014GL061413), 2014.
- Placidi, L., Hutter, K., and Faria, S. H.: A Critical Review of the Mechanics of Polycrystalline Polar Ice. *GAMM-Mitteilungen*, 29, 80–117, [10.1002/gamm.201490025](https://doi.org/10.1002/gamm.201490025), 2006.
- Praetorius, S. K.: North Atlantic circulation slows down news-and-views. *Nature*, 556, 180–181, [10.1038/d41586-018-04086-4](https://doi.org/10.1038/d41586-018-04086-4), 2018.
- Rahmstorf, S., Crucifix, M., Ganopolski, A., Goosse, H., Kamenkovich, I., Knutti, R., Lohmann, G., Marsh, R., Myzak, L. A., Wang, Z., and Weaver, A. J.: Thermohaline circulation hysteresis: A model intercomparison. *Geophysical Research Letters*, 32, L23 605, [10.1029/2005GL023655](https://doi.org/10.1029/2005GL023655), 2005.

- Rasmussen, S. O., Andersen, K. K., Svensson, A. M., Steffensen, J. P., Vinther, B. M., Clausen, H. B., Siggaard-Andersen, M. L., Johnsen, S. J., Larsen, L. B., Dahl-Jensen, D., Bigler, M., Röthlisberger, R., Fischer, H., Goto-Azuma, K., Hansson, M. E., and Ruth, U.: A new Greenland ice core chronology for the last glacial termination. *Journal of Geophysical Research: Atmospheres*, 111, D06 102, [10.1029/2005JD006079](https://doi.org/10.1029/2005JD006079), 2006.
- Rasmussen, S. O., Bigler, M., Blockley, S. P., Blunier, T., Buchardt, S. L., Clausen, H. B., Cvijanovic, I., Dahl-Jensen, D., Johnsen, S. J., Fischer, H., Gkinis, V., Guillevic, M., Hoek, W. Z., Lowe, J. J., Pedro, J. B., Popp, T., Seierstad, I. K., Steffensen, J. P., Svensson, A. M., Vallenga, P., Vinther, B. M., Walker, M. J., Wheatley, J. J., and Winstrup, M.: A stratigraphic framework for abrupt climatic changes during the Last Glacial period based on three synchronized Greenland ice-core records: Refining and extending the INTIMATE event stratigraphy. *Quaternary Science Reviews*, 106, 14–28, [10.1016/j.quascirev.2014.09.007](https://doi.org/10.1016/j.quascirev.2014.09.007), 2014.
- Rasmussen, T. L. and Thomsen, E.: The role of the North Atlantic Drift in the millennial timescale glacial climate fluctuations. *Palaeogeography, Palaeoclimatology, Palaeoecology*, 210, 101–116, [10.1016/j.palaeo.2004.04.005](https://doi.org/10.1016/j.palaeo.2004.04.005), 2004.
- Rasmussen, T. L., Thomsen, E., Van Weering, T. C., and Labeyrie, L.: Rapid changes in surface and deep water conditions at the Faeroe Margin during the last 58,000 years. *Paleoceanography*, 11, 757–771, [10.1029/96PA02618](https://doi.org/10.1029/96PA02618), 1996.
- Rasmussen, T. L., Thomsen, E., and Moros, M.: North Atlantic warming during Dansgaard-Oeschger events synchronous with Antarctic warming and out-of-phase with Greenland climate. *Scientific Reports*, 6, 20 535, [10.1038/srep20535](https://doi.org/10.1038/srep20535), 2016.
- Rial, J. A. and Saha, R.: Modeling Abrupt Climate Change as the Interaction Between Sea Ice Extent and Mean Ocean Temperature Under Orbital Insolation Forcing. in: *Abrupt Climate Change: Mechanisms, Patterns, and Impacts*, edited by Rashid, H., Polyak, L., and Mosley-Thompson, E., pp. 57–74, American Geophysical Union (AGU), [10.1029/2010GM001027](https://doi.org/10.1029/2010GM001027), 2011.
- Risken, H.: *The Fokker-Planck Equation - Methods of Solution and Applications*. Springer Verlag, Berlin, Heidelberg (Germany), 2. edn., [10.1007/978-3-642-61544-3](https://doi.org/10.1007/978-3-642-61544-3), 1989.
- Ritchie, P. D., Clarke, J. J., Cox, P. M., and Huntingford, C.: Overshooting tipping point thresholds in a changing climate. *Nature*, 592, 517–523, [10.1038/s41586-021-03263-2](https://doi.org/10.1038/s41586-021-03263-2), 2021.
- Roberts, A. and Saha, R.: Relaxation oscillations in an idealized ocean circulation model. *Climate Dynamics*, 48, 2123–2134, [10.1007/s00382-016-3195-3](https://doi.org/10.1007/s00382-016-3195-3), 2017.
- Robinson, A., Calov, R., and Ganopolski, A.: Multistability and critical thresholds of the Greenland ice sheet. *Nature Climate Change*, 2, 429–432, [10.1038/nclimate1449](https://doi.org/10.1038/nclimate1449), 2012.
- Rolinski, S., Müller, C., Heinke, J., Weindl, I., Biewald, A., Leon Bodirsky, B., Bondeau, A., Boons-Prins, E. R., Bouwman, A. F., Leffelaar, P. A., Roller, J. A., Schaphoff, S., and Thonicke, K.: Modeling vegetation and carbon dynamics of managed grasslands at the global scale with LPJmL 3.6. *Geoscientific Model Development*, 11, 429–451, [10.5194/gmd-11-429-2018](https://doi.org/10.5194/gmd-11-429-2018), 2018.
- Rooth, C.: Hydrology and ocean circulation. *Progress in Oceanography*, 11, 131–149, [10.1016/0079-6611\(82\)90006-4](https://doi.org/10.1016/0079-6611(82)90006-4), 1982.
- Rousseau, D. D., Antoine, P., Boers, N., Lagroix, F., Ghil, M., Lomax, J., Fuchs, M., Debret, M., Hatté, C., Moine, O., Gauthier, C., Jordanova, D., and Jordanova, N.: Dansgaard-Oeschger-like events of the penultimate climate cycle: The loess point of view. *Climate of the Past*, 16, 713–727, [10.5194/cp-16-713-2020](https://doi.org/10.5194/cp-16-713-2020), 2020.
- Rousseau, D. D., Bagniewski, W., and Ghil, M.: Abrupt climate changes and the astronomical theory: are they related? *Climate of the Past*, 18, 249–271, [10.5194/cp-18-249-2022](https://doi.org/10.5194/cp-18-249-2022), 2022.
- Ruth, U., Wagenbach, D., Steffensen, J. P., and Bigler, M.: Continuous record of microparticle concentration and size distribution in the central Greenland NGRIP ice core during the last glacial period. *Journal of Geophysical Research: Atmospheres*, 108, 4098, [10.1029/2002jd002376](https://doi.org/10.1029/2002jd002376), 2003.

- Ruth, U., Bigler, M., Röthlisberger, R., Siggaard-Andersen, M. L., Kipfstuhl, S., Goto-Azuma, K., Hansson, M. E., Johnsen, S. J., Lu, H., and Steffensen, J. P.: Ice core evidence for a very tight link between North Atlantic and east Asian glacial climate. *Geophysical Research Letters*, 34, L03 706, [10.1029/2006GL027876](https://doi.org/10.1029/2006GL027876), 2007.
- Sadatzki, H., Maffezzoli, N., Dokken, T. M., Simon, M. H., Berben, S. M., Fahl, K., Kjær, H. A., Spolaor, A., Stein, R., Vallelonga, P., Vinther, B. M., and Jansen, E.: Rapid reductions and millennial-scale variability in Nordic Seas sea ice cover during abrupt glacial climate changes. *Proceedings of the National Academy of Sciences of the United States of America*, 117, 29 478–29 486, [10.1073/pnas.2005849117](https://doi.org/10.1073/pnas.2005849117), 2020.
- Saha, R.: Millennial-scale oscillations between sea ice and convective deep water formation. *Paleoceanography*, 30, 1540–1555, [10.1002/2015PA002809](https://doi.org/10.1002/2015PA002809), 2015.
- Sakai, K. and Peltier, W. R.: A dynamical systems model of the Dansgaard-Oeschger oscillation and the origin of the bond cycle. *Journal of Climate*, 12, 2238–2255, [10.1175/1520-0442\(1999\)012<2238:adsmot>2.0.co;2](https://doi.org/10.1175/1520-0442(1999)012<2238:adsmot>2.0.co;2), 1999.
- Salati, E., Dall'Olio, A., Matsui, E., and Gat, J. R.: Recycling of water in the Amazon Basin: An isotopic study. *Water Resources Research*, 15, 1250–1258, [10.1029/WR015i005p01250](https://doi.org/10.1029/WR015i005p01250), 1979.
- Salazar, L. F. and Nobre, C. A.: Climate change and thresholds of biome shifts in Amazonia. *Geophysical Research Letters*, 37, L17 706, [10.1029/2010GL043538](https://doi.org/10.1029/2010GL043538), 2010.
- Schulz, M., Paul, A., and Timmermann, A.: Relaxation oscillators in concert: A framework for climate change at millennial timescales during the late Pleistocene. *Geophysical Research Letters*, 29, 2–5, [10.1029/2002GL016144](https://doi.org/10.1029/2002GL016144), 2002.
- Scoto, F. and Sadatzki, H.: Sea ice fluctuations in the Baffin Bay and the Labrador Sea during glacial abrupt climate changes. *Proceedings of the National Academy of Sciences of the United States of America*, 119, 1–9, [10.1073/pnas.2203468119/-/DCSupplemental.Published](https://doi.org/10.1073/pnas.2203468119/-/DCSupplemental.Published), 2022.
- Seierstad, I. K., Abbott, P. M., Bigler, M., Blunier, T., Bourne, A. J., Brook, E., Buchardt, S. L., Buizert, C., Clausen, H. B., Cook, E., Dahl-Jensen, D., Davies, S. M., Guillevic, M., Johnsen, S. J., Pedersen, D. S., Popp, T. J., Rasmussen, S. O., Severinghaus, J. P., Svensson, A., and Vinther, B. M.: Consistently dated records from the Greenland GRIP, GISP2 and NGRIP ice cores for the past 104ka reveal regional millennial-scale  $\delta^{18}\text{O}$  gradients with possible Heinrich event imprint. *Quaternary Science Reviews*, 106, 29–46, [10.1016/j.quascirev.2014.10.032](https://doi.org/10.1016/j.quascirev.2014.10.032), 2014.
- Sessford, E. G., Jensen, M. F., Tisserand, A. A., Muschitiello, F., Dokken, T., Nisancioglu, K. H., and Jansen, E.: Consistent fluctuations in intermediate water temperature off the coast of Greenland and Norway during Dansgaard-Oeschger events. *Quaternary Science Reviews*, 223, 105 887, [10.1016/j.quascirev.2019.105887](https://doi.org/10.1016/j.quascirev.2019.105887), 2019.
- Sigl, M., Fudge, T. J., Winstrup, M., Cole-Dai, J., Ferris, D., McConnell, J. R., Taylor, K. C., Welten, K. C., Woodruff, T. E., Adolphi, F., Bisiaux, M., Brook, E. J., Buizert, C., Caffee, M. W., Dunbar, N. W., Edwards, R., Geng, L., Iverson, N., Koffman, B., Layman, L., Maselli, O. J., McGwire, K., Muscheler, R., Nishiizumi, K., Pasteris, D. R., Rhodes, R. H., and Sowers, T. A.: The WAIS Divide deep ice core WD2014 chronology - Part 2: Annual-layer counting (0-31 ka BP). *Climate of the Past*, 12, 769–786, [10.5194/cp-12-769-2016](https://doi.org/10.5194/cp-12-769-2016), 2016.
- Singh, H. A., Battisti, D. S., and Bitz, C. M.: A heuristic model of dansgaard-oeschger cycles. part i: Description, results, and sensitivity studies. *Journal of Climate*, 27, 4337–4358, [10.1175/JCLI-D-12-00672.1](https://doi.org/10.1175/JCLI-D-12-00672.1), 2014.
- Skiba, V., Spötl, C., Trüssel, M., Schröder-Ritzrau, A., Plessen, B., Frank, N., Eichstädter, R., Tjallingii, R., Marwan, N., Zhang, X., and Fohlmeister, J.: Millennial-scale Alpine glacier dynamics during Marine Isotope Stage 8. *Communications Earth & Environment* [under review], 2023.

- Steffen, W., Rockström, J., Richardson, K., Lenton, T. M., Folke, C., Liverman, D., Summerhayes, C. P., Barnosky, A. D., Cornell, S. E., Crucifix, M., Donges, J. F., Fetzer, I., Lade, S. J., Scheffer, M., Winkelmann, R., and Schellnhuber, H. J.: Trajectories of the Earth System in the Anthropocene. *Proceedings of the National Academy of Sciences of the United States of America*, 115, 8252–8259, [10.1073/pnas.1810141115](https://doi.org/10.1073/pnas.1810141115), 2018.
- Steffensen, J. P., Andersen, K. K., Bigler, M., Clausen, H. B., Dahl-jensen, D., Fischer, H., Goto-azuma, K., Hansson, M., Johnsen, S. J., Jouzel, J., Masson-delmotte, V., Popp, T., Rasmussen, S. O., Röthlisberger, R., Ruth, U., Stauffer, B., Sveinbjörnsdóttir, Á. E., Svensson, A., and White, J. W. C.: High-Resolution Greenland Ice Core Data Show Abrupt Climate Change Happens in Few Years. *Science*, 321, 680–684, [10.1126/science.1157707](https://doi.org/10.1126/science.1157707), 2008.
- Stocker, T. and Schmittner, A.: Influence of CO<sub>2</sub> emission rates on the stability of the thermohaline circulation. *Nature*, 388, 862–865, [10.1038/42224](https://doi.org/10.1038/42224), 1997.
- Stocker, T. F. and Johnsen, S. J.: A minimum thermodynamic model for the bipolar seesaw. *Paleoceanography*, 18, 1087, [10.1029/2003PA000920](https://doi.org/10.1029/2003PA000920), 2003.
- Stommel, H.: Thermohaline Convection with Two Stable Regimes of Flow. *Tellus*, 13, 224–230, [10.1111/j.2153-3490.1961.tb00079.x](https://doi.org/10.1111/j.2153-3490.1961.tb00079.x), 1961.
- Svensson, A., Andersen, K. K., Bigler, M., Clausen, H. B., Dahl-Jensen, D., Johnsen, S. J., Rasmussen, S. O., Seierstad, I., Steffensen, J. P., Svensson, A., Vinther, B. M., Davies, S. M., Muscheler, R., Parrenin, F., and Röthlisberger, R.: A 60 000 year Greenland stratigraphic ice core chronology. *Climate of the Past*, 4, 47–57, [10.5194/cp-4-47-2008](https://doi.org/10.5194/cp-4-47-2008), 2008.
- Svensson, A., Dahl-Jensen, D., Steffensen, J. P., Blunier, T., Rasmussen, S., Vinther, B., Vallelonga, P., Capron, E., Gkinis, V., Cook, E., Kjær, H. A., Muscheler, R., Kipfstuhl, S., Wilhelms, F., Stocker, T., Fischer, H., Adolphi, F., Erhardt, T., Sigl, M., Landais, A., Parrenin, F., Buizert, C., McConnell, J., Severi, M., Mulvaney, R., and Bigler, M.: Bipolar volcanic synchronization of abrupt climate change in Greenland and Antarctic ice cores during the last glacial period. *Climate of the Past*, 16, 1565–1580, [10.5194/cp-16-1565-2020](https://doi.org/10.5194/cp-16-1565-2020), 2020.
- Tabar, M. R. R.: Analysis and data-based reconstruction of complex nonlinear dynamical systems. Springer Cham, Cham (Switzerland), 1. edn., [10.1007/978-3-030-18472-8](https://doi.org/10.1007/978-3-030-18472-8), 2019.
- Timmermann, A. and Lohmann, G.: Noise-induced transitions in a simplified model of the thermohaline circulation. *Journal of Physical Oceanography*, 30, 1891–1900, [10.1175/1520-0485\(2000\)030<1891:NITIAS>2.0.CO;2](https://doi.org/10.1175/1520-0485(2000)030<1891:NITIAS>2.0.CO;2), 2000.
- Timmermann, A., Gildor, H., Schulz, M., and Tziperman, E.: Coherent resonant millennial-scale climate oscillations triggered by massive meltwater pulses. *Journal of Climate*, 16, 2569–2585, [10.1175/1520-0442\(2003\)016<2569:CRMCOT>2.0.CO;2](https://doi.org/10.1175/1520-0442(2003)016<2569:CRMCOT>2.0.CO;2), 2003.
- Valdes, P.: Built for stability. *Nature Geoscience*, 4, 414–416, [10.1038/ngeo1200](https://doi.org/10.1038/ngeo1200), 2011.
- Vallelonga, P., Maffezzoli, N., Saiz-Lopez, A., Scotto, F., Kjær, H. A., and Spolaor, A.: Sea-ice reconstructions from bromine and iodine in ice cores. *Quaternary Science Reviews*, 269, [10.1016/j.quascirev.2021.107133](https://doi.org/10.1016/j.quascirev.2021.107133), 2021.
- Vélez-Belchí, P., Alvarez, A., Colet, P., Tintoré, J., and Haney, R.: Stochastic resonance in the thermohaline circulation. *Geophysical Research Letters*, 28, 2053–2056, [10.1029/2000GL012091](https://doi.org/10.1029/2000GL012091), 2001.
- Vettoretti, G. and Peltier, W. R.: Fast physics and slow physics in the nonlinear Dansgaard-Oeschger relaxation oscillation. *Journal of Climate*, 31, 3423–3449, [10.1175/JCLI-D-17-0559.1](https://doi.org/10.1175/JCLI-D-17-0559.1), 2018.
- Vettoretti, G., Ditlevsen, P., Jochum, M., and Rasmussen, S. O.: Atmospheric CO<sub>2</sub> control of spontaneous millennial-scale ice age climate oscillations. *Nature Geoscience*, 15, 300–306, [10.1038/s41561-022-00920-7](https://doi.org/10.1038/s41561-022-00920-7), 2022.

- Vinther, B. M., Clausen, H. B., Johnsen, S. J., Rasmussen, S. O., Andersen, K. K., Buchardt, S. L., Dahl-Jensen, D., Seierstad, I. K., Siggaard-Andersen, M. L., Steffensen, J. P., Svensson, A., Olsen, J., and Heinemeier, J.: A synchronized dating of three Greenland ice cores throughout the Holocene. *Journal of Geophysical Research: Atmospheres*, 111, D13 102, [10.1029/2005JD006921](https://doi.org/10.1029/2005JD006921), 2006.
- Voelker, A. H.: Global distribution of centennial-scale records for Marine Isotope Stage (MIS) 3: A database. *Quaternary Science Reviews*, 21, 1185–1212, [10.1016/S0277-3791\(01\)00139-1](https://doi.org/10.1016/S0277-3791(01)00139-1), 2002.
- Wang, S., Foster, A., Lenz, E. A., Kessler, J. D., and Stroeve, J. C.: Mechanisms and Impacts of Earth System Tipping Elements. *Reviews of Geophysics*, 91, e2021RG000 757, [10.1029/2021RG000757](https://doi.org/10.1029/2021RG000757), 2023.
- Wang, Y. J., Cheng, H., Edwards, R. L., An, Z. S., Wu, J. Y., Shen, C. C., and Dorale, J. A.: A high-resolution absolute-dated late pleistocene monsoon record from Hulu Cave, China. *Science*, 294, 2345–2348, [10.1126/science.1064618](https://doi.org/10.1126/science.1064618), 2001.
- Weijer, W., Cheng, W., Drijfhout, S. S., Fedorov, A. V., Hu, A., Jackson, L. C., Liu, W., McDonagh, E. L., Mecking, J. V., and Zhang, J.: Stability of the Atlantic Meridional Overturning Circulation: A Review and Synthesis. *Journal of Geophysical Research: Oceans*, 124, 5336–5375, [10.1029/2019JC015083](https://doi.org/10.1029/2019JC015083), 2019.
- Werth, D. and Avissar, R.: The local and global effects of Amazon deforestation. *Journal of Geophysical Research*, 107, 8087, [10.1029/2001jd000717](https://doi.org/10.1029/2001jd000717), 2002.
- Westerhold, T., Marwan, N., Drury, A. J., Liebrand, D., Agnini, C., Anagnostou, E., Barnet, J. S., Bohaty, S. M., De Vleeschouwer, D., Florindo, F., Frederichs, T., Hodell, D. A., Holbourn, A. E., Kroon, D., Laurentano, V., Littler, K., Lourens, L. J., Lyle, M., Pälike, H., Röhl, U., Tian, J., Wilkens, R. H., Wilson, P. A., and Zachos, J. C.: An astronomically dated record of Earth's climate and its predictability over the last 66 million years. *Science*, 369, 1383–1388, [10.1126/science.aba6853](https://doi.org/10.1126/science.aba6853), 2020.
- Winton, M.: Deep Decoupling Oscillations of the Oceanic Thermohaline Circulation. in: *Ice in the Climate System*, NATO ASI Series, vol.12, edited by Peltier, W. R., pp. 417–432, Springer, Berlin, Heidelberg (Germany), [10.1007/978-3-642-85016-5\\_24](https://doi.org/10.1007/978-3-642-85016-5_24), 1993.
- Wolff, E. W., Chappellaz, J., Blunier, T., Rasmussen, S. O., and Svensson, A.: Millennial-scale variability during the last glacial: The ice core record. *Quaternary Science Reviews*, 29, 2828–2838, [10.1016/j.quascirev.2009.10.013](https://doi.org/10.1016/j.quascirev.2009.10.013), 2010.
- Wunderling, N., Donges, J. F., Kurths, J., and Winkelmann, R.: Interacting tipping elements increase risk of climate domino effects under global warming. *Earth System Dynamics*, 12, 601–619, [10.5194/esd-12-601-2021](https://doi.org/10.5194/esd-12-601-2021), 2021.
- Zemp, D. C., Schleussner, C. F., Barbosa, H. M., Van Der Ent, R. J., Donges, J. F., Heinke, J., Sampaio, G., and Rammig, A.: On the importance of cascading moisture recycling in South America. *Atmospheric Chemistry and Physics*, 14, 13 337–13 359, [10.5194/acp-14-13337-2014](https://doi.org/10.5194/acp-14-13337-2014), 2014.
- Zemp, D. C., Schleussner, C. F., Barbosa, H. M., Hirota, M., Montade, V., Sampaio, G., Staal, A., Wang-Erlandsson, L., and Rammig, A.: Self-amplified Amazon forest loss due to vegetation-atmosphere feedbacks. *Nature Communications*, 8, 14 681, [10.1038/ncomms14681](https://doi.org/10.1038/ncomms14681), 2017.
- Zhang, X., Lohmann, G., Knorr, G., and Purcell, C.: Abrupt glacial climate shifts controlled by ice sheet changes. *Nature*, 512, 290–294, [10.1038/nature13592](https://doi.org/10.1038/nature13592), 2014.
- Zhang, X., Barker, S., Knorr, G., Lohmann, G., Drysdale, R., Sun, Y., Hodell, D., and Chen, F.: Direct astronomical influence on abrupt climate variability. *Nature Geoscience*, 14, 819–826, [10.1038/s41561-021-00846-6](https://doi.org/10.1038/s41561-021-00846-6), 2021.
- Zhang, Y., Chiessi, C. M., Mulitza, S., Sawakuchi, A. O., Häggi, C., Zabel, M., Portilho-Ramos, R. C., Schefuß, E., Crivellari, S., and Wefer, G.: Different precipitation patterns across tropical South America during Heinrich and Dansgaard-Oeschger stadials. *Quaternary Science Reviews*, 177, 1–9, [10.1016/j.quascirev.2017.10.012](https://doi.org/10.1016/j.quascirev.2017.10.012), 2017.